EXPLORING THE ROLES OF SEDIMENT PRODUCTION AND TRANSPORT ON CARBONATE PLATFORM EVOLUTION: A NUMERICAL MODELLING AND OUTCROP-BASED INVESTIGATION (LATE MIOCENE, UPPER CORALLINE LIMESTONE FORMATION, MALTA)

A thesis submitted for the degree of
Doctor of Philosophy at
Royal Holloway, University of London

Daniel Sultana

May 2018

Department of Earth Sciences,
Royal Holloway
University of London

DECLARATION OF AUTHORSHIP

I Daniel Sultana hereby declare that this thesis and the work presented in it is entirely my own. Where I have consulted the work of others, this is always clearly stated.

Signed: _____

Date: _____

ABSTRACT

Stratigraphic forward modelling (SFM) and evidence gathered from outcrops can be used together to improve our understanding of controls on carbonate platform evolution.

Grain size production curves representing common Cenozoic carbonate factories are applied in a SFM to investigate how carbonate factories may influence platform evolution. Results suggest platform evolution and geometry are strongly influenced by combined sediment production (PR) (m ky^{-1}) and diffusional transport (PR) (km^2 ky^{-1}) rates, expressed as a PR/TR ratio. It is the ratio, not the absolute values of each parameter, that influences platform geometry. Simulations with similar PR/TR ratios are practically indistinguishable. The PR/TR ratio that produces a good match between SFM and outcropping strata of the Upper Miocene reef complex of the Llucmajor area, Mallorca, are calculated. Similar parameter values should always create similar platform geometries.

Extensive fieldwork was carried out of the Late Miocene, Upper Coralline Limestone Formation in Malta. Sequence stratigraphic interpretations suggest that syndepositional tectonism significantly influenced platform evolution and depositional style. Identified facies associations and depositional sequences are characteristic of other Late Miocene Mediterranean carbonate platforms from the region, but relative sea level curves from each platform show important differences.

A range of numerical stratigraphic forward models matched the Maltese depositional system interpreted from outcropping strata. These SFM results show a close match with outcrop interpretations and demonstrate interpretations are theoretically plausible but non-unique with respect to rate of accommodation generation, variable sediment production, variable transport rates, and reduced model run time. These combined modelling and outcrop interpretations results indicate a need for more use of quantitative methods to evaluate multiple hypotheses and scenarios in outcrop and subsurface interpretations of carbonate platform evolution.

ACKNOWLEDGMENTS

I heartily thank Prof. Dan Bosence and Prof. Peter Burgess for their guidance and support. Both were always very approachable and enthusiastic when discussing questions and ideas. Through working with them, I have learnt an immense amount, on both academic and personal levels. I would also like to thank the entire academic and technical staff at the Department of Earth Sciences at Royal Holloway for their support. In particular I would like to thank Mr. Frank Lehane who helped with solving computer program related issues. I would also like to thank the laboratory staff, Dr. David Lowry in particular, for their assistance with the stable isotope analysis.

I would also like to thank Prof. Pauline Galea, Dr. Saviour Scerri, Dr. Godwin Debono, Dr. Stephen Schembri, Mr. Michael Gatt and Mr. Darrin Stevens for instilling and cultivating my interest in nature and geosciences.

I would like to thank my family – wife, mother, father and brother – for always supporting me in the lows and highs of life. I dedicate this work them, in particular my wife Sarah and son Matthew.

Finally, I would like to thank the Malta Government Scholarships Scheme (MGSS) for funding this study.

TABLE OF CONTENTS

LIST OF FIGURES AND TABLES

CHAPTER 1

CHAPTER 2

CHAPTER 3

CHAPTER 4

CHAPTER 5

CHAPTER 6

CHAPTER 7

CHAPTER 8

LIST OF ABREVIATIONS USED

AD	Coralline Algal Debris Facies (Dart, 1991)
AM	Coralline Algal Marl Facies (Dart, 1991)
BH	BoreHole
BR	Coralgal Barrier Reef Facies (Dart, 1991)
CAB FA	Coralline Algal Biostrome FA
CAD	Coralline Algal Debris Packstone Facies
CAF	Coralline Algal Floatstone Facies
CAP	Coralline Algal Pavement Rudstone to Framestone Facies
CASR	Coralline Algal Sand Ridge Packstone Facies
CFR	Coralgal Fore Reef Packstone Facies
CP	Coralline Algal Pavement Facies (Dart, 1991)
CPR	Coralgal Patch Reef Rudstone Facies
CR	Coralgal Reef Framestone Facies
DRS	Distal Reef Slope Wackestone Facies
DS	Depositional Sequence
DT	Distal Calciturbidite Facies (Dart, 1991)
EMT	Elapsed Model Time
ES	Evaporite Solution Breccia Facies (Dart, 1991)
FA	Facies Associations
FrS&S FA	Fore-Reef Slope and Shelf FA
FTSM	Flat-Top Steep Margin
GS	Genetic Sequence
GZ	Gozo
HSR	Highstand Systems Tract
IMF	Il Maghlaq Fault
IS	Inter Sand Shoal Facies (Dart, 1991)
ITCZ	Inter Tropic Convergence Zone
LST	Lowstand Systems Tract
MaxS	Maximum Platform Margin Gradient
MCAD	Massive Coralline Algal Debris Wackestone Facies
MMCO	Mid Miocene Climatic Optima
MMCT	Mid-Miocene Climatic Transition
MMS	Model Match for entire Simulation
MRN	Model Reference Numbers
MS	Model Set
MT	Malta

OP	Organ Pipe Porites Reef Facies (Dart, 1991)
OS FA	Open Shelf FA
OSGR	Open Shelf Glauconite-rich Packstone Facies
OSHR	Open Shelf Heterostegina-rich Packstone Facies
OShS	Open Shelf Sand Facies (Dart, 1991)
PCAD	Planar Bedded Coralline Algal Debris Wackestone Facies
PE	Peritidal Facies (Dart, 1991)
PR	Proximal Reef Slope Facies (Dart, 1991)
PR	Coralgal Patch Reef Facies (Dart, 1991)
PR	(Sediment) Production Rate
PRS	Proximal Reef Slope Packstone Facies
PT	Proximal Calciturbidite Facies (Dart, 1991)
RC	Reef-Core FA
RSL	Relative Sea Level
RT	Reef Talus Facies (Dart, 1991)
SaS FA	Sand Shoal FA
SB	Sequence Boundary
SFM	Stratigraphic Forward Model
ShS	Sheltered Shelf Facies (Dart, 1991)
SPIF	Saint Paul Island Fault
SR	Sand Ridge Facies (Dart, 1991)
SS	Sand Shoal Facies (Dart, 1991)
SS	Sand Shoal Facies (Dart, 1991)
SS FA	Sheltered Shelf FA
SS	Sand Shoal Grainstone Facies
TR	(Sediment) Transport Rate
TST	Transgressive Systems Tract
UCL	Upper Coralline Limestone
VLF	Victoria Lines Fault
VS	Vertical Section
WR	Wave Ripple Packstone Facies

CHAPTER 1: INTRODUCTION

1.1. Introduction

This thesis makes use of stratigraphic forward modelling (SFM) together with evidence gathered from outcrops to improve our understanding of controls on carbonate platform evolution. The thesis also applies quantitative methods to strengthen or reject conceptual models, test alternative hypotheses and explore issues of non-uniqueness (*sensu* Burgess & Prince, 2015) of real carbonate sedimentary systems.

This study develops and applies parameter rates and conditions in SFM that are characteristic of real outcrop examples. This ensures that numerical studies of carbonate platforms are not limited to a theoretical basis, but are characteristic of natural carbonate systems. The Late Miocene Upper Coralline Limestone (UCL) Formation of the Malta Platform is the outcrop example focused upon in this study. The exceptionally well-exposed Maltese outcrops enable the construction of elaborate conceptual models to help understand the influence that tectonic, sedimentologic, ecologic (carbonate associations) and eustatic features may have on platform evolution. These conceptual models are further evaluated through numerical SFM where the applied parameter rates are established for the Maltese carbonate system (including accommodation generation, sediment production and transport rates).

The UCL Formation was selected since both its lithofacies and platform evolution style are well studied in the Upper Miocene of the central Mediterranean region (e.g. Esteban, 1996; Pedley, 1996, 1998; Pomar *et al.,* 1996; Franseen & Goldstein, 1996). Insights into local dynamics of platform evolution may therefore reveal processes active in other carbonate systems and advance our understanding of carbonate platform evolution. Additionally, Miocene carbonates are intensively explored and locally exploited for hydrocarbons in parts of the Mediterranean region. The outcrop models presented in this study may serve as analogs for the highly productive Miocene carbonates from Gulf of Suez and for smaller reservoirs in other localities such as western Sicily, northern Tunisia, northern Morocco, north-eastern Spain, southern Turkey, Hungary, Romania, Bulgaria and Moldavia (Franseen *et al*., 1996).

This chapter introduces the geological setting of the Maltese region (section 1.2), the use of quantitative methods to investigate geological processes (section 1.3) and describes the aims of this thesis (section 1.4). The chapter concludes with an outline of the thesis structure (section 1.5). The research methodology applied is discussed in each respective chapter.

1.2. Geological setting

The Maltese Islands (35°54′N 14°31′E) are located in the central Mediterranean, within the Pelagian Sea. The islands comprise Malta (246 km^2), Gozo (67 km^2) and Comino (2.5 km^2) and a number of outlying islets that outcrop from the shallow shelf seas of the Malta-Hyblean Platform.

The Maltese Islands outcrop from the shallow shelf sea of the Malta-Hyblean Platform that forms the leading edge of the African Plate (Pelagian Platform) as it is subducted beneath the European Plate (figure 1.1). The northern margin of the Malta-Hyblean Platform collided with the European Plate and, in part, is subducted beneath it, forming the Apennine-Maghrebian chain of northern Sicily (Dart, 1991). The Malta Escarpment delineates the eastern margin of the platform before it descends down into the deeper Ionian Sea (figure 1.1). The western margin of the Malta Platform is poorly defined and forms a gently westward dipping shelf between Gela foredeep (S Sicily) and Gozo. The southern margin of the shelf extends towards the Medina Banks and is truncated by the NW to SE oriented Pantelleria Rift System (Reuther & Eisenbacher, 1985) (figure 1.1).

An Oligo-Miocene succession is exposed above sea level in the Maltese Islands. The Islands form the emergent part of the footwall shoulder of the most easterly rift of the Pantelleria Rift System (Malta Graben). Since the 20th century, many authors have described the Oligo-Miocene succession that is exposed above sea level in the Maltese Islands with increasing detail (Murray, 1980; Roman & Roger, 1939; House *et al*., 1961; Pedley, 1975; Pedley *et al*., 1976; Zammit-Maempel, 1977; Bosence *et al*., 1981; Pedley, 1987; Bosence, 1991; Dart, 1991, 1993; Gatt, 2012).

Pedley (1978) was the first to present a formal lithostratigraphy to Formation, Member and sometimes Bed level that is used in the Geological Maps of the Maltese Islands (Malta Oil Exploration Directorate, 1993). The carbonate stratigraphy has been divided into five formations (Pedley, 1976): the basal Lower Coralline Limestone Formation, Globigerina Limestone Formation, Blue Clay Formation, Greensand Formation and UCL Formation.

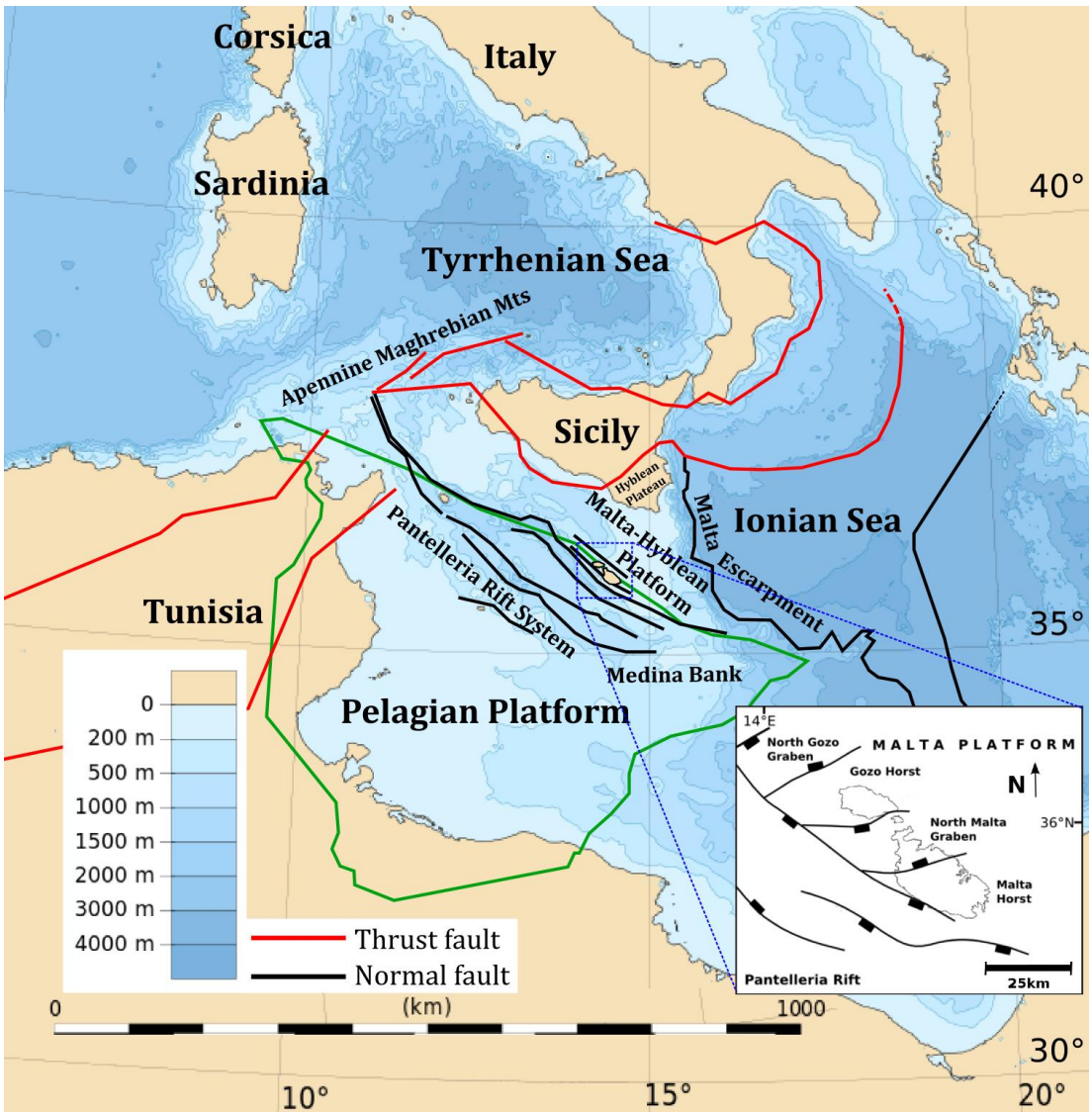

Figure 1.1: Location and tectonic setting of the Maltese Islands on the northern edge of the African Plate and the Pelagian Platform (green outline).

1.3. Use of quantitative methods to investigate geological processes

In sciences, models are developed to enhance our understanding of natural processes and their inter-relationships. The models are used to derive predictions that can be assessed against observations (Hardy, 1994). These may start out as conceptual models, but some may be augmented through numerical expressions into mathematical models. Quantitative mathematical models have various advantages over qualitative conceptual models. Paola (2000) notes that quantitative methods "*allows us to ask sharper questions, makes our hypotheses less ambiguous and hence easier to test, rules out some apparently plausible explanations and suggests new ones that would never have occurred to our unaided intuition*".

Forward modelling is a quantitative method that can be applied to test and better understand geological processes that cannot be directly observed. Forward modelling involves the

description of geological processes in mathematical models, simulating the processes by running algorithms of the model on a computer and outputting their effects (Warrlich, 2000). Over the past thirty years, significant work been done to develop stratigraphic forward models that reproduce 2D and 3D stratigraphies. These models have substantially contributed to identifying and quantifying the mechanisms that control platform evolution and the interplay/relationships between these mechanisms (e.g. Bice, 1988; Scaturo *et al*., 1989; Bosence & Waltham, 1990; Warrlich, 2000; Burgess & Steel, 2008; Williams *et al*., 2011; Prince & Burgess, 2013; Burgess & Prince, 2015). The recent stratigraphic forward models accurately replicate a variety of natural processes (e.g. CARBONATE 3D, CARBOCAT, DIONISOS). However, the values applied in various SFM based investigations do not adequately represent realistic parameter rates (e.g. Williams *et al*., 2011). Consequently, our understanding of how these parameters may influence platform development in natural systems remains incomplete. Additionally, a step-by-step quantitative method that builds on Paola's (2000) described potential application of quantitative techniques remains un-available.

1.4. Aims of research

This study applies quantitative techniques and assesses whether numerical methods can improve our understanding of platform evolution. The specific aims are:

1. To review and establish new grain-size production/depth profiles that can be applied in SFM and better represent Holocene carbonate factories. To use quantitative methods (SFM) to investigate how different aspects of carbonate factories may act independently and interact to influence carbonate platform development in natural systems.
2. To quantitatively bracket a range of diffusional sediment transport (diffusion coefficient) rates, relative to sediment production, which develop different platform geometries in SFM. To explore the relationship between slope angles and sediment composition of ancient carbonate platform systems.
3. To map and document the Late Miocene carbonate stratigraphy and facies distribution. To develop a facies scheme, characterise 3D stratal geometries and produce detailed carbonate facies models. To assess the influence of extensional tectonism on sedimentary style. To develop a sequence stratigraphy for the UCL Formation and improve the conceptual tectono-stratigraphy models for the UCL Formation.
4. To develop a method that quantitatively compares stratigraphic forward model simulation output to outcrop real data in order to constrain model parameters (chapter 4) and investigate conceptual models, alternative hypothesis and issues of non-uniqueness (chapter 7).
5. To combine modelling and outcrop interpretations to evaluate multiple hypotheses and scenarios of carbonate platform evolution.
6. To develop a step-by-step quantitative method that may improve our understanding of platform evolution. To apply the quantitative method to the Maltese UCL Formation conceptual

model and assess if it is a physically reasonable explanation, one of possibly several explanations, for what is observed in the real sedimentary system and whether there are issues of non-uniqueness (*sensu* Burgess & Prince, 2015).

1.5. Thesis structure

This thesis can be broadly subdivided into three sections. Chapters 3 and 4 undertake generic modelling of parameters that influence platform architecture. Chapters 5 and 6 constrain model parameters from the Maltese UCL Formation and identify features that can be used to quantitative compare SFM output to real strata. Hence, chapters 5 and 6 define a real data set from the UCL Formation that is used in chapter 7 to assess the applicability of the SFM-based hypothesis testing methods.

Chapter 2 is a description of literature on the controls on carbonate platform evolution (section 2.1), and the sedimentological and structural evolution of the Maltese Islands (section 2.2). The theory behind forward modelling programs is also described (section 2.3).

Chapter 3 establishes new depth production profiles from an extensive literature search that brackets average sediment production rates, depth distribution of sediment production, and proportions of grain-sizes produced for Cenozoic carbonate factories. These production profiles are applied in SFM to investigate how different aspects of carbonate factories may act independently and interact to influence carbonate platform development in natural systems. The aspects investigated in this study are sediment production profiles, sediment production rates, and production of different grain-size proportions with discrete diffusional transport rates.

Chapter 4 investigates the influence sediment production and diffusional transport has on facies architecture and stratal geometries. The chapter identifies which combination of sediment production and diffusional transport replicates facies architecture and stratal geometry of a well-studied Late Miocene flat-top steep margin (FTSM) platform, the Upper Miocene reef complex of the Llucmajor area, Mallorca. The chapter also explores whether different parameter values for the controlling processes (sediment production and diffusional transport) can develop facies architectures and stratal geometries that are not demonstrably different from one another and are thus non-unique (*sensu* Burgess & Prince, 2015).

Chapter 5 uses outcrop and borehole logs, thin sections and isotope analysis to develop a detailed sedimentological analysis of the Late Miocene UCL Formation across Malta and Gozo. Six facies associations (FA) and fifteen facies (table 5.3) were identified in the study area within the Greensand and UCL formations (figure 5.1).

Chapter 6 Uses outcrop data to propose stratigraphic relations, a depositional history and a conceptual model for the facies observed in the UCL Formation. The chapter also develops a sequence stratigraphic and chronostratigraphic scheme that enables the construction of a relative sea level curve. The Late Miocene Maltese relative sea level curve is then compared to that of other contemporaneous Mediterranean platforms that may together have been influenced by overriding paleoceanographic controls.

Chapter 7 presents and applies a step-by-step quantitative method that builds on Paola's (2000) described potential application of quantitative techniques. The method uses stratigraphic forward modelling (SFM) and enables the strengthening or rejecting of conceptual models for the UCL (developed in Chapter 5 and 6), the investigation of alternative hypothesis and issues of non-uniqueness with respect to the rate of accommodation generation, variable sediment production, variable transport rates, and reduced model run time. Thus, the method may improve our understanding of platform evolution and also help direct further research on platform evolution.

Chapter 8 summarises the key results of this study, discusses these in a broader context and describes how the study has advanced knowledge in the field.

CHAPTER 2: LITERATURE REVIEW

This chapter reviews previous published work on the controls on carbonate platform evolution (2.1), sedimentological and structural evolution of the Maltese Islands (2.2) and stratigraphic forward modelling (2.3).

2.1. Controls on carbonate platform evolution

2.1.1. Introduction

The analysis of the relatively shallow marine carbonate Upper Coralline Limestone (UCL) Formation of Malta forms a significant part of the work presented in this thesis (chapters 5 and 6). The lithofacies, dominant grain associations and platform evolution style observed in the UCL Formation are recorded in other shallow marine Mediterranean Late Miocene carbonates (e.g. Esteban, 1996; Cornée et al., 2004). The following section assesses the controls on the evolution of shallow marine carbonate associations.

"*Carbonates are born, not made*" (James, 1979). Shallow water carbonates are complex systems in which biological, physical and chemical factors interact to influence the occurrence of carbonate associations and platform evolution. It is for this reason that, when assessing shallow water carbonate facies, it is essential to consider the multitude of environmental factors that influence carbonate depositional environments. Changes in environmental conditions may force shifts in the active carbonate grain associations that in turn lead to variations in facies architecture and platform geometry. Carbonate systems can form a variety of platform geometries. These range from homoclinal ramps, which are low-gradient systems that lack steep platform margins (Ahr, 1973; Read, 1982; Burchette & Wright, 1992; Read, 1988), to flat-topped steep margin (FTSM) platforms with steep slope breaks and margins (Wilson, 1975; Read, 1982; Bosscher & Schlager 1992; Eberli & Ginsburg, 1989).

The first sub-section (2.1.2) of this chapter examines the controls and mechanisms that may influence the occurrence of different carbonate factories. The section is supplemented by examples from real sedimentary systems. Thus, discussions on parameters consist of two sub-sections: a general section, and a Mediterranean perspective. Ideas on how carbonate factories influence platform evolution are based on conceptual models or on numerical stratigraphic forward models (SFM). The sub-section that follows (2.1.3) reviews conceptual and numerical-based models that propose mechanisms whereby the dynamic processes in different carbonate factories may influence platform evolution. A detailed description of numerical SFM is available in section 2.3.

2.1.2. Controls on carbonate grain associations

The key overriding controls on carbonate sediment production are climate and geotectonics (Tucker, 1985). Changes in these primary controls directly influence water temperature, water depth, water energy levels and circulation patterns. These primary controls also influence, at local and regional scales, secondary environmental factors such as salinity, turbidity, terrigenous sediment influx, substrate nature, water chemistry (including Mg/Ca ratio), nutrient supply, and hydrodynamic regime. These controls in turn strongly influence the type and abundance of carbonate-producing organisms, whether inorganic carbonate precipitation or mixed carbonate clastic sedimentation occurs (Lees, 1975; Tucker & Wright, 1990). In addition to these allocyclic controls, the marine setting can be considerably modified by carbonate sedimentation through autocyclic mechanisms.

2.1.2.1. Climate

Climate is a principal control influencing the marine environment and consequently the nature of carbonate deposits (Tucker & Wright, 1990). Three major biogeographical zones can be defined on the basis of mean surface ocean temperatures and carbonate grain association type. These are the tropical, temperate and polar zones (Tucker & Wright, 1990). Most ancient and modern large carbonate systems were formed in tropical or subtropical areas with greatest production typically occurring in warm waters between latitudes 30°N and 30°S (Tucker & Wright, 1990). Lees & Buller (1972) identify two principal skeletal grain associations on the basis of fundamental differences between carbonate organisms. These are the chlorozoan and foramol carbonate grain associations (*sensu* Lees and Buller, 1972) (table 2.1). These distinct carbonate grain associations exemplify the control climate and oceanographic conditions have on carbonate secreting organisms.

Carbonate associations *sensu* Lees & Buller (1972)	**Descriptive association**	**Dominant or characteristic biota** (biota – in bold - form distinct factories in this thesis)	**Additional biota**	**Light-related term** (James, 1997)	**Latitude related terms** (Nelson, 1988; Schlager, 2000)
Chlorozoan	Chlorozoan (Lees & Buller, 1972)	**Zooxanthellate corals** and calcareous green algae	Benthic foraminifers, branching coralline algae, molluscs, non-skeletal grains	Photozoan	Tropical
	Chloralgal (Lees, 1975)	**Calcareous green algae**	Benthic foraminifers, branching coralline algae, molluscs		
Foramol	Foramol (Lees & Buller, 1972)	**Benthic foraminifers, molluscs and bryozoans**	Echinoderms, bryozoans, barnacles, ostracods, sponge spicules, worm tubes, ahermatypic corals and calcareous red algae	Heterozoan	Non-tropical or cool-water
	Bryomol (Nelson, 1988)	Bryozoans (>50%) and bivalve molluscs (infaunal and epifaunal)	Benthic foraminifers, echinoderms, calcareous red algae, barnacles		
	Rhodalgal (Carannente *et al.,* 1988)	**Coralline algae** (>80%) (rhodoliths as well as encrusting)	Bryozoans, benthic foraminifers, barnacles, bivalves, echinoderms		
	Molechfor (Carannante *et al.,* 1988)	Molluscs and benthic foraminifers	Echinoderms, barnacles, serpulids and bryozoans		
	Bimol (Hayton *et al.,* 1995)	Bivalves (infaunal and/or epifaunal: >60% up to 80%)	Bryozoans, benthic foraminifers, echinoderms, calcareous red algae, barnacles		

Table 2.1: Terminology of shallow water biotic carbonate grain associations (modified from Flugel, 2010). Dominant biota – in bold - form distinct factories in this thesis: scleractinian coral factory, calcareous green algal factory, coralline red algal factory and molluscan, bryozoan & benthic foraminifera factory.

The chlorozoan association develops exclusively in low latitudes (water temperatures > 15°C) and tolerates a narrow salinity range. Distribution patterns of modern chlorozoan association suggest that major environmental controls include; sea-water temperature, preferring growing primarily in tropical to subtropical climates, light availability, forming exclusively within shallow water euphotic zones (Flugel, 2010). The chlorozoan association tolerates a narrow range of tropical and subtropical environmental conditions. Under conditions unfavourable to chlorozoan growth, at tropical latitudes where salinities are too high or low, the chloralgal association is dominant (Lees, 1975).

Where water temperatures falls below 15°C, the chlorozoan and chloralgal associations are absent. Skeletal biota dominated by bryozoans, coralline red algae and molluscs, are present, forming the foramol association. These non-tropical carbonates are commonly found from mid to high latitudes. Foramol carbonate systems may also occur in localised tropical to temperate areas. Such zones are often characterised by environmental conditions unfavourable to chlorozoan and chloralgal growth, which may include; nutrient upwelling or terrestrial runoff (e.g. Henrich *et al.,* 1995; Pomar *et al.,* 2004; Wilson & Vecsei, 2005). Shallow-marine temperate carbonate sediments constitute nearly one third of the area of modern global shelf sediments (Nelson, 1988).

Modern temperate cool-water carbonates differ from tropical chlorozoan carbonates in several aspects. Temperate skeletal grains lack rapidly growing wave resistant calcareous frame-building organisms that develop in chlorozoan dominated tropical platforms. Temperate carbonate production rates are also significantly lower than tropical carbonate production (e.g. Bosence & Wilson, 2003).

2.1.2.1.A. Carbonate systems influenced by climate – a Mediterranean perspective

The following studies from the Central Mediterranean region illustrate how changing climatic conditions controlled biotic assemblages that in turn produced different shallow water carbonate facies.

Climatic variations through the Cenozoic controlled shallow water calcareous organisms and the facies they produce. Cenozoic carbonate platforms in the central Mediterranean region show vertical changes from photozoan to heterozoan skeletal assemblages. Gatt & Gluyas (2012) suggest that the development of Palaeogene Mediterranean photozoan assemblages coincides with periods when the inter tropic convergence zone (ITCZ) had shifted away from North Africa. Conversely, the heterozoan assemblages thrived during increased nutrient flux when the precipitation belt was located over the Sahara. The authors propose that meridional shifts in the ITCZ precipitation belt may have controlled nutrient flux from North African fluvial systems, and restricted conditions may have amplified its effect.

Bosellini (2006) compares two reef complexes that formed in the same physiographic and depositional setting at different times (Chattian and Messinian) in the eastern margin of the Apulia Platform. Despite the similar setting, two distinct reef complexes develop. The Chattian reef complex is characterized by a homogeneous reef-building biota that formed a single reef type while the Messinian reef shows a very low coral diversity but several other reef-building components. The author proposes the Oligocene to Miocene climatic cooling as the main factor controlling coral fauna turnovers. Bosellini also indicates that other environmental factors, such as changes in nutrient regimes and in hydrodynamic conditions, may also have exerted some influence.

2.1.2.2. Sea level fluctuations

Both climate and geotectonics control the position and fluctuations of sea level. Analysis by geoscientists in Exxon led to the publication of a 'global sea-level curve' (Vail *et al.,* 1991; Haq *et al.,* 1987; 1988). There are disputes regarding the timing and evidence for global synchroneity of their eustatic sea level cycles (e.g. Miall, 1992; 1997), however, the curves appear to show that there is a hierarchy of cycles of sea-level fluctuations through the Phanerozoic.

Various authors have proposed mechanisms for generating these cycles (Hallam, 1963; Worsley *et al.,* 1984). For first-order (duration hundreds of millions of years) sea level cycles there is a strong correlation between this curve and the patterns of continental dispersal and amalgamation through the Phanerozoic (Vail *et al.,* 1991; Worsley *et al.,* 1984). The causes of second-order (duration tens of millions of years) sea-level changes are thought to be changes in the rates of spreading at mid-ocean ridges (Hallam, 1963; Pitman, 1978). There is no general agreement on the mechanisms that may cause sea level fluctuations at the third order (duration one to ten million years) of cyclicity (Plint *et al.,* 1992). Glacio-eustasy is the more likely mechanism because it can generate the appropriate magnitude of sea-level change in a short period of time (Vail *et al.,* 1991; Haq *et al.,* 1988). Third and fourth order cycles are of the appropriate magnitude and period to cause the cycles of sea-level rise and fall that generate depositional sequences that have attracted the greatest amount of interest in sequence stratigraphy. However, not all depositional sequences are formed as a response to global sea-level change. Local tectonic activity can also generate relative sea level (RSL) fluctuations and develop depositional sequences. In many cases, the sea-level changes that are recorded in depositional sequences are a combination of global eustatic and local tectonic mechanisms.

2.1.2.2.A. Climate driven, eustatic sea level controls – a Mediterranean perspective

Esteban (1996) suggests that in the Mediterranean, rhodalgal units develop during Miocene transitions from glacial periods towards de-glaciation climatic optima. These scenarios are characterized by RSL rise, decreased salinity and increased nutrient concentration. Nutrient fluxes are brought to the marine environment through terrigenous fluvial discharge and entry of deep nutrient-rich Atlantic waters (Esteban, 1996). Esteban identifies an antipathetic relationship between rhodalgal units and coral reefs, which is strongly associated with climate and related sea level fluctuations as well as nutrient availability (Esteban, 1996). Esteban notes that Mediterranean chlorozoan reefs are present during 2nd order highstands (climatic optimum) while well-developed rhodalgal unit are characteristic of the TST of 3rd order depositional sequence. During such transgressions major coral-reef developments are excluded. In fact, the late Aquitanian transgression (his cycle 1.4) led to the drowning of many well-established reef tracts and was a time of coral decolonization. Such drowning also took place in the Maltese Islands (Pedley, 1978). Esteban (1996) thus suggests that in the Mediterranean, during the Miocene, rhodalgal carbonate ramps appear to be most common in the transgressive sections, while chlorozoan assemblages predominate during highstands. Esteban (1996), Pedley (1996) and Cornee *et al.* (2004) all emphasize the remarkable similarities of facies cycles in the Mediterranean region during the Miocene. They argue that the similarities indicate the dominance of large-scale regional climatic and eustatic palaeoceanographic controls on shallow water carbonate production.

In the Mediterranean, the most extensively developed Miocene carbonates are the rhodalgal ramp facies. During the climatic minima of the Burdigalian and Serravallian age, rhodalgal ramps are ubiquitous in the central Mediterranean (Esteban, 1996). For instance, in the south Appennines of Italy, the mid-Miocene (Langhian and Serravallian) climatic minimum was less conductive to coral reefs and favoured the development of a rhodalgal carbonate ramp (Pedley, 1996). The predominance of rhodalgal facies is a reflection of both colder climates and upwelling of nutrient rich waters (section 2.1.2.6.1).

2.1.2.2.B. Local tectonically driven sea level fluctuations – a Mediterranean perspective

The following examples demonstrate the control isostatic and palaeotopographic parameters have on shallow water carbonates.

Apennine Mountains (Italy)

During the Burdigalian, many areas in the Apennine Mountains were affected by an accelerating deformation regime. Deformation in most regions of Italy and along the north-south Axis of Tunisia reached a peak in the late Miocene to Pliocene. During the late Tortonian to early Messinian a number of reef systems developed in association with fold belts (Pedley,

1996). Through uplift, seafloor topographies experienced RSL shallowing and reefs were developed in areas of shallow seafloor. Such areas became available in greater numbers as the Alpine fold belts developed (Pedley, 1996). The emergent Apennine orogenic belts also led to a large influx of clastic sediment in areas flanking the uplift that led to vast gravity slides. This created extremely inhospitable environments for chlorozoan colonization. Shallow water carbonates in fact often share an antagonistic relation with clastic inputs (Pedley, 1996).

Cyprus

The development of late Miocene reefs in southern Cyprus was preceded by uplift (relative sea level fall) and crustal compression that created northwest-southwest-trending lineaments. The location and facies of the Koronia Member reefs were directly influenced by local tectonics. Some of these reefs developed on uplifted lineaments developed due to early Miocene compression in south Cyprus (Follows *et al.,* 1996). The reefs that developed on a recently stabilized lineament also shed large volumes of sediment talus into basinal areas (Follows *et al.,* 1996). These lineaments were thus important in localizing shallow water carbonate facies.

2.1.2.3. Water depth and light intensity

Many key carbonate producing organisms are photodependent. Phototrophs, such as calcareous algae, are completely dependent on light as the main energy source, while mixotrophs, that include many corals, partly rely on photosynthesis. Sediment production from these associations depends on calcification processes that are directly tied to light availability (McConnaughey & Whelan, 1997). Light availability decreases with an increase in water depth and turbidity. The dependence in some organisms of skeletal carbonate fixation on photosynthesis and light explains the decrease of carbonate production with an increase water depth and turbidity.

Photodependent carbonate organisms typically occur throughout the photic zone but flourish in the upper 10 to 15 m of the sea. This is the case for the green algae *Penicillus* and *Halimeda* and also for hermatypic corals. An excess of photic irradiance may however lead to photo-oxidative stress. Such a process causes "*bleaching*" the loss of symbiotic zooxanthellate algae in modern corals and other marine invertebrates (Fitt *et al.,* 2001; Lesser & Farrell, 2004).

2.1.2.4. Water energy

The distribution of carbonate-secreting organisms also depends on water circulation and current regime (Tucker & Wright, 1990). Certain types of carbonate organism, through their competitive adaptations, may favour particular water energy regimes. Some organisms, including corals, flourish in turbulent high-energy areas and so are concentrated along shelf

margins. Other calcareous associations, including certain chloralgal, flourish in more sheltered inner shelf environments.

The morphology of coralline algal frameworks is affected by hydraulic energy. Bosence (1983) crustose coralline frameworks from low energy environments are characterized by open leafy frameworks of a small number of species, and those from higher energy environments by dense closely superposed crusts of several species. Similarly, branching coralline algal frameworks become more densely branched in exposed environments.

Pomar *et al.* (1996) observe coral colonies across the reef core in the Llucmajor upper Miocene reef complex that are vertically zoned in the reef core and have distinct light and water energy (depth-controlled) growth morphologies. They suggest that deeper-water corals show platy forms, intermediate-depth corals are branching and shallower corals are hemispheroidal to columnar.

Corals and coralline algae frequently occur in the same or adjacent habitats. Various factors control whether a coral or coralline framework is produced in reefs. Bosence (1983) discusses that the occurrence of corallines on the windward intertidal side of reefs suggests that they can withstand conditions of higher hydraulic and light energy than corals.

2.1.2.5. Clastic influence; turbidity and sediment influx

The absence of clastic sediment is a prime requisite for carbonate production (Tucker & Wright, 1990). Turbidity inhibits carbonate production by cutting down the amount of light reaching the seafloor, thus discouraging the growth of photodependent associations. The chlorozoan and chloralgal associations are highly photodependent and thus develop mostly in clear water. Many filter feeding benthic organisms also do not tolerate suspended mud as this interferes with their feeding mechanisms (Tucker & Wright, 1990). Other organisms, such as deposit feeding organisms, may however thrive under turbid environments.

The climatic and geotectonic context, through their control on hinterland topography, drainage and rainfall, influence the quantity of material delivered to marine environments. Hence, turbidity is often brought about by suspended clay from rivers. Siliciclastic-free shelves may also become turbid as a result of lime mud (e.g. produced from *Penicillus*) that may be put into suspension by waves and storms (Tucker & Wright, 1990). Turbidity may also be the result of high surface water organic productivity in areas affected by high upwelling rates.

2.1.2.5.A. Clastic influence – a Mediterranean perspective

Various authors have studied the effects terrigenous clastic influxes have had on Mediterranean rhodalgal and chlorozoan associations (e.g. Esteban 1996; Pedley, 1996; Cornée et al. 2004). Observations of the role clastic input on carbonate growth have identified active and passive relationships. In active models, sediments of terrigenous origin are continually deposited and hinder coral growth (Esteban, 1996). However, when terrigenous sedimentation occurs at irregular intervals a different dynamic is developed. Troughs in sediment influx allow the stabilisation and growth of pioneer communities such as oysters, red algae and even chlorozoan associations. In affected Mediterranean areas, *Porites* corals have been observed (Esteban, 1996). Deposited sediments may even act as hard stabilizing substrates. Successive peak phases of terrigenous sedimentation may completely bury carbonate units thus halting or reducing carbonate production (Esteban, 1996).

Middle Miocene carbonate platforms developed on fault blocks rotated during Miocene extension and subsidence of the rift basin of the Gulf of Suez and northwest Red Sea. Early stages of rifting were dominated by siliciclastic sedimentation with sediment transport controlled by the evolving extensional fault systems and transfer zones (Purser et al., 1998; Bosence, 2005). Transfer zones and hangingwall sub-basins remained as sites of clastic sediment accumulation whereas footwall areas and horsts, isolated from clastic supply, accumulate subtropical, photozoan carbonates.

Miocene terrigenous sediments occur as the substratum for a large number of Miocene reefs in the Mediterranean. Reefs developed on passive type abandoned channel margins, stream-mouth bars and sand shoals (Esteban, 1996). Some Miocene reefs also developed in active type areas of repeated terrigenous sedimentation. *Porites* is well known for its ability to withstand high levels of fine-grained clastic sedimentation (Hubbard & Pocock, 1972).

2.1.2.6. Water chemistry

2.1.2.6.1. Nutrient Fluxes

Upwelling can introduce cold, nutrient rich oceanic bottom waters into shallow marine settings. Identifying the effects of oceanographically controlled nutrient supply in ancient successions is difficult but may be an important control on sediment production and shallow water carbonate facies (Wood, 1993; Wright, 1994; Hallock & Schlager, 1986).

Most large modern coral reefs grow in relatively nutrient-deficient waters. Coral associations are very efficient in recycling nutrients and thus predominate in oligotrophic conditions. In meso/eutrophic settings, the faster growing heterozoan associations (fleshy algae, red algae, soft corals, bryozoans, and sponges that tolerate such conditions) can out-compete and displace coral

associations (Hallock & Schlager, 1986). Increased nutrient levels also promote faster rates of bio-erosion that leads to an accelerated destruction of reef framework (Hallock & Schlager, 1986; Hallock, 1988; James, 1997; James *et al.,* 1999). Conversely, free-living coralline red algae (rhodoliths) can thrive under a wide range of temperatures, reduced light, and increased nutrient levels (Halfar & Mutti, 2005).

2.1.2.6.1.A. Nutrient flux – a Mediterranean perspective

Research over the past several decades has shown that benthic carbonate faunal or floral turnovers and community replacements are common throughout geologic history. Various climate feedback mechanisms are thought to have influenced shallow water ocean environments and forced shifts in carbonate communities. John & Mutti (2005) attempted to correlate termination phases and changes in biotic assemblages during the Miocene with climatic events and cooling steps (e.g. "Mi" oxygen isotope events). A direct relationship was however not found. The authors argue that other environmental factors may have caused the chlorozoan community shift. Organisms, which did not survive the mid-Miocene extinction peak, include associations (corals and larger foraminifera) with photosymbiont adaptations to oligotrophic conditions. Associations that survived were limited to genera tolerant of both high turbidity and nutrient levels (Edinger & Risk, 1995). Carbon isotope data ($d^{13}C$) from the Maiella platform (Abruzzi, Italy) (Mutti *et al.,* 1999) show that the second- order transgressive event in the central Mediterranean, spanning the Burdigalian to Serravallian, coincides with an increase in skeletal $d^{13}C$ values. This was interpreted as an indicator of increased surface water productivity.

In view of this, Mutti *et al.* (1999) suggest a mechanistic link between changes in carbonate facies of the Mediterranean region, from coral reef to rhodalgal facies, and increased surface water productivity. They argue that enhanced trophic resources triggered the dominance of red algae over coral reefs in the Burdigalian (long-term shift toward higher carbon isotope). Rhodalgal lithofacies further expanded in the mid-Miocene. This is interpreted to be the result of strengthened thermal gradients, associated with the establishment of the East Antarctic Ice Sheet, which enhanced upwelling. Climate change may also have increased weathering rates that introduced land derived nutrients into the oceans thus increasing marine trophic levels. The relative significance and control of temperature changes *versus* availability of nutrients or other environmental factors has led to significant debate (Mutti & Hallock 2003; Pomar *et al.,* 2004).

Pomar *et al.* (2004), discuss the shift from rhodalgal to chlorozoan that took place during the Late Miocene in the Balearic Islands (Spain). Although some decrease in surface water temperature might have taken place, the authors suggest that the major factor leading to the association change is related to a shift in marine trophic levels (Pomar, 2001). Pomar proposes that early Tortonian rhodalgal associations were formed in meso/euphotic conditions, while late

Tortonian reef complex grew in an oligotrophic setting. Nutrient availability thus may have exerted a stronger control on the skeletal composition of the Miocene carbonate platforms than temperature. Therefore interpretations based on nutrient variations and availability seems to better explain the resultant shallow water carbonates than temperature. Despite the significance of nutrients, other factors should also be considered (Pomar *et al.,* 2004).

Pomar (2001) attributes the nutrient change to climatic variations that occurred at the transitions from early to late Tortonian, from humid to arid (Calvo *et al.,* 1993). Calvo *et al.* (1993) report an early Tortonian humid period with a subsequent shift to drier conditions in the late Tortonian to Messinian. Such climatic change may have decreased fluvial runoff, thus reducing the delivery of nutrients from land and enabling the re-establishment of chlorozoan and chloralgal carbonate grain associations.

2.1.2.6.2. Calcium / Magnesium ratio

The material for carbonate sediments is extracted from the dissolved load of the sea. Precipitation of $CaCO_3$ may occur through biotic and abiotic pathways. The abiotic mode represents a purely inorganic method of carbonate precipitation. Ooids are broadly precipitated through this mechanism. The biotically induced mode occurs where metazoan organisms control precipitation whilst induced precipitation of $CaCO_3$ occurs in microbial communities.

Atmospheric CO_2 and Ca^{2+} concentration and Ca/Mg ratios influence precipitation of calcite and aragonite. Under high concentrations of atmospheric CO_2, and low marine Ca^{2+} and Mg/Ca ratios calcite precipitation is favoured over aragonite. Such conditions, characteristic of greenhouse climates, are likely to favour calcitic secreting biota while being detrimental to aragonite-secreting biota. Calcitic organisms, rather than aragonitic ones, are likely to dominate shallow water facies (Hallock, 2001).

Calcium and magnesium ratios have been found to exert a significant control over carbonate organisms. During episodes of high seawater Mg/Ca ratios, aragonite and high Mg calcite was preferentially deposited while at low Mg/ Ca ratios, calcite is dominant (Steuber & Veizer, 2002). Variations in Mg/Ca ratio may lead to the preferential development of certain carbonate producing organisms based on the availability of minerals for the formation of skeletons. A long-standing debate however exists regarding the degree to which various bio-mineralising organisms dictate skeletal mineralogy, as opposed to having it influenced, or even dictated, by environmental conditions (Weiner & Dove, 2003).

Laboratory experiments (Ries, 2010) have revealed that aragonite-secreting bryopsidalean (green) algae and scleractinian corals exhibit higher rates of calcification and growth in experimental seawaters formulated with seawater Mg/Ca ratios that favour their skeletal mineral. Laboratory experiments (Ries, 2010) therefore support the palaeontological evidence

(Stanley and Hardie 1998, 1999; Porter, 2007; Kiessling et al., 2008) that oceanic Mg/Ca was an important factor in determining the role that these organisms played in sediment production and reef building thoughout Phanerozoic time.

Abiotic precipitation in the form of ooids also significantly contributes towards shallow water carbonate production. The present consensus regarding ooids is that they form by chemical precipitation out of agitated waters saturated with calcium carbonate in warm waters (Tucker & Wright, 1990). It has also been proposed that bacteria may also play a role in the process, especially in less agitated environments. Sandberg (1975) attributes the change from pre-Cenozoic calcitic ooids to Cenozoic aragonitic ooids to an increase in the Mg/Ca ratio of seawater.

2.1.2.6.3. Salinity

Many organisms cannot tolerate great fluctuations in salinity and/or temperature, so that the number of species greatly decreases where these changing conditions occur. Lees (1975) in fact emphasise how shallow-marine carbonate-secreting organisms are highly affected by water chemistry particularly in relation to salinity (Lees & Buller, 1975).

Chlorozoan associations can only tolerate a narrow salinity range (32 to 40‰). Water temperature and salinity again appear to be the controlling factors in abiotically produced oolitic and grapestone grains. These grains occur where evaporation rates exceed precipitation and seawater salinity is high (Lees, 1975). At elevated and in lowered salinities the chloralgal associations dominate, replacing the chlorozoan organisms. Under hypersaline settings, microbial production can be very high, resulting in highly organic-rich sediment.

During the Tortonian, sediment production in the euphotic zone changed from rhodalgal to coralgal (Pomar et al., 2012). Esteban (1996) suggests that rhodalgal units correspond to the transition from climatic minimums (glacial periods) towards climatic optimums (de-glaciation) that correspond to pluvial periods in the Mediterranean. Esteban suggests that this setting would be characterised by decreased salinity and increased nutrient concentration. Conversely, coral reefs would have developed during interglacial (climatic optimum) periods that tend to evolve into semi-arid or arid climates in the Mediterranean-type settings that would have increased evaporation and salinity and decreases nutrients in the upper water layer.

2.1.3. Controls on platform evolution (including ramp to FTSM)

The above-mentioned environmental conditions control the type and abundance of carbonate-producing organisms and whether inorganic carbonate precipitation occurs. Carbonate

producing communities influence the rate of sediment production, the depth distribution of sediment production (production profiles) (e.g. James & Bone, 1991; Bosscher & Schlager, 1992; Schlager, 1981) and the grain sizes produced. These parameters are distinct for different calcareous associations and are thought to influence facies architectures to form the observed spectrum of carbonate platform geometries (e.g. Pomar, 2001; Pomar & Kendall, 2008).

Carbonate systems can form a variety of platform geometries ranging from homoclinal ramps to flat top steep margin (FTSM). The basinal and tectonic setting of carbonate platforms controls the occurrence, overall 3-D platform morphology, the large-scale stratigraphic features and depositional sequences (Bosence, 2005). Other factors, such as tectonic subsidence, antecedent topography, and relative sea-level oscillation also interact to determine platform geometry (e.g. Williams et al., 2011).

Various authors have discussed the influence that carbonate communities may have on stratal architecture and platform geometry (e.g., Wilson, 1975; Read, 1985; Wright & Faulkner, 1990; Aurell *et al.,* 1998; Bosence & Waltham 1990; Burchette & Wright, 1992; Bosence *et al.,* 1994; Bowman & Vail, 1999; Pomar, 2001; Schlager, 2005; Pomar & Kendall, 2008; Warrlich *et al.,* 2008; Williams *et al.,* 2011; Pomar *et al.,* 2012). Facies architectures and stratal geometries are both the result of an interaction between changes in accommodation, and the relative rates of sediment production to sediment transport (e.g. Bosence & Waltham 1990; Schlager, 1993; Helland-Hanse & Gjelberg, 1994; Carvajal *et al.,* 2009; Meijer, 2002; Burgess & Steel, 2008; Williams *et al.,* 2011; Prince & Burgess, 2013; Burgess & Prince, 2015).

The following section reviews the current ideas on how calcareous association are distinct from each other and which carbonate-association dependent aspects may influence the formation and maintenance of distinct carbonate platform geometries.

2.1.3.1. How are the carbonate photozoan and heterozoan associations different?

The photozoan association (*sensu* James, 1997) consists of the chlorozoan (Lees & Buller, 1972) and chloralgal (Lees, 1975) grain associations through the Phanerozoic. The photozoan association typically occurs in tropical, euphotic, oligotrophic settings. Organic production of photozoan association (e.g. corals) is greatest in the shallow euphotic zone and decreases exponentially with an increase in water depth (Bosscher & Schlager, 1992). The resulting euphotic production profile (production-depth curve) is characteristic of the photozoan association. Sediment production by the chlorozoan association is characteristically very high and spans several orders (0.35 to 23 mm yr^{-1}) (see appendix A).

The chlorozoan association produces organically bound sediments that develop coral framestone and reefal rudstones. These sedimentary textures are not easily dispersed and can aggrade to form steep reef margin slopes (e.g. Llucmajor Pomar *et al.,* 1996).

The heterozoan association (sensu James, 1997) consists of the foramol (Lees & Buller, 1972), bryomol (Nelson, 1988), rhodalgal (Carannante *et al.,* 1988), molechfor (Carannante *et al.,* 1988) and bimol (Hayton *et al.,* 1995) associations though the Phanerozoic (see table 1.1). These latter associations occur in a variety of climatic, nutrient, and bathymetric marine environments (Peres & Picard, 1964; Blanc, 1968; Bosence, 1976; Bosence, 1983, 1985; Iryu *et al.,* 1995; Basso, 1998; Pomar, 2001; Bosence & Wilson, 2003; Matsuda & Iryu, 2011). The rhodalgal association (coralline red algae) are photic organisms that can thrive in meso-oligophotic conditions equivalent to water depths up to 80 m (Halfar, 1999). Maerl beds are found from the low intertidal zone to depths of 150 m (Foster, 2001). The bryomol association exist in low and high latitudes and are abundant in depths between the intertidal zone and about 80 m (Flugel, 2010). The reduced photo-dependence of the heterozoan association develops an oligophotic production profile where sediment production is in the euphotic and oligophotic zone and gradually reduces with an increase in depth. Sediment production by the heterozoan association is typically several orders of magnitude lower (average 1.04 mm yr^{-1}) than for the chlorozoan association (see appendix A).

The heterozoan association produces a range of grain sizes, most of which are more easily dispersed than those produced by the chlorozoan association. The rhodalgal association may produce rhodolithic and crustal growth habits, both of these may be disintegrated into crustose and rhodolith branch debris of gravel, sand and mud grade sizes (e.g. Bosence & Pedley, 1982). Bioclasts from the bryomol association contribute towards the formation of carbonate particles of all grain-sizes (Flugel, 2010).

2.1.3.2. Controls on facies architecture, and platform geometry

Discussions on the possible biological controls carbonate gain associations may have on platform development are either based on qualitative conceptual models (e.g. Pomar, 2001; Pomar & Kendall, 2008; Pomar *et al.,* 2012) or numerical SFM (e.g. Bosence & Waltham, 1990; Bosence *et al.,* 1994; Williams *et al.,* 2011).

2.1.3.2.1. Conceptual qualitative models

Previous qualitative work has suggested the formation of distinct carbonate platform geometries are the result of particular relationships between water depth and sediment production i.e. the production/depth profile. In this scheme, FTSM platforms are thought to be the product of euphotic production profiles (e.g. Bosscher & Schlager 1992; Bowman & Vail 1999) while ramps are the result of oligophotic production profiles (e.g. Wright & Faulkner 1990; Pomar, 2001).

Pomar & Kendall (2008) propose that the variable character of carbonate platforms result from differences in the capacities of the carbonate systems to accumulate sediments above hydrodynamic base level (ecologically controlled accommodation). They argue that the interplay between different sediment production and redistribution processes form the various depositional profiles and facies belt distributions. In carbonate systems, sediment production and dispersal are strongly influenced by carbonate factories (table 2.1). Thus, different biotic systems have distinct competence in building-up above the hydrodynamic shelf equilibrium profile (Pomar, 2001b) and it is this ability that produces critical differences between carbonate platform geometries.

Pomar *et al.* (2012) investigate whether different types of carbonate production create distinct types of carbonate platforms, with diverse depositional profiles and facies belt distributions. Pomar & Kendall (2008) suggest that low-relief carbonate ramps are the result of fine-grained sediments produced in shallow areas that are shed basinward, or sediment produced and accumulated in the deeper part of the depositional profile. On the other end of the platform geometry spectrum, flat-topped steep margin (FTSM) platforms develop when biotic components are capable of accumulating to sea level (Pomar & Kendall, 2008). These conceptual models however do not quantitatively assess how individual or multiple parameters influence platform geometry. In view of these limitations, conceptual models are often insufficient for detailed analysis (Burgess, 2012).

2.1.3.2.2. Numerical stratigraphic forward models

More recent numerical SFM techniques provide a quantitative method to test the architectural response of a carbonate platform to different controlling parameters (e.g. Bosence *et al.,* 1994; Aurell et al., 1998; Williams *et al.,* 2011; Burgess & Prince, 2015). SFM are therefore better suited to improve our understanding on how carbonate factory dependent aspects influence carbonate systems. SFM are discussed in detail in section 2.3, the following section reviews the application of SFM that investigate the controls on platform evolution.

Recent SFM-based analysis shows that the dominant locus of sediment production within the production profile (euphotic *versus* oligophotic) does not exert a significant control on platform geometry (Williams *et al.,* 2011). Even oligophotic profiles, that were previously considered to favour ramp development, develop FTSM platforms (Williams *et al.,* 2011). Applying SFM, Williams *et al.* (2011) show that it is the relative sediment transport (diffusion coefficients) and sediment production rates that exert the greatest control on the evolution of platform geometries. Their numerical models show that when diffusion coefficients are high relative to production rates, both the euphotic and oligophotic production profiles produce ramp platforms. The authors suggest that low-gradient depositional systems are dominated by sediment transport. Such scenarios may occur in both low-energy conditions if carbonate factories

produce only sediment that is easily transportable and in high-energy conditions if natural processes can break down and transport bound sediments.

The leading hypothesis therefore argues that it is the carbonate sediment production and redistribution processes, relative to one another, that are critical in developing different types of platform geometries (e.g. Williams *et al.,* 2011; Pomar *et al.,* 2012). The hypothesis emphasises processes and aspects that are strongly influenced by carbonate factories. This is since carbonate factories determine the rate and depth distribution of sediment production (production profiles) and also determine the grain sizes produced that can greatly modify the rate of sediment dispersal/transport.

Previous SFM based investigations (e.g. Williams *et al.,* 2011) however do not adequately consider realistic values for various carbonate factory aspects. More specifically they do not investigate in detail the roles of sediment production profiles, sediment production rates, sediment grain-size, sediment transport rates or a combination of these. For instance Williams *et al.* (2011) assess the influence a very low maximum sediment production rate (0.47 m ky^{-1}), simulate arbitrary proportions of grain-sizes, and, a poorly constrained range of diffusion coefficient values (0 to 50 km^2 ky^{-1}). They also assess the influence different sediment production profiles have on platform geometry while simulating different total sediment production rates but these values are also poorly constrained. As a result, our understanding of how these different carbonate factory aspects influence platform development in natural systems remains incomplete.

2.2. Sedimentological and structural evolution of the Maltese Islands

This section is divided into two sub-sections. Section 2.2.1 reviews the plate tectonic setting of the Maltese islands by progressively focussing from the broad tectono-stratigraphic elements of the central Mediterranean, through the elements of the Pelagian Platform, down to the detail of the structure of the islands themselves. Section 2.2.2 reviews previous literature concerning the lithostratigraphy and biostratigraphy of the Maltese Islands. Published literature is then reviewed that develops conceptual models proposing the key controls on the Late Miocene evolution of the UCL Formation (Malta).

2.2.1. Structural evolution

The Pelagian platform mostly lies beneath the Pelagian Sea, but also comprises the onshore Hyblean plateau of SE Sicily, the Maltese and Pelagian Islands, and the Sahel area of eastern Tunisia (Snoke *et al.,* 1988) (Dart, 1991 p.26). A summary of the principal events in the tectono-stratigraphic evolution of the area is presented in figure 2.1. From well log geohistory

plots it can be calculated that the Pelagian Platform formed on the sinking passive continental margin of North Africa over approximately the last 180 My (Jongsma *et al.,* 1985) preserving a thick Mesozoic to Cenozoic carbonate stratigraphy. From the Neogene to present, the major Pantelleria Rift has bisected the platform while its northern margin has been subducted beneath the European plate (figure 1.1). At present, the deformation rate within the platform is low and restricted to the upper brittle crust.

2.2.1.1. Regional tectono-stratigraphic development

The Maltese Islands outcrop from the shallow shelf sea of the Malta-Hyblean Platform that forms the leading edge of the African Plate (Pelagian Platform) as it is subducted beneath the European Plate (figure 2.1).

2.2.1.1.1. Pantelleria Rift

The NW-SE trending Pantelleria Rift (Reuther & Eisbacher, 1985) is bathymetrically expressed by the greater than 1km deep Pantelleria, Linosa and Malta troughs, and the Malta-Medina channel (figures 1.1 and 2.2). The zone of extensional deformation is up to 100 km wide south-west of the Maltese Islands, and as narrow as a single 30 km wide graben beneath the Malta-Medina channel (Jongsma *et al.,* 1985; 1987). The Rift divides the Pelagian Platform into two structural blocks. The northern block comprises the Malta Platform, Gela Basin and Adventure Plateau, the southern block, the Lampedusa-Medina Plateau (Dart, 1991).

Seismic reflection profiles show that the Pantelleria Rift consists of a zone of symmetrical graben structures produced by extensional faulting and tilting (Finetti & Morelli, 1972; Finetti, 1982; 1984; Jongsma *et al.,* 1985; 1987; Winnock, 1979; 1981; Winnock & Bea, 1979) (figure 2.2). Some faults displace the sea floor. These grabens have a bathymetric expression and are partially filled with Plio-Quaternary deposits, the most recent of which are turbiditic (Maldonado & Stanley, 1976). These deposits have a thickness of 1 km beneath the Pantelleria, 2 km beneath the Linosa, and 1.5 km beneath the Malta Troughs (Colantoni et al., 1985; Winnock, 1981).

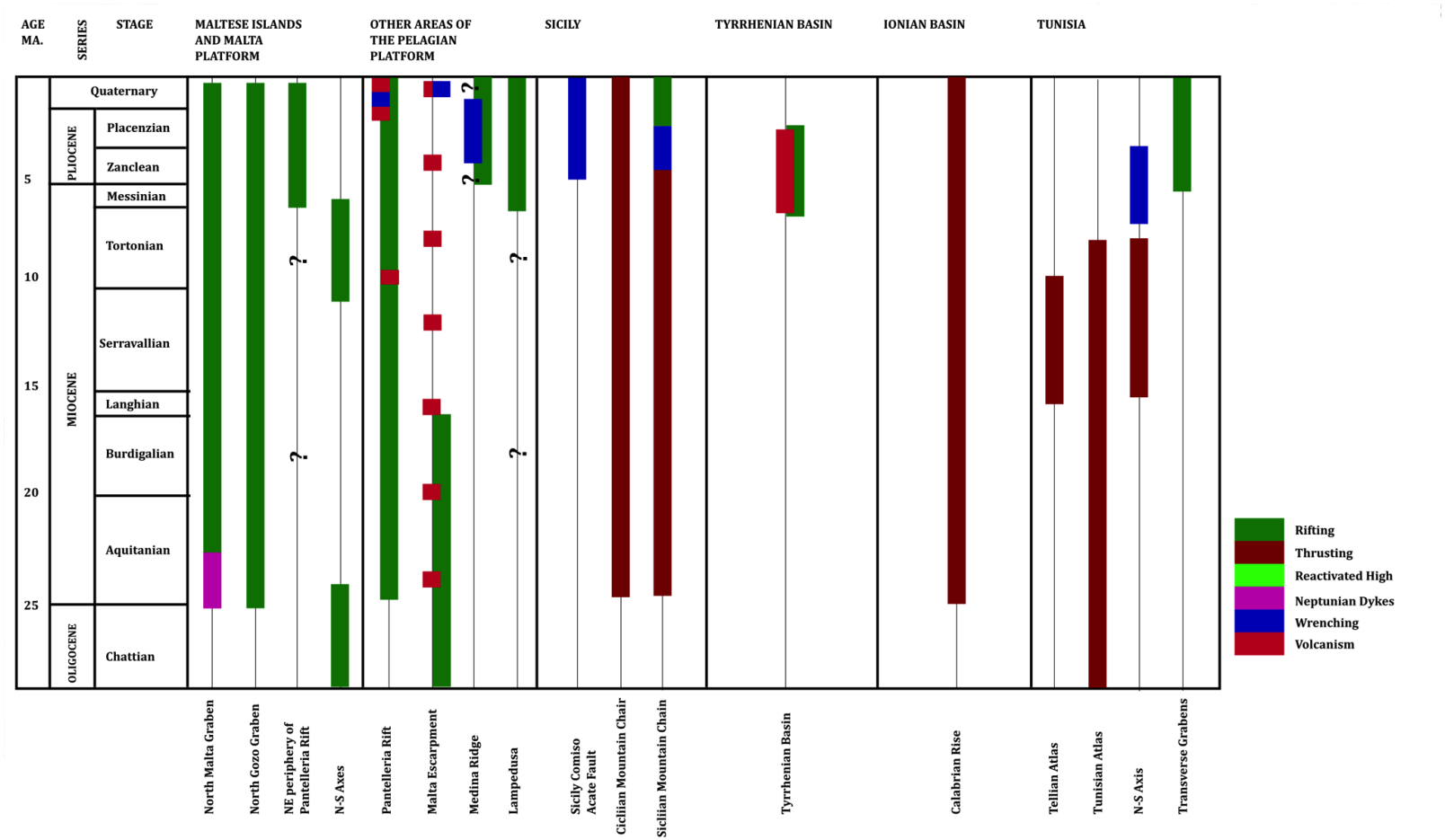

Figure 2.1: Timing of major tectonic events within the central Mediterranean compared to those within the Malta Platform. (Modified from Dart, 1991).

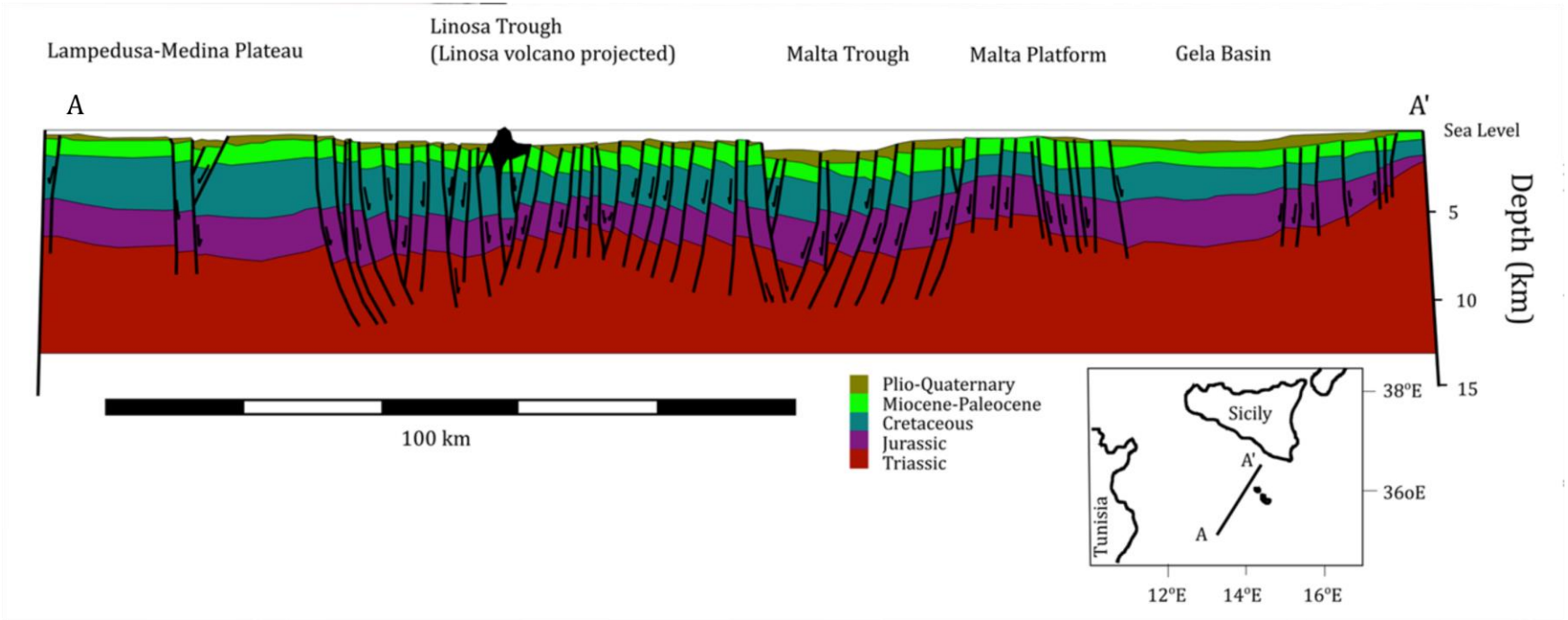

Figure 2.2: Depth converted reflection seismic section across the Pantelleria Rift system. (Modified from Dart, 1991 figure 2.8 who modifies from Finetti, 1984).

2.2.1.1.2. Malta Platform

The NNW-SSE trending 100 km wide Malta Platform (figure 1.1), lies beneath the Malta Plateau and extends to the south of the Hyblean Plateau. It displays a particularly thick Mesozoic to Tertiary pre-M reflector (top Messinian evaporites or erosion surface) succession (Jongsma *et al.,* 1985). The Cenozoic thins to the north-east exposing Mesozoic strata in SE Sicily. Faulting and volcanics are associated with four rifting phases; Middle-Late Triassic, Middle Jurassic, Middle-Late Cretaceous and Neogene-Quaternary (Finetti, 1982). Onshore exposure of an Oligo-Miocene carbonate sequence, transected by the 14 km ENE-WSW trending North Malta Graben, is provided by the Maltese Islands. A second ENE-WSW trending graben of similar width, and with fault throws of up to 800 m, occurs to the north west of Gozo (North Gozo Graben) (Dart, 1991).

2.2.1.2. Tectonic development of the Maltese Islands

The Maltese graben system comprises a series of Miocene to Quaternary extensional basins and forms a small part of the arcuate Pantelleria (Reuther & Eisbacher, 1985) rift system. The rift system lies within the African plate, in the foreland of the Sicilian Apennine-Maghrebian thrust and fold belt (Hill & Hayward 1988; Argnani 1990). Regional seismic reflection data indicates that the Pantelleria Rift is characterized by half and full grabens (figure 2.2) (Finetti 1984; Jongsma *et al.,* 1985; Argnani 1990). The Maltese graben system consists of five distinct tectonic units: North Gozo Graben, Gozo Horst, North Malta Graben, Malta Horst and Pantelleria Rift (Dart *et al.,* 1993; figure 1.1).

The Maltese graben system is characterized by two intersecting extensional fault trends: NW-SE and ENE-WSW (Pedley, 1976; Illies 1980; Reuther & Eisbacher 1985; Dart, 1991; Dart *et al.,* 1993) (figures 1.1, 2.3 and 2.5).

(i) To the SW of Malta lies the 100 km wide NW-SE-trending Pantelleria Rift (Reuther & Eisbacher, 1985). The Malta Platform forms the Pantelleria Rift's NE footwall crest. The NW-SE-trending Il-Maghlaq Fault is located on the periphery of the Pantelleria Rift and throws > 210 m. The main bounding fault (il-Maghlaq Fault) of the Pantelleria Rift lies approximately 10 km to the SW and throws 2.2 km (figures 2.3 and 2.5). There is a very gentle eastward dip of less than 1° across the Malta Horst and to the Malta Platform away from the Pantelleria Rift (Dart *et al.,* 1993).

(ii) The Malta platform is also dissected by ENE-WSW trending faults that effectively subdivide the Maltese graben system into four distinct tectonic units: North Gozo Graben, Gozo Horst, North Malta Graben and Malta Horst (Dart *et al.,* 1993; figures 2.3 and 2.5). The ENE-WSW trending North Gozo Graben and the North Malta Graben intersect the Pantelleria Rift at acute angles of 66° and 32° (figures 2.3 and 2.5). The North Gozo Graben has a throw of 1600

m on its northwestern bounding fault and the Victoria Lines fault has a displacement of 195 m within the North Malta Graben (Costain 1957-1958) (Dart *et al.,* 1993). Displacement on faults in the aforementioned grabens dies out eastwards and cannot be recognized in seismic data from the Malta Platform east of the islands (Dart *et al.,* 1993). In addition to the main graben described, there are numerous minor ENE-WSW-trending faults (Dart *et al.,* 1993). Fault plane solutions from both ENE-WSW trending fault set of the North Malta Graben, and NW-SE-trending Il-Maghlaq fault can be interpreted to result from a N-S-directed extension axis (Dart *et al.,* 1993).

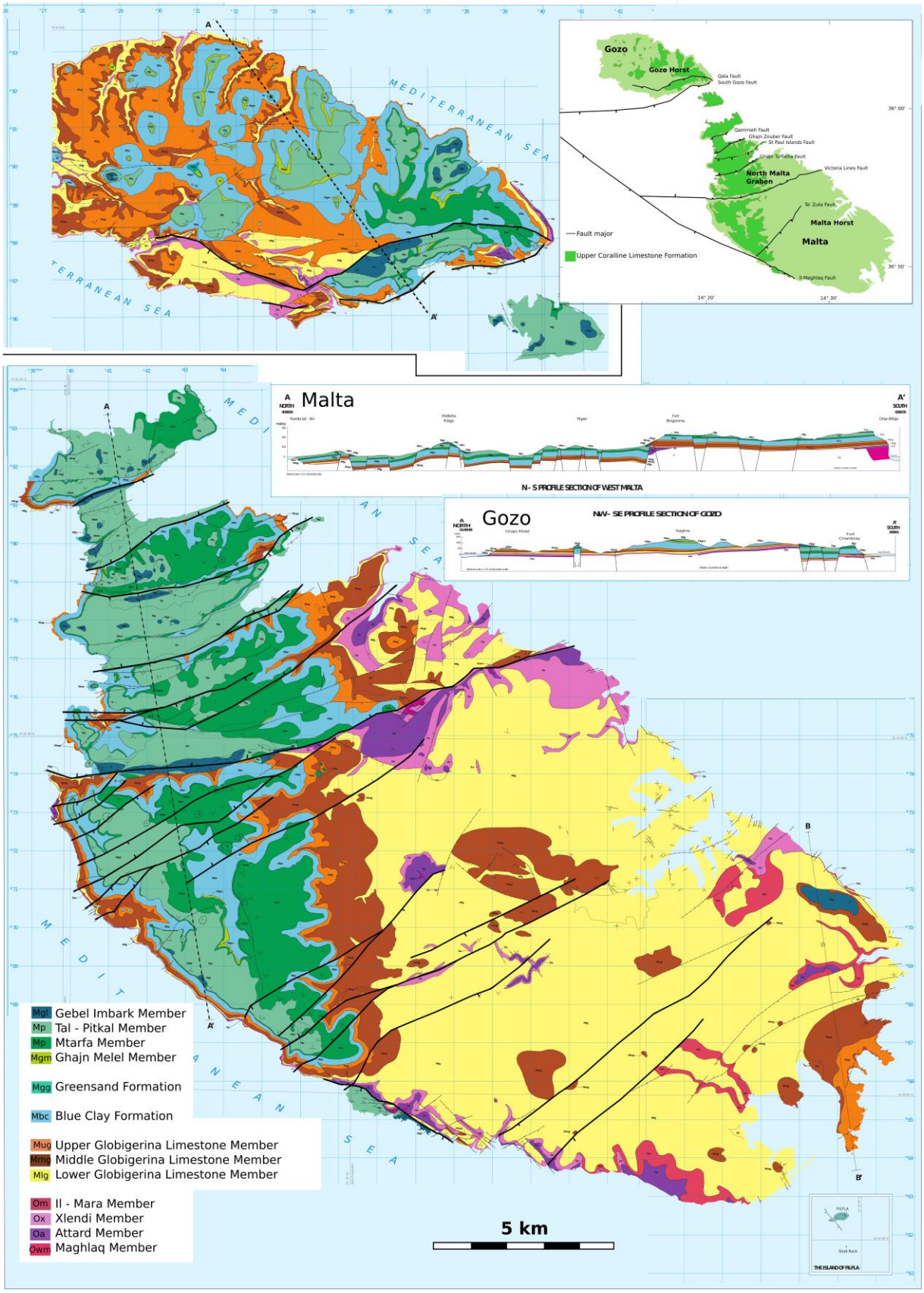

Figure 2.3: Geological Map of the Maltese Islands. (Modified from Pedley et al., 1993).

2.2.1.3. Tectono-stratigraphic evolution of the Maltese grabens

Four tectono-stratigraphic phases have been recognized that are coeval throughout the graben system. (i) Pre-rift (>21 Ma), (ii) early syn-rift (21 to 6 Ma), (iii) late syn-rift (<5 Ma) and (iv) post-rift (probably <1.5 Ma) (Dart, 1991; Dart *et al.,* 1993; figure 2.4). Rifts significantly influenced sedimentary deposition from the early Miocene to the present day in the central Mediterranean Pelagian Platform (Dart *et al.,* 1993)(figure 2.4). Early syn-rift strata occurred throughout the Miocene and led to minor extension and fault-related thickness variations in hangingwall depocentres (Illies 1980; Bosence & Pedley 1982; Pedley 1987). The Plio-Quaternary was the most active period of extension on both fault trends (Finetti 1984; Jongsma *et al.,* 1985) and the Plio-Quaternary succession demonstrates significant fault-related thickness variations.

2.2.1.3.1. Pre-rift phase

Lower Coralline Limestone Formation platform carbonates and Lower Globigerina Limestone Member pelagic carbonates comprise the pre-rift strata of the Maltese Islands (figure 2.4). These deposits are characterized by parallel stratal geometries, have facies architectures that show no relationship to fault traces, and show no fault-related thickness changes. The Lower Globigerina Limestone Member is capped by a submarine hardground, the C1 phosphate conglomerate bed (Pedley, 1974). Neptunian dykes cut the C1 and mark the onset of the early syn-rift phase (Dart *et al.,* 1993).

2.2.1.3.2. Early syn-rift phase

Maltese early syn-rift strata include the Middle and Upper Globigerina Limestone Members, Blue Clay Fm, Greensand Fm, and parts of the UCL Formation (figure 2.4) (Dart *et al.,* 1993). Deposits accumulating during this phase are typified by minor fault-related thickness variations, and minimal fault-related bathymetric relief that may have influenced facies distribution. Local tectonic processes did not erase evidence of unconformities and sedimentary hiati, produced by regional base-level changes, which are preserved in both uplifted and downthrown fault blocks (Dart *et al.,* 1993).

- Upper Coralline Limestone Formation

Dart (1991) suggests that the coralline algal biostrome facies (Bosence & Pedley, 1982) and the coral and algal patch-reef facies (Pedley, 1987b) were formed during the early syn-rift phase. These facies are arranged in a N-S oriented facies belt that is sub-perpendicular to the faults of ENE-WSW-trending North Malta Graben (figure 2.7) (Dart *et al.,* 1993).

The Victoria Lines Fault (VLF) disrupts the Coralline algal biostrome (Bosence & Pedley 1982;

Pedley 1987; Dart 1991; figure 2.4). In the VLF hangingwall depressions a thin succession of algal marl facies were deposited while in the VLF footwall high, an up to 10 m thicker higher energy algal debris succession accumulated (Dart, 1991). The bathymetric relief that led to the partitioning of the Coralline algal biostrome facies is not thought to have been significant. This is since the overlying shallow water (<10 m) patch reef facies (depositional sequence 2) occur on both the footwall and hanging-wall of the VLF (Dart, 1991). Isopach analysis (Bosence & Pedley, 1982) suggests that within the North Malta Graben other faults may also have been active at this time. In SW Malta the Gebel Mtarfa beds (sheltered shelf facies) of depositional sequence 2 thickens from the footwall to the hangingwall (12 to 35 m) of the Il-Maghlaq Fault (Dart, 1991).

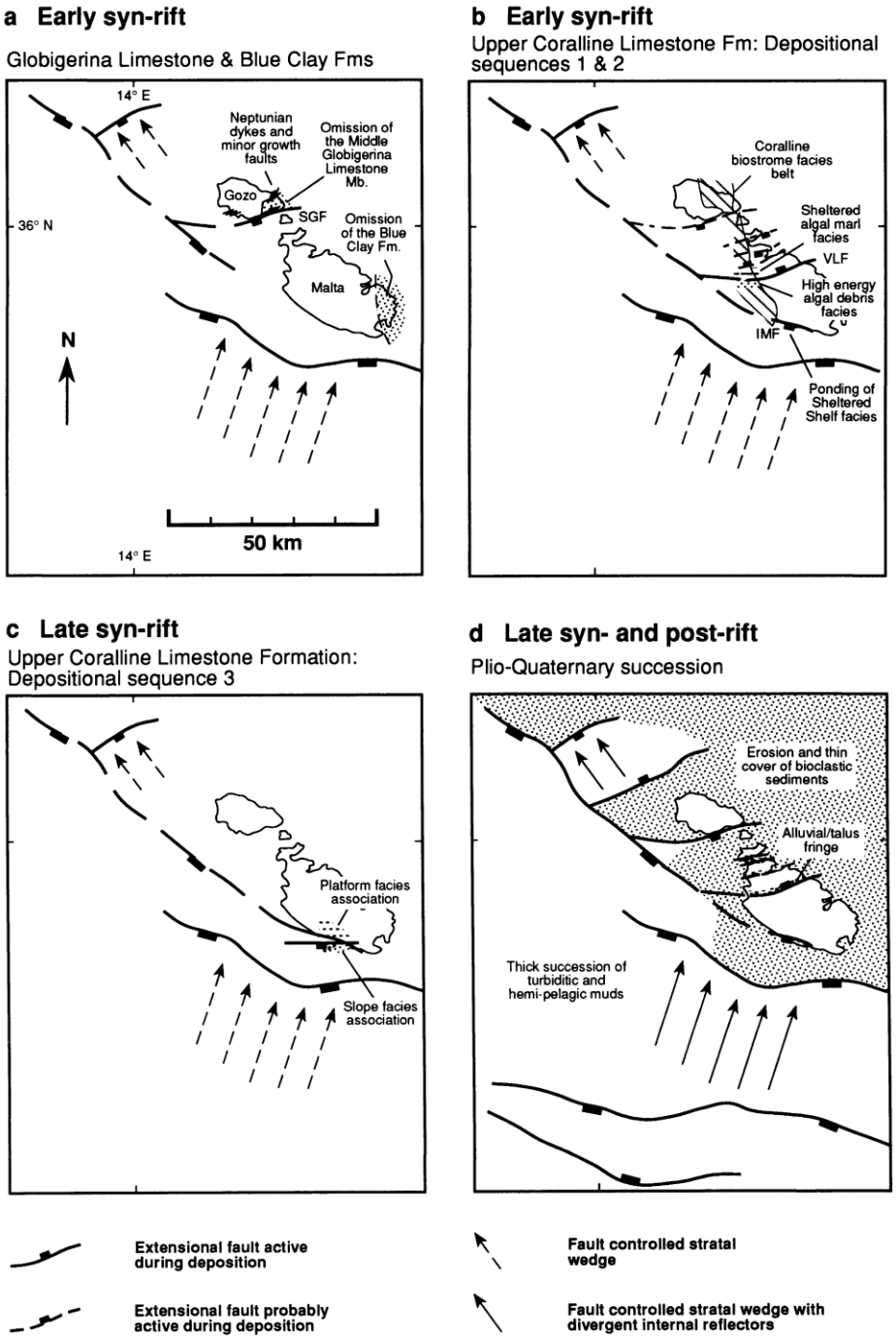

Figure 2.4: Series of palaeogeographic and palaeotectonic summaries for the Maltese graben system. Data sources include Dart (1991), Pratt (1990) and Bosence & Pedley (1982). Ornament indicates areal extent of features described in the text. (a) Distribution of early syn-rift fault-related thickness variations and neptunian dykes from the Aquitanian to Tortonian. SGF, South Gozo Fault. (b) Distribution of early syn-rift fault-related facies distributions and thickness variations during the early Messinian. VLF, Victoria Lines Fault; IMF, I1 Maghlaq Fault. (e) Distribution of late syn-rift fault-related facies distributions and thickness variations during the late Messinian. RHF, Ras Hanzir Fault. (d) Distribution of late syn-rift to post-rift fault-related facies distributions and thickness variations during the Plio-Quaternary. (From Dart *et al.,* 1993).

2.2.1.4. Kinematic evolution

The kinematic evolution of the Maltese graben system can most simply be explained by a single phase of N-S orientated extension, which resulted in the formation of two distinct fault trends (Dart, 1991; Dart *et al.,* 1993). Three different kinematic models propose a mechanism for the formation of the Pantelleria Rift (Jongsma *et al.,* 1987; Grasso & Reuther, 1988; Argnani, 1990). Argnani (1990) proposed that the N-S oriented foreland extension in the region of the Pantelleria Rift that is coeval and causally related to back-arc extension in the Tyrrhenian Sea, and compression in the Apennine- Maghrebian thrust belt. A N-S-trending transfer fault (Separation Belt) lies between the Pantelleria and Linosa Troughs (figure 2.5) characterized by a line of volcanic centres and localized basins and uplifts. The kinematic evolution of the Maltese graben system derived by Dart (1991 in Dart *et al.,* 1993) strongly support this model. The N-S extension direction data from Malta fit well, and the model does not require the influence of substantial strike-slip motions, for which there is no evidence in the Maltese region.

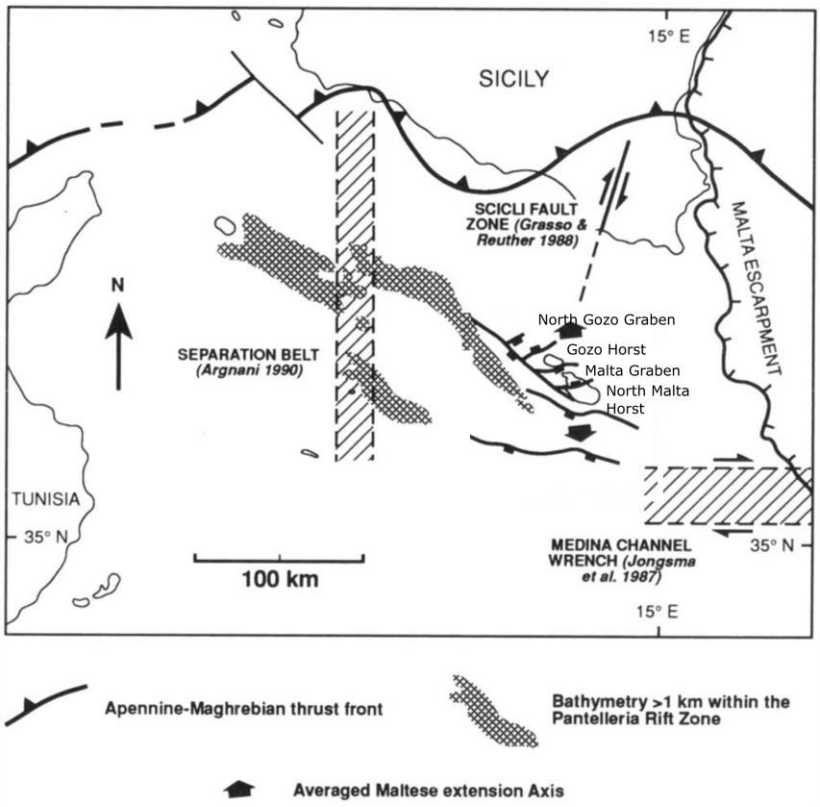

Figure 2.5: Kinematic evolution of the Maltese graben system and Pantelleria Rift. Location of Medina Channel Wrench after Jongsma *et al.,* (1987), location of the Scicli fault zone after Grasso & Reuther (1988), location of the Separation Belt transform zone after Argnani (1990). The kinematic evolution of the Maltese graben system derived from this study is consistent with the orientation of Argnanis separation transfer belt. Modified from Dart *et al.,* 1993.

2.2.2. Sedimentological evolution of the Maltese Islands

The Maltese Islands display an Oligo-Miocene stratigraphy (figure 2.6) up to 450m thick, unconformably capped by thin Quaternary calcretes, lacustrine, alluvial and raised beach deposits (Pedley, 1976; Rose, 1985). The Oligo-Miocene succession is underlain by Oligocene to Cretaceous, Jurassic and Triassic shallow water limestones and dolomites (Dart, 1991).

Since the Eocene, Malta has been situated a few 100 km northeast of exposed land with a clastic sediment fringe in what is present-day Tunisia. A shallow carbonate platform environment dominated in the Maltese area in the Eocene and Oligocene with deeper waters to the west, and probably also to the east. During the early to mid Miocene deeper waters prevailed accumulating pelagic carbonate facies (and some deep water clays) but shallow carbonate environments returned in the late Miocene. Since the late Miocene the Maltese Islands and surrounding areas have been intermittently exposed following the sea level draw-down associated with Messinian desiccation of the Mediterranean (Pedley, 1974; Dart, 1991 see table 6.1 samples (4)). No Pliocene strata are recorded from the Islands, implying uplift prior to this period. At present, the Islands have a maximum elevation of 272 m above sea level in western Malta.

Since the 20th century, successions of authors have described the outcropping Oligo-Miocene succession in the Maltese Islands with increasing detail (Murray, 1980; Roman & Roger, 1939; House *et al.,* 1961; Pedley, 1975, 1976; Zammit-Maempel, 1977; Bosence *et al.,* 1985; Pedley, 1987; Bosence, 1990; Dart, 1991, 1993; Gatt, 2012). The carbonate stratigraphy has been furmally divided into five formations (Pedley, 1976): the basal Lower Coralline Limestone Formation, Globigerina Limestone Formation, Blue Clay Formation, Greensand Formation and UCL Formation (figure 2.6).

Iaccareno & Salvatorini (1982) erect biostratigraphic zonations for the Maltese onshore succession on the basis of foraminifera. The stratigraphic subdivisions (figure 2.6) have been tied to Strontium isotope dates (Jacobs *et al.,* 1996; Follmi *et al.,* 1994). The following ages have been attributed to the Maltese succession; Chattian age (> 24.5 Ma) for the Lower Coralline Limestone Formation, an Aquitanian to Langhian (24.5-15 Ma) age for the Globigerina Limestones, a Serravalian (15-11.5 Ma) for the Blue Clay and a Tortonian age for the Greensand Fm and the lower part of the UCL Formation.

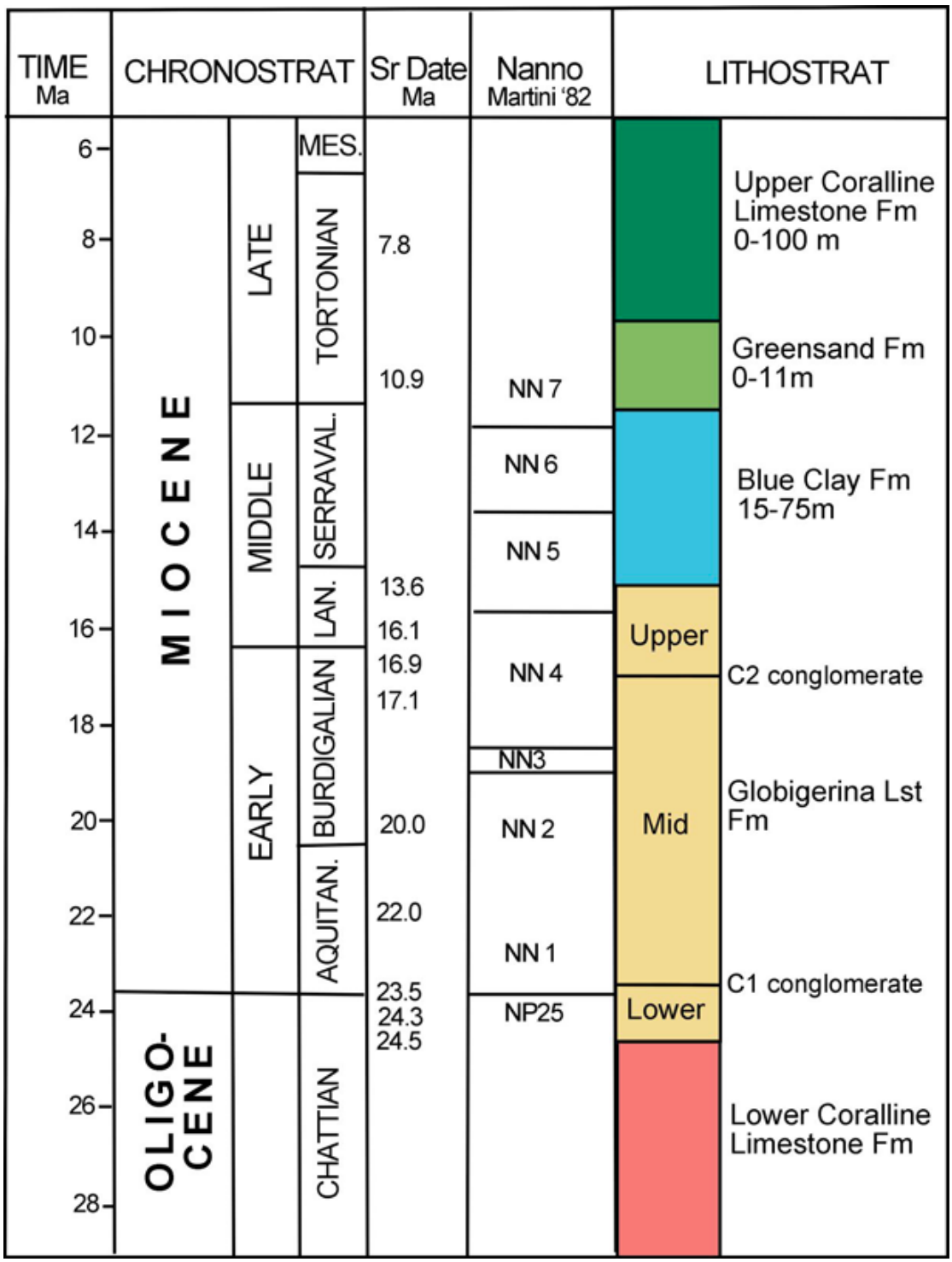

Figure 2.6: Stratigraphic subdivisions and biostratigraphic and chemostratigraphic ages for the Oligo-Miocene of Malta and Gozo (after Pedley, 1978; Pedley et al., 1993; Jacobs *et al.,* 1996; Follmi *et al*, 2008).

The below review is largely based on the formal terminology described by Pedley (1974; 1975; 1978; 1979). The more recent facies names (Bosence & Pedley, 1982; Dart, 1991) for deposits observed within the UCL Formation are also described.

2.2.2.1. Lower Coralline Limestone Formation

At the base of the exposed succession is the Lower Coralline Limestone Formation that is subdivided into four members (Pedley, 1975; 1978) (figure 2.3). It consists of at least 140 m of shallow water limestones that are capped by a hardground surface (Felix, 1973; Bennett *et al.,* 1979; Pratt, 1990). The Formation is characterised by N-S striking facies belts on an easterly sloping carbonate ramp succession. The facies show the development of several common Neogene ramp facies (Buxton & Pedley, 1989). Gatt & Gluyas (2012) subdivide the Lower Coralline Limestone Formation into eight facies associations. The facies consist of carbonate grains of coral, coralline red algae and large benthic foraminifera that dominated some units.

The formation is interpreted as having been deposited within a transgressive shallow water (<40 m) carbonate sequence (Bennett *et al.,* 1979; 1980). The formation passes upwards from the near shore lagoonal Maghlaq Member (oldest), via the Attard and Xlendi Members, to outer ramp Il-Mara Member (youngest) (Pedley, 1978). The thickest accumulation of the Il-Mara Member is developed in the east, which suggests deeper water invaded from the east (Pedley, 1978).

Facies of the Maghlaq and Attard Members are indicative of inner ramp (Buxton & Pedley, 1989) or near-shore lagoonal setting (water depths of 5 to 40 m). The inner ramp is characterised by a broad rhodolitic algal sequence (Attard Member) containing an easterly facing, north-south belt of patch-reefs. This is preserved in the westernmost outcrops of western Malta and Gozo. Facies of the Xlendi Member are thought to have been deposited in turbulent shallow marine sand shoal environments (water depths < 5 m). Deposits of the Il-Mara Member, considered to be laterally equivalent to the Xlendi Member (Pedley, 1975; 1978), suggest an outer ramp (Buxton & Pedley, 1989) or fore-reef environment (water depths 5 to 20 m) (Chalis, 1980). The deeper water (outer ramp) Il-Mara Member consists of finer-grained wackestones and packstones and occurs to the east of the patch reef and rhodolith facies.

2.2.2.2. Globigerina Limestone Formation

The Globigerina Limestone Formation consists of massively bedded, yellow and grey foraminiferal wackestones and white coccolith-rich carbonate mudstones. These deposits indicate pelagic deposition in an outer shelf environment. The Formation has been subdivided into three members (Lower, Middle and Upper) that are separated by two thin and laterally

persistent phosphatic conglomerates (Wigglesworth, 1964; Pedley, 1974, 1976) (figure 2.3). The facies of the Lower Globigerina Limestone indicate shallow sub-tidal environments (water depths 10 to 75 m) (Pratt, 1990), the Middle Globigerina Limestone suggest deposition in deep pelagic waters (water depths 250 to 750 m) (Bennett *et al.,* 1979; Berger & Winterer, 1974), while the echinoid biofacies of the Upper Globigerina Limestone suggest water depths of 140 to 250 m (Chalis, 1979; Bennett *et al.,* 1979; Pratt, 1990). The Formation demonstrates significant thickness variations with a minimum thickness of 20 to 25 m in eastern Gozo (Wigglesworth, 1964; Felix, 1973; Pedley, 1976) and an estimated maximum thickness of 207 m (Felix, 1973) in eastern Malta (Pedley, 1976).

2.2.2.3. Blue Clay Formation

The Blue Clay Formation overlies the Upper Globigerina Limestone Member with a narrow 1 m transition in western Malta and throughout Gozo (figure 2.3). The deposits are interpreted as having been formed in an open marine environment (<400 m water depth) although water depths become shallower in the upper 15 m (Chalis, 1979). The Formation is found throughout Gozo and western Malta and overlies the Upper Globigerina Limestone Member with a thin transitional contact. The Formation exhibits considerable thickness variations (0 to 75 m). In western Malta, the upper boundary. that underlies the Greensand and UCL Formations, is a slight angular unconformity. In eastern Malta, the Blue Clay Formation has been eroded in its entirety and the UCL Formation rests disconformably on the Globigerina Limestone.

The shift from Globigerina Limestone to Blue Clay Formations was the result of an abrupt shift from clay-rich carbonate slope system (middle Miocene) toward clay-dominated marls (*circa* 13 Ma). John *et al.* (2003) suggest that the deposition of the Blue Clay Formation was largely the result of global climate change and an associated change in the rate of continental weathering. Marl deposition persisted until the Tortonian (*circa* 12 Ma) after which shallow water carbonate ramp was re-established. John *et al.* (2003) suggest that a regional increase in rainfall during cooler periods increased continental weathering and runoff from the North African Margin.

2.2.2.4. Greensand Formation

The Greensand Formation is commonly less than 1 m thick except in syn-depositional depressions of western Gozo where the deposits can be up to 11 m thick (Pedley, 1978) (figure 2.3). At the type section (Il-Gelmus 36.048058, 14.233351) (figure 2.3), the il-Gelmus Beds of this formation consist of massive-bedded, friable, greyish-green, marly sediment. Petrographic analysis of the il-Gelmus Beds shows that the beds consist of bioturbated, friable, marly lithoclastic and bioclastic sediments (Pedley, 1978).

At Il-Gelmus, the Greensand strata develop a transitional basal contact with the Blue Clay and a sharp upper contact with the overlying UCL Formation (Pedley, 1978). Elsewhere in east Gozo and throughout Malta, the Greensand Formation has a sharp basal contact with the Blue Clay. West of a line from Marsalforn (Gozo) to Mgarr ix-Xini (Gozo), there is an extensive disconformity between the Greensand Formation and the overlying Ghajn Melel Member of the UCL Formation (Pedley, 1978). This is most pronounced in western areas of Gozo, where a significant portion of the Il-Gelmus Beds and an upper part of the Blue Clay Formation were eroded before the Ghajn Melel Member was deposited (Pedley, 1978). Giannelli & Salvatorini (1975) argue that the hiatus is marked by an absence of zones NI6 and Nl7 of Blow (1969). Pedley (1978) refers to this hiatus as the basal Upper Coralline Limestone erosion surface. At Qolla s-Safra (36.073379, 14.254869) and Tas-Salvatur (36.066425, 14.254395) (Gozo) (figure 2.3), the Qolla s-Safra Beds are preserved below the basal UCL Formation. These beds lie conformably above the Il-Gelmus Beds are preserved due to pre-erosional downwarping along the eastern margin of the northern Greensand basin (Pedley, 1978).

2.2.2.5. UCL Formation

The analysis of the relatively shallow-marine carbonate UCL Formation forms a significant part of the work presented in this thesis (chapters 5 and 6). The subdivision of the 104 m thick formation has primarily been achieved by the recognition of many facies changes and the establishment of a formal lithostratigraphy (Pedley, 1978). The following account gives a lithostratigraphic division for the whole Islands based principally on three key sources Pedley (1974; 1975; 1987), Bosence & Pedley (1982) and Dart (1991).

Pedley describes lithologies observed across the Maltese Islands and divides the formation into four members and twelve beds (Pedley, 1975; 1987) (table 2.2). Bosence & Pedley (1982) describe lithologies and stratigraphic units associated with the Coralline algal biostrome and distinguish six facies. Dart (1991) describes lithologies encountered in the Fomm ir-Rih (35.898059, 14.334623) and Il-Maghlaq (35.830087, 14.419002) areas (Dart, 1991 p.219). Dart divides the outcropping formation into three genetic sequences (Dart, 1991 p.220; figure 2.11 and table 5.4). Each genetic sequence comprises a series of genetically related facies bounded by significant, rapid and laterally continuous facies change, or an unconformity and its time equivalent surface (Dart, 1991 p.220). This new sequence stratigraphic scheme interprets the facies in terms of their presumed environment of deposition. Most of the genetic sequences and facies defined by Dart (1991) are equivalent, or related, to Pedley's (1978) lithostratigraphic scheme. A stratigraphic comparison table (tables 2.2, 5.4) has been developed that indicates which depositional units presented by the different authors correspond to each other.

Spratt (1843)	**Murray (1890)**	**Wigglesworth (1964)**	**Pedley (1974; 1975; 1978; 1979) Lithostratigraphy**	**Bosence & Pedley (1982)**	**Dart (1991) GS: Genetic Sequence**	
Upper Limestone, Coarse Grained Sandstone	Upper Coralline Limestone	Upper Coralline Limestone	UCL Fm, Tal- Pitkal Member, Ghar Lapsi Beds	*Not assessed in study*	GS3: Slope Facies Association (Dart, 1991 p.241)	Reef Talus Facies (RT)
						Proximal Calciturbidite Facies (PT)
						Distal Calciturbidite Facies (DT)
						Evaporite Solution Breccia Facies (ES)
					GS3: Platform Facies Association (Dart, 1991 p.236)	Sand Shoal Facies (SS)
						Inter Sand Shoal Facies (IS)
						Organ Pipe *Porites* Reef Facies (OP)
Upper Limestone, White Rubbly Sandstone			UCL Fm, Gebel Imbark Member, Gebel Imbark Beds		GS2: Peritidal Facies (PE) (Dart, 1991 p.264)	
			UCL Fm, Gebel Imbark Member, Tat-Tomna Beds		GS2: Sand Shoal Facies (SS) (Dart, 1991 p.262)	

Upper Limestone, White or Grey-Brown Bed			UCL Fm, Tal- Pitkal Member, Ghadira beds			GS2: Proximal Reef Slope Facies (PR) (Dart, 1991 pp.232, 262)	
			UCL Fm, Tal- Pitkal Member, Depiru Beds (Dart, 1991 pp260)			GS 2: Coralgal Barrier Reef Facies (BR) (Dart suggests the Facies is previously un-described in literature in Dart, 1991 pp229. In this study it is proposed that these Facies are similar to Pedley's Depiru Beds)	
			UCL Fm, Tal- Pitkal Member, Tal Pictal Beds			GS2: Coralgal Patch Reef Facies (PR) (Dart, 1991 p.260)	
Upper Limestone, Red Coralline stratum			UCL Fm, Mtarfa Member, Gebel Mtarfa Beds	Gebel Mtarfa Beds		GS 1: Open Shelf Sand Facies (OShS) (Dart, 1991 p.227)	
			UCL Fm, Mtarfa Member, Rdum il-Hmar Beds	*Not assessed in study*		(?) GS2: Sheltered Shelf Facies (ShS) (Dart, 1991 p.232)	
			UCL Fm, Tal-Pitkal Member, Rabat Plateau Beds	Coralline Algal Biostrome	Algal Crust Packstone Facies	GS1: Coralline Algal Biostrome (Dart, 1991	Coralline Algal Debris Facies (AD)
					Algal Branch		

					Packstone Facies	p.226)	
			UCL Fm, Mtarfa Member, Coralline Algal Bioherm		Crustose Pavement Facies		Coralline Algal Pavement Facies (CP)
					Rhodolith Pavement Facies		
					Crustose Algal Wackestone Facies		Coralline Algal Marl Facies (AM)
					Crustose Algal Marl Facies		
					Considered as Ghajn Znuber Beds (below)		*Considered as Sand Ridge Facies (below)*
		Greensand *Note: Wigglesworth (1964) incorporates the Greensand Formation and overlying light*	UCL Fm, Ghajn Melel Member, Zebbug Beds	Zebbug Beds		Zebbug Beds	
			UCL Fm, Ghajn Melel Member, Ghajn Znuber Beds	Ghajn Znuber Beds		GS1: Sand Ridge Facies (SR) (Dart, 1991 p.221)	
			Greensand Formation	Greensand Formation		Greensand Formation	

Blue Clay	(Murray's (1890) Greensand is a sub-division of Blue Clay Formation)	Greensand	*brown biosparites (Pedley's Ghajn Melel Member) within the Upper Coralline Limestone Formation (Pedley, 1974 p.78)*			
	Blue Clay	Blue Clay	Blue Clay	Blue Clay Formation	Blue Clay Formation	Blue Clay Formation

Table 2.2: Stratigraphic chart indicating history of stratigraphic divisions of the Upper Coralline Limestone.

2.2.2.5.1. Ghajn Melel Member (Pedley ,1974)

Previous authors included the strata of the Ghajn Melel Member as part of the Greensand Formation. Pedley (1978) identifies that the member overlies his basal "*Upper Coralline Limestone erosion surface"* and in view of this, the member was included within the UCL Formation. The member consists of the Ghajn Znuber Beds in the east and the Zebbug Beds (previously Ghajn Melel Beds) in the west.

The division of this member is partly based on the different faunas they contain. More certain evidence for the subdivision is from their respective petrologies (Pedley, 1978). The Zebbug Beds contain un-abraded and un-mineralised *Heterostegina* foraminifera. The Ghajn Znuber Beds contain 40 to 60% derived glauconite, limonitic lithoclasts and *Heterostegina* fragments that were impregnated by goethite prior to fragmentation and transportation. This subdivision of the Ghajn Melel Member is not recognised on the current geological map of Malta (figure 2.3).

2.2.2.5.1.A. Ghajn Melel Member, Zebbug Beds

The Zebbug Beds consist of ginger to yellowish-brown coloured, thickly bedded, biomicrites and biosparites that are occasionally rich in *Heterostegina* (Pedley, 1978). In outcrop, the strata comprise thickly bedded, rubbly weathering limestones (Pedley, 1978). Up to 80% of the contained material consists of unabraded *Heterostegina*. The beds attain their greatest thickness in western Gozo (16 m at Zebbug) where they overlie truncated or rest unconformably upon the Greensand and Blue Clay Formations (Pedley, 1978). In Malta, the beds are represented by a few centimetres of *Heterostegina* rich sediment at Ta' Lippija (Mgarr, Malta) (figure 2.7). The beds are thought to have formed in quiet marine conditions with waters depths of less than 50 m (Pedley, 1978). This interpretation is supported by the original micritic nature of the sediments and the benthonic foraminifera.

2.2.2.5.1.B. Ghajn Melel Member, Ghajn Znuber Beds

The Ghajn Znuber Beds consist of massive-bedded, dark brown, bioturbated, medium to coarse-grained foraminiferal packstones and grainstones (biosparrudite) composed of limonitic lithoclasts, Heterostegina fragments and allogenic glauconite (Greensand) at their base (Pedley, 1974, 1978; Bosence & Pedley, 1982; Dart, 1991). Macrofauna are well developed and include echinoids, oysters and bryozoan colonies (Pedley, 1978; Bosence & Pedley, 1982; Dart, 1991). Faunas are dominantly thick shelled and frequently reworked and bored (Bosence & Pedley, 1982) and rhodoliths are present near the top of the sand waves (Bosence & Pedley, 1982). The bed corresponds to Dart's (1991) Sand Ridge Facies (Genetic Sequence 1).

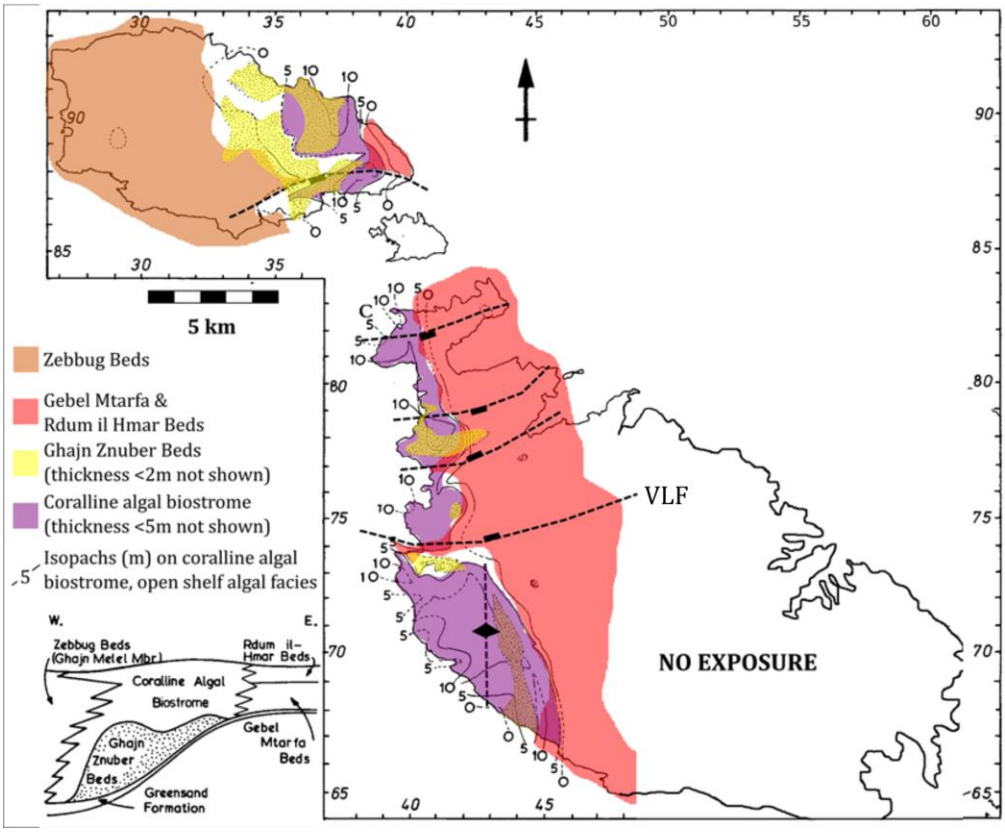

Figure 2.7: Geological distribution of the Ghajn Melel Member and Mtarfa Members for the onshore UCL Formation. Facies distributions from Bosence & Pedley (1982) and Pedley (1990). Biostrome isopachs superimposed on distribution of Ghajn Znuher Beds (modified from Bosence & Pedley, 1982). Sedimentary analysis conducted as part of Dart (1991) thesis confirms that the Victoria Lines Fault (VLF) was active during the deposition of the Coralline Algal Biostrome (modified from Dart, 1991).

The Ghajn Znuber Beds overlie the Blue Clay with a sharp basal contact (Pedley, 1978). In western areas of Malta and eastern Gozo, the beds frequently underlie the Coralline Algal Biostrome (Pedley, 1978; Bosence & Pedley, 1982; Dart, 1991). In Gozo, the Ghajn Znuber Beds generally lie to the east of the Zebbug Beds where they occur along the cliffs that extend from Mgarr harbour north-eastwards towards Qala (Pedley, 1978). Here the beds overlie Greensand and underlie the Coralline Algal Biostrome. A similar situation is also seen throughout western Malta where the Ghajn Znuber beds either form east-west oriented ridges (type locality), or are restricted to a north-south ridge-like structure (extends beneath Dingli Cliffs) (Pedley, 1978) (figure 2.7).

Distribution of the thinnest beds is patchy, however, the beds occur as NNSE-SSW or N-S ridges that vary in amplitude from 4 to 13 m (Pedley, 1975; 1978; Bosence & Pedley, 1982). Dart (1991) indicates that the Sand Ridge Facies (comparable to the Ghajn Znuber Beds) can form 1km wide 15m amplitude N-S oriented ridges in the west of Malta (figure 2.7). Dart (1991) also recognises an east-west ridge parallel to the Victoria Lines Fault. Dart (1991 p.266)

suggests that the east-west oriented sand ridge was controlled by syn-depositional extensional tectonism of the Victoria Lines Fault and resulting RSL change.

Pedley (1978) proposes that the Ghajn Znuber Bed was deposited as elongate linear, sublittoral sand ridges orientated parallel to a coastline lying to the west of the present islands. This is based on outcrop and isopach trends that indicate the major areas of occurrence are parallel to the erosional areas that are thought to have lain to the west of the islands. Further evidence for the structural high with the depositional areas of the Comino Straits is from Dart *et al.* (1993) who indicates that the Blue Clay Formation thins southward across Gozo (60 to 10 m) and is attenuated on the footwall crest of the South Gozo fault (SGF) (Dart, 1991; Dart *et al.,* 1993).

The coarse grain size, dominance of lithoclastic material and thick-shelled fauna indicate a high-energy environment of deposition (Pedley, 1978). The absence of primary cross-stratification is due to the intense penecontemporaneous bioturbation (Pedley, 1987). Limonitic lithoclasts and goethite impregnated *Heterostegina* fragments are an indication of reworking and slow sedimentation rates. These grains were either reworked from an adjacent shallow water area or formed *in situ* upon the Greensand Formation during a sea level fall (Pedley, 1987; Bosence & Pedley, 1982). Bosence & Pedley (1982) argue that prior to the deposition of the Coralline algal biostrome, the sand waves of the Ghajn Znuber Beds were relatively static structures, subjected occasionally to high-energy conditions. Dart (1991) interprets the facies as having been deposited as a series of high-energy sand waves.

2.2.2.5.2. Mtarfa Member (Pedley, 1974)

The Mtarfa Member consists of the Coralline Algal Biostrome, the Gebel Mtarfa Beds and the Rdum Il-Hmar Beds. The latter two Beds of the Member overlie and lie to the east of the Ghajn Melel Member. The *Terebratula-Aphelesia* Bed is present at the base of the Mtarfa Member and provides a stratigraphic marker horizon at the base of the UCL (Pedley, 1978 pp209) (figure 2.8). The marker horizon is present across the Islands and permits correlation within the member during early stages of accumulation (Pedley, 1976; 1978).

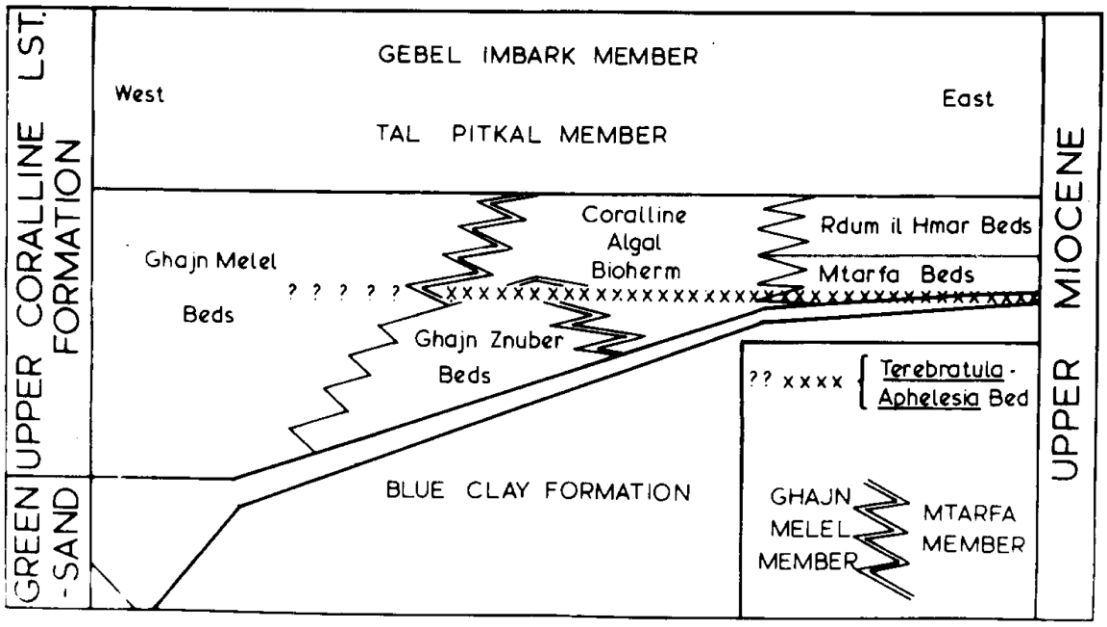

Figure 2.8: Lithostratigraphy of the Basal UCL Formation. (From Pedley, 1976).

2.2.2.5.2.A. Mtarfa Member, Coralline Algal Biostrome (Bosence & Pedley, 1982)

The Coralline Algal Biostrome, originally the Coralline Algal Bioherm of Pedley (1975; 1978), is up to 16 m thick and occurs in a north to south oriented belt, 5 to 6 km wide, that extends throughout eastern Gozo and western Malta (20 km) (Bosence & Pedley, 1982; Pedley, 1987; Pedley, 1990) (figure 2.9). The coralline algal biostrome overlies the Blue Clay and Greensand Formations. Lateral persistence of the facies is poor and correlation is difficult (Bosence & Pedley, 1982). The only biostratigraphic marker bed (*Terebratula-Aphelesia* Bed; Pedley, 1976) indicates that a mosaic of facies existed at any one time during biostrome deposition (Bosence & Pedley, 1976). The Biostrome is interpreted to have formed in an open shelf environment free from terrigenous sediment in water depths of 50 to 60m (Bosence & Pedley, 1982). A study by Pedley (1976) on facies distributions and the form of bryozoan growth suggests easterly-directed current flow.

Bosence & Pedley (1982), Pedley (1987) and Dart (1991) present facies and isopach maps of the Coralline algal biostrome. The authors suggest syn-depositional fault movement within the North Malta Graben (figure 2.3). Evidence of tectonic activity is from the thickened successions in hanging-wall depocentres and thinned successions over footwall highs. Data collected by Dart (1991) across the Victoria Lines Fault indicate that thickened Coralline Algal Biostrome successions accumulated upon footwall highs in areas of better illumination, and hence enhanced algal productivity (Dart, 1991).

Bosence & Pedley (1982) subdivide the Coralline Algal Biostrome into six facies: crustose algal marl, crustose algal wackestone, rhodolith pavement, algal branch packstone, crustose pavement and algal crust packstone (Bosence & Pedley, 1982). Each facies is characterised by different rhodolith morphologies and coralline crusts that are constructed mainly by *Mesophyllum commune*. The *in situ* Crustose algal marl and algal debris wackestone facies, derived from the former facies, are most common in the basal parts of the biostrome particularly in troughs between sand ridges (Bosence & Pedley, 1982). The bulk of the biostrome consists of Rhodolith pavement and Crustose pavement and their derived Algal branch and Algal crust packstone facies. The biostrome is most commonly capped by the Algal branch packstone facies. Dart (1991) simplifies these facies division and combines the crustose algal marl and crustose algal wackestone (Coralline algal marl facies), the rhodolith pavement and crustose pavement (Coralline algal pavement facies), and the algal branch packstone and algal crust packstone facies (Coralline algal debris facies).

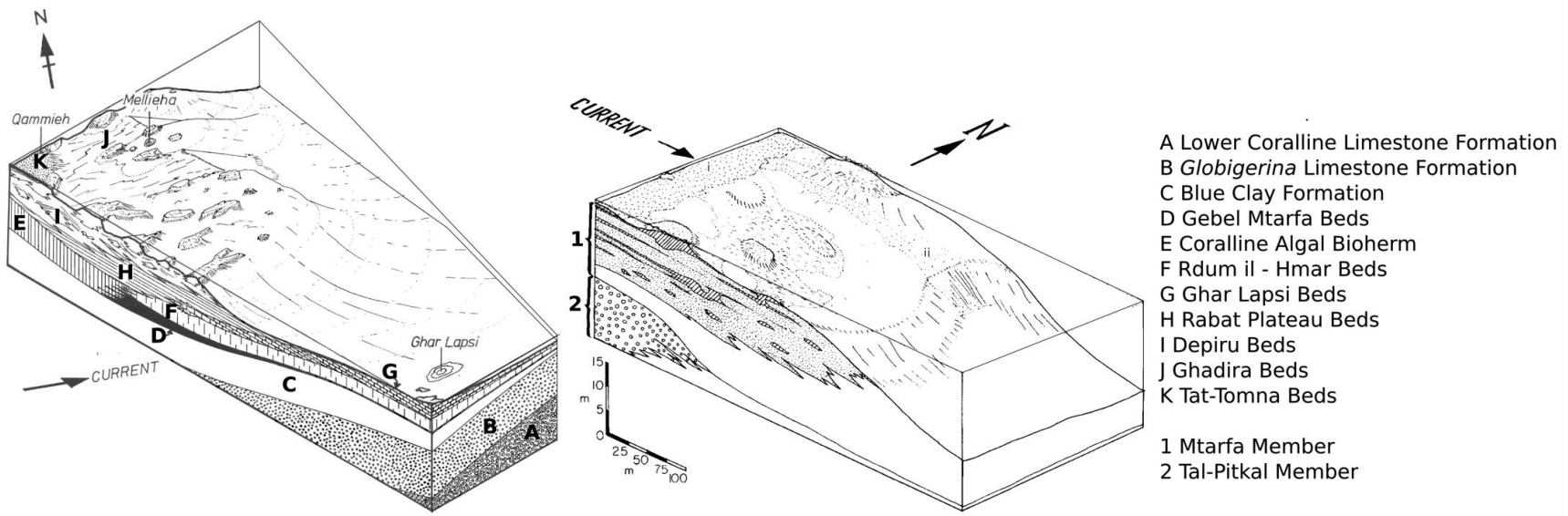

Figure 2.9: 3D block diagrams illustrating the palaeogeography and sedimentological associations of the UCL Formation (modified from Pedley, 1978; Pedley, 1979).

2.2.2.5.2.A.i. Crustose Algal Marl Facies

When present, the facies forms 0.4 to 1.3 m thick units at the base of the coralline algal biostrome. The facies consists of a kaolin-rich pale grey micrite matrix. *In situ* crust growths of *Mesophyllum commune* (Lemoine) and macrofauna occur within the matrix. Common macrofauna include brachiopods, lucinid bivalves, echinoids and bryozoan (Bosence & Pedley, 1982). The marl matrix of the coralline algal marl facies suggests it was deposited in a sheltered setting. Sheltered, low energy environments necessary for the marls and *in situ* biota to accumulate may have been present in troughs between the still forming coarse-grained sand ridges of the Ghajn Znuber facies (Bosence & Pedley, 1982 pp21). The brachiopod and coralline assemblage suggest water depths in excess of 30 to 40 m (Thompson, 1927; Pajaud, 1974; Adey & Boykins, 1982; Bosence & Pedley, 1982).

2.2.2.5.2.A.ii. Algal Debris Wackstone Facies

The facies occurs vertically and laterally adjacent to the Crustose Algal Marl facies. The Algal Debris Wackestone typically infill low-relief erosional channels that truncate into the Crustose algal marls. This wackestone consist of large intraclasts of the Crustose algal marls and contain a higher percentage of coralline algal crusts (40.3%) than the Crustose algal marls (Bosence & Pedley, 1982). These authors suggest that the reworked nature of the sediments, along with the dense branching and size of the corallines indicate that the Algal Debris Wackstone is the higher energy transported counterpart of the Crustose algal marl.

2.2.2.5.2.A.iii. Rhodolith pavement

The Rhodolith pavement facies is the most widespread (both vertically and laterally) of the Coralline Algal Biostrome facies. Rhodoliths occur in their greatest abundance, attain their greatest size (up to 20cm) within this facies. The rhodoliths are predominantly densely branched and spheroidal in shape. *Mesophyllum commune* are the most common coralline. The facies develops alternations of rhodoliths and wackestones as plane beds or cross beds 10 to 30 cm thick and set up to 150 cm thick (Bosence & Pedley, 1982). Large-scale trough cross-stratification and shallow (50 cm) channels are recognised in the alternating rhodolith and wackestone bed. These structures indicate two main current directions: a NNE-SSW bidirectional group and an E-W bidirectional group. The bimodality of each group suggests a tidal influence (Bosence & Pedley, 1982).

The dominance of coralline genera *Mesophyllum* and brachiopod genera suggest medium water depths (greater than those for sea-grass growth) and a tide-swept submarine platform. The large-scale trough cross-bedding and alternations of rhodoliths and wackestone suggests sub-marine dunes. The sequence of branch-lateral growth and laminar growth is a growth response by the

coralline algae to increased turning and apical abrasion following transport (Bosellini & Ginsburg, 1971; Bosence, 1976). The repeated sequences observed within the facies therefore suggests fluctuation (months or possibly years) low and high hydraulic energy during growth of the Rhodolith (Bosence & Pedley, 1982). Bosence & Pedley (1982) interpret the facies as having formed under high hydraulic energy conditions.

2.2.2.5.2.A.iv. Algal Branch Packstone

Bosence & Pedley (1982) describe the facies as massively bedded units composed of coralline algal debris with sparsely distributed small and spheroidal densely branching rhodoliths; the external surfaces of which are commonly abraded (Bosence & Pedley, 1982). Macrofauna are transported. The facies is commonly interbedded with the Rhodolith Pavement facies and frequently forms the final deposit capping the Coralline algal biostrome. The similar composition and close association to the Rhodolith pavement suggests that the Algal Branch Packstone are in part eroded and transported material from the Rhodolith Pavement facies (Bosence & Pedley, 1982). Widespread shallowing in western areas of the Maltese Islands reworked the coralline algae biostrome and generated the coralline algal branch debris beds (Pedley, 1978).

2.2.2.5.2.A.v. Crustose Pavement

The facies is characterised by leafy *in situ Mesophyllum commune* crusts. The crusts commonly bifurcate and re-join that form an *in situ* three-dimensional framework. Bosence & Pedley (1982) observe similarities between the crustose coralline framework and the rhodoliths within the Rhodolith pavement facies. This, the authors argue, suggests that the rhodoliths within the latter facies develop from eroded fragments of the Crustose Pavement. Fragmented and detached framework crusts were developed into rhodoliths; thereby generating the rhodolith pavement (Bosence & Pedley, 1982; Dart, 1991). The crusts are thought to have formed a low-profile, current-swept three dimensional framework with sediment-free surfaces. The absence of relief in the crustose pavement beds and its association with debris and crustose rhodoliths allows comparisons to be drawn with the present-day Mediterranean “Coralligene de Plateau” (Peres, 1967) that occurs in open shelf water depths of 50 to 130 m (Bosence & Pedley, 1982).

2.2.2.5.2.A.vi. Algal Crust Packstone

The facies primarily consists of algal crust debris or yellow micrite containing foraminiferal debris. The facies is commonly interbedded with the Crustose Pavement and frequently overlie it. The similar composition and close association to the Crustose pavement suggests that the Algal Crust Packstone are in part eroded and transported material from the Crustose Pavement facies (Bosence & Pedley, 1982). When the crusts of the crustose pavement were subject to

more turbulent conditions under higher energy levels, crusts were fragmented thereby developing the algal crust packstone facies (Bosence & Pedley, 1982).

2.2.2.5.2.B. Mtarfa Member, Gebel Mtarfa Beds (Pedley, 1974)

Pedley (1975; 1978) describes the strata as a yellow, thickly bedded biomicrite, containing bivalves and occasional echinoids. Dart (1991) considers his Open Shelf Sand Facies (Genetic Sequence 1) to be equivalent to Pedley's (1974) Gebel Mtarfa Beds (Dart, 1991 p.227) and describes the facies as consisting of yellow bioturbated bioclastic fine to coarse-grained packstones and grainstones that are bedded on a 1 to 2 m scale.

The facies occurs throughout eastern Gozo and central Malta, and contains the *Terebratula-Aphelesia* Bed near their base (Pedley, 1975; 1978) (figure 2.8). In Malta, the beds are well developed and extend as a broad belt from the eastern Marfa Ridge southwards throughout the entire outcrop to Gebel Ciantar, at the southern end of the UCL Formation plateau (Pedley, 1987). Pedley (1976; 1987) states that bioclasts are dominated by coralline algal, molluscan and echinoid debris. Thus, it is proposed that the Gebel Mtarfa Beds may be eastern lateral equivalents of the Coralline Algal Biostrome and represent storm and/or current sands reworked eastward of the biostrome (figures 2.8 and 2.9). Bosence & Pedley (1982) and Dart (1991 p.227) argue that field relations demonstrate contemporaneity with the Coralline Algal Biostrome facies.

2.2.2.5.2.C. Mtarfa Member, Rdum il-Hmar Beds

The unit is also the eastern lateral equivalent of the Coralline Algal Biostrome and rests upon and occupies a similar area to the Gebel Mtarfa Beds (figure 2.9). Pedley (1974) describes the beds as white biomicrite containing bivalves and occasional echinoids. Trace fossils include *Thalasinoides*, *Ophiomorpha*, *Lockeia* and *Teichichnus*. Macrofauna and flora are either absent, extremely sparse or patchily distributed and faunas are limited to benthonic foraminifera, small bivalves and *Halimeda* moulds (Pedley, 1974). Depositional textures and ichnofacies were interpreted to indicate deposition on a shallow shelf with water depths no greater than 100 m (Pedley, 1978).

2.2.2.5.3. Tal-Pitkal Member (Pedley, 1974)

Porites and *Montastrea* patch reefs (Depiru Beds) developed in the shallowest western areas (figures 2.3). Pedley (1978; 1979) indicates that material was shed from these western areas eastward into deeper leeward waters via sub-tidal wash-over deltas (Ghadira Beds) (figure 2.9).

Dart (1991) argues that his Coralgal Patch Reef facies is equivalent to Pedley's (1975; 1978; 1979) Depiru Beds (Tal-Piktal Member) and that his Coralgal Barrier Reef Facies were

previously unidentified in the Maltese Islands. Sedimentological descriptions by the two authors suggest that Dart's Coralgal Patch Reef facies are in fact equivalent to Tal-Piktal Beds and his Coralgal Barrier Reef Facies are equivalent to Depiru Beds.

2.2.2.5.3.A. Tal-Pictal Member, Tal-Pictal Beds

At the type locality (Rdum Depiru, near Tal Pitkal) small lensoidal carbonate mounds, containing a high coralline algae and coral component, are developed in the sediments (Pedley, 1974). The facies are described as grey to white massively bedded algal debris packstones that display small caves and vugs up to 50 cm across produced by the dissolution of originally aragonitic *Porites* and *Montastrea* coral colonies (Dart, 1991). Dart (1991) observes this facies in the footwall and hanging-wall successions of the Fomm ir-Rih area. In Malta the beds transitionally succeed the Rabat Plateau Beds and are best developed in western areas of the Islands (Pedley, 1974). The facies records the build up of coral colonies as small patch reefs within bedded platform deposits (Dart, 1991 p.260).

2.2.2.5.3.B. Tal-Piktal Member, Depiru Beds

The Depiru Beds are composed of massive framestones, bindstones, packstones and grainstones containing coralgal bioherms and biostromes (Pedley, 1974; 1975; 1978; 1979). The biostromes are constructed from coralline algae and corals *Porites* and *Tarbellastraea* that are often bored by *Lithophaga* (Pedley, 1974; 1975; 1978; 1979). Dart (1991) describes the facies as being dominated by white coralgal framestones consisting of both *Porites* and *Montastrea* corals. Massive and botryoidal coral morphologies are preserved as moulds. Pedley (1974; 1978) describes the bioherms as having cross-sections up to 32 m long and 4 m high and were formed originally as patch reefs, but probably had relief of no more than 1 to 1.5 m on the sea bed. Dart (1991) observes individual coral colonies that are up to 1 m in diameter and coalescing modern caves that record dissolution of intergrowing frameworks that were more than 6 m in height and 15 m across. Interstices between the coral colonies consist of fine to very coarse-grained bioclastic packstones and grainstones. Peloids, coralline algal and molluscan debris also occur. The Depiru Beds are laterally equivalent to the Ghadira Beds in the west (Dart, 1991 p.60). The Depiru Beds are found above the Rabat Plateau Beds in western Malta and eastern Gozo. In the Il-Maghlaq area, the Coralgal Barrier Reef facies (Dart, 1991) is found where up to 13m thick (Dart, 1991 p.229).

In the il-Maghlaq study area the Barrier reef Facies is bounded to the east by the Proximal Reef Slope Facies of Dart (1991) that is traced across the islands. The close spatial relationship of both facies suggests that the Coralgal Barrier Reef Facies may have formed a north-south oriented barrier (Dart, 1991 p.229) but that in order to determine whether a continuous

framework could be traced northward away from the Il-Maghlaq would require further field study. The significant occurrence of coralgal framework suggests a shallow-water high-energy windward shelf margin environment (Dart, 1991 p.229). Pedley (1978) interprets the deposits as having formed in a shallow-water, high-energy marine environment in water depths of less than 25 m (figure 2.9).

2.2.2.5.3.C. Tal-Piktal Member, Ghadira Beds

The Ghadira Beds (Pedley, 1974) correspond to Dart's (1991) Proximal Reef Slope Facies (Genetic Sequence 2). The deposits consist of fine to granule grade packstones and grainstones. The facies is well bedded on a 20 to 100 cm scale. Bioclasts are well-rounded and include coralline algae, corals and originally aragonitic debris now preserved as mouldic porosity (Pedley, 1978; Dart, 1991) and are similar to the flanking sediments of the Depiru Beds (figure 2.9). The Ghadira Beds may also contain abundant ooliths that are absent from the Depiru Beds. These Ghadira Beds occasionally occur to the east of the Depiru Beds patch reef belt, are up to 30 m thick and display sigmoidal clinoforms with slopes up to 30° that prograde eastwards for a distance of 1 km (Pedley, 1978; Dart, 1991 pp.60, 232).

Pedley (1978; 1979) suggested these beds indicate wash-over, sub-tidal delta from deposition of sediments entering a deep leeward depression, funnelled between adjacent patch reef areas. Dart (1991) interprets these beds as Proximal Reef Slope Facies upon a windward margin. Dart (1991) argues the facies forms part of a N-S belt of fore-reef slope deposits on the eastern margin of a poorly preserved coralgal barrier reef (described in Dart, 1991 p.229).

2.2.2.5.4. Gebel Imbark Member (Pedley, 1974)

Shallowing in western areas continued and the Tat-Tomna Beds were deposited (Pedley, 1978; 1979). The Qammieh Beds were then deposited as the platform became restricted and eventually emergent (Pedley, 1987). In southwest Malta during this period, and possibly also during the deposition of the Tal-Pitkal Member, Pedley (1987) and Dart (1991) indicate that debris flow and turbidite sediments of the Ghar Lapsi Limestones accumulated in a hanging-wall low associated with the NW-SE trending Il-Maghlaq Fault. Emergence then occurs across the Maltese Islands, both on the up-thrown Malta Horst and in the Il-Maghlaq intra platform palaeobasin. This reflects the onset of the regional Messinian salinity crises (Dart, 1991 p.102).

2.2.2.5.4.A. Gebel Imbark Member, Tat-Tomna Bed

In the west of Malta, the Tat-Tomna beds are found with an erosive base above the Depiru Beds (Pedley, 1975; 1978). The beds exhibit small-scale bimodal cross-stratification and are composed of oopelsparites and pelmicrites and pelmicrites (Pedley, 1975; 1978). The beds are equivalent to Dart's (1991 pp.236, 262) Sand Shoal Facies (Genetic Sequence 2). The facies is a

white bioclastic to ooidal fine to very coarse-grained grainstone that sometimes exhibits small-scale bimodal cross stratification. Bioclasts are well rounded and consist of coralline algal, echinoid and indeterminate debris.

Pedley (1978) suggests the Tat-Tomna Beds were deposited in a shallow agitated environment of migrating intertidal sand shoals. Dart (1991) also argues that the cross bedding, coated grains and well-rounded bioclasts observed within the Sand Shoal Facies indicate deposition in a sand shoal environment (tidal shoal and inter shoal sands). Extensive bioturbation and small-scale cross-bedding suggests the sand shoals may have frequently been inactive. This precludes interpretations of high-energy shelf margin environments. Dart observes that the occurrence of sand shoals in association with *Halimeda* implies that water in the back-reef lagoon, or restricted shelf, was probably less than 10 m (certainly <100 m depth). He further suggests that the coarser bioclastic grainstone beds may be interpreted as wash over bodies produced by storm surges cutting through the reef barrier.

2.2.2.5.4.B. Gebel Imbark Member, Qammieh Beds

The Qammieh Beds occur above the Tat-Tomna beds and consist of microsparite, micrite and dolomite (Pedley, 1975; 1978). The Beds correspond to Dart's (1991) Peritidal Facies (Genetic Sequence 2) that he subdivides into three sub-facies. The first sub-facies consists of white bioclastic wackestone, packstones and grainstones. The second consists of pale grey to green clays that display a basal root system and alternate with the first sub-facies. The third terminates the facies and consists of stromatolites composed of laminated domes and broken crusts.
Pedley (1978) interprets the deposits as having formed in a sheltered marine to intertidal mudflat environment. Dart (1991 p.264) interprets the clay interbeds of the second sub-facies as palaeosols. The facies may have been subject to periodic emergence and consolidation of sand shoals with sub-aerial vegetation. Stromatolites and a fauna of restricted diversity suggest high salinities and possibly intertidal conditions just prior to final emergence.

2.2.2.6. Pliocene and Quaternary deposits

Pliocene deposits are absent from the Maltese Islands. The Islands were subject to emergence and erosion starting in the late Messinian and continues to present (Pedley, 1978). Quaternary deposits, consisting of terrestrial deposits, fresh water tufa and raised beaches, form locally on the Islands.

2.2.2.7. Comparison to the Hyblean-Plateau (South East Sicily)

Late Miocene sedimentary patterns observed in the Maltese Upper Coralline Limestone Formation are similar to contemporaneous sediments observed in South East Sicily. In Sicily,

Heterostegina-rich coarse bioclastic packstones, with inferred water depths of about 40m, give way to rhodolithc coralline algal biostromal beds of the Siracusa Limestone Member. Small patch reefs occur in the shallowest eastern zone. These commonly contain scattered *Porites* and *Tarbellastraea* colonies and crustose corallines. Off-reef packstones and grainstones occur westwards of the patch reefs and are often *Halimeda*-rich. Shorewards of the patch reefs lay an outer shoal zone and inner restricted lagoon (Pedley, 1996; Pedley & Grasson, 1992).

The Sicilian deposits can be readily tied to those observed in Malta. The Sicilian *Heterostegina*-rich coarse bioclastic packstones correspond to the Maltese Ghan Melel Member, the rhodolithc coralline algal biostromal beds of the Siracusa Limestone Member correspond to the Maltese Mtarfa Member, the Sicilian patch reefs to the Maltese Tal-Pictal Beds, the Sicilian off-reef packstones and grainstones correspond to the Maltese Ghadira Beds, and the Sicilan outer shoal zone and inner restricted lagoon correspond to the Maltese Tat-Tomna Beds (table 2.2).

Pedley (1996) suggest both regions develop a similar sedimentary pattern since they occur within a similar carbonate ramp setting that provides a setting for coral patch reefs, with the additional important development of coralline algal biostromes immediates basinwards of the lime-mud dominated patch reefs.

2.2.3. Sequence Stratigraphy of the Upper Coralline Limestone, Malta

Dart (1991 p.272) develops the first sequence stratigraphic scheme for some of the outcropping deposits of the Maltese UCL Formation. The scheme is however limited to two study areas, the Il-Maghlaq and the Fomm ir-Rih. Combined, these areas comprise 23% (20 km^2 of 83 km^2) of the outcropping UCL Formation across the Maltese Islands.

Dart divides the vertical succession into three genetic sequences (GS) bounded by four sequence boundaries (SB) (Dart, 1991 p.220) (figure 2.10). Dart (1991 p.272) suggests that the facies of the N-S facies belts of the UCL Formation are developed in response to cyclical variations in RSL (figure 2.10). Dart supports his claim by making reference to facies palaeobathymetry, relative elevations of successive platform facies, thickness of platform facies and stratal geometries. Dart (1991) develops a RSL curve for the Maltese UCL Formation by combining data from the previous literature, and from the Fomm ir-Rih and Il-Maghlaq study areas.

Genetic sequence 1 (GS1)

Before the deposition of the cycle of sea-level change represented by GS1, pelagic sediments of the Blue Clay Formation accumulated in water depths in access of 200 m. At the base of GS1, the Greensand Formation and the Sand Ridge Facies (Ghajn Znuber Beds – Pedley, 1974) sediments record a low stand in sea level. The basal sequence boundary (SB1) is marked by a hiatus and a condensed sequence of Greensand Formation glauconite sands. The overlying

coarse packstones of the Sand Ridge Facies are interpreted as the products of sub-tidal sand waves in, or adjacent to, a shallow shelf area. Both facies therefore indicate a substantial decrease in water depth relative to the Blue Clay Formation. This is evidenced by an increase in current winnowing and a tendency to non-deposition. The Sand Ridge Facies are thus interpreted as a low stand or transgressive deposits. Wackestones and marls of the overlying Coralline Algal Marl (Crustose Algal Wackestone Facies and Crustose Algal Marl Facies – Bosence & Pedley, 1982) indicate a deepening of water following progressive sea-level rise. The overlying succession of Coralline Algal Marl, Coralline Algal Pavement and Coralline Algal Debris sub-facies within the Coralline algal biostrome then suggest shallowing upward conditions.

Genetic sequence 2 (GS2)

Dart (1991 p.275) interprets a sequence boundary (his SB2) between GS1 and GS2. He proposes that SB2 is not marked by a sharp erosion surface, but rather by a regional up sequence increase in the degree of colonisation by coral knobs, patches and barriers. Dart (1991) interprets GS2 as having been deposited in shallower water conditions than GS1. Dart (1991) suggests that coral colonisation of the Coralgal patch reef facies (Tal Pictal Beds – Pedley, 1974) and Barrier Reef Facies (Depiru Beds – Pedley, 1974) (GS2) was limited to western Malta. As RSL rose and peaked, during an interpreted marine transgression and highstand, the coralgal barrier built up and shed debris eastwards, creating prograding sigmoidal clinoforms of the Proximal Reef Slope facies (Ghadira Beds – Pedley, 1974) (GS2). The Coralgal Patch Reef facies pass up-section to Sand Shoal Facies (Tat-Tomna Beds – Pedley, 1974) and Peritidal Facies (Gebel Imbark Beds – Pedley, 1974) of the inner lagoon. This progradation and shallowing of lagoon sediments are interpreted to correspond to the same genetic sequence (GS2) and are thought to reflect a slowing in the rate of RSL rise (figure 2.10). The Peritidal Facies displays several, metre scale, shallowing upwards cycles capped by palaeosols. These may have been formed in response to higher frequency sea level oscillations (possibly 5^{th} or 6^{th} order).

Genetic Sequence 3 (GS3)

GS3 deposits were only recorded by Dart (1991) in the Il-Maghlaq study area in the hangingwall sub-basin of the Il-Maghlaq fault. The onset of GS3 records somewhere in the region of a 40 m of RSL fall to generate the post Peritidal Facies emergence surface that terminated GS2 lagoonal deposition on the Il-Maghlaq fault footwall. Eastern exposures of the Slope Facies Association pass up sequence from Proximal to Distal Calciturbidite Facies. This most probably records up sequence deepening produced by a RSL rise. The Distal Calciturbidite Facies is sharply overlain by, and reworked into, the Evaporite Solution Breccia Facies. Both fore-reef slope erosion and evaporite deposition are indicative of a following RSL fall. This

culminated in the formation of the erosion surface (SB4) that terminated shallow water carbonate deposition across the Maltese Islands and the Malta Platform. Karst formation and meteoric diagenesis associated with SB4 from the Messinian to the present day would have over printed that generated in the lagoonal area of GS2 during the formation of SB3.

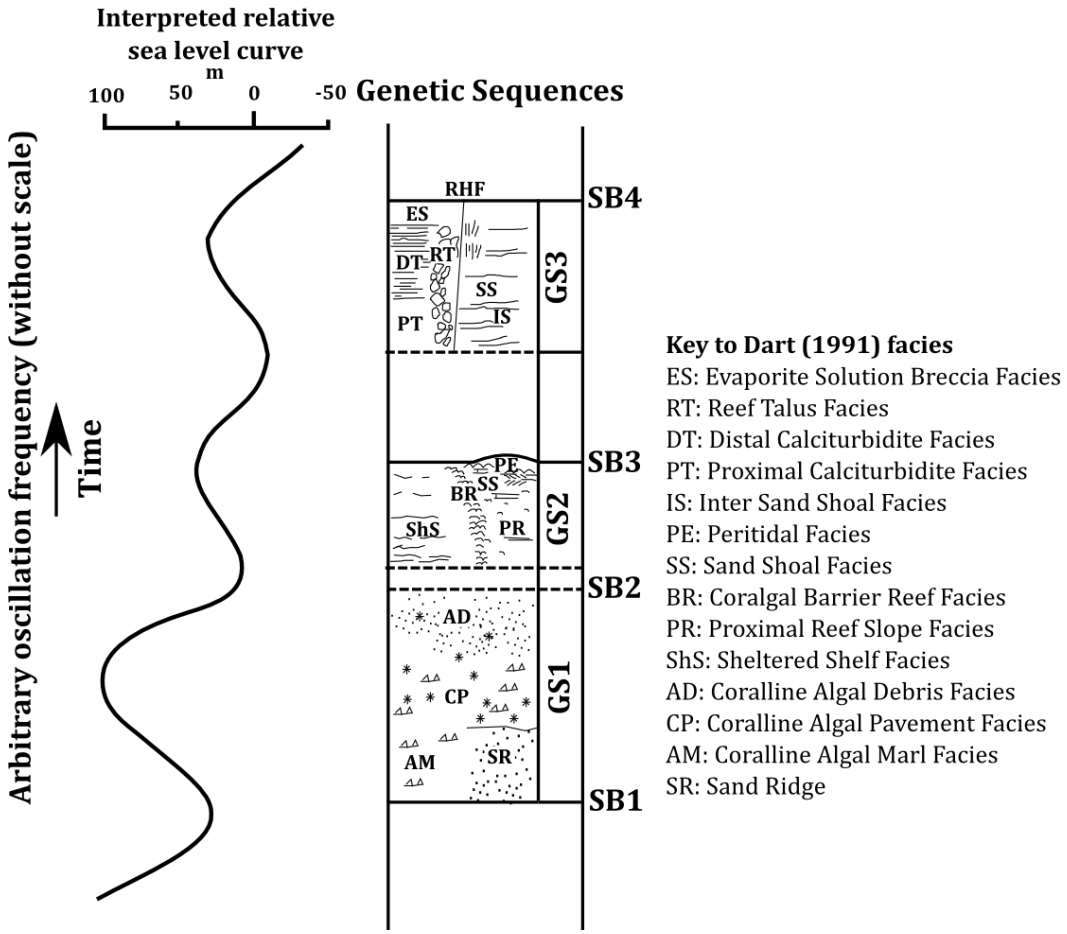

Figure 2.10: Interpreted relative sea level curve derived from palaeobathymetric and stratal geometry data derived from both the Fomm Ir-Rih and Il-Maghlaq study areas. See table 5.4 for facies abbreviations. RHS, Ras Hanzir Fault strand. (Modified from Dart, 1991 p.274). See table 2.2 for facies abbreviations.

2.3. Stratigraphic forward models

2.3.1. Introduction

This section introduces the concept of numerical modelling of carbonate platform evolution. The progress made in simulating platform dynamics in one, two and three-dimensional numerical stratigraphic models is reviewed. The strengths and weaknesses of the approaches followed by these respective models are also assessed. The chapter also provides a description and justification for the use of Dionisos SFM applied in the thesis.

2.3.2. Qualitative conceptual models and quantitative models

In essence, a model is an "*intellectual device for making processes easier to understand*" (Lehr, 1990). Models are used to make predictions that can be tested against observations. Comparisons between model predictions and observations allow scientists to refine the model and improve their understanding of natural processes and relationships.

A model however only represents and replicates aspects of the process that the model developer can observe and describe. A model therefore does not necessarily represent the real processes; rather it represents our understanding and ability to describe the process. Consequently, when testing the validity of a model, one can only prove a model to be incorrect, never correct. A model that consistently and accurately predicts natural processes is a good model. One can however never be certain that a yet unidentified feature of a process cannot produce results that were not predicted by the model.

There are two types of models, qualitative/conceptual and quantitative/mathematical models. Both types of models describe a concept of a process, however they use different languages. Conceptual models use words and/or graphics while quantitative models use equations (figure 2.11). Both types of models are used in geology (Warrlich, 2000).

Paola (2000) argues that quantitative models have several advantages over conceptual models. He observes that quantitative models "*allow us to ask sharper questions, makes our hypotheses less ambiguous and hence easier to test, rules out some apparently plausible explanations and suggests new ones that would never have occurred to our unaided intuition*". Issues of scale and internal consistency also limit conceptual models. These are therefore unable to quantitatively assess how individual or multiple parameters influence platform geometry. In view of these limitations, conceptual models are often insufficient for detailed analysis (Burgess, 2012). Numerical SFM is a more rigorous approach that relies on equations and algorithms that ensure internal consistency. SFM is able to quantify and simulate the physical and biological processes acting over geological time scales to reproduce the morphology and internal structure of

stratigraphic bodies (Watney *et al.,* 1999). In view of this, over the past few decades, the science has matured when describing geological principles. It is shifting from being exclusively qualitative and descriptive to increasingly incorporating quantitative methodologies.

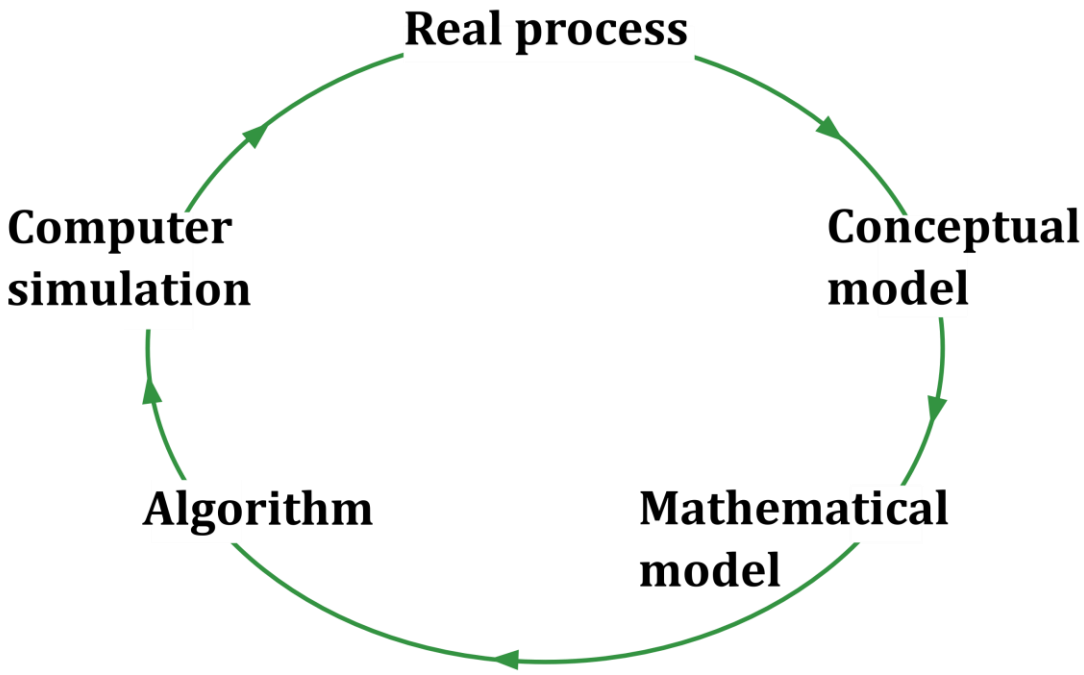

Figure 2.11: The relation between real process and simulating algorithm. (From Warrlich, 2000).

2.3.2.1. Forward models

In many cases, experiments can be developed to assess whether a model adequately simulates a process. In such instances, experiment results are compared to the model predictions. In some cases however, the space and/or time dimension of a process may exceed our observation abilities and a direct experiment is not possible. In such instances a mathematical model must be developed that simulates the effects of the process over unobservable time and/or space dimensions (figure 2.12). The mathematical model is typically run in a computer and the simulated outputs are compared to real results of the modelled process. If the match between the simulation output and real data is sub-optimal, the input parameters and/or numerical model are altered until an optimal match is obtained. This method of testing a model of a process against a process result is called 'forward modelling'. A forward model can therefore be defined as the simulation of product from the known response of a process to a given set of input parameters (Cross, 1999; Watney *et al.,* 1999).

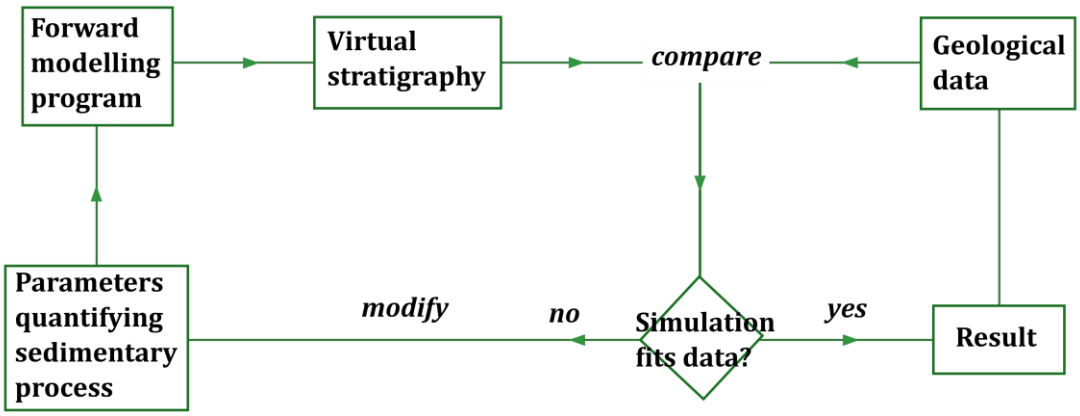

Figure 2.12: The principle of forward modelling explained using the example of stratigraphic simulation. (From Warrlich, 2000).

Computer forward models are often applied in geology to quantitatively investigate and better understand specific processes or the interrelation of a set of processes. Forward models are used since most geological processes take place over time dimensions that cannot be directly observed by humans and unknown portions of the results (strata) are not preserved in the geological record. Forward modelling is applied in various fields in geology, including tectonics, geochemistry and stratigraphy. Forward modelling methods applied to stratigraphy are termed stratigraphic forward models (SFM). SFMs are a quantitative representation of our understanding on how certain Earth-surface systems work (Watney *et al.,* 1999; Paola, 2000). SFM use algorithmic methods to produce synthetic strata based on the simulated tectonic and stratigraphic processes and their rates. Processes that are typically simulated include RSL cycles (subsidence and uplift), sediment supply variations, and various processes of sediment erosion, transport and deposition.

SFMs have some important advantages over qualitative conceptual models used for the same purpose. Even simple rule based forward models are better able to address issues of scale and internal consistency than qualitative models (Burgess, 2012). Consequently, SFM are a better suited to test the validity of a concept about the probable behaviour of a particular physical system. Burgess (2012) also notes that SFM can also exhibit counter-intuitive behaviour that, if correct, may improve our understanding in unexpected directions.

Over the past few decades, SFM of the processes forming carbonate platform stratigraphies has enabled us to identify and quantify the mechanisms and interplay between mechanisms controlling platform evolution (e.g. Bice, 1988; Scaturo *et al.,* 1989; Bosence & Waltham, 1990; Burgess & Steel, 2008; Williams *et al.,* 2011; Prince & Burgess, 2013; Burgess & Prince, 2015). SFM has also been applied to investigate the development of particular stratigraphies (e.g. Lawrence *et al.,* 1990; Bosence *et al.,* 1994; Huessner *et al.,* 2001; Warrlich *et al.,* 2008; Granjeon and Joseph, 1999; Granjeon *et al.,* 2002; Borgomano *et al.,* 2014). A number of

precautions must be taken when defining SFM parameters that seek to replicate particular platform cases. This is in order to avoid issues of circular reasoning (see section 4.2.2 for details). The integration of outcrop and subsurface data with forward modelling and simulation of basin fill/platform evolution helps to understand how stratigraphic sequences develop (e.g. Bosence *et al.,* 1994, Bowman & Vail, 1999; Warrlich *et al.,* 2008).

2.3.2.2. Inverse models

Inverse modelling is a systematic procedure to determine model parameters by minimising the deviation between model output and real data (after Lessenger & Lerche, 1999). An inverse model is therefore a method of identifying the nature of a process through examining the effects the process has on some observable feature within its environment (Warrlich, 2000).

Observable strata show the final production of stratigraphic processes, but we do not truly know what the processes were in any particular case; this is the inverse problem in sedimentary geology (Burgess, 2012). The simulation and replication of specific strata is attractive because this suggests that the SFM adequately reproduced the key stratigraphic processes involved, thereby solving the inverse problem. This example of model inversion involved running the stratigraphic model, comparing the simulated output with the real data (via an objective function), adjusting the model parameters in proportion to the difference between model and real data, until an acceptable match is obtained (e.g. Cross & Lessinger, 1999; Charvin *et al.,* 2009).

There are two key problems with this approach. First, one needs to create an effective quantitative objective function to meaningfully compare the synthetic strata to the real data. This is difficult since the process often requires smoothing of both the data and the model output. This may reduce our ability to adequately quantify synthetic to real match. Secondly, even if a good match between model and real data is achieved, there are issues of non-uniqueness. That is, different parameter values for the controlling processes (e.g. sediment production and diffusional transport) may develop facies architectures and strata geometries that are not demonstrably different from one another (e.g. Burton *et al.,* 1987; Heller *et al.,* 1993; Burgess & Prince, 2015).

2.3.3. Stratigraphic forward modelling of carbonate platforms - purpose and approaches

There are various types of SFM, each with strengths and weaknesses. These cover the rage of depositional systems, from alluvial to deep-marine, and represent both siliciclastic and carbonate deposition. These models have been improved over time and now increasingly simulate important and complex stratigraphic processes in both siliciclastic and carbonate

systems, e.g. interactions between sediment production and transport.

Recent model developments are from collaborations of large groups of geologists and programmers. These community-developed SFM enable the science to move beyond cartoon depictions of depositional environments and are becoming the repository for established ideas about how depositional systems operate and evolve (Burgess, 2012). Such SFM are being applied in both a predictive sense for modelling specific cases, although there are important limitations, and in a more general experimental sense to gain insight into basin fill dynamics.

SFM based experiments may provide insights that conceptual models of depositional environments or conventional sedimentological analysis have difficulty answering (e.g. Warrlich *et al.,* 2008; Burgess, 2012). These models will prompt fieldwork on modern and ancient depositional systems (to constrain realistic parameter values) and to test whether the processes in the model reflect observations in real systems. The use of SFM could help geoscientists move towards a hybrid of observation, experimentation, testing, and guided model refinement, thereby helping sedimentary geology mature as a science (Burgess, 2012).

2.3.3.1. Types of SFM

The following section reviews progress made in SFM over the past three decades in moving towards the goals described above. Basin modelling is experiencing rapid growth and researchers are investigating a variety of approaches. Models that are currently being used have been classified and defined by Paola (2000) in the following nonexclusive axes: geometric *versus* dynamic models, deductive *versus* rule-based models, coupled *versus* uncoupled models, analytical *versus* simulation models, deterministic *versus* stochastic and one-dimensional *versus* two-dimensional *versus* three-dimensional models. A summary, of the model types is given below.

Geometric *versus* dynamic models

The sediment surface within a geometric model is represented by one or several surfaces with a predefined geometry. A rigid-lid model is the simplest type of geometric models, where the surface is a fixed horizontal plane. A major improvement on rigid-lid geometric models is the ability to conserve sediment mass and to allow for variations in sediment supply. While such models are computationally simple, they may replicate key stratal geometry features such as unconformities. Geometric models allow a high degree of flexibility, they however incorporate few process-based constraints on what natural transport processes can and cannot do. They also fail to replicate stratal features that are influenced/dependent on sediment surface. These weaknesses are treated in dynamic ("process-based") models where the surface is produced on the basis of some representation of how the interaction of sedimentation, transportation and deposition interact with subsidence (Burgess, 2012).

Deductive *versus* rule-based models

Deductive models use mathematical methods to define and manipulate governing equations (based on Newtonian mechanics) and their boundary conditions. Deductive models are supported by a well-defined link with basic physics that enhances confidence in the model predictions. Deductive models are however limited by issues of sensitivity dependence and by the fact that various aspects of sedimentary systems are not well understood in terms of the governing equations and boundary conditions. Even in instances where the governing equations and boundary conditions are understood, the resulting equations can be difficult and/or computationally taxing, especially in three dimensions (Burgess, 2012).

Rule-based models seek to reduce model complexity by only simulating the critical dynamics within a sedimentary system. Geometric models and cellular-automata are examples of rule-based models. These models benefit from simple formulations and fast computational speed. This enables them to assess complicated interacting processes (likely typical of real sedimentary systems). It is however difficult to assess how realistic and predictive these types of models are (Burgess, 2012).

Coupled *versus* uncoupled models

Coupling refers to the connections between two or more model elements. Conversely, uncoupling refers to the disconnection between various model elements. For instance, isostatic subsidence that is driven by sediment loading effects should be strongly coupled to a depositional model predicting thickness and density of strata. Conversely, tectonic subsidence due to lithospheric stretching is independent of and therefore not coupled to sedimentation (Burgess, 2012). Different sedimentary processes can also be coupled, for example fluvial and shoreline processes. While it seems likely that many sedimentary systems are strongly coupled, the representation of these connections in SFM is still in early phases of development (Burgess, 2012).

Analytical/experimental *versus* simulation models

Analytical SFMs are used to explore the behaviour of sedimentary systems without simulating all the processes that produced particular strata (Burgess, 2012). The purpose of these models is therefore to conduct numerical experiments that systematically investigate generic sedimentary processes and their interactions in carbonate systems through for example sensitivity and parameter space analysis (e.g. Harbaugh & Bonham-Carter, 1970; Bosence & Waltham, 1990; Eberli *et al.,* 1994; Warrlich *et al.,* 2002; Bitzer & Salas, 2002; Burgess & Wright, 2005; Emmerich *et al.,* 2003; Williams *et al.,* 2011; Burgess & Prince, 2015). Simulation models are constructed to reproduce specific outcrop or subsurface examples in greater detail than analytical models (Burgess, 2012). These models often simulate more parameters and are

consequently more difficult to use. In fact, simulations models often require an inversion method to adequately replicate specific real examples (Cross & Lessinger, 1999).

Deterministic *versus* stochastic

Deterministic models do not contain any random variables. Consequently, iterations will produce the same result if the runs are repeated with identical parameter values (Burgess, 2012). Stochastic/probabilistic, models include random variables that are set by probability density functions and implemented using pseudo-random number generators seeded with a particular value (Burgess, 2012). The same model results will also be given when using the same start value, however different results will be generated with the application of different seed values. This allows probabilistic models to run multiple times for the same parameter values to generate numerous stochastic scenarios. Random variables are typically introduced to simulate processes that are more complicated than those replicated in deterministic models (Burgess, 2012). This approach is useful in small-scale models that attempt to replicate high levels of strata heterogeneity observed in certain natural depositional systems (Burgess & Wright, 2005).

While strongly coupled models and certain types of rule-based models are deterministic, these may also develop outputs that are practically indistinguishable from random. This blurs the distinction between deterministic and stochastic models (Burgess et al., 2006; Burgess & Emery, 2004).

One-dimensional *versus* two-dimensional *versus* three-dimensional models

While natural depositional systems are three-dimensional, the development of one- and two-dimensional models is a key and necessary first step in basin modelling (Paula, 2000). The first dimension in stratigraphy is the vertical. Two-dimensional models add the horizontal dimension parallel to the mean transport direction. Two-and-a-half dimensional models seek to partly simulate three-dimensional processes and effects (e.g. out-of-plane mass transfers). If three-dimensional/out-of-plane/lateral processes and effects are not substantial, three-dimensional models can be envisaged as a series of two-dimensional cross sections. This however is seldom the case in natural systems. Various natural sedimentary basins have multiple interacting source points, complex subsistence, combined lateral and transverse flow. In these scenarios, fully three-dimensional models are required (Paula, 2000).

Simulations of sediment dispersal in carbonate platforms

Bosence & Waltham (1990) demonstrate that the evolution of carbonate platforms is strongly influenced by sediment erosion rates. In view of this, they develop a process-based sediment dispersal function where the simulated geometries are produced by the disintegration, transport and redeposition of sediment. Through this approach, the authors re-connect with clastic simulation programs that already applied this approach. The simulating of disintegration,

transport and deposition was necessary to produce better results than the first order fits to real stratigraphies achieved so far (Lerche *et al.,* 1987; Koerschner & Read, 1989; Osleger & Read, 1991). Simulations of sediment dispersal can be broadly subdivided in three main categories. These are discussed below.

Diffusion of sediments

Various forms of the diffusion equation have been used to model fluvial morphology in engineering and geomorphology (Begin *et al.,* 1974; Garde *et al.,* 1981; Jain, 1981; Soni, 1981; Gill, 1983; Jaramillo & Jain, 1984; Ribberink & var der Sander, 1985; Zhang & Kahawita, 1987; Paola, 2000). Dionisos (Granjeon & Joseph, 1999) is the most sophisticated program that mainly uses diffusion. The model uses a generalised diffusion equation to simulate sediment dispersion. Dionisos also takes water discharge into account to simulate fluvial- and gravity-dominated sediment transport. Dionisos is a remarkable basin-modelling program that can replicate many important aspects of basin evolution.

Despite the importance of the diffusion coefficient parameter, estimates of the value from natural systems are poorly constrained. This is particularly true of carbonate systems. Additionally, diffusion rates estimated from natural systems range from 0.0001km^2 ky^{-1} from data from the St. Croix reef-rimmed shelf (Hubbard *et al.,* 1990; Bosence *et al.,* 1994), to 7 km^2 ky^{-1} in pelagic strata on the flanks of the Galapagos spreading centre (Mitchell *et al.,* 1996), and 560 km^2 ky^{-1} in the Mississippi delta (Kenyon & Turcotte, 1985). As a consequence, numerical studies of carbonate platforms have been limited to a theoretical basis, assessing a wide range of diffusion values. For instance, Williams *et al,* (2011) applied a range of diffusion coefficient values that is quite extreme, spanning from 0 to 50 km^2 ky^{-1}. Bosence *et al.* (1994) and Williams *et al.* (2011) argue that diffusion coefficients in the lower end of this range may more accurately represent shallow to deep-marine carbonate settings.

Simulating sediment dispersal by moving sediment 'quanta' down slopes

Cao & Lerche (1994) simulate sediment transport by moving discrete quantities of sediment "quanta" from the site of erosion to deposition down a slope or energy gradient. This approach exceeds the limitations of the slope diffusion approach and enables sediment simulation on a sub-basin scale.

Hardy & Gawthorpe (1998) develop a program that simulates clastic deltas. The model simulates moving sediments from a point source to open water using random walk when the surface is sub-horizontal, and movement down the steepest slope on inclined surfaces. Slope diffusion above a critical angle is used to simulate slumping and avalanching (Warrlich, 2000).

These simulations establish a fluid velocity field that disperse sediments along that field.

Bonham-Carter & Sutherland (1968) was an early attempt that combines a flow model for an open channel with a jet flow model to simulate the fluid velocity field in a delta. Sediment discharge of fine and coarse-grained sediment is then simulated (Warrlich, 2000).

2.3.3.2. Latest Stratigraphic Forward Models

Recent research and development in the field of three-dimensional numerical stratigraphic models focus on two main sectors. Research either focuses on developing models that predict geometries and facies away from data points and help interpret vast quantities of data obtained by the new technologies in data acquisition. Alternatively, research develops models that are used to address more analytic and conceptual questions that improve our understanding on sediment dynamics.

CARBONATE 3D

CARBONATE-3D is a finite difference stratigraphic forward simulator written by the SedTec modelling group at the Royal Holloway University of London. The program simulates the evolution of carbonate platforms and mixed carbonate siliciclastic systems at macroscopic time and spatial scales (Warrlich *et al.,* 2001, 2002). After inputting temporal and spatial scales, initial surface, and a relative sea-level history, CARBONATE-3D can simulate the major processes operating in carbonate systems. Sea level and differential subsidence control accommodation space. Carbonate sediment production varies with water depth and production is simulated in the platform margin, platform interior, and pelagic environments. Production rates within these environments also depends on a restriction effect related to the distance from the aforementioned platform areas (see Warrlich *et al.,* 2002). Siliciclastic sediment can be introduced as line sources along the edges of the mode. The simulated strata can be eroded by dissolution or mechanical erosion at a user defined rate. If shear stress is above a grain-size specified critical shear stress, the sediment is entrained and transported. Transport is dependent on currents, waves and slopes. This replicates bed-load and suspended-load. Within this transport framework, coarse-grained sediments tend to flow downslope, but fine sediments follow currents and waves (Warrlich *et al.,* 2002). Transported sediment is deposited in areas where shear stress is below the critical shear stress.

CARBONATE-3D calculates sedimentary geometries as time surfaces and simulates facies. The facies can either be described on the basis of the processes that formed the largest faction of the accumulated sediment, or on the basis of grain size proportions from each carbonate factory (above mentioned environments).

Results of simulated surfaces can be viewed as three-dimensional images, as maps or cross-sectional views. This enables a qualitative comparison between real and simulated stratigraphies. The degree of model to outcrop match can also be quantified using a facies comparator. The comparator compares the real and simulated stratigraphies (in any location) to

assess the percentage match or mismatch of a simulation.

More recent work on CARBONATE-3D has developed CARB3D+ (Peterson *et al.* 2006). The SFM is an innovative process-based 3D forward model that can simulate sedimentary facies, geometries, and early diagenesis of isolated carbonate platforms in a sequence stratigraphic context. It differs from the earlier model in employing an explicit simulation of the evolving hydrodynamic environment and sedimentary processes. The algorithm includes sediment production in reef, shoal-margin, interior, and pelagic carbonate environments. Sediments are entrained by waves and currents, and are transported by currents and by grain avalanching on slopes. CARB3D+ also includes dynamic feedback between platform morphology and sediment production and transport (Peterson *et al.* 2006).

CarboCAT (Burgess, 2013)

Various numerical SFM have successfully replicated large-scale aspects of carbonate stratal architectures (e.g., Bosence & Waltham, 1990; Aurell *et al.,* 1998; Paterson *et al.,* 2006; Warrlich *et al.,* 2008). While these models helped to explain how various features of carbonate strata were produced, few of these have been successful in reproduced the finer scale heterogeneity observed in carbonate strata. The origin of these heterogeneities remains relatively unknown.

CarboCAT (CAT being short for Cellular AuTomata) models multiple carbonate lithofacies deposited in carbonate deposystems, particularly within a platform interior setting. While the model is entirely deterministic, it can generate dynamic behaviour and produce heterogeneous carbonate strata. CarboCAT uses a cellular automata to calculate the spatial distributions of lithofacies and to calculate the accumulation of heterogeneous carbonate strata in three dimensions. Cellular automata are a type of discrete numerical model that can be entirely deterministic in their calculation. These models may produce complicated results from relatively simple rule-based computational algorithms that are associated to biological concepts of space, competition, and population dynamics (Flake, 2000). The discrete numerical models partly enable the reproduction of finer scale heterogeneities observed in carbonate strata (Burgess, 2013). Cellular automata consist of cells that have a finite, usually small, number of possible states (e.g. Wolfram, 2001) that is determined with reference to surrounding cells within a specified distance – termed the "cell's neighbourhood". Simple rules, based for instance on the number cells within the cell's neighborhood with the same state, is used to determine the future state of a cell at the next iteration of a cell (Burgess, 2013).

CarboCAT includes the ability to simulate various geological processes, including: tectonic subsidence, eustatic sea-level oscillations, water depth-dependent carbonate production rates for

several carbonates factories, and a simple representation of sediment transport (Burgess, 2013). Sediment transport in CarboCAT is modeled using a simple gradient-based method. The function distributes a proportion of produced sediment into adjacent lower elevation model cells not already occupied by producing carbonate facies (Burgess, 2013).

Despite its simplicity and lack of stochastic elements CarboCAT simulates heterogeneous platform interior strata and exhibits stratigraphically interesting behaviours that includes complex histories of lateral migration and interfingering of lithologies (Burgess, 2013).

DIONISOS

Dionisos (Diffusion Oriented Normal and Inverse Simulation of Sedimentation) is a three-dimensional forward stratigraphic model developed by the Institut Français du Pétrole (Granjeon & Joseph, 1999; Granjeon *et al.,* 2002). The program simulates geometries and lithologies of coastal environments on time and spatial macroscopic scales (100s of ky to 10s of My and 10s to 100s of km). Synthetic strata are based on a defined range of input parameters. Sediment production can be simulated in the model as being depth dependent, constant through the model run or vary through time. A generalised diffusion equation is used to simulate sediment dispersion. It takes into account water discharge to simulate fluvial- and gravity-dominated sediment transport as well as moderate wave- and tidal-dominated environments (Granjeon & Joseph, 1999). Simulations of sediment transport in Dionisos are based on two sets of equations that model the interactions between the short-term and long-term evolution of sedimentary processes (Ku Shafie & Madon, 2008). These equations allow the calculation of sediment erosion, transport and deposition. The short-term transport rate element depends on water velocity and inertia. The long-term transport rates are determined by a generalized modified sediment diffusion formulation, which is a smoothing algorithm that simulates the approximate net effect of all gravity driven and water driven processes (Granjeon & Joseph, 1999; Granjeon *et al.,* 2002; Ku Shafie & Madon, 2008). Simulations of sediment transport by diffusion apply a generalized modified sediment diffusion formulation calculated via an implicit finite-difference method. The diffusion coefficient is a smoothing algorithm that simulates the net effect of all gravity driven and water driven processes. The formulation defines sediment transport at a point on the model grid on the basis of the topographic gradient at that point and the diffusion coefficient attributed for the grain-size group (Granjeon & Joseph 1999; Granjeon *et al.,* 2002). Sedimentary textures and facies can be differentiated from Dionisos on the basis of depth of deposition and/or on the grain size proportions/ratios.

DIONISOS is an impressive basin-modelling program that can reproduce many key elements of the development of a whole basin. The program can reproduce coastal plain, shoreface and upper offshore clastic and carbonate environments. The program can be applied to prospect (e.g.

carbonate platform) or to basin scale (e.g. Lower Cretaceous of the Paris basin) and uses an inversion loop to calibrate the input parameters on subsurface or field data.

Dionisos 3.85 has been used in this thesis to create a series of two-dimensional models that combine spatially and temporally variable carbonate sediment production and sediment transport at the platform scale. At the time when this thesis was started, DIONISOS was the best SFM available at the Department of Earth Sciences (Royal Holloway). Other SFM (e.g. CarboCAT) would require significant development to be able to do the analysis carried out in this thesis.

CHAPTER 3: CONTROLS ON CARBONATE STRATAL ARCHITECTURE AND PLATFORM GEOMETRY

3.1. Introduction

Discussions on the controls on platform evolution are either based on qualitative conceptual models (e.g. Pomar, 2001; Pomar & Kendall, 2008; Pomar *et al.,* 2012) or quantitative numerical stratigraphic forward models (SFM) (e.g. Bosence & Waltham, 1991; Bosence *et al.,* 1994; Williams *et al.,* 2011) (section 2.1.3.2). Issues of scale and internal consistency limit conceptual models. SFM are better suited to improve our understanding on how carbonate factory dependent aspects influence carbonate systems. Previous SFM based investigations on controls of platform evolution however do not fully consider realistic values for various carbonate factory aspects (e.g. Williams *et al.,* 2011) (sections 2.1.3.2 and 3.2.3). As a result, our understanding of how carbonate factories may influence platform development remains incomplete.

This chapter applies DIONISOS SFM to investigate how different aspects of carbonate factories may act independently and interact to influence carbonate platform development. The aspects investigated in this study are sediment production profiles (production profiles), sediment production rates, and production of different grain-size proportions with discrete diffusional transport rates. This study is distinct from and builds on previous investigations in three ways:

(I) It produces new depth production profiles that brackets average sediment production rates, depth distribution of sediment production, and proportions of grain-sizes produced for five carbonate factories from Holocene systems (section 3.2.2). These different aspects are combined to form production profiles that better represent particular natural Cenozoic carbonate factories.

(II) New equalised production profiles (section 3.2.3) are developed. These enable a comparison of the influence distinct production profiles have on platform geometry. The tested production profiles are made equal in terms of total sediment that can be produced within a defined time interval across the depth range producing sediment. This method ensures that the only difference being compared between production profiles is the depth distribution of sediment production. This is an improvement on the tests by Williams *et al*., (2011) which also investigate production profiles (section 2.1.3.2.2).

(III) Four grain-sizes (mud, sand, gravel and cobble-boulder) are simulated and the proportions each grain-size contributes towards total sediment production are systematically altered. This enables an investigation of the full spectrum of grain-size proportions. The method allows us to assess the influence different proportions of grain-sizes, and their attributed diffusion coefficients, have on stratal architecture and platform geometry.

This study focuses on Cenozoic carbonate systems for three principal reasons. Firstly, Holocene carbonate factories are well known and a global data set is reviewed here to produce new depth

production profiles for four carbonate factories. The carbonate factories in these Holocene systems are well documented for Cenozoic carbonate systems, e.g. Llucmajor area, Balearic Islands (e.g. Pomar, 1991, 1993; Pomar & Ward, 1994, 1995; Pomar *et al*., 1996), the Las Negras platform, Southern Spain (e.g. Franseen, 1989; Goldstein *et al*., 1990; Franseen & Mankiewicz, 1991), the Nijar Basin, South Eastern Spain (e.g. Mankiewicz, 1987, 1996; Warrlich et al., 2005), the Malta platform (e.g. Pedley, 1974, 1976; Bosence & Pedley, 1982; Dart, 1991) and Miocene Latium-Abruzzi ramp (Carminati *et al*., 2007; Brandano *et al*., 2009). Secondly, there exist a number of well-exposed and investigated Cenozoic carbonate platforms (e.g. previously mentioned platforms). This allows the stratal architectures that result from the simulation of particular carbonate factories to be compared to those developed in real carbonate systems. Thirdly, a lot of the debate of the control of carbonate factories on carbonate platform geometry is tied to Pomar's work (e.g. Pomar, 2001; Pomar & Kendall, 2008; Pomar *et al*., 2012) that has been done within the sphere of Cenozoic carbonate systems.

3.2. Methods: model formulations, initial conditions and parameters

3.2.1 Dionisos, Maximum topographic gradients and Parameter space plots

Dionisos (Granjeon & Joseph, 1999; Granjeon *et al.,* 2002) SFM has been used here to create a series of two-dimensional models that combine spatially and temporally variable carbonate sediment production and sediment transport. Refer to chapter 2 (section 2.3.3.2) for a detailed description of the SFM.

A quantitative metric was developed (modified from Williams et al., 2011) so as to compare the resulting simulated stratal architecture in terms of maximum topographic gradient (MaxS) along the depositional profile (measured in degrees). A high MaxS indicates steep slope-breaks and represents flat-top steep margin (FTSM) platforms while a low MaxS indicates low-gradient systems and implies a ramp type platform. Homoclinal ramps are composed of a distally dipping surface with approximately constant regional gradients of 0.1° to 1.0° (Burchette & Wright, 1992), > 1° but < 5° are distally steepened ramps and FTSM platform form when platform margins gradients are greater than 5.0°.

Model sets, consisting of several hundred models each, were made. Each model set tests a different equalised production profile (section 3.2.3), and assesses the same range of sediment production (200 to 4000 m My^{-1}) and diffusional transport rates (0 to 2.5 km^2 ky^{-1}). Each model in the model set therefore simulates a different sediment production and diffusional transport rate. Parameter space plots (PSP) were developed for each model set, these display maximum topographic gradient (MaxS). The PSP demonstrate the extent to which various production

profiles, sediment production and diffusional transport rates influence MaxS and by inference platform geometry.

A summary table (table 3.1) is presented below that indicates what model parameters were applied in this chapter. The parameter rates are described in more detail in the following sections within the chapter.

SFM parameters applied in section	3.3.1	3.3.2	3.3.3
DIONISOS	✓	✓	✓
Model iterations	2	160	190
Duration (My)	5	5	5
Time step (My)	0.05	0.05	0.05
Cell size (km)	0.5	0.5	0.5
Initial bathymetry (figure)	3.3	3.3	3.3
Sea level history (figure)	3.5	3.5	3.5
Sediment production equalised production profile	✗	✓	✓
Sediment production natural production profile	✓	✗	✗
Single grain size	✗	✓	✗
Multiple grain size	✓	✗	✓
Sediment transport by diffusion (km^2 ky^{-1}).	0 to 2.5	0 to 2.5	0 to 2.5
Wave and current modelling.	✗	✗	✗
Sediment transport by slope failure	✗	✗	✗
Sub-aerial erosion	✗	✗	✗

Table 3.1: Summary of initial model conditions and input parameters.

3.2.2. Cenozoic multiple grain-size production profiles

SFM carbonate production *versus* water-depth curves (production profiles) that seek to simulate/replicate sediment production of real/natural Cenozoic carbonate factories must match them as closely as possible in terms of (i) sediment production rates, (ii) depth distribution of sediment production (production profiles), and (iii) grain-size proportions produced.

This study brackets (from literature) the sediment production rates, depth distribution of sediment production, and grain-sizes produced for five different carbonate factories from

Holocene carbonate platforms (Appendix A). These aspects are combined to form a distinct production profile for each carbonate factory. The production profiles are defined by the depth distribution of sediment production and grain-sizes produced. The assessed carbonate factories are: (I) scleractinian reef-building z-corals (chlorozoan *sensu* Lees & Buller, 1972), (II) calcareous green algae (chloralgal *sensu* Lees, 1975), (III) coralline red algae (rhodalgal *sensu* Carannante *et al.,* 1988), (IV) molluscan & bryozoan (brymol *sensu* Nelson, 1988) and (V) planktonic foraminifera (nannofor *sensu* Hayton *et al.,* 1995) (table 2.1). These factories are well documented for the Cenozoic, e.g. Llucmajor area, Balearic Islands (e.g. Pomar *et al*., 1996), the Las Negras platform, Southern Spain (e.g. Franseen & Mankiewicz, 1991), the Nijar Basin, South Eastern Spain (e.g. Warrlich, 2000), the Malta platform (e.g. Pedley, 1978; Dart, 1991) and Miocene Latium-Abruzzi ramp (Brandano *et al*., 2009).

These new production profiles are distinct from previous profiles in that each profile consists of a number of distinct grain-size production profiles, one production profile for each grain-size produced by the carbonate factory. The new production profiles allow grain sizes to be simulated and enable a proxy for facies to be obtained from the models on the basis of relative proportions of accumulated grain-sizes (cf. Boylan *et al.*, 2002 see section 8.4.1). Various proportions of each grain-size simulated in SFM produces the range of carbonate depositional textures (Dunham, 1962 and its modification by Embry & Klovan, 1971) that occur in natural carbonate systems.

In this study, four grain-sizes are considered and simulated in SFM: mud (< 62 μm) forming mudstone, sand (62 μm to 2 mm) forming grainstone, gravel (2 to 64 mm) forming rudstone, and cobble-boulder (> 64 mm) is used to represent framestone. Sediment production from carbonate factories falls within one or more of these grain-sizes (based on literature descriptions). Wackestones, packstones, and floatstone textures are formed from a mixture of the above grain sizes. Textures were differentiated from Dionisos based on the following grain size proportions: mudstone > 90% mud with <10% sand, wackestone >50% mud with 10 to 49% sand, floatstone >50% mud with 10 to 49% gravel, packstone >50% sand with 10 to 49% mud, rudstone >50% gravel with 10 to 49% mud or sand, grainstone 100% sand, framestone >20% cobble and boulder.

The following definitions of sediment production and accumulation are necessary. Sediment accumulation rate (m yr^{-1}) is a result of autochthonous *in situ* produced sediment, deposited allochthonous sediment, and eroded fraction. Literature accounts of ancient carbonate factories provide accumulation rates. Sediment production rate is the total *in situ* sediment production by the carbonate factory over a defined time period present in an area or point. Sediment production may be in (g $CaCO_3$ m^2 yr^{-1}) or in (*in situ* m yr^{-1}). The production rates do not

account for deposited allochthonous sediment, and eroded fraction. Literature accounts of modern carbonate factories provide sediment production rates.

Dionisos SFM simulates sediment production as *in situ* m yr^{-1}, not in kg $CaCO_3$ m^{-2} yr^{-1}. In view of this, where literature only provides production rates as kg $CaCO_3$ m^{-2} yr^{-1}, these were converted to *in situ* m yr^{-1} following the Bosence & Waltham (1990) method. The calculation is based on carbonate factory production rates (kg $CaCO_3$ m^{-2} yr^{-1}), skeletal mineral density and skeletal porosity. The following values were used in the calculation of production rates (*in situ* m yr^{-1}): aragonite mineral density of 2.93 g cm^3 for the scleractinian coral and calcareous green algal factories and a calcite mineral density of 2.71g cm^3 applied for the coralline red algal and molluscan, bryozoans and foraminiferal factories. An average 50% initial skeletal porosity was applied to all factories. For example aragonitic (density 2.93 g cm^3) hermatypic coral *Diploria labyrinthiformis* has bulk density of 1.65g cm^3 (Ghiold & Enos, 1982), the hermatypic coral therefore consist of 56% aragonite skeletal mineral density and 44% initial skeletal porosity).

Sediment production rates (g $CaCO_3$ m^2 yr^{-1}) in any carbonate factory may differ by several orders of magnitude (e.g. scleractinian coral factory) (Appendix A). Variations in sediment production rates in any one factory may be due to differences in growth rates between species of the same carbonate factory, habitat suitability and intensity of predation (e.g. Adey & Vassar 1975; Stearn *et al*. 1977).

3.2.2.1. Scleractinian coral factory – Photozoan factory

The scleractinian coral factory forms part of the photozoan factory (*sensu* James, 1997). The coral factory occurs in tropical, euphotic, oligotrophic settings. Published and calculated sediment production rates vary by two orders of magnitude from 0.77 to 31.00 kg $CaCO_3$ m^{-2} yr^{-1} and 0.35 to 23.00 m ky^{-1} across the depth range producing sediment (Appendix A). An average scleractinian coral production rate 7.48 m ky^{-1} is calculated when averaging all production rates between 0 to 20 m depth (assuming 100% cover) (figure 3.1). Considering a 50% coral seabed cover (e.g., Longman, 1981; Done, 1982; Dinesen, 1983; Sweatman *et al.,* 1998 in Vecsei, 2001), the factory has a production rate of 3.74 m ky^{-1}. Sediment production was calculated as scaling linearly to the proportion of seabed cover.

Bosscher & Schlager (1992) measure Caribbean coral production rates *versus* depth and develop an equation based on these observations. The Bosscher & Schlager equation was used to approximate coral factory production rates at depth intervals where Holocene literature production rates are sparse (typically at depths >40 m).

Biological and mechanical processes break down a portion of scleractinian coral framestone production into finer grain-sizes. Erosion commonly removes 25 to 50% of the sediment (Land, 1979; Hubbard *et al.,* 1990; Harney & Fletcher, 2003). In this study, scleractinian coral factories maintain 75% of their initial cobble to boulder grain-size (producing framestone) and 25% of the sediment produced is as sand grain-size (grainstone) (figure 3.1A).

3.2.2.2. Calcareous green algal factory – Photozoan factory

The Calcareous green algal factory forms part of the photozoan factory (*sensu* James, 1997). Literature-based descriptions of sediment production from tropical calcareous green algal factory largely relates to the benthic *Halimeda* and *Penicillus* genera. Published and calculated sediment production rates within tropical and warm temperate environments range from 0.05 to 1.67 kg $CaCO_3$ m^{-2} yr^{-1} and 0.04 to 1.23 m ky^{-1} (Appendix A). An average calcareous green algal factory production rate of 0.33 m ky^{-1} is obtained when averaging all production rates between 0 to 20 m depth (figure 3.1). A rate of 0.17 m ky^{-1} is calculated when the factory occupies 20 to 50% of the seabed cover (e.g. Liddell *et al.,* 1988).

The production profile of this photo-dependent factory has been modelled to reduce with depth following Liddell *et al.* (1988) descriptions of *Halimeda* occurrence in North Jamaica. Liddell *et al*. demonstrate that *Halimeda* is an important space-occupier over the bathymetric range of 1m to 75 m and the alga' s lower depth limit is controlled by light intensity, with the rapid decrease in the alga below 75 m.

The disintegration of calcareous green algae, especially *Halimeda* and *Penicillus*, is often identified as the source of large quantities of sand and mud in Jamaica and Florida respectively (e.g. Liddell *et al.,* 1988; Bosence, 1989). In view of this, the factory has been modelled to produce mud and sand in equal proportions (Neuman & Land, 1975; James *et al.,* 2009) (figure 3.1B).

3.2.2.3. Coralline red algal factory – Heterozoan factory

The coralline red algal factory forms part of the heterozoan factory (*sensu* James, 1997). The coralline red algal factory is heterotrophic and occurs in a variety of climatic, nutrient, and bathymetric marine environments (Peres & Picard, 1964; Blanc, 1968; Bosence, 1971; Bosence, 1983, 1985; Iryu *et al.,* 1995; Basso, 1998; Bosence & Wilson, 2003; Matsuda & Iryu, 2011). Published and calculated sediment production rates vary considerably from 0.008 to 10.3 kg $CaCO_3$ m^{-2} yr^{-1} and 0.10 and 8.30 m ky^{-1} (Appendix A). An average production rate 1.04 m ky^{-1} is obtained when averaging all production rates between 0 to 60 m depth (figure 3.1). An average production rate 0.50 m ky^{-1} is obtained when the factory occupies 50% of the seabed

cover (Steam *et al.,* 1977; Matsuda & Iryu, 2011).

Crustose red algae are photic organisms that can thrive in meso-oligophotic conditions equivalent to water depths up to 80 m (Halfar, 1999). Maerl beds are found from the low intertidal zone to depths of 150 m (Foster, 2001). Matsuda & Iryu (2011) indicate that living biotic cover on rhodoliths is approximately 50% down to water depths of 100 m. The authors also note that production decreases rapidly at depths greater than 100 m. These observations, along with data on production rate at certain depths (Appendix A), were used to constrain the coralline red algae factory production profile.

The factory may produce rhodolithic and crustal growth habits, both of these may be disintegrated into crustose and rhodolith branch debris of gravel, sand and mud grade sizes (e.g. Bosence & Pedley, 1982). Peres (1967) and Laborel (1961) described Mediterranean coralline algal construction associated with carbonate sands and gravels in intertidal and shelf areas to depths of 150 m (Bosence, 1983). In view of this, sediment production of the coralline algal factory has been modelled to consist of 40% gravel, 40% sand and 20% mud sized sediment (figure 3.1C).

3.2.2.4. Mollusc, bryozoan and foraminiferal factory – Heterozoan factory

The Molluscs, bryozoan and benthonic foraminiferal factory forms part of the heterozoan factory (*sensu* James, 1997). This factory is tied to sediment production by the molluscan, bryozoan and foraminifera factories as benthos and epibionts (e.g. on sea grasses and scleractinian corals). Published and calculated production rates for the factory range from 0.0002 to 2.76 kg $CaCO_3$ m^{-2} yr^{-1} and production rates range from 0.01 to 2.04 m ky^{-1} (Appendix A). The factory can occur very commonly to very rarely in the seabed. An average production rate of 0.2 m ky^{-1} is obtained when averaging all production rates between 0 to 60 m depth (figure 3.1). An average production rate of 0.04 m ky^{-1} is calculated when the factory covers 20% of the seabed (e.g. Bosence, 1989; Noble *et al.,* 1995).

Bryozoans exist in low and high latitudes and are abundant in depths between the intertidal zone and about 80 m (Flugel, 2010). This information, along with direct measures of production rates at defined depths, were used to construct the association's production profile.

Bryozoan bioclasts are abundant constituents of modern and ancient cool-water shelf carbonates and contribute towards the formation of carbonate particles of all grain-sizes (Flugel, 2010). In this study, the factory is modelled to produce 100% sand (figure 3.1D).

3.2.2.5. Planktonic foraminiferal factory

The nannofor grain association (Hayton *et al.,* 1995) primarily consists of mud grade sediment produced by planktonic foraminifera factory that are found in large numbers throughout the sunlit zone of the ocean. Literature provides values for sediment accumulation rates at the sea floor. This is a function of the supply of biogenic skeletal components from the planktonic foraminifera factory, mineral grains carried from continents, and authigenic particles created at the sea floor (Cita *et al.,* 1978). In view of the sparse literature on sediment production rates of the factory, the separation of the three aforementioned sedimentary sources to isolate and quantify factory production rates was not possible (Appendix A). Values characteristic of accumulation rates of deep marine environments are used in our SFM. Average accumulation rates for deep-sea environments range from 0.001 to 0.3 m ky^{-1} (Appendix A). An average of 0.05m ky^{-1} was applied at water depths greater than 60 m (e.g. Cita *et al.,* 1978; Ku & Broecker, 1965; Scholle *et al.,* 1983).

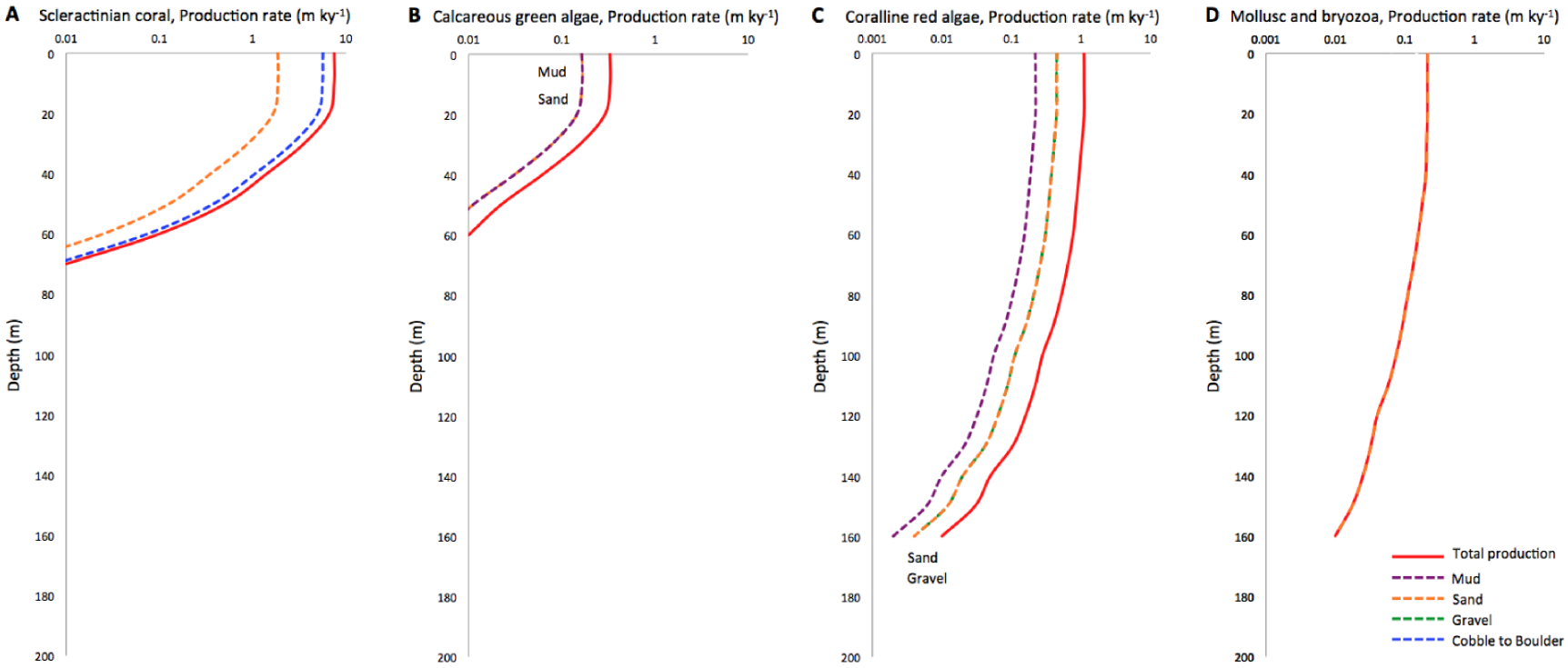

Figure 3.1: Average sediment production rates (m ky^{-1}) at different depths (m) for the (A) scleractinian coral, (B) calcareous green algal, (C) coralline red algal and (D) molluscan, bryozoans and foraminiferal carbonate factories obtained from literature (Appendix A). The full red curve represents the average factory sediment production rate assuming 100% seabed cover (used in these models); the curve does not distinguish between the grain-sizes produced. The dashed curves represent average sediment production rate (assuming 100% seabed cover) of various grain-sizes. Calculations for dashed curves are dependent on total sediment production rate, and proportions of grain-sizes produced by the factory.

3.2.3. "Equalised" euphotic and oligophotic production profiles

Carbonate production profiles can be described in terms of sediment production loci, for example euphotic or oligophotic production profiles. A euphotic production profile is a profile where sediment production is largely concentrated in the euphotic zone (0 to 40 m), while an oligophotic production profile is a profile where sediment production only diminishes below the oligophotic zone (>100 m).

Williams *et al.* (2011) use SFM to quantitatively investigate the influence euphotic and oligophotic production profiles have on platform geometry. However they also simulate significantly distinct sediment production rates, applying higher production rates for the oligophotic production profiles. Williams *et al.* (2011) conclude that oligophotic profiles produce FTSM platforms, not ramps as previously assumed. This results in better-developed slope-breaks and higher maximum slope gradients than euphotic profiles. We argue that these results are misleading. The oligophotic profiles may have developed steeper platform margins as a result of higher overall production rates rather than a result of the shape of the tested production profiles. Given the limitations of the forward modelling methods applied, their conclusions require further investigation.

Two distinct carbonate production profiles are tested in this study. The euphotic production profile (figure 3.2A) is based on the production profile of the photozoan scleractinian coral factory (figure 3.1A). The oligophotic production profile (figure 3.2B) is based on the production profile of the heterozoan coralline red algal factory (figure 3.1C). Production profiles were developed from these carbonate factories since they are well supported by literature data on sediment production *versus* depth and grain-size proportions produced. To assess the influence distinct production profiles have on platform geometry, the tested euphotic and oligophotic production profiles were made equal in terms of total sediment that could be produced within a defined time interval across the depth range producing sediment. This method ensures that the only difference being compared between production profiles is the depth distribution of sediment production. These production profiles are termed "equalised production profiles".

The method applied to produce equalised production profiles is the following. The amount of sediment produced at a depth interval was calculated as a fraction of total sediment produced (e.g., 0.2/1.9 (20%) of total sediment is produced at 0 to 10 m depth, 0.15/1.0 (15%) of total sediment is produced at 10 to 20 m depth etc.). The total sediment produced across the entire production profile then multiplied the fraction. The total sediment production was kept equal between the tested euphotic and oligophotic production profiles. The calculation was repeated at all depth intervals for all tested production profiles. When only one grain-size was considered,

the resulting profile was termed equalised single-grain-size production profiles (figures 3.2A and 3.2B full black lines).

Equalised production profiles producing multiple grain-sizes were also calculated. These were termed equalised multiple-grain production profiles. In these production profiles, the sediment production of the equalised single-grain-size production profile was divided into several production profiles, one for each grain-size produced by the carbonate factory. The sediment production rate of each grain-size is proportional to its contribution towards total sediment production by the factory (e.g. at 10 m depth the scleractinian coral factory produces 75% cobble to boulder and 25 % sand-sized sediment. If the equalised single-grain-size production rate at 10 m depth is 10 m My^{-1}, the equalised multiple-grain-size production rate at 10 m depth is 7.5 m My^{-1} cobble to boulder and 2.5 m My^{-1} sand) (figures 3.2A and 3.2B dotted coloured lines).

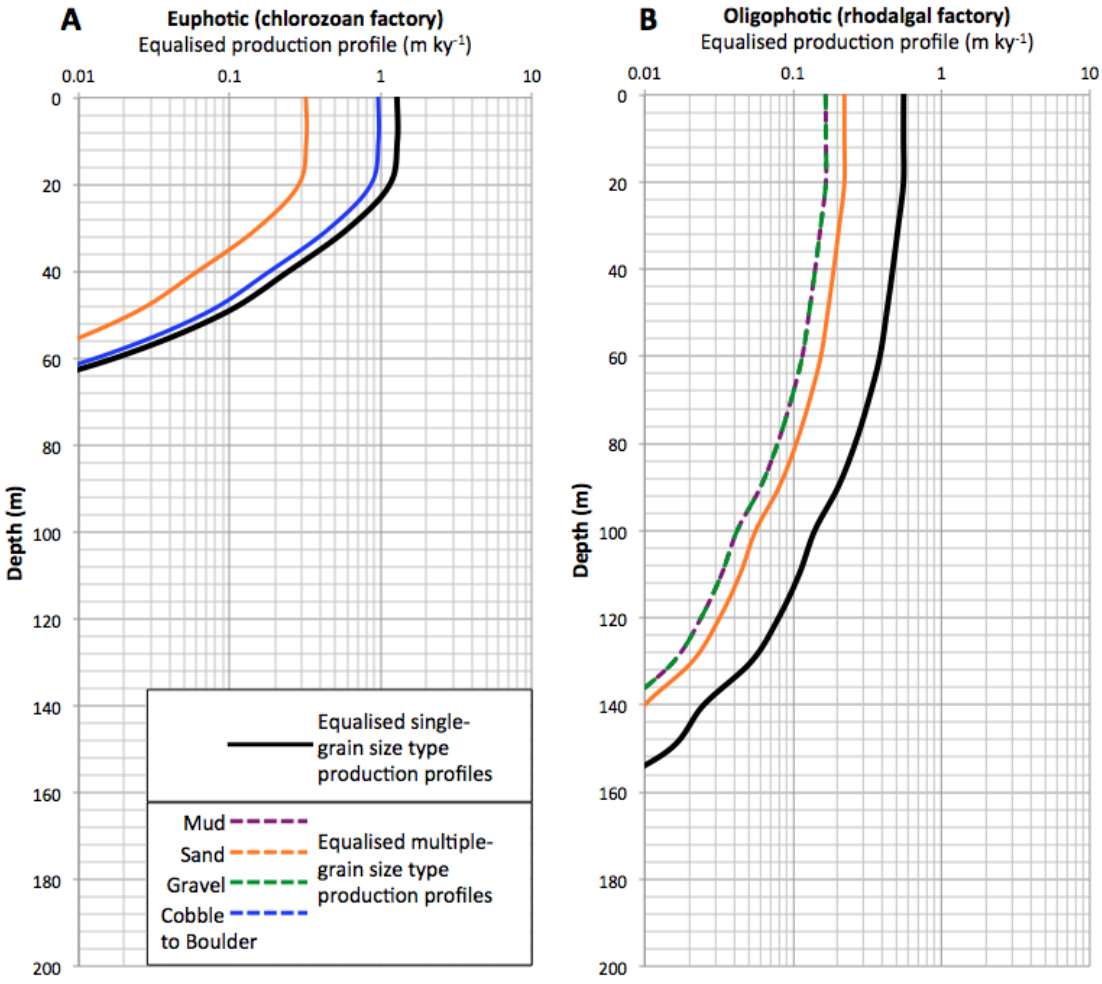

Figure 3.2: Equalised single grain-size and multiple grain-size production for (A) euphotic, and (B) oligophotic production profiles. Full black lines are equalised single-grain-size production profiles. Dashed coloured lines are equalised multiple grain-size production profiles. The euphotic production profile simulates the production profile and the grain-sizes of the photozoan scleractinian coral factory. The oligophotic production profile simulates the production profile and the grain-sizes of the heterozoan coralline red algal factory.

3.2.4. Initial surface

The initial bathymetry used in these models is similar to those recorded underlying Cenozoic platforms from the Mediterranean. The chosen profile is largely comparable with antecedent gradients inferred from the Latium Abruzzi and Llucmajor Mediterranean Miocene carbonate systems on which various platform types formed, ranging from homoclinal ramps to reef rimmed platforms (e.g. Pomar & Kendall, 2008). The initial surface configuration applied in this study simulates a 400 km long two-dimensional grid with a 1300 m relief and a 0.21° slope that passes distally into a 1000 m deep flat-bottomed basin (figure 3.3) (Poulain & Zambianchi, 2007).

The production profiles determine sediment production rates, at a defined time period in an area or point, through an interaction with bathymetry. Since production profiles tested here are simulated on the same initial bathymetries, the influence initial bathymetry has on production profiles can be discounted and the influence production profiles have on altering initial bathymetry, sediment accumulation and platform geometry can be investigated.

A sensitivity test assessing variable cell sizes (1.0 km, 0.5 km and 0.25 km applying same 0.1 My time step) shows that, within the grid size range tested, model accuracy in terms of MaxS is not significantly influenced by grid size (figure 3.4A). A cell size of 0.5 km was selected as it produces accurate results.

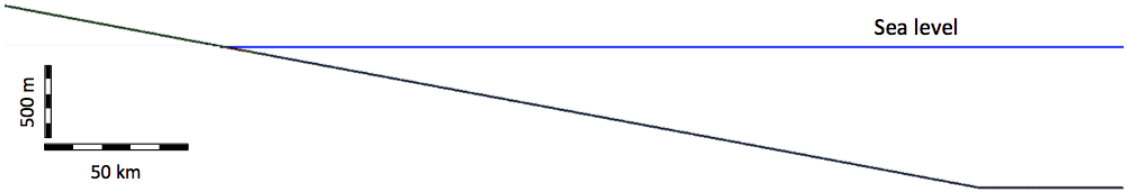

Figure 3.3: The initial topography used in all the model runs (vertical exaggeration V.E. 50). Black line depicts initial surface, and blue line depicts initial sea level

3.2.5. SFM run time (elapsed model time)

A model run time of 5 My was selected. This run time enables platforms to achieve a platform dynamic equilibrium - where platforms maintain a particular platform margin gradient and geometry over time, despite changing variable values, in this case rising relative sea-level and sediment production and transport (stable MaxS in figure 3.4).

Sensitivity test assessing variable time steps (0.5 My, 0.05 My, and 0.005 My applying same 0.5 km grid size) indicate that as time step duration decreases (finer time resolutions) the recorded maximum platform margin gradients increase (figure 3.4B). This is since synthetic

surfaces are more often calculated and this allows for a more precise analysis of maximum platform gradient change over time. However, as time step duration decreases, a threshold is reached where model accuracy is at a maximum. Finer time steps therefore do not significantly influence the simulations output. A time step of 0.05 My was selected as the best compromise between increased accuracy from smaller time steps, and manageable run times from longer time steps.

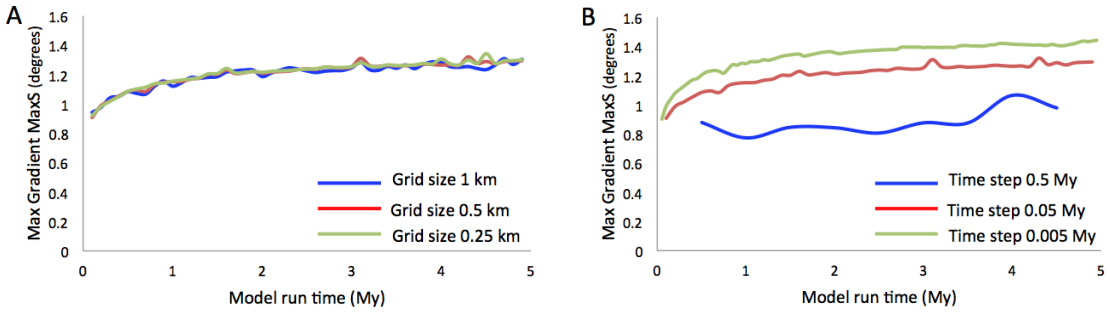

Figure 3.4: (A) Sensitivity test assessing the influence variable grid size has on maximum platform margin gradients. Three models were simulated that apply a common time step (0.1 My), a common diffusion coefficient (0.1 km^2 ky^{-1}) and variable grid sizes. (B) Sensitivity test assessing the influence variable time steps have on maximum platform margin gradients. Three models were simulated that apply common grid size (0.5 km), a common diffusion coefficient (0.1 km^2 ky^{-1}) and variable time steps. (Elapsed model time – EMT).

3.2.6. Sea level history

A late Miocene (10.3 to 5.3 Ma) eustatic sea level curve (Miller *et al.,* 2005; Kominz *et al.,* 2008) was applied in all our SFM to simulate sea level conditions affecting Miocene platforms. A late Miocene sea level curve was selected since section 3.3.1 compares simulated strata with large-scale outcropping strata of two late Miocene carbonate platforms, the Llucmajor reef rimmed platform and the Latium Abruzzi ramp platform. The same sea level curve is applied to all model runs.

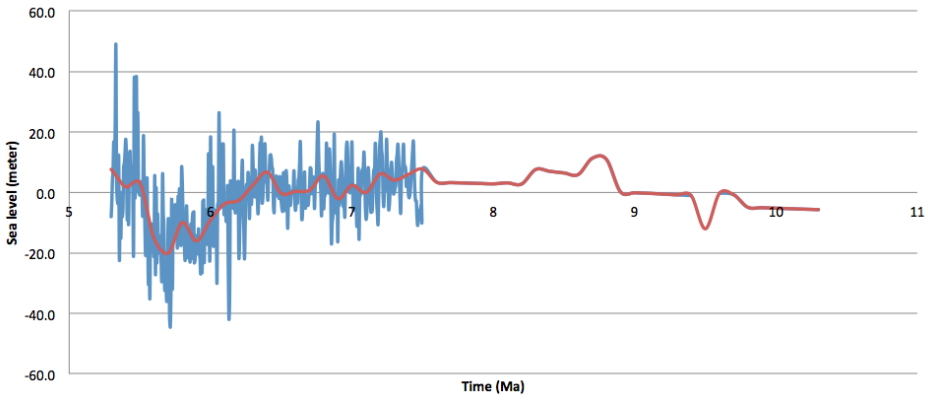

Figure 3.5: Miocene sea level estimates (Miller *et al.,* 2005). Blue curve smoothed to form red line that is used in this study.

3.2.7. Sediment transport

Sediment transport in Dionisos is calculated using a generalized modified sediment diffusion formulation (section 2.3.3.1, 2.3.3.2). Dionisos does not explicitly represent the range of transport processes that can occur in natural carbonate systems (e.g., Playton *et al.,* 2012). Despite the importance of the diffusion coefficient parameter, estimates of the value from natural systems are poorly constrained (section 2.3.3.1). This is particularly true of carbonate systems.

In this study, SFM runs apply diffusion coefficient values ranging from 0 to 2.5 km^2 ky^{-1}. A range is tested so as to represent a variety of possible natural sediment transport situations, from cases with very little transport, to ones that are transport-dominated. The full spectrum of carbonate platform geometries (low angle homoclinal ramp to FTSM platform) was simulated with the tested range of diffusion coefficients and sediment production rates tested. Simulations applying diffusion coefficients greater than 2.5 km^2 ky^{-1} did not accumulate sediment *in situ* and were therefore not assessed in this study.

The relationship between grain-size and transport rate has been expressed by attributing different diffusion coefficients to different sedimentary grain-sizes. Coarser material is expressed as sediment with a low diffusion coefficient and hence a lower transport rate than finer-grade material. The diffusion coefficient is therefore inversely proportional to grain-size. The diffusion coefficient ratios for each grain-size vary from no differentiation (1x mud: 1x sand: 1x gravel: 1x cobble to boulder) (i.e. no distinction between grain sizes) to significant difference (1x mud: 0.05x sand: 0.0025x gravel: 0.0001x cobble to boulder), where x is the diffusion coefficient (km^2 ky^{-1}).

3.3. Stratigraphic Forward Model results and discussions

Results are presented in three sections.

(i) Section 3.3.1 simulates sediment production of the photozoan and the heterozoan factories. This section determines whether these distinct carbonate factories develop distinct stratal architectures and platform geometries. The tested factories are distinct from one anther in terms of (a) production profiles, (b) sediment production rates, and (c) production of different grain-size proportions (with distinct diffusional transport rates). The first section therefore does not quantify how these different aspects of carbonate factories influence platform geometry. This analysis is done in the succeeding sections (3.3.2 and 3.3.3).

(ii) Section 3.3.2 assesses different production profiles, sediment production rates and sediment diffusional transport rates and determine their influence on platform evolution. All tests in this section simulate the production of one grain-size, and therefore represent the simplest type of carbonate factory (produces only one grain-size).

(iii) Section 3.3.3 assesses the influence that multiple grain-sizes and relative quantities have on stratal architecture, platform evolution and geometry. In these runs several grain-sizes are produced by multiple production profiles that represent grain production from one or more carbonate factories (figure 3.1). These two sections add to Williams *et al.* (2011) experiments by testing equalised production profiles, and investigating sediment production rates, grain sizes, and transport rates that are more characteristic of natural Cenozoic carbonate systems.

It is important to note that tests in section 3.3.2 and 3.3.3 apply equalised euphotic (figure 3.2A) and oligophotic (figure 3.2B) production profiles. The tested equalised production profiles were made equal in terms of total sediment that could be produced within a defined time interval across the depth range producing sediment. In this scheme, total sediment production of the euphotic production profile was reduced to match that produced by the oligophotic production profile. This method ensures that the only difference being compared between production profiles is the depth distribution of sediment production. Since the sections investigate equalised production profiles, the simulations of equalised euphotic production profiles do not achieve the steep slopes associated with FTSM platforms.

3.3.1. Photozoan and Heterozoan factories producing multiple grain-sizes

Two distinct carbonate factories are investigated in this section, the photozoan factory (James, 1997) and the heterozoan factory (James, 1997). The photozoan factory is the sum of sediment production by the scleractinian coral and calcareous green algae factories (sum of sediment production in figures 3.1A and 3.1B). The heterozoan factory is the sum of sediment production by the coralline red algal and molluscan, bryozoan and benthic foraminiferal factories (sum of sediment production in 3.1C and 3.1D). Chlorozoan reef-rimmed carbonate platforms are characteristically dominated by *in situ* accumulation with limited transport, and heterozoan are

transport-dominated ramp systems where significant quantities of produced sediment are transported basinwards. In view of this, distinct grain size diffusion coefficients were applied for the chlorozoan and heterozoan factories. Photozoan grain size diffusional transport rates: mud 0.005 km^2 ky^{-1}, sand 0.00125 km^2 ky^{-1} and cobble to boulder 0 km^2 ky^{-1}. Heterozoan grain size diffusional transport rates: mud 0.05 km^2 ky^{-1}, sand 0.0125 km^2 ky^{-1} and gravel 0.0031 km^2 ky^{-1}.

Results from numerical SFM clearly indicate that distinct carbonate factories developed different stratal architecture and platform geometries (figure 3.6).

The simulated photozoan factory developed platform margin gradients of 14.5° forming FTSM platform geometry (figure 3.6A). This is comparable to descriptions of the late Miocene reef rimmed Llucmajor chlorozoan dominated platform where basinward-dipping clinobeds are 10 to 30° (Pomar *et al*., 1996). Simulations of the photozoan factory develop framestone to rudstone textures in the euphotic zone (0 to 60 m), grainstones and packstones are simulated basinwards within the oligophotic to aphotic zones (>60 m) (figure 3.6B). The simulated chlorozoan factory develops stratal architecture characteristic of reef-rimmed platforms. Both the simulation and the late Tortonian to early Messinian Llucmajor reef-rimmed platform develop reef core framework facies in euphotic depths. Outcrop of the Llucmajor platform demonstrate that the coral reef facies interfinger basinwards with proximal fore-reef slope deposits consisting of grainstone, packstone, rudstone and floatstone facies.

The simulated heterozoan factory develop distally steepened ramp geometries, steep and sudden breaks in platform margins are not developed, and form gradients of up to 4.8° (figure 3.6A). This is comparable to the ramp geometries developed by the heterozoan dominated Latium Abruzzi platform (Brandano *et al*., 2009). Numerical simulations of heterozoan factories develop floatstone to rudstone textures in the upper euphotic zone (0 to 30 m), rudstone textures in the lower euphotic zone (30 to 60 m) to mesophotic zone (60 to 100 m), and packstones to mudstones textures in the oligophotic to aphotic zone (110 to >200 m) (figure 3.6C). The simulated stratal architecture is similar to that observed in the outcropping Latium Abruzzi ramp where rudstone to floatstone facies accumulate in inner (euphotic) to middle (oligophotic) environments and packstones to mudstones accumulate in outer (oligophotic to aphotic) ramp settings (Brandano *et al*., 2009).

The photozoan and heterozoan factories are distinct from each other in 3 ways: (i) the depth distribution of sediment production, (ii) the sediment production rates, and (iii) the grain-sizes produced. The photozoan factory has a euphotic production profile while the heterozoan factory has an oligophotic production profile. Compared against the heterozoan factory, the photozoan factory has a significantly higher total sediment production rate, and produces a larger proportion of coarse grains characterised by a lower-transport rate.

This section does not quantify which carbonate factory aspects and to what extent these different carbonate factory aspects contributed towards the developing of distinct carbonate platforms. The following sections investigate these carbonate factory aspects separately and quantify their influence on platform evolution.

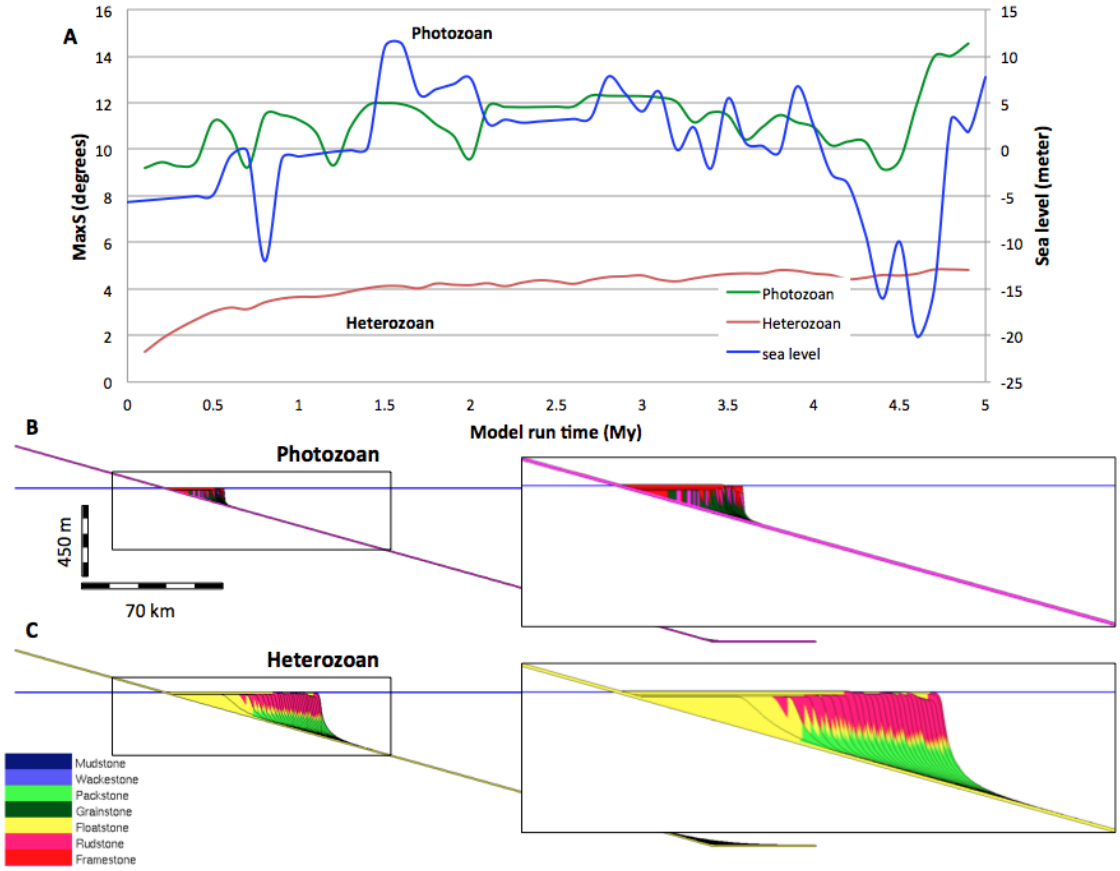

Figure 3.6: (A) Maximum platform margin gradient (MaxS) in degrees at each time step plotted against time (million years) for the photozoan (green curve) and heterozoan (maroon curve) factories. Simulated sea level curve superimposed (blue curve). (B) Photozoan SFM 2D architecture and platform geometry (V.E. 75 with time lines every 0.38 My) – magnification of stratal architecture to the right. (C) Heterozoan SFM 2D architecture and platform geometry (V.E. 75 with time lines every 0.38 My) magnification of stratal architecture to the right.

3.3.2. Carbonate factories producing only one grain-size

3.3.2.1. Control of sediment production and sediment transport on platform geometry in single-grain-size systems

Two distinct carbonate factories and production profiles are tested here; the equalised euphotic production profile (figure 3.2A) and the equalised oligophotic production profile (figure 3.2B). All tests in this section simulate the production of one grain-size, and therefore represent the simplest type of carbonate factory (produces only one grain-size).

Over the range of sediment production and diffusion coefficient rates tested, both euphotic and oligophotic equalised single grain-size production profiles develop a spectrum of platform geometries. The euphotic production profile produces synthetic strata with MaxS that range from 0.22° to 9.31° (figure 3.7A). The oligophotic production profile develops synthetic strata with MaxS that range from 0.22° to 20.88° (figure 3.7B). Geometries range from homoclinal ramps to FTSM platforms.

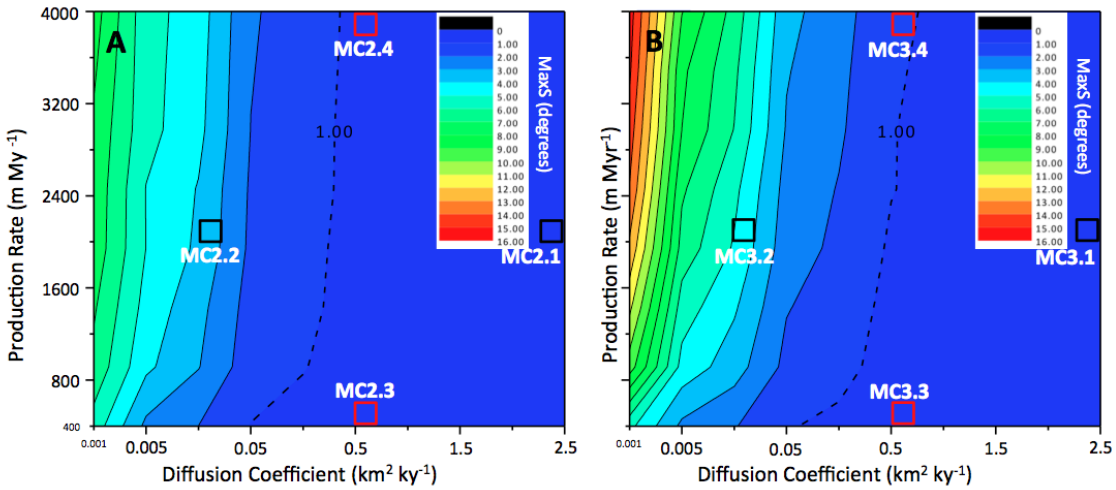

Figure 3.7: Parameter space plot for (A) euphotic, and (B) oligophotic applying *equalised* single grain-size production profiles (figure 3.2 full black curves). Euphotic equalised production profile is characteristic of the scleractinian coral factory production profile, while the oligophotic equalised production profile is characteristic of coralline red algal factory production profile. Red and black boxes are parameter values within the parameter space plot for which SFM results are displayed as 2D cross sections in figure 3.8 (red boxes) and figure 3.9 (black boxes).

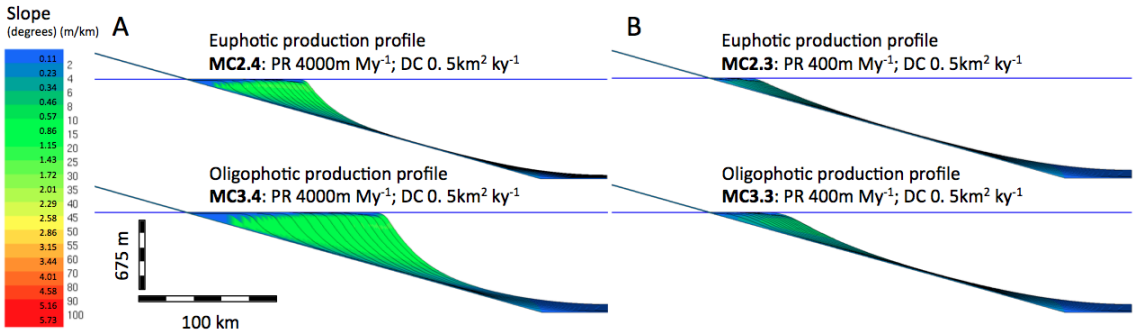

Figure 3.8: SFM 2D profiles (V.E. 75 with time lines every 0.38 My) formed under sediment diffusion coefficient (DC: 0.5 km^2 ky^{-1}) and a range of sediment production rates (PR) (figure 3.7 red boxes); (A) high (PR: 4000 m My^{-1}) and (B) low (PR: 400 m My^{-1}) sediment production rates for the euphotic and oligophotic production profiles. All tested equalised single grain-size production profiles (figure 3.2 full black line) develop FTSM platforms under high sediment production rates, and ramps under low production rates.

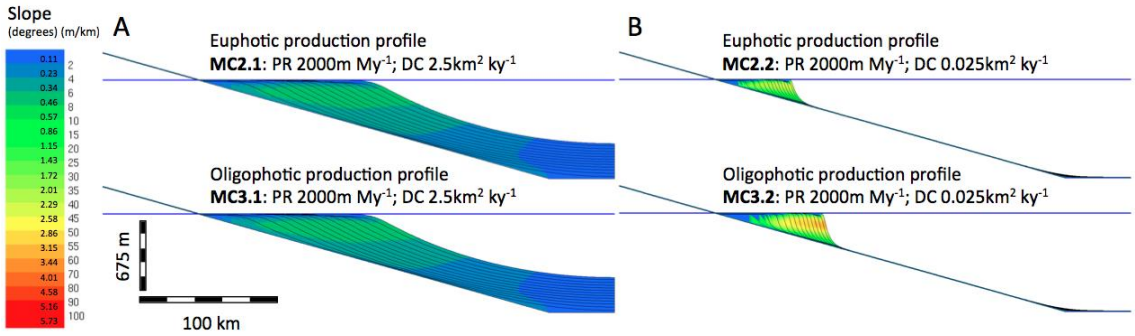

Figure 3.9: SFM 2D profiles (V.E. 75 with time lines every 0.38 My) developed under sediment production rate (PR: 2000 m My^{-1}) and a range of sediment diffusion coefficients (DC) (figure 3.7 black boxes); (A) high (DC: 2.5 km^2 ky^{-1}) and (B) low (DC: 0.025 km^2 ky^{-1}) diffusion coefficient values for the euphotic and oligophotic production profiles. All tested equalised single grain-size production profiles (figure 3.2 full black line) develop FTSM platforms under low diffusion coefficients, and ramps under high diffusion coefficients.

For a defined diffusion coefficient (0.5 km^2 ky^{-1}) over a range of production rates (400 to 4000 m My^{-1}), equalised euphotic single grain-size production profile tests (figure 3.7A) develop MaxS that is lowest (MaxS 0.52°) with least production rates (400 m My^{-1}) and highest (MaxS 0.76°) for greatest production rates (4000 m My^{-1}) (red boxes in figure 3.7A and 2D sections in figures 3.8A and 3.8B). MaxS results for a defined production rate (2000 m My^{-1}) over a range of diffusion coefficients (0.05 to 1 km^2 ky^{-1}) are lowest (MaxS 0.65°) for high diffusion coefficient rates (1 km^2 ky^{-1}) and highest (MaxS 4.98°) for the lowest diffusion coefficient rates (0.05 km^2 ky^{-1}) (black boxes in figure 3.7A add 2D sections in figures 3.9A and 3.9B). Results for the oligophotic profile (figure 3.7B) follow the same pattern.

Results demonstrate that platform geometry in numerical models is controlled by a combination of sediment production (PR) and sediment transport (TR) rates. The control can be expressed as a production-transport ratio or proportion (PR/TR). This relationship is observed for both euphotic and oligophotic equalised single grain-size production profiles. Tests that simulate high PR relative to TR (high PR/TR ratio) develop steep platform margin gradients and form FTSM platforms (e.g. MC2.2 in figures 3.7A and 3.9B). In such scenarios, sediments rapidly accumulate and prograde, forming steep platform margins. Conversely, models that simulate low PR relative to TR (low PR/TR ratio) develop low platform margin gradients and form ramps (e.g. MC2.1 in figure2 3.7A and 3.9A). In such scenarios, high sediment transport rates redistribute sediment across the underlying topography that prevents the steepening of platform margins. Simulations with *similar PR/TR ratios* develop similar platform margin gradients. It is the ratio, not the absolute values of each parameter, that influences platform geometry. For instance PR 600 m My^{-1} / DC 0.75 km^2 ky^{-1} and PR 1800 m My^{-1} / DC 2.25 km^2 ky^{-1} have a similar PR/TR and both develop platform margin gradients of 0.47° (figure 3.7). The PR/TR ratio is a simple, but new and useful way of considering the spectrum of carbonate platform geometries.

3.3.2.2. Control of euphotic and oligophotic single-grain-size production profiles on platform geometry

Both equalised euphotic and oligophotic single-grain-size parameter space plots were superimposed and MaxS values subtracted (figures 3.7A and 3.7B). This allowed for direct comparison of the influence distinct equalised euphotic and oligophotic production profiles (figure 3.2) have on MaxS and by inference platform geometry. The resulting parameter space plot (figure 3.10A) quantifies the influence production profiles have on platform geometry over a range of sediment and production rates.

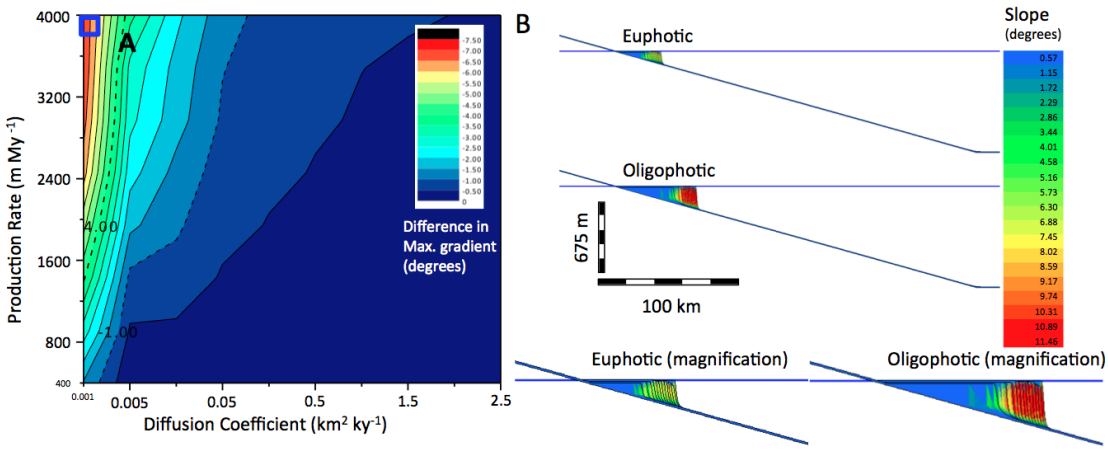

Figure 3.10: (A) Parameter space plots 9A and 9B superimposed and subtracted (euphotic - oligophotic parameter space plot). The blue box (top left corner of PSP) locates the parameter values that produce the greatest difference between the two production profiles. The blue box also identifies the parameter values producing the 2D SFM displayed in in figure 3.9B. (B) SFM 2D profiles (V.E. 75 with time lines every 0.38 My) showing that the greatest MaxS difference of -6.99° (MaxS euphotic < oligophotic production profile) occurs under high sediment production (4000 m My^{1}) and low sediment transport (0.001 km^2 ky^{-1}) conditions (2D section is parameter values of blue square in parameter space plot).

In all the tested sediment production and diffusion transport rates, equalised single grain-size oligophotic production profiles develop steeper platform margins than equalised single grain-size euphotic profiles at the end of the model run time. This is shown by the negative values in the parameter space plot (figure 3.10A). Sediment production by the oligophotic production profile is over a large depth range, while that of the euphotic profile is concentrated in shallow depths. Sediment production and accumulation by the oligophotic production profile is therefore less limited by the available accommodation, which in these tests is defined by the simulated late Miocene sea level curve (section 3.2.6). Additionally, as sediment accumulates at depth, the deeper bathymetries are brought within the oligophotic and euphotic sediment production zone. Consequently, in these equalised production profile runs, the oligophotic profile has a greater sediment production rate over the entire platform slope (per unit time) that leads to greater rates of sediment accumulation, progradation and platform margin steepening.

3.3.3. Carbonate factories producing multiple grain-sizes

3.3.3.1. Control of sediment production and sediment transport on platform geometry in multiple-grain-size systems

The following section tests equalised euphotic and oligophotic multiple grain-size production profiles. The equalised multiple-grain euphotic production profile (figure 3.2A) is based on the scleractinian coral factory and produces cobble to boulder and sand grain-sizes. The equalised

multiple-grain oligophotic production profile (figure 3.2B) is based on the coralline red algal factory and produces gravel, sand and mud grain-sizes.

Over the range of sediment production (400 to 4000 m My^{-1}) and diffusion coefficients (0 to 2.5 km^2 ky^{-1}) tested, both equalised multiple-grain-size euphotic and oligophotic production profiles develop synthetic strata that build the full range of platform geometries (figures 3.11A and 3.11B). Maximum platform margin gradient developed by the euphotic production profile ranges from 0.49 to 9.8° (figure 3.11A) and for the oligophotic production profile from 0.37 to 18.08° (figure 3.11B).

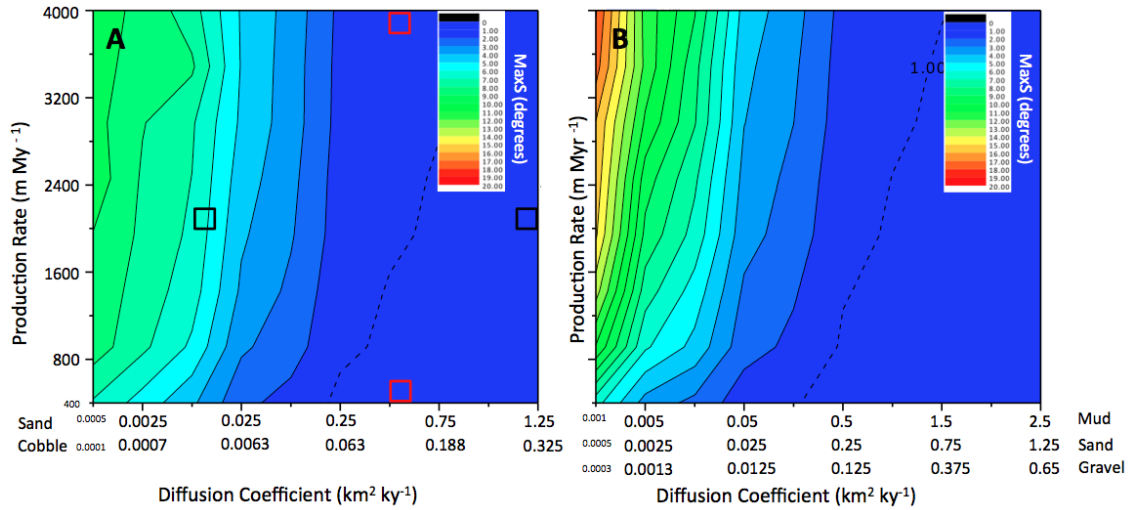

Figure 3.11: Parameter space plot for equalised multiple grain-size (A) euphotic, and (B) oligophotic production profiles (figure 2 coloured lines). The boxes in red and black boxes in figure are parameter values referred to in the paragraphs tied to this sub-section. The euphotic production profile is based on the scleractinian coral factory and produces cobble to boulder and sand grain-sizes (figure 3.2A). The oligophotic production profile is based on the coralline red algal factory and produces gravel, sand and mud grain-sizes (figure 3.2B).

For a defined diffusion coefficient (0.5 km^2 ky^{-1}) over a range of production rates (400 to 4000 m My^{-1}), equalised euphotic multiple grain-size production profile tests (figure 3.11A) produce MaxS that are lowest (0.79°) with lowest production rates (400 m My^{-1}) and highest (1.75°) for greatest production rates (4000m my^{-1}) (red boxes in figure 3.11A). MaxS results for a defined production rate (2000m My^{-1}) over the range of diffusion coefficients (0.05 to 2 km^2 ky^{-1}) are lowest (0.79°) for high diffusion coefficient rates (2 km^2 ky^{-1}) and highest (4.16°) for the lowest diffusion coefficient rates (0.05 km^2 ky^{-1}) (black boxes in figure 3.11A). Results from the equalised multiple grain-size oligophotic production profile (figure 3.11B) follows the same pattern discussed above.

Results from the multiple-grain-size systems indicate that platform geometry is controlled by a combination of sediment transport (TR) and sediment production (PR) rates. These results are the same as those developed in single-grain-size systems (section 3.2.1). This indicates that even in a mixed-grain-size, mixed transport rate system, the production-transport ratio is an key control on platform geometry.

3.3.3.2. Control of euphotic and oligophotic multiple-grain-size production profiles on platform geometry

Both equalised multiple grain-size parameter space plots were superimposed and MaxS values subtracted (figures 3.11A and 3.11B). The resulting parameter space plot (figure 3.12A) quantifies the influence distinct equalised production profiles and distinct grain-size produced (and their attributed diffusion coefficients) has on platform geometry.

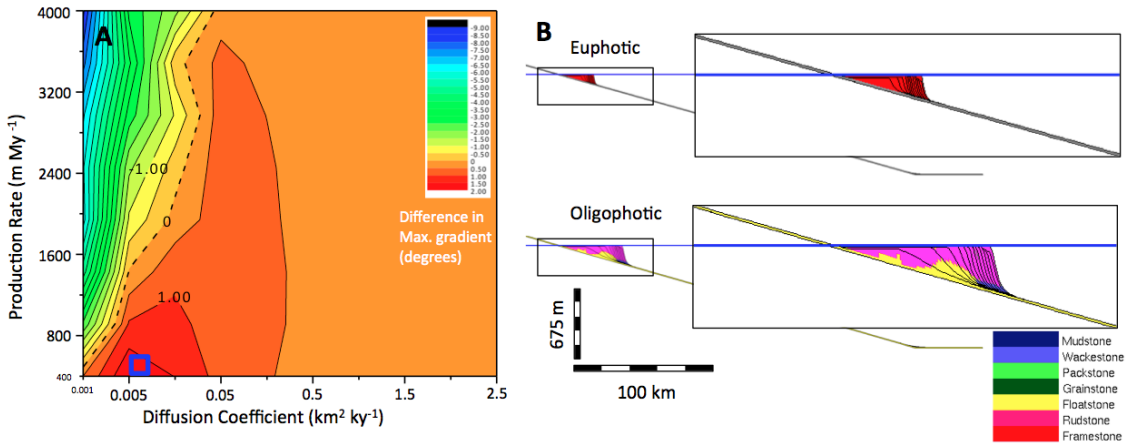

Figure 3.12: (A) Parameter space plots figure 3.11A (euphotic) and 11B (oligophotic) superimposed and subtracted. The blue box (bottom left corner of PSP) locates the parameter values that produce the greatest difference between the two production profiles. The blue box also identifies the parameter values that develop the 2D SFM displayed in in figure 3.12B. (B) SFM 2D facies profiles (V.E. 75 with time lines every 0.38 My) showing the greatest MaxS difference of 1.98° (MaxS euphotic > oligophotic) under low sediment production (400 m My^{-1}) and low sediment transport (0.001 km^2 ky^{-1}) conditions (2D section is parameter values of blue square in parameter space plot).

Results indicate that under low-to-high diffusion coefficient values (>0.001 km^2 ky^{-1}) and all tested sediment production rates, the euphotic production profile develops steeper platform margins than the oligophotic production profile. This relationship is the opposite of that observed for single grain-size profiles (section 3.2.2), where oligophotic production profiles developed steeper platform margins than euphotic production profiles. The effects of the

simulated grain-sizes have in this case outweighed the influence that production profiles have on platform geometry.

These tests show that the size, quantity and transport rate (diffusion coefficient) of grains produced significantly influence platform geometry. Carbonate factories control the quantity of grain-sizes produced that influences platform sediment transport rates. This in turn influences the PR/TR ratio and platform geometry. The scleractinian coral factory produces coarse grains, develops a higher PR to TR ratio and forms FTSM platforms. The coralline red algal factory produces finer grains and develops a higher TR to PR ratio forming ramps. The control carbonate factories exert on stratal architecture and platform geometry through their control on grain sizes and quantities produced is further investigated in section 3.3.3.4 below.

3.3.3.4. Systematic analysis of different proportions of mud, sand and gravel and their influence on platform geometry

Thirty models are tested in this section. Each model simulates different proportions of mud, sand and gravel (e.g. 10% mud and 90% gravel *versus* 90% mud and 10% gravel). The different proportions of sediment grain sizes and model reference numbers (MRN) are provided in table 3.2. The only difference between models is the grain-size proportions simulated, and the attributed grain-size diffusion coefficient. Other models parameters are equal.

Maximum platform margin gradients (MaxS degrees) increase with an increase in contribution (of total sediment production) of low diffusion coefficient grain-sizes in a linear relationship (figure 3.13). This is evident for MRN6.1 to 6.10 that represent an increasing proportion of sand relative to mud (blue rhombus), MRN6.11 to 6.20 that represent an increase in proportion of gravel relative to mud (green triangle), and MRN6.21 to 6.30 that represent an increase in proportion of gravel relative to mud (blue asterisk). No threshold grain-size proportion and platform margin steepening were observed. The lower the diffusion coefficients used, the steeper the maximum platform margins developed and vice-versa.

The difference in maximum platform margin gradients (MaxS diff degrees) between successive models for red squares MRN6.1 to 6.10 (mud and sand), green violet cross MRN6.11 to 6.20 (mud and gravel), orange circles MRN6.21 to 6.30 (sand and gravel). These results demonstrate that as the contribution of low diffusion coefficient grain-sizes towards total sediment production increases, the difference between previous models - simulating larger proportions of higher diffusion coefficient grain-sizes - maximum platform gradient decreases.

MRN	1	2	3	4	5	6	7	8	9	10	11
Sand & Gravel											
Mud % of total PR	100	90	80	70	60	50	40	30	20	10	0
Sand % of total PR	0	10	20	30	40	50	60	70	80	90	100
Gravel % of total PR	0	0	0	0	0	0	0	0	0	0	0

MRN	12	13	14	15	16	17	18	19	20
Mud & Gravel									
Mud % of total PR	90	80	70	60	50	40	30	20	10
Sand % of total PR	0	0	0	0	0	0	0	0	0
Gravel % of total PR	10	20	30	40	50	60	70	80	90

MRN	21	22	23	24	25	26	27	28	29	30
Sand & Gravel										
Mud % of total PR	0	0	0	0	0	0	0	0	0	0
Sand % of total PR	90	80	70	60	50	40	30	20	10	0
Gravel % of total PR	10	20	30	40	50	60	70	80	90	100

Table 3.2: Grain size proportions and model reference number (MRN).

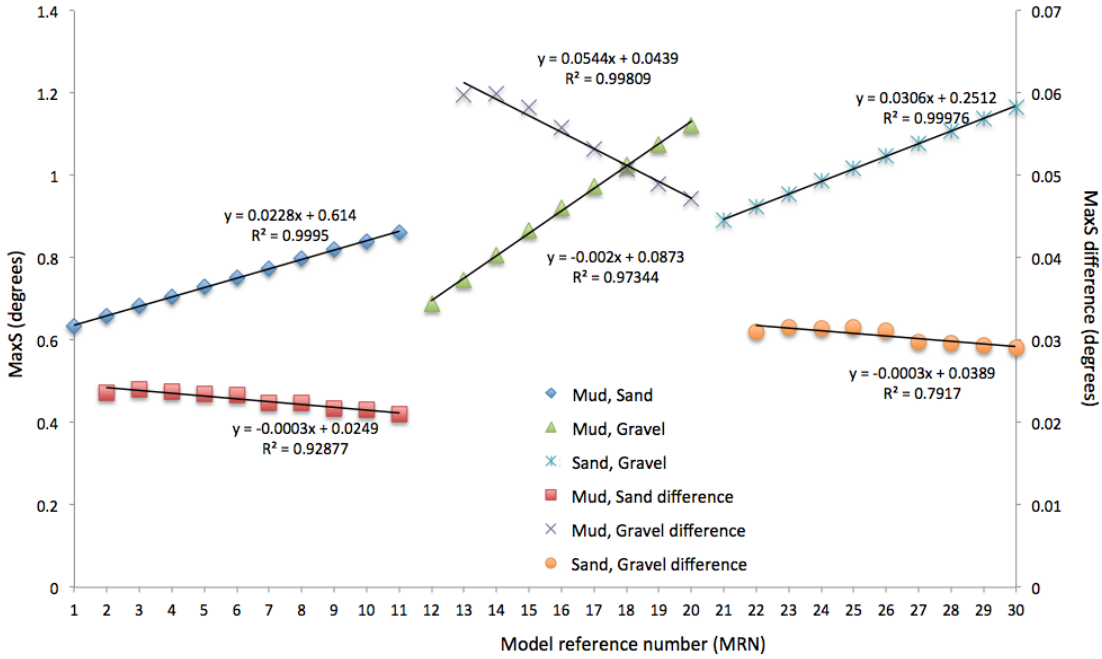

Figure 3.13: Each MRN simulates a distinct grain-size proportion – refer to table 3.2 for grain size proportions. Horizontal axis demonstrates the model number (table 3.2), the left vertical axis displays the MaxS (degrees) and the right vertical axis displays the trend line (MaxS difference (degrees) between successive models).

Distinct platform geometries were formed through the simulation of distinct grain-size proportions. Simulations assessing grain-sizes with lower diffusion coefficients (e.g. sand-gravel) develop steeper platform margin gradients than those simulating grain-sizes with higher diffusion coefficients (e.g. mud-sand). For instance a model simulating 10% mud and 90% sand (MRN6.10) develops a MaxS of 0.84°, a model simulating 10% mud and 90% gravel (MRN6.20) develops a MaxS of 1.12°, and a model simulating 10% sand and 90% gravel (MRN6.29) develops a MaxS of 1.34° (figure 3.13). Results clearly indicate that the relative proportions of grain-size produced, and their attributed diffusion coefficients, significantly influence platform geometry. This is since fine-grained systems are transport-dominated systems (sediment transport rate relatively higher than sediment accumulation) and develop ramp geometries. Conversely, coarse-grained systems are deposition-dominated systems (sediment accumulation rate is relatively higher than sediment transport) and develop FTSM platforms.

Tests confirm a strong positive correlation between the maximum platform margin gradient and the proportions of grain-sizes simulated. Platform margin gradients increase as the proportion of coarse, low transport rate, grains increases. Maximum platform margin gradients increase linearly with an increase in the contribution of low diffusion coefficient grain-sizes. This relationship is observed in the trend lines of all tested grain-size proportions (figure 3.13 mud-sand blue rhombus, mud-gravel green triangle and sand-gravel blue asterisk).

As proportions of coarser grain-size are increased, and finer grain-size proportions decreased, the mud-gravel simulations develop a steeper dipping trendlines than mud-sand and sand-gravel simulations (figure 3.13 mud-sand blue rhombus, mud-gravel green triangle and sand-gravel blue asterisk). Results therefore show that the presence of very low diffusion coefficient material (e.g. gravel) can have a greater influence on steepening platform margin gradient than larger quantities of lower diffusion coefficient material (e.g. sand). Mud-sand (MRN6.1 to 6.10) and sand-gravel (MRN6.21 to 6.30) simulations develop a similar increase in maximum platform margin gradient with an increase in proportion of low diffusion coefficient grain-sizes. A trend line of 0.023 is developed for mud-sand simulations and 0.031 for sand-gravel simulations (figure 3.13). It is interesting to note that within the range of tested diffusion coefficients, as long as one grain-size diffusion coefficient is half as great as the other, the behaviour is observed independently of the diffusion coefficient used (figure 3.11). Mud-gravel (MRN6.11 to 6.20) simulations also demonstrate an increase in maximum platform margin gradient developed with an increase in proportion of low diffusion coefficient grain-sizes. The mud-gravel slope trend line is steeper (0.054) than those developed by sand-gravel (0.031) (figure 3.11, compare green triangles to blue stars). The distinct trend lines are interpreted to be the consequence of the following SFM process. As low diffusion coefficient gravel-sized grains accumulate, the platform margin steepens. The mud-sized higher diffusion coefficient grain

fraction does not accumulate *in situ* and is transported basinwards. Since the gravel-sized sediment dominates *in situ* accumulation, the gravel grains build the platform margin gradient. This is the case even if they constitute a minor portion of total sediment production.

3.4. Conclusions

Holocene grain size production profiles

The study brackets average sediment production rates, depth distribution of sediment production, and proportions of grain-sizes produced for five carbonate factories from Holocene systems (section 3.2.2). These different aspects are combined to form production profiles that better represent particular natural carbonate factories.

The production profiles can be applied in SFM to more accurately simulate sediment production of particular natural carbonate platforms than realised in previous SFM-based attempts. A more realistic simulation of sediment production contributes to the building of accurate forward models. As discussed by Bosence *et al*. (1994), accurate forward models enable: the testing of sequence stratigraphic interpretations, the reconstruction of partially exposed or imaged carbonate stratigraphies, the locating and quantifying of likely reservoir facies, illustrating the development and likely interconnections of reservoir facies, analysing the primary depositional controls on reservoir heterogeneities, and predict stratigraphies around a basin margin.

Control of production profiles on platform geometry

In all the tested sediment production and diffusion transport rates, equalised single grain-size oligophotic production profiles develop steeper platform margins than equalised single grain-size euphotic profiles (see section 8.2.1 for discussion).

Control of grain-sizes and their relative quantities on platform geometry

Results clearly indicate that the relative proportions of grain-size produced, and their attributed diffusion coefficients, significantly influence platform evolution and geometry. Tests confirm a strong positive correlation between the maximum platform margin gradient and the proportions of grain-sizes simulated. Platform margin gradients increase as the proportion of coarse, low transport rate, grains increases. Maximum platform margin gradients increase linearly with an increase in the contribution of low diffusion coefficient grain-sizes.

These results may be a consequence of the Dionisos diffusional transport computation and is consequently only a hypothesis for how natural systems might work. This result thus requires further testing.

Control of sediment production and transport rates on platform geometry

Results suggest that hypotheses emphasising production profiles, production rates or transport rates, as separate, more-or-less dominant, controls are misleading. Rather, platform evolution and geometry is controlled by a combination of both production and transport rate. These aspects are, to a large extent influenced by carbonate factories. The control can be expressed as a production-transport (PR/TR) ratio. The production-transport ratio is the control in both tested production profiles, and even in a mixed-grain-size, mixed transport rate system.

Simulations with similar PR/TR ratios develop similar platform margin gradients. It is the ratio, not the absolute values of each parameter, that influences platform evolution and geometry. Tests that simulate high PR relative to TR (high PR/TR ratio) develop steep platform margin gradients and form FTSM platforms. Conversely, models that simulate low PR relative to TR (low PR/TR ratio) develop low platform margin gradients and form ramps. Carbonate factories control the quantity and type of grain-sizes produced. This in turn influences the PR/TR ratio and platform geometry. The photozoan factory has a high PR relative to TR and produces a FTSM platform while the heterozoan factory has a high TR relative to PR and forms a ramp. The distinct platform geometries are therefore the consequence of distinct PR/TR ratios.

Control of carbonate factories on stratal architecture and platform geometry

The photozoan factory has a greater sediment production rate than the heterozoan factory. The photozoan factory also produces grain-sizes that are less easily transported - expressed with a lower diffusion coefficient. The photozoan factory has a high PR relative to TR and produces a FTSM platform while the heterozoan factory has a high TR relative to PR and forms a ramp. The distinct platform geometries are therefore the consequence of distinct PR/TR ratios. In the tests carried out in this chapter, the different simulated stratal architecture and platform geometries are the consequence of different carbonate factories that lead to a different PR/TR ratio.

CHAPTER 4: EXPLORING THE ROLES OF SEDIMENT PRODUCTION AND TRANSPORT ON CARBONATE PLATFORM GEOMETRY

4.1. Introduction

The chapter applies an inverse modelling method to construct a numerical model that replicates platform features (facies architecture and stratal geometry) observed in real carbonate platforms or models constructed from outcrop observations and interpretations (conceptual models). Numerical SFM that replicate depositional systems may be valuable in testing sequence stratigraphic interpretations, reconstructing partially exposed or imaged carbonate stratigraphies, locating and quantifying likely reservoir facies, illustrating the development and likely interconnections of reservoir facies, analysing primary depositional controls on reservoir heterogeneities and predicting stratigraphies around a basin margin (e.g. Bosence *et al.,* 1994; Burgess & Steel, 2008; Warrlich *et al.,* 2008).

The method is applied to a cliff section through the reef-rimmed Llucmajor platform that formed during the late Miocene (Tortonian-Messinian) in Mallorca. This outcrop example was chosen because the controls on the stratigraphic processes have been extensively studied and are relatively well understood (e.g. Pomar, 1991, 1993; Pomar & Ward, 1994, 1995; Pomar *et al*., 1996). The numerical model that best matches the Llucmajor conceptual model in terms of stratal geometry and facies architecture is used to provide insights that conventional sedimentological analysis has difficulty answering (e.g. Warrlich *et al*., 2008). This work investigates two key aspects:

(i) (Section 4.3.1) Assesses the influence of sediment production and diffusional transport on facies architecture and stratal geometry. The section identifies which combination of sediment production and diffusional transport best replicates facies architecture and stratal geometry of the Llucmajor conceptual model. These sedimentary production and more general transport rate (resulting from diffusional transport) can be applied in other SFM based studies that attempt to re-create sediment production, transport and accumulation dynamics that develop particular stratal geometries and platform types. The specific sediment production and diffusional transport values can be applied to diffusion-based SFM (e.g. Dionisos).

(ii) (Section 4.3.2) Whether different parameter values for the controlling processes (sediment production and diffusional transport) develop facies architectures and stratal geometries that are not demonstrably different from one another and are thus non-unique (*sensu* Burgess & Prince, 2015). The section also describes the sediment production and transport processes that control platform evolution. Previous work has investigated non-uniqueness (e.g. Heller *et al*., 1993; Flemings & Grotzinger, 1996; Burgess & Prince, 2015). However, this work is different from previous attempts because it tests if non-unique platform features can be developed in models that simulate distinct sediment production and diffusional transport rates that are better constrained and characteristic of real carbonate systems. If these tests develop

models that are not significantly different from one another, this would demonstrate non-uniqueness within a realistic parameter range. This would emphasise the need for a shift towards sequence stratigraphic methods based on constructing and evaluating multiple rather than single hypotheses and scenarios (Burgess & Prince, 2015).

4.2. Methods

4.2.1 Stratigraphic Forward Model applied

Dionisos SFM (section 2.3.3.2) (Granjeon & Joseph, 1999; Granjeon *et al.,* 2002) is applied in this study.

A summary table (table 4.1) is presented below that indicates what model parameters were applied in this chapter. The parameter rates are described in more detail in the following sections within the chapter.

SFM parameters applied in section	4.3.1	4.3.2
DIONISOS	✓	✓
Model iterations	1085	1085
Duration (My)	2.1	2.1
Time step (My)	0.05	0.05
Cell size (km)	0.25	0.25
Initial bathymetry (figure)	4.1	4.1
Sea level history (figure)	4.2	4.2
Sediment production equalised production profile	✗	✗
Sediment production natural production profile	✓	✓
Single grain size	✗	✗
Multiple grain size	✓	✓
Sediment transport by diffusion ($km^2\ ky^{-1}$)	0 to 1	0 to 1
Wave and current modelling.	✗	✗
Sediment transport by slope failure	✓	✓
Sub-aerial erosion	✓	✓

Table 4.1: Summary of initial model conditions and input parameters.

4.2.2. Method to simulate facies architecture and stratal geometry that match outcrop

The study applies a SFM inverse method (section 2.3.2.2) to identify which sediment production and diffusional transport rates simulate facies architectures and stratal geometries are similar to those observed in real carbonate systems/platforms. In this study, the method is applied to a cliff section through the reef-rimmed Llucmajor platform that formed during the late Miocene in Mallorca.

Stratigraphic inverse methods consist of a SFM that simulate stratigraphy, a set of observed real world data that can be compared to SFM outputs, and a set of equations that quantitatively compare SFM outputs to observations of real world data (Cross & Lessenger, 1999; Charvin *et al*., 2009). The method first (i) requires input parameters characterizing the modelled basin and its evolution through time (section 4.2.2.1). This is to ensure that synthetic facies architectures and stratal geometries are the result of processes and parameter rates characteristic of the investigated natural system. Sediment diffusional transport rates cannot be directly constrained from outcrop. Consequently, a range of diffusional transport rates must be tested. The method then (ii) applies an objective function that quantitatively compares the synthetic and real platforms in terms of facies architectures and stratal geometries (section 4.2.2.2). The metric that is calculated from the objective function identifies which combination of sediment production and diffusional transport develops a model that best matches outcrops of the real platform.

4.2.2.1. SFM Parameters and Processes

The parameters and processes that influence the evolution of the Llucmajor carbonate platform include: initial surface, time of formation, sea level and relative sea level history, carbonate sediment production, slope failure, sub-aerial erosion and diffusional transport. These parameters and processes were constrained from literature descriptions of subsurface and outcrop data and from analogue ancient and modern carbonate systems.

Wile the chapter attempts to simulate an outcrop example, literature descriptions of the platform (e.g. Pomar, 1991, 1993; Pomar & Ward, 1994, 1995; Pomar *et al*., 1996) are more a conceptual model than an actual data directly observed. This is since most of the elements discussed by the aforementioned authors require interpretation of various different elements that can be more directly observed from outcrop.

A number of precautions must be taken when defining SFM parameters that seek to replicate particular platform cases. This is in order to avoid issues of circular reasoning. SFM parameters should not be based on interpretations of how features observed in that specific platform were formed. If the simulated SFM parameters represent conceptual models, the SFM will simply replicate the conceptual model for the platform, not the natural processes that may have affected platform evolution. The conclusions drawn from SFM would therefore represent the initial

assumptions/interpretations made to construct the conceptual model. New insights into the natural processes governing platform evolution therefore would not be possible.

SFM parameters should rather be based on independent observations of the real sedimentary system. This helps ensure that the SFM parameters are objective observations and do not reflect conceptual model-building interpretation. This is possible for certain SFM parameters (e.g. carbonate factories). However, other model parameters invariably contain an element of interpretation (e.g. relative sea level history). In this chapter, we explain what the SFM parameters are based on (table 4.2). This allows the reader to know exactly the basis on which the modelling is being done and know which parameters are more robust (based on more direct platform observation) and which are more speculative interpretations (based on conceptual model interpretations).

Model parameter	**Explanation**	**Certainty** (decreasing order): (i) Direct outcrop observation, (ii) Robust interpretation, (iii) Speculative interpretation
Initial surface	Outcrop and core-hole data (Pomar *et al*., 1996; Pomar, 2001)	Direct outcrop observation
Sea level curve	Based on (i) fossil in facies and their interpreted paleobathymetries, (ii) relative elevations of successive facies, (iii) thickness of platform facies, and (iv) stratal geometries.	Robust interpretation
Formation time	Regional considerations, biochronozone, Sr isotopes and K-Ar dates	Robust interpretation
Sediment production	Carbonate factories active at various depth zones based on facies model	Robust interpretation

Table 4.2: Evidence used to define/constrain model parameters. The table indicates the basis on which the modelling is being done – which model parameters are more robust and which are more speculative interpretation.

4.2.2.1.1. Initial surface (and selection of grid size and time step)

The initial topography and bathymetry for the Llucmajor model follows the pre-Miocene basement as seen in sea-cliff exposures along the southern Llucmajor platform (Pomar, 1991; Pomar *et al*., 1996). The initial bathymetric surface has been modelled as a 50 km long two-dimensional grid with a 335 m relief (35 m above sea level to 300 m below sea level) (figure 4.1).

Figure 4.1: (A) Locations and simplified geological maps of the Llucmajor platform (modified from Pomar *et al*., 1996). Red line in map indicates location of SFM initial bathymetry. (B) Initial surfaces of the Llucmajor platform model (V.E. 20) based on literature descriptions and diagrams (modified from Pomar *et al*., 1996). Dashed vertical lines indicate the location of Cap Blanc area. Outcrop based lithological logs are available for the Cap Blanc area and are used in this study to compare real and synthetic/simulated facies.

Sensitivity tests assessing variable gird sizes (1 km, 0.5 km and 0.25 km applying same 0.1 My time step) and variable SFM time steps (0.5 My, 0.05 My and 0.005 My applying same 0.5 km grid size) were carried out to assess the influence grid size have on model accuracy in terms of maximum platform gradient (sections 3.2.4 and 3.2.5). In view of this, a grid size of 0.25 km and a time step of 0.05 My was select as suitable for the study as the best compromise between increased accuracy from smaller time steps, and manageable run times from longer time steps.

4.2.2.1.2. Llucmajor formation time

Bizon *et al*. (1973), Pomar *et al*. (1983), Pomar (1991), Alvaro *et al*. (1984) and Oswalr (1992) provide a chronostratigrpahic framework for the three sequences observed in the Llucmajor platform (Pomar, 2001; Pomar *et al*., 1996). The lower sequence corresponds to a carbonate ramp consisting of rhodalgal lithofacies. The *Heterostegina* unit of the rhodalgal-ramp, which is immediately overlain by the Cap Blanc reefal unit (Pomar, 2001 figure 2), is attributed to the early Tortonian (N16 in Alvaro *et al*., 1984). The middle sequence corresponds to a well-developed progradational reef platform. Regional considerations have attributed the Cap Blank Reef to the late Tortonian – early Messinian (Pomar *et al*., 1983) and more precisely the late Tortonian global cycle TB3.2 of Haq *et al.* (1988) (Pomar, 1991). This is consistent with Bizon *et al*. (1973) and Alvaro *et al*. (1984) who determine that samples from the Cap Blanc area are

from the N17 (late Tortonian) biochronozone. Age estimations from Sr isotopes (Oswalr, 1992) also give a late Tortonian age for the reef complex. The upper sequence consists of oolites and stromatolies. Ar–Ar dates in the middle of the 20 km wide Llucmajor Platform indicates an early Messinian age (6.2 Ma on the sanidines and 6.5 Ma on the biotites). This gives a late Tortonian–early Messinian age for the whole platform (Pomar *et al*., 2012).

This study simulates the middle and upper sequences that correspond to the progradational reef-rimmed and back-reef Llucmajor platform that formed during the late Tortonian – early Messinian in Mallorca. Literature descriptions of chronostratigraphy suggest the sequences may have been deposited between 8.4 to 6.3 Ma (Pomar *et al*., 1996; Pomar *et al*., 2012). This entails a SFM run time of 2.1 My.

4.2.2.1.3. Sea level curve

The Llucmajor reef crest trajectory, at the platform margin, was predominantly progradational but also contains an element of aggradation (Pomar, 1991; Pomar & Ward, 1994; Pomar *et al*., 1996). Pomar (1991) and Pomar & Ward (1994) propose that the vertical shifts are the result of Late Miocene eustatic sea level changes. Pomar *et al*. (1996) observe that the coral colonies growth morphology in outcrop is vertically zoned in the reef core. They suggest the coral growth morphologies are depth-controlled such that deeper-water corals show platy forms, intermediate-depth corals are branching and shallower corals are hemispherical to columnar (Pomar *et al*., 1996). The vertical zonation of coral-colony morphologies with respect to depth corresponds to modern depth-controlled coral growth morphologies. Pomar uses coral growth forms and reef-crest lines as a proxy to interpret depositional paleo-depth and sea level amplitude fluctuations. Using this information, they develop the amplitude variations to the Llucmajor sea level curve. The sea level curve applied in this study follows that proposed by Pomar (1991) and represents the reef crest line of cosets of sigmoids (figure 4.2). The sea level history time component is based on the length of reef progradation time (2.1 My) defined in the previous section (4.2.2.1.2).

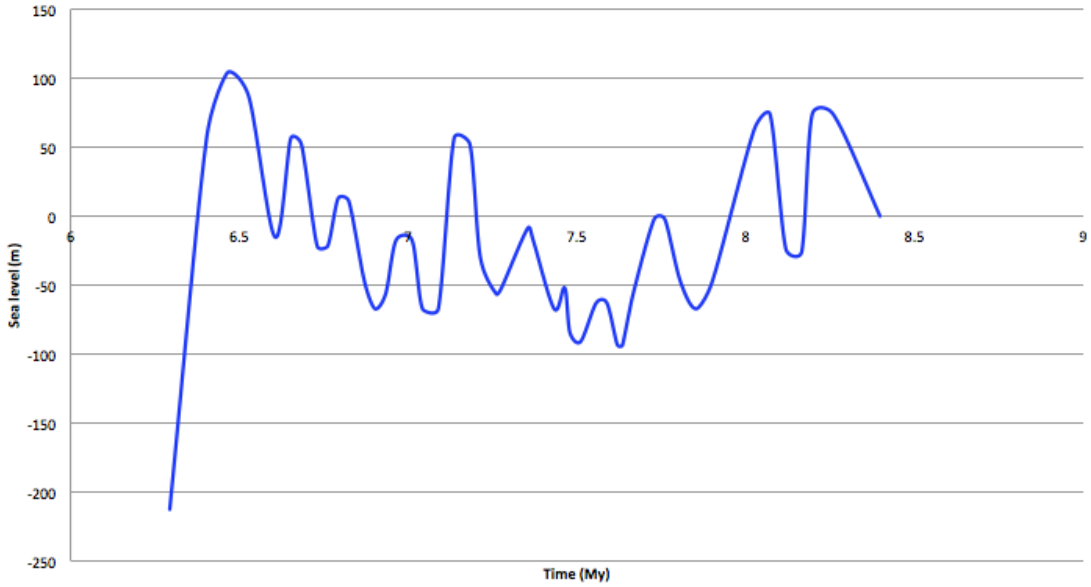

Figure 4.2: Sea level curve developed by Pomar (1991) for the Llucmajor platform on the basis of reef crest positions. This sea level curve is applied in SFM simulations. The time component (horizontal axis) of the sea level history was tied to the length of time during which the reef prograded (2.1 My) established in section 4.2.2.1.2.

4.2.2.1.4. Depositional conceptual model of the Upper Miocene Llucmajor Reef Complex

Pomar *et al*. (1996) develop a depositional conceptual model (figures 4.3 and 4.4) for the lithofacies observed in the Upper Miocene Llucmajor Reef Complex. The model represents the various depositional environments and is built on differences in facies lithology, skeletal/non-skeletal constituents, bedforms and geometric relationships. The lithofacies are the off-reef open-shelf, fore reef slope, reef core, and the back-reef lagoon lithofacies. The facies model is a conceptual model and is consequently an interpretation of observed outcrop features. It is therefore necessary to review which objective outcrop observations support the facies model and where the certainty in the facies model arises.

The key to the facies model is the position of lithofacies relative to the coral rich reef-core lithofacies that is interpreted to form the platform margin. The reef-core lithofacies consists of coral framework and reefal rudstone and contains secondary reef core framework components that include encrustations of red algae, foraminifera and bryozoans (Pomar, 2001). The lithofacies develops progradational sigmoids that dip (<45°) south-westwards in what was presumably a paleo-seaward direction (Pomar *et al*., 1996). Within the sigmoids, the coral colonies are vertically zoned according to depth-controlled growth morphologies. The coral morphologies change down depositional dip (south-westward) from domal and massive, to branching and platy. The change in coral morphology is observed in modern corals and represents an increase in paleo-depth from the shallow marine reef-crest, to intermediate water-

depths and deeper-water depths. These outcrop observations ground the interpreted depositional model in observational truths. The reef-core lithofacies is convincingly placed within the platform margin and can be used to indicate which lithofacies are basinwards (south-westwards) and landwards (north-eastwards) relative to the reef-core lithofacies.

Basinwards (south-westwards) of the reef-core lithofacies is the fore-reef slope lithofacies and then the off-reef open shelf lithofacies. The proximal fore-reef slope deposits consist of basinward-dipping (10 to 30°) clinothems composed of skeletal and intraclastic grainstone, packstone, rudstone and floatstone that interfinger landward with coral reefs. In distal fore-reef slope positions, slope deposits consist of gently inclined red algae-mollusk packstone/grainstone with rhodoliths, whole-shell bivalves and oysters, locally with branching red-algae biostromes (Pomar, 2001). Open shelf lithofacies consist of fine-grained highly burrowed and flat-lying packstone/wackestone beds. These are composed of planktonic foraminifera, ostracods, and fine-grained detritus of bivalves, echinoids and red algae (Pomar, 2001).

Landward (north-eastward) of the reef-core lithofacies is the back-reef lagoon lithofacies that consist of the outer and inner lithofacies. The outer-lagoonal lithofacies consist of skeletal grainstone, packstone and coral patch reefs. The dominant sediment-producing organisms include echinoids, mollusks, benthic foraminifera, with minor contributions from Halimeda, planktonic foraminifera and bryozoans. Further landwards is the inner-lagoonal lithofacies that consists of bedded grainstones, packstones and wackestones-mudstones. Skeletal components include miliolids, thin bivalves and gastropods (Pomar, 2001).

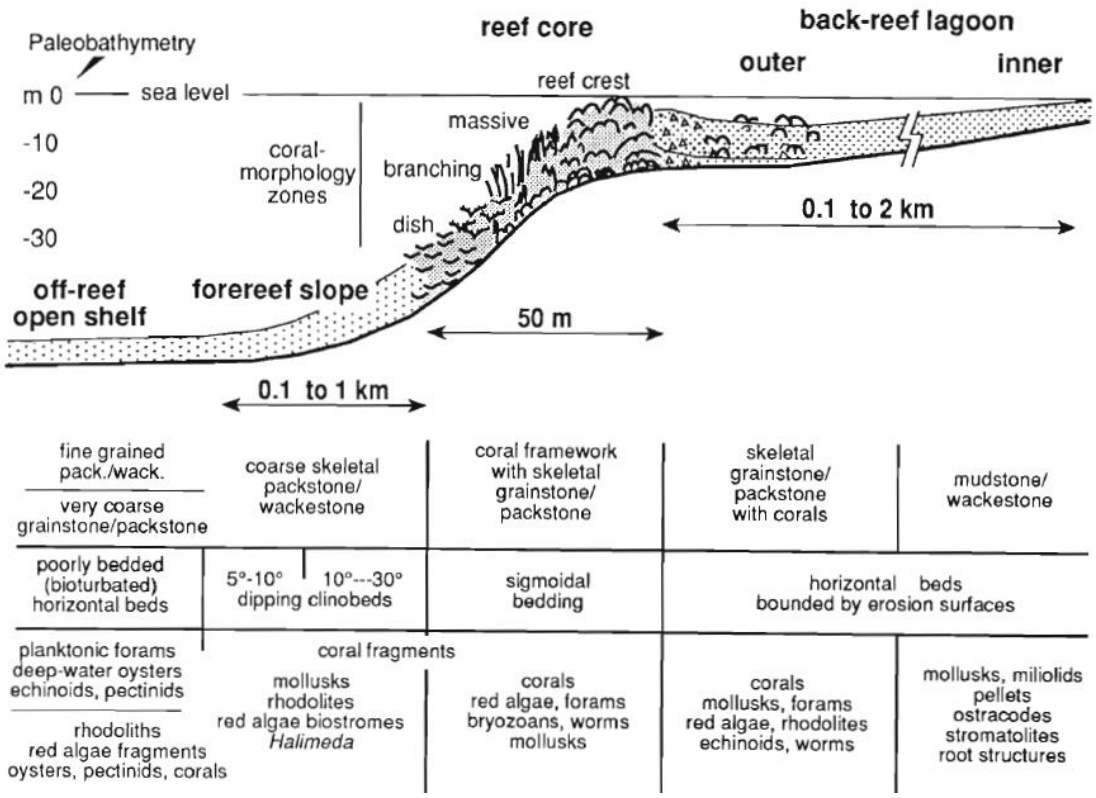

Figure 4.3: Depositional model and main facies characteristics of the Upper Miocene Reef Complex of the Llucmajor Platform (from Pomar *et al*., 1996).

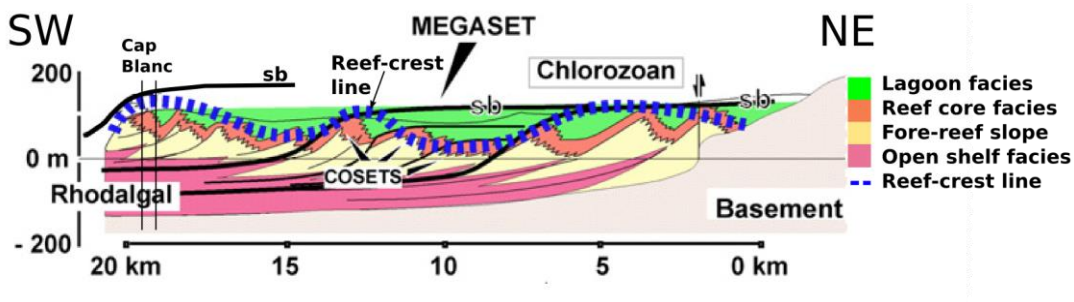

Figure 4.4: Cross-section with platform geometry, facies architecture and reef-crest line (platform margin trajectory – blue dashed line) based on interpretation of water-well cores (modified from Pomar, 2001 and Pomar *et al*, 2012).

The facies model allows the carbonate factories active at various depth zones to be identified (table 4.3). This is necessary to define sediment production rates (section 4.2.2.1.5) that are characteristic of the investigated depositional systems.

	Carbonate factories active at various depth zones		
	Euphotic (<60 m depth)	Mesophotic (60 to 110 m depth)	Oligophotic and Aphotic (>110 m depth)
Llucmajor platform, Mallorca, Spain, late Miocene, Reef-rimmed platform	- Scleractinian coral - Calcareous green algae - Coralline red algal - Molluscan, bryozoans and foraminiferal	- Molluscan, bryozoans and foraminiferal - Coralline red algal - Nannofor	- Coralline red algal - Molluscan, bryozoans and foraminiferal - Nannofor

Table 4.3: *In situ* carbonate factories at various depths in the Llucmajor platforms (modified from Pomar & Kendall, 2008). Three depth zones are defined depending on light availability: euphotic (<60 m), mesophotic/oligophotic (60 to 110 m) and aphotic (>110 m).

4.2.2.1.5. Sediment production and synthetic facies

The aim is to simulate sediment production that is characteristic of the natural carbonate factories and replicate facies architectures (vertical and lateral arrangement of several facies as particular grain sizes) that may have resulted form real carbonate factories. A new method is applied in this study to better adjust the simulated sediment production to that produced in natural carbonate system. Through the method, simulations of carbonate sediment production better replicate that occurring in real/natural carbonate systems in terms of total sediment production, depth distribution of sediment production (production profiles), and grain size proportions produced. The new method first (i) identifies the carbonate factories producing sediment *in situ* at various depth zones (table 4.3), and then (ii) simulates sediment production for each carbonate factory as a number of distinct grain size production profiles, one production profile for each grain size produced by the carbonate factory (figure 4.1). Erosion and transport of sediment is represented through the diffusion coefficient that is simulated as inversely proportional to the grain-size (section 4.2.2.1.8).

A production profile was developed (figure 4.5) on the basis of the identified carbonate factories observed in the Llucmajor platform (table 4.3) and the sediment production rates for those factories (figure 3.1). Since carbonate factory sediment production falls within a range, seven distinct sediment production rates were tested; PR 100, PR 500, PR 1000, PR 1500, PR 2000,

PR 2500, and PR 3000. PR 1000 represents the average sediment production (m ky^{-1}) by the carbonate factories (figure 4.5). PR 100 represents one tenth of sediment produced in PR 1000. PR 3000 represents three times the average sediment production of PR 1000. All seven tested sediment production rates fall within the natural range, from low PR 100 to high PR 3000, of sediment production of Holocene carbonate factories (section 3.2.2).

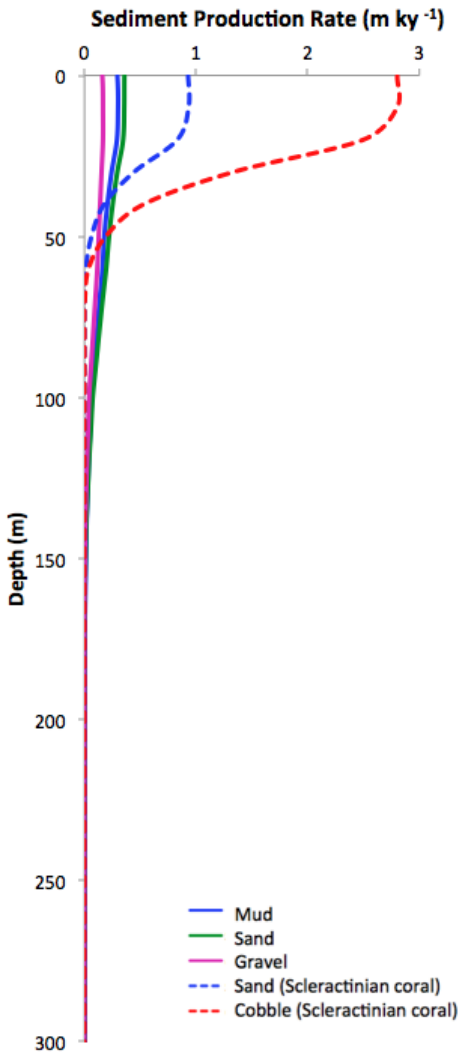

Figure 4.5: Production profile applied in SFM based on the carbonate factories observed in the Llucmajor platform (table 4.3).

The simulation of grain size production profiles (figure 4.5) enables facies to be identified in SFM on the basis of relative proportions of accumulated grain sizes. Various proportions of each grain size simulated in SFM produces the range of carbonate depositional textures (Dunham, 1962 and its modification by Embry & Klovan, 1971) that occur in natural carbonate systems. Textures were differentiated from Dionisos based on the following grain size proportions: mudstone > 90% mud with <10% sand, wackestone >50% mud with 10 to 49% sand, packstone >50% sand with 10 to 49% mud, grainstone 100% sand, floatstone >50% mud with 10 to 49% gravel, rudstone >50% gravel with 10 to 49% mud or sand, framestone >20% cobble and boulder.

4.2.2.1.6. Slope failure

Literature on slope angle and sediment texture is very limited. The most extensive and commonly referred to work is by Kenter (1990) and Adams *et al.,* (2002). Kenter carried out a quantitative literature based study exploring the relationship between slope angles and sediment composition of ancient carbonate platform systems (Appendix B). The study suggested that sediment texture is a major control on slope angle and slope curvature of carbonate platform flanks. The study concluded that in systems built to the angle of repose, slope angles and critical slopes are directly correlated to grain sizes.

Despite the work being commonly cited, the study has a number of limitations that restrict its applicability. Firstly, the sediment fabric is divided into four classes: grain supported no matrix, grain supported with mud matrix, mud-supported, and mud supported. These classes do not specify grain size and do not follow the currently used textural classes (e.g. Dunham, 1962 and modifications by Embry & Klovan, 1971 and James, 1984). This limits the applicability of these slope angle and texture values. Secondly, the study only includes 25 data points. This may not be sufficient to identify relationships between slope angle and slope curvature of carbonate platform flanks.

In this study, literature data on outcropping Mediterranean Miocene carbonate platforms were reviewed in terms of the slope angle, overall sediment texture and other details that may influence these two parameters (Appendix B). This study adds forty-four slope angle and sediment texture data points to Kenter's (1990) original data set (Appendix A). This data set is used to assess whether textures and slope dips reported by Kenter are similar to those developed by Mediterranean Miocene carbonate systems. Through this data, we will establish the min, max and average slope angles developed by various sedimentary textures. The maximum value can be used in SFM to define a threshold gradient beyond which textures are unstable and transported down-slope to less steep gradients. These values are used in this study.

A plot of sediment texture against slope gradient (figure 4.6) indicates that the steepest slope gradients (30 to 45°, average 33°) are formed within biologically bound and framework textures. These observations compare well to those made by Kenter (1990) that show that the three steepest slope angles (20 to 45°, average 35°) are facies stabilized by organic frame-building organisms (figure 4.6). Grain-supported rudstone (20 to 40°, average 33°), grainstone (10 to 30°, average 22°) and packstone (10 to 35°, average 15°) textures develop lower slopes than biologically bound and framework textures. These results also correspond to Kenter's (1990) results that suggest grain-supported textures build slope angles varying from circa 12 to 40°. As proposed by Kenter, results presented in this thesis also show that within the grain-supported categories the mud-free rudstone and grainstone textures develop slightly steeper slopes than the mud containing packstone texture. Mud-supported floatstone and wackestone

(10 to 30°, average 14°) textures form lower gradients than grain-supported textures. Kenter (1990) demonstrates that mud-supported textures show slope angles up to 15°. No mudstone textures were recorded in the studied Miocene outcrops. Kenter (1990) notes that mudstones build slope angles of up to 5°.

Results from analysis in this thesis suggest a relationship between the inclinations of slope profiles from outcropping carbonate platforms and sediment texture (figure 4.6). Despite the differences in age, geographic location and environmental contexts, the slope angles formed by the various sediment textures are similar in both this and Kenter's study. The study carried out in this thesis therefore supports Kenter (1990) suggestion that sediment texture is a major control on slope angle and slope curvature of carbonate platform flanks.

In circumstances where sediment accumulation rates exceed transport rates, slope gradients tend to steepen. A threshold may eventually be reached where gravitational sheer stress exceeds the shear strength of the constituent materials. Beyond this critical slope threshold, sediment becomes unstable and is transported down-slope to gradients below the critical threshold (Schlager and Camber, 1986). Based on the values derived in this chapter, biologically bound framework textures have been set to develop a maximum slope of 50° (1200 m/km), rudstone textures 30° (577 m/km), grainstone textures 20° (364 m/km) and mudstone textures 5° (87 m/km). Sediment aggrading beyond this critical angle becomes unstable, and is transported down slope via mass transport processes. Dionisos represents the mass transport process using algorithms such that sediments are transported downslope by slumps and debris flows and sediment accumulates in areas below the critical slope threshold (Granjeon, 2008). The texture-slope failure angles from this study can be applied in other SFM to establish thresholds beyond which slope failure will occur.

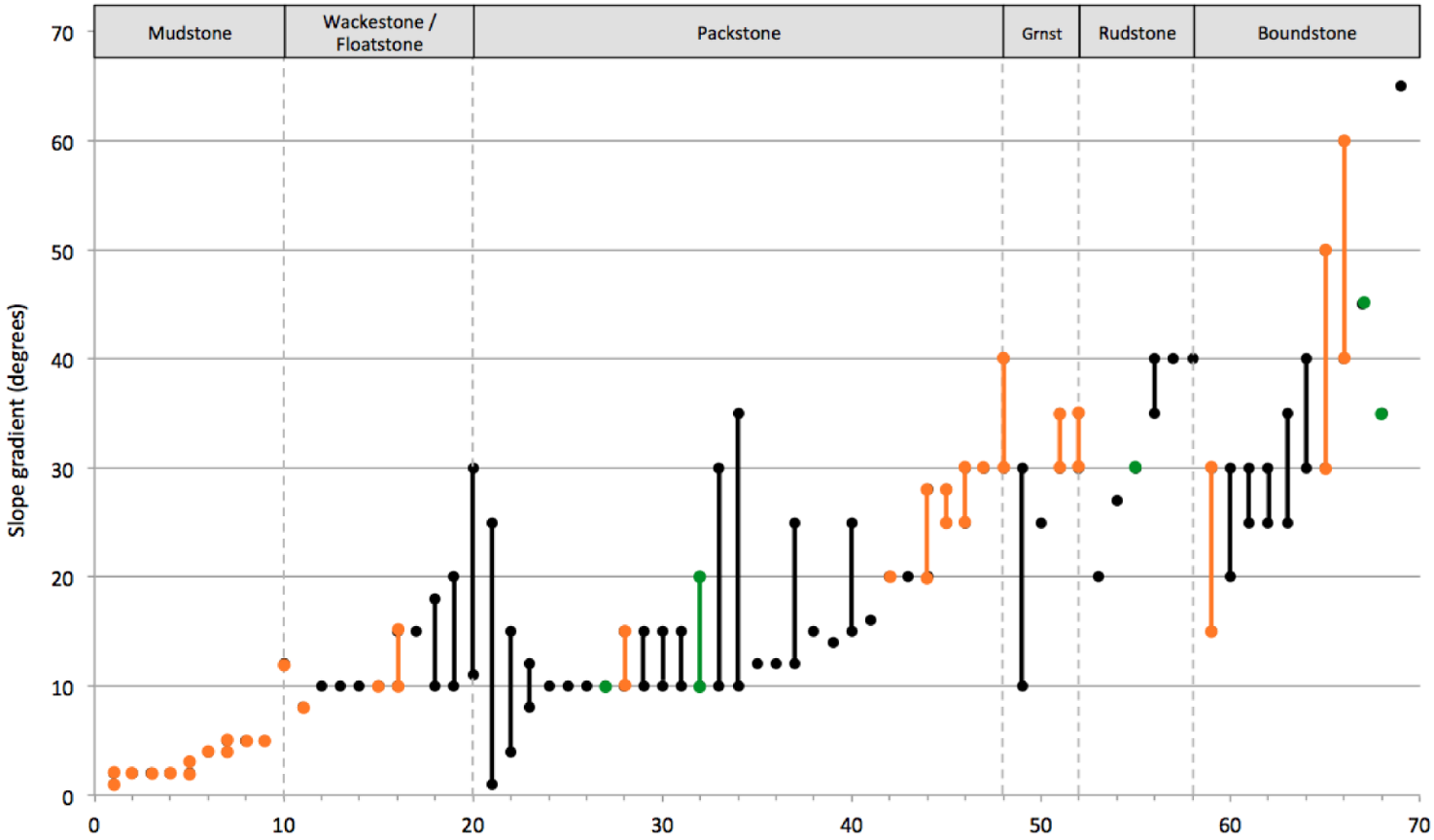

Figure 4.6: Gradients and sediment textural class (Dunham, 1964; Embry Klovan, 1971) in outcropping carbonate slopes. Data points in orange are from Kenter (1990), data points in black and green are new data points from various literature sources (Appendix A). Data points in green are from the Llucmajor platform. Refer to Appendix A for literature sources and measurements of texture type and slope angle used to create figure.

Based on these data, slope angle measured from clinoform foreset dip (e.g. measured from a depth-converted seismic image), can give some indication of likely grain size/sediment texture in the clinothem strata. This can help distinguish between siliciclastic and carbonate strata (e.g. reef-rimmed platform margins).

4.2.2.1.7. Sub-aerial erosion

Rates of sub-aerial karst dissolution are highly variable in different regions in the world. Rates in tropical areas range between 0.015 to 0.099 m ky^{-1} (Kukall, 1990). In Irish Lower Carboniferous strata, Williams (1966) uses MEM (micrometre erosion metre) and obtained values ranging from 0.003 to 6.3 m ky^{-1}. Sweeting (1972) suggests that mean dissolution rates of limestone is between 0.015 and 0.1 m ky^{-1}. MEM data in north Yorkshire, UK, indicate current rates of erosion of the order of 0.01 to 0.05 m ky^{-1} (Trudgill, 1989). Stephenson & Kirk (1996) measured erosion rate of shore platforms in South Island, New Zealand and using MEM indicate average annual lowering rate of 1.1 m ky^{-1} for limestone platforms and 1.48 m ky^{-1} mudstone platforms. MEM data by Muhammad and Beng (2002) indicate Noegene limestone dissolution rates in the area of Kinta and Lenggong valleys (Malaysia) of 0.005 to 1.830 m ky^{-1}.

Given the above modern day analogues, an average sub-aerial dissolution rate of 0.03 m ky^{-1} is simulated in SFM. Sub-aerial dissolution however does not significantly influence platform evolution. This is since the platform top is very infrequently and briefly sub-aerially exposed, and the rates of sub-aerial erosion are relatively low.

4.2.2.1.8. Diffusional transport

Calcareous grains produced by carbonate factories may be transported at different rates depending on grain size and bulk density. In this study, the relation between grain size and transport rate has been expressed by attributing a diffusion coefficient that is inversely proportional to grain size. In this context, coarser material is expressed as sediment with a low diffusion coefficient and hence a lower transport rate than finer-grade material that has a higher diffusion coefficient.

The diffusion coefficients for the different grain sizes produced with the models were systematically varied across the models tested but maintains the relationship that coarser sediment always has the same or lower diffusion coefficient value than finer sediment, never a higher value. The tested diffusion coefficients range from 0 to 1 $km^2\ ky^{-1}$. Diffusion coefficients greater than 1 $km^2\ ky^{-1}$ are not simulated as model mismatch increases drastically beyond this value. The diffusion coefficient ratio for each of the grain sizes varies from no difference (mud 1 $km^2\ ky^{-1}$; sand 1 $km^2\ ky^{-1}$; gravel 1 $km^2\ ky^{-1}$; cobble 1 $km^2\ ky^{-1}$) to significant difference in terms of the order of magnitude (mud 1 $km^2\ ky^{-1}$; sand 0.13 $km^2\ ky^{-1}$; gravel 0.016 $km^2\ ky^{-1}$;

cobble 0.002 km^2 ky^{-1}) (refer to x-axis in figure 4.8 for range of tested grain size diffusion coefficient ratios).

4.2.2.2. Functions to describe model match

Objective functions were developed that quantitatively assess which combination of sediment production and diffusional transport develops modelled facies architectures and stratal geometries similar to those observed in the real carbonate system/platform. The degree of match is quantified on the basis of three factors that represent some key aspect of the strata observed in the Llucmajor outcrop (table 4.4). These factors are, where possible, directly tied to outcrop observations to avoid circular logic (discussed in section 4.2.2.1). This is particularly the case for platform margin gradients (F_1) and reef crest total progradation distance (F_3).

The first factor (F_1) compares maximum platform margin gradients observed in Llucmajor to those simulated in SFM [equation 1]. The objective function [equation 1] is a ratio of the simulated to outcrop margin maximum gradient (MaxS) (measured in degrees). The second factor (F_2) compares the facies recorded at Cap Blanc in outcrop (figure 4.9 black dashed lines) to the facies simulated at the same location [equation 2]. The more matches expressed along the vertical section, the greater the factor match (figure 4.7). A 100% match (F_2 1.00) requires each facies to be exactly the same thickness and exactly the same position within the one Cap Blanc vertical section, but not necessarily in the whole model. It is important to note that a match at a single log location does not imply a perfect match across the whole 2D section. The facies outcropping at the Cap Blanc area was chosen for facies comparison since the area contains some of the best outcrop records available in literature for the Upper Miocene Reef Complex (e.g. Pomar *et al*., 1996). The third factor (F_3) compares reef crest total progradation distance to that simulated [equation 3]. The objective function [equation 3] is a ratio of the simulated to outcrop reef crest progradation distance (measured in km).

Equation 4 (table 4.5) quantifies the match between numerical model and outcrop data (MMS) based on the results of the three individual factors (F_1 F_2 and F_3 in table 4.5). The MMS [Equation 4] metric is mapped in parameter space plots (figure 4.8A to 4.8F). Seven distinct sediment production rates were tested (section 4.2.2.1.5). Each production rate simulates one hundred fifty five models that test a different grain size diffusion coefficient (section 4.2.2.1.8). Each of the one thousand and eighty five two-dimensional models therefore simulates a unique combination of sediment production and diffusional transport.

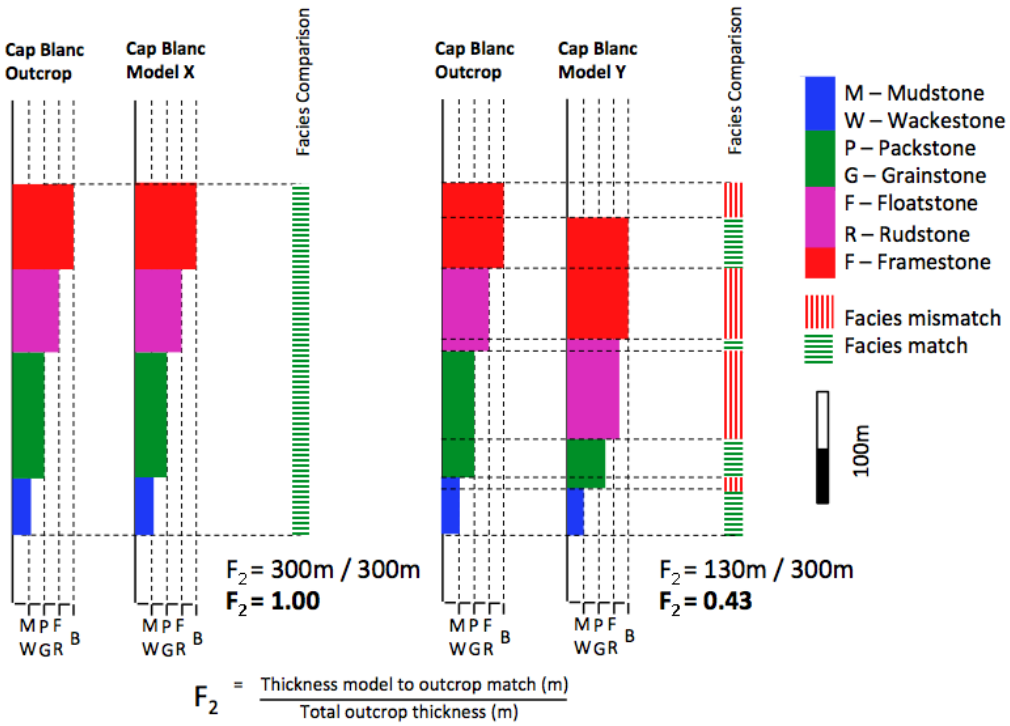

Figure 4.7: The second factor (F_2) compares the facies recorded at Cap Blanc in outcrop (figure 4.4) to the facies simulated at the same location. A 100% match (F_2 1.00) requires each facies to be exactly the same thickness and exactly the same position within the one Cap Blanc vertical section, but not necessarily in the whole model.

Factor 1 (F_1) Platform geometry maximum gradient	**Factor 2 (F_2) Facies comparison at Cap Blanc location**	**Factor 3 (F_3) Reef crest progradation and position (platform margin trajectory)**
Proximal-reef slope deposits dip >10° (Pomar *et al.,* 1996)	Measures the goodness of fit in terms of facies architecture between simulated and real strata at the Cap Blanc. Location of Cap Blank and lithological cross section at the Cap Blanc outcrop in figures 4.9A and 4.10. (Stratigraphic section from Pomar *et al*., 1996)	The Llucmajor platform prograded 21 km towards the SW (Pomar, 1991). Refer to figure 4.9A for reef crest position over time.

Table 4.4: The match between model run and Llucmajor outcrop data depends on three quantitative functions, based on gradient, succession thickness and facies distribution identified in the Llucmajor platform. Refer to figure 4.9Afor cross-section diagram depicting platform geometry and maximum platform gradient (F_1), facies architecture (F_2) and reef-crest progradation (F_3).

The degree of model match in F_1, F_2, F_3 and MMS [equations 1 to 4] is quantitatively expressed as a fraction where a score of 1 is a perfect match between the simulated and real factor. The three factors (F_1, F_2 and F_3) are given equal importance in equation 4. Consequently, models that have different factor values (F_1, F_2, F_3) may develop similar MMS values [equation 4]. For instance, a model with a poor match in F_1 with a good match in F_2 and F_3 may give the same MMS value as a model that has a moderate match in F_1 and F_2 and a good match in F_3. It is however important to note that a high MMS value [equation 4] requires a high match in all factors (F_1, F_2 and F_3). A high MMS value reflects a good match in all three factors (F_1, F_2 and F_3). A comparison of Llucmajor conceptual model, two-dimensional SFM simulations, model factors (F_1, F_2 and F_3) and MMS values [equation 4] is available in figure 4.9.

[Equation 1] F_1: Platform margin gradients
$F_1 = (SF_1/OF_1)$ *(use this equation when simulated MaxS ≤ Llucmajor MaxS)*
$F_1 = (OF_1/SF_1)$ *(use this equation when simulated MaxS ≥ Llucmajor MaxS)*
F_1 = Model Match Factor 1 (maximum platform gradient)
SF_1 = Simulated Factor 1 (simulated maximum platform margin gradient)
OF_1 = Outcrop Factor 1 (Llucmajor maximum platform margin gradient)

[Equation 2] F_2: Facies at the Cap Blanc area (figure 4.9A for location and vertical facies)
$F_2 = (TM / TOL)$
F_2 = Model Match Factor 2 (facies comparison at Cap Blanc)
TM = Thickness of Match between simulated facies and outcropping facies in Cap Blanc
TOL = Total outcrop log height (m) that compared against simulated facies

[Equation 3] F_3: Reef crest progradation and platform margin trajectory (figure 4.9A)
$F_3 = (SF_3/OF_3)$
F_3 = Model Match Factor 3 (reef crest progradation distance)
SF_3 = Simulated Factor 3 (simulated reef crest progradation distance)
OF_3 = Outcrop Factor 3 (Llucmajor reef crest progradation distance)

[Equation 4]
$MMS = F_1 * F_2 * F_3$
MMS = Match between numerical model and outcrop data (MMS units)

Table 4.5: Mathematical equations that quantitatively assess which combination of sediment production and diffusional transport develop platform margin gradients (F_1), facies architectures (F_2) and reef crest progradation and platform margin trajectories (F3) similar to those observed in the Llucmajor outcrop. Equation 4 quantifies the match between numerical model and outcrop data (MMS) based on the results of the three individual factors (F_1 to F_3).

4.3. Results and discussions

4.3.1. SFM of real strata

4.3.1.1. Model match

A range of MMS values, from 0.008 to 0.87 MMS [equation 4], were developed across the tested sediment production and grain size diffusion coefficient rates (figure 4.8). This demonstrates that sediment production and diffusional transport rates are important controls on facies architecture and platform geometry. The highest model match achieved between Dionisos model and the Llucmajor conceptual model (figures 4.8E and 4.9) is 0.87 MMS. The match was achieved when applying a sediment production rate of PR 2000 with grain size diffusion coefficients: mud 0.1 km^2 ky^{-1}, sand 0.033 km^2 ky^{-1}, gravel 0.00 83km^2 ky^{-1} and cobble 0.0021 km^2 ky^{-1}. A comparison of Llucmajor conceptual model, two-dimensional SFM simulations, model factors (F_1, F_2 and F_3) and MMS values [equation 4] is available in figure 4.9.

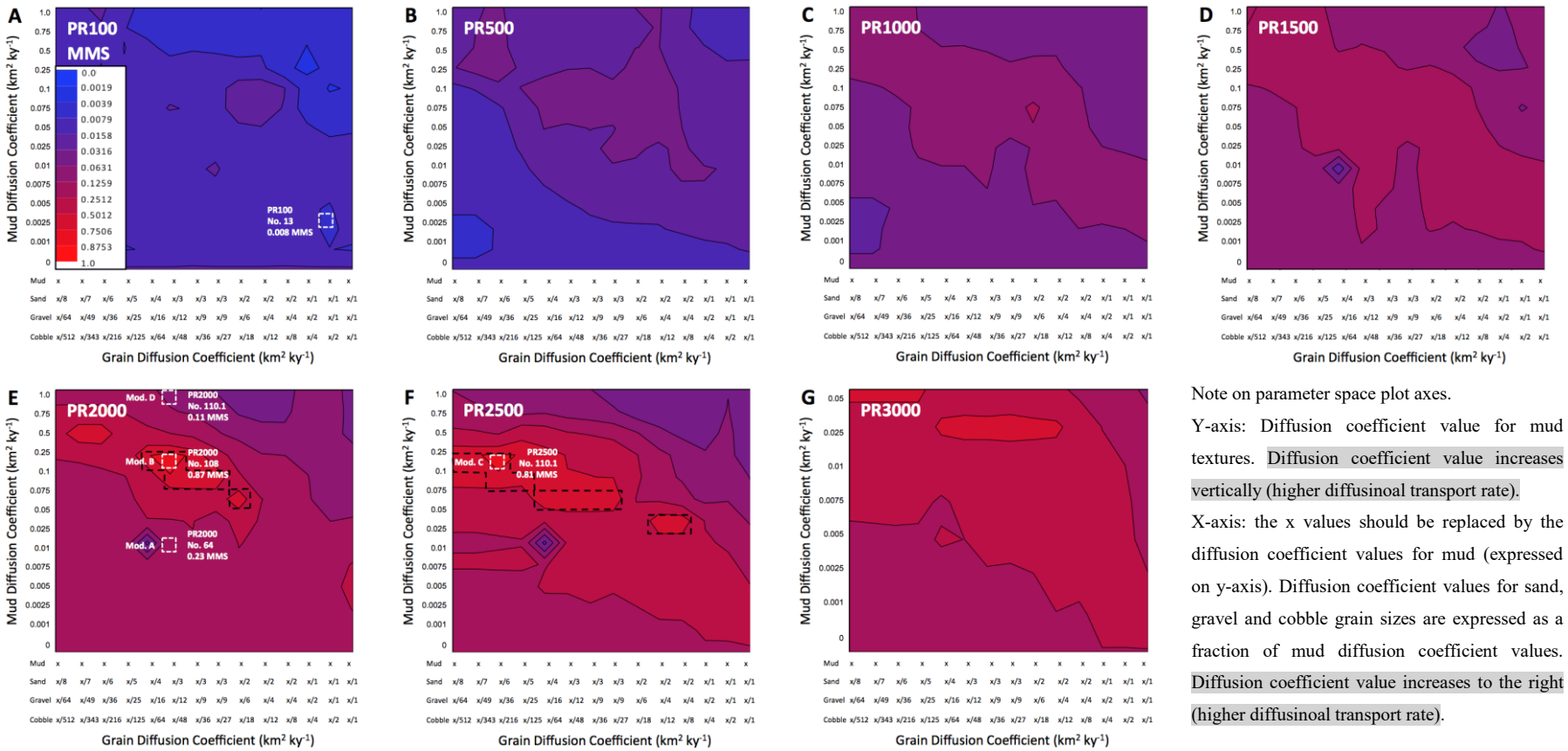

Note on parameter space plot axes.

Y-axis: Diffusion coefficient value for mud textures. Diffusion coefficient value increases vertically (higher diffusinoal transport rate).

X-axis: the x values should be replaced by the diffusion coefficient values for mud (expressed on y-axis). Diffusion coefficient values for sand, gravel and cobble grain sizes are expressed as a fraction of mud diffusion coefficient values. Diffusion coefficient value increases to the right (higher diffusinoal transport rate).

Figure 4.8: Parameter space plots showing the match between numerical model and outcrop data [MMS] values [equation 4]. Seven parameter space plots are displayed for the seven different sediment production rates tested: (A) PR 100, (A2) PR 500, (A3) PR 1000, (A4) PR 1500, (A5) PR 2000, (A6) PR 2500, and (A7) PR 3000. All parameter space plots used the same colour scale that is displayed in figure A. The highest model match achieved between model and Llucmajor conceptual models is 0.87 MMS [equation 4] achieved when applying PR 2000 with grain size diffusion coefficients: mud 0.1 $km^2\ ky^{-1}$, sand 0.033 $km^2\ ky^{-1}$, gravel 0.0083 $km^2\ ky^{-1}$ and cobble 0.0021 $km^2\ ky^{-1}$ (model reference: PR 2000 model number 108).

The white dashed box in figures A, E and F denote the models that are further discussed in the subsequent sections. Two-dimensional cross sections for model PR 100 No.13 in figure 4.9B; model PR 2000 No.64 in figure 4.9C and model PR 2000 No.108 in figure 4.9D. Model B (No.108) in parameter space plot A5 is the model that develops the best match for simulation value (0.087 MMS) that best matches the Llucmajor platform based on the three factors assessed (F_1, F_2 and F_3 in table 4.5). The black dashed lines in figure E and F denote models that develop similar F_3 (Reef crest progradation and platform margin trajectory) values.

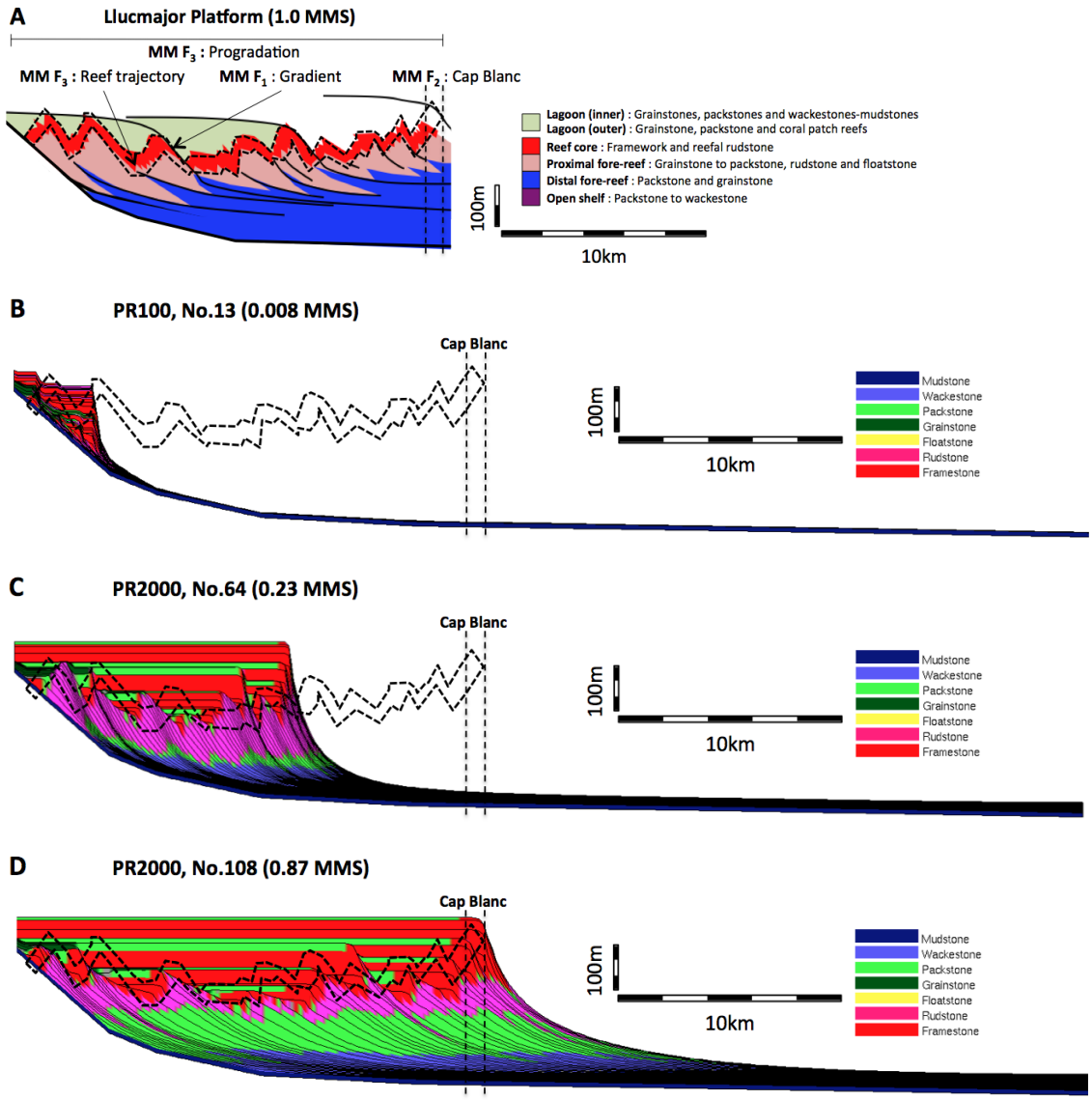

Figure 4.9: A comparison of Llucmajor conceptual models (7A), two-dimensional SFM simulations, model factors (F_1, F_2 and F_3) and MMS values. 2D cross-sections for conceptual model (A) and SFM simulations (B, C and D). (A1) Displays a diagram of the Llucmajor conceptual model (Pomar *et al.,* 1996). The diagram shows the three model factors (F_1, F_2 and F_3) that represent some aspect of the strata observed in the Llucmajor outcrop. These model factors are used to quantify the degree of match between simulated and real facies architectures and stratal geometries (equations 1, 2, 3, and 4 in table 4.5). If MMS was calculated for the conceptual model, a score of 1.0 MMS (a perfect match) would therefore be obtained. (B, C and D) Display two-dimensional simulations developing a range of MMS values [equation 4]. The MMS value is calculated following equations 1, 2, 3 and 4 (table 4.5). Model factors F_3 (Reef crest progradation and platform margin trajectory) and F_2 (Cap Blanc area for facies comparison) are displayed in each of the three SFM simulations. The overlay of F_3 onto the 2D sections enables a visual comparison between real and simulated reef crest progradation and platform margin trajectory. (B) Displays the SFM that produces the worst match to conceptual model (0.008 MMS); the model has a poor match for all three model factors (F_1, F_2 and F_3), Refer to figure 4.8A for location of model PR100 No.13 within parameter space plot. (C) Displays the SFM that produces a moderate match to conceptual model (0.023 MMS). Refer to figure 4.8E for location of model PR 2000 No.64 within parameter space plot. (D) Displays the SFM that produces a best match to conceptual model (0.87 MMS) the model has a good match for all three model factors (F_1, F_2 and F_3). Refer to figure 4.8E for location of model PR 2000 No.108 within parameter space plot. All two-dimensional cross-sections have a vertical exaggeration (V.E.) of 20; time lines are shown for every 0.04 My.

4.3.1.2. Comparison between model displaying highest MMS and real strata

The following section compares the numerical model that best matches the Llucmajor conceptual model. The comparison is in terms of outcrop factors (F_1 to F_3). In terms of the platform maximum gradient factor (F_1), the best model match develops maximum gradients of 12.36°. The gradient is within the observed gradient range of 10 to 30° developed in proximal fore-reef slope settings (Pomar *et al*., 1996). In view of this, the factor was calculated as $1.00F_1$ [Equation 1]. The facies observed in outcrop in the Cap Blanc area (figure 4.9A) were compared against the facies produced in the same area in the best-fit model through factor (F_2). Results demonstrate an overall facies match of $0.94F_2$ [Equation 2]. SFM develop a perfect match for the distal fore-reef and lagoonal facies, and a minor mismatch in the fore-reef slope (3.4% of total mismatch) and reef core facies (3.4% of total mismatch) (figure 4.10). In terms of total reef crest progradation and position (F_3), the SFM that best matches Llucmajor progrades a total distance of 22.3 km (figure 4.9D). This is comparable to the estimated 21km that the Llucmajor platform progrades (figure 4.9A). The reef crest closely matches that described in outcrop (compare figure 4.9A and 4.9D). The factor was calculated at $0.93F_3$ [Equation 3]. Based on these results, a 0.87 MMS was calculated [equation 4].

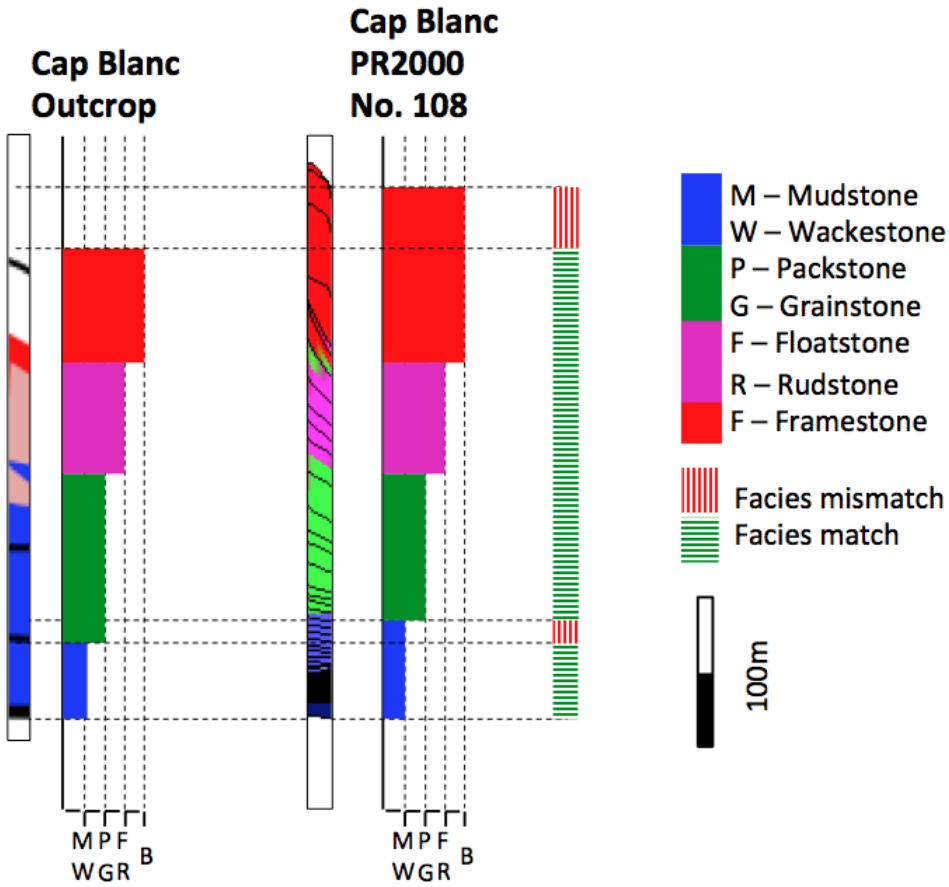

Figure 4.10: Comparison of facies (F_2) formed in the Cap Blanc area in the Llucmajor outcrop and the facies developed in the model that best matches outcrop (highest MMS value of 0.87MMS). The quantitative comparison [equation 2] enables the quantification of model factor 2 (F_2 Facies at Cap Blanc area). Results demonstrate a facies match of 0.94 (F_2) [Equation 2]. Two-dimensional cross-section of facies has a vertical exaggeration (V.E.) of 20; time lines are shown for every 0.04My.

4.3.2. Unique and non-unique platform characteristics

4.3.2.1. Investigation of non-uniqueness at large-scale in terms of reef crest progradation

To investigate non-uniqueness, we assess how many of the 1085 models (each simulate a unique combination sediment production and diffusional transport), demonstrate similar total reef crest progradation values (F_3). The investigation is in terms of F_3 since it is the best suited to distinguish which unique sediment production and diffusional transport parameter values develop models displaying similar large-scale stratal geometries.

Across the range of parameter values tested, 19 of the 1085 simulated models develop F_3 value between 0.9 to 0.95 F_3 [equation 3] (black dashed lines in figure 4.8E and 4.8F). This indicates that despite the application of distinct sediment production and diffusional transport rates, 1.8%

of the tested models develop total reef crest progradation that are similar. This investigation provides evidence to issues of non-uniqueness in terms of reef crest progradation. While the result is notable, non-uniqueness in terms of progradation distance (F_3) is only developed over a small range of sediment production and diffusional transport values. This suggests that the system is mostly too sensitive to be significantly non-unique.

Despite the small number of non-unique progradation distance examples that occur, the range of parameter values that produce these non-unique models is interesting. Models that simulate a relatively low sediment production rate (PR 2000) and a higher diffusional transport rate can have similar F_3 values to models that simulate a relatively high sediment production rate (PR 2500) and a lower diffusional transport rate. Similar F_3 values [equation 3] also occur across models that simulate the same sediment production rates. In such instances, similar F_3 values are the result of slightly different grain size diffusion coefficients. These models have distinct individual grain sizes diffusion coefficient, however the overall diffusion coefficient is largely similar. E.g. Both PR 2000 mud 0.05 $km^2\ ky^{-1}$, sand 0.025 $km^2\ ky^{-1}$, gravel 0.0083 $km^2\ ky^{-1}$, cobble 0.0028 $km^2\ ky^{-1}$ and PR 2000 mud 0.075 $km^2\ ky^{-1}$, sand 0.033 $km^2\ ky^{-1}$, gravel 0.0083 $km^2\ ky^{-1}$, cobble 0.0028 $km^2\ ky^{-1}$ develop similar F_3 [Equation 3]. These results suggest that similar sediment production to transport ratios (PR/TR) may produce similar (non-unique) stratal geometries. This finding, and the processes that developed similar stratal geometries, is further investigated in the following section.

4.3.2.2. Detailed investigation of non-uniqueness

Across the parameter range tested, Models B and C (figure 4.8E and F) are similar across all three factors investigated [F_1, F_2 and F_3] and produce similar MMS values [equation 4]. Model B, the model that best matches Llucmajor conceptual model, has a model match of 0.87 MMS and was achieved by applying a sediment production rate PR 2000 with grain size diffusion coefficients: mud 0.1 $km^2\ ky^{-1}$, sand 0.033 $km^2\ ky^{-1}$, gravel 0.0083 $km^2\ ky^{-1}$ and cobble 0.0021 $km^2\ ky^{-1}$ (figure 4.8E). A similar MMS value of 0.81 MMS was achieved by Model C which applies a higher sediment production rate PR 2500 and lower grain size diffusion coefficients: mud 0.1 $km^2\ ky^{-1}$, sand 0.0167 $km^2\ ky^{-1}$, gravel 0.0028 $km^2\ ky^{-1}$ and cobble 0.0005 $km^2\ ky^{-1}$ (figure 4.8F). Model B therefore simulates a lower production rate and higher diffusional transport rate than Model C. Models B and C develop a similar MMS value despite applying distinct sediment production and diffusional transport rates.

Both Model A (PR 2000 No.64) and Model D (PR 2000 No.152) develop poorer model match to the Llucmajor conceptual model, 0.234 MMS and 0.107 MMS respectively (figure 4.8E). These are discussed here to draw comparisons between the models with better and poorer model MMS values. Models A and D simulate a sediment production rate of PR 2000 (similar to Model B). Model A applies a grain size diffusion coefficients that is one order of magnitude

lower than Model B (best model match) and Model D applies a grain size diffusion coefficients that is one order of magnitude lower than Model B (best model match). Model A is characterised by a relatively low diffusion coefficient and represents an *in situ* accumulation dominated system, while Model D is characterised by relatively high diffusion coefficients and represents a transport dominated system. Model A has a sediment production rate of PR 2000 and a grain size diffusion coefficient of mud 0.01 $km^2\ ky^{-1}$, sand 0.0033 $km^2\ ky^{-1}$, gravel 0.0008 $km^2\ ky^{-1}$ and cobble 0.0002 $km^2\ ky^{-1}$. Model D has a sediment production rate of 2000 m My^{-1} and a grain size diffusion coefficient of mud 1.0 $km^2\ ky^{-1}$, sand 0.333 $km^2\ ky^{-1}$, gravel 0.0833 $km^2\ ky^{-1}$ and cobble 0.0208 $km^2\ ky^{-1}$.

4.3.2.2.1. Comparison of features developed by Models A, B, C and D

Models A, C and D are compared to Model B in terms of the platform margin gradients (F_1), facies architecture, (F_2), total progradation distance (F_3), platform margin position over time, and stratal geometries (table 4.6). This analysis is done to assess whether distinct sediment production and diffusion coefficients can develop similar model factors at the large and smaller scales.

Model features	Model A	Model B	Model C	Model D
(F_3) Progradation distance (Figure 4.11)	13.8 km	22.3 km	23.4 km	>50 km
Platform margin position over time (Figure 4.12)	Significantly different from Model B	Figure 4.12	Very close match to Model B	Significantly different from Model B
Stratal geometries (Figure 4.11)	Significantly different from Model B	See figure 4.11	Very close match to Model B	Significantly different from Model B
(F_1) Platform margin gradients (Figures 4.11 and 4.12)	25.91°	12.36°	23.83°	3.52°
(F_2) Facies architecture (Figure 4.13)	39%	See figure 4.13	87%	64%

Table 4.6: Models A, C and D are compared to Model B in terms of the platform margin gradients (F_1), facies architecture, (F_2), total progradation distance (F_3), platform margin position over time, and stratal geometries.

Progradation distance, platform margin trajectory over time and stratal geometry

The similarity between Models B and C is greatest in terms of progradation distance (F_3), platform margin trajectory over time (figure 4.12) and stratal geometry (figure 4.11).

In terms of progradation distance over the entire model run time, Model B progrades a total distance of 22.3 km, Model C progrades 23.4 km (1.1 km more progradation than Model B), Model A progrades 13.8 km (8.5 km less progradation than Model B) and Model D progrades >50 km (27.7 km more progradation than Model B) (figure 4.11).

In terms of platform margin position over time, Model C very closely matches that of Model B. In 52% of the model run time, the position of the platform margin in Model C perfectly matches that of Model B and in 48% of the model run time it very closely matches (<0.5 km from platform margin) the platform margin location in Model B. Models A and D develop platform margin trajectories that are significantly different from Model B. The platform margin trajectory of Model A only closely matches Model B in 36% of the model run and for Model D 26% of the model run (figure 4.12).

The stratal geometries developed by model B and are very similar to those formed by Model C. This is evidenced by the overlaying of stratal geometries developed by Model B onto Model C (figure 4.11). In contrast the stratal geometries developed by Model A and Model D are clearly different from those developed by Model B. Model A develops steep platform margins and steep clinoform stratal geometries while model D produces sigmoidal clinoforms (figure 4.11).

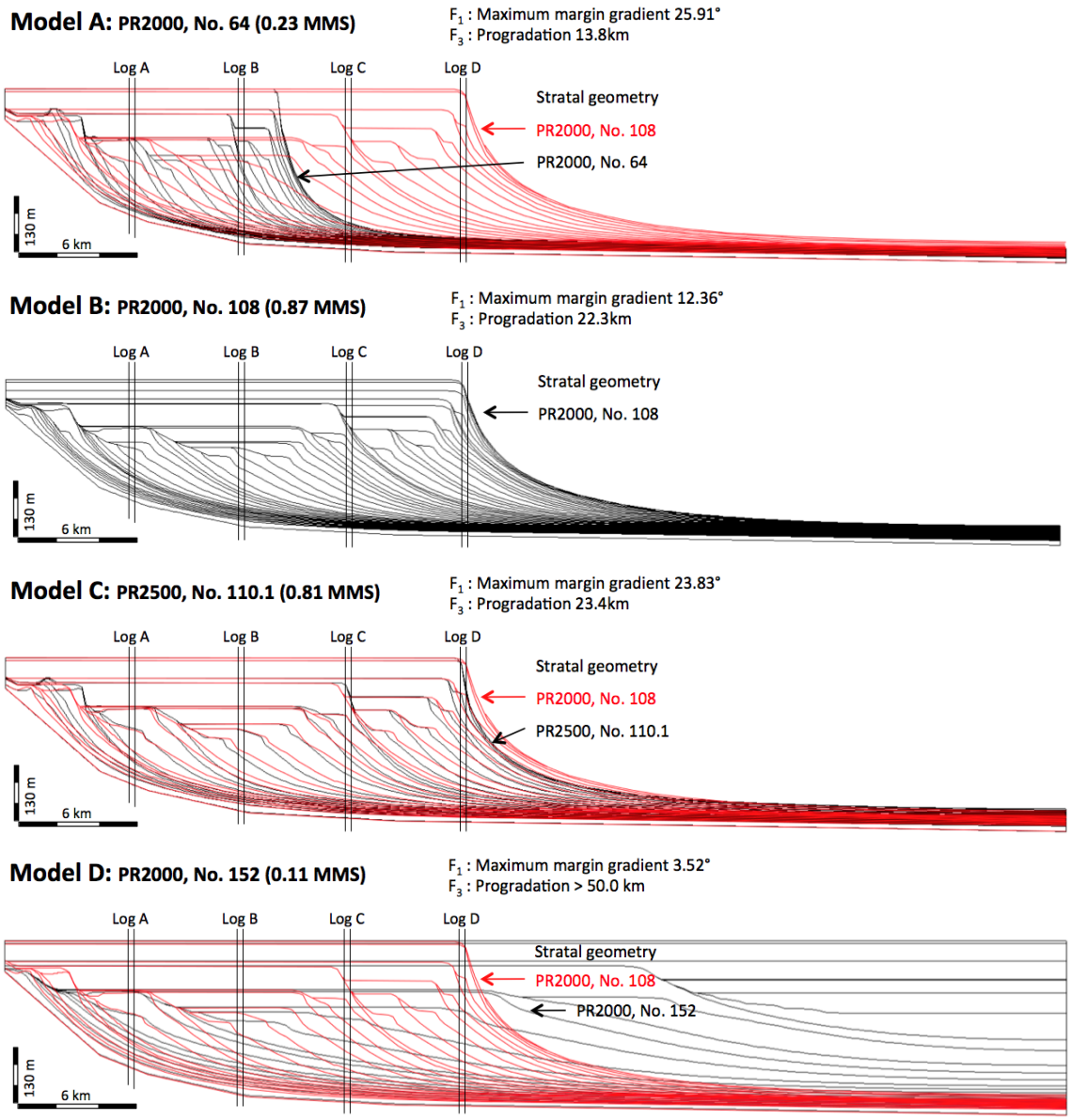

Figure 4.11: SFM models A, B, C and D are compared in terms of platform margin gradients (F_1), reef crest progradation (F_3) and large-scale stratal geometries. The stratal geometries developed by model B (model that best matches Llucmajor conceptual model 0.87MMS) are overlain onto Models A, C and D for visual comparison. Models B and C have similar stratal geometries, reef crest progradation (F_3) and platform margin gradients (F_1) – these models are non-unique. Models A and D are clearly distinct from model B. Two-dimensional cross-section of facies has a vertical exaggeration (V.E.) of 20, and time lines are shown for every 0.04My.

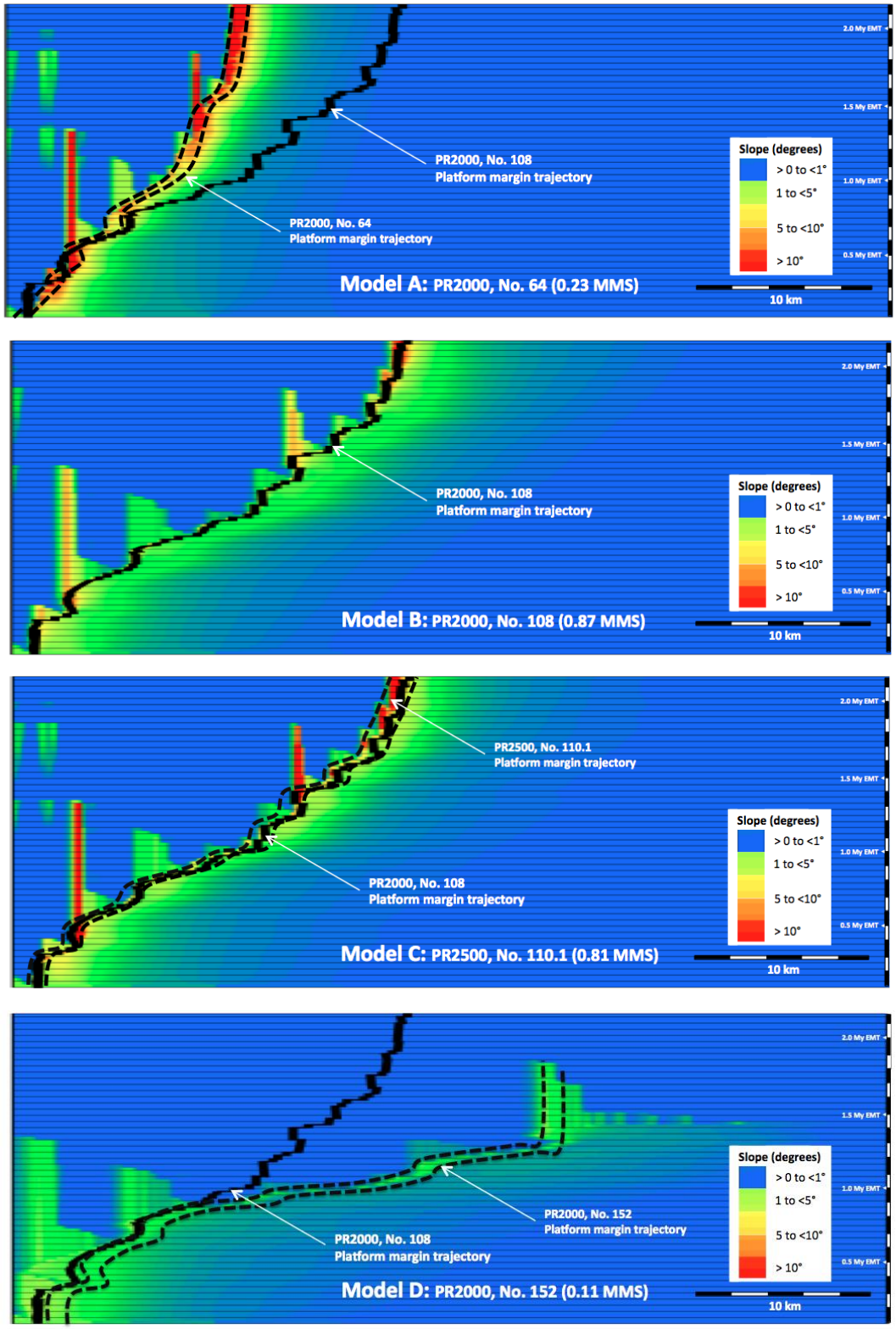

Figure 4.12: Diagrams show elapsed model time plotted on the y-axis (My EMT), and horizotal distance across simulated platform as the x-axis on which platform slope (degrees) is displayed. The diagram allows the four models to be compared in terms of platform margin slope (F_1) and platform margin position over time. The full black line indicates the platform margin position of Model B (model that best matches Llucmajor conceptual model). The full black line (Model B) is overlain on the other models (Models A, C and D) and indicates how closely the platform margins in latter models match those formed in Model B. The platform margin positions for models A, C and D are shown dashed black lines. Models B and C have similar platform margin slope (F_1) and platform margin position over time - these models are non-unique. Models A and D develop distinct platform margin slope (F_1) and platform margin position over time).

Platform margin gradients

In terms of maximum platform margin gradients (F_1), Model B and Model C develops maximum gradients (across entire model run) of 12.36° and 23.83° respectively (figure 4.11). While the maximum gradients are different, these steep gradients are only briefly developed in Model C during short time intervals (at 0.32My and 1.24My elapsed model time). The platform margin gradients developed by Model C are otherwise similar to those developed by Model B (figure 4.12). Maximum platform margin gradients of Model C have in fact not significantly impacted the resulting stratal geometries that determine the large-scale similarity between models (figure 4.11). Model A and Model D develop maximum platform margin gradient of 25.91° and 3.52° respectively. In both cases, these gradients are maintained across the model run simulation (figure 4.12).

Facies architecture

A finer-scale examination of facies architecture (F_2) is necessary to assess whether the synthetic facies architectures of Model B and C are also non-unique. To assess this factor (F_2) and fine-scale, the facies developed by Model A, C and D are compared to those developed by Model B at four different locations (figure 4.11 for locations of facies comparison and figure 4.13 for facies comparison). Model A develops an overall facies match of 39%, Model C an overall facies match of 87% and Model D an overall facies match of 64%. Individual logs (A, B, C and D) and their respective match are also calculated (figure 4.13). The facies architecture developed by Model C very closely matches Model B. Both models display the same cycles/alternations of facies and have only very slight thickness variations. This facies architecture can therefore be considered as largely (87%) non-unique. The imperfect match is likely the result of a subtle interplay between *in situ* carbonate production, gradient size dependent diffusion coefficient rates and gradients that are developed.

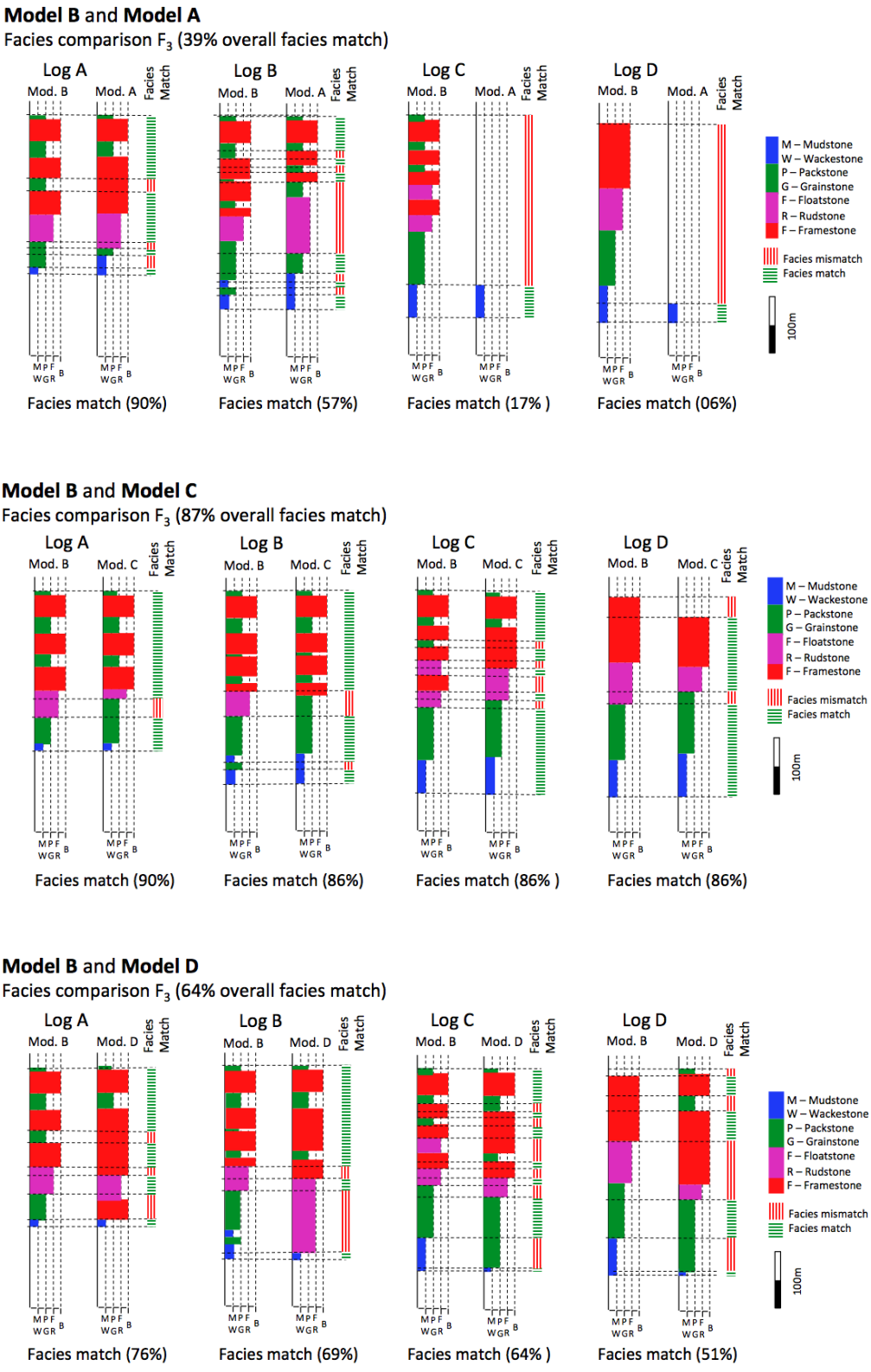

Figure 4.13: SFM models A, B, C and D are compared in terms of facies architecture (F_2) at four different locations (figure 4.11). Models A, C and D are compered to the facies architecture developed by Model B. Model A develops an overall facies match of 39%, Model C an overall facies match of 87% and Model D an overall facies match of 64%. Individual logs (A, B, C and D) and their respective match is also calculated. The facies architecture developed by Model C very closely matches Model B. These facies architecture is largely (87%) non-unique until.

4.3.2.2.2. Comparison of sediment production and transport dynamics of Models A, B, C and D

This section investigates the SFM processes that enable different sediment production and diffusional transport values to develop models (Model B and C) that display similar non-unique platform features.

A series of profiles showing sediment production, transport and accumulation rates of processes along each cross-section were developed that allow the definition and analysis of sediment processes along the simulated depositional profile (figures 4.14 and 4.15). The graphs define sediment production (m/0.02 My), sediment transport (m/0.02 My), depositional slope (degrees) and sediment accumulation (m/0.02 My) along the modelled depositional profile. The analysis is carried out during model run time 0.9 to 0.88 My (one time step of 0.02 My EMT) under a relative sea level rise from 19.3 to 47.7 m (+ 28.4 m) (figure 4.2).

Sediment production simulates a euphotic production profile (figure 4.5) that has highest sediment production rates within the shallow euphotic zone (<40 m water depth). The depth zone corresponds to topset areas of Models A, B, C and D. The extent of the topset (platform top) is relatively limited in Model A (0 to 10700 m) when compared to Models B (0 to 15900 m), Model C (0 to 16100 m) and D (0 to 30300 m) (figures 4.14 and 4.15). Consequently, Model A produces the least sediment and model D the most sediment over the entire platform topset. In all models, sediment production and accumulation (in the form of progradation and aggradation) in the topset area is from newly created accommodation produced by a relative sea level rise (+ 28.4 m) over the 0.02 My EMT investigated. Sediment production rates in all models are greater than the rate of relative sea level rise. Consequently, the maximum sediment accumulation rates in all models are limited by sea level. Despite simulating different diffusion coefficients, all models have similar sediment transport and accumulation rates across the topset (figures 4.14 and 4.15). As sediment accumulates within the platform top (over one time step of 0.02 My EMT) a low gradient slope is formed (figure 4.12) and a small volume of sediment is transproted (figure 4.14) basinwards away from the platform top through the diffusion formulation.

Model D, B, C and A develop increasingly steep platform margins (due to a decreasing diffusional transport rate). The highest rates of sediment erosion occur at the platform margin. This corresponds to the steepest slope in the simulated platforms (Model A from 10100 to 10700 m, Model B from 15500 to 15900 m and Model C from 15900 to 16100 m) (figures 4.14 and 4.15). The steep slopes in Model A were developed as a result of the low diffusion coefficient that accumulates a large proportion of sediment *in situ*. The quantity of eroded and transported sediment at the platform margins and foreset is significantly greater in Model D

(figures 4.14 and 4.15). The higher quantities of eroded sediment in Model D are the result of a higher diffusion coefficient and higher quantities of sediment produced in the forest area. A high diffusion coefficient therefore redistributes sediment across the underlying topography. This prevents the steepening of platform margins and forms ramp-like stratal geometries.

The foreset of Model A is characterised by the steepest slope compared to models B, C and D. This leads to a rapid increase in depth over a short horizontal span which forces a very rapidly decrease of sediment production. In fact, very little to no sediment is produced in the forest areas of Model A (near-vertical green line from 10700 to 11300 m) (figures 4.14 and 4.15). The foreset slopes of Models B, C and D are not as steep as Model A. This leads to a more gradual increase in depth along the foreset. Consequently, sediment production rates decline more gradual along the foreset and the horizontal extent over which sediment is produced is greater (less steep green line from 30300 to 40000 m) (figures 4.14 and 4.15). The foreset areas of Model B, C and D in particular therefore produce a larger quantity of sediment than Model A. The vast majority of Model D sediment production in forest areas is eroded and transported along the platform margin and bottomsets. Models B and C, with their lower diffusion coefficients, accumulate a larger proportion of the sediment produced in the foreset areas. The forest is key to understanding how Models B and C are similar, despite simulating different sediment production and diffusional transport rates. The higher sediment production rates of Model C are offset by a lower diffusional transport rate (relative to Model B). This has the effect of steepening the Model C foreset gradients without significantly affecting other platform features. Consequently, Models B and C are different in terms of platform margin gradients but not distinct in other platform aspects.

In all models, sediment erosion rapidly declines basinwards along the foreset depositional slope (figure 4.14). This is the result of a gradual decline in slope gradient and to a lesser extent a reduced sediment production rate. The deposition of transported sediment is demonstrated by positive values in blue line (figure 4.14). The sediment deposited at the base of the foreset and bottomset originates from topset and forest areas. The quantity and horizontal extent over which the sediment is deposited is proportional to the sediment eroded in the topset and foreset areas. This is in turn dependent on sediment production and diffusional transport rates. Consequently, sediment deposition in bottomset areas is greatest in Model D and lowest in Model A.

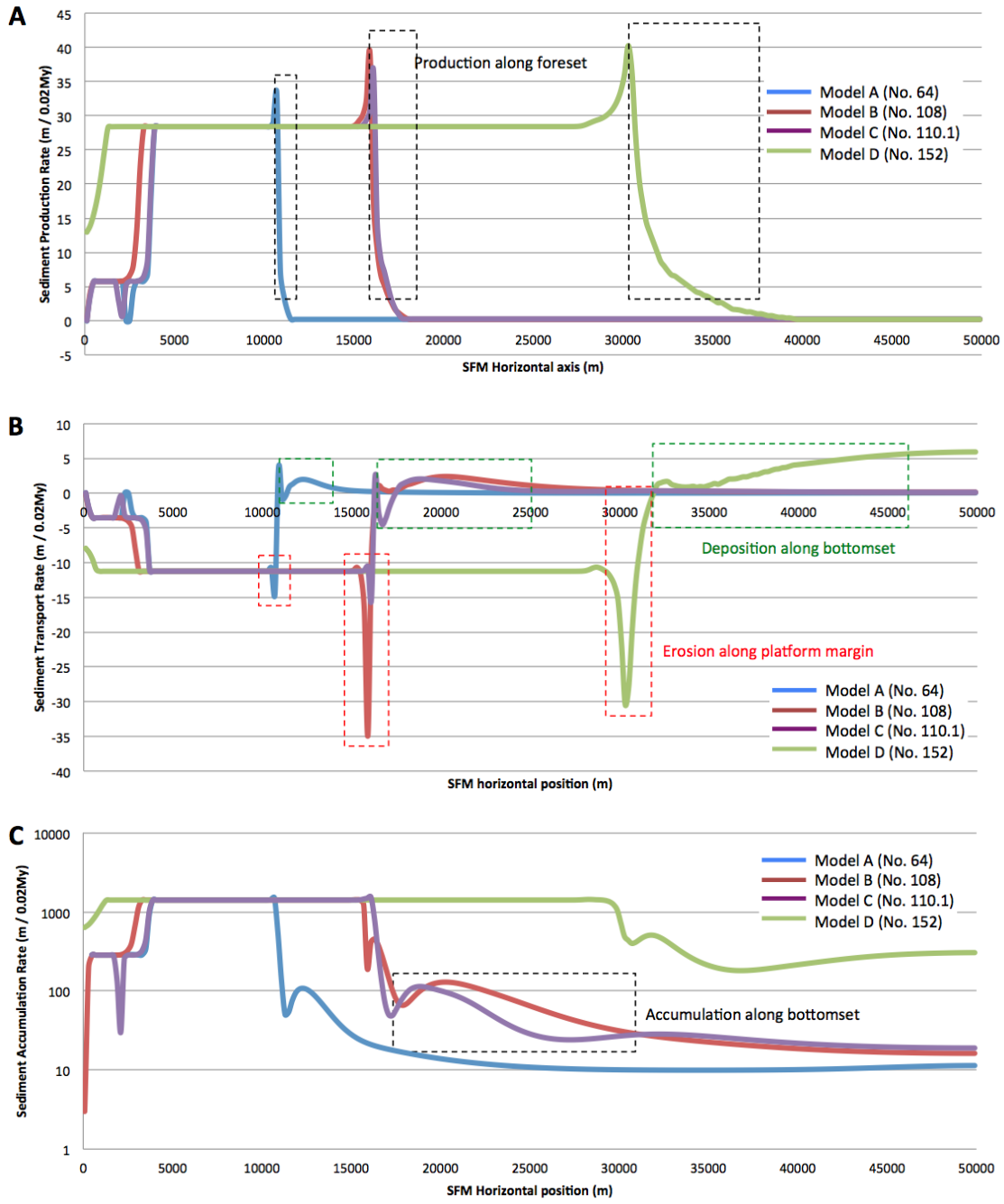

Figure 4.14: Graphs showing (A) Sediment PR, (B) Sediment TR, (C) Sediment Accumulation Rate for models A, B, C and D. Refer to figure 4.15 for profiles showing the rates of processes along each modelled cross-section. As sediment accumulates within the platform top (over one time step of 0.02 My EMT) a low gradient slope is formed (see wheeler diagram depicting slope in figure 4.12) and a small volume of sediment is transproted (B) basinwards away from the platform top through the diffusion formulation.

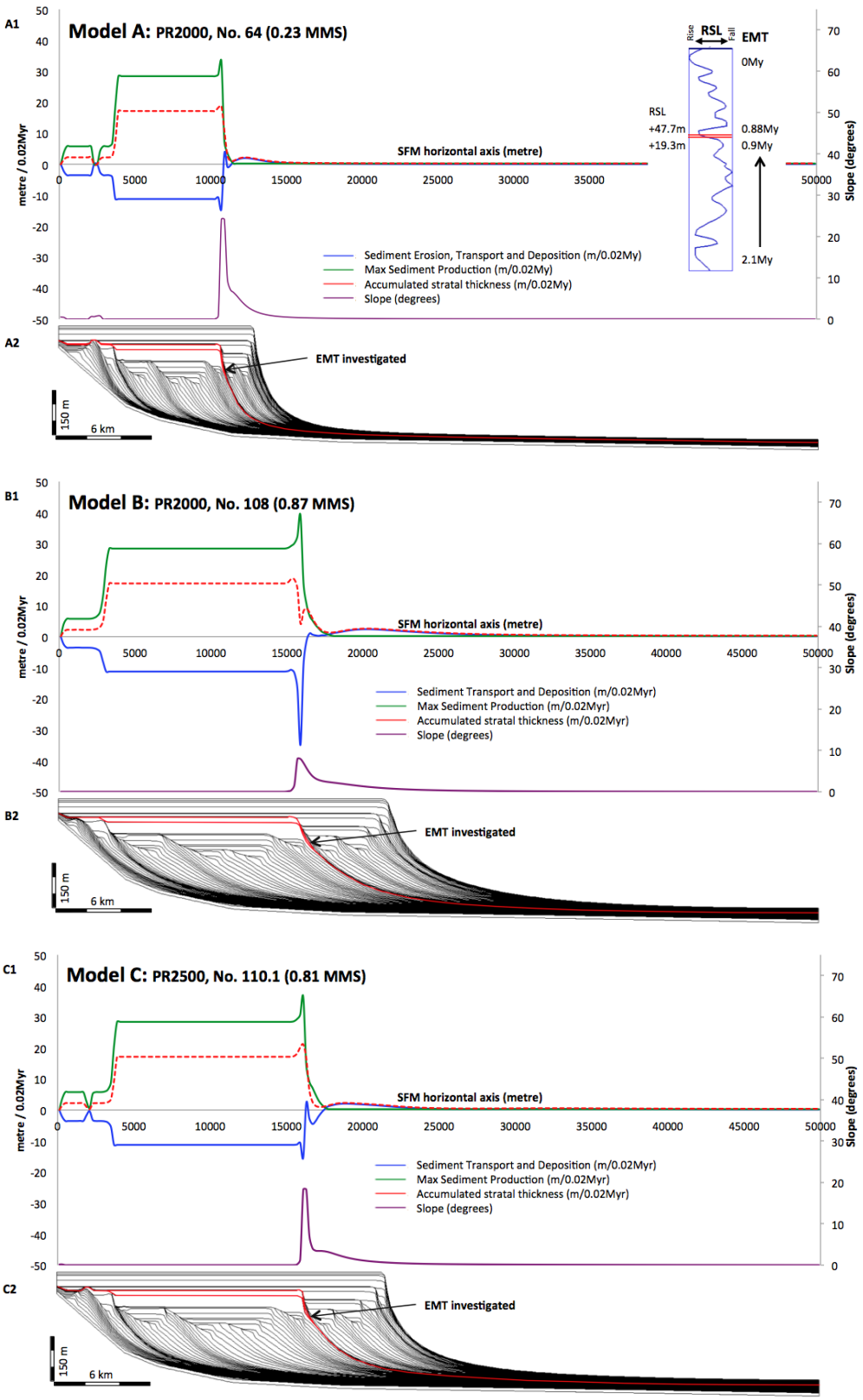
A1
Model A: PR2000, No. 64 (0.23 MMS)
RSL
Rise
Fall
EMT
0My
RSL
+47.7m
+19.3m
0.88My
0.9My
2.1My
SFM horizontal axis (metre)
metre / 0.02Myr
Slope (degrees)
Sediment Erosion, Transport and Deposition (m/0.02My)
Max Sediment Production (m/0.02My)
Accumulated stratal thickness (m/0.02My)
Slope (degrees)
A2
EMT investigated
150 m
6 km
B1
Model B: PR2000, No. 108 (0.87 MMS)
SFM horizontal axis (metre)
metre / 0.02Myr
Slope (degrees)
Sediment Transport and Deposition (m/0.02Myr)
Max Sediment Production (m/0.02Myr)
Accumulated stratal thickness (m/0.02Myr)
Slope (degrees)
B2
EMT investigated
150 m
6 km
C1
Model C: PR2500, No. 110.1 (0.81 MMS)
SFM horizontal axis (metre)
metre / 0.02Myr
Slope (degrees)
Sediment Transport and Deposition (m/0.02Myr)
Max Sediment Production (m/0.02Myr)
Accumulated stratal thickness (m/0.02Myr)
Slope (degrees)
C2
EMT investigated
150 m
6 km

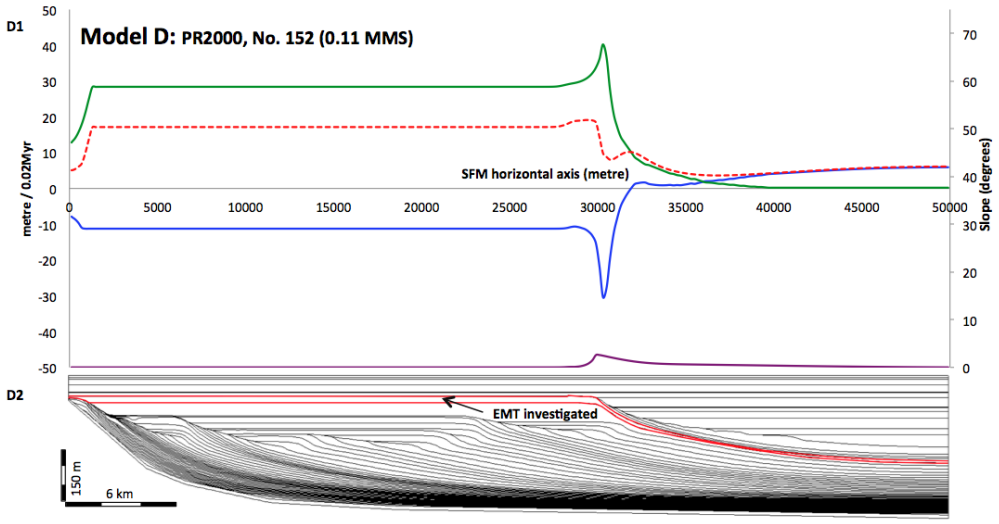

Figure 4.15: SFM models A, B, C and D are compared in terms of sediment production, sediment transportation, sediment accumulation and slope. The time interval investigated Graphs is 0.9 to 0.88 My (i.e. 0.02 My model run time). The graphs define sediment production (m/0.02 My), sediment transport (m/0.02 My), depositional slope (degrees) and sediment accumulation (m/0.02 My) along the modelled depositional profile. The analysis is carried out during model run time 0.9 to 0.88My (one time step of 0.02 My) under a relative sea level rise from 19.3 to 47.7 m (+ 28.4 m). The graphs (X1) record sediment production, sediment transportation, sediment accumulation on the left y-axis and slope is recorded on the right y-axis. The horizontal axis is the SFM horizontal distance. Graphs record these features for each model for the time interval 0.9 to 0.88 My (i.e. 0.02 My EMT). The time interval investigated produces stratal geometries shown in red in the two-dimensional cross-sections below each graph (A2, B2, C2 and D2). The blue line (sediment erosion, transport and deposition) was calculated by subtracting accumulated sediment thickness from in situ maximum sediment production rate (thickness – Max PR). Negative values indicate sediment accumulation is less than *in situ* sediment production, this suggests a fraction of the in situ produced sediment was eroded and transported. Positive values indicate sediment accumulation is greater than *in situ* sediment production, this suggests *ex situ* transported sediment was deposited and increased sediment accumulation beyond maximum *in situ* sediment deposition.

Note: Despite Model C simulating a greater sediment production than Model B, the maximum sediment production rate in Model C is greater than Model B. Maximum sediment production rate quantifies the maximum sediment production that cannot exceed sea level. Earlier time steps of Model C had greater aggradation than Model C and consequently, Model C maximum production rate is less than Model B.

Sedimentary processes that develop different sigmoidal geometries

Sedimentary production and diffusional transport dynamics of Model A develops steep platform margins and steep clinoform stratal geometries that produce FTSM platforms. A low diffusional transport limits basinwards (topset to bottomset) sediment transport. This leads to a low sediment accumulation and aggradation rate within bottomset areas that are in water depths deeper than *in situ* carbonate production. This sedimentary dynamic has the consequent effect of reducing the rate of foreset aggradation and shallowing that in turn limits progradation rates (figures 4.14A and 4.16 Model A).

In contrast, Model D is subject to higher total sediment production (over a more widespread topset and foreset which is within the *in situ* carbonate production zone - more gradual forest gradients) and diffusional transport rates. Eroded sediment is deposited in the foreset and bottomset. Aggradation in the area brings the zone up to shallower depths within the range of *in situ* carbonate sediment production. This further increases sediment production rates within the foreset areas and diminishes foreset gradients. This both increases the area within the sediment production zone and increases the fraction of *in situ* accumulation (lower gradients). The process first develops sigmoidal clinoforms that gradually evolve into ramp-like geometries that area subject to an accelerated rate of foreset and bottomset shallowing and progradation (figures 4.14D and 4.16 Model D).

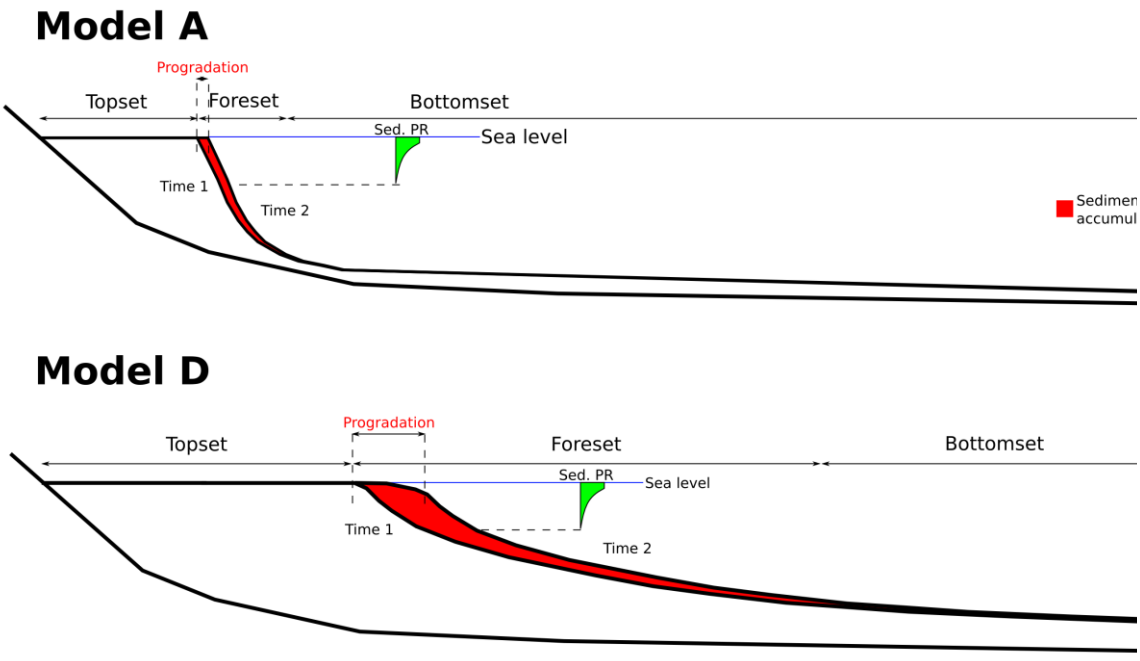

Figure 16: Models (not to scale) that depict the key sedimentary production and diffusional transport dynamics of Model A and Model C. Model A develops steep platform margins and steep clinoform stratal geometries that produce FTSM platforms. Model D first develops sigmoidal clinoforms that gradually evolve into ramp-like geometries. Refer to figure 4.15A and 4.15D for scaled versions.

Do non-unique models have similar PR/TR

The section investigates whether Models A, B, C and D have a similar or distinct sediment production and diffusional transport ratio (PR/TR). The ratio was calculated by summing the maximum sediment production rate and transport across one time step (0.02 My) across the topset and foreset areas. This area was chosen for the calculation since sediment production, diffusional transport and platform evolution is largely defined within these areas. Results (table 4.7) indicate that Models A, B/C and D have distinct PR/TR and Models B and C have a similar PR/TR. This suggests that models simulating distinct sediment production and transport rates can have a similar PR/TR that in turn develops similar platform features. Conversely, models that have a different PR/TR (e.g. Models A, B and D) develop distinct platform features.

Model Ref.	PR/TR
Model A	1102.12 : 459:50
Model B	1975.90 : 825.89
Model C	1924.59 : 779.65
Model D	4434.10 : 1814.57

Table 4.7: PR/TR calculated by summing the maximum sediment production rate and transport across one time step (0.02 My) in the topset and foreset areas. Maximum sediment production rate quantifies the maximum sediment production that cannot exceed sea level.

4.4. Discussions

4.4.1. Discussion of section 4.3.1

The similarity 0.87 MMS [equation 4] between SFM and real facies architecture and stratal geometry confirms that the method (section 4.2.2) used in this study can be used to simulate facies architecture and geometries that match those observed/developed in the Llucmajor platforms. To replicate Llucmajor FTSM platform stratal geometries, an average sediment production and relatively low diffusional transport are required (section 4.3.1). The rates are relative to the ranges of these parameters observed in natural systems (section 3.2.2). The natural range of carbonate sediment production for the scleractinian coral factories in the euphotic zone is 0.18 to 11.50 m ky^{-1} (50% cover) (section 3.2.2). A scleractinian coral sediment production rate of 7.48 m ky^{-1} was needed for the best match between SFM and Llucmajor conceptual model. Diffusion rates estimated from natural systems range from 0.0001 km^2 ky^{-1} from data from the St. Croix reef-rimmed shelf (Hubbard *et al.,* 1990; Bosence *et al.,* 1994), to 7 km^2 ky^{-1} in pelagic strata on the flanks of the Galapagos spreading center (Mitchell *et al.,* 1996), and 560 km^2 ky^{-1} in the Mississippi delta (Kenyon & Turcotte, 1985). Relative to these rates, the grain size diffusion coefficients that produce the best match between SFM to and

Llucmajor conceptual model are relatively low.

Despite the inverse and iterative method, a perfect match between SFM and Llucmajor conceptual model was not achieved. Two issues probably contribute towards this mismatch. Firstly, SFM simulations of sediment transport do not perfectly represent the natural processes that actively contribute different volumes of sediment towards total sediment transport. Sediment transport processes active in natural systems may not be accurately represented by the simplified diffusion formulation. Secondly, a more accurate model match might be achieved with a more extensive exploration of the parameter space tested in the simulations.

4.4.2. Discussion of section 4.3.2

Non-unique models need not be absolutely identical in every comparison that one can theoretically make. Rather, non-unique models are models that are practically indistinguishable (Burgess & Prince, 2015). Despite the application of a unique combination of sediment production and diffusional transport rates (i) 19 of the 1085 simulated models (1.8%) develop total reef crest progradation that are similar (section 4.3.2), and (ii) two models (Model B and C) are practically indistinguishable. The latter two models are similar for both the large-scale (F_1 and F_3) and fine-scale (F_2) platform characteristics. These results therefore support previous arguments of non-uniqueness *at the stratal geometry scale* but also demonstrate non-uniqueness at the finer facies scale.

The distribution of non-unique results (F_3) within the sediment production and diffusional transport parameter space tested (figures 4.8E and 4.8F) suggest that models simulating distinct sediment production and transport rates can have a similar PR/TR that in turn develops similar platform features. Conversely, models that have a different PR/TR develop distinct platform features. Calculations of PR/TR across the topset and foreset areas of Models A, B, C and D confirm this hypothesis. Models B and C, which are practically indistinguishable (non-unique), have similar PR/TR while Models A, B/C and D, which develop distinct platform features, have different PR/TR (table 4.7). These results demonstrate that the simulation of distinct rates for key processes (sediment production and diffusional transport) can develop similar non-unique platform features. This shows that similar (non-unique) stratal geometries and facies architectures can occur across a range of parameter values for particular processes. Thus, non-uniqueness of stratal geometries challenges the assumed ability to identify a single explanation or history for a given stratal geometry, for example, when attempting to interpret sediment bypass and RSL histories (Burgess & Prince, 2015). This provides support for a need to shift towards sequence stratigraphic methods based on constructing and evaluating multiple hypotheses and scenarios (e.g. Burgess and Prince, 2015).

4.5. Conclusions

The highest match achieved between Dionisos model and the Llucmajor conceptual model (constructed from outcrop observations and interpretations) is 0.87 MMS. The match was achieved when applying a sediment production rate of PR 2000 (section 4.3.1) with grain size diffusion coefficients: mud 0.1 km^2 ky^{-1}, sand 0.033 km^2 ky^{-1}, gravel 0.0083 km^2 ky^{-1} and cobble 0.0021 km^2 ky^{-1}. Relative to parameters rates observed in natural systems, these values represent average sediment production rates and relatively low diffusional transport rates. The parameter values may be used in other SFM studies that seek to simulated similar FTSM platform geometries.

Despite the simulation of unique combinations of sediment production and diffusional transport rates (i) 19 of the 1085 simulated models (1.8%) develop total reef crest progradation that are similar, and (ii) two models (Model B and C) are practically indistinguishable. This investigation provides evidence to issues of non-uniqueness in terms of reef crest progradation. While the result is notable, non-uniqueness in terms of F_3 is only developed over a small range of sediment production and diffusional transport values. This suggests that the system is mostly too sensitive to be significantly non-unique. The distribution of non-unique results suggest that similar sediment production to transport ratios (PR/TR) may produce similar (non-unique) stratal geometries. This shows how important the PR/TR ratio is as a control on stratal and platform evolution and geometry. Models simulating distinct sediment production and transport rates can have a similar PR/TR that in turn develops similar platform features (e.g. Model B and C). Conversely, models that have a different PR/TR (e.g. Models A, B and D) develop distinct platform features.

CHAPTER 5: LATE MIOCENE STRATIGRAPHY AND SEDIMENTOLOGY, MALTESE ISLANDS

5.1. Introduction

This chapter establishes a new facies scheme for the Late Miocene shallow water Upper Coralline Limestone Formation of Malta and Gozo and provides interpretations of depositional environments and sequence stratigraphy. In this thesis, facies were recognised, described and classified on the basis of lithology, fossil content and sedimentary structures. Facies descriptions were also supplemented by details on colour, biogenic features (when present) and geometry (thickness, lateral extent, shape, boundary types). Microfacies analysis also contributes towards facies descriptions and helps recognize various sedimentological and palaeontological components. From this analysis a revised facies model and new sequence stratigraphic model is presented for the UCL Formation.

The chapter begins by reviewing the methods used to collect the data, and then describes the facies associations and their facies. New findings are discussed and put in context with the previous work on this formation (section 2.2.2.5).

The chapter also aims to obtain field-based data from a relatively well-exposed succession that, in addition to the facies and sequence stratigraphic models, can be used to assess the applicability of the *SFM-based hypothesis testing method* of Chapter 7. Hence the focus of this fieldwork was to (A) constrain model parameters necessary for the subsequent computer simulations and (B) identify features that can be used to quantitatively compare SFM output to real strata. The model parameters established through observations made in this chapter are initial surface of deposition, relative sea level curve, time framework, and the carbonate factories present at different times. The features identified to enable a comparison between SFM and real strata are the facies distribution, facies relations and depositional sequences in three dimensions, stratal dip, depositional textures, and stratal stacking patterns.

5.2. Methods

5.2.1 Outcrop sedimentary logs

In the course of the study 48 sedimentary logs were measured at outcrop and recorded in a standard format. The localities represent the better-developed and thicker outcrops within the study area and were selected to ensure, as far as possible, an even high-density distribution of outcrop data (figure 5.1; Appendix C1.1 for outcrop logs). All logs are referenced to 0 m at the top of the Blue Clay Formation that is the most widely distributed and recognisable horizon (figure 5.3). The Greensand Formation is only locally present and was not studied in detail in

outcrop. The thickness and distribution of the Greensand Formation is in this study assessed through water borehole data (section 5.2.4).

Samples were collected from the logged outcrops (Appendix C1.1) for further laboratory study (thin section and isotope analysis). Allochem composition was initially determined in the field with the aid of a hand lens and later checked in thin sections. Depositional texture, using Dunhams (1962) classification as modified by Embry & Klovan (1971), was attempted in the field and confirmed following microscopic examination. Observations and interpretations derived during sedimentary logging were used to erect a facies association and facies classification (table 5.3).

Excellent cliff face outcrops and quarry exposures have enabled the investigation of facies distribution, thickness, geometry and stratigraphic relationships. This information was used to construct a series of facies maps (e.g. figure 5.6) and also enables a three-dimensional representation with a series of cross sections (Appendix C2). The outcrop logs, facies maps and cross sections were used in the comparison between real and simulated model outputs (chapter 7). In instances where facies are not observed to interfinger, so that the facies are not seen in lateral stratigraphic contact with other units, evidence for the interpreted stratigraphic relationships is either from marker beds (e.g. *Terebratula-Aphelesia* Bed) or the application of Walther's law.

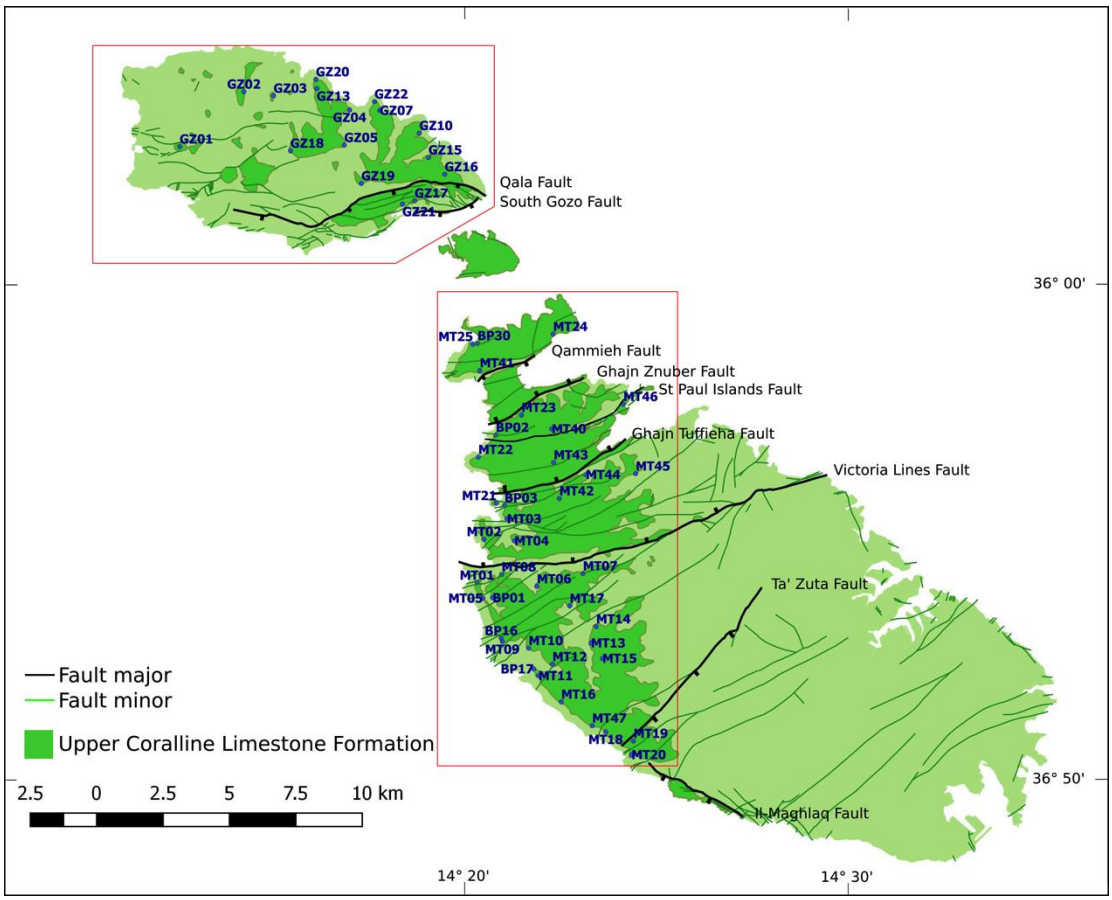

Figure 5.1: The light green area indicates the area of the Maltese Islands. The darker green area indicates the outcrops of Upper Coralline Limestone Formation of Malta and Gozo. Blue circles and numbers indicate the locations where outcrop logs within the Upper Coralline Limestone Formation were taken. The study area (red boxes and polygon) excludes the Il-Maghlaq area that is separated by a major fault and was extensively studied by Dart (1991). MT (Malta) and GZ (Gozo) logs were carried out in this course of this study (Appendix C1.1), BP logs are from Bosence & Pedley (1978).

5.2.2 Thin section analysis

Representative samples from each facies were selected for microscopic study. A total of 19 thin sections were manufactured by hand (table 5.1) and a further 32 were used from previous studies. These were vacuum impregnated with epoxy (Struers EpoFix Kit) and a fluorescent dye (Struers EpoDye). The impregnation treatment was necessary in order to preserve soft matrix and recognize original porosity. Thin sections were assessed using the point counting method (Flugel, 2010). Point counting of microfacies samples was done on photographs and photomosaics of thin sections. A two-dimensional grid is used in point counting. Accuracy of the point counting method is tied to selected grid density and the number of points counted. In this study, grid spacing was approximately one quarter of the diameter of the largest grain observed in the photomicrographs. In order to keep sampling errors small, several hundred points were counted (Flugel, 2010). The number of points counted for each microfacies sample

is stated in the petrographic descriptions section for each facies. The estimated volume of a particle type is proportional to the counted number of particles of that type (Chayes, 1956). Every grain, matrix and cement that falls under a grid point was counted. Grid sizes were classed as mud (<0.063 mm), fine to very fine sand (F-VF Sd) (0.063 to 0.25 mm), medium sand (M Sd) (>0.25 to 0.5 mm), Very coarse to coarse sand (VC-C Sd) (>0.5 to 2 mm), Very fine gravel (VF Grv) (>2 to 4 mm) and Pebble (>4 to 64 mm). The microfacies analysis was used to determine depositional texture and for frequency analyses of different grain types.

Facies Association (FA)	**Facies**	**Thin Section (outcrop reference/sample number)**
Sand Shoal FA	Wave Ripple Packstone Facies (WR)	MT16/S7
	Sand Shoal Grainstone Facies (SS)	BP Tat-Tomna 2 (close to MT22)
Fore-Reef Slope and Shelf FA	Proximal Reef Slope Packstone Facies (PRS)	MT15/S4; MT23/S4
	Distal Reef Slope Wackestone Facies (DRS)	MT44/S3
Sheltered Shelf FA	Massive Coralline Algal Debris Wackestone Facies (MCAD)	MT15/S1a
	Planar Bedded Coralline Algal Debris Wackestone Facies (PCAD)	MT20/S8; MT24/S4
Coralline Algal Biostrome FA	Coralline Algal Debris Packstone Facies (CAD)	BP 15i (close to MT04); BP 30 (close to MT25)
	Coralline Algal Pavement Rudstone to Framestone Facies (CAP)	Rhodolith Pavement Rudstone Sub-Facies: BP 14f (close to MT06); BP 21c (close to GZ21) Crustose Pavement Framestone Sub-Facies: BP 14e (close to MT06)
	Coralline Algal Floatstone Facies (CAF)	BP 15 (close to MT04); BP Facies B/A
	Coralline Algal Sand Ridge Packstone Facies (CASR)	MT01/S1
Open Shelf FA	Open Shelf *Heterostegina*-rich Packstone Facies (OSHR)	BP 2(45) (close to GZ02); BP 19a (close to MT18); BP 42 (close to MT22)

Table 5.1: List of thin section examined. Thin sections labelled MT were prepared in this study and are located in outcrop logs (Appendix C1.1). Thin sections labelled BP are from Bosence & Pedley (1978) and were re-assessed in this study.

5.2.3 Fossils - Recognizing Paleoenvironmental Conditions

Fossils listed from literature (Pedley, 1974; Bosence & Pedley, 1982; Dart, 1991; Gatt, 2006) and those that were identified from investigations carried out in this course of study are listed in Appendix C3. The fossils used in the paleoenvironmental analysis are listed in the description of each facies. These fossils were compared with their present-day habitats and environments to develop interpretations of paleo-depositional environments of the Late Miocene facies.

5.2.4 Water Borehole Data

Seven hundred and seventeen water borehole records provide subsurface data into the Greensand and Upper Coralline Limestone Formations across the Maltese Islands (figure 5.2). The borehole reports provide information on depth of the formations and their hydrogeological properties. Efforts were also made by the operators (Russell, 1955; Costain, 1957, 1958) to record, with varied success, the stratigraphic/lithologic intervals.

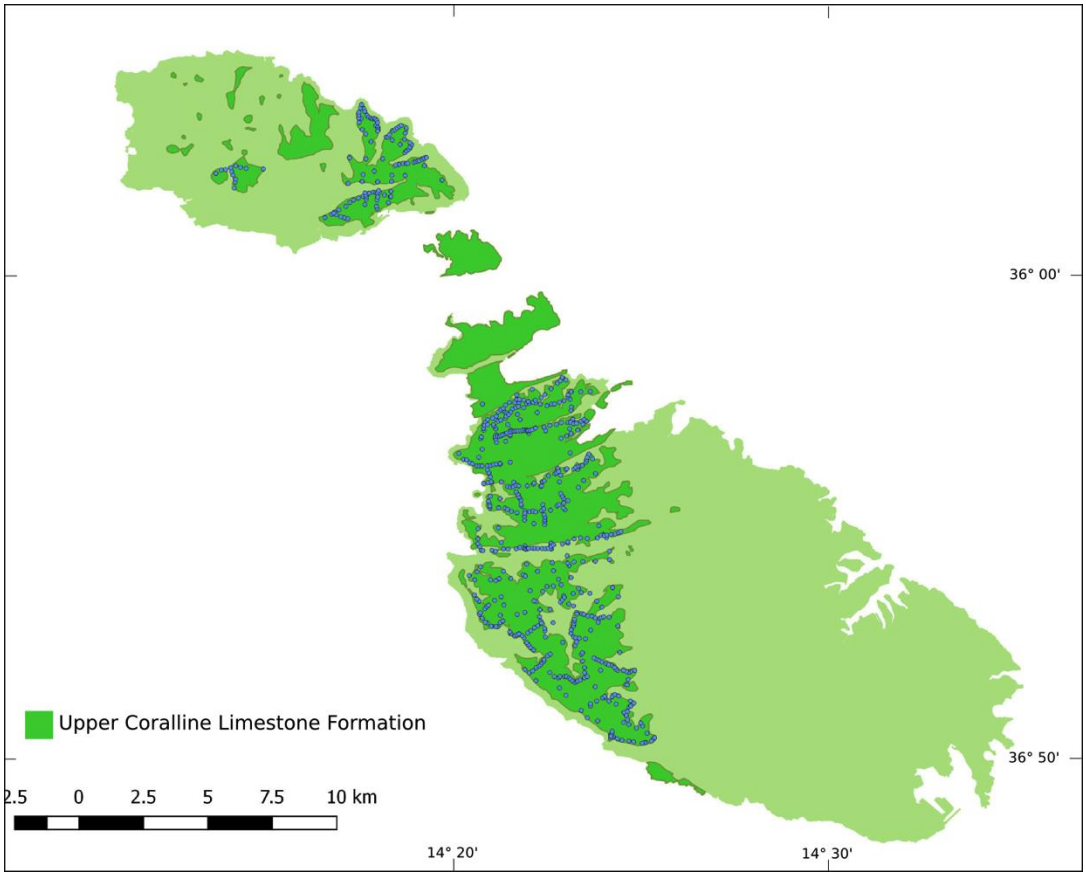

Figure 5.2: Distribution of water boreholes (blue dots) that provide subsurface data on the top Blue Clay, Greensand and the Upper Coralline Limestone Formation across the Maltese Islands (Russell, 1955; Costain, 1957, 1958).

When compared to outcrop-based lithological logs produced in this study, the water borehole data are of lower stratigraphic resolution but of greater spatial resolution. Descriptive terms used in water borehole stratigraphic columns cannot be tied exactly to discrete lithostratigraphic or sedimentological units identified in this and previous outcrop-based studies (e.g. Pedley, 1974; Bosence & Pedley, 1982; Dart, 1991). However, a systematic comparison of 54 borehole logs to 36 nearby outcrops (<50m) carried out in the course of this study has allowed a scheme to be developed that indicates which descriptive terms used in the borehole logs relate to which stratigraphic divisions (table 5.2 and Appendix C1.2).

In this study, the water borehole records (Russell, 1955; Costain, 1957, 1958) were used to identify the thickness distribution of certain stratigraphic divisions (table 5.2). Borehole data outliers (with thicknesses that are well in excess of what is expected for the area) are not used for modeling. Thickness maps for the six identified divisions were produced across the Malta Horst, North Malta Graben and Gozo Horst (e.g. figure 5.4). Water borehole logs close to outcrop logs were used to accurately determine where the top of the Blue Clay and Greensand Formations occurs.

Borehole Log Division (Russell, 1955; Costain, 1957, 1958)	**Stratigraphic / sedimentological units used in this thesis (table 5.3)**
Division 0	Blue Clay Formation
Division 1	Open Shelf Glauconite-rich Packstone Facies (OSGR)
Division 2	Coralline Algal Floatstone Facies (CAF)
Division 3.1	Open Shelf *Heterostegina*-rich Packstone Facies (OSHR)
Division 3.2	Coralline Algal Pavement Rudstone to Framestone Facies (CAP), Coralline Algal Debris Packstone Facies (CAD), and Massive Coralline Algal Debris Wackestone Facies (MCAD)
Division 4.1	Planar Bedded Coralline Algal Debris Wackestone Facies (PCAD), and Distal Reef Slope Wackestone Facies (DRS)
Division 4.2	Reef-Core FA, Proximal Reef Slope Packstone Facies (PRS) and Sand Shoal FA

Table 5.2: Scheme indicating which borehole log divisions relate to which stratigraphic divisions. See Appendix C1.2 for an outline of which borehole log descriptive terms correspond to stratigraphic divisions.

5.2.5 Thickness of Upper Coralline Limestone and Greensand formations

The depth to Blue Clay Formation gives information on the preserved thickness of the Upper Coralline Limestone (UCL) and Greensand formations. The UCL demonstrates significant thickness variation across the study area but has an average exposed thickness of 28 m and a maximum exposed thickness of 109 m (figure 5.3). The top of the Upper Coralline Limestone Formation is not seen as it is the youngest Miocene unit on Malta. In most cases it forms the top of the studied outcrops, however, sub-aerial Quaternary deposits can locally cap the Formation. Consequently, the true thickness of the UCL as a stratigraphic unit is not known, and has caused vagaries in data and correlation.

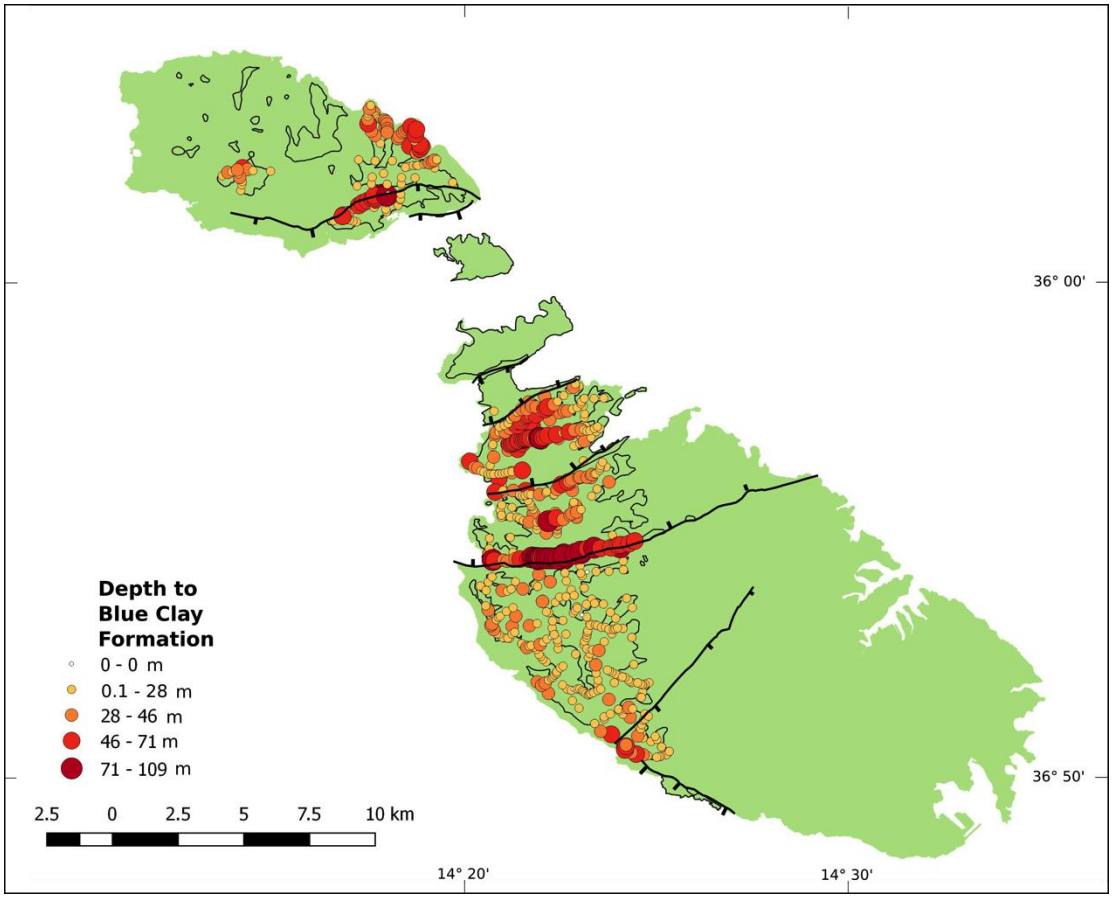

Figure 5.3: Depth to Blue Clay Formation gives information on the preserved thickness of the Upper Coralline Limestone and Greensand formations based on seven hundred and seventeen water borehole records. The UCL demonstrates significant thickness variation across the study area but has an average exposed thickness of 28 m and a maximum exposed thickness of 109 m.

5.3. Description of facies associations and facies within the Greensand and Upper Coralline Limestone formations

The identified facies were grouped into facies associations. Six facies associations (FA) and fifteen facies (table 5.3) were identified in the study area (figure 5.1) within the Greensand and

Upper Coralline Limestone (UCL) formations (figure 5.1). Formal stratigraphic terminology has been previously proposed for the UCL and a stratigraphic comparison chart (table 5.4) indicates which FA and facies of this study are equivalent to, or relate to, previous divisions in the literature. The six FA recognised (table 5.3) are typical for those also reported in the Upper Miocene of the central Mediterranean region (e.g. Esteban, 1996; Pedley, 1996, 1998; Pomar *et al.,* 1996; Franseen & Goldstein, 1996).

Platform type	**Facies Association (FA)**	**Facies**
Fault-Block Platform (*sensu* Bosence, 2005)	Sand Shoal FA (SaS)	Wave Ripple Packstone Facies (WR) Sand Shoal Grainstone Facies (SS)
	Fore-Reef Slope and Shelf FA	Distal Reef Slope Wackestone Facies (DRS) Proximal Reef Slope Packstone Facies (PRS)
	Reef-Core FA	Coralgal Reef Framestone Facies (CR) Coralgal Patch Reef Rudstone Facies (CPR) Coralgal Fore Reef Packstone Facies (CFR)
	Sheltered Shelf FA (SS)	Planar Bedded Coralline Algal Debris Wackestone Facies (PCAD) Massive Coralline Algal Debris Wackestone Facies (MCAD)
	Coralline Algal Biostrome FA	Coralline Algal Debris Packstone Facies (CAD) Coralline Algal Pavement Rudstone to Framestone Facies (CAP) Coralline Algal Floatstone Facies (CAF) Coralline Algal Sand Ridge Packstone Facies (CASR)
	Open Shelf FA	Open Shelf *Heterostegina*-rich Packstone Facies (OSHR) Open Shelf Glauconite-rich Packstone Facies (OSGR)

Table 5.3: Summary facies scheme erected in this thesis for the UCL Formation.

Pedley (1974; 1975; 1978; 1979) Lithostratigraphy	**Bosence & Pedley (1982)**	**Dart (1991) GS: Genetic Sequence**		**Facies Association (FA)**	**Facies**
Upper Coralline Limestone Formation (UCL Fm), Tal-Pitkal Member, Ghar Lapsi Beds	*Not assessed in study*	GS3: Slope Facies Association (Dart, 1991 p.241)	Reef Talus Facies (RT)	*Area where Facies Association outcrops (Ghar Lapsi - west of Il-Maghlaq fault) was not investigated in this thesis*	
			Proximal Calciturbidite Facies (PT)		
			Distal Calciturbidite Facies (DT)		
			Evaporite Solution Breccia Facies (ES)		
		GS3: Platform Facies Association (Dart, 1991 p.236)	Sand Shoal Facies (SS)		
			Inter Sand Shoal Facies (IS)		
			Organ Pipe *Porites* Reef Facies (OP)		
UCL Fm, Gebel Imbark Member, Gebel Imbark Beds		GS2: Peritidal Facies (PE) (Dart, 1991 p.264)		*Area where Facies Association outcrops (Ghar Lapsi - west of*	

			Il-Maghlaq fault) was not investigated in this thesis	
UCL Fm, Gebel Imbark Member, Tat-Tomna Beds		GS2: Sand Shoal Facies (SS) (Dart, 1991 p.262)	Sand Shoal FA	Wave Ripple Packstone Facies (WR)
				Sand Shoal Grainstone Facies (SS)
UCL Fm, Tal- Pitkal Member, Ghadira beds		GS2: Proximal Reef Slope Facies (PR) (Dart, 1991 pp.232, 262)	Fore-Reef Slope and Shelf FA	Distal Reef Slope Wackestone Facies (DRS)
				Proximal Reef Slope Packstone Facies (PRS)
UCL Fm, Tal- Pitkal Member, Depiru Beds		GS 2: Coralgal Barrier Reef Facies (BR) (Dart, 1991 p.229 suggests facies is previously un-described. In this study the facies corresponds to Depiru Beds)	Reef-Core FA	Coralgal Reef Framestone Facies (CR)
UCL Fm, Tal- Pitkal Member, Tal Pictal Beds		GS2: Coralgal Patch Reef Facies (PR) (Dart, 1991 p.260)		Coralgal Patch Reef Rudstone Facies (CPR)
				Coralgal Fore Reef Packstone Facies (CFR)
UCL Fm, Mtarfa Member, Gebel Mtarfa Beds	Gebel Mtarfa Beds	GS 1: Open Shelf Sand Facies (OShS) (Dart, 1991 p.227)	Sheltered Shelf FA	Massive Coralline Algal Debris Wackestone Facies (MCAD)

UCL Fm, Mtarfa Member, Rdum il-Hmar Beds	*Not assessed in study*		GS2 (?) see section 5.3.3: Sheltered Shelf Facies (ShS) (Dart, 1991 p.232)			Plane Bedded Coralline Algal Debris Wackestone Facies (PCAD)
UCL Fm, Tal-Pitkal Member, Rabat Plateau Beds	Coralline Algal Biostrome	Algal Crust Packstone Facies	GS1: Coralline Algal Biostrome (Dart, 1991 p.226)	Coralline Algal Debris Facies (AD)	Coralline Algal Biostrome FA	Coralline Algal Debris Packstone Facies (CAD)
		Algal Branch Packstone Facies				
UCL Fm, Mtarfa Member, Coralline Algal Bioherm		Crustose Pavement Facies		Coralline Algal Pavement Facies (CP)		Coralline Algal Pavement Rudstone to Framestone Facies (CAP)
		Rhodolith Pavement Facies				
		Crustose Algal Wackestone Facies		Coralline Algal Marl Facies (AM)		Coralline Algal Floatstone Facies (CAF)
		Crustose Algal Marl Facies				
		Considered as Ghajn Znuber Beds (below)		*Considered as Sand Ridge Facies (below)*		Coralline Algal Sand Ridge Packstone Facies (CASR)

UCL Fm, Ghajn Melel Member, Zebbug Beds	Zebbug Beds	Zebbug Beds	Open Shelf FA	Open Shelf *Heterostegina*-rich Packstone Facies (OSHR)
UCL Fm, Ghajn Melel Member, Ghajn Znuber Beds	Ghajn Znuber Beds	GS1: Sand Ridge Facies (SR) (Dart, 1991 p.221)		
Greensand Formation	Greensand Formation	Greensand Formation		Open Shelf Glauconite-rich Packstone Facies (OSGR)
Blue Clay Formation	Blue Clay Formation	Blue Clay Formation	Blue Clay Formation	

Table 5.4: Stratigraphic chart indicating history of stratigraphic divisions of the Upper Coralline Limestone and how these relate to the Facies Associations (FA) and Facies of this thesis.

5.3.1. Open Shelf Facies Association

The Open Shelf Facies Association (FA) consists of the Open Shelf Glauconite-rich Packstone Facies (OSGR) and the Open Shelf *Heterostegina*-rich Packstone Facies (OSHR). The Open Shelf FA is locally absent and varies in thickness from 0 to 47 m (sum of divisions 1 and division 3.1, figures 5.4 and 5.7 respectively).

In this study, the Greensand Formation has not been studied in detail. It has been treated as one facies, the Open Shelf Glauconite-rich Packstone (OSGR) Facies, within the Open Shelf Sand Facies Association. However, this facies is likely to consist of a number of different facies/sub-facies if studied in detail.

5.3.1.1. Open Shelf Glauconite-rich Packstone Facies (OSGR)

Description

The OSGR Facies is a friable greyish-green packstone that is extensively bioturbated and massive-bedded. Petrographic analysis of the Il-Gelmus Beds (type locality) shows that the beds consist of friable, marly lithoclastic sediments (Pedley, 1978). Derived clasts are common in all outcropping areas, and the strata are uncommonly rich in abraded “waterworn” gypsum grains and glauconite (Pedley, 1978).

Facies thickness, distribution, timing and association with other beds

Water borehole data suggest that the facies is locally absent. When present, it has an average thickness of 0.9 m and a maximum thickness of 25 m (figure 5.4). Thicker accumulations occur along the west of Malta and east of Gozo.

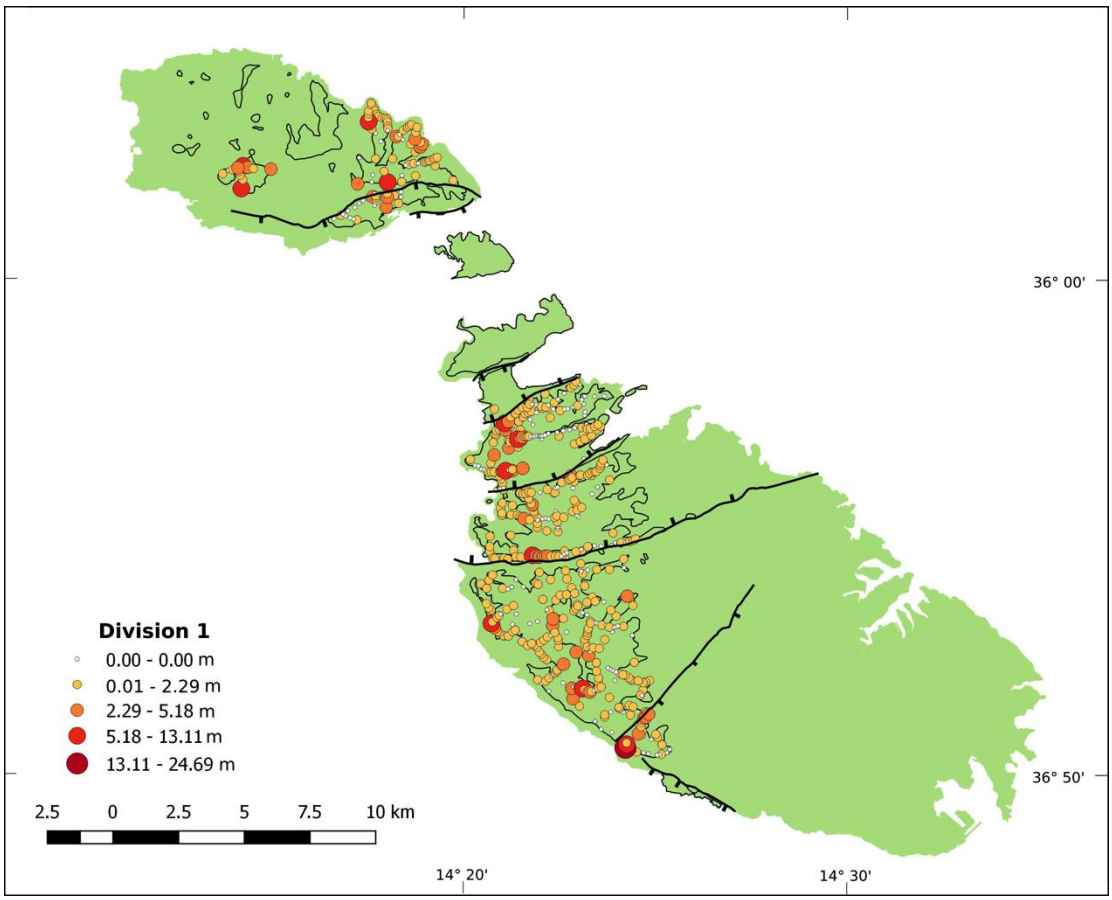

Figure 5.4: Thickness distribution of division 1 within outcrop area of the UCL Fm based on seven hundred and seventeen water borehole records. Division 1 (table 5.2) equates to the OSGR Facies.

Fauna and Flora

The fossils that are most characteristic and/or provide information on depositional environments include *Heterostegina depressa* (d'Orbigny), *Cellepora sp.* (Lineaus), *Textularina sp.* (Defrance), *Bairdia sp.* (M'Coy), *Myliobatis sp.* (Cuvier), *Sparus auratat* (Linnaeus), *Trachypatagus tuberculatus* (Wright), and *Strombus sp.* (Swainson). See Appendix C3 for a detailed list of all the fauna and flora recorded in the facies.

Depositional environment

In the Red Sea, *Heterostegina depressa* is distributed over almost the complete photic zone and is replaced in deeper waters by the totally evolute species *Heterostegina operculinoides* (Hofker) (Hottinger, 2006). In Indo-Pacific Miocene carbonates, the association of *Amphistegina* (d'Orbigny), *Myogypsina* (Sacco) and *Heterostegina* (d'Orbigny) is diagnostic of shallow, high-energy conditions (Flugel, 2010). *Heterostegina depressa* lives on hard substrates in high-energy conditions (Reiss & Hottinger, 1984; Hottinger 2006). However, in the deeper parts of the photic zone (below 60–80 m), the nature of the substrate is of secondary importance for the distribution of the deeper species (Hottinger 2006). More recent studies suggest that light

intensity plays a very important role in influencing the water depth distribution of larger benthic foraminifera (Eder *et al.,* 2016). *Heterostegina depressa* (d'Orbigny) copes better with low light conditions than with high light conditions (Nobes *et al.,* 2008). The larger benthic foraminifera *Textularina sp.* (Defrance) is frequently observed in the inner neritic environment (0 to 40m depth) (Chukwu *et al.,* 2012). However, various authors suggest that the larger benthonic foraminifera *Heterostegina depressa* (d'Orbigny) and *Textularina sp.* (Defrance) occupy almost the entire photic zone (<80 m), though the prior genus copes better with low light conditions (Nobes *et al*., 2008).

Cellepora sp. (Lineaus) overcomes fast water currents and high rate of sedimentation (>100 $cm/10^3$ yr) by the articulation of the long narrow internodes, thereby forming celleporiiform growth forms (El Sorogy *et al.,* 2004). The species' growth form is generally observed to be adapted for living in warm, shallow, high-energy water environments of the littoral zone (Holcova & Zagorsek, 2008). It is argued that the relationship between the taxonomic composition and bryozoan colony growth−patterns implies nearshore environments, with considerable wave action, and warm climatic conditions (Hara, 2015).

The ostracod *Bairdia sp.* (M'Coy) is an epifaunal detritivore-grazer that is commonly recorded in shallow, sub-tidal environments (Sebe *et al.,* 2013). The vertebrate *Myliobatis sp.* (Cuvier) lives in warm, shallow coastal waters (Sepkoski, 2002) whilst the vertebrate *Sparus auratat* (Linnaeus) is typically found at depths of 0 to 30 m (up to 150 m) near seagrass or over sandy bottoms (Froese & Pauly, 2015). The echinoderm *Trachypatagus tuberculatus* (Wright) typically suggests moderately agitated water at depths less than 40m (Philippe & Lary, 1990). *Strombus costatus* (Gmelin), or *Lobatus costatus* (Gmelin), is typically found in depths that vary from 3 to 20 m (Brownell, 1977). *Strombus sp.* (Swainson) is primarily found in shallow marine habitats, such as seagrass meadows, sand beds, and algal flats (Tewfik & Guzman, 2003). Overall, the habitats where the latter species is found are shallow enough for light to penetrate through the water column, which allows the surrounding plant life to photosynthesize.

The faunal assemblage observed within the OSGR Facies suggests deposition in warm, shallow (*circa* 50 m), high-energy water environments of the shoreface/littoral zone. The skeletal and glauconitic grains are fragmented and abraded which indicates the grains were extensively transported. Additionally, the packstone texture supports the interpreted moderate-high energy depositional environment. The extensively bioturbated and massive-bedded nature of the facies suggests the high-energy marine conditions may have been intermittently interrupted by periods of lower-energy.

These observations indicate that the sediments were extensively reworked/transported and accumulated in a high-energy marine environment over a considerable period of time. In conclusion, both faunal and sedimentary evidence suggest that the OSGR Facies was deposited under turbulent conditions, associated with an open-water shifting substrate in a platform environment. This paleoenvironmental interpretation corresponds to that by Pedley (1974, 1978).

5.3.1.2. Open Shelf Heterostegina-rich Packstone Facies (OSHR)

Pedley subdivides the Ghajn Melel Member into the Zebbug Beds in the west of Gozo and the Ghajn Znuber Beds in the east of Gozo and west of Malta (table 5.4, Pedley, 1978). Pedley's (1978) divisions are partly based on the different faunas they contain. Pedley (1978) indicates that more certain evidence for the subdivision is from their respective petrologies as the Zebbug Beds contain un-abraded and un-mineralised *Heterostegina* whereas the Ghajn Znuber Beds contain 40 to 60% derived glauconite, limonitic lithoclasts and *Heterostegina* fragments that were impregnated by goethite prior to fragmentation and transportation. Dart's (1991) Sand Ridge Facies is comparable to the Ghajn Znuber Beds of Pedley (1978).

Certain of Pedley's (1978) criteria, to distinguish between the Zebbug and Ghajn Znuber Beds, are observed in petrographic/microfacies analysis (sections below). However, both beds are rich in *Heterostegina* and share many common features at outcrop scale (compare MT47 and GZ22 in figure 5.5). This suggests that the beds in Gozo and Malta are similar. The microscopic differences between beds goes beyond the resolution of stratigraphic forward model outputs. In view of this, these two beds of the Ghajn Melel Member have been combined for this thesis into this one facies.

Description

The OSHR Facies in Malta and Gozo consists of orange-brown to yellowish-brown, *Heterostegina*-rich packstones and rudstones (figure 5.5A and B). The beds are typically extensively bioturbated and massive-bedded (e.g. in localities MT47, GZ22). Certain localities in the west of Gozo (GZ02, GZ03) display thick bedding at a 1 to 2 m scale that dip to the NNE (e.g. locality GZ02 in figure 5.5C). The main bioclastic components are benthonic foraminifera *Heterostegina*, bryozoan, echinoid and bivalve debris.

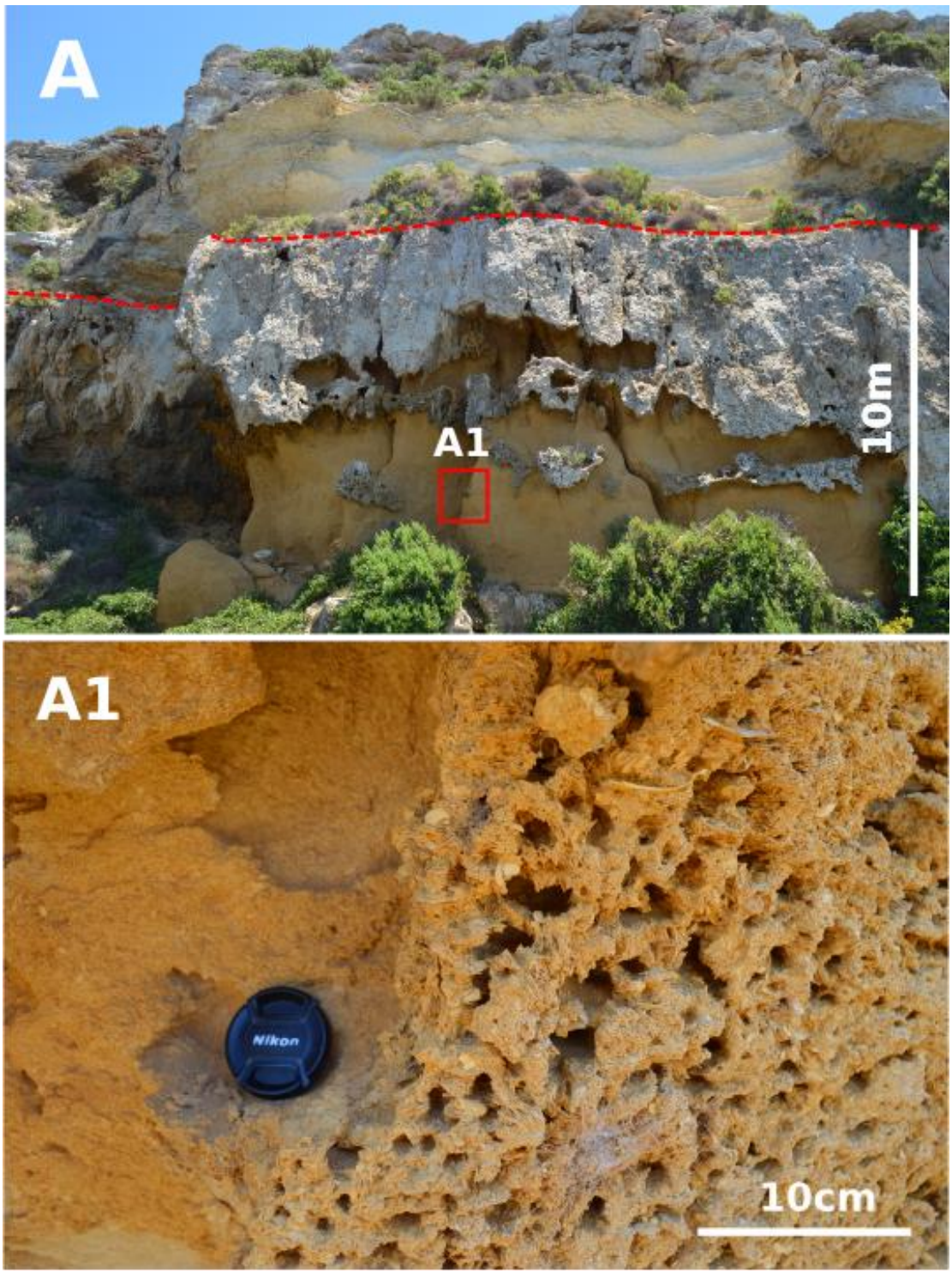
A
A1
10m
A1
Nikon
10cm

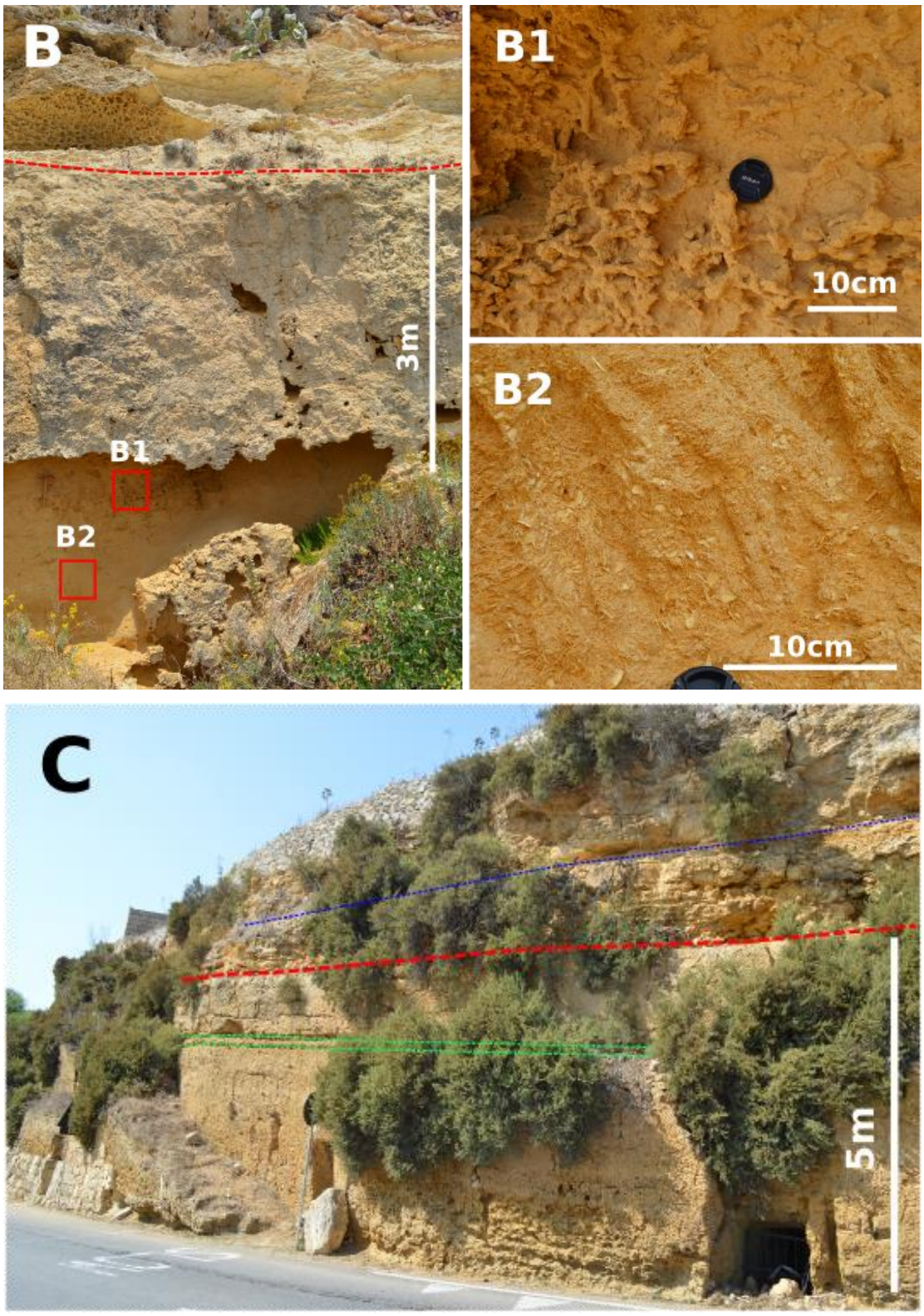

Figure 5.5: Features of the OSHR Facies. (A and B) Outcrops contain a thick (<15 m) accumulation of OSHR Facies (pale orange) that is overlain by Coralline Algal Biostrome FA (cream). A laterally extensive sharp planar or undulating boundary (red dashed line in figure A and B) exists between these units (A, locality GZ22; B, locality MT47). (A1, B1 and B2) Detail of the OSHR Facies with a large proportion of bioclastic debris, is extensively bioturbated and massive-bedded. (C) A sharp erosive bed boundary (red dashed line) separates the underlying OSGR Facies from the overlying OSHR Facies. The beds in these two units are concordant at this location as shown by dashed green lines for bedding in the OSGR Facies and dashed blue line for the bedding in the OSHR Facies (locality GZ02).

Facies thickness, distribution, timing and association with other beds

The OSHR Facies overlies the Blue Clay and, in places, the OSGR Facies (figure 5.5C). In western areas of Gozo (localities GZ02, GZ03) there is a sharp erosive bed boundary between the OSGR and overlying OSHR facies (e.g. locality GZ02 figure 5.5C) but no angular discordance. Pedley (1978 pp8) interprets the contact between the OSGR and OSHR facies as a disconformity. Evidence for a break in time is however not provided.

The Coralline Algal Biostrome FA overlies the OSHR Facies. A laterally extensive sharp planar or undulating boundary exists between these latter units in Malta and Gozo (e.g. red dashed line in MT47, GZ22 figure 5.5A and 5.5B). In certain locations the topmost 0.3 m of OSHR deposits, that directly underlie the Coralline Algal Biostrome FA, demonstrate a centimetre to decimetre scale coarsening-upwards trend that contains an increasing proportion of coralline algal debris (e.g. MT47, GZ02, GZ20, GZ21).

The OSHR Facies can be observed across Gozo except for the easternmost outcrops (GZ15 and GZ16) where the beds are absent (figure 5.6 and 5.7). In Gozo, the beds are best developed in GZ03, GZ17 and GZ22 where they can form accumulations up to 16 m thick. In Malta, the OSHR Facies only occurs in the westernmost areas and diminishes eastwards (figure 5.6 and 5.7). Outcrop data suggest the distribution of the facies in Malta is patchy and may be locally absent even in western areas of Malta (figure 5.6 and 5.7).

Water borehole data correctly identifies thick accumulations of OSHR Facies in the north east of Gozo. This accumulation corresponds to the thick succession observed in outcrop localities GZ22. The borehole data however does not record the thick accumulation of OSHR Facies observed in outcrop in the south west of Malta (localities MT16, MT47, MT18). This mismatch between water borehole and outcrop data may be the result of inaccurate and/or inconsistent borehole descriptions. In view of this, water borehole data tied to division 3.1 may not be as reliable in identifying certain lithological units as the other borehole log divisions. Therefore, interpretations on the distribution of the OSHR Facies (figure 5.6) are here based on new outcrop and literature descriptions (Pedley, 1974; 1978; Bosence & Pedley, 1982; Dart, 1991).

Thicker accumulations of the OSHR Facies are localised (e.g. MT47 and BP02) and form lens-like isolated northerly trending ridges 1km wide and 10m amplitude. These observations correspond to those made by Pedley (1974; 1978), Bosence & Pedley (1982) and Dart (1991).
Dart also notes that an accumulation of Sand Ridge Facies (Ghajn Znuber Beds) is aligned parallel to the Victoria Lines Fault (VLF) (Dart, 1991). Dart's Sand Ridge Facies are here re-interpreted here as part of the Coralline Algal Sand Ridge Facies within the Coralline Algal Biostrome FA (see section 5.3.2.1).

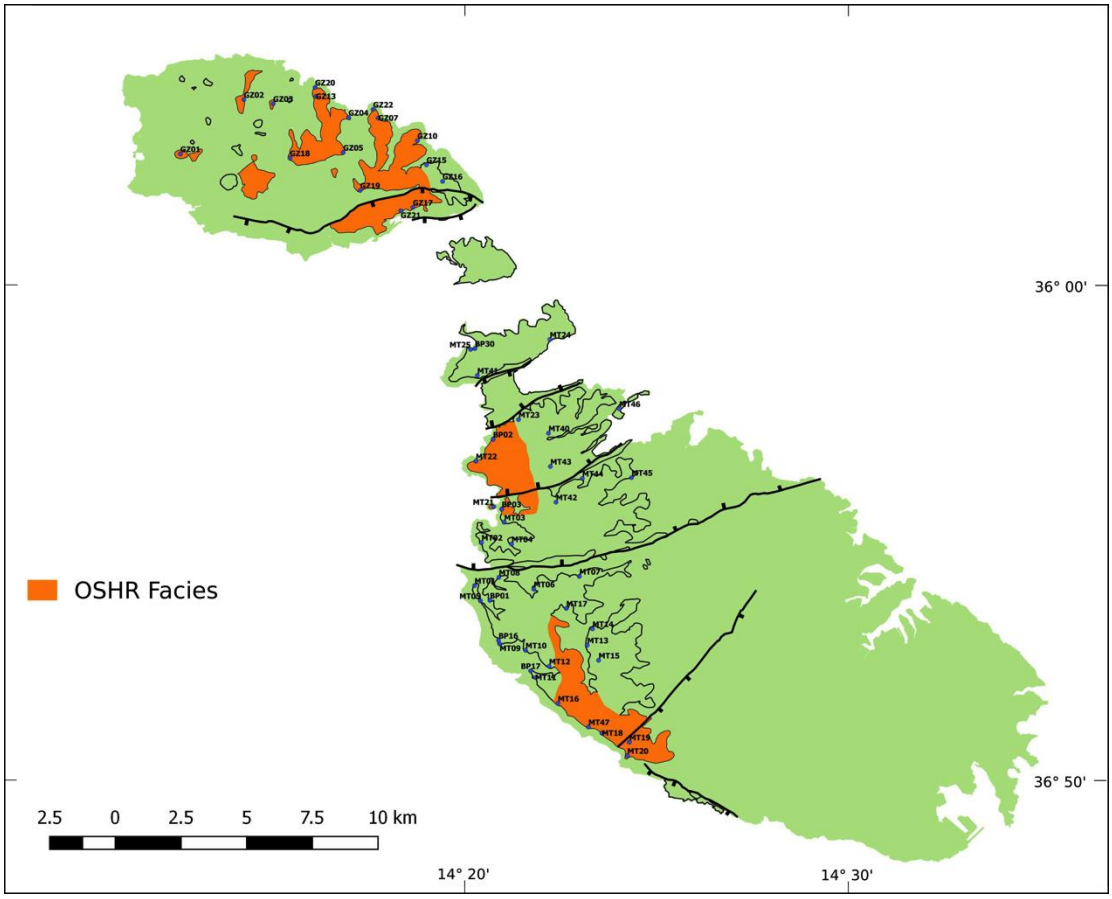

Figure 5.6: Open Shelf Heterostegina-rich Packstone (OSHR) Facies map based on new outcrop and literature (Pedley, 1974; 1978; Bosence & Pedley, 1982; Dart, 1991) descriptions. Information on the thickness and distribution of division 3.1 was not used in developing the OSHR facies map.

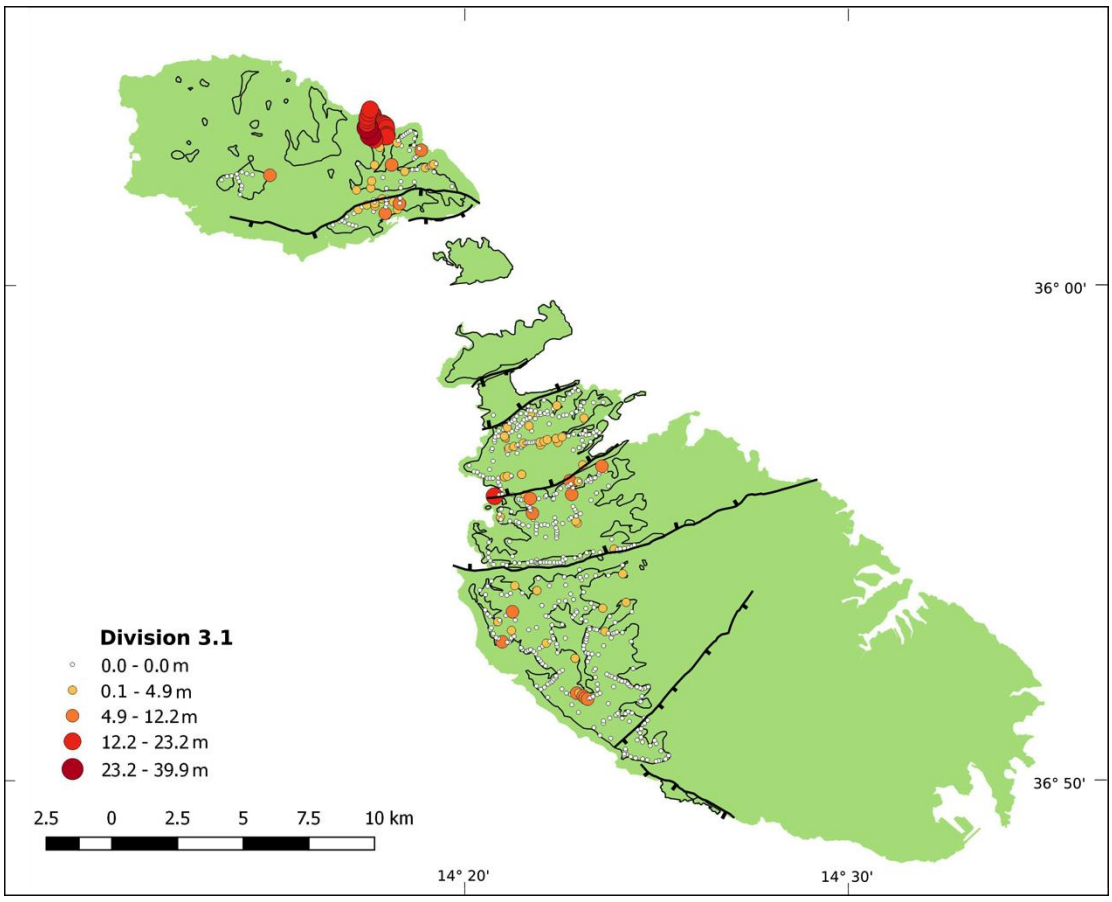

Figure 5.7: Thickness distribution of Open Shelf Heterostegina-rich Packstone (OSHR) Facies within outcrop area of the UCL Fm (black line) based on seven hundred and seventeen water borehole records. This facies equates to division 3.1 (table 5.2).

Petrography

Samples BP 2(45), BP 19a and BP 42 (figure 5.8A) were assessed in terms of grain sizes, grain composition, porosity and cement (table 5.5). Results indicate that BP 42, BP 2(45) and BP 19a are progressively coarser. Samples BP 2(45) and BP 19a are moderately well sorted and sample BP 42 is moderately sorted. Larger benthic foraminifera (*Heterostegina*) fragments are the dominant skeletal-grains in all three samples and make up 37% to 52% of all points counted. The *Heterostegina* fragments in samples BP 2(45) and BP 19a are finer and better rounded than those observed in BP 42. The foraminiferal fragments in all samples are iron (goethite/limonite) impregnated, though samples BP 2(45) and BP 19a are more intensely iron impregnated. Grain morphometry of the foraminifera (*Heterostegina)* fragments indicates they are rounded to sub-rounded and demonstrate intermediate sphericity (0.4). BP 19a and BP 42 contain 2 and 5% intact *Heterostegina*. Glauconite grains occur in BP 2(45) and BP 19a and account for 10% and 5% of all points counted. The glauconite grains are well rounded and demonstrate high sphericity (0.9). Glauconite grains are not present in BP 42. All thin sections contain minor portions of planktonic foraminifera (2% to 3% of all counted points) preserved as intact tests and fragments. Echinoid fragments (0.5% of all counted points) were also noted. Sample BP

2(45) contained undifferentiated coralline algae (1% of all counted points). All three samples correspond to the molechfor (Carannante *et al.,* 1988) grain association.

Thin Section	Mud matrix %	F-VF Sd %	M Sd %	VC-C Sd %	VF Grv %	Pebble %	Porosity %	Cement %
BP 2(45)	22.86	16.03	29.93	3.74	0.53	0.00	9.05	17.86
BP 19a	19.76	8.14	37.01	16.28	0.00	0.00	2.86	15.95
BP 42	45.00	26.76	17.31	6.82	0.52	0.00	2.38	1.19

Table 5.5: Grain sizes, porosity and cement observed in the assessed thin sections. 420 points were counted in each thin section.

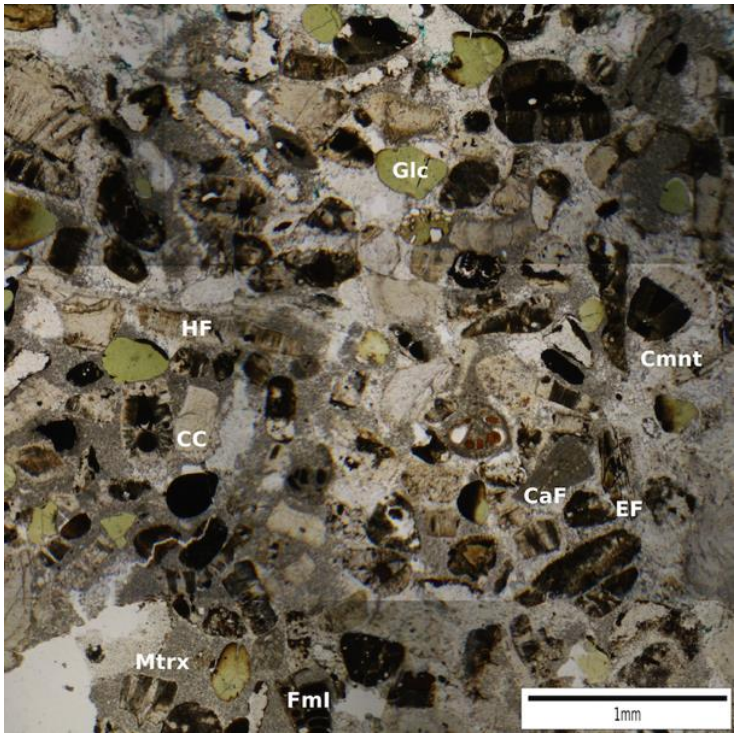

Figure 5.8: (A) Photomosaic of photomicrographs of thin section BP 2(45) of OSHR Facies. Glc, Glauconite; FmI, Foraminifera intact; HF, Heterostegina fragments; EF, Echinoid fragments; CaF, Coralline algal fragments; Mtrx, Matrix; Cmnt, Cement; CC, Calcite Crystal. Brown to dark brown grains are limonite-impregnated bioclasts.

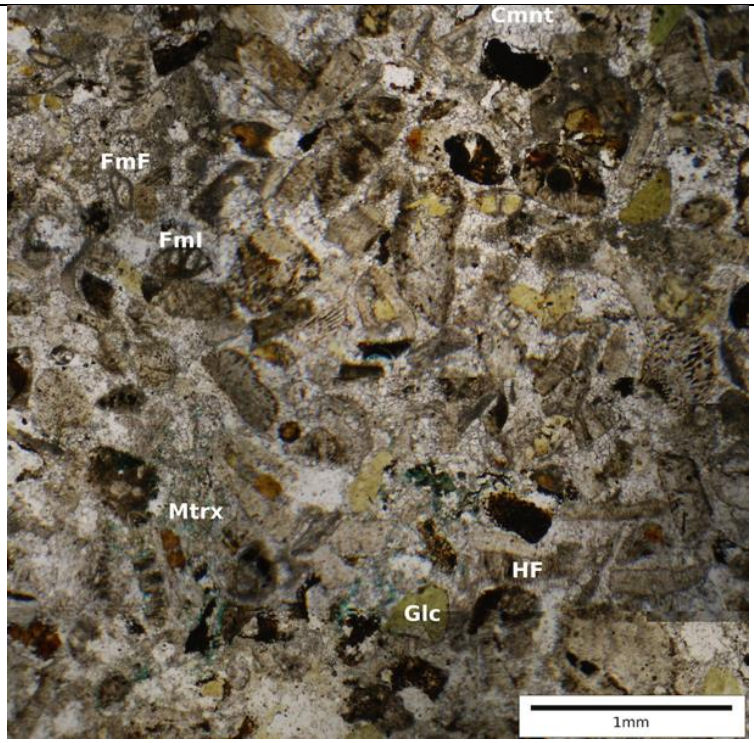

Figure 5.8: (B) Photomosaic of photomicrographs of thin section BP 19a of OSHR Facies. FmF, Foraminifera fragments; FmI, Foraminifera intact; Glc, Glauconite; HF, *Heterostegina* fragments; Mtrx, Matrix; Cmnt, Cement.

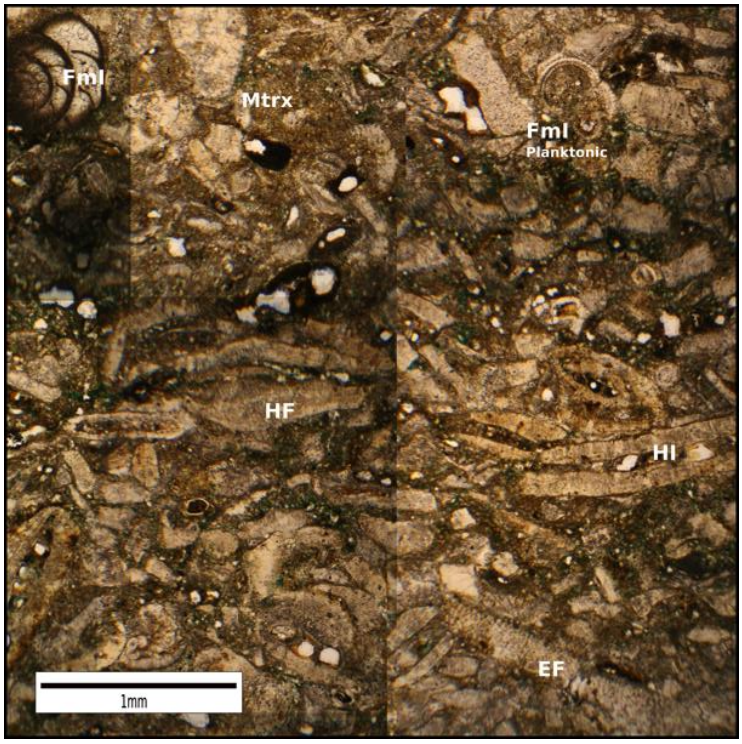

Figure 5.8: (C) Photomosaic of photomicrographs of thin section BP 42 of OSHR Facies. FmI, Foraminifera intact; HF, *Heterostegina* fragments; HI, *Heterostegina* intact; EF, Echinoid fragment; Mtrx, Matrix.

Samples BP 2(45) and BP 19a (figure 5.8A and 5.8B) were taken from outcrops in the west of Malta that correspond to Pedley's (1978) Ghajn Znuber Beds. Sample BP 42 (figure 5.8C) was taken from Zebbug Gozo that corresponds to Pedley's (1978) Zebbug Bed. A comparison of the three samples indicates that samples are different at a microfacies level. BP 2(45) and BP 19a are relatively well sorted and well rounded mixed bioclastic grain packstone with glauconite. Sample BP 42 is relatively poorly sorted, and less- well rounded *Heterostegina*-rich debris packstones.

Pedley (1978) suggests that the *Heterostegina* in the Zebbug Beds are invariably un-abraded and un-mineralised whilst in the Ghajn Znuber Beds contain 40 to 60% derived glauconite, limonitic lithoclasts and *Heterostegina* fragments that were impregnated by goethite. Petrographic analysis carried out in this study corroborates certain of Pedley's (1978) claims. Samples BP 2(45) and BP 19a appear to be more intensely iron impregnated than sample BP 42. Petrographic analysis however indicates that both the Ghajn Znuber and Zebbug samples are dominated by *Heterostegina* debris and have similar proportions of skeletal and non-skeletal grains. The *Heterostegina* debris in samples BP 2(45) and BP 19a are however finer-gained and better rounded than those observed in BP 42. Additionally, samples BP 42 and BP 19a, corresponding to Pedley's Zebbug and Ghajn Znuber Beds respectively, contain similar low proportions of intact *Heterostegina* tests. The assessed samples therefore do not match the criteria proposed by Pedley to differentiate between the Zebbug and the Ghajn Znuber Beds.

While the difference between samples is noticeable, field observations indicate that the Zebbug and Ghajn Znuber Beds contain interbedded coarser and finer intervals. In view of this, further microfacies analysis, assessing a larger number of thin sections, may be necessary to conclusively identify similarities and differences between the Ghajn Znuber and Zebbug Beds. If further petrographic analysis concludes that the beds are in fact distinct, this would be at the microscopic level that goes beyond the resolution of stratigraphic forward model outputs (see chapter 8).

Fauna and Flora

The fossils that are most characteristic and/or provide information on depositional environments in the OSHR Facies include *Heterostegina sp.* (d'Orbigny) and *Cellepora sp.* (Lineaus), *Clypeaster altus* (Leske) and *Chlamys (Macrochlamys) lattissima* (Huelva) (for details see Appendix C3).

Depositional environment

The facies consists of overturned, disarticulated and abraded macrofossils. These characteristics are indicative of high-energy marine conditions. Present day benthonic foraminifera *Heterostegina sp.* (d'Orbigny) live at depths less than 50m (Vaughan & Cole, 1941) and is found living of modern, shallow, sub-tropical seas of Australia and the West Indies (Carpenter, 1986). In Indo-Pacific Miocene carbonates, the association of *Amphistegina* (d'Orbigny), *Myogypsina* (Sacco) and *Heterostegina sp.* (d'Orbigny) is diagnostic of shallow high-energy conditions (Flugel, 2010). *Heterostegina sp.* (d'Orbigny) tests are broken and are sub-rounded to well-rounded suggesting that the grains were extensively transported and abraded. This indicates that the deposits were subject to high-energy environments. The celleporiform bryozoan *Cellepora sp.* (Lineaus) is observed in this unit and Pedley (1974) argues that they are

adapted to sub-littoral environments exposed to moderate to high velocity currents and subject to extensive sediment reworking. Recent literature on the habitat of celleporiform bryozoa (Holcova & Zagorsek, 2008) supports Pedley's (1974) interpretation.

Microfacies analysis indicates that the facies is grain-supported and consists of coarse grains (medium-grained to very coarse-grained) that demonstrate high roundness and sphericity (sub-rounded to well-rounded). This suggests that deposition occurred within environments with sufficient current velocity to winnow mud and transport coarser grains. *Heterostegina* tests are preserved as debris, corresponding to highly fragmented tests (level 3 of Beavington-Penney, 2004). Larger benthic foraminifera are known to be resistant to abrasion (Beavington-Penney, 2004) so that fragmentation is the result of long transport times and reworking. This indicates that the sediments were subject to high-energy marine environments that extensively transported and reworked the sediments. A distinctive brown colouration is provided by limonitic lithoclasts and *Heterostegina* fragments that are impregnated with goethite (Pedley, 1987; Bosence & Pedley, 1982). This is an indication of reworking and slow sedimentation rates.

The massive nature of the beds indicates destruction of original sedimentary structures due to extensive bioturbation. This, in combination with the faunal and petrographic characteristics of the beds suggests that the beds may have been subject to episodes of turbulent water conditions (storm reworking?) that were followed by lower energy conditions. During periods of high-energy, large volumes of sediment were deposited in the area thereby forming N-S orientated patches (figures 5.6 and 5.7) interpreted as sand-waves and ridges. During periods of lower energy, relatively low quantities of sediment reached the area and the previously deposited and new accumulating deposits were bioturbated. OSHR deposits that are more micritic may have occupied environments subject to lower energy conditions and formed contemporaneously with the coarser grained deposits that were in higher energy environments.

In conclusion, the OSHR facies is interpreted to have formed littoral-sublittoral sand waves and ridges. The deposits formed in high-energy shallow shelf (*circa* 20 to 50 m) environment within the storm/fair weather wave base. This environmental interpretation corresponds to that made by Pedley (1974, 1978), Bosence & Pedley (1982) and Dart (1991).

5.3.2. Coralline Algal Biostrome Facies Association

Certain of Bosence & Pedley's (1982) detailed Coralline Algal Biostrome Facies (section 2.2.2.5.2) have been combined for this study as they share a number of petrographic characteristics that can be encompassed in Embry & Klovan's (1971) classification for coarse-grained bioclastic limestones. Thus, their Crustose Algal Marl Facies and Crustose Algal

Wackestone Facies are combined and termed the Coralline Algal Floatstone Facies (CAF) (table 5.4). The Rhodolith Pavement and Crustose Pavement Facies combined as the Coralline Algal Pavement Rudstone to Framestone Facies (CAP) and the Algal Branch Packstone Facies and Algal Crust Packstone Facies are combined and termed the Coralline Algal Debris Rudstone Facies (CAD) (table 5.4). Outcrop and borehole data indicate that the Coralline Algal Biostrome FA outcrops in Gozo and in western areas of Malta. The association is absent in central and eastern areas of Malta.

Previous studies have identified a facies that outcrops in the Fomm ir-Rih area (VLF footwall) as Ghajn Znuber Beds (Pedley, 1974, 1978; Bosence & Pedley, 1982), and the Sand Ridge Facies (Dart, 1991). In this study, this unit has been interpreted as a new distinct facies – the Coralline Algal Sand Ridge Packstone (CASR) Facies - based on its lithology, sedimentary structures and geometry. The CASR underlies the Rhodolith Pavement Facies and is interpreted to have formed contemporaneously with the Coralline Algal Floatstone Facies (CAF). The facies is therefore included within the Coralline Algal Biostrome Facies Association and not with the underlying Ghajn Znuber beds of previous authors.

5.3.2.1. Coralline Algal Sand Ridge Packstone Facies (CASR)

Description

The CASR Facies is a yellow bioclastic packstone to rudstone that is rich in coralline algal debris. The facies can be divided into two sub-facies. The coarse-grained basal sub-facies (up to 5 m) has massive beds on a 0.1 to 0.2 m scale and is moderately bioturbated (figure 5.9). These consist of alternating rhodolith-rich rudstone beds and very coarse-grained coralline algal, molluscan and echinoid debris packstone beds. The spheroidal rhodoliths average 8 cm in length and 7 cm in height and contain abraded branch tips. Intervals that are less extensively bioturbated display dune scale cross-stratification (figure 5.9A1). The large-scale prograding cross-beds are orientated to the south-west (MT01: 120/08/SW). The basal sub-facies demonstrates a gradual fining upward trend into the overlying sub-facies (figure 5.9A2). The latter sub-facies is a pale-yellow to white fine-grained packstones to wackestones (up to 10 m in thickness) that shows a gradual fining upward trend. The sub-facies is extensively bioturbated resulting in massive beds (figure 5.9A3). Coralline algal, molluscan and echinoid debris are less common and finer-grained than the basal section and rhodoliths are absent.

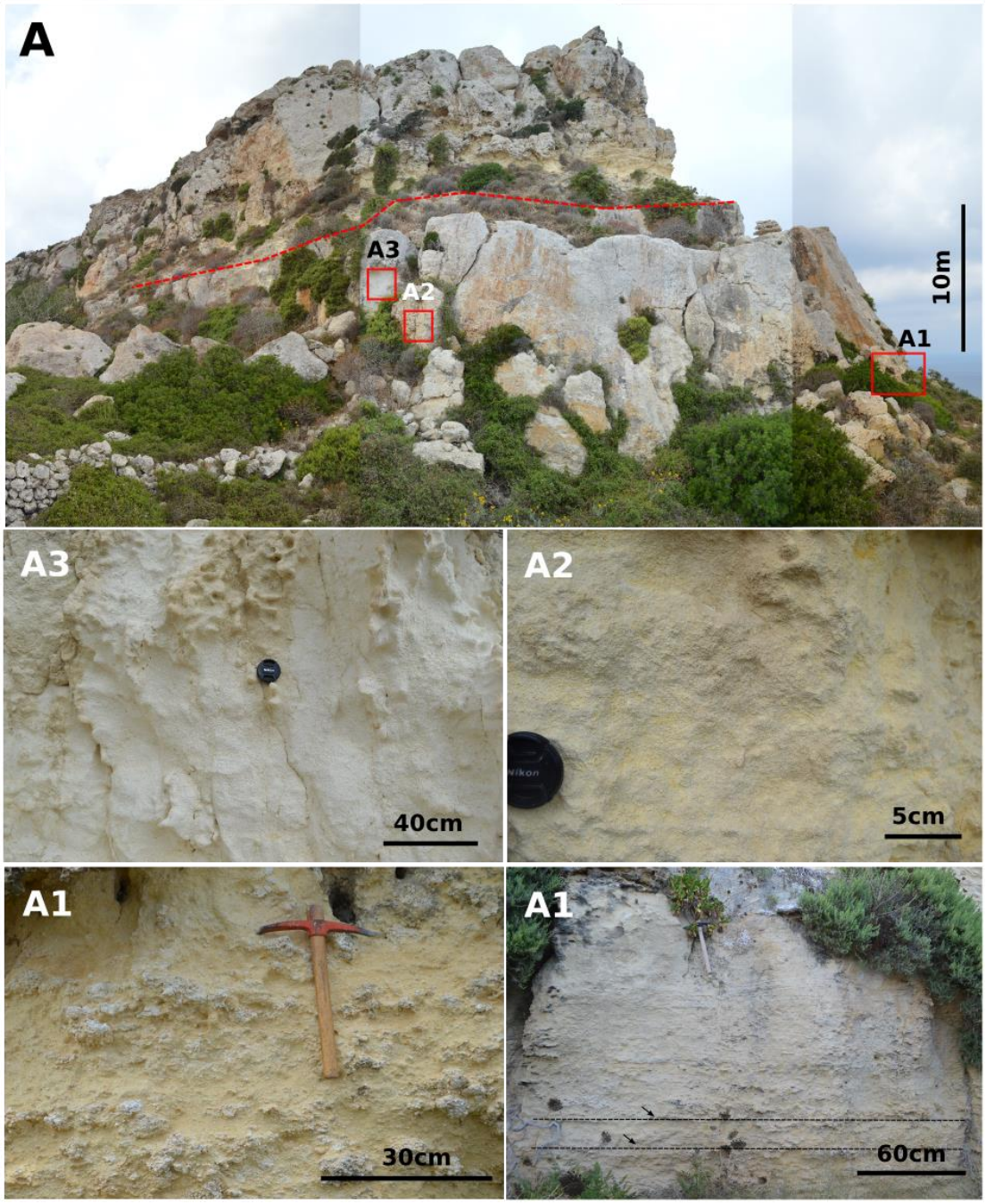

Figure 5.9: Features of the Coralline Algal Sand Ridge Packstone (CASR) Facies. (A) Outcrop contains a thick (<15 m) accumulation of CASR Facies that is overlain by the Coralline Algal Pavement Rudstone to Framestone Facies (CAP). A sharp laterally extensive bed boundary (red dashed line) is observed between the two units (locality MT01). (A1) Detail of coarse-grained basal sub-facies, (A1 left) containing rhodolith rich rudstone beds, (A1 right) base displaying prograding cross-beds (black dashed lines and arrows) are orientated to the south-west, middle and top (above black dashed lines) displaying dune scale cross-stratification. (A2) Detail of basal sub-facies gradually fining upward into the overlying sub-facies. (A3) Fine-grained packstones to wackestones that shows a gradual fining upward trend and are extensively bioturbated.

The basal contact of the CASR Facies is not observed in outcrops. The Upper Coralline Limestone Formation thickness observed in outcrop is similar to that recorded in neighbouring water borehole logs (<25m). This suggests that the CASR Facies may directly overlie the Blue Clay or OSGR (Greensand Formation). The Coralline Algal Pavement (CAP) Facies overlies the CASR Facies and a sharp laterally extensive bed boundary is observed between the two units (e.g. figure 5.9A).

Facies thickness, distribution, timing and association with other beds

The CASR Facies forms a west-east ridge parallel to the VLF footwall succession (figure 5.10). The facies is only observed in Fomm ir-Rih (MT01) and to the east of Fomm ir-Rih (MT08). The thickest accumulation is observed at MT01 (>10 m) and diminishes eastwards (MT08 *circa* 5 m) (Appendix C2, Outcrop cross section 5).

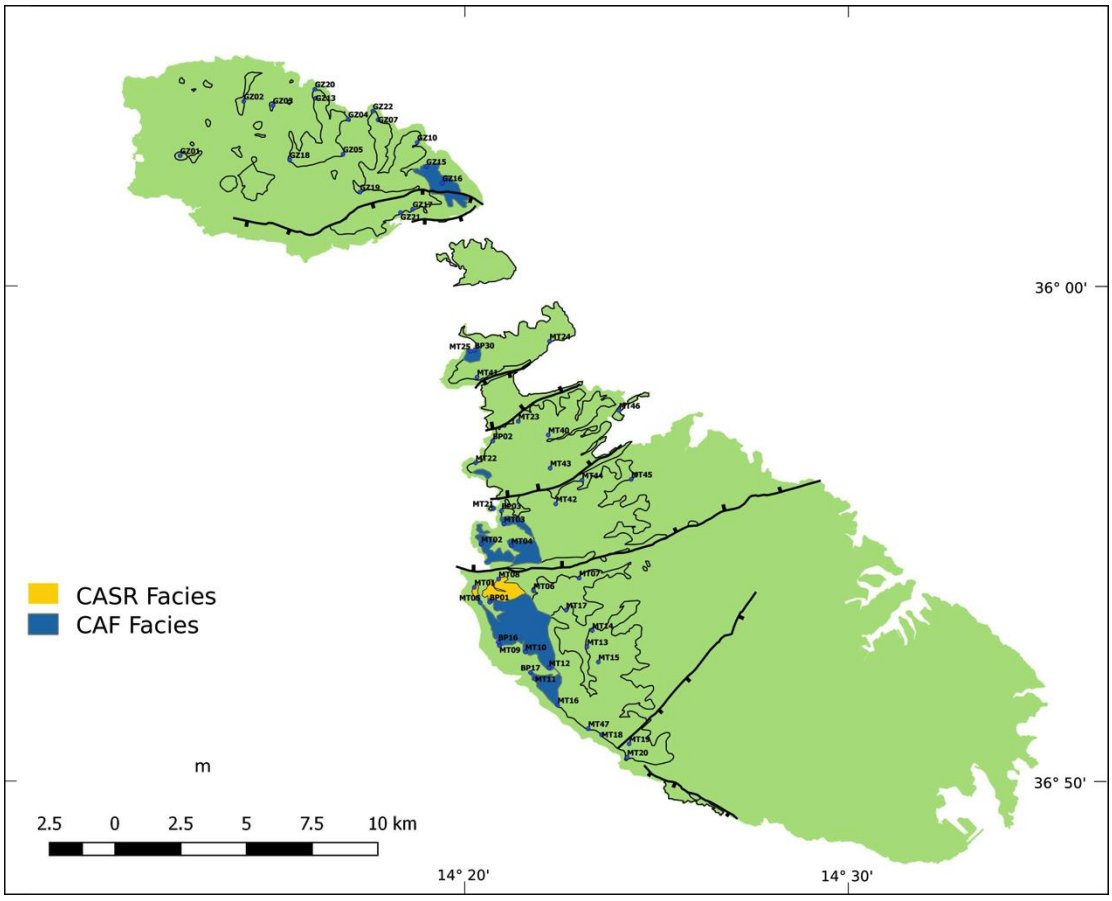

Figure 5.10: Coralline Algal Sand Ridge Packstone (CASR) and Coralline Algal Floatstone (CAF) Facies map based on outcrop observations carried in this the course of this study. Both CASR and CAF facies are mutually exclusive and can, therefore, be presented in the same facies map.

The contemporaneity of the CASR Facies and the Coralline Algal Floatstone (CAF) Facies is supported by the following observations. (i) The *Terebratula-Aphelesia* Bed (interpreted as a time horizon by Pedley, 1976) is observed at the base of the CASR facies and continues laterally into the CAF facies (Appendix C1.1 outcrop logs localities MT01 and MT05). Pedley (1976) observations are consistent with those made in this study. Pedley's observed *Terebratula terebratula* (Linne) in both locations MT01 in what he describes as friable yellow biomicrites (Pedley, 1976 p.210) that corresponds to the CASR Facies of this thesis and in location MT05 in what he describes as grey, marly, algal biomicrites that correspond to the Coralline Algal Floatstone (CAF) Facies. (ii) Both facies underlie the Rhodolith Pavement Facies and therefore occupy a similar stratigraphic position. (iii) Both facies contain similar amounts of coralline algal material.

Petrographic description

Sample MT01/S1 (figure 5.11) was assessed in terms of grain sizes, grain composition, porosity and cement (table 5.6). Results indicate that the sample is a moderately to poorly sorted coarse-grained packstone. Ranking of observed grains demonstrates a dominance of coralline algal debris present in 31% of all points counted. The observed coralline algal debris ranges between medium sand (53%) and very coarse to coarse sand (46%). Coralline algal grains demonstrate high roundness and sphericity (sub-rounded to well-rounded). Foraminifera (*Heterostegina*) are present in 12% of points. The foraminifera are very commonly present as fragments (7%) and sparsely as intact specimens (5%). Grains that are less common include other foraminifera (2%) and echinoid (2%) debris and glauconite (0.5%). The sample corresponds to the Rhodalgal (Carannante *et al.,* 1988) grain association.

Thin Section	Mud matrix %	F-VF Sd %	M Sd %	VC-C Sd %	VF Grv %	Pebble %	Porosity %	Cement %
MT01/S1	24.76	4.51	26.17	20.75	0.00	0.00	3.81	20.00

Table 5.6: Grain sizes, porosity and cement observed in the assessed thin section. 420 points were counted in the thin section.

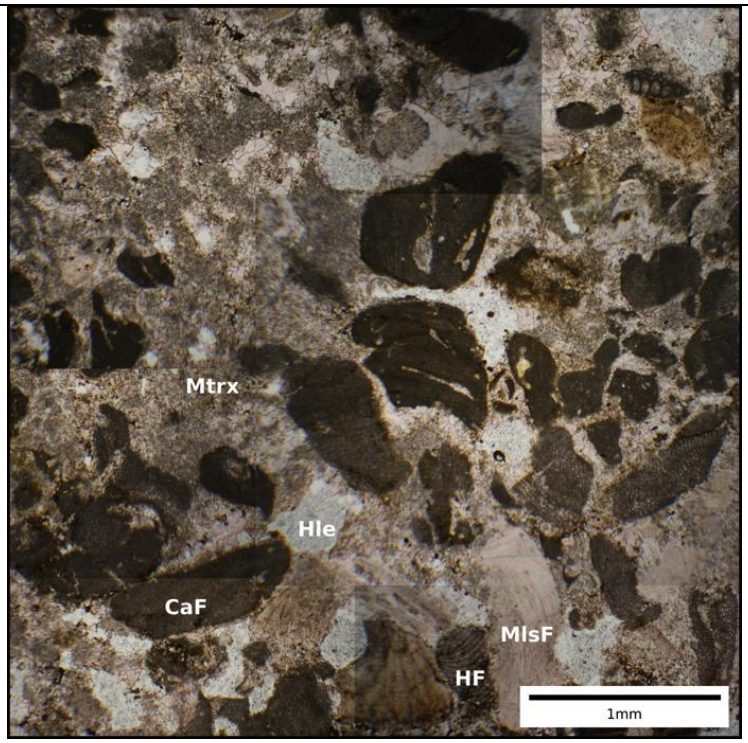

Figure 5.11: Photomosaic of photomicrographs of thin section (MT01/S1) of CASR Facies. MlsF, calcitic mollusc fragment; HF, *Heterostegina* fragments; CaF, Coralline algal fragments; Mtrx, Matrix; Hle; holes in slide (no crystal boundaries visible or cement under cross polarisation).

At the microfacies level, the CASR Facies is distinct from the OSHR Facies in terms of coralline algal and *Heterostegina* content. When compared with the OSHR facies skeletal grains in the CASR Facies are dominated by coralline algal debris with lower portions of *Heterostegina* debris.

Fauna and Flora

A rich biota is observed in the basal rudstone sub-facies and includes bryozoan colonies, echinoids, brachiopods, coralline red algae and calcitic bivalves. Densely branching spheroidal rhodoliths (average 8 cm in length and 7 cm in height) are also commonly observed. Bioclastic components include coralline algal branch debris, echinoid and bivalve debris with lesser contributions from bryozoan. Skeletons are frequently fragmented and abraded. As the facies fines upward, the aforementioned biotas are less commonly observed, bioclastic grains are finer and rhodoliths are entirely absent.

Depositional environment

The CASR Facies consists of overturned, disarticulated and abraded marine macrofossils. These features are indicative of high-energy marine conditions. Present-day benthonic foraminifera *Heterostegina sp.* (d'Orbigny) live at depths less than 50m (Vaughan and Cole, 1941). The *in situ* foraminifera *Heterostegina* is typical of modern, shallow, sub-tropical seas of Australia and the West Indies (Carpenter, 1986). The celleporiform bryozoan *Cellepora sp.* (Lineaus) is observed in the Beds. Pedley (1974) argues that they are adapted to sub-littoral environments exposed to moderate to high velocity currents and subject to extensive sediment reworking.

Recent literature on the habitat of celliporiform bryozoa (Holcova & Zagorsek, 2008) supports Pedley's interpretation. Rhodoliths present towards the base of the Coralline Algal Sand Ridge Facies demonstrate abraded branch tips indicate frequent turning. Coralline red algae provide some indication of water depth. Coralline algae can thrive in meso-oligophotic conditions equivalent to water depths down to 80m (Halfar, 1999). Matsuda & Iryu (2011) indicate that living biotic cover on rhodoliths is approximately 50% down to water depths of 100 m beyond which production decreases rapidly with depth.

Microfacies analysis indicates a moderately to poorly sorted coarse-grained packstone primarily consisting of medium sand and very coarse to coarse sand. The grains demonstrate high roundness and sphericity (sub-rounded to well-rounded). This evidence suggests that sediments were subject to high-energy marine environments that extensively transported and reworked the sediments. A distinctive brown colouration is provided by limonitic lithoclasts and *Heterostegina* fragments that are impregnated with goethite (Pedley, 1987; Bosence & Pedley, 1982). This is an indication of reworking and slow sedimentation rates.

In conclusion, the CASR Facies is interpreted to have formed linear, littoral-sublittoral sand waves and ridges within the VLF footwall high (*c.f.* Dart, 1991). The deposits formed in high-energy shallow shelf (*circa 20 to* 50 m) environment within the storm/fair weather wave base. The CASR Facies demonstrates a fining upward sequence. This suggests that the VLF footwall area was subject to increasingly deeper and lower energy marine environments.

5.3.2.2. Coralline Algal Floatstone Facies (CAF)

Description

The CAF Facies is vaguely to massively bedded and occurs at the base of the coralline algal biostrome (figure 5.12). The facies consists of up to 10 m (figure 5.13) of dark grey marls containing millimetre thick crusts of coralline algae. These are locally observed to be preserved in their original growth position as are *Terebratula* brachiopods. The beds also contain minor proportions of molluscan debris, *in situ* bryozoan and benthonic foraminifera.

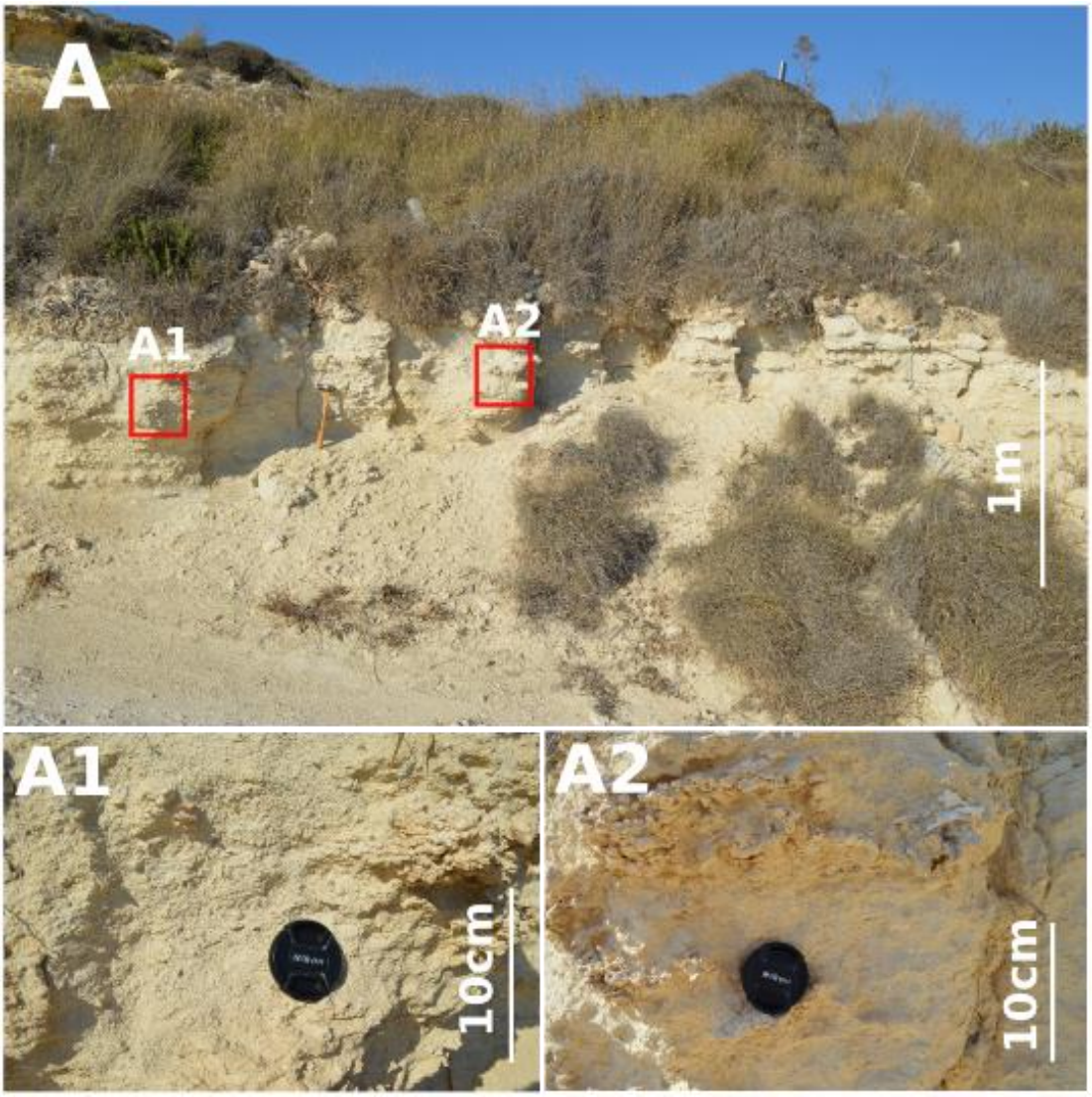

Figure 5.12: Features of the Coralline Algal Floatstone (CAF) Facies. (A) Outcrop contains an accumulation (<5 m) accumulation of dark grey marls containing millimetre thick crusts of coralline algae (locality MT05). (A1) Detail of dark-grey marl and (A2) detail of rhodoliths and coralline algae crusts.

Facies thickness, distribution, timing and association with other beds

The CAF Facies occurs where the OSHR Facies is absent or poorly developed at the base of the Coralline Algal Biostrome FA. Where the OSHR Facies is absent, the CAF Facies directly overlies the Blue Clay Formation (e.g. MT05). The facies relation is supported by evidence from outcrop (figure 5.10 facies map) and water borehole records that indicate that where accumulations of division 2 (figure 5.13) occur, accumulations of division 1 (figure 5.4) and 3.1 (figure 5.7) are absent or relatively underdeveloped.

The CAF Facies occurs within the VLF hanging-wall succession (e.g. MT04) and south of the VLF footwall (e.g. MT09). The *Terebratula-Aphelesia* Bed is present in the CAF Facies and is locally observed in the CASR Facies (MT01).

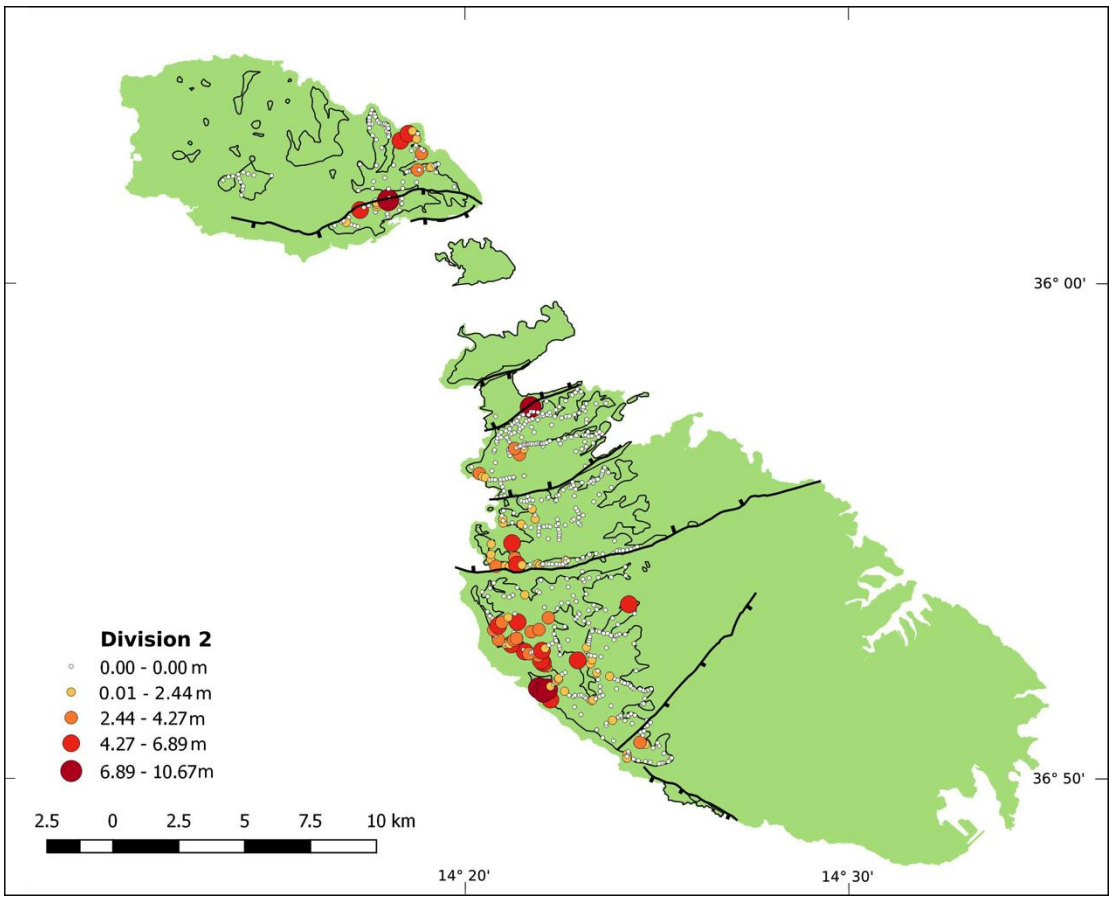

Figure 5.13: Thickness distribution of Coralline Algal Floatstone (CAF) Facies within outcrop area of the UCL Fm based on seven hundred and seventeen water borehole records. This facies equates to division 2 (table 5.2).

Petrographic description (microscopic)

Samples BP 15 and BP 1 (figure 5.14) were assessed in terms of grain sizes, grain composition, porosity and cement (table 5.7). Results indicate that the samples are moderately to poorly sorted rudstone (BP 15) and wackestone (BP 1). Ranking of observed grains show that coralline algal crusts and undifferentiated algal fragments typically rank first in both assessed samples and are present in 15% to 57% of all points counted. In either case, coralline algal crusts and undifferentiated coralline algal fragments display a grain morphometry that is angular to sub-angular with intermediate sphericity (0.4). Bivalve and brachiopod shell fragments are observed in both samples and account for 3% to 5% of all counted points. Similarly, foraminifera are present in both samples and are preserved as intact and fragments tests. These occur in 1% to 8% of points counted. In both samples, glauconite grains account for 1% of all counted points. These are well rounded and demonstrate high sphericity (0.8). BP 15 also contains echinoid fragments (1% of counted points) and bryozoan colony fragments (0.8% of counted points). Both samples correspond to the Rhodalgal (Carannante *et al.,* 1988) grain association.

Thin Section	Mud matrix %	F-VF Sd %	M Sd %	VC-C Sd %	VF Grv %	Pebble %	Porosity %	Cement %
BP 15	32.60	8.63	21.42	20.19	8.93	1.23	7.00	0.00
BP 1	63.09	12.54	12.54	3.51	0.50	0.00	7.82	0.00

Table 5.7: Grain sizes, porosity and cement observed in the assessed thin sections. 420 points were counted in each thin section.

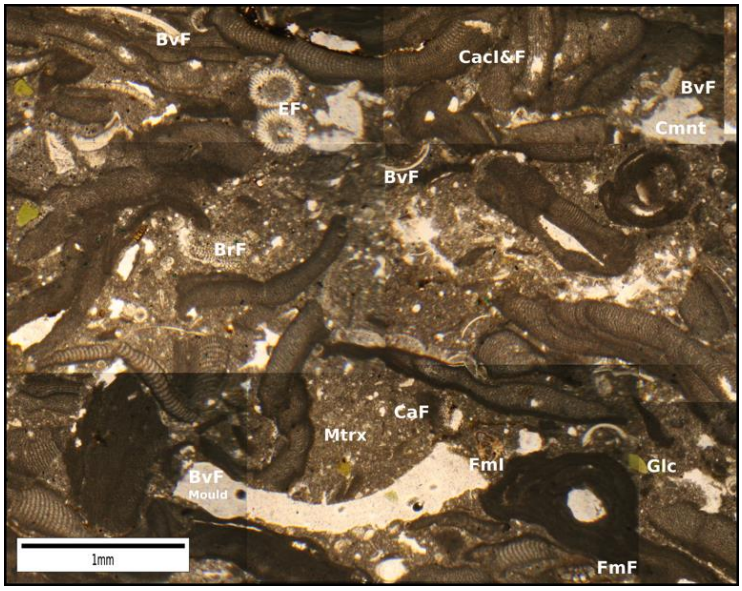

Figure 5.14: (A) Photomosaic of photomicrographs of thin section BP 15 of coarse poorly-sorted rudstone interval within the beds CAF Facies. Bvf, Bivalve and brachiopod fragments; CaC, Coralline algal crust intact and fragments; EF, Echinoid spine fragments; FmF, Foraminifera fragments; FmI, Foraminifera intact; Glc, Glauconite; CaF, Coralline algal fragments; Mtrx, Matrix; Cmnt, Cement.

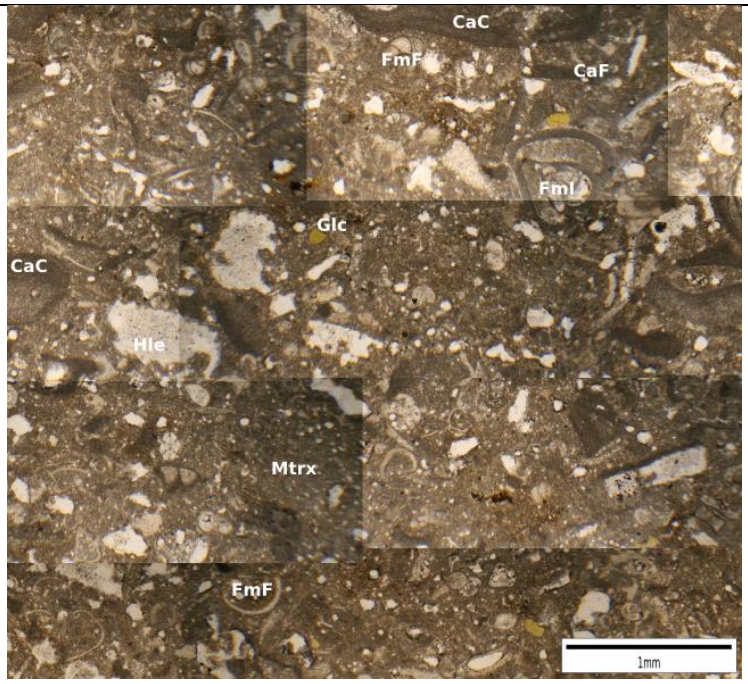

Figure 5.14: (B) Photomosaic of photomicrographs of thin section BP 1 of the CAF Facies. CaC, Coralline algal crust intact and fragments; CaF, Coralline algal fragments; FmI, Foraminifera intact; Glc, Glauconite; FmF, Foraminifera fragments; Mtrx, Matrix; Hle, mould porosity (distinctive serrated upper edges suggest mould of dissolved unknown skeletal fragment).

Fauna and Flora

Observed macrofauna include brachiopods (*Terebratula*), bivalves, foraminifera, echinoids, bryozoan sheets and tubes (for details see Appendix C3). Fauna are heavily encrusted. Rhodoliths are relatively small (5 cm height and 10 cm diameter) and are developed in either a crustose habit or in a branching and columnar form, characterised by relatively open-branched thalli. These observations correspond to those made by Bosence & Pedley (1982) for their Crustose Algal Wackestone and Crustose Algal Marl facies.

Depositional environment

The muddy matrix and *in situ* biota suggest that the facies was deposited in a sheltered marine environment. This interpretation is supported by the presence of thin crusts and delicate open-branch coralline algal growth-forms that developed on muddy substrates. Comparison with modern environments, based on brachiopod and coralline assemblages, suggests that the facies accumulated in water depths greater than 30 to 40 m (Thompson, 1927; Pajaud, 1974; Adey and Boykins, 1982; Bosence & Pedley, 1982).

Microfacies analysis demonstrates wackestone and rudstone textures. While the grains present range from very fine sand to pebbles (>4 to 64 mm), the coarser grains are *in situ* coralline algal crusts. These should therefore not be interpreted as indicative of high-energy marine conditions. The matrix comprises between 33 to 63% of the rock sample. This suggests sediment deposition

in quiet/sheltered mud-dominated marine environment.

It is suggested that sheltered, lower-energy environment necessary for the CAF Facies to accumulate, may have been present where the sand ridges of the OSHR Facies are not developed (*cf.* Bosence & Pedley, 1982).

5.3.2.3. Coralline Algal Pavement Rudstone to Framestone Facies (CAP)

The CAP Facies has been subdivided into the Crustose Pavement Framestone and the Rhodolith Pavement Rudstone Sub-Facies. Both sub-facies contain different growth forms of coralline algae.

Description

The ***Rhodolith Pavement Rudstone Sub-Facies*** consists of alternating rhodolith rich beds and coralline algal debris rich interbeds (figure 5.15A). Rhodolith rich beds occur as plane beds or cross beds and range from 0.2m to 2m in thickness (e.g. MT05). The facies is typically massively bedded, however shallow (0.5m) channels and trough cross-bedding are locally discernable (e.g. MT05). Near the base of the facies, the beds demonstrate aggradational planar beds and up-section these develop into large-scale progradational trough cross-beds (figure 5.15A).

Rhodoliths attain their greatest size and abundance in the Rhodolith Pavement Facies. The rhodoliths occur as large (longest axis up to 20 cm), slightly flattened spheroids and ellipsoids and are predominantly densely branched (figure 5.15 A1). Bosence & Pedley (1982) indicate that the dense branching in these rhodoliths is brought about by a repeated sequence of lateral growth and apical coalescence.

Locally, wavy or platy corals form lenticular beds within the Rhodolith pavement sub-facies (e.g. Dingli MT16) (figure 5.15B). The lateral and vertical extent of these coral-rich accumulations are smaller than those found in the Coralline Algal Debris Packstone Facies that are in turn smaller than those noted in the Coralgal Patch Reef Facies.

The ***Crustose Pavement Framestone Sub-Facies*** is up to 4m thick and dominated by leafy *Mesophyllum commune* (Lemoine) crusts that form an *in situ* three-dimensional framework (Bosence & Pedley, 1982). In Tas-Santi (MT06) the framework forms isolated crusts that bifurcate and join to form an open framework interbedded with debris from the same crusts (figure 5.16). These observations correspond to those made by Bosence & Pedley (1982).

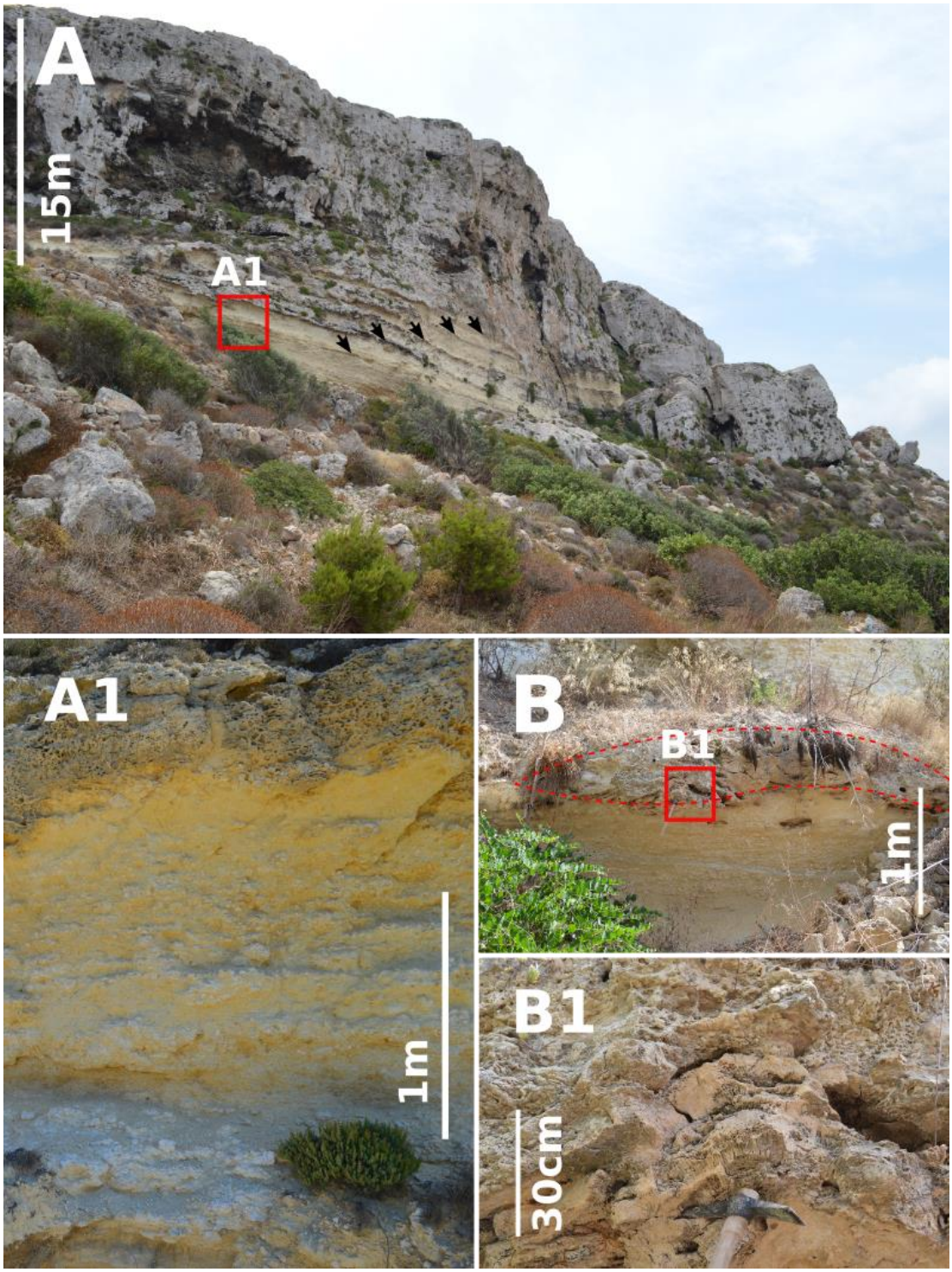

Figure 5.15: Features of the Rhodolith Pavement Sub-Facies from the Coralline Algal Pavement (CAP) Facies. (A) Outcrop contains a thick (15 to 20 m) succession of Rhodolith Pavement Sub-Facies consisting of aggrading to prograding beds (black arrows) (locality MT01). (A1) Detail of Rhodolith Pavement Sub-Facies that consists of alternating rhodolith rich beds and coralline algal debris rich interbeds. (B) Outcrop of Rhodolith Pavement Sub-Facies where (B1) wavy or platy shaped corals (above geological hammer) form lenticular shaped accumulations (red dashed line in B) (locality MT16).

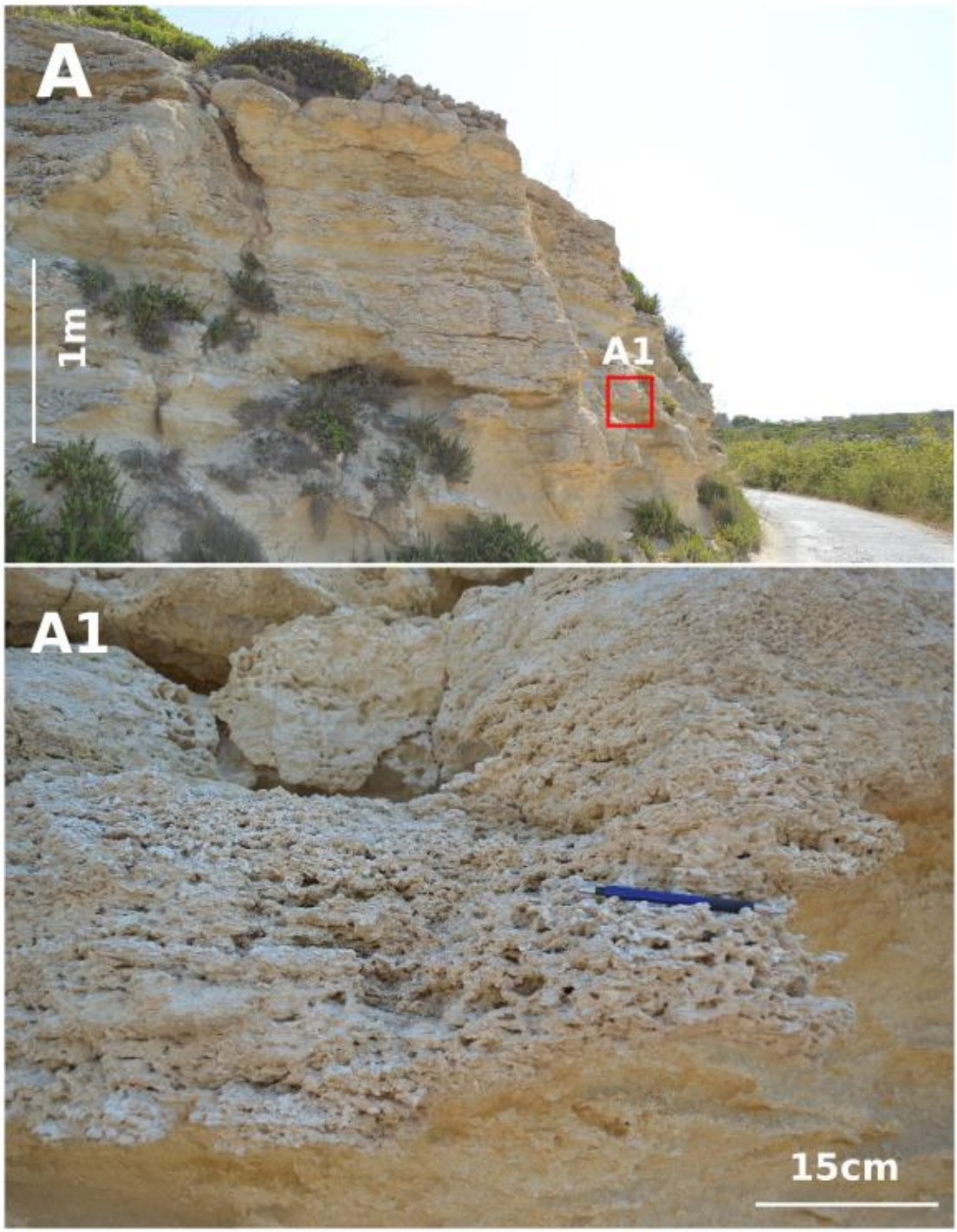

Figure 5.16: Features of the Crustose Pavement Sub-Facies from the Coralline Algal Pavement (CAP) Facies. (A) Outcrop contains a succession (<4 m) of Crustose Pavement Sub-Facies consisting of (A1) *Mesophyllum commune* (Lemoine) crust that form an *in situ* three-dimensional framework (locality MT06).

Facies thickness, distribution, timing and association with other beds

The Rhodolith Pavement Sub-Facies is the most abundant in western areas of Malta and eastern Gozo (figure 5.17 facies map; Appendix C1.1 outcrop logs; Appendix C2 outcrop cross sections). The sub-facies occurs across the Maltese islands and is thickest in eastern areas of Gozo and western areas of Malta. The sub-facies diminishes eastwards where it passes laterally into the CAD Facies (figure 5.21).

Outcrop-based, cross-sections (Appendix C2 outcrop cross section 1 and 8) show thickened accumulations of CAP Facies on footwall highs of the VLF, south Gozo fault (SGF) and Qala fault. The thickness distribution map of division 3.2, that includes the CAP, CAD and MCAD Facies, shows thickened accumulations in the SGF and Qala Fault (figure 5.18 blue polygon). The thickness distribution map also indicates a thickened accumulation in the Mellieha horst block (figure 5.18 red polygon). The division 3.2 thickness distribution map (figure 5.18) does not show significant thickness variation across the VLF. Outcrop observations however indicate that there is a significant change in facies across the VLF; the footwall is dominated by CAP facies (e.g. MT01, MT05, BP01) while the hanging-wall by the Sheltered Shelf FA (e.g. MT02) (see section 5.3.3).

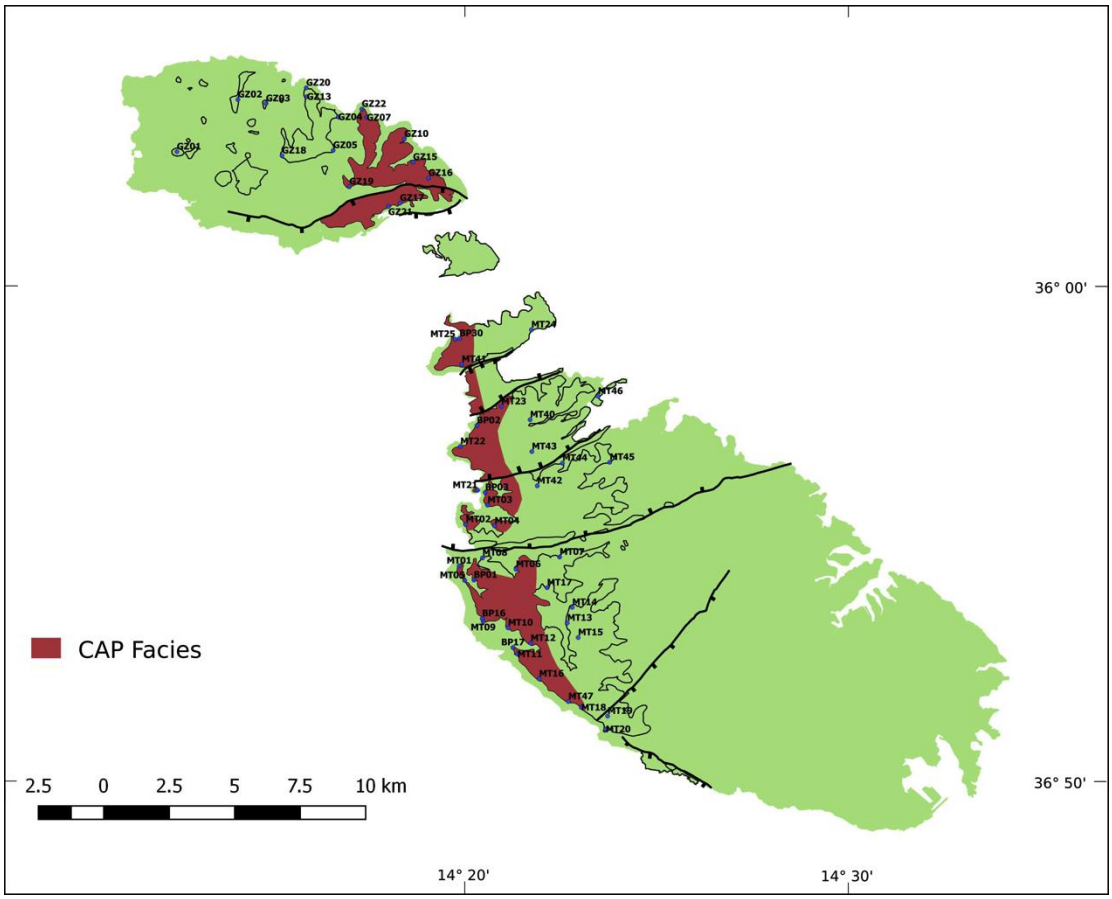

Figure 5.17: Coralline Algal Pavement Rudstone to Framestone (CAP) Facies map based on outcrop observations carried in this the course of this study.

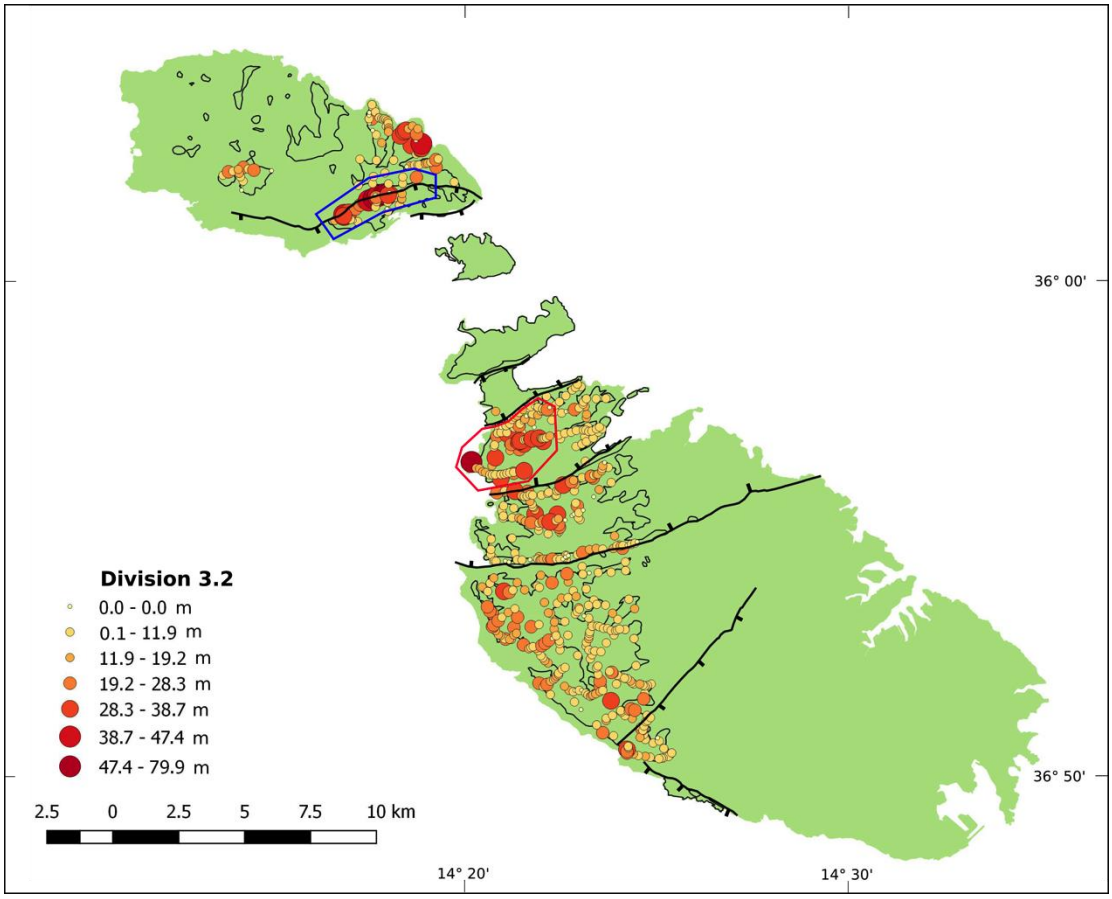

Figure 5.18: Thickness distribution of Coralline Algal Pavement Rudstone to Framestone (CAP), Coralline Algal Debris Packstone (CAD) Facies of the Coralline algal biostrome Facies Association, and Massive Coralline Algal Debris Wackestone (MCAD) Facies within outcrop area of the UCL Fm based on seven hundred and seventeen water borehole records. These facies equate to division 3.2 (table 5.2). Red and blue polygons indicate thickened accumulations of division 3.2 in the in the SGF and Qala Fault (blue polygon) and Mellieha horst block (red polygon).

Accumulations of the Crustose Pavement Sub-Facies are less extensive, both in height and lateral extent, than the Rhodolith Pavement Sub-Facies. The former facies was only observed in Tas-Santi (MT06).

Petrographic description (microscopic)

Samples BP 14f and BP 21c (figure 5.19A and B) of the *Rhodolith Pavement Sub-Facies* were assessed in terms of grain sizes, grain composition, porosity and cement (table 5.8). Results indicate that the samples are moderately to poorly sorted floatstones (BP 14f) and rudstones (BP 21c). In terms of ranking of observed grains, coralline algal branch and crust fragments, are dominant and comprise 28 to 49% of all points. Coralline algal fragments display a sub-rounded grain morphometry with low sphericity (0.3). Foraminifera rank second in both samples and are

preserved as intact and fragments tests. Well-rounded and high sphericity (0.8) glauconite grains account for 1 % of all counted points in both samples. Both samples also contain minor quantities of foraminifera, ostracods and bivalve debris. Both samples correspond to the Rhodalgal grain association of Carannante *et al.* (1988).

Sample BP 14e (figure 5.19C) of the *Crustose Pavement Sub-Facies* was assessed in terms of grain sizes, grain composition, porosity and cement (table 5.8). Results indicate that the sample is a moderately to poorly sorted wackestone. Ranking of observed grains demonstrates a dominance of coralline algae crust fragments present in 38% of all counted points. Twenty-eight coralline algae fragments were measured in terms of their grain sizes; results indicate that 11% are fine to very fine sand, 39% are medium sand, and 39% are very coarse to coarse sand, and 11% are granule. Foraminifera rank second occurring in 3% of points counted, 0.8% as undifferentiated and multichamber trochospiral intact tests and 1.9% as undifferentiated fragments. Bivalve fragments (1% of counted points), bryozoan colony fragments (0.5% of counted points) and glauconite grains (0.2% of all counted points) are also observed. The sample corresponds to the Rhodalgal (Carannante *et al.,* 1988) grain association.

Thin Section	Mud matrix %	F-VF Sd %	M Sd %	VC-C Sd %	VF Grv %	Pebble %	Porosity %	Cement %
BP 14f	61.83	7.54	12.08	3.51	6.03	3.51	5.50	0.00
BP 21c	47.57	20.69	14.59	6.48	5.86	4.24	0.57	0.00
BP 14e	48.16	8.96	15.68	14.56	3.36	0.00	7.36	1.92

Table 5.8: Grain sizes, porosity and cement observed in the assessed thin sections. 625 points were counted in each thin section.

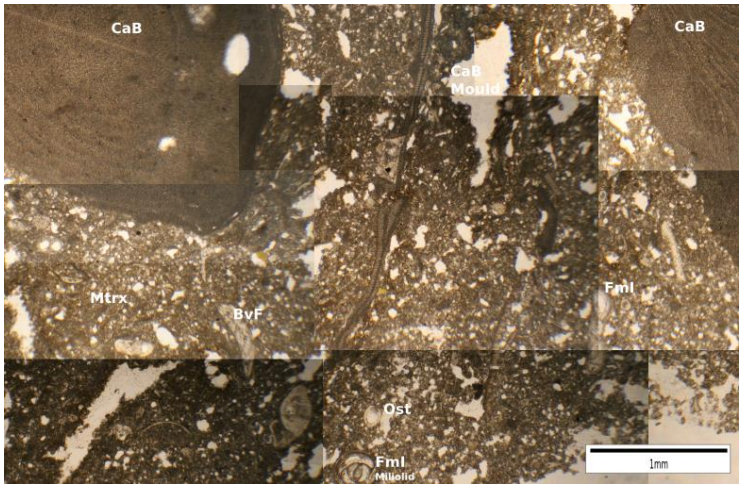

Figure 5.19: (A) Photomosaic of photomicrographs of thin section BP 14f of Rhodolith Pavement Sub-Facies. Bvf, Bivalve fragments; CaB, Coralline algal branch fragments; FmF, Foraminifera fragments; FmI, Foraminifera intact; CabF, Coralline algal branch fragments; Ost, Ostracod; Mtrx, Matrix

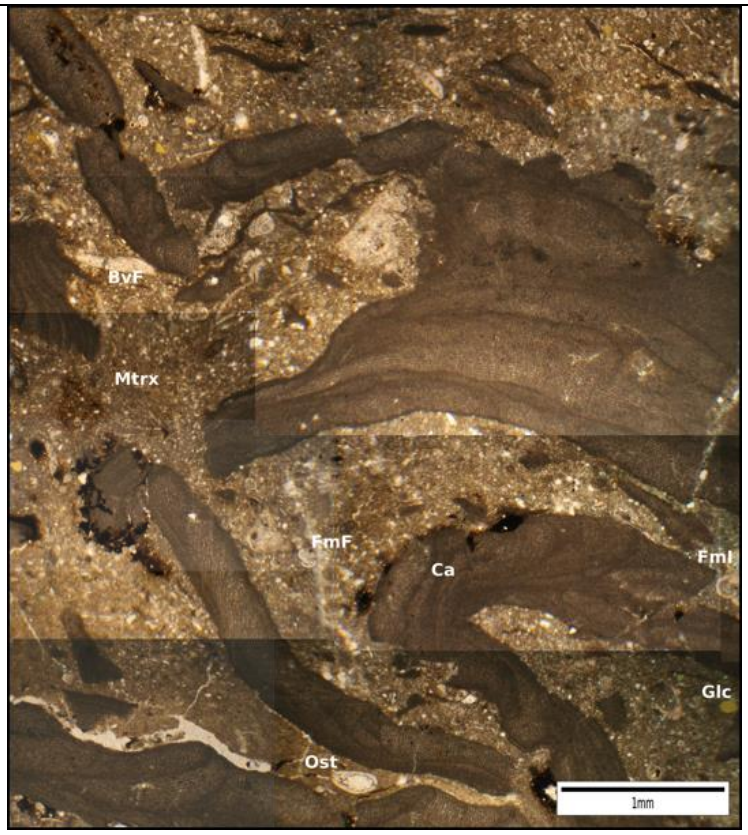

Figure 5.19: (B) Photomosaic of photomicrographs of thin section BP 21c of Rhodolith Pavement Sub-Facies. Bvf, Bivalve fragments; Ca, Coralline algal fragments; FmF, Foraminifera fragments; FmI, Foraminifera intact; Glc, Glauconite; Ost, Ostracod; Mtrx, Matrix.

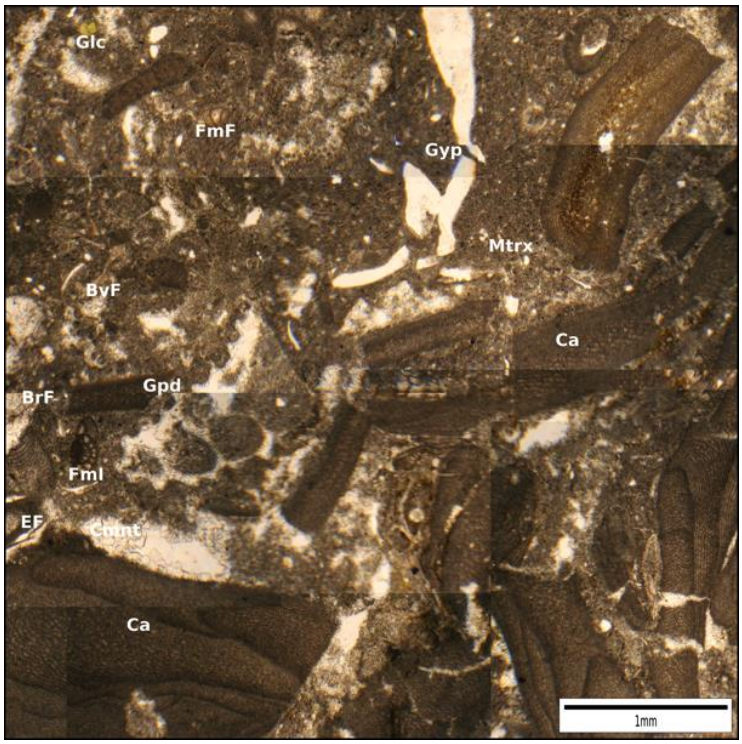

Figure 5.19: (C) Photomosaic of photomicrographs of thin section BP 14e of Crustose Pavement Sub-Facies. Bvf, Bivalve fragments; BrF, Bryozoan fragments; Ca, Coralline algal fragments; EF, Echinoid fragments; FmF, Foraminifera fragments; FmI, Foraminifera intact; Gpd, Gastropod with micrite filled chambers and dissolved out shell; Gyp, Calcite spar pseudomorphic gypsum crystals growing in matrix; Mtrx, Matrix.

Fauna and Flora

Rhodolith Pavement Facies: A diverse epifauna and infauna encrust the rhodoliths and include bryozoans, foraminifera, serpulid tubes, oysters and brachiopods (for details see Appendix C3). The remaining macrofauna is varied and includes *Chlamys* (Roding) and *Lucina* (Fleming) bivalves, gastropods and echinoids. Bryozoan colonies are uncommon and mainly of sheet-like encrusting habit and frequently encrust corallines. Locally, wavy or platy unidentified corals form lenticular beds within the Rhodolith pavement sub-facies.

Crustose Pavement Facies: The Crustose Pavement Facies framework is characterised by coralline algal crusts that form an *in situ* three-dimensional framework (for details see Appendix C3).

Depositional environment

Rhodolith Pavement sub-facies: When hard substrates are absent, a number of coralline algal species can occur as free-living rhodolith nodules inhabiting sandy seafloors (Halfar and Mutti, 2005). Coralline red algae live in a wide range of environments, from arctic to tropical settings, under both high- and low-nutrient conditions and in depths down to 100 m (e.g., Adey & Macintyre, 1973; Bosence, 1983a, 1983b; Testa & Bosence, 1999, 2005; Johansen, 1981; Steneck, 1986). Rhodalgal facies, defined as containing abundant coralline red algae (Carannante *et al.,* 1988), frequently occur in nutrient-rich upwelling areas subject to reduced-light conditions (in Halfar & Mutti, 2005). By calibrating modern carbonate assemblages to local oceanographic parameters in the Gulf of California, Halfar *et al.* (2004) quantitatively demonstrated the predominance of rhodalgal lithofacies under mesotrophic and slightly eutrophic conditions (in Halfar & Mutti, 2005). Coralline red algae can also thrive in meso-oligophotic conditions equivalent to water depths of up to 80 m (Halfar, 1999). Matsuda & Iryu (2011) indicate that living biotic cover on rhodoliths is approximately 50% down to water depths of 100 m, beyond which production decreases rapidly with depth.

The dominance of coralline algae *Mesophyllum* and *Lithophyllum* in the rhodolith pavement sub-facies (Bosence & Pedley, 1982; Bassi, 1995; Bassi *et al*., 2009) suggests water depths of circa 40 to 100 m. Within the rhodolith rich beds, the repeated sequence of branching, lateral growth and laminar growth is thought to be a response of coralline algae to abrasion following turning and transport (Bosellini & Ginsburg, 1971; Bosence, 1976). The repeated rhodolith growth sequence suggests that the sub-facies was subject to alternating low and high-energy environments during their growth. In all of the assessed samples, microfacies analysis indicates that coralline algal branch and crust fragments are common to very common. The sizes of these transported and abraded grains ranges from very fine to pebble sized fragments, with the majority of grains being medium to very coarse sands. The coarse nature of these abraded grains

suggests sediment deposition in moderately agitated water and the observed channels and cross stratification may have been formed during storm conditions. This indicates that the facies may have been deposited within the storm weather wave based in water depths of 40 to 60 m.

In summary, the Rhodolith Pavement Sub-Facies is interpreted to have formed in the littoral zone at *circa* 40 to 60 m depths. This zone was subject to fluctuating, hydraulic conditions (possibly within storm weather wave base) that locally developed sub-marine dunes. This subjected the rhodoliths to cycles of burial, erosion and transportation. This interpretation corresponds to that presented by Bosence & Pedley's (1982).

Crustose Pavement Sub-Facies: The absence of relief in the crustose pavement beds and its association with debris and crustose rhodoliths allows comparisons to be drawn with the present-day Mediterranean "Coralligène de Plateau" (Peres, 1967) that occurs in open shelf water 50 to 130 m deep. Similar crustose coralline pavement communities also occur in the 8 to 30 m deep fore-reef from Hawaii (Littler, 1973), the 30 to 80 m deep shelves of the Indo-Pacific region (Adey, 1979) and the 50 to 100 m deep Eocene Priabonian open shelf (Bassi, 1995). The Maltese Crustose Pavement Sub-Facies formed an *in situ* framework that produced a low relief on the current swept seabed (Bosence & Pedley, 1982; Bassi, 1995). The close spatial and temporal association of the Maltese Crustose Pavement and Rhodolith Pavement Sub-Facies suggests the prior sub-facies may have been deposition within the shallower depth range *circa* 50 to 80 m.

5.3.2.4. Coralline Algal Debris Packstone Facies (CAD)

Description

This CAD Facies is a pale yellow to yellow coarse to very coarse-grained, massively bedded wackestone to packstone. It primarily consists of coralline algal, molluscan and echinoid debris with occasional small spherical rhodoliths with abraded branch tips. The facies is often interbedded with the Rhodolith Pavement Sub-Facies and commonly forms the final deposits capping the Coralline Algal Biostrome FA (figure 5.20A). The facies may gradually coarsen upwards. Unidentified wavy plate and dish corals, corresponding to Pomar *et al.* (1996) dish coral zone, are locally observed within the facies (e.g. MT18) (figure 5.20B). A laterally extensive sharp contact is locally discernable between the pavement facies and overlying algal debris facies in the Bahrija section (e.g. MT05) but this may be the result of extensive recrystallization (possibly Quaternary?).

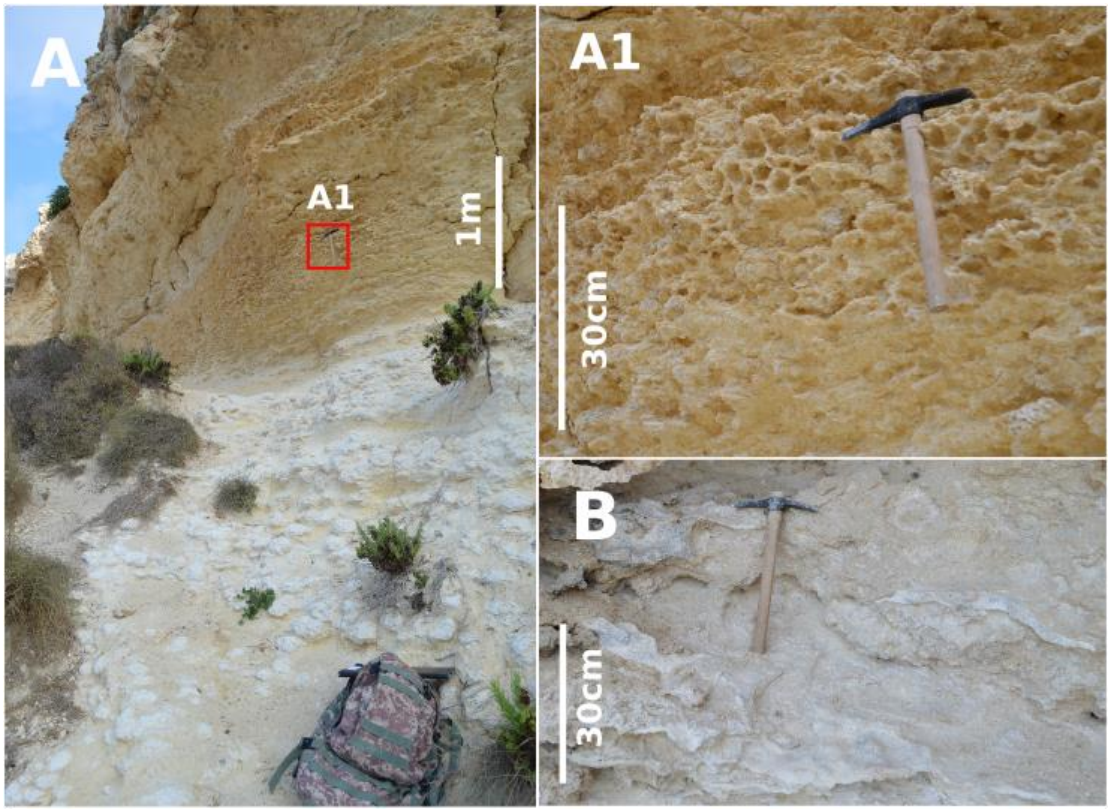

Figure 5.20: Features of the Coralline Algal Debris Packstone (CAD) Facies. (A) Outcrop contains an (<5 m) accumulation of CAD Facies (yellow) that overlies the CAP Facies (pale yellow) at the bottom of image (locality MT11). (A1) Detail of coarse to very coarse-grained, massively bedded floatstone to with occasional small spherical rhodoliths (whiter than matrix). (B) Outcrop of CAD Facies containing unidentified wavy platy and dish-shaped corals (locality MT18).

In the west areas of Malta (MT01, MT02, MT18), extensively cemented beds, between 0.1 and 0.5 m thick, weather positively with respect to the rest of the facies. The cemented beds occur within the facies and develop sharp, laterally extensive and undulating basal and upper surfaces. The cemented beds also develop encrusted and bored upper surfaces. These surfaces are tentatively interpreted as hardground surfaces.

Facies thickness, distribution, timing and association

The CAD Facies is the most widespread facies of the Coralline Algal Biostrome FA (figure 5.21). To the west and southwest of Malta, in both the Malta Horst and Graben, the facies is up to 4 m in thickness and frequently overlies the Rhodolith Pavement Sub-Facies. The Rhodolith Pavement Sub-Facies diminishes to the east of Malta and is gradually replaced by the CAD Facies that, in turn, gradually diminishes further eastwards (Appendix C2, outcrop cross sections 4, 5 and 6).

Pedley (1987) suggests that CAD Facies is thickest north of the VLF within the hanging wall. In this study, the sedimentary accumulation within the VLF hanging wall is interpreted to consist of a thick succession of Planar Bedded Coralline Algal Debris Wackestone Facies (PCAD) (section 5.3.3.2) that is overlain by a thin succession of CAD Facies. (Appendix C2, OCS 1 and figure 5.18 division 3.2 thickness map). The CAD facies is better developed within the footwall successions of syn-depositional faults; eastwards of IMF in western areas of Malta (MT01, MT05, MT09, MT10, MT12, MT11, MT16, MT18), southwards to the VLF (MT01, MT06, MT08), and southwards of the SPIF (Appendix C2, e.g. OCS 1, 8 and figure 5.18 division 3.2 thickness map). Similar observations were made by Dart (1991) regarding the VLF area (Dart, 1991 p.258). The CAD Facies is therefore better developed in the footwall succession of syn-depositional faults of the VLF and SPIF than in the hangingwalls where it is relatively underdeveloped (figure 5.18 division 3.2 thickness map).

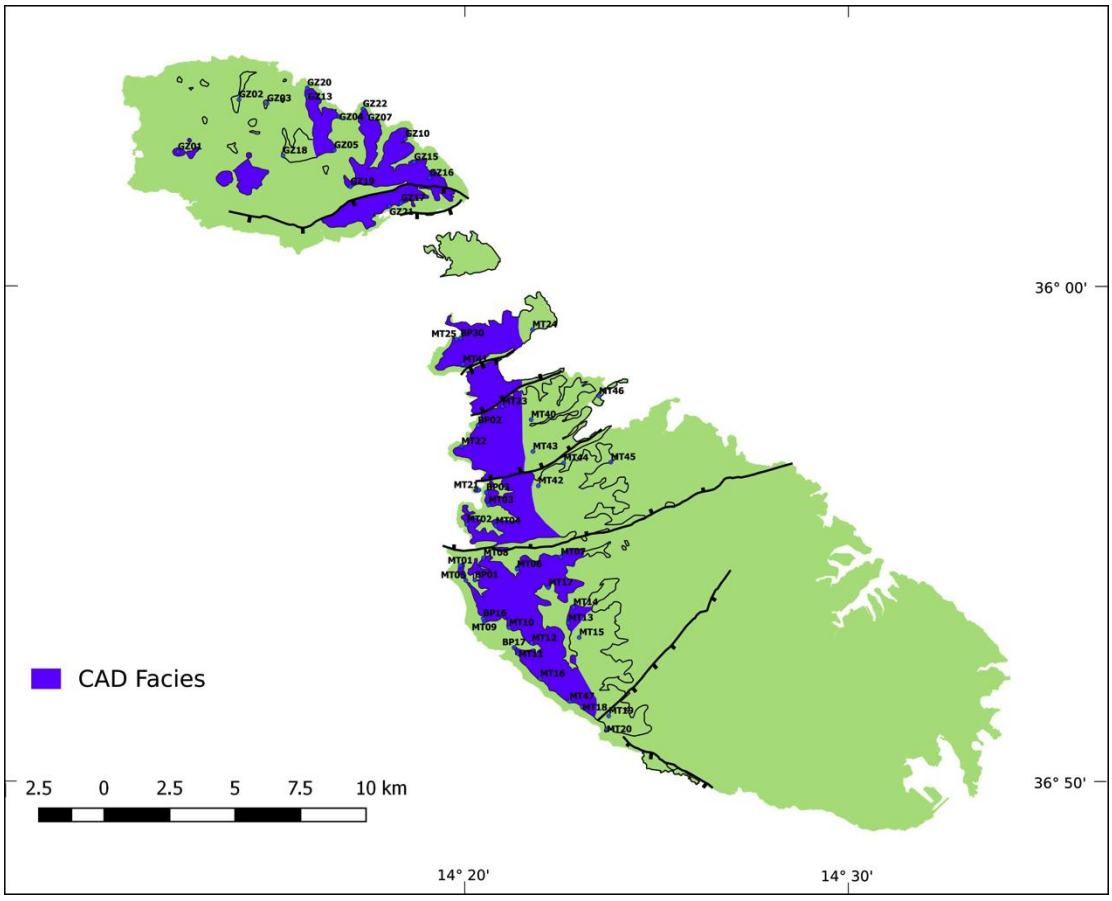

Figure 5.21: Coralline Algal Debris Packstone (CAD) Facies map based on outcrop observations carried in this the course of this study.

Petrographic description

Samples BP 15i and BP 30 (figure 5.22) were assessed in terms of grain sizes, grain composition, porosity and cement (table 5.9). Results indicate that both samples are well to moderately well-sorted. Sample BP 15i and BP 30 have a similar wacke-packstone texture. In

terms of ranking of observed grains, coralline algae, predominantly in the form of coralline algal branch fragments, are dominant in both assessed samples and are present in 28% to 35% of all points respectively. Coralline algal fragments display a sub-rounded grain morphometry with intermediate sphericity (0.5). Foraminifera rank second in both samples and are preserved as primarily as fragments, though intact tests are also observed; these occur in 6% to 8% of points counted. Echinoid fragments (2% of counted points), bivalve fragments (1%) and bryozoan fragments (0.5%) were also observed in BP 15i facies H. In sample BP 30, molluscan fragments are observed in 6% of counted points. Glauconite grains are present 1% to 2% in both samples; these are well rounded and demonstrated high sphericity (0.9).

Thin Section	Mud matrix %	F-VF Sd %	M Sd %	VC-C Sd %	VF Grv %	Pebble %	Porosity %	Cement %
BP 15i	54.10	20.44	13.23	4.41	0.40	0.00	7.43	0.00
BP 30	47.24	25.61	16.43	9.66	0.48	0.00	0.57	0.00

Table 5.9: Grain sizes, porosity and cement observed in the assessed thin sections. 420 points were counted in each thin section.

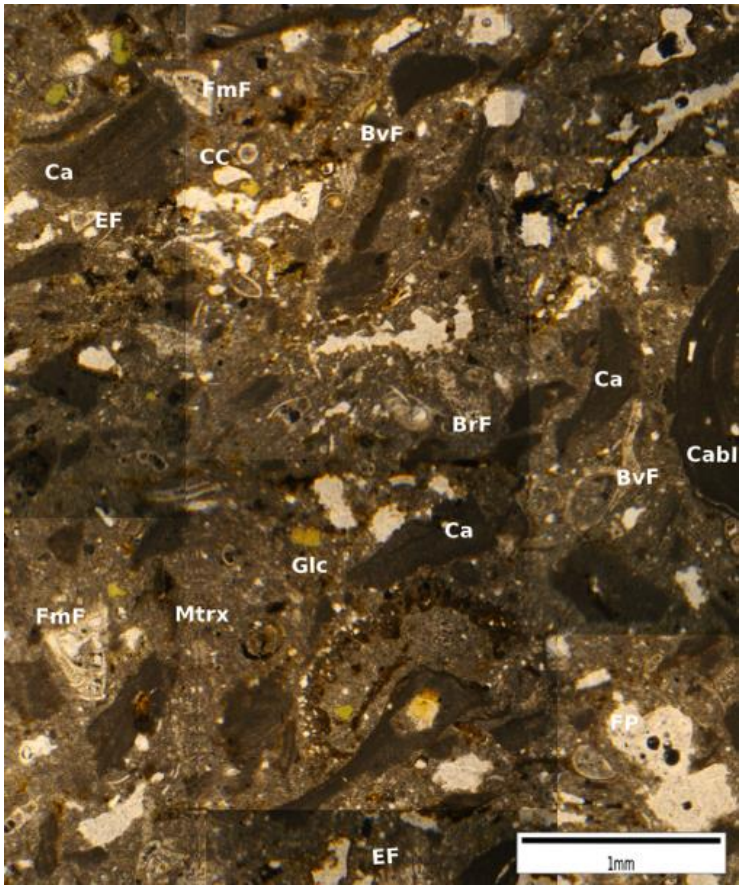

Figure 5.22: (A) Photomosaic of photomicrographs of thin section BP 15i of the CAD Facies. CabI, Coralline algal branch intact; Ca, Coralline algal fragments; BrF, Bryozoan fragments; EF, Echinoid fragments; FmF, Foraminifera fragments; Glc, Glauconite; CC, Calcitic crystal; FP, Fenestral porosity; Mtrx, Matrix.

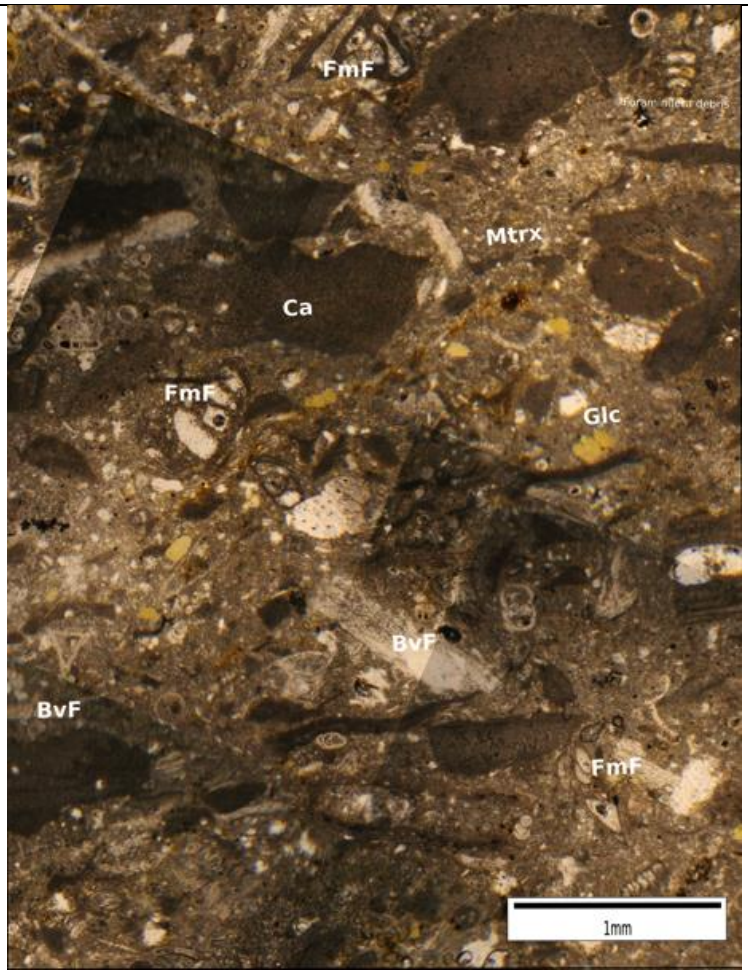

Figure 5.22: (B) Photomosaic of photomicrographs of thin section BP 30 of the CAD Facies. BvF Bivalve fragments; Ca, Coralline algal fragments; FmF, Foraminifera fragments; Glc, Glauconite.

Macrofaunal and floral components are invariably transported and include fragments of coralline algal branches and crusts, echinoids, mollusc and pectinid valve fragments (for details see Appendix C3). Rhodoliths are sparsely distributed in the algal branch packstone. These are smaller (up to 8 cm along their longest axes) than those found in the Rhodolith Pavement facies (up to 20 cm along longest axes). Their spheroidal morphologies have external surfaces that are commonly abraded. In the west of Malta, coral moulds are locally seen (MT16; MT18; MT23) in certain horizons of this facies. These moulds are formed by coral colonies that display wavy plates and dish morphologies.

Depositional environment

Macrofaunal components are invariably transported and include fragments of coralline algal crusts and branches, echinoids, mollusc and pectinid valve fragments. Spherical rhodoliths display dense branching spheroidal morphologies with external surfaces that are commonly abraded. Microfacies analysis indicates that the sizes of these transported and abraded grains ranges from very fine to pebble sized fragments, with the majority of grains being medium to very coarse sands. The size of these transported coarse grains suggests sediment deposition in moderately agitated water

Coral moulds are more commonly observed in the CAD Facies than in the underlying Rhodolith Pavement Facies. The corals observed in the Coralline Algal Biostrome FA display an up-section change in morphology. These change from wavy plate in the Rhodolith Pavement Sub-Facies to wavy plate and domal dish morphologies in the CAD Facies. Their wavy plates and dish morphology therefore indicates formation in water depths between 30m and 60m (Pomar *et al.,* 1996).

The CAD Facies is interpreted to have formed with increasingly turbulent and higher energy environments possibly within or close to the storm/fair weather wave base (< 50 m). When compared to the depositional environment of the CAP Facies, which is interpreted to have been deposited in littoral zone in water depths <100 m, this implies a fall in sea level. Shallowing may have eroded the CAP Facies and currents transported and deposited the debris forming the CAD Facies. Eroded material was transported basinwards and deposited in western and central areas of the Malta Horst and in southeastern areas of the Gozo Horst. The similar nature of allochemical constituents and the close spatial associations of the CAP and CAD Facies support this interpretation. This interpretation corresponds to that made by Pedley (1974) and Bosence & Pedley (1982).

5.3.3. Sheltered Shelf Facies Association

In this work, the Sheltered Shelf FA is subdivided into two distinct facies that are contemporaneous and occupy a similar area. The facies association consists of the Massive Coralline Algal Debris Packstone Facies (MCAD) and the Plane Bedded Coralline Algal Debris Wackestone Facies (PCAD). The MCAD is equivalent to Pedley's (1974) Gebel Mtarfa Beds and Dart's (1991 p.227) Open Shelf Sand Facies (table 5.4). The PCAD is equivalent to Pedley's (1974) Rdum il-Hmar Beds (table 5.4). Pedley (1975; 1978) suggests the Rdum il-Hmar beds may be the eastern lateral equivalents of the Coralline Algal Biostrome FA and occupies a similar area to the MCAD Facies. New evidence from this study (see sections 5.3.3.1, 5.3.3.2) supports this interpretation. Dart (1991 p.222) however suggests his Sheltered Shelf Facies, equivalent to that the Rdum Il-Hmar Bed (table 5.4), are contemporaneous with the Fore-Reef Slope and Shelf FA and Reef-core FA that overlie the Coralline Algal Biostrome. Dart's interpretation is not supported by this study.

The MCAD is massive-bedded and consists of fine to coarse-grained packstones while the PCAD demonstrates plane-parallel bedding consisting of fine-grained wackestones. In other aspects, the two facies demonstrate similar constituent composition and macrofaunal content. It is suggested that the MCAD represent a relatively higher energy/less sheltered environment, while the PCAD were deposited in a relatively lower energy/more sheltered shelf setting.

When the Sheltered Shelf FA is present at outcrop it typically averages <10 m in thickness, though in the south west and north east of Malta it can locally be up to 23 m thick (e.g. MT19, MT24). Water borehole thickness records in areas where the MCAD and PCAD facies are exclusively developed within division 4.2 and 4.1 indicate that the FA may be as thick as 35 m in certain south-western locations (log 1991).

The Sheltered Shelf FA lies immediately to the east of the Coralline Algal Biostrome FA and forms a broad N-S oriented facies belt across the eastern areas of Malta. In Malta, the Sheltered Shelf FA is well developed and extends from the eastern Marfa Ridge locality (MT24) southwards to Mtarfa locality (MT15) and to Gebel Ciantar locality (MT19, MT20) (figure 5.23, 5.24 and 5.25). These observations correspond to descriptions by Pedley (1987). Pedley (1987) also indicates that the Sheltered Shelf FA (Gebel Mtarfa Bed) is poorly expressed in Gozo and its occurrence is limited to the eastern extremity of the island where the beds are often less than 2 m thick and lie directly on Greensand Formation (Pedley, 1987). In this study, the Sheltered Shelf FA was not observed in Gozo.

Pedley (1976) records the *Terebratula-Aphelesia* (T-A) Bed in the Sheltered Shelf FA in the east of Malta (figure 2.8). This suggests that the Sheltered Shelf FA and the Coralline Algal Biostrome FA, which also contains the T-A Bed at its base, are penecontemporaneous (Pedley, 1975; 1978; Dart, 1991 p.227). Pedley (1975; 1978) and Bosence & Pedley (1982) suggest an eastward transition from the Coralline Algal Biostrome FA to the Sheltered Shelf FA. Vertical and lateral facies relations observed in this study support this interpretation. The eastern margin of the Coralline Algal Biostrome FA is observed to interfinger eastwards with the Sheltered Shelf FA at Fiddien Valley locality (figure 5.23). This lateral interfingering was also observed by Bosence & Pedley (1982).

The PCAD is locally overlain by the CAD Facies (MT07). This suggests the Sheltered Shelf FA predates the CAD Facies deposits that towards the end of depositional sequence 1 (see section 6.3.2), prograded eastwards to overlie the Sheltered Shelf FA (MT07). In other localities, the Sheltered Shelf FA is overlain by the Fore-Reef Slope and Shelf FA (section 5.3.5) (figure 6.2 OCS2 e.g. MT15, MT19, MT20, MT40, MT43). The latter FA is contemporaneous with the Reef-Core FA (section 5.3.4) that overlies the CAP and CAD Facies of the Coralline Algal Biostrome FA.

These observations and facies relations indicate that the Sheltered Shelf FA is penecontemporaneous to the CASR, CAF and CAP Facies of the Coralline Algal Biostrome. The Sheltered Shelf FA predates the CAD Facies (Coralline Algal Biostrome FA), Reef-Core FA and the Fore-Reef Slope and Shelf FA.

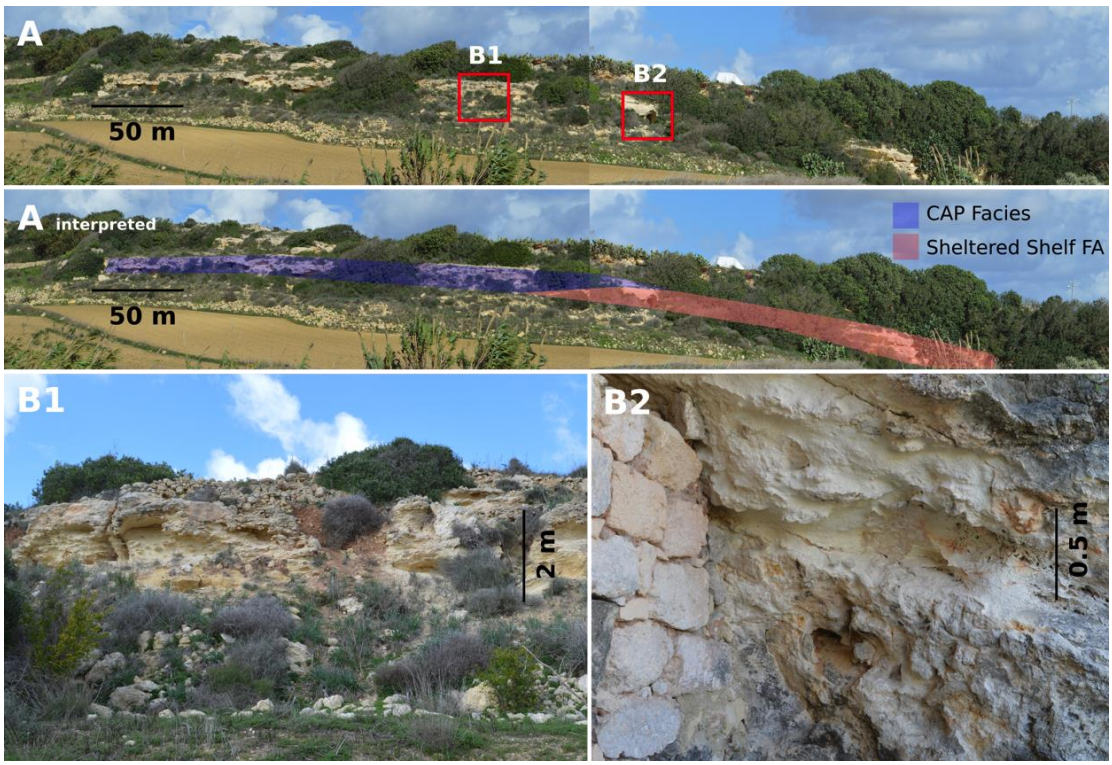

Figure 5.23: (A) Eastern margin of the Coralline Algal Biostrome FA interfingers eastwards (A interpreted) with the Sheltered Shelf FA at Fiddien Valley locality (38.891092, 14.377251). (B1) Depicts accumulation of CAP Facies, (B2) depicts accumulation of Sheltered Shelf FA. Palaeobathymetric slope of 0.4° to 1.8°.

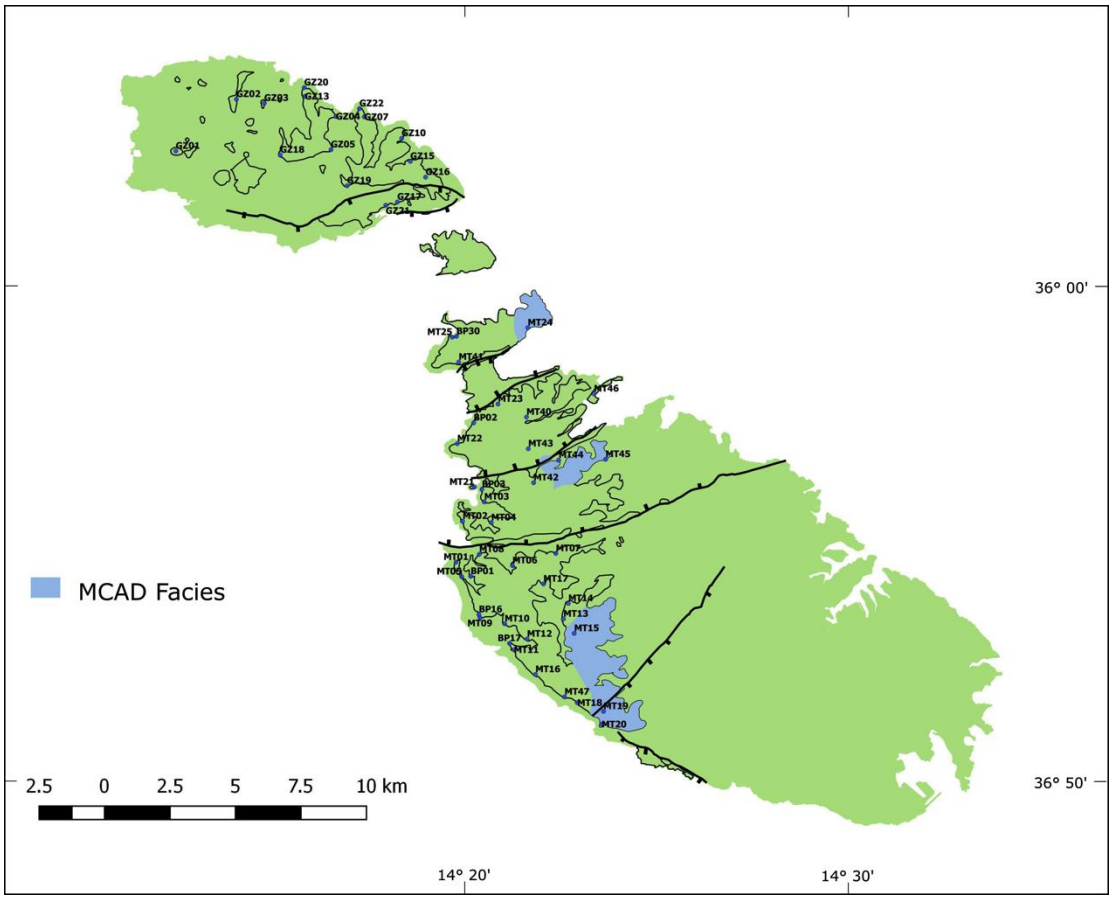

Figure 5.24: Facies map of the MCAD. Facies map is based on new outcrop observations.

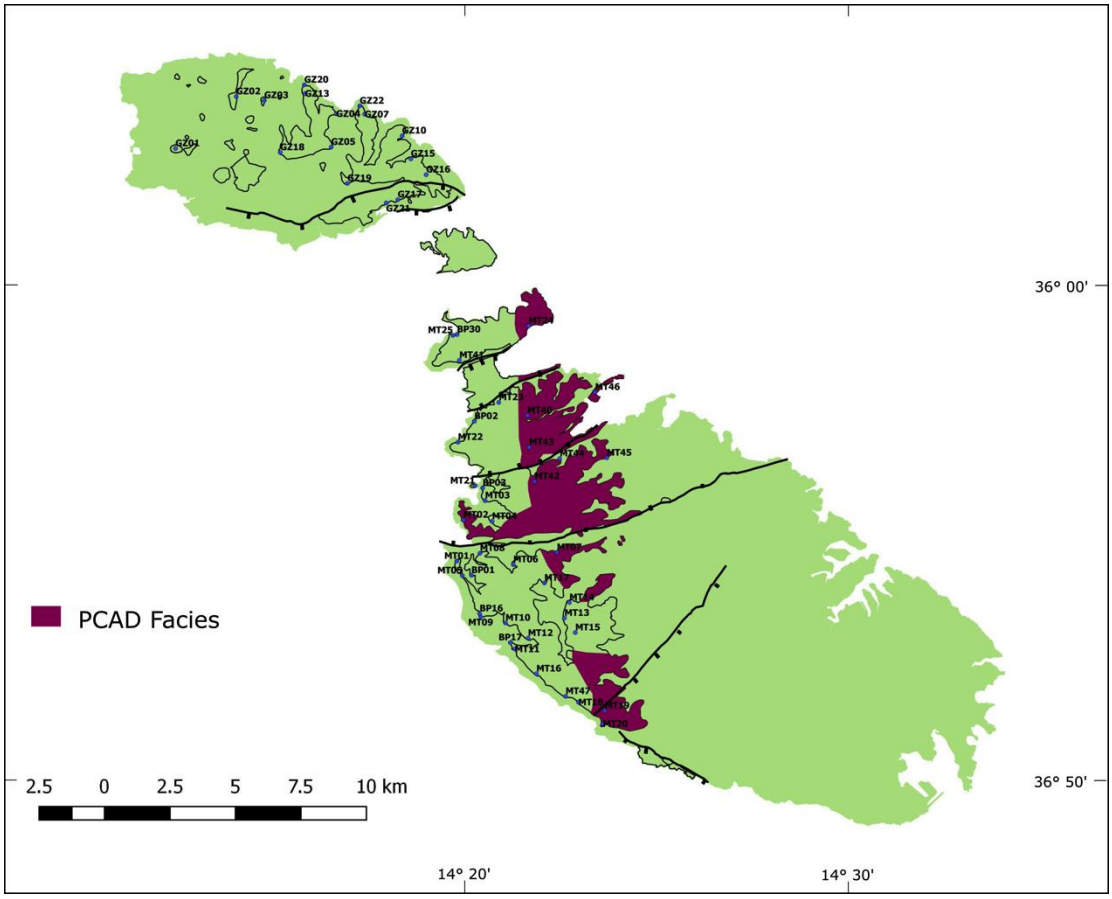

Figure 5.25: Facies map of the Plane bedded coralline algal debris wackestone Facies (PCAD). Facies map is based on new outcrop observations and thickness distribution of division 4.1 when supported by outcrop and field investigations (division 4.1 corresponds to PCAD and Distal Reef Slope Wackestone (DRS) Facies).

5.3.3.1. Massive Coralline Algal Debris Wackestone Facies (MCAD)

The MCAD Facies and the CAD Facies of the Coralline Algal Biostrome FA are comparable in their constituent composition. However, the MCAD Facies typically consists of finer-grained coralline alga debris than that observed in the CAD Facies and it does not interbed with the CAP Facies. The CAD Facies commonly contains abraded rhodoliths (<10 cm in diameter) while the MCAD Facies very rarely contains abraded rhodoliths (<5 cm in diameter). The MCAD can also be differentiated from the PCAD Facies (see section 5.3.3.2) based on the prior's finer-grained composition.

Description

These pale-yellow beds are coarse-grained bioclastic wackestones. The beds are extensively bioturbated and appear massive. However, when the bioturbation is not pervasive, bedding on a 1m to 2m scale is observed. Coralline algal debris and large fossil, molluscs in particular, are also commonly found. Spheroidal rhodoliths, typically less than 5cm in diameter, are very

rarely observed. When these are seen, they are densely branched and contain abraded branch tips (e.g. MT15) (figure 5.26).

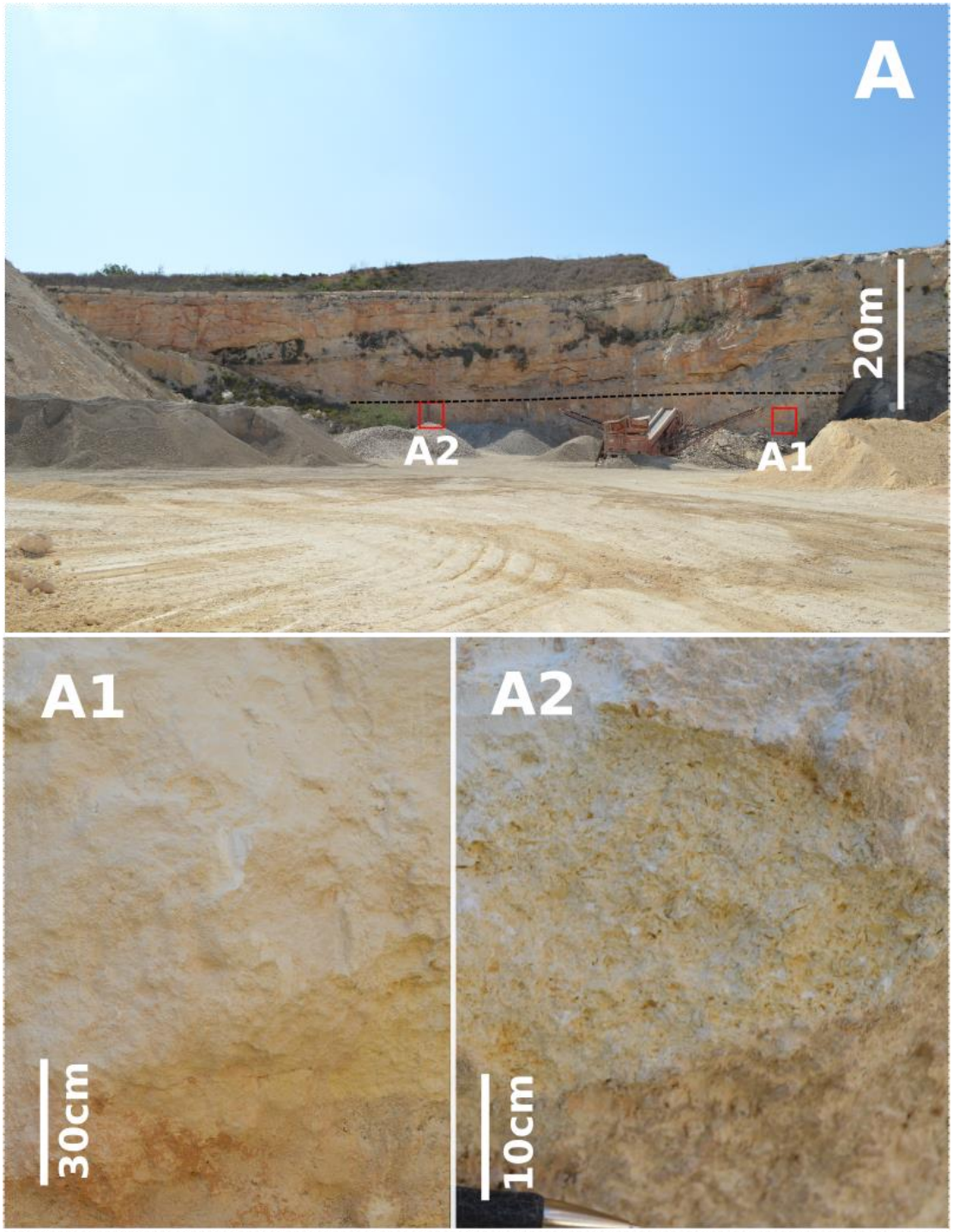

Figure 5.26: Features of the Massive Coralline Algal Debris Wackestone (MCAD) Facies. (A) Quarry section contains a thick (<20 m) accumulation of MCAD Facies that is overlain (black dashed line) by the Distal Reef Slope Wackestone (DRS) Facies (locality MT19). (A1 and A2) Detail of the MCAD Facies coarse-grained bioclastic packstones containing coralline algal debris and large fossils debris

Petrographic description

Sample MT15/S1a (figure 5.27) was assessed in terms of grain sizes, grain composition, porosity and cement (table 5.10). Results indicate that the sample is a moderately to poorly-sorted coarse-grained wackestone. Ranking of observed grains demonstrates a dominance of undifferentiated coralline algal fragments, present in 24% of all points counted. The grain size of twenty nine coralline algal fragments were measured; results indicate that 34% of grains are fine to very fine sand, 48% are medium sand and 17% are very coarse to coarse sand sized. Grain morphometry is rounded and of intermediate sphericity (0.5). Bivalve shell fragments rank second and are present in 6% of all counted points. The two calcitic foliaceous bivalve grain fragments observed were very coarse to coarse sand in size. Foraminifera rank third and are present in 4% of all counted points. Three very coarse to coarse sand foraminifera grains were observed that were either preserved as fragments (1%) or as intact tests (3%) with multichamber uniserial and multichamber planspiral (Miliolid) test shapes. The sample corresponds to the rhodechfor grain association (Hayton *et al*., 1995).

Thin Section	Mud matrix %	F-VF Sd %	M Sd %	VC-C Sd %	VF Grv %	Pebble %	Porosity %	Cement %
MT15/S1a	53.57	9.15	12.21	9.39	0.00	0.00	15.68	0.00

Table 5.10: Grain sizes, porosity and cement observed in the assessed thin sections. 420 points were counted in the thin section.

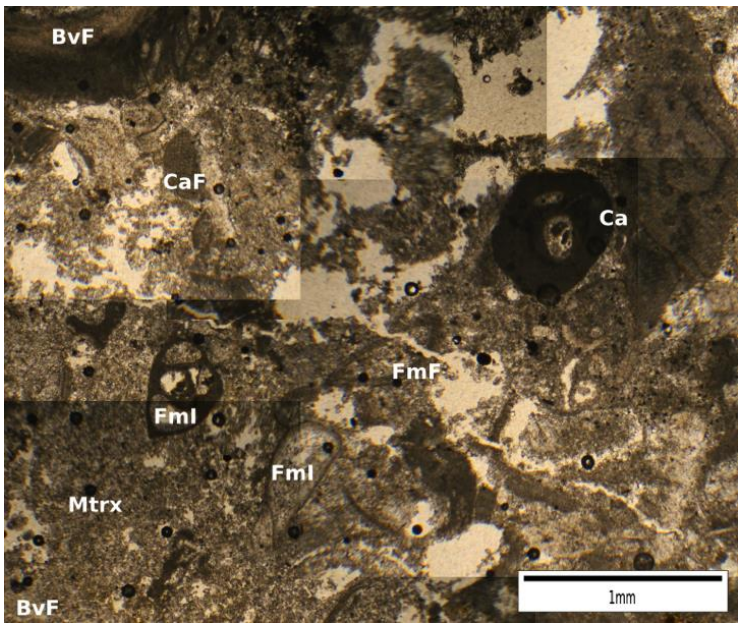

Figure 5.27: Photomosaic of photomicrographs of thin section MT15 S1a of the MCAD Facies. Bvf, Bivalve fragments; Ca, Coralline algae, CaF Coralline algal fragments; FmI, Foraminifera intact; FmF, Foraminifera fragments; Mtrx, Matrix. Clear areas and fracture are holes from section making.

Fauna and Flora

The biota observed in the MCAD Facies includes coralline algae, disarticulated small bivalves, brachiopods, gastropods, bryozoans, benthonic foraminifera and echinoids (the latter two were preserved as complete specimens). Fossils observed and reported in the Sheltered Shelf FA are given in Appendix C3.

Depositional environment

The MCAD Facies is a moderately to poorly sorted coarse-grained wackestone. Bioclasts are reworked and rounded coralline algal and foraminiferal fragments. The facies is extensively bioturbated, suggesting periods of low energy. This suggests that the MCAD Facies was deposited in moderately agitated water.

5.3.3.2. Plane Bedded Coralline Algal Debris Wackestone Facies (PCAD)

Description

The PCAD Facies consists of white to pale yellow coloured very fine to fine-grained wackestone. Macrofaunal content is absent or very locally distributed. The facies develops 0.1 to 1.5 m plane parallel beds that themselves are massive (figure 5.28: outcrop photos MT07, MT20). The facies slope 0.4° to 1.8° to the southeast.

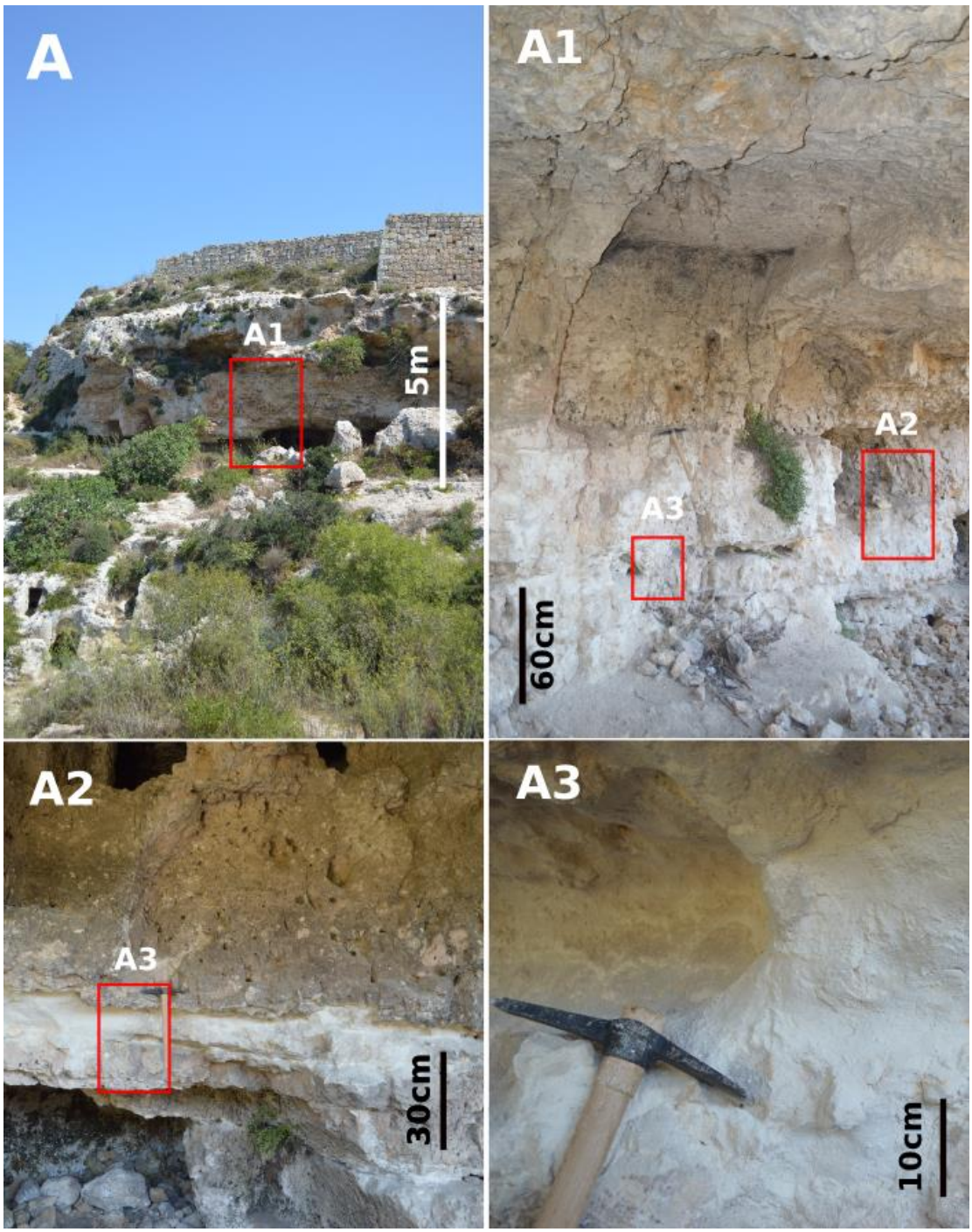
A
A1
5m
A1
A2
A3
60cm
A2
A3
30cm
A3
10cm

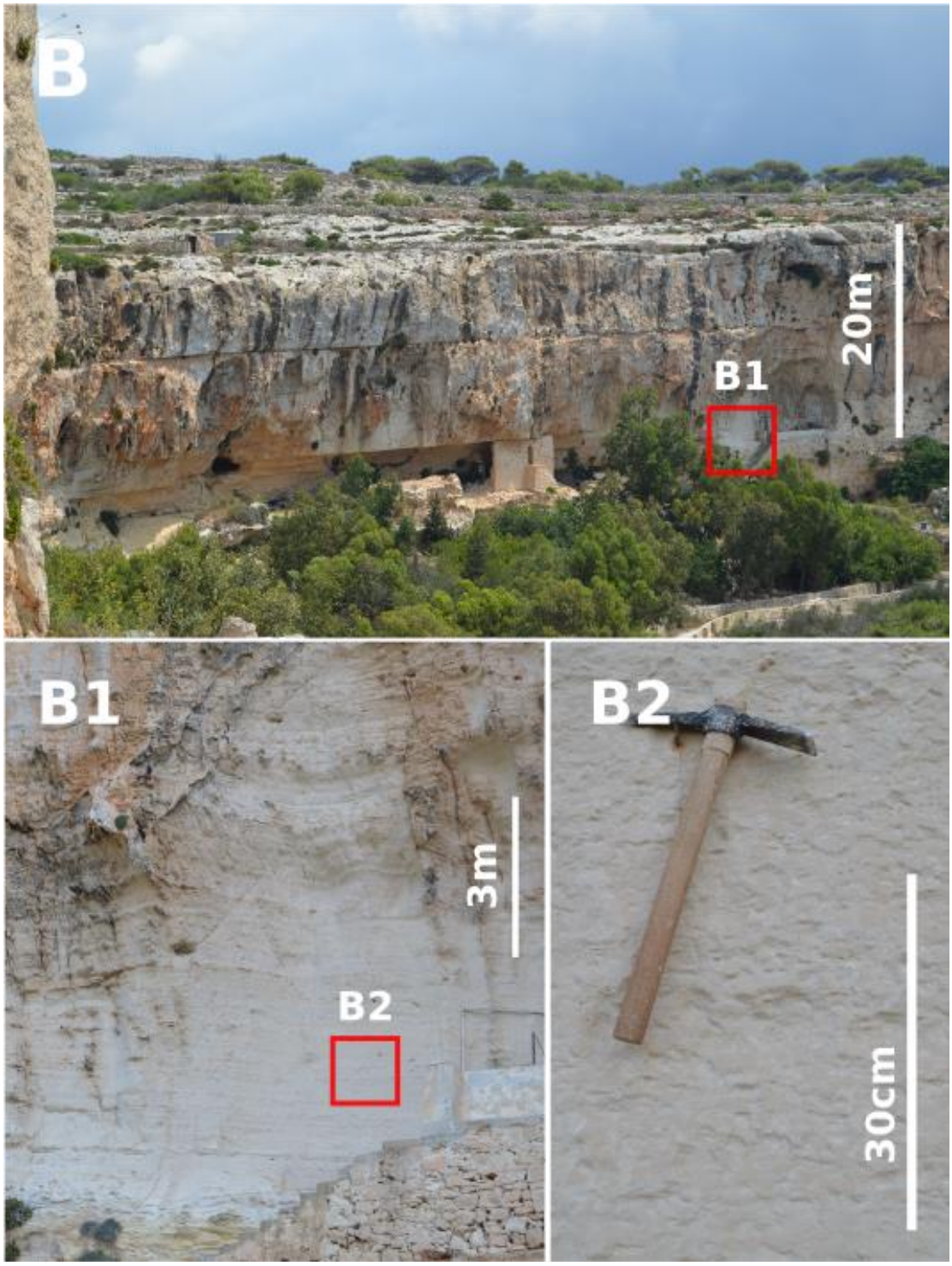

Figure 5.28: Features of the Plane Bedded Coralline Algal Debris Wackestone (PCAD) Facies. (A) Outcrop containing a thick (<10 m) accumulation of PCAD Facies (locality MT07). (A1 and A2) Detail of 0.1 to 1 m plane parallel beds (brown material in upper part of A2 are Quaternary deposits). (A3) Detail of fine-grained wackestone that contains very few macrofauna. (B) Outcrop containing a thick (<20 m) accumulation of PCAD Facies (locality MT20). (B1) Detail of 0.1 to 1 m plane-parallel bedding. (B2) Detail of fine-grained wackestone that contain very few macrofauna but irregular beds suggesting bioturbation.

Facies thickness, distribution, timing and association with other beds

Pedley (1974) suggests that the PCAD Facies (Rdum il-Hmar Beds) are poorly developed in Gozo and limited to areas east of Qala (Pedley, 1974). In this study, the PCAD Facies was not recognised in Gozo. On Comino, Pedley (1974) suggests that the Santa Marija Bay outcrops may be tied to the PCAD Facies (Rdum il-Hmar Beds), the author however cautions that the interpretation is uncertain due to the poor quality of the exposed surface seen today.

Thickness distribution maps of division 4.1 (figure 5.29), which correspond to PCAD and Distal Reef Slope Wackestone (DRS) Facies, show thickened accumulations within graben areas and hangingwall areas (e.g. VLF hanging wall). Thickness records for division 4.1, in areas where the PCAD Facies is exclusively developed, indicate that the FA may be as thick as 30 m in certain north-eastern locations (log 1041). Observations from outcrop (e.g. MT02) indicate that the thickened accumulations within the VLF hanging wall consist of the PCAD Facies (Appendix C2, OCS1, 2). The PCAD Facies do not form the top of outcrops in these areas and their true thickness is therefore preserved. The stratigraphically thickened succession is therefore thought to be the result of syn-depositional tectonic activity that produced hanging-wall depocentres.

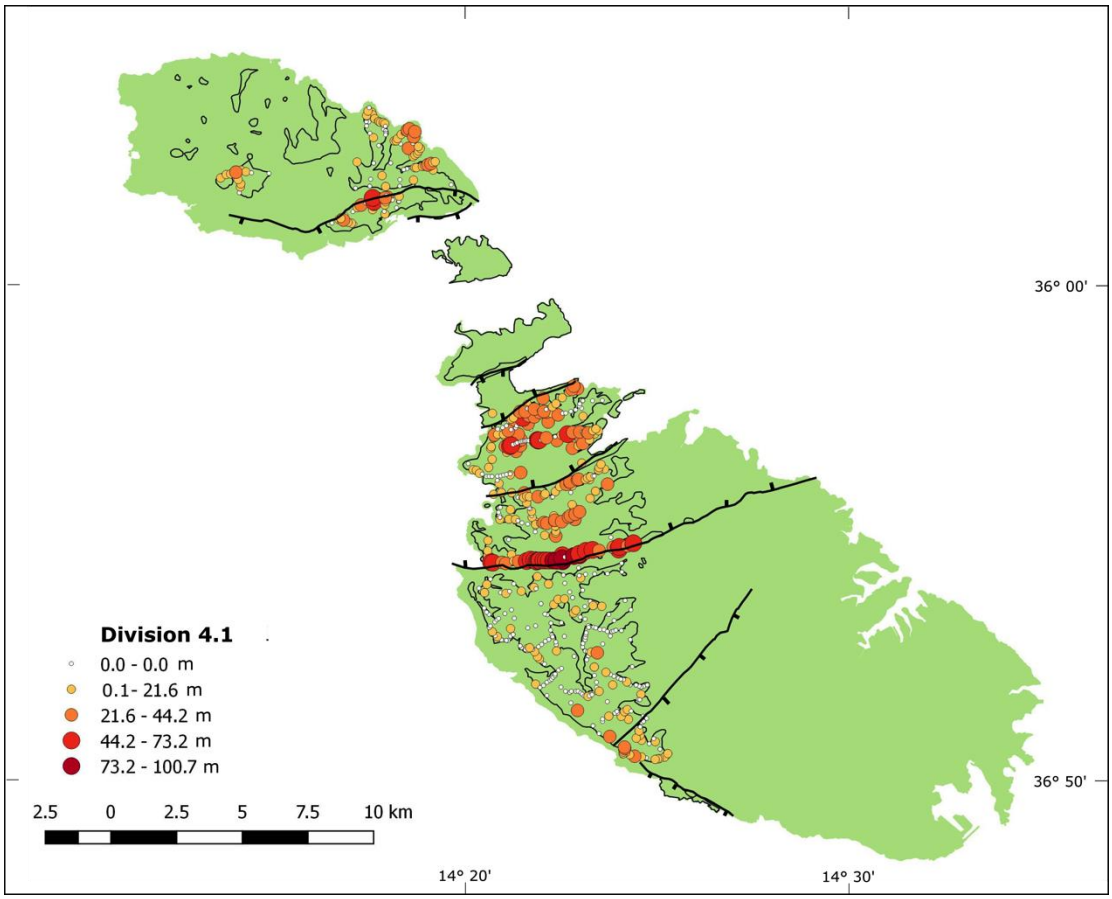

Figure 5.29: Thickness distribution of PCAD and DRS Facies based on seven hundred and seventeen water borehole records. These facies equate to division 4.1 (table 5.2). Refer to Appendix C2 for related outcrop cross sections that cross the VLF.

Petrographic description

Samples MT20/S8 and MT24/S4 (figure 5.30) were assessed in terms of grain sizes, grain composition, porosity and cement (table 5.11). Results indicate that the MT20/S8 is a very well to well sorted fine-grained wackestone and MT24/S4 is a very-well to well sorted very fine-grained packstone. Ranking of observed grains demonstrates a dominance of undifferentiated coralline algal fragments, present in 19% of all points counted in MT20/S8 and 41% of all points counted in MT24/S4. The grain size of fifty one coralline algal fragments were measured; results indicate that 92% of grains are fine to very fine sand and 8% are medium sand. Grain morphometry of sample MT20/S8 is rounded to well-rounded and of intermediate sphericity (0.5). Grain morphometry of sample MT24/S4 grains are rounded to well-rounded and demonstrate intermediate to high sphericity (0.6). Undifferentiated foraminifera fragments rank second occurring in 11% of points counted in sample MT20/S8 and 6% of points counted in sample MT24/S4. Molluscan shell fragments rank third in both samples and are present in 1% of all counted points in sample MT20/S8 and 5% of counted points in sample MT24/S4. The latter sample may also contain ostracods debris. Both sample correspond to the rhodechfor (Hayton *et al*., 1995) grain association.

Thin Section	Mud matrix %	F-VF Sd %	M Sd %	VC-C Sd %	VF Grv %	Pebble %	Porosity %	Cement %
MT20/S8	65.14	26.20	4.28	0.00	0.00	0.00	4.38	0.00
NT24/S4	48.00	47.36	4.64	0.00	0.00	0.00	0.00	0.00

Table 5.11: Grain sizes, porosity and cement observed in the assessed thin sections. 525 points were counted in the thin section.

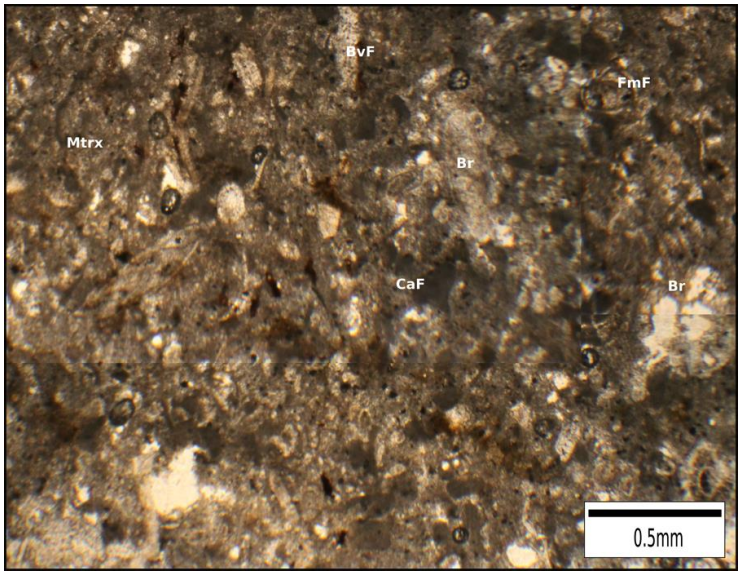

Figure 5.30: (A) Photomosaic of photomicrographs of thin section MT20 S8 of the PCAD Facies. Ca, Coralline algal fragments; Br, Bryozoan fragment; FmF, Foraminifera fragments; BvF, Bivalve fragment; Mtrx, Matrix.

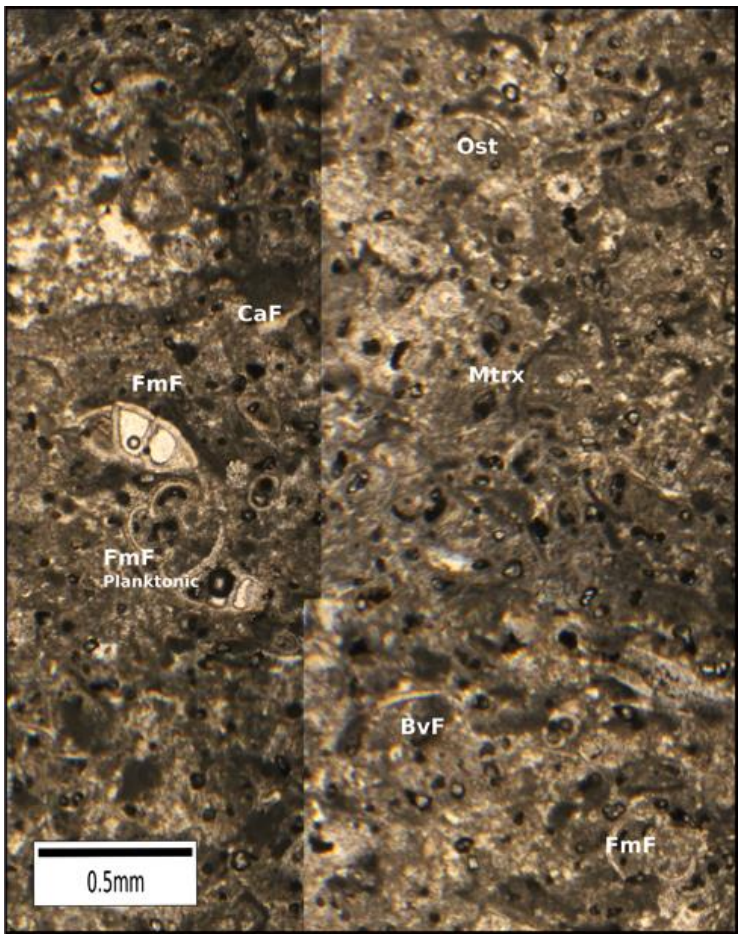

Figure 5.30: (B) Photomosaic of photomicrographs of thin section MT24/S4 of the PCAD Facies. Bvf, Bivalve fragments; Ost, Ostracods; FmF, Foraminifera fragments; FmI, Foraminifera intact; CaF, Coralline algal fragments.

A petrographic comparison of the MCAD and PCAD Facies shows significant differences. The MCAD has a larger proportion of coarser bioclasts while the PCAD contains a larger proportion of micritic matrix and finer bioclasts. Coralline algal fragments ranks highest in both facies. However, algal fragments in the MCAD are coarser than those observed in the PCAD Facies. The PCAD is better sorted than the MCAD Facies; PCAD very well-to-well sorted wackestone, while MCAD moderately to poorly sorted wackestone. These observations suggest that the MCAD accumulated in a higher-energy environment than the PCAD Facies.

Fauna and Flora

The PCAD Facies contains comminuted bioclastic debris with coralline algal fragments dominating. Macrofauna in the facies are typically rare and include small bivalves, brachiopods, gastropods, echinoids, bryozoans, benthonic foraminifera and serpulid worms (for details see Appendix C3).

Depositional environment

The fine-grained PCAD Facies are very well-to-well sorted fine-grained wackestones with abundant micritic matrix (65% of points counted). Fine to very fine sand bioclastic grains are characteristically transported coralline algal fragments that are generally broken, abraded are well-rounded to rounded. The absence of *in situ* photic biota and the predominantly micritic

sediments suggests environments below the storm wave base where lime mud accumulated. Facies distributions and the high occurrence of coralline algal debris suggest the facies may have accumulated eastward of the Coralline Algal Biostrome FA within sheltered/deeper marine environments. The coarser nature of the MCAD Facies suggests accumulation in more turbulent/higher energy conditions than the PCAD Facies.

The PCAD Facies displays prominent vertically burrowed horizons at their base (Pedley, 1974). The extensive bioturbated horizon suggests that during early periods of deposition there may have been relatively low quantities of sediment reached the shallow shelf. As the Coralline Algal Biostrome FA prograded eastwards, the volume of derived sediment reaching the shelf increased. This may have reduced the effect of bioturbation and producing the less bioturbated middle and upper PCAD Facies.

The Sheltered Shelf FA lies immediately to the east of the Coralline Algal Biostrome FA. Both FA are interpreted as being penecontemporaneous (section 5.3.3 introduction). The Rhodolith Pavement Sub-Facies is interpreted to have formed in the littoral zone at circa 40 to 60 m depths and the Crustose Pavement Sub-Facies open shelf water 50 to 80 m deep. The close spatial and temporal association of the Sheltered Shelf FA and Coralline Algal Biostrome FA, combined with the lack of evidence for a marked change (<5°) in topographic slope in outcrop (Fiddien Valley area) (figure 5.23), suggests that the MCAD and PCAD Facies may have been deposited in a similar depth range to the Coralline Algal Biostrome FA. In view of this, the MCAD and PCAD Facies are interpreted to have been deposited in sheltered environments with depths similar to or greater than the maximum depth of *in situ* coralline algal accumulation (>80 m).

It is suggested that water currents flowing eastward over the Coralline Algal Biostrome FA, particularly the CAP Facies, eroded and transported coralline algal debris eastward, thereby forming the Sheltered Shelf FA. As the currents flowed over the Biostrome, friction diminished its strength to produce the eastern sheltered environment within which the Sheltered Shelf FA accumulated.

5.3.4. Reef-Core Facies Association

The Reef-Core FA consists of the Coralgal Fore Reef Facies (CFR), the Coralgal Patch Reef (CPR) and the Coralgal Reef Framestone (CR) Facies (table 5.3). The successive facies demonstrate a change in coral morphology, from platy to massive corals, and an increase in coral abundance and size up-section. The CFR Facies is a new facies proposed in this study that represents deeper fore-reef deposits than the CPR Facies. The latter facies corresponds to the Tal-Pitkal Beds of Pedley (1974) and the Coralgal Patch Reef Facies of Dart (1991). The CR

Facies corresponds to Dart's (1991) Coralgal Barrier Reef Facies and Pedley's (1975, 1978) Depiru Beds (Table 5.4).

When the Reef-Core FA is present in outcrops it typically is <6 m in thickness, though in the south west of Malta it can locally be up to 16 m thick (MT16). Pedley (1975; 1978; 1979) suggests that the Tal- Pitkal Member (Reef-Core FA) overlies the CAD Facies (Coralline Algal Biostrome FA) in eastern Gozo, and overlies the OSHR Facies in western Gozo. In this study, the Reef-Core FA is only observed in western areas of Malta and northern areas of Gozo where it is seen to overlie the Coralline Algal Biostrome FA and be overlain by the Sand Shoal FA (e.g. MT01). The FA is arranged in a NNW-SSE oriented facies belt across the Maltese Islands (figure 5.31). The FA may have also occurred in western areas of the Gozo Horst. This is supported by the presence of eastward prograding Proximal Reef Slope Packstone Facies (PRS) and Distal Reef Slope Wackestone Facies (DRS) in the western area of Gozo (GZ01). Thin sections of this facies association were not prepared because of the very coarse grained nature of these deposits.

An extensive sharp erosive surface is commonly observed across the Maltese Islands between the Reef-Core FA and the underlying CAD Facies (see chapter 6 section 6.3.2.1). Evidence has been gathered in this study that indicates the erosive surface was the result of a substantial relative sea level fall that exposed the upper levels of the Coralline Algal Biostrome FA to sub-aerial conditions in the west of Malta (chapter 6 section 6.3.2.1 and Appendix C4). The surface is interpreted as a sequence boundary (SB3) and is a key horizon that marks the shift from heterozoan factories to photozoan factories (*sensu* James, 1997).

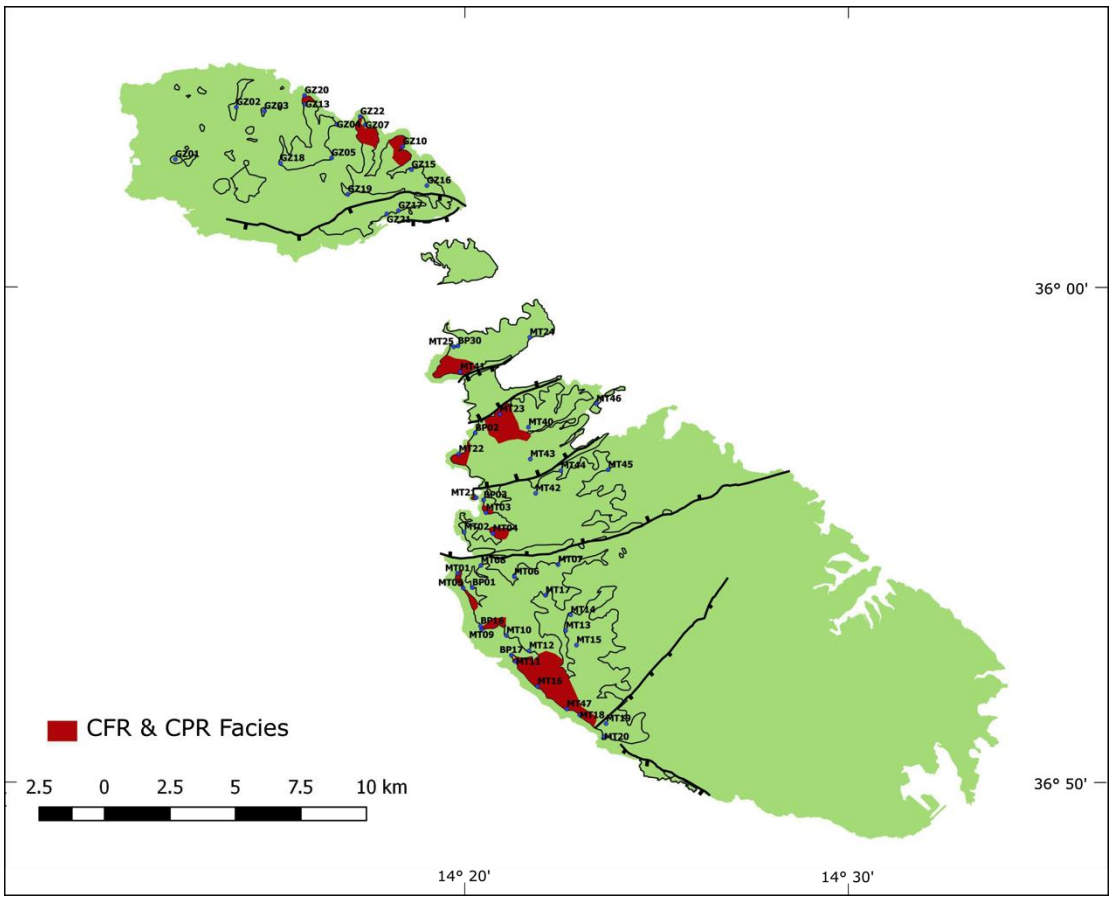

Figure 5.31: Facies Map of the Coralgal Fore Reef (CFR) and Coralgal Patch Reef (CPR) Facies of the Reef-Core FA. The Coralgal Reef (CR) Facies only outcrops in localities MT01 and MT05 (west of Malta, footwall of VLF). Facies map is based on new outcrop observations and thickness distribution of division 4.2 when supported by outcrop and field investigations (division 4.2 corresponds to Reef-Core FA and Proximal Reef Slope Packstone (PRS) Facies).

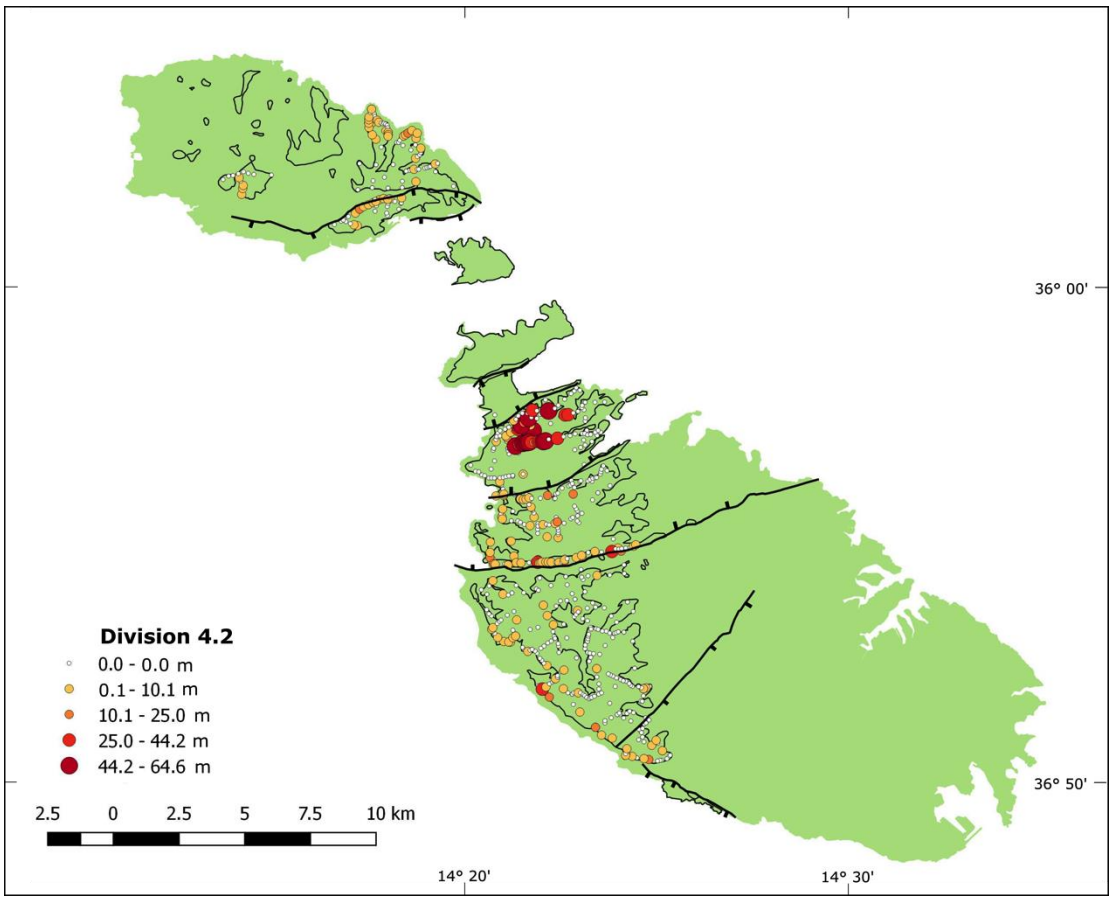

Figure 5.32: Thickness distribution of Reef-Core FA and Proximal Reef Slope Packstone (PRS) Facies within outcrop area of the UCL Fm based on seven hundred and seventeen water borehole records. These facies equate to division 4.2 (table 5.2).

5.3.4.1. Coralgal Fore Reef Packstone Facies (CFR)

Description

The facies are characteristically pale-grey to pale-yellow, bioturbated and massively bedded algal debris packstones. Where bioturbation is less extensive, large-scale progradational tabular cross bedding is discernible that is orientated to the east-northeast (e.g. MT01) (figure 5.33). Small corals are commonly (up to 20% of rock volume) present within the facies. The corals range from 5 to 15 cm in height and 10 to 45 cm in length and display wavy plate to flattened domal morphologies that correspond to Pomar *et al*. (1996) dish coral zone (figure 5.33). The corals are either preserved in calcite or as moulds (e.g. MT01, MT05, MT09, MT18). The corals occur in a matrix similar to that of the underlying CAD Facies.

The chlorozoan CFR Facies occurs in western areas of the Malta Horst and Malta Graben (MT01, MT03, MT05, MT09, MT18, MT21, MT22). This facies was also observed in one outcrop in the east of Gozo (GZ10) (figure 5.31 facies map and Appendix C2 for cross sections).

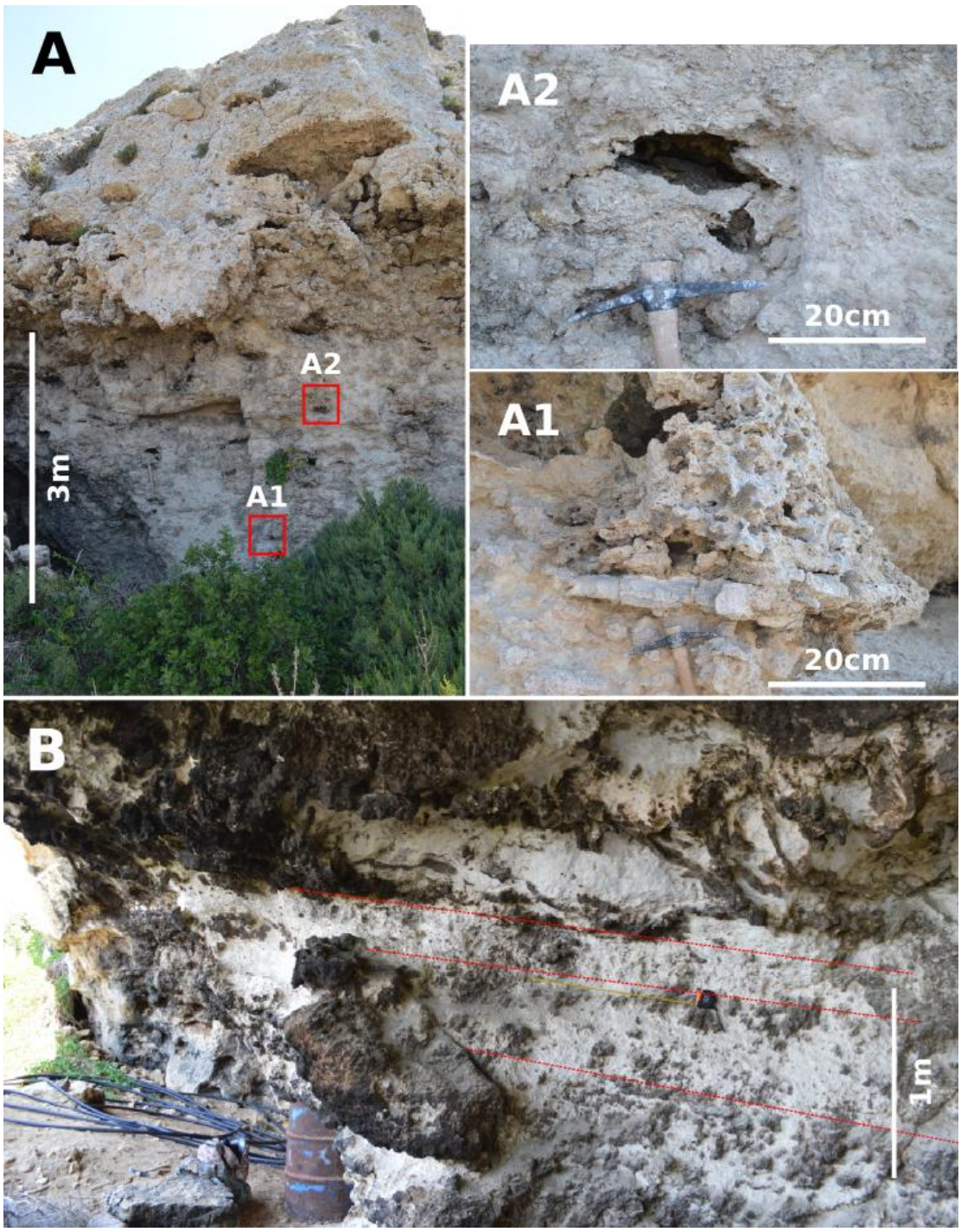

Figure 5.33: Features of the Coralgal Fore Reef Packstone (CFR) Facies. (A) Outcrops contain a thick (<5 m) accumulation of CFR Facies (locality MT18). (A1 and A2) Detail of the CFR Facies containing unidentified corals displaying wavy plate and flattened domal morphologies that correspond to Pomar *et al*. (1996) dish coral zone. (B) Outcrop displaying large-scale progradational tabular cross-bedding (red dashed lines) orientated to the east-northeast (locality MT01).

Fauna and Flora

The CFR Facies contains scleractinian corals, bryozoans, benthonic foraminifera, echinoids, bivalves, gastropods *Strombus costatus* (Gmelin), *Lobatus costatus* (Gmelin) and rarely *Halimeda* (Lamouroux) (for details see Appendix C3). Rhodoliths are sparsely observed and coralline algal fragments together with molluscan and echinoid debris are common. Compared to the CPR Facies (below), the CFR Facies contains fewer photozoan fossils (e.g. corals and *Halimeda*) and a larger fraction of heterozoan fossils (e.g. rhodoliths).

Depositional environment

The wavy plate and small domal coral morphologies suggest formation in water depths between 30 to 60m (*cf.* Pomar *et al*., 1996). The depth interpretation is corroborated by the limited occurrence of photozoan/photodependent organisms, namely *Halimeda sp.* (Lamouroux). Additionally *Strombus sp.* (Swainson) is found in shallow marine habitats, such as seagrass meadows, sand beds, and algal flats (Tewfuk & Guzman, 2003). *Strombus costatus* (Gmelin) and *Lobatus costatus* (Gmelin) are typically found in depths that vary from 3 to 20m (Brownell, 1977). Overall, the habitats are shallow enough for light to penetrate through the water column, which allows the surrounding plant life to photosynthesize (Appeldoorn 1985). The packstones textures of the CFR Facies are less coarse than the overlying CPR Facies. This suggests that the CFR Facies may have occupied conditions were more sheltered than those accommodating the CPR Facies.

5.3.4.2. Coralgal Patch Reef Rudstone Facies (CPR)

Description

The CPR Facies is a pale-grey to white massively bedded packstone, floatstone and rudstone. The facies very commonly (<50%) contains aragonitic *Porites* (Verrill) and *Montastraea* (Blainville) corals that have been dissolved to form caves and moulds 20 to 50cm in height and 30 to 60cm in length (e.g. MT03, MT09, MT18) (figure 5.33: outcrop photos MT09 and MT18). The corals display domal morphologies that correspond to Pomar *et al.* (1996) massive coral zone. The corals occur in a matrix similar to the CAD Facies that consists of yellow to pale-yellow packstone composed of coralline algal, molluscan, and echinoid debris. Small spherical rhodoliths are occasionally observed in the massive beds. The CPR Facies locally develops lensoidal beds (3 to 5 m wide and 1 m thick) that are especially coral rich (e.g. Dingli Cliffs MT18) and of similar dimensions to modern coral patch reefs. These observations correspond to those made by Pedley (1974). The CPR Facies commonly overlie the CFR Facies. The key difference between the CFR and CPR Facies is the increased abundance of photodependent organisms and coarser texture in the latter facies.

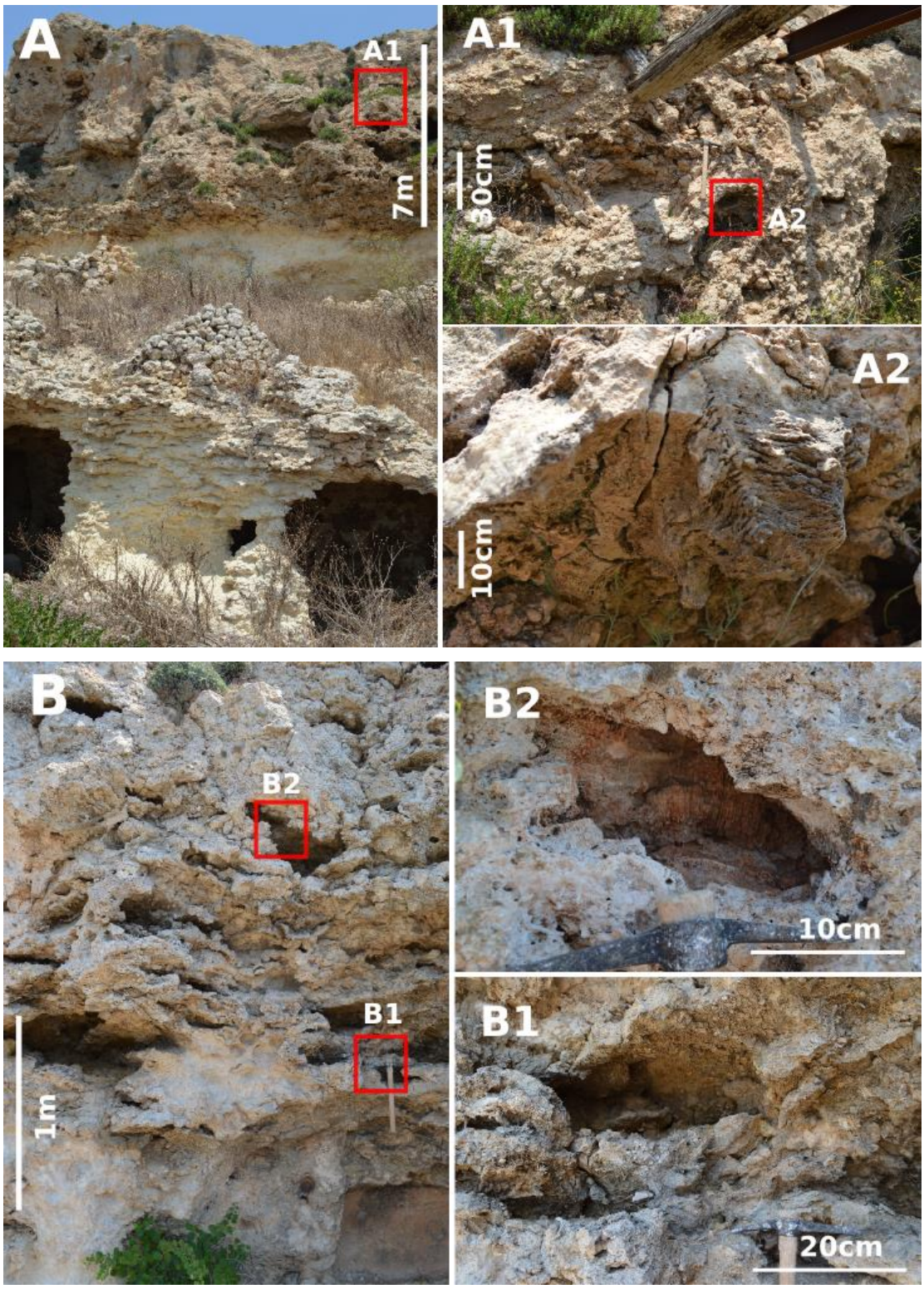

Figure 5.34: Features of the Coralgal Patch Reef Rudstone (CPR) Facies. (A) Outcrop contains an accumulation of CPR Facies (brown) that overlies the Coralline Algal Biostrome FA (pale yellow) (locality MT09). (B) Outcrop contains accumulation of CPR Facies (locality MT18). (A1, A2 and B1, B2) Detail of CFR Facies containing *Porites* (Verrill) and *Montastraea* (Blainville) corals that have been dissolved to form small caves and moulds 20cm to 50cm in height and 30cm to 60cm in length. The corals display domal morphologies that correspond to Pomar's (2004) massive coral zone.

Facies thickness, distribution, timing and association with other beds

Thickness maps of division 4.2 (figure 5.32) show thickened accumulations along the VLF and SPIF footwalls. The VLF and SPIF footwalls may have developed a positive relief, thereby placing the areas in shallower waters. This would have enhanced coral growth, producing a thickened successions within the uplifted VLF and SPIF footwall structural highs. Relief on the footwall structural highs may have been a relic of initial throw influencing the Coralline Algal Biostrome FA, or as a result of syn-depositional tectonic activity.

Fauna and Flora

In addition to scleractinian corals the fauna and flora include bryozoans, bivalves, Chlorophyta namely *Halimeda (Lamouroux)*, benthonic foraminifera and molluscan moulds (for details see Appendix C3). *Glycymeris sp.* (Costa) is widespread on shallow sea-beds that consist of heterogeneous-grained sediments of fine shell-gravels, or sandy-muddy gravels offshore to about 100 m (Freneix *et al*., 1988). *Lithophaga* (Roding) commonly bore the *Porites* (Verrill) and *Montastraea* (Blainville) corals producing pholad borings and their internal structure is preserved inside the coral mould. Rhodoliths and encrustations of coralline red algae are sparse and bioclasts are principally coralline algal fragments together with molluscan and echinoid debris.

Depositional environment

The isolated coral moulds display domal morphologies which, based on zonation of coral-colony morphologies with respect to paleo-depth (Pomar *et al*., 1996), suggest depths of approximately 10 to 20 m. The observed fauna and flora, including corals, pholad borings (likely *Lithophaga*) and encrustations of red algae, suggest accumulation in the shallow-zone patch-reefs similar to the upper Miocene Llucmajor platform of Mallorca (*cf.* Pomar *et al*., 1996). Additionally, the calcareous green alga *Halimeda* (Lamouroux) is commonly observed in lagoonal and reef environments throughout the tropical world (e.g. Hine *et al*., 1988; Liddell *et al*. 1988; Multer, 1988).

5.3.4.3. Coralgal Reef Framestone Facies (CR)

Description

The facies is dominated by white massive coral framestones containing large coralgal bioherms. The corals observed in the CR Facies are the most abundant and largest of the Reef-Core FA facies and display massive and domal morphologies. Coalescing caves record intergrown coralgal frameworks that are more than 6m high and 32m across (e.g. MT01, MT05) (figure 5.35). Individual corals are 1.5 to 2 m in height and 3.5 to 4 m in length (e.g. MT05). The coral bioherms may have had a relief of no more than 1 to 1.5 m on the seabed and may have formed by the coalescing of coral patch-reefs. Pedley (1974) indicates that the longer axes of the barrier

reefs are approximately oriented east-west. Facies map of the CFR and CPR Facies of the Reef-Core FA (figure 5.31) however suggest the Reef-Core FA is oriented north-south. The corals occur in a matrix similar to the CAD Facies that consists of yellow to pale-yellow packstone composed of coralline algal, molluscan, and echinoid debris. Rhodoliths were rarely observed in the facies.

Facies thickness, distribution, timing and association with other beds

This facies was only observed in the westernmost areas of the Malta Horst along the VLF footwall high (MT01 and MT05). The full succession of CAD Facies, erosive surface (sequence boundary), CFR Facies, CPR Facies and CR Facies is only observed in the IMF footwall in the west of Malta from Fomm ir-Rih (MT01) to Bahrija (MT05). The VLF footwall may have contained a fault scarp that produced optimal marine conditions for higher chlorozoan production. This may have allowed the local accumulation and coalescing of coral patch-reef sediments to form a more extensive coral reef. Where the CR Facies occurs it conformably overlies the CPR Facies.

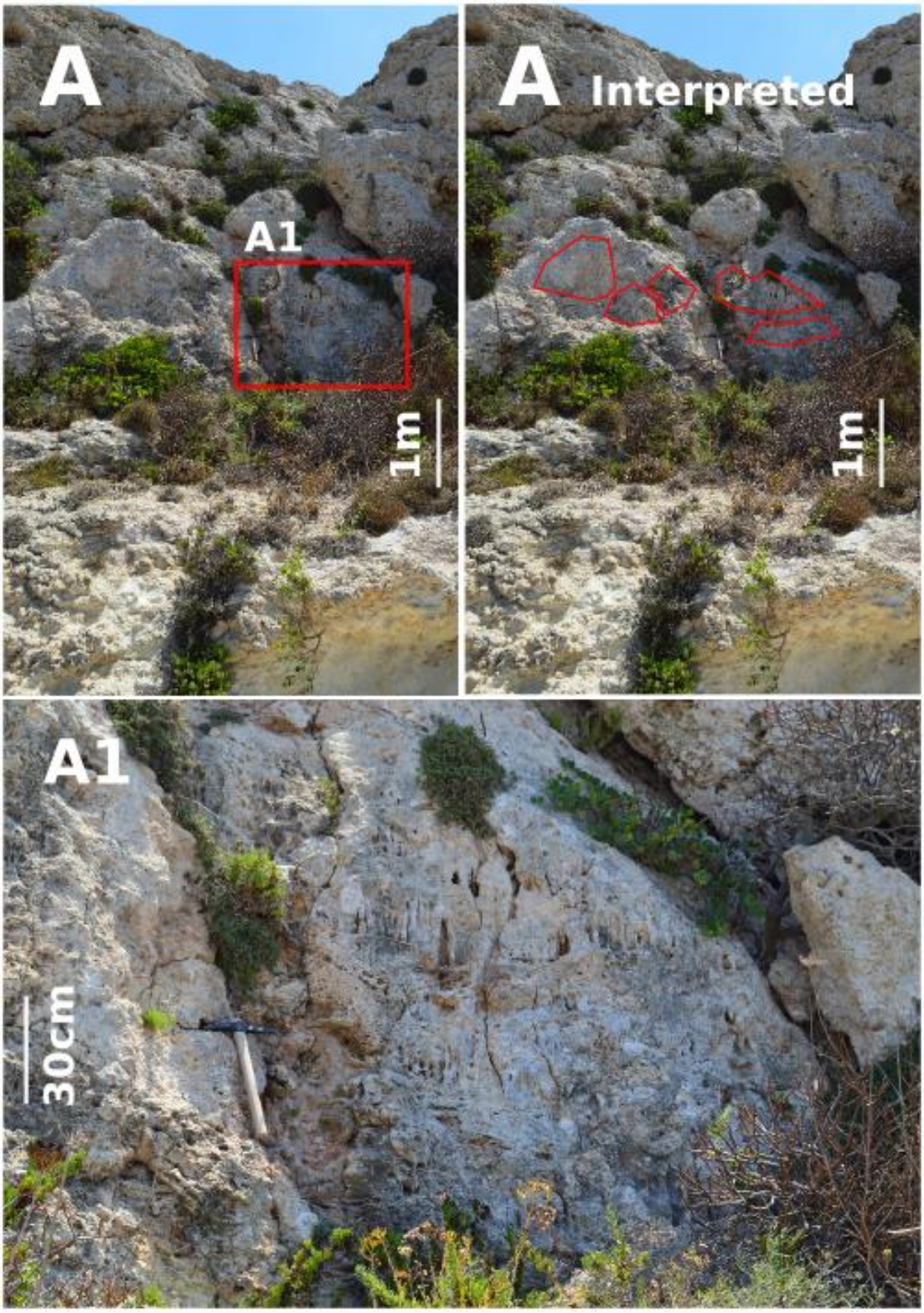

Figure 5.35: Features of the Coralgal Reef Framestone (CR) Facies. (A) Outcrop contains a thick accumulation (<5 m) of CR Facies (locality MT05). (A interpreted) Indicates the position and dimensions of corals with massive and domal morphologies (red polygons). (A1) Detail of CR Facies, particularly the *in situ* coral framework.

Fauna and Flora

Fauna and flora includes both *Porites* (Verrill) and *Montastrea* (Blainville) corals, bryozoans, bivalves, chlorophyta namely *Halimeda (Lamouroux)*, benthonic foraminifera and molluscan moulds (for details see Appendix C3). Coralline crusts intergrow with the corals. *Lithophaga* (Roding) commonly bore the corals producing pholad borings.

Depositional environment

The corals display head like morphologies that correspond to the Pomar *et al*. (1996) massive coral zone suggesting water depths of 10 m or less. The corals *Porites* (Verrill)*, Tarbellastraea* (Alloiteau), *Acropora* (Oken) and *Favites* (Link) (Pedley, 1974), observed in the facies, thrive in the shallow photic zone of tropical oceans. Bosscher & Schlager (1992) reviewed Caribbean coral production rates *versus* depth and noted that coral growth is photo-dependent. Highest coral production rates occur in the euphotic zone, down to approximately 20 m depth, and decreases exponentially with increasing depth to a minimum at 60 m depth. In particular, *Favites abdita* is observed to have a lower depth limit of 40 m (Stimson *et al*., 2002). *Acropora* is most common in shallowest reef environments within moderate to high water energies (Shinzato *et al*., 2011).

5.3.5. Fore-Reef Slope and Shelf Facies Association

The Fore-Reef Slope and Shelf FA contains facies that were deposited basinwards (eastwards) of the Reef-Core FA in either a fore-reef slope or off-reef shelf marine setting. The FA consists of the Proximal Reef Slope Packstone (PRS) Facies and Distal Reef Slope and Shelf Wackestone (DRS) Facies. The PRS and DRS Facies correspond to Dart's (1991) Proximal Reef Slope Facies and Pedley's (1974, 1978) Ghadira Beds. When the Fore-Reef Slope and Shelf FA is present in outcrop it typically is <6 m in thickness, though in the south west of Malta it can locally be up to 30 m thick (MT20). The PRS represent foresets and DRS represent bottomsets of prograding clinoforms.

5.3.5.1. Proximal Reef Slope Packstone Facies (PRS)

Description

The pale-grey to white PRS Facies is composed of coarse-grained bioclastic wackestones and packstones. The facies is well bedded on a 0.5m to 1.5m scale and develops large-scale sigmoidal clinoforms that are up to 30m thick. The clinoforms dip between 15° to 30° and prograde eastwards (figure 5.36). Basal parts of the clinoform beds develop erosive bases and groove casts. Sedimentological descriptions and observations correspond to those made by Pedley (1974) and Dart (1991).

Figure 5.36: Outcrop of Proximal Reef Slope Packstone (PRS) (red-dashed lines) and Distal Reef Slope Wackestone (DRS) Facies with interpreted (blue-dashed lines) large-scale sigmoidal clinoforms that are up to 30m thick, display dips between 15° to 30° and prograde eastwards (locality MT20). PRS represent foresets and DRS represent bottomsets (blue dashes lines) of the prograding sigmoidal clinoforms. Green line demarcates the boundary with the Reef-Core FA at MT18.

Facies thickness, distribution, timing and association with other beds

The PRS Facies forms a NNW-SSE oriented facies belt across the Maltese Islands. The PRS Facies form eastward prograding sigmoidal clinoforms along the eastern margin of the Reef-Core FA. The Gebel Ciantar locality displays a near continuous west-east section where the Reef-Core FA (e.g. MT47, MT18), PRS and DRS Facies (MT19 and MT20) are in stratigraphic contact with each other (figure 5.36). The PRS Facies is interpreted to represent reworked sediment originating from the Reef-Core FA and Sand Shoal FA to the west. This interpretation is supported by the close spatial relationship and the similar nature of the PRS allochems to those observed in the Reef-Core FA (e.g. MT23/S4 in petrographic description) and Sand Shoal FA (e.g. MT15/S4 in petrographic description).

In this study the PRS and DRS Facies were recorded in the Malta Horst and Graben (MT15, MT19, MT20, MT23, MT40, MT44, MT43) and Gozo Horst (GZ01, GZ15) (figure 5.37 facies map). The PRS and DRS Facies overlie the MCAD Facies (MT15, MT19, MT20, MT44, GZ01) and the PCAD Facies (MT40, MT43). The PRS Facies overlies the DRS Facies in southwest (MT15) areas of Malta. In eastern parts of the Island, the DRS Facies is present and the PRS is missing (MT23, 44). The observed spatial distribution of PRS Facies with adjacent facies suggests an eastwards prograding reef slope. Water borehole thickness records for division 4.2 (which includes the Proximal Reef Slope Packstone Facies) in areas where the PRS facies is exclusively developed indicate that the FA may be as thick as 47 m in certain north-eastern locations (log 1175).

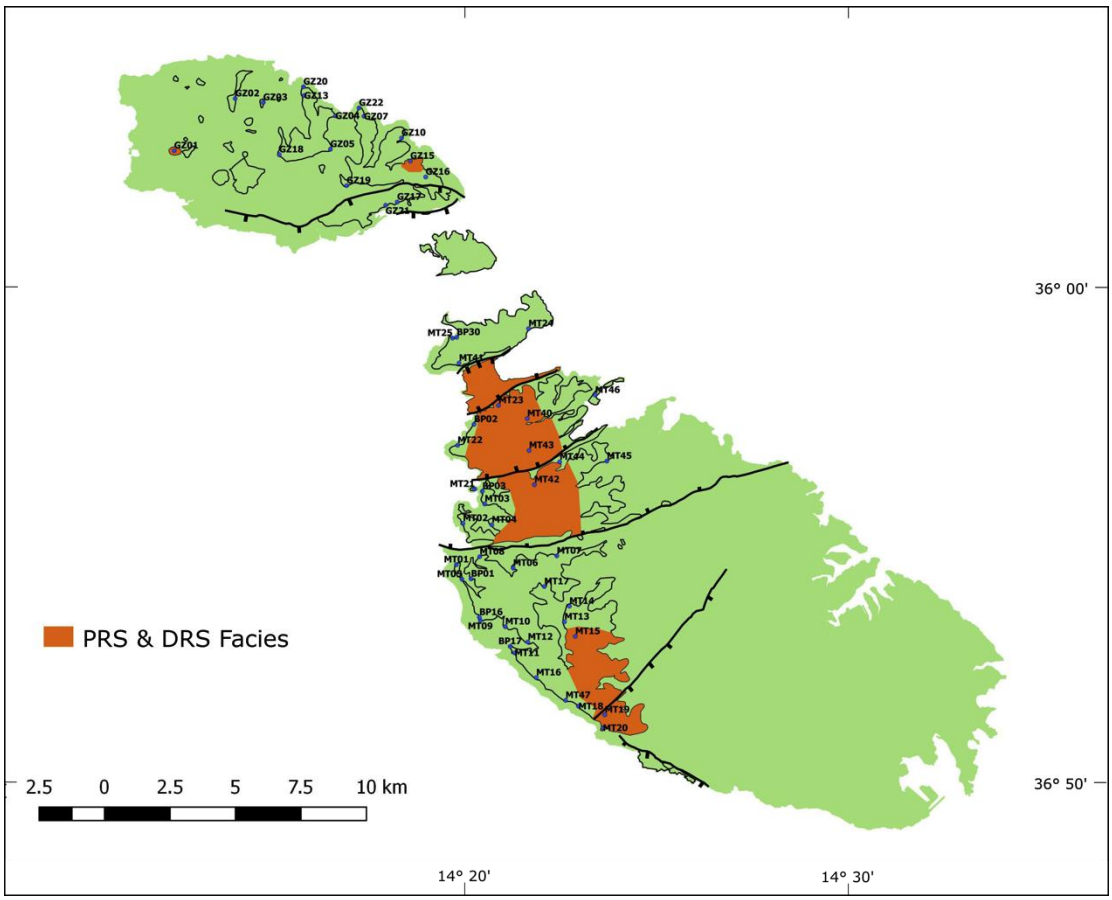

Figure 5.37: Facies map of the Proximal Reef Slope Packstone (PRS) Facies and the Distal Reef Slope Wackestone (DRS) Facies. Facies map is based on new outcrop observations and thickness distribution of division 4.1 and division 4.2 when supported by outcrop and field investigations.

Petrographic description

Samples MT15/S4 and MT23/S4 (figure 5.38) were assessed in terms of grain sizes, grain composition, porosity and cement (table 5.12). Results indicate that sample MT15/S4 is moderately well to moderately sorted, while sample MT23/S4 is well to moderately well sorted. Sample MT15/S4 is a coarse-grained packstone, while MT23/S4 is a fine-grained wackestone.

Ranking of observed grains in sample MT15/S4 demonstrates a dominance of medium to very coarse sand ooids present in 43% of all counted points. Ooid laminae are obliterated or absent, due to a pervasive micritization of the cortex (Flugel, 2010). Molluscan fragments rank second (1% of counted points) and peloids rank third (1% of counted points). Peloidal grains were observed, both fine to very fine sand in size. The peloids were interpreted to be fecal pellets (diagnostic criteria: peloids are rounded elongated, rod-shaped or ovoid dark-colored micritic grains, rarely spherical, commonly homogeneous or with silt-sized inclusions; rarely with defined internal structures with sizes <100 μm to several millimeters) (Flugel, 2010). The sample corresponds with the oopeloid.

Ranking of observed grains in sample MT23/S4 demonstrates a dominance of undifferentiated coralline algal fragments that is present in 15% of all counted points. Grain sizes of twenty-seven coralline algal fragments were measured; results indicate that 52% of grains are fine to very fine sand, 33% are medium sand. Grain morphometry is rounded to sub-rounded and demonstrates intermediate to high sphericity (0.6). Foraminifera are preserved as fragments and undifferentiated intact tests (6% of points counted). Molluscan fragments (5% of counted points) and echinoid (0.4% of counted points) were also observed. The sample corresponds with the oopeloid grain association.

Thin Section	Mud matrix %	F-VF Sd %	M Sd %	VC-C Sd %	VF Grv %	Pebble %	Porosity %	Cement %
MT15/S4	43.17	5.00	25.00	14.17	0.83	0.00	11.83	0.00
MT23/S4	69.00	16.97	6.13	3.30	0.00	0.00	4.60	0.00

Table 5.12: Grain sizes, porosity and cement observed in the assessed thin sections. 600 points were counted for thin section MT15/S4 and 500 points were counted for thin section MT23/S4.

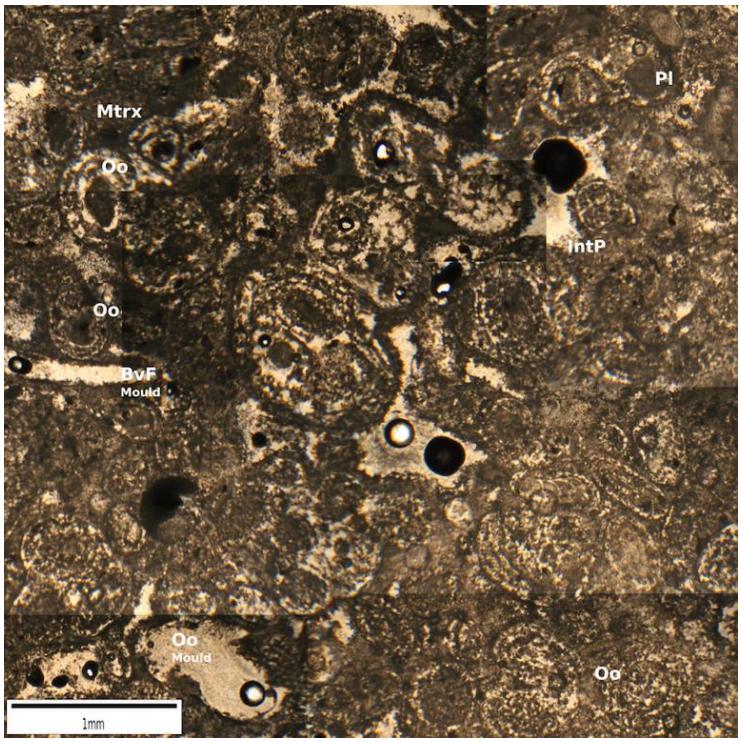

Figure 5.38: (A) Photomosaic of photomicrographs of thin section MT15/S4 of the PRS Facies. Oo, Ooids; Bvf, Bivalve fragments; Pl, Peloids; Mtrx, Matrix; IntP, Interparticle and intraparticle/mouldic porosity.

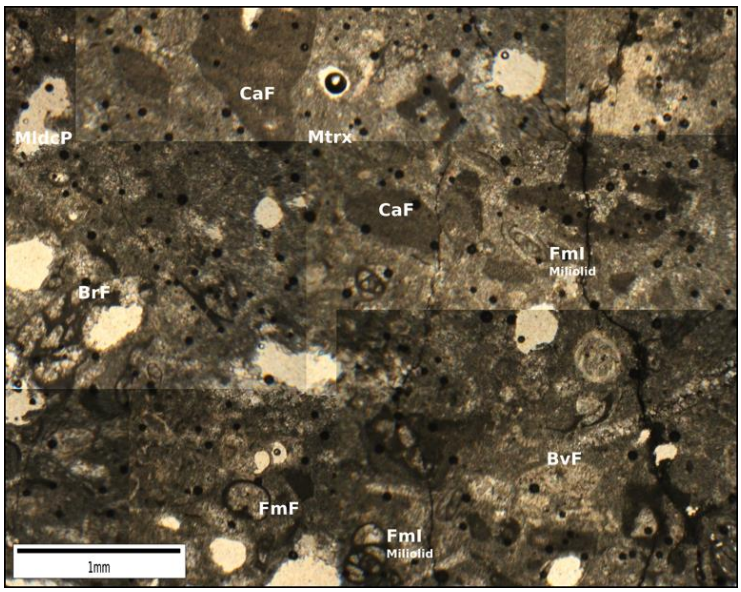

Figure 5.38: (B) Photomosaic of photomicrographs of thin section MT23/S4 of the PRS Facies. EF, Echinoid fragments; FmF, Foraminifera fragments; FmI, Foraminifera intact; Bvf, Bivalve fragments; BrF, Bryozoan fragments; Ca, Coralline algal fragments; MldcP, Moldic porosity (some may be dissolved out coral debris); Mtrx, Matrix.

While the assessed thin section samples (MT15/S4 and MT23/S4) are distinct from each other, these are still thought to belong to the same facies. This is since their depositional geometries, bedforms, bed contacts, macro and micro faunal and floral, facies distribution, and relationship with other facies are similar.

Fauna and Flora

Macrofauna is relatively sparse and includes echinoid, molluscan and coralline algal debris. Originally aragonitic debris now preserved as mouldic porosity has been interpreted as *Halimeda* (Lamouroux). Microfauna includes foraminifera (figure 5.38).

Depositional environment

Pedley (1978) observes that that the Ghadira beds (PRS Facies) contains coarse bioclastic and oolitic material and form wedge like bodies along the eastern margin of the Tal- Pitkal Member (Reef-Core FA). He suggests that the Ghadira beds represent subtidal delta-front sediments that entered a fairly deep depression in the east from shallow-water areas to the west (Pedley, 1978). Dart (1991) later argued that the facies are fore-reef deposits with sediment being primarily derived from the westward occurring and contemporaneous coralgal patch and barrier reefs (Dart, 1991 p.229).

Pedley (1978) and Dart (1991) suggest that the sediment supply of the PRS, that contains coarse bioclastic and oolitic material, was the Reef-Core FA. Microfacies analysis carried out in this study provides an alternative to previous paleoenvironmental interpretations. The abundance of first bioclastic (MT23/S4) and then oolitic (MT15/S4) material in the PRS Facies suggests a change in sediment source. The nature of the allochems and their stratigraphic positions suggest that the stratigraphically lower PRS bioclastic sediments may be contemporaneous with and

sourced from the Reef-Core FA. The stratigraphically higher PRS oolitic sediments may be contemporaneous with and sourced from the Sand Shoal FA (see section 5.3.6). Additional petrographic analysis across the PRS Facies would be necessary to verify this hypothesis. The allochems within the PRS Facies were likely transported eastwards down a depositional slope by tide and gravity processes. The lack of *in situ* shallow water fossils within the PRS Facies substantiates the interpretation that the ooids and peloids were transported.

The PRS Facies forms eastward (basinward) prograding sigmoidal clinoforms. The height of the prograding clinoform geometries in the PRS Facies is up to 30 m. This suggests a reefal platform margin relief up to 30 m in height. If the Reef-Core FA (section 5.3.4) is considered to have formed in water depths of <30 m, the PRS Facies must have been deposited in water depths of > 30 to 60 m.

5.3.5.2. Distal Reef Slope Wackestone Facies (DRS)

Description

The facies is typically white to very pale-grey fine-grained mudstones and wackestones. The facies consist of east-northeasterly directed progradational cross-beds that characteristically dip less than 10° (e.g. MT15, MT19, MT20, MT44). The facies comprises 0.2 to 0.8 m thick cemented interbedded with 0.2 to 0.5 m thick less well-cemented beds. Beds display normal grading. The well-cemented beds are bioclastic packstones and wackestones, which are interbedded with friable very fine-grained wackestones and mudstones (e,g, MT15, MT19, MT40, MT44, GZ01) (figure 5.40). The DRS Facies are recorded in the eastern parts of the Island (MT23, 44).

Petrographic description

Sample MT44/S3 was assessed in terms of grain sizes, grain composition, porosity and cement. The sample was taken from the finer-grained beds. Results indicate that the sample is entirely (100%) composed of micrite matrix. The sample is therefore a very well sorted mudstone.

Fauna and Flora

Fauna are sparser than in the proximal reef slope beds and appear to include similar bioclastic material though these are preserved as finer grains that are more fragmented and difficult to identify.

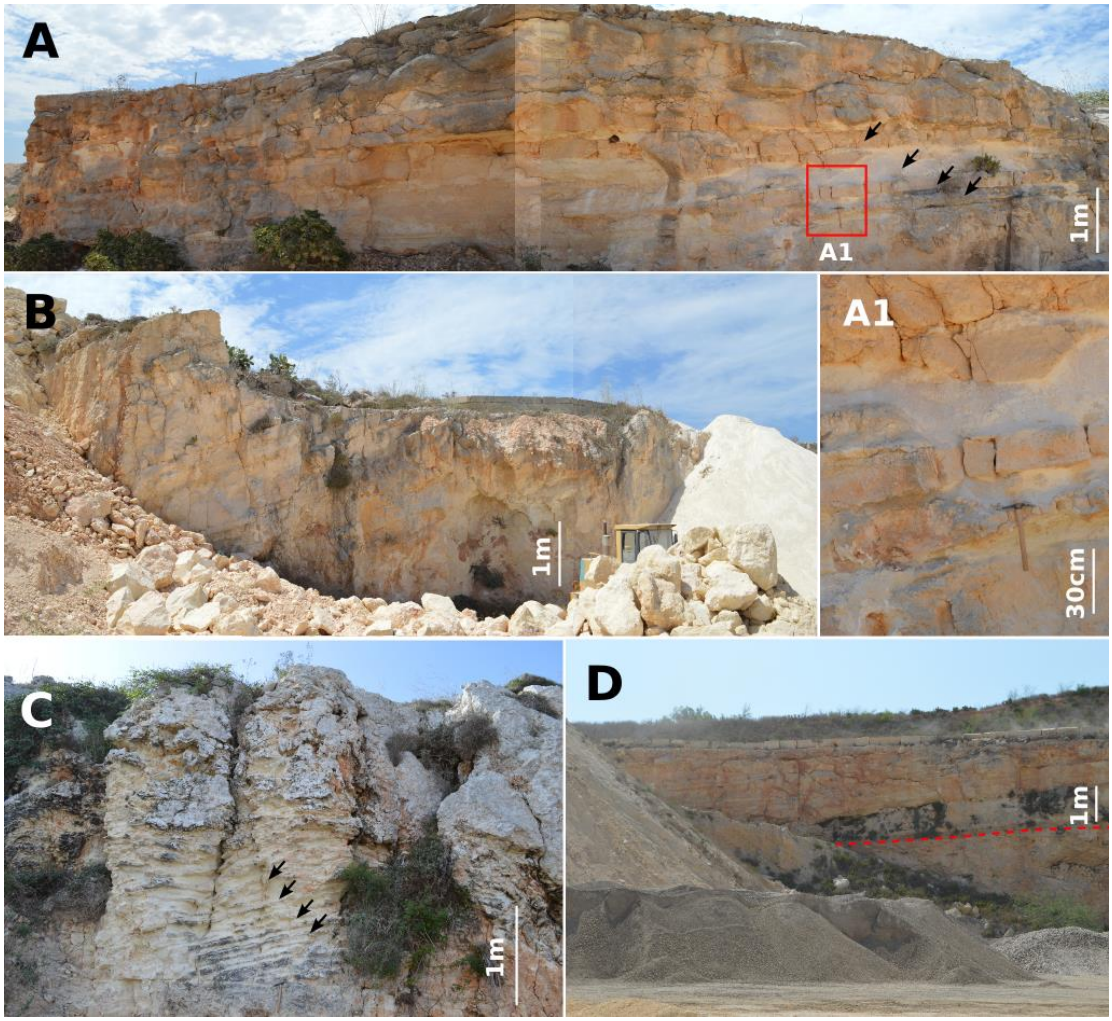

Figure 5.39: Features of the Distal Reef Slope Wackestone (DRS) Facies. (A, B and D) Quarry sections and (C) outcrop containing DRS Facies that display progradational trough cross beds (black arrows) which dip less than 10° (A and B at locality MT15, C at locality MT44 and D at locality MT19). (B) Beds demonstrate tectonic dip to the left. (A1 and C) Detail well-cemented bioclastic wackestone beds and interbedded with friable very fine-grained wackestones and mudstones. (D) Demonstrates MCAD Facies that is overlain by the DRS Facies (red dashed line shows boundary between the two facies) (locality MT19).

Depositional environment

The decimetre scale interbedded very-fine and fine beds of DRS Facies display normal grading and gradational contacts. This sequence is characteristic of transport and deposition by gravitational processes such as turbidites. The DRS Facies forms the bottomsets of the large-scale PRS prograding sigmoidal clinoforms (figure 5.36). If the Reef-Core FA is considered to have formed in water depths of <30 m (section 2.4), and the reefal platform margin relief was up to 30 m in height (section 2.5.1), the DRS Facies must have been deposited in water depths of >60 m.

5.3.6. Sand Shoal Facies Association (FA)

The Sand Shoal FA consists of the Sand Shoal Grainstone Facies (SS) and the Wave Ripple Packstone Facies (WR). These two facies correspond to Pedley's (1974, 1978) Tat-Tomna Beds and Dart's (1991) Sand Shoal Facies (table 5.4). The FA is interpreted as migrating/constantly-shifting ooidal and peloidal sand shoals formed in shallow-marine, tropical high-energy environments.

In northwest and west areas of Malta, a basal surface to this facies association is a sharp erosive contact that separates it from the underlying Reef-Core FA (figure 5.40). Reef-Core FA. Above this contact, reef growth is abruptly ended and the facies are dominated by cross-bedded packstones and grainstones of the Sand Shoal FA. The surface may have been produced by a relative sea-level fall followed by sea-level rise, but no evidence of subaerial exposure is seen.

5.3.6.1. Sand Shoal Grainstone Facies (SS)

Description

This facies is a pale-grey, fine-grained peloidal, ooidal and bioclastic grainstone. The facies exhibits trough cross-bedding with sets that are 0.1 to 0.3 m thick and co-sets that are 0.2 to 0.5 m thick (figure 5.41C). Pedley (1974) argues that trains of migrating straight and sinuous crested ripples formed the cross-beds. When bioturbation is extensive, cross beds are destroyed producing massively bedded grainstone beds.

The facies is only developed in the westernmost areas of the Malta (close to MT16, MT18 and MT22). When present the facies forms accumulations 3 to 5m thick. The SS Facies underlies the WR Facies (e.g. MT22).

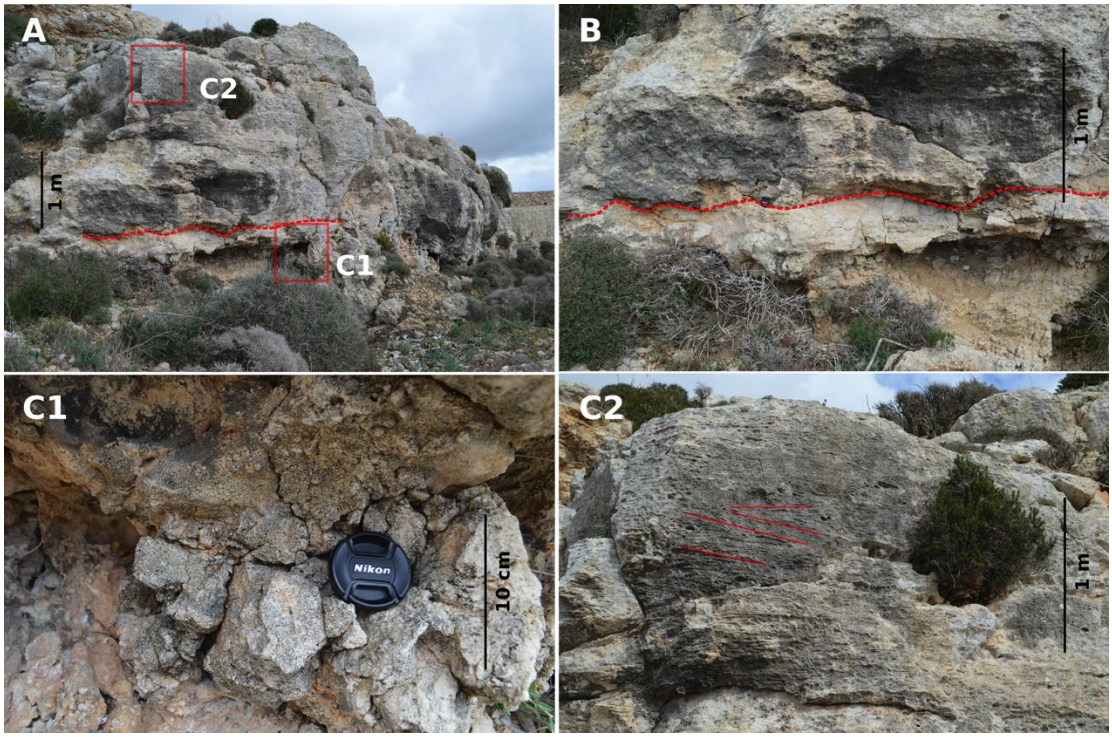

Figure 5.40: Detail of the sharp erosive contact that separates the Sand Shoal FA from the underlying Reef-Core FA. (A) Outcrop displaying sharp contact (red dashed line) that separates the Sand Shoal FA (above red dashed line) from the underlying Reef-Core FA (below red dashed line). (B) Closer view of the sharp contact (red dashed line). (C1) Detail of the Reef-Core FA, and (C2) detail of the Sand Shoal FA indicating cross-bedding (locality Dingli MT16).

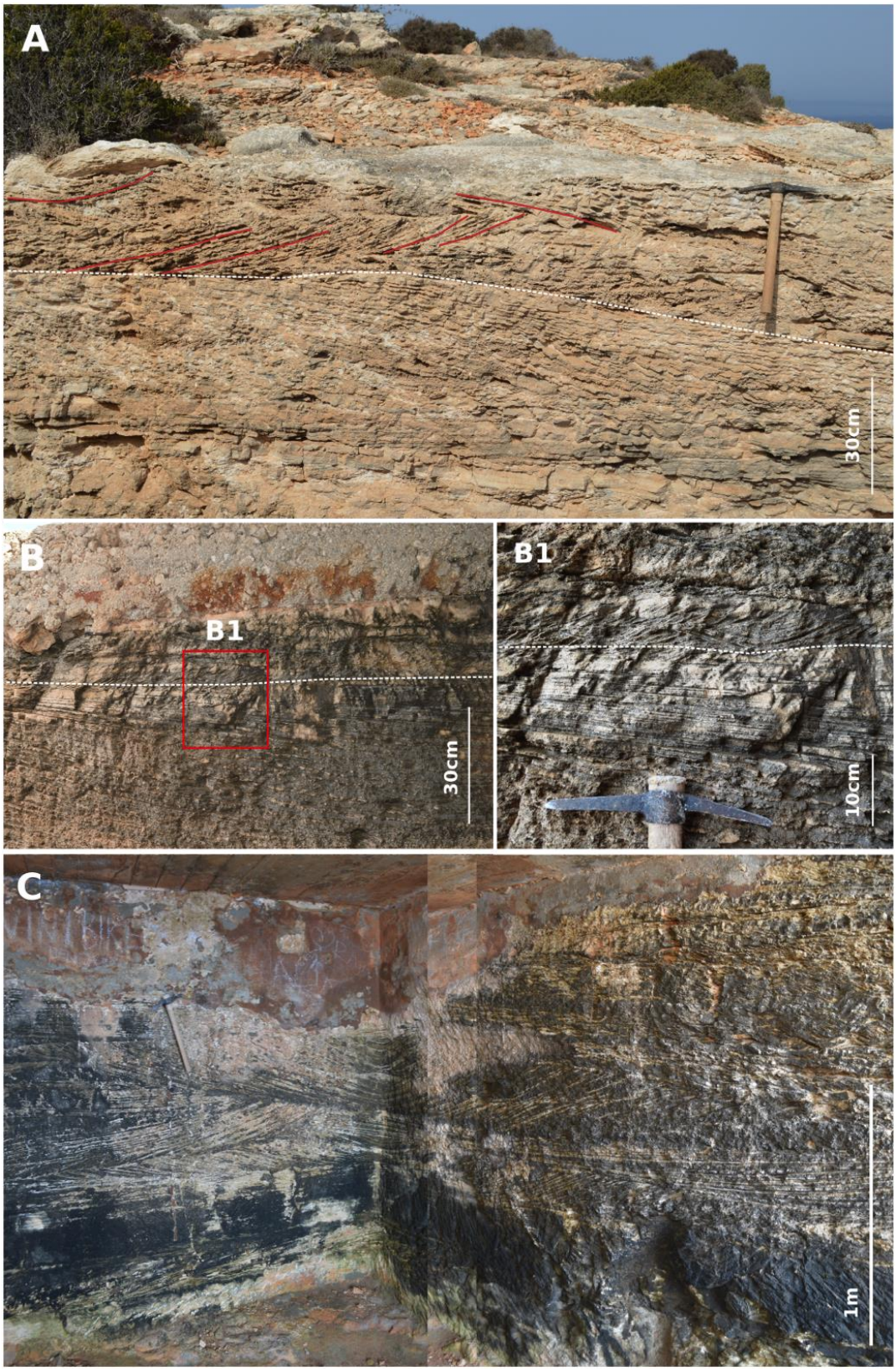

Figure 5.41: Features of the SS and WR Facies. (A, B and C) Outcrops contain a thick (<5 m) accumulation of SS Facies (locality MT22). (A and B) White dashed line demarcates the underlying SS Facies from the overlain WR Facies. (B1) Detail of the SS and WR Facies cross-bedding bedforms. WR Facies consists of cosets that are 10 to 20 cm thick with individual cross-lamina being 1 to 5 mm thick. (C) Detail of SS cross-bedding bedforms in 90 degree re-entrant illustrating trough cross-bedding with sets that are 0.1 to 0.3 m thick and co-sets that are 0.2 to 0.5 m thick.

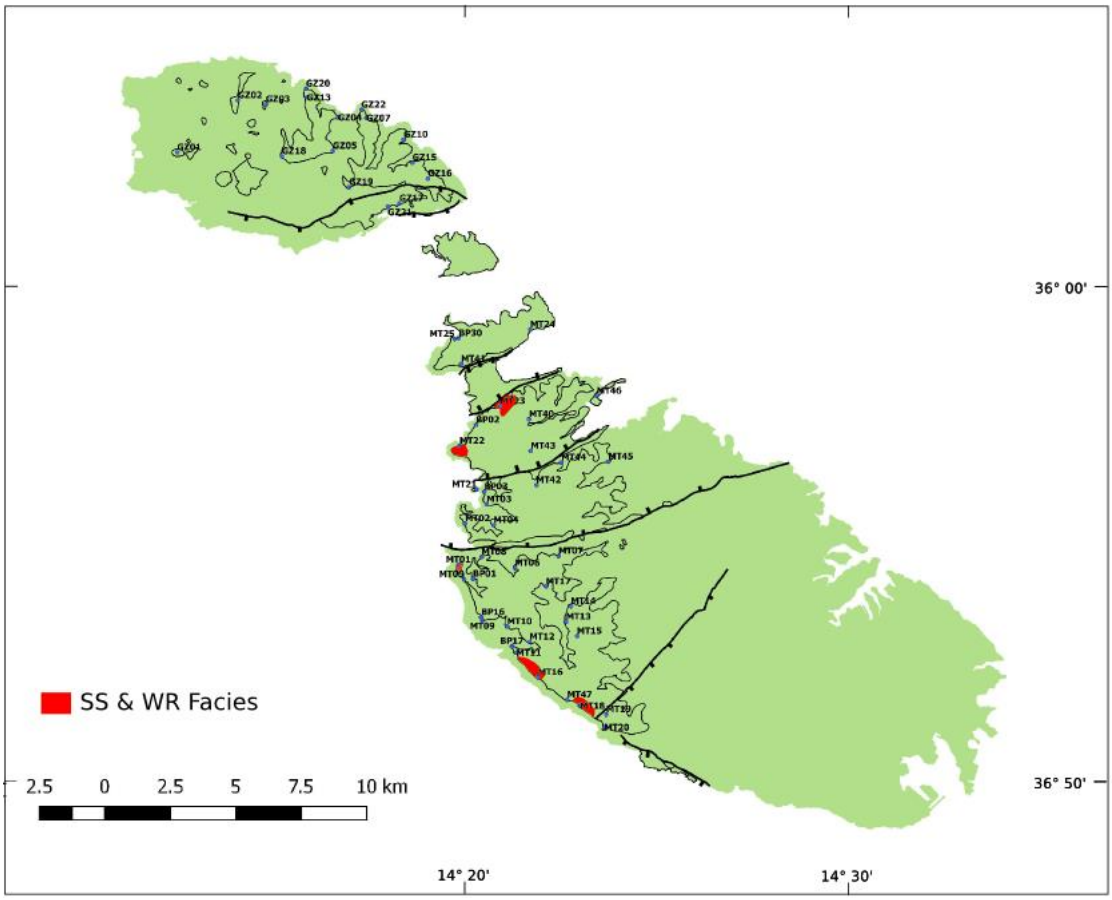

Figure 5.42: Facies map of the Sand Shoal Facies Association. Facies map is based on outcrop observations.

Petrographic description

Sample DB Tat-Tomna 2 (figure 5.43) was assessed in terms of grain sizes, grain composition, porosity and cement (table 5.13). Results indicate that sample is a very-well to well sorted grainstone. Ranking of observed grains demonstrates a dominance fine to very fine-grained peloids that are present in 35% of all counted points. The peloids are elongate, ovoid, dark-coloured micritic grains that are homogeneous and do not show internal structures with sizes <100µm. These observed characteristics are diagnostic criteria of fecal pellets (Flugel, 2010). Foraminifera rank second occurring in 4% of points counted, 2% as undifferentiated intact tests and 2% as Miliolid intact tests (<0.6 mm). Fine to very fine sand sized ooids rank third and are present in 1% of all counted points. In thin section the micritic ooids appear dark, featureless and microcrystalline due to pervasive micritization of the cortex (*cf.* Flugel, 2010). Aragonite ooids can be transformed to micritic and microsparitic ooids by the activity of microborers or *in situ* calcitization (Popp & Wilkinson 1983; Flugel, 2010) or dissolved and preserved as moulds (figure 5.43). Undifferentiated coralline algal fragments and molluscan fragments were very rarely observed in the sample.

Thin Section	Mud matrix %	F-VF Sd %	M Sd %	VC-C Sd %	VF Grv %	Pebble %	Porosity %	Cement %
Tat-Tomna 2	0.00	38.34	0.70	0.35	0.00	0.00	23.00	37.60

Table 5.13: Grain sizes, porosity and cement observed in the assessed thin section. 500 points were counted for both thin sections.

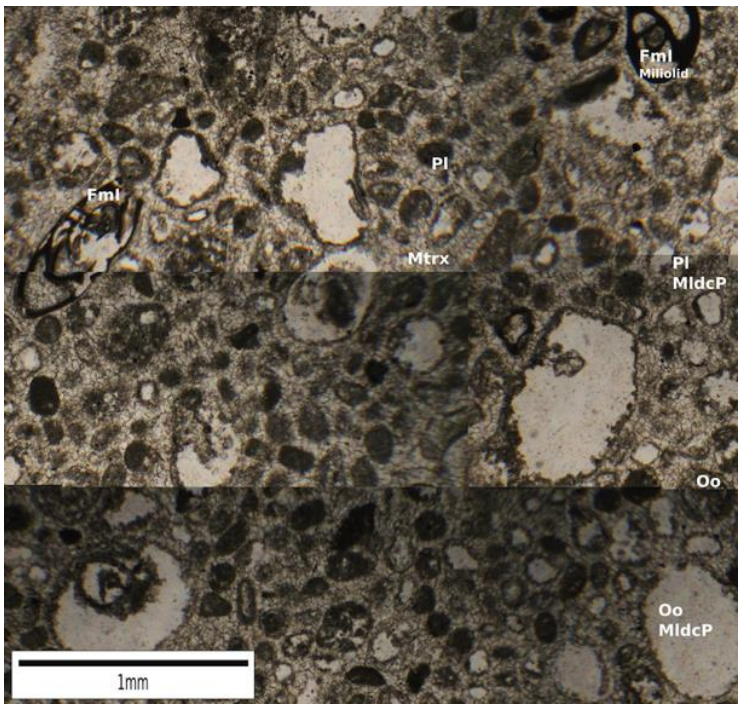

Figure 5.43: Photomosaic of photomicrographs of Tat-Tomna 2 of the SS Facies. The thin section consists of Oo, Ooids; FmI, Foraminifera intact; Pl, Peloids; MldcP, Moldic porosity from dissolution of unknown, abraded, possibly skeletal clasts and ooids (e.g. bottom right of micrograph); Mtrx, Matrix.

Fauna and Flora

Fossil components are sparse but bivalve, gastropod and echinoid debris are occasionally observed.

Depositional environment

The trough cross-stratification observed in the facies was probably produced by migrating 3-dimensional sand dunes. Dunes are the next bedform to develop with increasing flow strength beyond the upper limit of ripples. The change in bedforms, from dunes in the SS Facies to wave ripples in the overlying WR Facies, is interpreted to result of a reduction in flow strength. This may be the due to a relative shallowing from the shallow nearshore to foreshore zones.

The scarcity of sessile and mobile benthos in the facies suggests that periods of stabilization were not long enough for shelled organisms to become established. Feldman & McKenzie

(1993) suggests that a decrease in faunal diversity commonly correlates with increased sediment mobility. Highly unstable and constantly shifting substrates are inhabited by only a few shelly benthos. In view of the very sparse fauna observed in the SS Facies, it is suggested that the grains were frequently shifting, and consequently inhabited by only a few shelly benthos. The extensive bioturbation also suggests that the shoals may have become temporarily inactive. This suggests that the turbulent energy conditions may have been transient.

Peloids (faecal pellets) and ooids were also observed in thin section. Faecal pellets are produced in tropical shallow-marine tidal marine and in non-marine environments. They are more commonly preserved in sub-tidal and lower intertidal zones of inner platform or ramp settings subject to low water energy and reduced sedimentation rates (Flugel, 2010). The laminae within the observed ooids are obliterated or absent. This suggests a shallow-marine environment (Flugel, 2010). Marine ooids occur in intertidal and shallow sub-tidal marine environments (e.g. Simone, 1981). Excellent examples of modern marine ooids include those from the Bahamas, the Persian Gulf, the Red Sea and the Great Barrier Reef where the distribution of ooid sand shoals is restricted to high-energy zones along open bank margins (Flugel, 2010).

The SS Facies is interpreted to represent migrating 3D sand shoals formed in very shallow intertidal and shallow sub-tidal high-energy inshore marine environments. Interpretations correspond to those made by Pedley (1975; 1978; 1979) and Dart (1991). The facies may have formed a shoal margin to a shallow area of the platform. This implies a change in margin from reef rimmed (Reef-Core FA) to shoal margin as is observed in the Bahamas today.

5.3.6.2. Wave Ripple Packstone Facies (WR)

Description

The WR Facies is a pale-grey fine-grained peloidal, ooidal and bioclastic packstone. The cross-bedded facies exhibits cosets that are 10 to 20cm thick with individual cross-lamina being 1 to 5mm thick (figure 5.41A and 5.41B). The cross-beds exhibit small-scale scour and fill and small-scale (wave?) ripples. Bedding is commonly disrupted by bioturbation. The beds are only developed in the westernmost areas of the Malta and when present are typically 1 to 2 m thick.

Petrographic description

Sample MT16/S7 (figure 5.44) was assessed in terms of constituent composition, grain size and sedimentary constituents (table 5.14). Results indicate that sample is a moderately well to moderately sorted packstone. Ranking of observed grains demonstrates a dominance of very fine to medium sand-sized peloids present in 28% of all counted points. The peloids are similar to those observed in the SS Facies and were therefore interpreted as fecal pellets. Very fine to medium sand-sized ooids rank second and are present in 13% of counted points. Ooid laminae

are obliterated or absent, due to a pervasive micritization of the cortex (Flugel, 2010). In thin sections micrite ooids appear dark, featureless and microcrystalline and are similar to those described from the SS Facies. Foraminifera rank third occurring in 7% of points counted, 4% as intact multichamber triserial and multichamber planspiral foraminifera tests and 3% as undifferentiated foraminifera fragments (<0.6mm). Undifferentiated very fine to medium sand-sized coralline algal ranks fourth (2.5% of counted points). The sample corresponds with the oopeloid grain association.

A key difference between the SS and WR Facies is the absence of matrix and presence of cement (37.6% of all points counted) in the prior facies and the absence of cement and presence of matrix (41.60%) in latter facies. Otherwise, both facies have comparable quantities of non-skeletal grains (36% to 41%) and skeletal grains (5% to 10%). Peloids also rank first in both samples (28% to 35% of all counted points). While the facies cannot be distinguished at the microfacies scale, the key distinct criteria at their different bedforms.

Thin Section	Mud matrix %	F-VF Sd %	M Sd %	VC-C Sd %	VF Grv %	Pebble %	Porosity %	Cement %
MT16/S7	41.60	46.05	47.37	6.58	0.00	0.00	8.20	0.00

Table 5.14: Grain sizes, porosity and cement observed in the assessed thin section. 500 points were counted for the thin section.

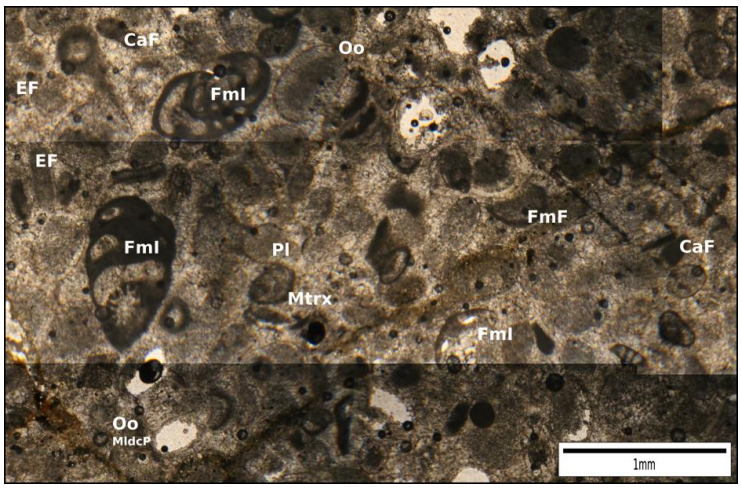

Figure 5.44: Photomosaic of photomicrographs of MT16/S7 of the WR Facies. The thin section consists of Pl, peloids; FmF, Foraminifera fragments; FmI, Foraminifera intact; CaF, Coralline algal fragments; Oo, Ooids; EF, Echinoid fragments; MldcP, Moldic porosity from dissolution of unknown, abraded, possibly skeletal clasts and ooids; Mtrx, Matrix.

Fauna and Flora

Fossil components are sparse but bivalve, gastropod and echinoid debris are occasionally observed.

Depositional environment

Cross-beds exhibit small-scale scour and fill and small-scale ripples. These bedforms are interpreted as 3D asymmetrical linguoid wave ripples. This interpretation corresponds to that by Pedley (1974). The bed is often bioturbated, suggesting that the sand shoals may have at times been inactive. Microfacies analysis indicates the assessed sample consists of moderately to poorly sorted very fine to medium sand. Grains are transported particles that are generally broken and abraded, sub-rounded to well-rounded fossils. This suggests that the WR Facies was deposited in moderately agitated water. Additionally, the WR Facies contains matrix (41.60%) while the SS Facies does not. This indicates that the WR Facies was deposited in lower-energy environments that the SS Facies. Such low-energy environments may have been developed within a sheltered foreshore marine environment. The WR Facies therefore represents a shallowing-up in marine depth from a higher-energy nearshore (SS Facies) to a lower-energy foreshore marine environment.

The observed depositional geometries and microfacies analysis suggests the WR Facies consists of wave ripples formed in very shallow conditions within the fair weather wave base. The vertical sequence observed in the Sand Shoal FA, from SS to WR Facies, records a progressively shallower marine depositional environment.

CHAPTER 6: DEPOSITIONAL HISTORY AND SEQUENCE STRATIGRAPHY

6.1. Introduction

This chapter investigates stratigraphic relations and the depositional history (section 6.2) for the facies within the Greensand and Upper Coralline Limestone (UCL) formations described in chapter 5. A sequence stratigraphic (section 6.3) and chronostratigraphic (section 6.4) scheme are then constructed. On the basis of this, a relative sea level curve is developed for the Late Miocene, Greensand and UCL formations (section 6.5).

The Late Miocene depositional units (Esteban, 1996; Cornée *et al*., 2004) developed in other Mediterranean carbonate platforms are then compared to those observed in Malta (section 6.5). This comparison investigates whether the relative sea level curve for the shallow-water Upper Coralline Limestone Formation may have been largely controlled by local tectonic processes or by eustatic factors (driven by variations in accommodation) or by other controls (e.g. climate, marine chemistry). The Maltese Late Miocene relative sea level curve is then compared to other sea level curves that have been constructed for contemporaneous carbonate platforms across the Mediterranean (section 6.6). The section also discusses the controls that may have contributed towards the similarities and differences in relative sea level curves for these contemporaneous Mediterranean carbonate platforms.

6.2. Stratigraphic relations (3D facies relations & correlations) and depositional history

6.2.1. Open Shelf FA

Dart *et al*. (1993) indicate that depth converted seismic sections of the Pantelleria Rift, including the Il-Maghlaq Fault (IMF), show thickness increases (up to 250 m) down hanging-wall dip slopes. Depth conversion was using the Dix equation and internal velocity analyses were used to derive specific depths for specific locations on the seismic section (Dart, 1991 p.114). The deposits, which accumulated within the hanging-wall during the early syn-rift, include the Middle and Upper Globigerina Limestone Members, the Blue Clay Formation, OSGR Facies (table 5.4), and Genetic Sequences 1 and 2 of the Upper Coralline Limestone Formation (Dart *et al*., 1993). Seismic interpretations are supported by field evidence from the hanging wall sub-basin of the IMF where a unique succession of Upper Coralline Limestone Formation platform and slope facies develops along the IMF footwall and hanging-wall respectively (Pedley, 1987; Dart, 1991 p.235; Dart et al., 1993). These observations suggests that the IMF developed fault-related bathymetric relief before the Late Miocene at which time the Greensand and Upper Coralline Limestone formations formed (section 2.2.2). In view of this, the IMF is defines the westernmost border of the Late Miocene Malta Fault-Block Platform (figures 6.1 and 6.7).

In east Gozo and throughout Malta, the OSGR Facies has a sharp basal contact with the Blue Clay Formation (Pedley, 1978). A relative sea level fall ended the deposition of the pelagic Blue Clay sediments and started the deposition of shallow marine OSGR Facies. The OSGR Facies was deposited under very turbulent conditions, associated with an open-water shifting substrate in a platform environment (see chapter 5 section 5.3.1.1).

Eustatic sea level fall and/or sustained uplift of the IMF footwall and the South Gozo Fault (SGF) footwall may have forced a further fall in relative sea level across the Maltese Islands. Progressively shallowing marine conditions extensively eroded into the OSGR Facies as indicated by the erosion surface between OSGR and overlying OSHR Facies (see chapter 5 section 5.3.1.2 figure 5.5C). The erosion surface is observed west of a line from Marsalforn (Gozo) to Mgarr ix-Xini (Gozo) (Pedley, 1978). Erosion was most pronounced in western Gozo within the Gozo Horst regional high where a significant portion of the Il-Gelmus Beds (OSGR Facies) and an upper part of the Blue Clay Formation were eroded before the OSHR Facies (Ghajn Melel Member) was deposited (Pedley, 1978) (literature review section 2.2.2.4). Pedley (1978) refers to this hiatus as the "*basal UCL erosion surface"*. Giannelli & Salvatorini (1975) argue that the hiatus is marked by an absence of zones NI6 and Nl7 of Blow (1969). At Qolla s-Safra and Tas-Salvatur (Gozo) (figure 2.3), the Qolla s-Safra Beds (OSGR Facies) are preserved below the basal UCL Formation. Pedley (1978) suggests that Qolla s-Safra Beds (OSGR Facies) are preserved due to pre-erosional downwarping along the eastern margin of the northern Greensand basin (Pedley, 1978). In view of this, it is suggested that the northern areas of the Gozo Horst may have presented deeper marine environments than southern areas. The deeper bathymetry would have preserved the beds from subsequent erosion from a relative sea level fall.

Following the "*basal Upper Coralline Limestone erosion surface"*, relative sea level rose. This created the accommodation within which the OSHR Facies accumulated. In Gozo, the OSHR Facies is observed across the entire Gozo Horst (Comino Straits). In Malta, the facies occurs in the west of Malta to the north-east of the IMF footwall high (figure 5.6).

The OSHR Facies is interpreted to represent linear sublittoral sand ridges orientated parallel to a coastline lying to the west of the present islands. As sea level rose wave ravinement in nearshore environments in western areas (within the IMF footwall high) of the Maltese Islands eroded into seabed deposits that consisted of OSGR deposits. The sediments that were reworked from adjacent shallow water areas were subsequently transported eastwards (basinwards) forming the OSHR Facies. The reworked and Fe-impregnated sands of the OSHR Facies are here interpreted as a transgressive lag. As relative sea level continued to rise, less material was eroded and re-deposited within the Maltese Islands and deposition of the OSHR facies ended.

6.2.2. Coralline Algal Biostrome Facies Association (FA)

The Coralline Algal Biostrome FA consists of a mosaic of sedimentary facies that formed a low relief platform of rhodalgal carbonate factory in moderate water depths (Bosence & Pedley, 1982). The biostrome is arranged in a NNW-SSE oriented facies belt that in Malta trends obliquely across the IMF footwall high (figure 6.1 facies map and Appendix C2 for related outcrop cross sections). A study by Pedley (1976) on facies distributions and the form of bryozoan growth-forms suggests an easterly-directed current flow. This is supported by easterly oriented cross beds observed in the field (e.g. MT01). This is consistent with paleocurrents for central Mediterranean at this time that was subject to eastward flow at the surface (e.g. Meijer *et al*., 2004).

As RSL rose, deposition of the OSHR Facies (Open Shelf FA) gradually diminished and accommodation space within the uplifted Victoria Lines Fault (VLF) footwall high was created. The VLF footwall high may have been better illuminated than deeper areas south and southwest of VLF and hanging wall lows (northeast of VLF). Illuminated areas accumulated CASR Facies while deeper and more sheltered areas accumulated the CAF Facies (figure 7.2 OCS1 MT16 to BP1). The orientation of CASR prograding beds also suggests SSW progradation (see chapter 5 section 5.3.2.1) into deeper waters where the lower energy CAF Facies outcrops (e.g. MT05, MT09, MT10). The CASR Facies demonstrates a fining upward sequence. This suggests that the VLF footwall area was subject to increasingly deep and low energy marine environments. Relative sea level rise outpaced CASR Facies sedimentation rates and the deposition of this facies diminished. It is suggested that under these deeper and lower energy marine conditions deposition of the lower energy CAF Facies may have continued. As the rate of relative sea level rise gradually diminished and sea levels stabilised, sedimentation rates of the CAP Facies outpaced the rates of base-level rise. This developed the aggradational and progradational geometries observed in western area of Malta. Relative sea level then gradually fell, exposing the CAD Facies to increasingly turbulent and higher energy environments possibly within or close to the storm/fair weather wave base that brought to an end the shallowing-upward trend of the Coralline Algal Biostrome. The corals observed in the Coralline Algal Biostrome FA display an up-section change in morphology. These change from wavy plate in the Rhodolith Pavement Sub-Facies to wavy plate and domal dish morphologies in the CAD Facies. Their wavy plates and dish morphology therefore indicates formation in water depths between 30m and 60m (see Pomar *et al.,* 1996). Thus the widespread shallowing in the Maltese Islands reworked the Coralline Algae Biostrome FA and generated the CAD Facies. As relative sea level continued to fall, a regionally extensive erosive boundary was formed that eroded into the CAD Facies (figure 5.33 and 5.34). The relative sea level fall exposed westernmost parts of Malta (e.g. MT01, MT05) to sub-aerial environments (see section 5.3.4).

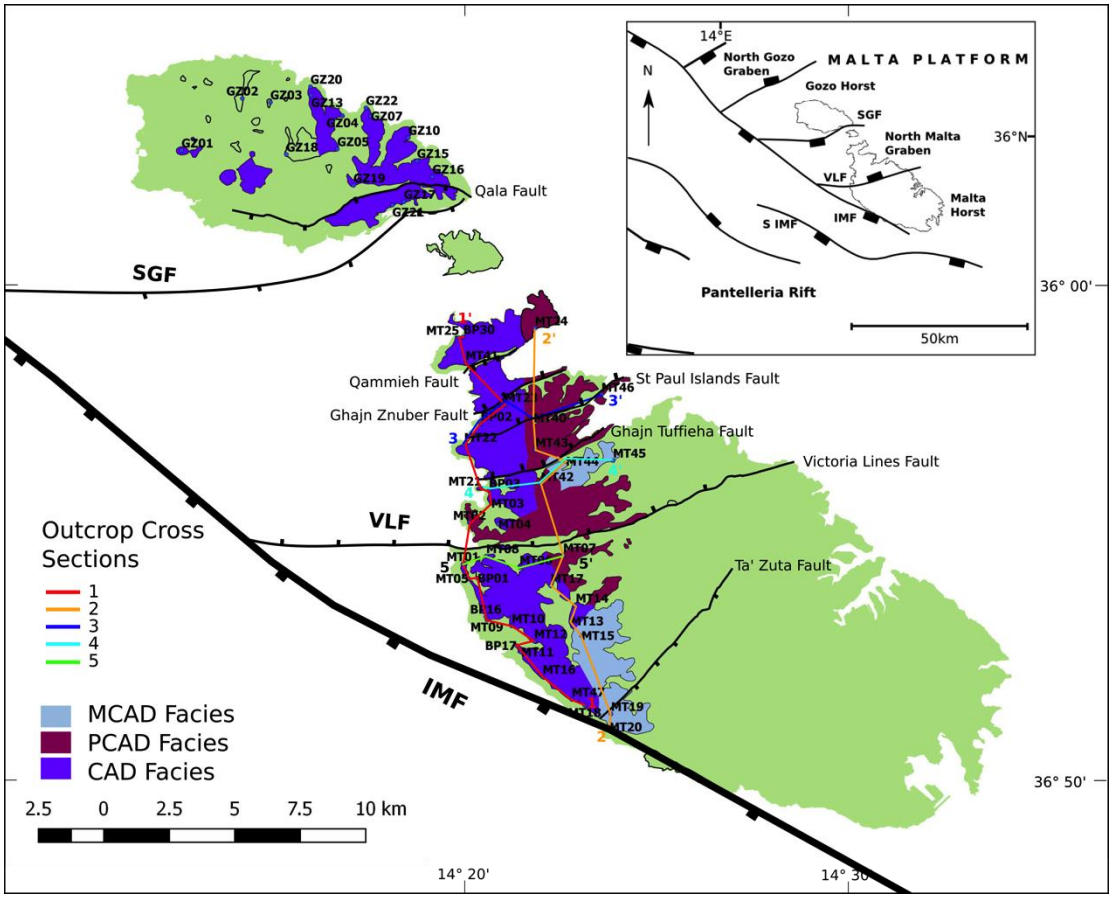

Figure 6.1: Facies map depicting the facies of the Coralline Algal Biostrome FA and the Sheltered Shelf FA are visible in this facies map. For facies maps that show the entire distribution of particular facies see figure 5.10 for CASR and CAF Facies, figure 5.17 for CAP Facies, figure 5.21 for CAD Facies, figure 5.23 for MCAD Facies and figure 5.24 for PCAD Facies. Smaller scale map of Malta platform (top right corner) showing the extent of the IMF and SGF and how these relate to the Pantelleria rift (modified from Dart, 1991 and Dart *et al*., 1993). See figure 6.2 for generalised lithostratigraphic and sequence stratigraphy diagram with average stratigraphic thickness of facies and facies associations.

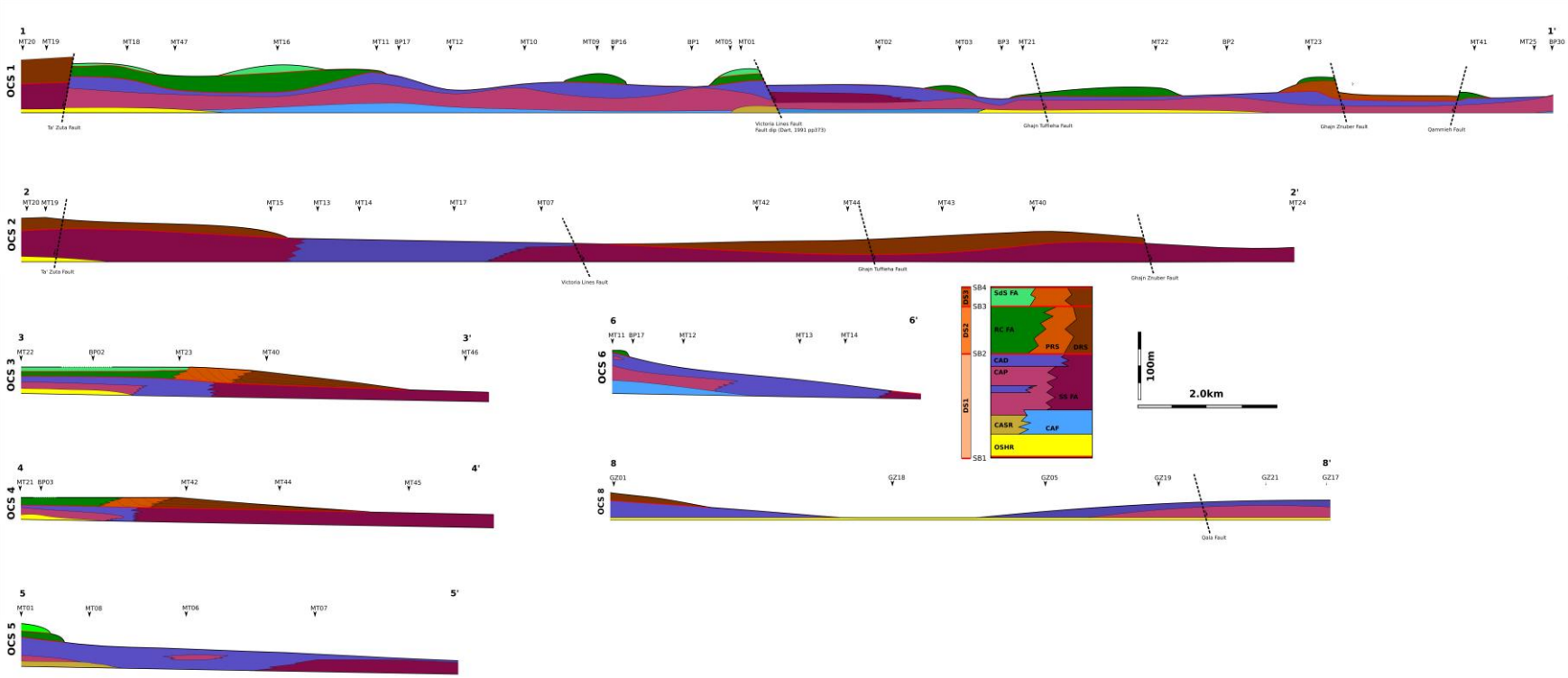

Figure 6.2: Outcrop cross sections (OCS 1, 2, 3, 4, 5, 6 and 8). When these are viewed alongside facies maps this allow a 3D picture of facies relations can be considered. See figure 6.1 and 6.3 for position of outcrop cross sections in maps. Base of OCS logs correspond to top of Blue Clay Formation. Fault dips are from Dart, 1991 (pp. 370, 373 and 374). The OCS 1 and 2 are South to North along facies strike. The facies in cross section 1 do not significantly vary along strike (except across the Ta' Zuta and Victoria Lines Fault). The OCS 3, 4, 5 and 6 are west to east in Malta and show similar proximal to distal facies changes. The OCS 8 represents a west to east section in Gozo and shows a different facies change (proximal to distal) than west to east sections in Malta (e.g. OCS 4). This is because the east part of the OCS 8 is in the footwall high of the South Gozo and Qala faults (southeast of Gozo). These eastern areas in Gozo are shallower than central parts of Gozo and eastern areas in Malta. Consequently, there are different west to east facies changes in Gozo than in Malta (e.g. OCS 4). Note: bold black line represents modern day surface, bold red line represents Miocene sequence boundaries.

Palaeobathymetry

Accumulations of the *in situ* CAF and CAP Facies are limited to the western areas of Malta and gradually diminish eastwards (figure 6.1 and 6.2 OCS3, 4 and 5). The absence of *in situ* coralline algal facies in central and eastern areas indicates that these regions were hostile to coralline algal growth.

The distribution of *in situ* CAF and CAP Facies may be the result of eastward flowing currents that upwell on the westerly facing margins of the IMF footwall. Upwelling may have produced favourable conditions for coralline algal growth. The dominance of rhodalgal facies could thus represent the influence of cooler, nutrient-rich waters or persistent upwellings (Esteban, 1996). Such currents may have previously existed within the Pelagian Block and are thought to have developed the phosphatic hardground surfaces within the Globigerina Limestone Formation (Pedley & Bennett, 1985).

Coralline algae, however, occur in a wide range of climatic settings (from arctic to tropical), can thrive in depths to 100 m and under high- and low-nutrient conditions (e.g. Peres & Picard, 1964; Blanc, 1968; Bosellini & Ginsburg, 1971; Adey & Macintyre, 1973; Testa & Bosence, 1999 Bosence, 1983, 1985; Iryu *et al*., 1995; Basso, 1998). Additionally, global distributions illustrate that rhodalgal facies reached peak abundances from the late-early to early-late Miocene (Burdigalian–early Tortonian) in part due to globally cooler temperatures following a climatic optimum in the early-middle Miocene contributed (e.g. Halfar & Mutti, 2005). It is unlikely that marine chemical or thermal conditions differed so significantly between western and eastern areas of Malta (across <2.5 km) to prevent coralline algal growth. In view of this, it is proposed that the eastern Maltese areas may have been deeper than the maximum depth at which coralline algal development occurs, that is > *circa.* 100 m (e.g., Adey & Macintyre, 1973; Bosence, 1983; Testa & Bosence, 1999; Johansen, 1981; Steneck, 1986; Matsuda & Iryu, 2011). There also is an eastward decline and transition from the CAP Facies, to the CAD facies and then the Sheltered Shelf FA (figure 6.2 OCS 3,4).

Observations carried out in this thesis suggest that during the deposition of the Coralline Algal Biostrome FA and Sheltered Shelf FA, the Malta Fault-Block Platform (Malta Horst and Graben) may have been characterised by a <2° dip to the east (figures 6.7, 6.8 and 6.9). This interpretation is based on the distribution of the contemporaneous CAP, CAD, MCAD and PCAD Facies and their interpreted depth of deposition. The CAP Facies transitions to the Sheltered Shelf FA over a distance of 1.8 to 3 km (e.g. MT44-MT24, BP02-MT40, MT22-MT43, MT03-MT43, MT06-MT07, MT44-MT24). The Sheltered Shelf FA may have been deposited in sheltered environments with depths similar to or 20 to 40 m greater than the maximum depth of *in situ* coralline algal accumulation (>100 m). This is supported by the lack of evidence for a marked change (<5°) in topographic slope in outcrop (figure 5.23). On the basis of these values, one can interpret an eastward dipping palaeobathymetric slope of between

0.4° (3 km horizontal distance and 20 m relief) to 1.8° (1.8 km horizontal distance and 40 m relief) across the tilted North Malta Graben and Malta Horst fault blocks.

Tectono sedimentary development

The CASR, CAP and CAD Facies are the first to record thickening along the VLF footwall high (figure 6.1 and 6.2 OCS1). This corresponds to interpretations by Dart (1991 p.373). The CAP and CAD facies also record thickening along the SPIF footwall in the Mellieha horst block (figure 5.18). These observations suggest that VLF and SPIF developed bathymetric footwall relief during deposition of the Coralline Algal Biostrome FA. During early stages of Coralline Algal Biostrome FA deposition, the VLF produced sufficient bathymetric relief to develop the CASR Facies on the VLF footwall and not within the hanging-wall.

During the early stages of CAP deposition, the bathymetric relief on the VLF was however not significant enough to cause facies partitioning of the CAP Facies between footwall and hanging-wall successions. This is supported by the presence of Rhodolith Pavement Sub-Facies in both the Malta Graben north of the VLF (e.g. MT02; MT03, MT04, MT21, MT22, MT41, MT25) and Malta Horst (e.g. MT01, MT05, MT16) (figure 6.1 and 6.2 OCS1). The CAP Facies in the VLF footwall (e.g. MT01, MT05) is however thicker than that observed in the VLF hanging wall (e.g. MT02) (figures 6.2 OCS1 and 6.9). Thicker accumulations of CAP Facies formed in uplifted areas relative to downthrown areas (figure 6.1 and 6.2 OCS1 see MT08, MT10, MT16, MT18 figure 5.18 division 3.2 thickness map). The uplifted footwall highs of the IMF, VLF and SPIF faults may have been shallower, better-illuminated areas than the hanging-wall lows allowing for enhanced coralline algal production (figure 6.9). The Coralline Algal Biostrome in uplifted areas would also have been subject to higher wave and current energy with cleaner and clearer sediment-free waters. As the CAP Facies formed, eroded sediments may have contributed towards the formation of CAD Facies (e.g. MT13, MT14, MT17). With shallowing, large quantities of coralline algal debris were generated from the uplifted areas and transported eastwards, contributing to the formation of the Coralline Algal Debris Packstone Facies (MT13, MT14, MT17).

The westernmost outcrop of the VLF hanging wall (MT02) contains a unique succession where the CAP Facies is overlain by the Sheltered Shelf FA (figure 6.1 and 6.2 OCS1 see outcrop log MT02). It is suggested that as throw on the VLF increased, during the deposition of CAP Facies, this led to facies partitioning between the VLF footwall high (Malta Horst) and the VLF hanging wall lows (Malta Graben) (figure 6.9). Within the VLF footwall, high-energy, shallow marine environments predominated and deposition of the CAP Facies continued (MT01). In the VLF hanging wall depressions, sheltered deeper-marine environments were formed leading to the deposition of PCAD Facies. Thus, fault induced differential subsidence rate influenced

sedimentary processes such that the rate of hanging-wall sea level rise would have been greater than the rate of footwall sea level rise.

6.2.3. Sheltered Shelf Facies Association (FA)

The Sheltered Shelf FA is interpreted as the eastern seaward lateral equivalent of, and contemporaneous with, the Coralline Algal Biostrome FA (figures 5.23, 6.1 and 6.2 OCS3 and OCS4). This corresponds to Pedley's (1975; 1978) and Bosence & Pedley's (1982) interpretations. Evidence for contemporaneity of the Sheltered Shelf FA and Coralline Algal Biostrome FA is from three observations made in this study (section 5.3.3).

The Sheltered Shelf FA may represent storm and/or current reworked sediment originating from the Coralline Algal Biostrome FA. This interpretation is supported by the similar nature of the allochems of the aforementioned facies associations and a west to east decline in coralline algal debris grain size. Initially this reworking developed a thick sequence of coarse-grained CAD Facies (e.g. MT06), and when transported further eastward, develops the Facies of the Sheltered Shelf FA (e.g. MT07). Sedimentological and petrographic observations suggest the MCAD Facies was formed under higher-energy environments than the PCAD Facies. The MCAD may have formed within an exposed shelf environment while the PCAD may have formed in sheltered shelf environment. Over time the CAD Facies prograded eastwards and locally overlies the Sheltered Shelf FA (MT07) (figures 6.1 and 6.2 OCS5). The occurrence of higher-energy Coralline Algal Biostrome FA in the west of Malta and lower-energy Sheltered Shelf FA in the east of Malta suggests an eastward deepening slope and/or reduction in current energy across the Malta Platform.

In the southwest of the Malta Horst (MT19, MT20), the OSHR Facies (relatively high energy) are overlain by a thick accumulation of Sheltered Shelf FA (figure 6.2 OCS2). This succession is distinct from that observed in western areas of the Malta Horst where the OSHR Facies underlies the Coralline Algal Biostrome FA (e.g. MT16, MT47, MT18). These observations suggest that western areas of Malta were subject to shallower marine environments than south-western areas of Malta that were subject to sheltered and deeper marine environments. The southwest of the Malta Horst (outcrops MT19 and MT20) display a shallowing-upward succession of PCAD (relatively low energy) to MCAD (relatively higher energy) Facies. This shallowing may coincide with the upward shallowing observed in the Coralline Algal Biostrome FA. The boundary between the MCAD Facies and overlying DSR Facies in MT19 and MT20 may also correlate to the SB2 between the Coralline Algal Biostrome FA and the Reef Core FA.

The VLF hanging wall (MT02) also contains a distinct succession. The relatively shallow-water and high-energy CAP Facies are overlain by the sheltered/deep water PCAD Facies that are in

turn overlain by the shallow water and high-energy CAD Facies. The deepening and then shallowing trend is distinct from that observed in the rest of the Maltese Islands where the Coralline Algal Biostrome FA is subject to a continuous upward shallowing and increase in water energy. It is suggested that during the deposition of CAP Facies, bathymetric relief on the VLF hanging wall increased to gradually reduce then halt deposition of CAP Facies. The PCAD Facies was then deposited with sediment probably originating from uplifted VLF footwall areas where the CAP Facies continued to form. This interpretation is supported by thickness distributions of the Sheltered Shelf FA. The VLF contains a thickened succession of the PCAD Facies (figure 5.29) that may have resulted from syn-depositional tectonic activity that produced hanging-wall depocentres. As relative sea levels subsequently fell across the Maltese Islands, the VLF hanging wall was exposed to higher energy regimes and the CAP Facies formed.

6.2.4. Reef-Core FA

After the west of Malta was subject to erosion, at the top of the Coralline Algal Biostrome FA (section 6.3.2.1), relative sea level subsequently rose and western areas of the Maltese Islands (along the IMF footwall) formed shallow marine environments within the photic zone. A chlorozoan (coral) factory, producing the Reef-Core FA, was subsequently established within western areas of the Maltese Islands. Both the CAD and CFR Facies contain a similar skeletal assemblage, though in different proportions, of coralline algal debris, rhodoliths and small corals with wavy plate to flattened domal morphologies. This suggests that, following the relative sea level fall that generated the widespread erosion surface, both facies formed in relatively shallow water depths within the photic zone (*circa* 30 to 60 m). However, following the deposition of CFR Facies, the high sedimentation rates from the chlorozoan factory in relation to the increase in accommodation led to aggradation and progradation that progressively reduced water depths. This led to the succession of progressively shallower marine Reef-Core FA, from CFR, CPR to the CR Facies, observed in western Malta (figure 6.3 and 6.4 OCS3 and OCS5). As relative sea levels fell, the chlorozoan factory gradually replaced the rhodalgal factory. A gradual change in other marine conditions (e.g. temperature, salinity and nutrients), are thought to have controlled the shift from rhodalgal to coralgal factories (see chapter 8 section 8.3.2).

The Reef-Core FA is arranged in a NNW-SSE oriented facies belt across the Maltese Islands and trends obliquely across the IMF footwall high (figure 6.3). This corresponds to Dart's (1991 pp297) observations. In Gozo, the Reef-Core FA may have also occurred in offshore areas possibly towards the IMF footwall high. This is supported by the presence of eastward dipping PRS and DRS Facies in the western area of onshore Gozo (GZ01) (figure 6.2 OCS8). The observed facies orientation and trend may be the result of more rapid progradation of the Reef Core FA in west and northwest areas of the Maltese Islands than in southwest areas within

the Malta Horst (MT20 and MT19). The uneven rate of progradation would have produced NNW-SSE facies trend that is obliquely to, and not parallel to, the IMF. Field evidenced supports the interpreted eastward prograding Reef Core FA (see section 5.3.4.1 and 5.3.5.1). Additionally, the presence of deeper-water PCAD, MCAD, DRS Facies in the southwest areas in the Malta Horst (MT19 and MT20) than in western areas of Malta, where shallow-water CAP FA and Reef Core FA occur (e.g. MT16, MT22 and GZ10), supports the interpreted difference in depth between west and southwest areas within the Malta Horst.

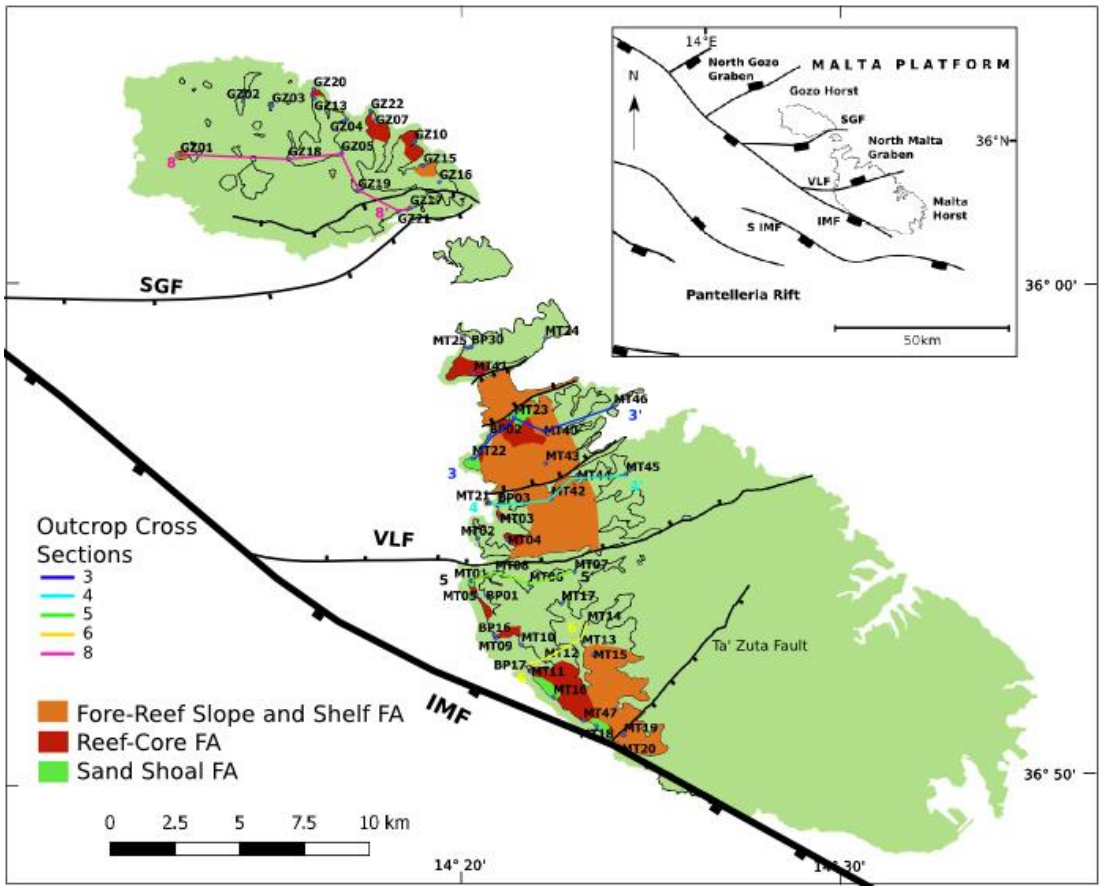

Figure 6.3: Facies map depicting the facies that cap the Coralline Alga Biostrome FA and the Sheltered Shelf FA. Offshore extent of IMF and Pantelleria rift also shown. Not all the facies of the Reef-Core FA, Fore-Reef Slope and Shelf FA and Sand Shoal FA are visible in this facies map. For facies maps that show the entire distribution of particular facies see figure 5.30 for Reef-Core FA Facies map, figure 5.37 for Fore-Reef Slope and Shelf FA facies map, and figure 5.42 for Sand Shoal FA facies map. Smaller scale map of Malta platform (top right corner) showing the extent of the IMF and SGF and how these relate to the Pantelleria rift (modified from Dart, 1991, Dart *et al*., 1993). See figure 6.2 for generalised lithostratigraphic and sequence stratigraphy diagram with average stratigraphic thickness of facies and facies associations.

6.2.5. Fore-Reef Slope and Shelf Facies Association

The shallow marine Reef-Core FA is replaced eastwards (basinwards) by the deeper marine Fore-reef slope and Shelf Facies Association. The Fore-Reef Slope and Shelf FA occurs immediately eastward of the Reef-Core FA and Sand Shoal FA and forms a NNW-SSE oriented facies belt across the Maltese Islands (figure 6.3). The Fore-Reef Slope and Shelf FA is interpreted to represent reworked sediment originating from the Reef-Core FA and Sand Shoal FA to the west. This interpretation is supported by the close spatial relationship and the similar nature of the PRS allochems to those observed in the Reef-Core FA (e.g. MT23/S4 in petrographic description) and Sand Shoal FA (e.g. MT15/S4 in petrographic description). The Gebel Ciantar locality displays a near continuous west-east section where the Reef-Core FA (e.g. MT47, MT18), PRS and DRS Facies (MT19 and MT20) are in stratigraphic contact with each other (figure 5.36).

The Reef-Core FA and Sand Shoal FA produced large volumes of coral and coralline algal bioclasts and ooids. The sediments were shed from western areas and transported eastwards (basinwards) down a depositional slope by tide and gravity processes. Deposited sediments developed the eastwards (basinwards) prograding sigmoidal clinoforms observed within the PRS and FRS Facies. Clinoform geometries in the PRS Facies are up to 30 m thick (figure 5.36 interpreted cliff outcrop). This suggests a reefal platform margin relief up to 30 m in height. The PRS overlie the DRS Facies in western and central areas of Malta. This also suggests an eastwards prograding reef slope. The facies distribution suggests shallow marine environments existed along the IMF footwall area and progressively deeper marine environments occurred eastwards (basinwards).

6.2.6. Sand Shoal Facies Association (FA)

Following the deposition of the Reef-Core FA, marine shallowing continued in western areas a sharp erosive contact was developed that separates the underlying Reef-Core FA from the overlying Sand Shoal FA (section 6.3.4 and figure 5.40). This corresponds to observations by Pedley (1978) who notes that the CR Facies (Depiru Beds) were truncated by a prominent erosion surface. Shallowing may be the result of normal regression and/or relative sea level fall. Subsequently, relative sea level rose to establish marine depths of 10 m or less within which the Sand Shoal FA were deposited.

The Sand Shoal FA caps the Reef-Core FA in western areas of both the Malta Horst (MT01, MT16) and Graben (MT22, MT23) (figure 6.2 OCS1, OCS3 and OCS5 and figure 6.3). This suggests that western areas of Malta were of similar paleodepth. That is, while the ENE-WSW VLF and SPIF may have locally expressed bathymetric relief, it was significant enough to cause facies partitioning/distribution across the entire North Malta Graben.

6.3. Sequence Stratigraphy

The facies described in this chapter are here divided into three depositional sequences (DS) (figures 6.6, 6.7, 6.8 and 6.9. Each depositional sequence comprises a relatively conformable succession of genetically related strata bounded by unconformities or their correlative conformities. One can demonstrate that the depositional sequences are the response to cyclical variations in relative sea level by considering (i) facies palaeobathymetry, (ii) relative elevations of successive facies, (iii) thickness of platform facies, and (iv) stratal geometries.

6.3.1. Depositional Sequence 0 (DS0)

The OSGR Facies (Greensand Formation) was deposited in warm, shallow (*circa* 50 m) and high-energy marine environments of the shoreface/littoral zone. Continued shallowing marine conditions formed an extensive erosion surface between the OSGR Facies (DS0) and the overlying OSHR Facies (DS1) (Pedley, 1978 p.8). Erosion was most pronounced in western Gozo where a significant portion of the Il-Gelmus Beds (Greensand Formation) and an upper part of the Blue Clay Formation were eroded before the OSHR Facies was deposited (Pedley, 1978). Pedley (1978) refers to this hiatus as the *basal Upper Coralline Limestone erosion surface*. Giannelli and Salvatorini (1975) argue that this hiatus is marked by an absence of zones NI6 and Nl7 of Blow (1969). The erosion surface, which marks the end of DS0, forms a possible/proposed sequence boundary (SB1). No evidence of subaerial exposure was however observed in the areas assessed in this study.

6.3.2. Depositional Sequence 1 (DS1)

Following SB1, relative sea level rose thereby creating space within which the OSHR Facies accumulated. The OSHR Facies is interpreted to have formed in shallow shelf (*circa 20 to* 50 m) marine environments. Additionally, an average of 10 m of the OSHR Facies is preserved in the south west of Malta (MT47) and north of Gozo (GZ22). This suggests that the relative sea level rise must have been in the order of 30 to 60 m.

The OSHR Facies is interpreted to have formed linear, littoral-sublittoral sand waves and ridges deposited in high-energy shallow shelf within the storm/fair weather wave base. During early stages of relative sea level rise, wave ravinement may have eroded into shallow marine nearshore deposits that existed in western areas of the Maltese Islands (footwall high of IMF). Wave ravinement transported eroded sediments eastwards (basinwards) forming the OSHR Facies. The OSHR Facies is thus interpreted as transgressive lag deposits (figure 6.7A).

As relative sea level rise outpaced OSHR accumulation, OSHR accumulation rates decreased. The CASR and CAF Facies replace the OSHR Facies and accumulate in western areas of the Maltese Islands. The up to 10 m thick CASR Facies is interpreted to have formed in high-

energy shallow shelf (*circa* 20 to 50 m) environment within the storm/fair weather wave base. The contemporaneous CAF Facies may have accumulated in sheltered/deeper marine environments water depths greater than 30 to 40 m. The CASR facies is only observed within the VLF footwall high while the CAF Facies occurs in VLF footwall (south and southwest of VLF) and hanging wall lows (north of VLF) (figure 6.1, 6.2 OCS1 and 6.7A). The CASR Facies demonstrates a fining upward sequence. This suggests that the VLF footwall area was subject to increasingly deep and/or low energy marine environments. It is suggested that under these deeper and/or lower energy marine conditions deposition of the CAF Facies may have continued (figure 6.7A). Both CASR and CAF Facies are thus interpreted as transgressive deposits.

The CAP Facies conformably overlies the CASR and CAF Facies (figure 6.7B). The CAP Facies is interpreted to have formed in the littoral zone at *circa* 40 to 100 m depths. An average of 25 m of the Coralline Algal Biostrome FA are preserved in the south west of Malta and south of Gozo (figure 5.18). For this amount of sediment to accumulate, a relative sea level rise of similar magnitude must have occurred. The aggradational and progradation bedforms developed within the CAP Facies suggest production rates must have kept pace then exceeded the relative rise in sea level (figure 6.7B). It is interpreted that the CAP Facies as representing late transgressive and highstand deposits. The MCAD and PCAD Facies were generated from debris shed eastward off the coralline algal biostrome (CAP Facies).

The CAD Facies conformably overlies the CAP Facies (figure 6.7C). The CAD Facies is interpreted to have formed under increasingly turbulent and higher energy environments possibly within or close to the storm/fair weather wave base (*circa* 30 to 60 m). The higher-energy marine environments are the result of a relative sea level fall representing a normal regression. The CAD Facies are thus interpreted as late highstand and falling stage deposits. An extensive sharp erosive sequence boundary (SB2) is commonly observed across the Maltese Islands between the Reef-Core FA and the underlying CAD Facies (figure 6.7D). Evidence has also been gathered in this study that indicates the erosive surface was the result of a substantial relative sea level fall that exposed the upper levels of the Coralline Algal Biostrome FA to sub-aerial conditions in the west of Malta (section 6.3.2.1). This surface is labelled sequence boundary 2 (SB2) and terminates depositional sequence 1.

6.3.2.1. SB2: erosive bed boundary between Reef-Core FA and underlying Coralline Algal Biostrome FA

The sharp erosive bed boundary, between the Reef-Core FA and the underlying CAD Facies of the Coralline Algal Biostrome FA, is observed in both the Malta Horst (e.g. Dingli figure 6.4C) and the Malta Graben (e.g. Majjistral Park MT22 figure 6.4B).

A number of observations indicate that the erosive surface was the result of a substantial relative sea level fall that exposed the deposited Coralline Algal Biostrome FA to sub-aerial conditions. The nature of the surface is supported by three observations: (i) the regionally extensive erosive surface is frequently observed to truncate into the underlying Coralline Algal Debris Packstone Facies (figure 6.4). (ii) A "*brown bed*", interpreted as a palaeosol preserved in karstic features, is observed 20cm to 50cm below the surface of interest (figure 6.5). (iii) Oxygen and Carbon isotope analysis from the Mellieha area (MT22) carried out in this the course of this study (Appendix C4) suggest sub-aerial conditions at the boundary. In view of the above information, the erosional surface has been interpreted as a sequence boundary.

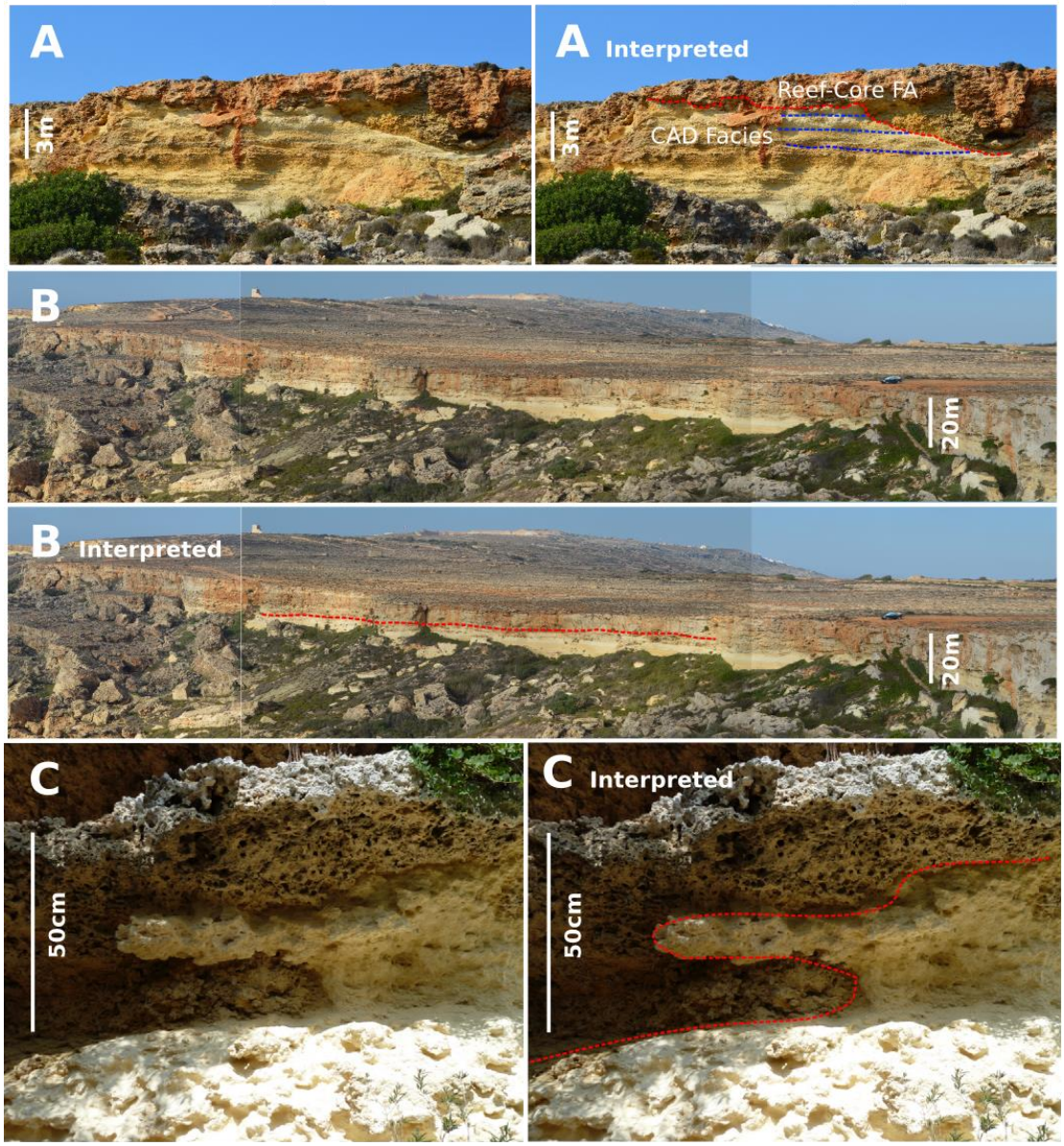

Figure 6.4: A sharp erosive bed boundary (red dashed line) is observed between the Reef-Core FA and the underlying CAD Facies - Coralline Algal Biostrome FA. (A) Is at L-Iskorvit locality (MT04). (B) Is at Majjistral Park - Mellieha locality (MT22). (C) Detail of sharp erosive bed boundary (red dashed line) at Tal-Pitkal outcrop in Dingli (grid reference 432688) that shows lithification of and erosion into CAD Facies that is overlain by Reef-Core FA.

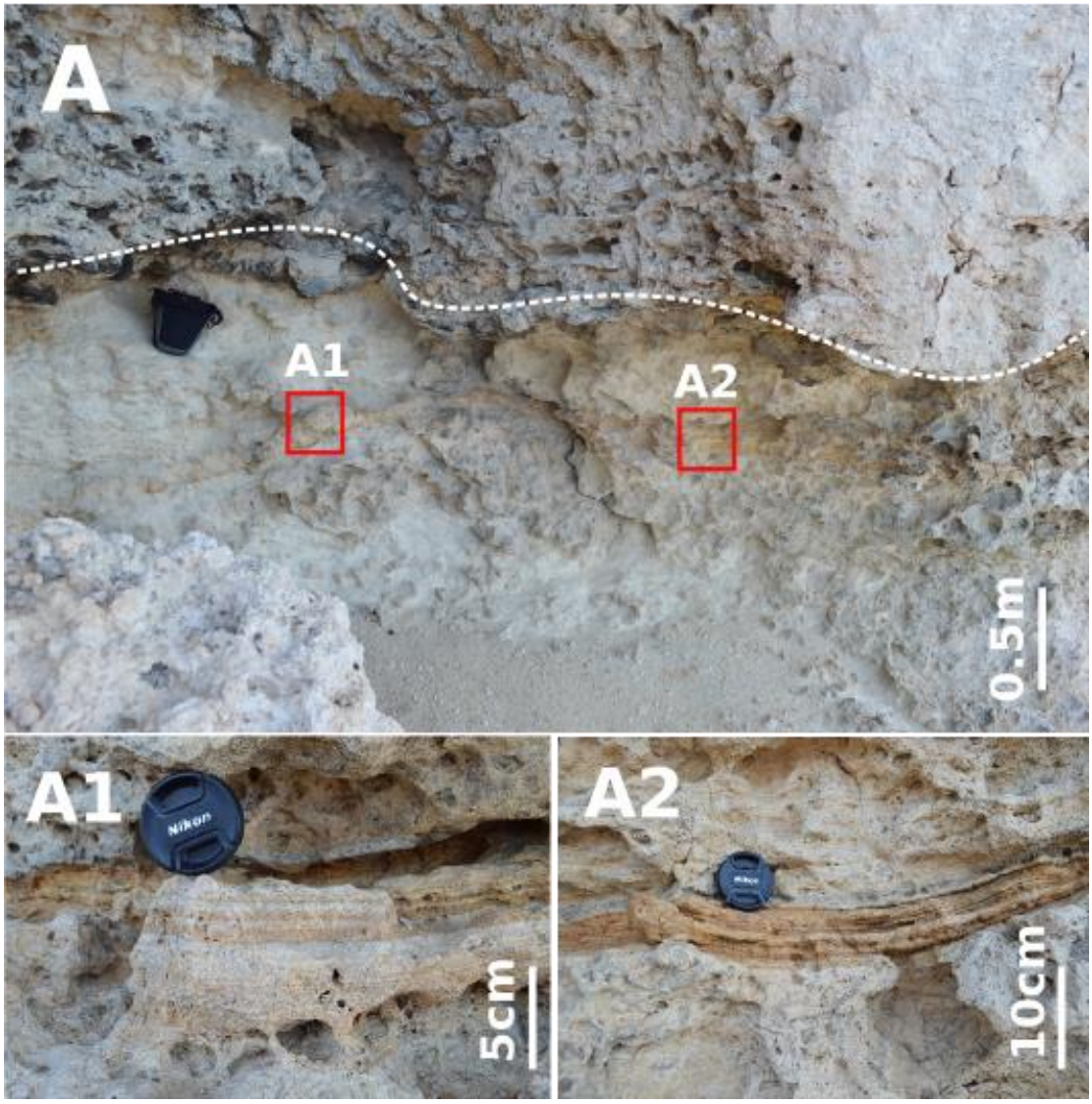

Figure 6.5: (A) "*Brown bed*", a subsurface infill of brown (oxidised iron) material of a subsurface cavity is observed 20cm to 50cm below the sharp erosive bed boundary (surface of interest - white dashed line) which separates the Coralline algal biostrome FA from the Reef-Core FA (locality MT05). The brown infill is interpreted as a speleothem. (A1 and A2) Detail of "*brown bed*". See Appendix C4 for oxygen and carbon isotope analysis.

6.3.3. Depositional Sequence 2 (DS2)

Following the creation of SB2, relative sea level rose and accommodation space for the Reef-Core Facies Association was created (figure 6.7E). This FA records an upward shallowing marine succession. The CFR Facies is interpreted to have formed in water depths between 30 to 60 m, the CPR Facies suggest depths of approximately 10 to 20 m and the CR Facies suggests water depths of 10m or less. An average of 20 m (5 to 25 m) of the Reef-Core FA are preserved in the south west of Malta (figure 5.32). For this amount of sediment to accumulate, a relative sea level rise of up to 80 m must have occurred. The colonisation of chlorozoan (coral) factories

would have significantly increased sediment production rates. The high chlorozoan sediment production rates likely outpaced the rates of base-level rise. This led to progradational bedforms developed within the Reef-Core FA, normal regression and relative sea level shallowing in both transgressive and highstand phases (*cf.* Upper Miocene Reef Complex of the Llucmajor area, Mallorca Spain e.g. Pomar *et al*., 1996). The CFR, CPR and CR Facies may therefore represent transgressive to highstand deposits (figure 6.7E).

6.3.4. Depositional Sequence 3 (DS3)

In certain localities in western areas of Malta (MT16) a basal surface forms a sharp, erosive lower contact that separates the underlying Reef-Core FA from the overlying Sand Shoal FA (section 5.3.6 and figure 5.40). Shallowing may be the result of normal regression and/or a low-amplitude sea level fall. If sea level fell, this must have been in the order of less than 10 m. This is since the CR Facies, that underlies the erosive surface, may have formed in water depths of 10 m or less, and sub-aerial features were not observed within the erosion surface. For this reason, this erosion surface is tentatively labelled as sequence boundary 3 (SB3) and it terminates depositional sequence 2 (figure 6.7F and E).

Following SB3 relative sea level rose to establish marine depths of 10 m or less within which the Sand Shoal FA accumulated. Subsequent marine shallowing, inferred through the succession of SS to WR Facies in the Sand Shoal FA, may be the result of normal regression and/or relative sea level fall. The SS and WR Facies are interpreted to represent migrating 3D sand shoals and wave ripples formed in very-shallow intertidal and shallow sub-tidal (<10 m) high to moderate energy marine environments. The shallowing and progradation of lagoonal deposits is interpreted to reflect a slowing of the rate of relative sea level rise (figure 6.7G). These deposits are interpreted as highstand deposits.

Following the deposition of the Sand Shoal FA, the central Mediterranean region is subject to the Messinian evaporitic drawdown (Dart, 1991 table 6.1 samples (4), Friedman, 1958; Hsü *et al*., 1973; Stoffers and Kühn, 1974; Schreiber & Tabakh, 2000). The Maltese region may have been subaerialy exposed and formed an upland karst plateau for much of its subsequent history (*cf.* Dart *et al*., 1993). This marks the sequence boundary 4 (SB4) and terminates depositional sequence 3 and the UCL Formation (figure 6.7H).

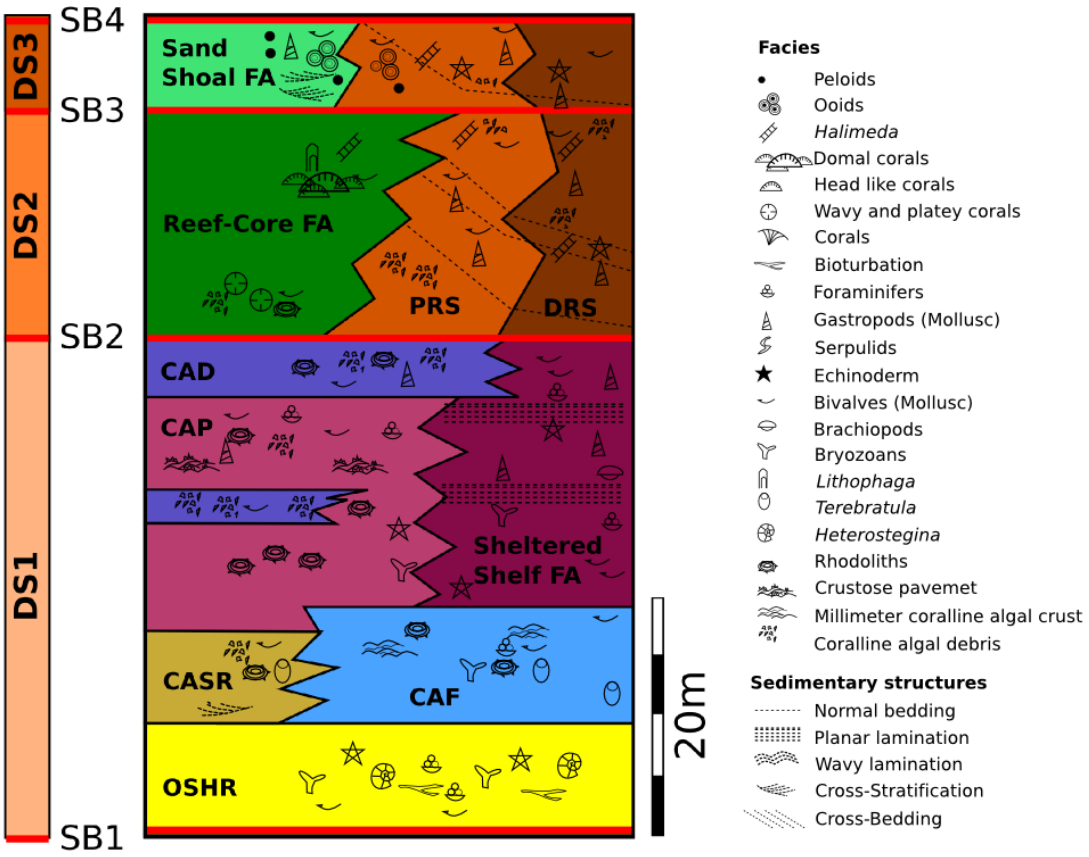

Figure 6.6: Generalised lithostratigraphic and sequence stratigraphy diagram with average stratigraphic thickness of facies and facies associations. The characteristic fossils observed in outcrop are displayed in the lithostratigraphic diagram. Full terms of facies available in table 5.3.

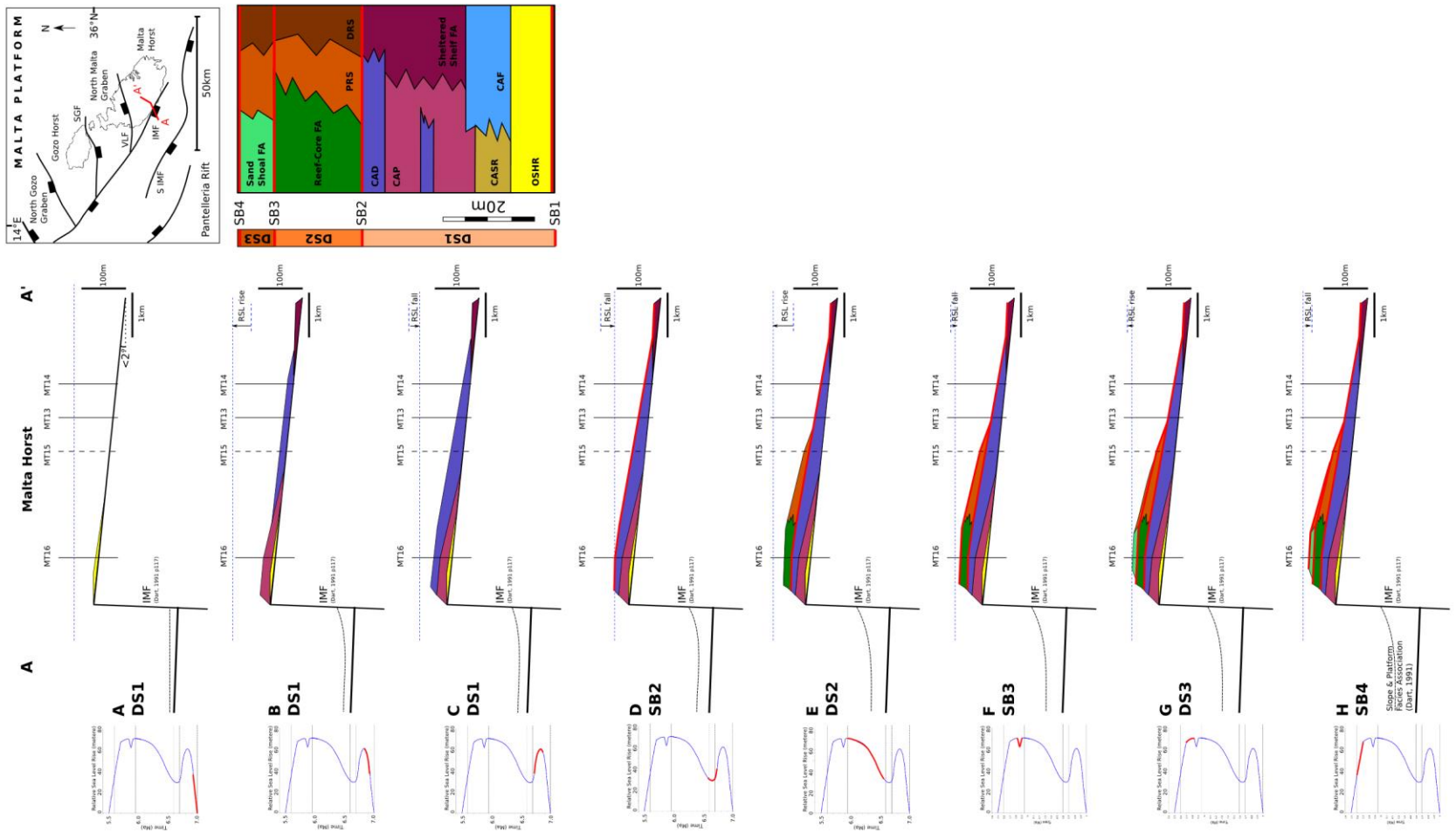

Figure 6.7: A west to east (dip section) 2D section across the Malta Horst that formed part of the Malta Fault-Block Platform. The depositional facies associations (FA) and facies are tied to an interpreted relative sea level cycles (right margin). Time scale, on relative sea level curve, developed in section 6.4. Facies association and facies abbreviations as in table 5.3. Figures A to C correspond to depositional sequence 1 (DS1), figure D represents the sequence boundary 2 (SB2), figure E represents depositional sequence 2 (DS2), figure F represents sequence boundary 3 (SB3), figure G represents depositional sequence 3 (DS3), and figure H represents sequence boundary 4 (SB4).

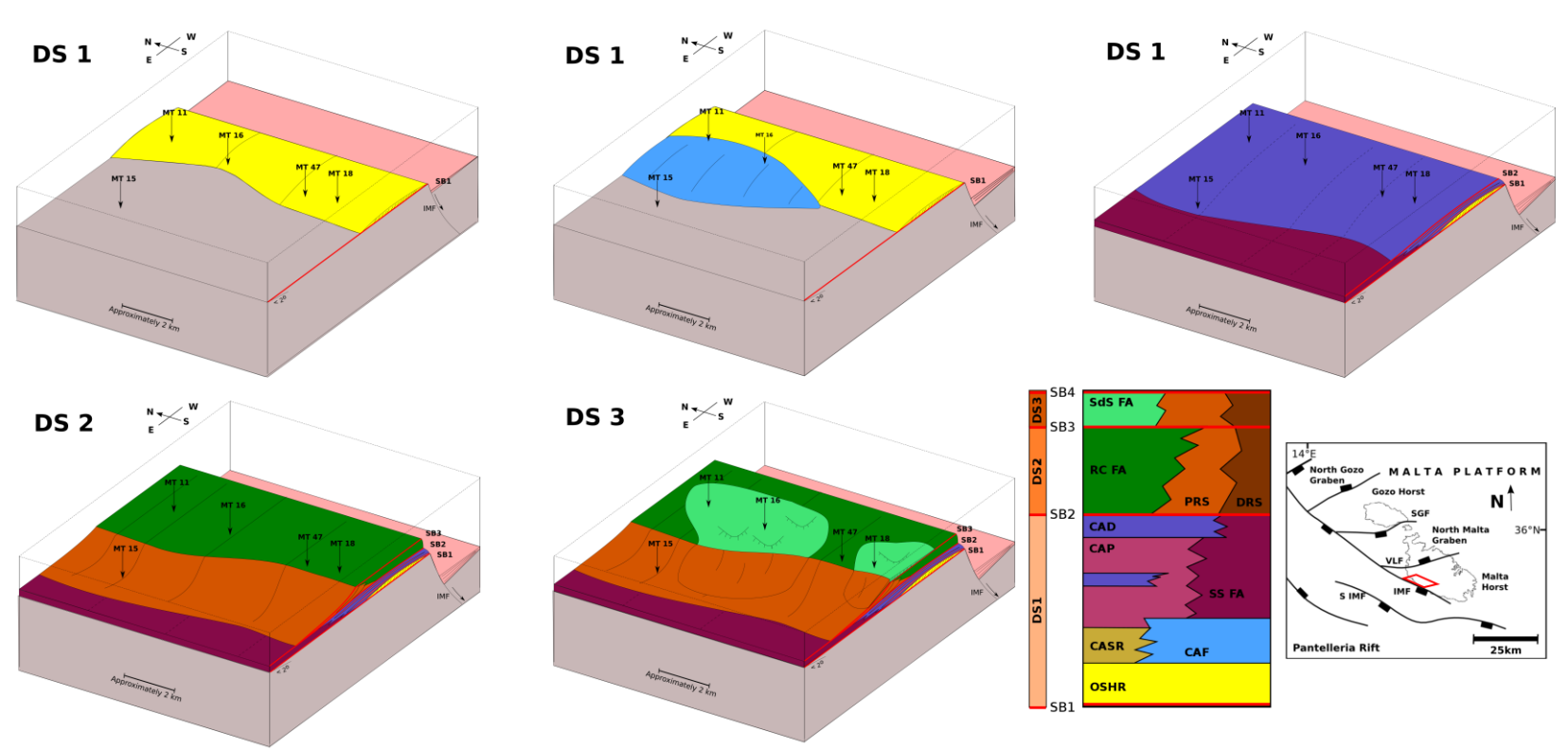

Figure 6.8: 3-D conceptual model of the Late Miocene, UCL Formation (Malta) across a typical west (shallow) to east (deep) section of the Malta Fault-Block Platform. The conceptual model summaries of field observations and interpretations. The 3-D diagram shows the depositional sequences (DS1, DS2 and DS3), facies distribution within the depositional sequence and key sedimentary geometries. Throw on the IMF is increasing as the UCL Formation is deposited.

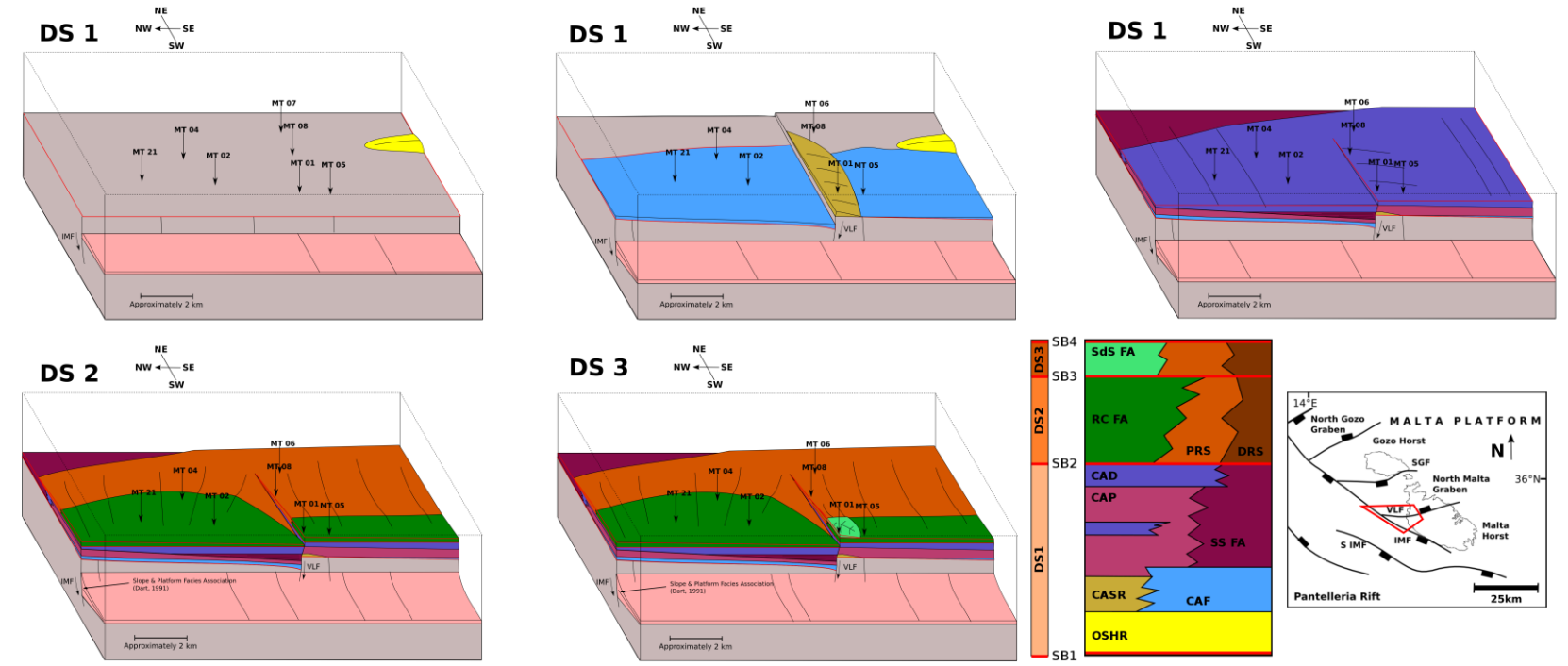

Figure 6.9: 3-D conceptual model of the Late Miocene, UCL Formation (Malta) across the Victoria Lines Fault (VLF) – part of the Fault-Block Platform. The conceptual model summaries of field observations and interpretations. The 3-D diagram shows the depositional sequences (DS1, DS2 and DS3), facies distribution within the depositional sequence and key sedimentary geometries. Throw on the IMF is increasing as the UCL Formation is deposited.

6.4. Chronostratigraphic scheme

The following section attempts to develop a chronostratigraphic scheme for the facies associations within the UCL Formation. While biostratigraphy does provide a broad band of dates for the overall formation, it does not provide the duration of deposition for the facies or the facies associations observed in this study. This information is necessary to develop a relative sea level curve that incorporates the temporal aspect and for numerical stratigraphic forward models (chapter 7).

Previous authors have attempted various other methods to refine the chronostratigraphy of Late Miocene Mediterranean platforms; e.g. Malta (Dart, 1991), Llucmajor (Pomar *et al*., 2012), Las Negras (Franseen & Goldstein, 1996) and Nijar (Warrlich, 2000). Results from these studies indicate that all of these the successions are difficult to accurately date. This is because biostratigraphy only provides a broad band of dates for the depositional units and their duration of deposition. While strontium dating may be more precise, the error bands tied to this method are commonly substantial as the Late Miocene carbonate deposits are commonly extensively diagenetically altered (e.g. Dart, 1991 Sr values for Malta, table 6.1). As a result, these attempts to date the successions were of very limited success. In view of these limitations, and the need for approximate dates, this study attempts to further refine the chronostratigraphy of the facies associations within the UCL Formation through regional correlations of well-dated depositional units and marine planation surfaces (section 6.4.3).

6.4.1. Biostratigraphy

The biostratigraphic age ranges for the combined Greensand and UCL formations was proposed by Mazzei (1985) and corresponds to those proposed earlier by Gianelli & Salvatorini (1975). Mazzei (1985) suggests CN9B, which occurs between 6.38 to 5.5 Ma (using Dart, 1991 p.65) or 7.167 to 5.54 Ma (using Raffi *et al*., 2006, Lourens *et al*., 2005). Both age ranges were defined using the same CN9B, however the latter provides a revised date for the CN9B fossils using Raffi *et al*., (2006). Gianelli & Salvatorini (1975) suggest N17, which occurs between 7.09 to 5.73 Ma. Both the CN9B (using Raffi *et al*., 2006) and N17 age rage are comparable and are used as reference point throughout the remaining of the chronostratigraphic analysis.

6.4.2. Strontium isotopes ($^{87}Sr/^{86}Sr$)

Dart (1991) used $^{87}Sr/^{86}Sr$ values obtained from the Maltese UCL Formation to assign absolute ages. Values for the UCL range between 0.708920 and 0.708985 and based on the standard $^{87}Sr/^{86}Sr$ curve of Hodell *et al*., (1989), an age range between 4.9 and 5.5Ma was determined by Dart (1991 p.72). Excluding the possibility of a Pliocene age, Dart's results indicate an upper Messinian age for the formation. This supports the biostratigraphical scheme of Gianelli & Salvatorini (1975) and Mazzei (1985) (section 6.4.1). The age determinations from stable Sr isotope analysis are not as precise as those determined biostratigraphically. This is due to

analytical error within the calibration curves, and Sr ratio values falling within flat portions of the calibration curves. Based on both stable strontium and biostratigraphic methods, Dart (1991 p.74) argues that a wholly Messinian age is preferred for the UCL Formation.

Dart's (1991) $^{87}Sr/^{86}Sr$ values were re-assessed and re-calibrated for this study using the more recent Gradstein *et al*. (2004) Sr lookup tables. Based on the standard $^{87}Sr/^{86}Sr$ curve of Gradstein *et al*. (2004), an age range between 6.06 and 9.07Ma is estimated for the Maltese UCL Formation. The different Sr samples that Dart (1991) took throughout the succession of UCL stratigraphy show similar age ranges (table 6.1). Also, when the Sr derived ages considered against stratigraphic height, results suggest that average ages seem to increase up section (table 6.1). This would imply that samples in lower elevations, deposited first, are older than the more recently deposited. Despite the re-interpreted results, the age determinations derived from the stable Sr isotope analyses do not allow age brackets to be unambiguously tied to particular facies associations. The age determinations derived from stable Sr isotope analyses (table 6.1) are not as precise as those determined biostratigraphically.

Fm	Ref.	Sample type	Elevation (m)	$^{87}Sr/^{86}Sr$ (2)	S.E. (3)	$^{87}Sr/^{86}Sr$	$^{87}Sr/^{86}Sr$	Ma Min	Ma Avg	Ma Max
UCL	S10	Sediment	Uppermost (4)	0.708931	±9	0.708894	0.708922	7.37	8.18	9.07
UCL	S9	Pectinid	Uppermost (4)	0.708956	±11	0.708967	0.708945	6.48	6.96	7.59
UCL	S8	Oyster	Uppermost (4)	0.708953	±11	0.708964	0.708942	6.56	7.07	7.75
UCL	S7	Sediment	Uppermost (4)	0.708944	±12	0.708956	0.708932	6.83	7.50	8.56
UCL	S6	Sediment	24.5	0.708971	±16	0.708987	0.708955	6.06	6.51	7.16
UCL	S5	Oyster	23	0.708952	±9	0.708961	0.708943	6.65	7.10	7.69
UCL	S4	Pectinid	23	0.708949	±13	0.708962	0.708936	6.62	7.23	8.35
UCL	S3	Sediment	11.5	0.708964	±110 (5)	/	/	/	/	/
UCL	S2	Oyster	11.5	0.708953	±18	0.708971	0.708935	6.38	7.10	8.40
UCL	S1	Sediment	2.5	0.708999	±156 (5)	/	/	/	/	/

Table 6.1: Minimum, average and maximum age of depositions (Ma) obtained from $^{87}Sr/^{86}Sr$ values (Dart, 1991) using Gradstein *et al*. (2004) Sr lookup tables. (1) Elevation above base of stratigarphic division, (2) Results normalized, (3) Analytical uncertainty represents two standard errors of mean ratios and reflect the last two digits of $^{87}Sr/^{86}Sr$, (4) Collected from the hanging wall sequence of Il-Maghlaq Fault and therefore most likely the uppermost strata within the Formation, (5) Results rejected due to unacceptable standard error.

The most recent Sr isotope analysis was carried out by Jacobs *et al*. (1996). They provide Sr ratios for the Blue Clay, Greensand and UCL Formations (Jacobs *et al.,* 1996) based on calcitic samples (brachiopod, foraminifera shells). The $^{87}Sr/^{86}Sr$ data was normalised to Hodell (1991) measurements (Jacobs *et al*., 1996). Jacobs *et al*. (1996) indicate that the age derived from samples taken with the Greensand Formation is 6.30 Ma (sample IG8) and for the UCL Formation 7.81 Ma (sample IG8). The ages for the Sr ratio values were re-assessed in this thesis using the more recent Gradstein *et al*. (2004) Sr lookup tables. Based on the standard $^{87}Sr/^{86}Sr$ curve of Gradstein *et al*. (2004), the Blue Clay sample taken at Qammieh (Qabb 19) is 11.81 Ma, the Greensand sample taken at Il-Gelmus (IG8) is 5.86 Ma, and the UCL is 9.21 Ma (table 6.2). This would imply that Greensand samples in lower elevations, deposited first, are younger than the more recently deposited and overlying UCL samples. Consequently, the age determinations derived from the stable Sr isotope analyses do not allow age brackets to be unambiguously tied to particular depositional units.

Formation	Sample and elevation (m)	Sample type	$^{87}Sr/^{86}Sr$ of Hodell (1991)	Age, after correlation to Hodell (1991) (Ma)	Age correlation with Gradstein *et al*. (2004) Sr lookup chart		
					Min	Avg	Max
UCL Fm, Qammieh	UCL (*circa.* 15m from base of UCL)	Brachiopod	0.708912	7.81	8.91	9.21	9.46
Greensand Fm, il-Gelmus	IG8 (*circa.* 6m from base of GS)	*Undisclosed*	0.709002	6.3	5.81	5.86	5.91
Blue Clay Fm	Qabb19 (*undisclosed*	Foraminifera	0.70884	10.87	11.37	11.81	12.14

Table 6.2: Minimum, average and maximum age of depositions (Ma) obtained from $^{87}Sr/^{86}Sr$ values (Jacobs *et al*., 1996) using Gradstein *et al*. (2004) Sr lookup tables.

6.4.3. Regional correlations

Cornée *et al*. (2004) proposed long distance correlations of eight late Tortonian–Messinian carbonate platforms in the western and central Mediterranean, namely in Morocco (Melilla–Nador & Kebdana), in Algeria (Murdjadjo and Tessala-Beni Chougrane), in SE Spain (Sorbas basin), in Malta, and in Italy (Lampedusa and Salemi). The Melilla–Nador platform (Morocco) and Sorbas basin (Spain) where carbonate complexes have been tentatively dated (Carree *et al.,* 2006). Dating of the Melilla–Nador platform and basin has been attempted with high precision $^{40}Ar/^{39}Ar$ geochronological studies (Cunningham *et al*. 1994, 1996; Roger *et al*. 2000; Cornée *et al*. 2002). Dating of the Sorbas basin has been attempted with GPTS and APTS calibration (Gautier *et al*., 1994; Krijgsman *et al*., 2001) and margin-basin correlations (Martin & Braga, 1994; Braga & Martin, 1996; Conesa *et al*., 1999). Correlations are based on the identification of three lithological units (T1, T2, T3), two major biological sedimentary cycles (C1 (T1+T2), C2 (T3)) and of two index surfaces (surface A separates T1 and T2; surface B separates T2 and T3) (figure 6.10).

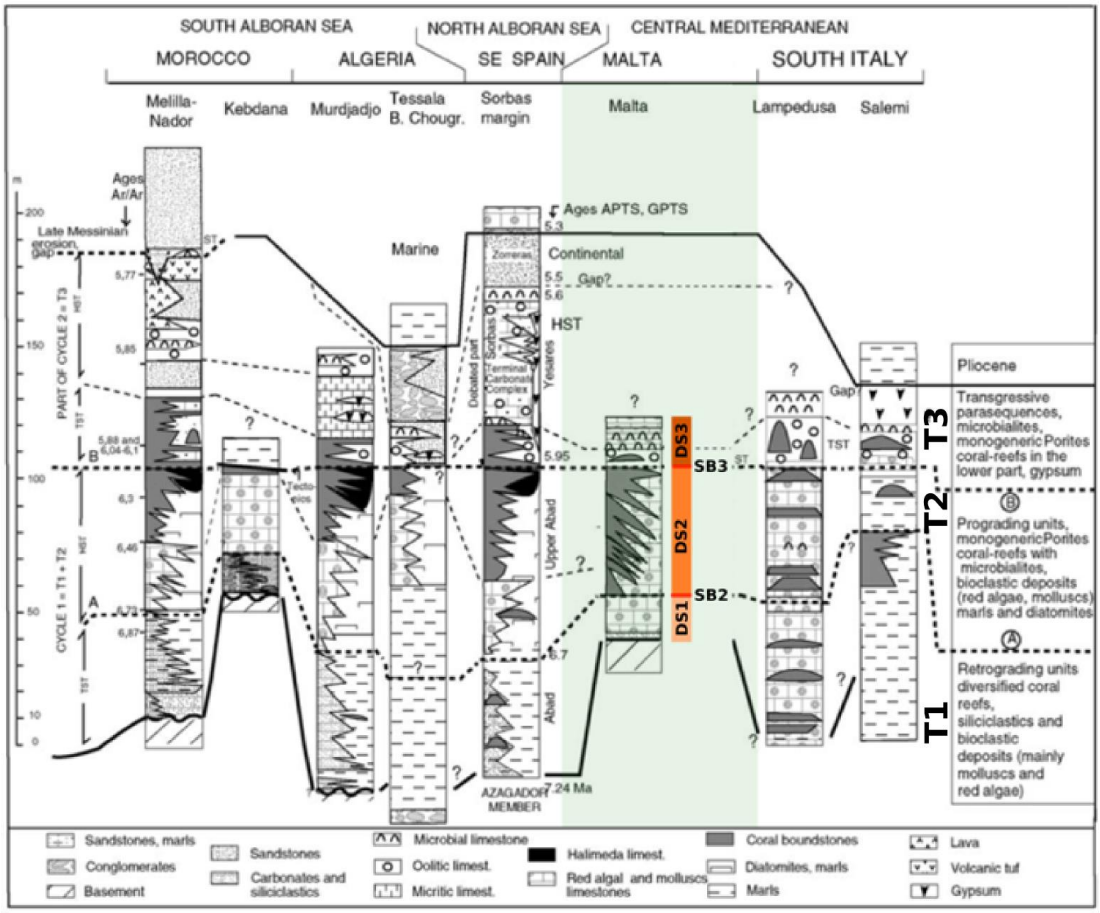

Figure 6.10: Summary logs and correlations proposed by Cornée *et al*. (2004) between the eight investigated Messinian carbonate platforms. Morocco (Melilla–Nador and its opposite southern margin, Kebdana: Saint Martin & Rouchy 1990; Saint Martin 1990; Saint Martin *et al*., 1991; Saint Martin & Cornée 1996; Chennouf *et al*., 1996; Cornée *et al*., 1996; Saint Martin *et al*., 2007b; Roger *et al*., 2000; Munch *et al*., 2001; Cornée *et al*., 2004; Pestrea-Saint Martin *et al*., 2003; Munch *et al*., 2003a; Garcia *et al*., 2003), in Algeria (Murdjadjo and its opposite southern margin, Tessala- Beni Chougrane: Saint Martin 1990; Saint Martin & Rouchy 1990; Saint Martin & Andre, 1992; Cornée *et al*., 1994; Saint Martin *et al*., 1995; Pestrea *et al*., 1999), in SE Spain (Sorbas basin: Saint Martin & Rouchy 1990; Conesa 1997; Conesa *et al*., 1999; Conesa & Babinot 1999; Lacour *et al*., 2000; Saint Martin *et al*., 2000, 2001), in Malta (Saint Martin & Andre 1992; Saint Martin *et al*., 2007a), and in south Italy (Lampedusa: Andre *et al*., 2002; Sicily: Saint Martin & Cornée, 1996; Saint Martin 2001; Pestrea & Saint Martin 2002). Melilla–Nador ages from Roger *et al*. (2000) and Cornée *et al*. (2002), Sorbas ages from Krijgsman *et al*. (2001). Figure modified from Cornée *et al*. (2004).

Chronological data indicate rather similar ages for the units T1 to T3 in Melilla–Nador and in Sorbas, as follows (figure 6.10). Retrograding T1 units accumulated during the latest Tortonian to early Messinian, up to 6.7 Ma. Prograding bioclastic then reefal T2 units developed between 6.7 and around 5.95 Ma. Marine T3 deposits accumulated between 5.95 and 5.6 Ma. The age of T3 (Terminal Carbonate Complex) in Melilla–Nador from $^{40}Ar/^{39}Ar$ ages indicates it is coeval with the Sorbas gypsum (Cornée *et al*., 2004). On the basis of chronological data in Melilla–Nador and Sorbas, Cornée *et al*. (2004) suggest surface A to date at around 6.7 Ma (latest accumulation of T1 unit) and surface B to date at around 5.95 Ma (latest accumulation of T2 unit). Cornée *et al*. (2004) interpret cycle 1 deposition (from around 6.9 Ma *at least* to around 5.95 Ma) as a third-order cycle (lasted 1 Ma) and cycle 2 (from around 5.95 and to around 5.6 Ma) as a fourth-order cycle (lasted 0.35 Ma).

The marine planation surface B should date at around 5.95 Ma, this is supported by GPTS (geomagnetic polarity time scale) data in Cabo de Gata where the Terminal Carbonate Complex deposition began at the base of chron C3r (Franseen *et al*., 1998; Montgomery *et al*., 2001). On the basis of Cornée *et al*. (2004) inferred correlations deposition of cycle 1 is interpreted as a third-order cycle (from around 6.9 Ma to around 5.95 Ma) and cycle 2 may be a fourth-order cycle (from around 5.95 and to around 5.6 Ma). Cornée *et al*. (2004) indicates that the 5.6–5.3-Ma time span is poorly documented in the described sites. The main desiccation event of the Mediterranean occurred in the 5.6–5.32-Ma time-span (Cornée *et al*., 2004).

The chronological data of the lithological units and index surface identified by Cornée *et al*. (2004) were correlated to the Maltese units in the Cornée *et al*. (2004) study. These units and index surfaces can also be applied to the Maltese facies associations and erosional surfaces defined in this thesis (table 6.3). This helps constrain the time during which the Maltese sequences and sequence boundaries formed. Within this scheme, lithological unit T1, that consists mainly of red algae, corresponds to the Open Shelf FA, Coralline Algal Biostrome FA and Sheltered Shelf FA that may have formed from around 6.9Ma. Since the base of cycle C1 (base of UCL Formation) is not well constrained (Cornée *et al*., 2004 "*from around 6.9 Ma at least*"), the base of cycle C1 was in this study set at 7.00 Ma. This corresponds to the biostratigraphic CN9B and N17 zones (Mazzei, 1985; Gianelli & Salvatorini, 1975). Surface A (corresponding to SB2 section 6.3.3) formed around 6.7 Ma. Lithological unit T2, consists of prograding units of coral-reefs, corresponding to Reef-Core FA and Fore-Reef Slope and Shelf FA that may have formed between 6.7 and around 5.95 Ma. Cycle 1, which consists of lithological unit T1 and T2, formed from around 6.9 Ma to around 5.95 Ma. Surface B (corresponding to SB 3 section 6.3.4) separates cycle 1 from cycle 2 and formed around 5.95 Ma. Lithological unit T3 tied to cycle 2 (corresponding to the Sand Shoal FA) formed from around 5.95 and to around 5.6 Ma.

Sedimentary cycle	Lithological Units/Index Surface (of Cornée *et al*., 2004)	Age and notes (of Cornée *et al*., 2004)	Correlation with Malta Facies Associations and Sequence Boundaries (this thesis)
C2	T3: transgressive parasequences, microbialites, monogeneric *Porites* coral-reefs in the lower part, gypsum	Around 5.95 to around 5.6 Ma	Sand Shoal FA
	Surface B	Around 5.95 Ma	SB3
C1	T2: prograding units, monogeneric Porites coral-reefs with microbialites, bioclastic deposits (red algae, molluscs), marls and diatomites	Around 6.7 to around 5.95 Ma	Reef-Core FA and Fore-Reef Slope and Shelf FA
	Surface A	Around 6.7 Ma	SB2
	T1: consists of retrograding units diversified coral reefs, siliciclastic and bioclastic deposits (mainly mollusc and red algae)	Around 6.9 Ma (in this thesis, the base of cycle C1 was set at 7.00 Ma)	Open Shelf FA, Coralline Algal Biostrome FA and Sheltered Shelf FA

Table 6.3: Chronological data of the lithological units and index surface (Cornée *et al*., 2004) applied to the Maltese facies associations (on the basis of sedimentology) and erosional surfaces. This provides the correlation and dating of the Late Miocene Maltese sequence that is required for numerical stratigraphic forward modeling of chapter 7. Biostratigraphic and geochronological studies (section 6.4.1 and 6.4.2) provide similar/comparable (albeit inconclusive) age ranges for the UCL Formation. Description of lithological units (T1, T2 and T3) from Cornée *et al*. 2004.

6.4.4. Proposed chronostratigraphy for the UCL Fm

Biostratigraphic and geochronological studies provide similar/comparable (albeit inconclusive) age ranges for the UCL Formation. The biostratigraphic age ranges for the Greensand and UCL Formations proposed by Mazzei (1985) corresponds to those proposed by Gianelli & Salvatorini (1975) and are from 7.167 to 5.5 Ma (section 6.4.1). The age proposed by biostratigraphic work also corresponds to that suggested by distance correlations of late Tortonian–Messinian littoral carbonate complexes (Cornée *et al*., 2004; Cunningham *et al*. 1994, 1996; Roger *et al*. 2000; Cornée *et al*. 2002; Gautier *et al*. 1994; Krijgsman *et al*. 2001; Martin & Braga, 1994; Braga and Martin, 1996; Conesa *et al*., 1999). Regional correlations based on Cornée *et al*. (2004) suggest that the UCL formed from 6.9 (*at least*) to 5.6 Ma.

Cornée *et al.* (2004) identify and correlate three lithological units, two sedimentary cycles and two index surfaces, across the Late Tortonian–Messinian carbonate complexes of western and central Mediterranean (including the Maltese UCL Formation).

The ages for these units, cycles and surfaces have also been determined at some, but not all, locations (section 6.4.3). The Cornée *et al*. (2004) regional correlations provide the most complete chronostratigraphic scheme for the facies associations within the Maltese UCL Formation and is applied in this study. It is however important to note that the regional correlations do not provide definitive evidence for the ages of the sequences within the Maltese UCL Formation (see discussion on cyclostratigraphy and circular arguments section 6.6) but are considered the best that can be achieved with current understanding and the attempts that have been made by previous workers and in this study to date these late Miocene carbonate rocks.

6.5. Relative Sea Level Curve

A relative sea level curve (figure 6.6) has been constructed for the Maltese Late Miocene UCL Formation. The relative sea level curve is based on the chronostratigraphic scheme (section 6.4) and the interpreted depositional environments and thicknesses for the observed facies.

It is difficult to determine from field evidence alone, whether the overall relative sea level curve was superimposed with high frequency oscillations. High frequency oscillations are to be expected for sediments of the same age in the Mediterranean (e.g. Franseen *et al*., 1998; Pomar *et al*., 1996; Pomar, 2001; Warrlich, 2000) and from the forward modelling work done on reefs of the same age in Mallorca (Bosence *et al*., 1994).

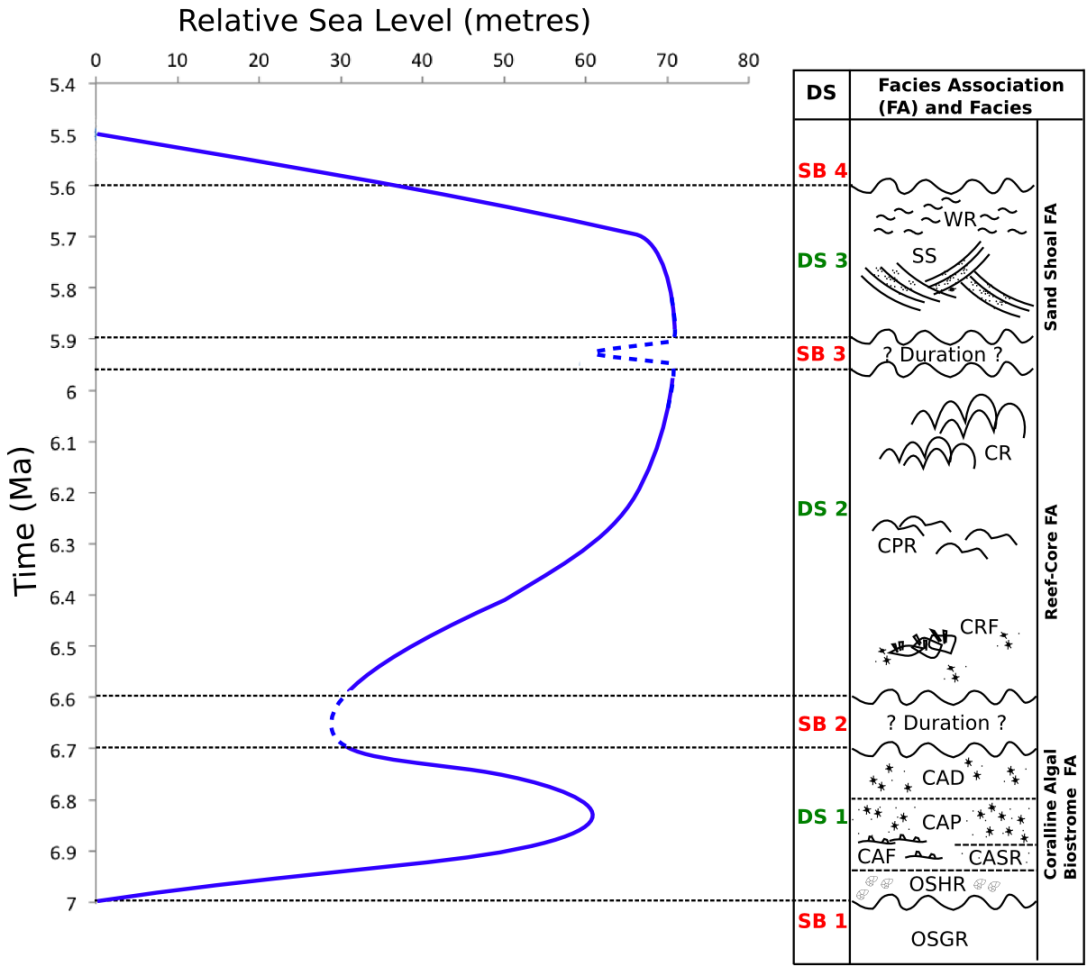

Figure 6.11: Interpreted relative sea level (RSL) curve defined from palaeobathymetric and stratal geometry data, dating and correlation of depositional sequences from central Mediterranean area. The sea level at 5.5 Ma represents Messinian drawdown event and RSL would have fallen well beyond this point height (Friedman, 1958; Hsü *et al*., 1973c; Stoffers & Kühn, 1974; Schreiber & Tabakh, 2000). Abbreviations of facies associations and facies discussed as in table 5.3. Depositional sequences (DS) and sequence boundaries (SB) discussed in section 6.3.

The relative sea level curves developed by Dart (1991) and in this thesis are comparable. Both contain three depositional sequences and three (Dart, 1991) or four (this study) sequence boundaries. The investigation undertaken in this thesis however is a broader study throughout the Maltese Islands that added more observations, added new data on sequence boundary (SB2) identification, and added a tentative time scale.

There are two slight differences between the relative sea level curve interpreted by Dart (1991) and the one developed in this study. First, Dart (1991) does not take the time component into consideration. In this study, the time component is based on regional correlations (section 6.4). The time component is necessary in SFM simulations that are carried out in the following chapter. Second, the relative sea level curve for Dart's depositional sequence 1 has a 100 m

change in relative sea level while that developed in this study shows a < 60 m change in sea level. In this study, palaeobathymetric, stratal geometry and numerical stratigraphic forward modeling data support the interpreted change in relative sea level. The amplitude of sea level change for depositional sequence 2 is similar.

6.6. Comparison with previous relative sea level curves for Late Miocene Mediterranean carbonate platforms

The Late Miocene relative sea level curve constructed for the Maltese Islands is here compared to three other well-studied Late Miocene carbonate platforms, namely the Llucmajor area, Balearic Islands (e.g. Pomar, 1991, 1993; Pomar & Ward, 1994, 1995; Pomar *et al*., 1996), the Las Negras platform, Southern Spain (e.g. Franseen, 1989; Goldstein *et al*., 1990; Franseen & Mankiewicz, 1991), the Nijar Basin, South Eastern Spain (e.g. Mankiewicz, 1987, 1996; Warrlich, 2000) and the Malta platform (e.g. Dart, 1991). The section also discusses the controls that may have contributed towards the similarities and differences in relative sea level curves for the contemporaneous Mediterranean carbonate platforms.

6.6.1. RSL for Late Miocene Mediterranean carbonate platforms

The following section reviews the information, interpretations and assumptions previous authors have applied in order to construct relative sea level curves for the aforementioned Mediterranean Late Miocene carbonate systems (table 6.4 and figure 6.12).

Platform	**Chronostratigraphic temporal resolution** (decreasing order): good, moderate and poor	**Sea level amplitude resolution** (decreasing order): good, moderate and poor
Llucmajor (Pomar *et al*., 1996; Pomar *et al*., 2012)	*Poor resolution*: Deposition start time and end time not precisely defined, precise dates/duration of depositional units not defined. The halfway point of this relative sea level curve corresponds to the Ar–Ar dates for the middle of the 20 km wide Llucmajor Platform (6.2 Ma on the sanidines and 6.5 Ma on the biotites).	*Good resolution*: Amplitude based on reef crest curve. The amplitude uncertainty for the Reef Complex Unit is represented by the addition of a ± 10 m range along the relative sea level curve of Pomar *et al*. (1996).
Las Negras	*Poor resolution*: Deposition start time known, end time not precisely	*Moderate resolution*: Maximum extent of relative sea level fall and rise poorly

(Franseen & Goldstein, 1996)	defined, precise dates/duration of depositional sequences not defined. The temporal uncertainty starts at +/- 0.1 Ma (based on SB1a age range in Franseen & Goldstein (1996)) and increases to +/- 0.4 Ma towards the Messinian-Pliocene transition (age range less well constrained - end at approximately ~5.3 Ma, corresponding to the Messinian-Pliocene transition in Franseen & Goldstein, 1996).	defined for DS1A, DS1B and DS2, these are well defined for DS3 and TCC. In this thesis, the amplitude uncertainty is represented by the addition of a ± 15 m range along the complete lines and a ± 25 m range along the dashed lines of Franseen & Goldstein's (1996) relative sea level curve. In this thesis, an additional ± 20 m is factored in for the Rhodalgal unit and a ± 10 m has been factored in for the Coralgal reef unit and the stromatolitic unit. This represents the uncertainty depth range within which the units may be deposited.
Nijar (Warrlich, 2000 p.180)	*Good resolution*: Deposition start and end time known, approximate dates/duration of depositional sequences well defined. The temporal uncertainty expressed in Warrlich (2000) relative sea level curve.	*Moderate resolution*: Maximum extent of relative sea level fall and rise is moderately well defined for all depositional sequences. The amplitude uncertainty has already been expressed in Warrlich (2000) relative sea level curve.
Malta Chapter 6	*Moderate resolution*: Deposition start and end time not precisely known (established from regional correlations). Range defined by $^{87}Sr/^{86}Sr$ (Dart, 1991) and regional correlations (Cornée *et al*., 2004) (section 6.4)	*Moderate resolution*: Extent of relative sea level fall and rise moderately well defined for all depositional sequences The amplitude uncertainty is represented by an addition of ± 20 m has been factored in for the Rhodalgal unit and a ± 10 m has been factored in for the Coralgal reef unit and the stromatolitic unit.

Table 6.4: Uncertainty in temporal and relative sea level amplitude resolution for the Late Miocene carbonate platforms: the Llucmajor area, Balearic Islands (e.g. Pomar, 1991, 1993; Pomar & Ward, 1994, 1995; Pomar *et al*., 1996), the Las Negras platform, Southern Spain (e.g. Franseen, 1989; Goldstein *et al*., 1990; Franseen & Mankiewicz, 1991), the Nijar Basin, South Eastern Spain (e.g. Mankiewicz, 1987, 1996; Warrlich, 2000) and the Malta platform (e.g. Pedley, 1974, 1976; Bosence & Pedley, 1982; Dart, 1991).

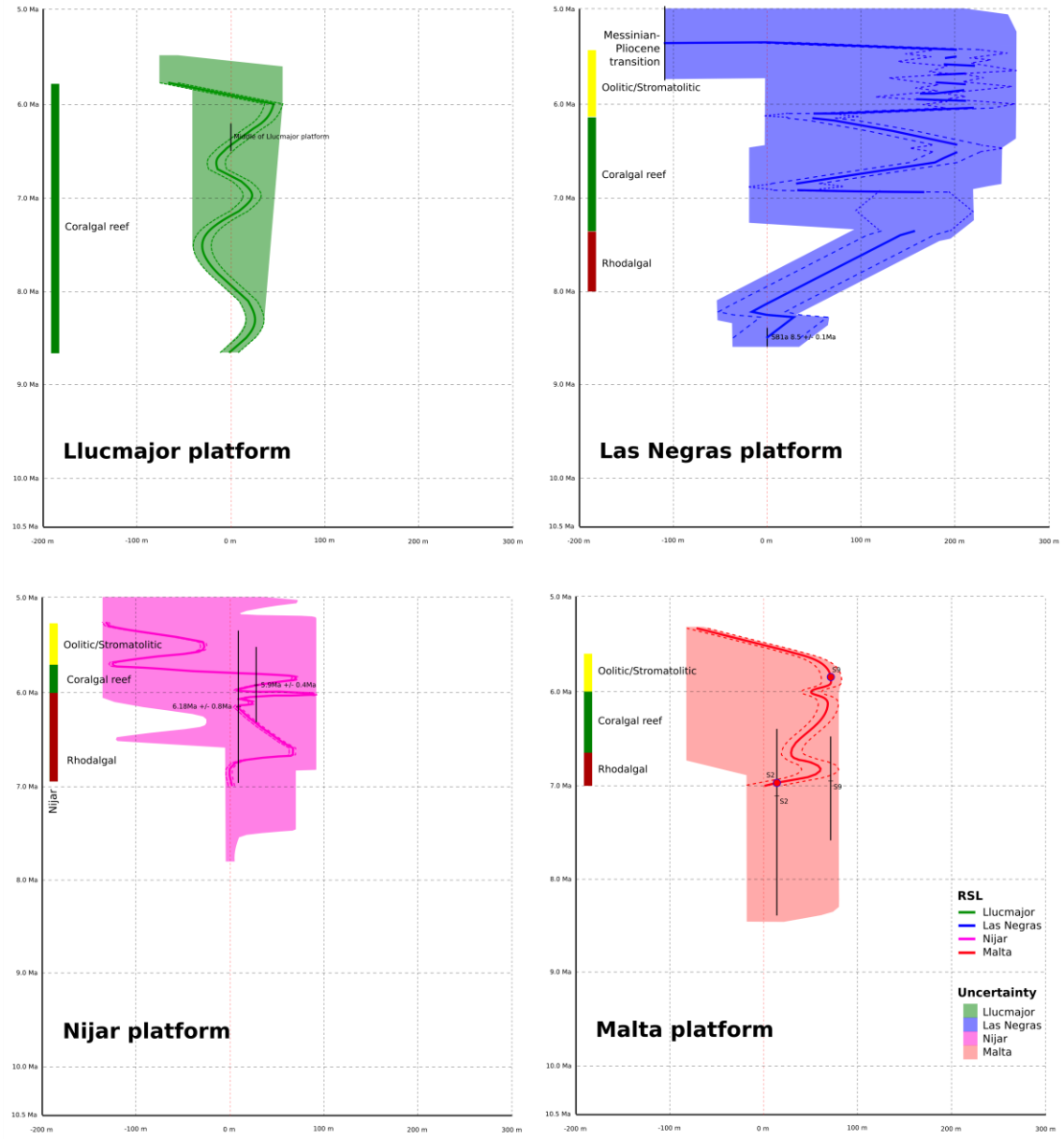

Figure 6.12: RSL curves and uncertainty a result of uncertainty in ages of strata, and water-depth interpretations. Shaded zones, colour coded for each platform, indicate the range of possible oscillation amplitude and frequency. Solid curve represents the original interpreted relative sea level curve presented in literature. Vertical error bars represent the age uncertainty reported in literature that is tied to particular deposits. Dashed sea-level curve lines represent the RSL amplitude uncertainty interpreted in this thesis. Coloured area represents the combination of temporal and amplitude uncertainties. Temporal uncertainty has been expressed in these graphs by moving the relative sea level curve (solid curve line) to correspond to the maximum and minimum temporal uncertainty. The RSL curve provided in the literature could technically fill any space within the shaded area for each graph. The bars demonstrating carbonate factories are correctly located on the temporal (vertical) scale and are based on interpreted stratigraphic age. The base level (0 m) of relative sea level is the same as in literature descriptions and represents the present-day sea level.

6.6.2. Sensitivity analysis of a multiple platform correlation

Comparison of how the curves are similar/different

At a broad level, the four *interpreted* relative sea level curves display three 3rd order sea level cycles (figure 6.12). The Nijar platform has a 4th order sea level cycle superposed onto the 3rd order cycle from 6.15 to 5.85 Ma. These 3rd order sea level cycles are however not tied/associated with the same carbonate factory (rhodalgal, coralgal reef or oolitic/stromatolitic units). E.g. for the Llucmajor and Nijar platforms, three sea level peaks are tied to the coralgal reef factory, for the Las Negras platform two peaks are tied to the coralgal reef factory and one peak to the oolitic/stromatolitic factory, while for the Malta platform each sea level peak is tied to a different carbonate factories.

Despite the suggested contemporaneity of Cornée *et al*. (2004) (figure 6.10) and the regional controls thought to have influenced the deposition of these units (section 6.4.3), the interpreted relative sea level curves are quite distinct in detail both in frequency and in amplitude (figure 6.13). A comparison of relative sea level peak and trough frequencies (black arrows) across the investigated platforms demonstrates that these are largely not contemporaneous. Only certain of the relative sea level peaks (A, B, C and D) and troughs (E) occur within ≤0.1 My of each other across the platforms and within the same depositional units (figure 6.13). E.g. Relative sea level peaks B and C are contemporaneous and tied to the coralgal reef unit for both the Las Negras and Nijar platforms and peak C is common to all platforms. It is important to note that the relative sea level curves of Llucmajor, Las Negras and Nijar were constructed independently of each other, by different authors and on the basis of interpreted facies depositional environment and depositional timing. This indicates that contemporaneity of certain relative sea level peaks and troughs are not the result of circular reasoning.

The peak-to-trough amplitudes for relative sea level cycles/periods that are contemporaneous vary significantly between platforms (figure 6.13). E.g. Cycle/period A peak-to-trough amplitude vary from 55 m in the Llucmajor platform to 188 m in the Las Negras platform and cycle/period E peak-to-trough amplitude vary from 155 m in the Las Negras platform and 17 m in the Malta platform.

The quality of outcrops also influences interpretations of relative sea level amplitude variations and the number of relative sea level cycles/periods for particular depositional units. E.g. the excellent outcrops of the Llucmajor platform demonstrate vertical shifts in prograding reef crest line over large distances. Conversely, the Maltese outcrop of the coralgal reef unit is relatively limited. The Llucmajor outcrop therefore enables a more thorough investigation of amplitude variations in relative sea level and more precise investigations of relative sea level

cycles/periods than is possible for the Maltese Platform. This situation may also lead to mismatches in the interpreted relative sea level curves between contemporaneous platforms even if the platform were in fact affected by the same relative sea levels.

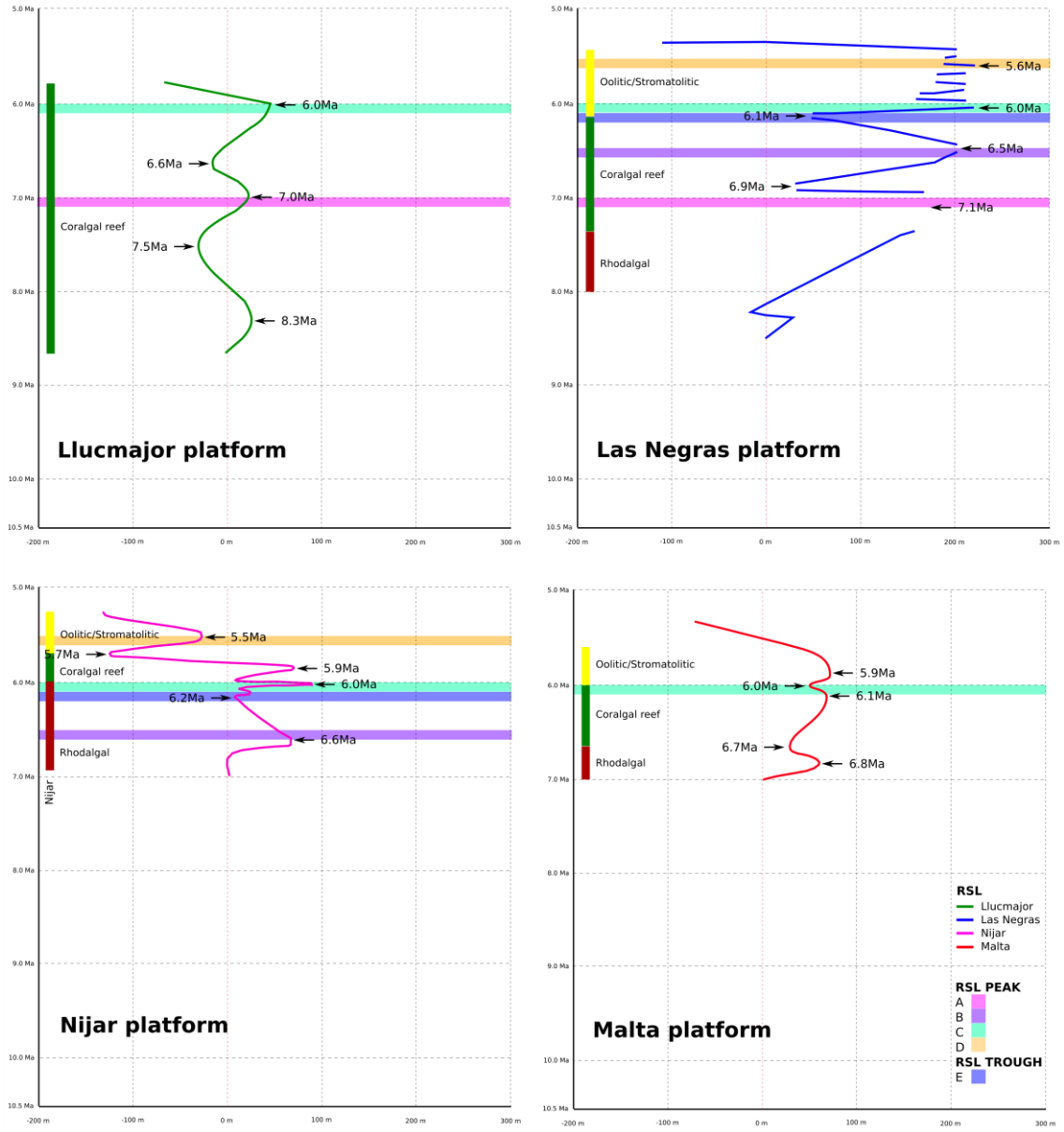

Figure 6.13: Relative sea level curve for the Mediterranean Late Miocene platforms (Llucmajor, Las Negras, Nijar and Malta) with temporal and amplitude uncertainties interpreted in this study. The full line represents the original interpreted relative sea level curve presented in literature. The arrows represent the age at which peaks and troughs in relative sea level occur – this represents the frequency content (power spectra) of each relative sea level curve. The shaded area highlights the peaks and troughs in interpreted relative sea level that are contemporaneous across the assessed Late Miocene carbonate platforms. 3rd order sea level cycle duration range 5 to 0.5 My, 4th order sea level cycle duration range 0.5 to 0.1 My.

Why are the curves so variable?

The frequency and amplitude content of each relative sea level curve has a strong element of uncertainty/error tied to it (figure 6.13 shaded areas). The implied precision of the RSL temporal scale is not supportable, because it is greater than that of the best available chronostratigraphic techniques (see Miall, 1992 and section 6.4). Late Miocene carbonate depositional sequences are difficult to accurately date. Biostratigraphy only provides a broad band of dates for the depositional units and does not provide the precise age and duration of deposition for the depositional units. Strontium dating may be more precise, however the error bands tied to this method are commonly substantial as the carbonate deposits are commonly extensively dolomitised. E.g. Late Miocene reefs are commonly dolomitised and accurate strontium dating is not possible since errors on ages are common very large (e.g. Dart, 1991 Sr values for Malta, section 6.4.2, table 6.1). There is therefore no direct evidence supporting the interpretations of particular sea level cycle orders - e.g. Pomar & Ward (1994) interpret the Llucmajor megasets of sigmoids to represent 3rd order sea level cycles. This makes the suggested temporal scale of the investigated relative sea level curves tentative at best. In addition to this, one also needs to consider that there exists a large range of possible sediment production (section 3.2.2) and transport rates (section 2.3.3.1). Similar sediment production and transport ratios, produced by different sediment production and transport rates, can produce the same platform geometries and facies architectures (e.g. Bosence *et al.,* 1994; section 4.3.2). These different (non-unique) solutions to the depositional geometries observed in the Mediterranean platforms indicate that the geometries/platforms may be plausibly interpreted as a result of various sea level cycle orders.

The amplitude component of the relative sea level curve can also be difficult to precisely determine. This aspect strongly depends on whether the deposition of the sediments can be constrained to a well-defined depth range. Where reefs rise and fall through stratigraphy, amplitude can be well constrained (e.g. Llucmajor reef complex unit *circa* ±10 m; Pomar *et al.,* 1996). However, where a wide range of depositional depths is interpreted for the deposits the amplitudes of sea level cycles/periods will be poorly constrained (e.g. coralline algae can occur in a variety of depths). The corollary of this is that when one takes the error/uncertainty in frequency and amplitude content into account, a detailed sea level curve cannot (normally) be constructed. The mismatch between relative sea levels for the four Late Miocene carbonate platforms may be the result of this uncertainty.

The temporal occurrence of three different carbonate factories (rhodalgal, coralgal reef and stromatolitic units) is also indicated for the different platforms. It is worth noting that the same factories are not contemporaneous across the four Late Miocene platforms (figure 6.12). This can either be since (i) the timing of the occurrence of the three carbonate factories is incorrect,

or (ii) that the carbonate factories are not contemporaneous across platforms. This uncertainty calls in to question the evidence for long distance cyclostratigraphic correlations (e.g. Esteban, 1996; Cornée *et al*., 2004) and Esteban's model (1996). The validity of using these published sea-level cycles for correlation is also questionable as this then makes a perfect circular argument.

Within the uncertainty space (shaded area figure 6.14) one can develop a composite relative sea level curve that fits, in terms of sea level frequency and amplitude, the relative sea level curves interpreted for each of the assessed carbonate platforms (figure 6.14). The composite relative sea level curve consists of one sea level cycle/period for the rhodalgal unit, this corresponds to the Malta and Las Negras platforms, three sea level cycles/periods for the coralgal reef unit that corresponds to the Llucmajor and Nijar platforms (the Las Negras and Malta platforms are interpreted to represent two and one cycles/periods respectively), and the oolitic/stromatolitic unit consists of one sea level cycle/period that corresponds to the Las Negras, Nijar and Malta platforms (figure 6.14). The composite relative sea level curve assumes the mismatch between relative sea level curves is the effect of temporal and amplitude uncertainty. The ability to construct a common RSL curve, within the uncertainty range (shaded area), for all platforms may suggest that that different RSL curves reported in literature may in part be the effect of uncertainty in relative sea level frequency and amplitude content. However, in view of the large uncertainty and the distinct relative sea level curves for platforms, developing a common RSL for different platforms might not be particularly revealing.

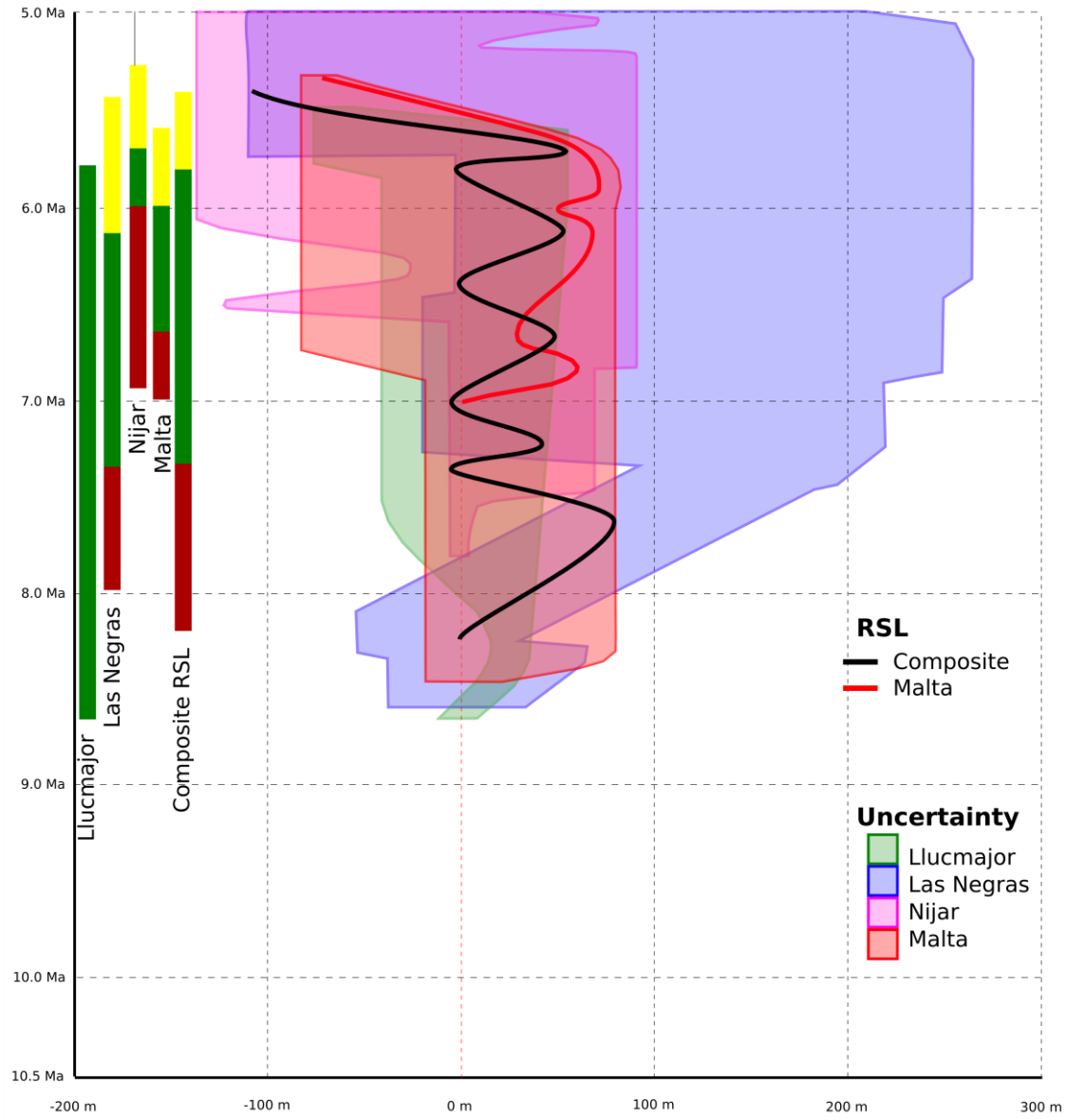

Figure 6.14: Relative sea level curve for each platform (figure 6.12) and associated uncertain due to a combination of uncertainty in ages of strata, and uncertainty in the water-depth interpretations. Shaded zones, colour coded for each platform, indicate the range of possible oscillation amplitude and frequency. The composite relative sea level curve (black line) fits the shaded zones interpreted for each of the assessed carbonate platforms (figure 6.12). The composite relative sea level curve consists of one sea level cycle/period for the rhodalgal unit, this corresponds to the Malta and Las Negras platforms, three sea level cycles/periods for the coralgal reef unit that corresponds to the Llucmajor and Nijar platforms (the Las Negras and Malta platforms are interpreted to represent two and one cycles/periods respectively), and the oolitic/stromatolitic unit consists of one sea level cycle/period that corresponds to the Las Negras, Nijar and Malta platforms. The columns in the left margin of graph represent the occurrences of factories in the respective carbonate platforms. The red bar is the rhodalgal factory, the green bar is the coralgal reef unit and the yellow bar is the oolitic/stromatolitic unit.

The different relative sea level curves proposed for the Late Miocene Mediterranean platforms may also be the consequence of multiple combined processes controlling nature of the strata at each location. Some controls may be shared (eustatic sea level), while others may be different and unique to each platform. Some examples of local processes include regional relative sea level rise and fall, local tectonically generated relative sea level, sediment production and transport changes, autocyclic effects (and their possible misinterpretation as changes in relative sea level) etc. Issues of uncertainty may obscure the extent to which sea level frequency and amplitude aspects were influenced by shared and unique processes/controls.

Conclusion

The Late Miocene relative sea level curves are different for different Mediterranean platforms. This is despite the implied contemporaneity and the regional controls, including eustasy, thought to have influence the deposition of these units (section 6.4). Whether the difference is due to uncertainty and/or multiple local controls, the validity of these different scenarios and interpretations need to be investigated using quantitative methods (e.g. SFM – chapter 7). Stratigraphic forward models (SFM) can be used to perform this sensitivity analysis and assess multiple theoretically plausible scenarios as explored in the following chapter (chapter 7).

CHAPTER 7: INVESTIGATING THE CONCEPTUAL MODEL, ALTERNATIVE HYPOTHESIS AND ISSUES OF NON-UNIQUENESS

7.1. Introduction

This chapter presents and applies a step-by-step quantitative method (figure 7.1) that builds on Paola's (2000) described potential application of quantitative techniques (section 2.3.2). The method integrates forward modelling with outcrop observations and enables the strengthening or rejecting of conceptual models (best fit analysis section 7.3), the investigating of alternative hypothesis and issues of non-uniqueness (sensitivity analysis section 7.4). The method may thus improve our understanding of platform evolution and also helps direct further research on platform evolution.

7.1.1. The method

Construct a conceptual model (*violet boxes in flow chart*)

Features observed in real sedimentary systems (e.g. skeletal grains, platform geometry, facies architecture, stacking patterns etc.) are used to construct conceptual models. Conceptual models represent a qualitative interpretation of how the sedimentary system might have evolved and are here treated as hypotheses. Issues of scale and internal consistency limit conceptual models. Consequently, qualitative conceptual models alone tend to be ineffective for improving our understanding of geological processes (section 2.3.2).

Best-fit analysis (*blue boxes in flow chart*)

Numerical SFM can overcome the limitations of conceptual models. SFM rely on equations and algorithms that support internal consistency and can now replicate features observed in real situations (e.g. Granjeon & Joseph, 1999; Bosence *et al*., 1994; Huessner *et al*., 2001; Granjeon *et al*., 2002; Warrlich *et al*., 2008; Chapter 4). This indicates that the models are governed by functions that replicate natural processes and dynamics. Additionally, when compared to conceptual models, SFM can help us investigate processes that are not obvious. Non-uniqueness (*sensu* Burgess & Prince, 2015) is an example of non-obvious behaviour, not least because this behaviour can only be properly explored via multiple runs of quantitative models.

The first part of the method requires the user to define model parameters and processes for SFM from the real sedimentary system (observations) and develop a conceptual model of how the real system might have evolved (interpretation) (section 7.3.1). This is necessary to ensure the model is characteristic of the depositional systems investigated and the controls that are thought to influence its evolution (conceptual model).

The resulting *numerical model* represents the conceptual model in terms of the processes and parameters selected. The computation of the numerical model will produce synthetic features

(stratal geometries, depositional thickness, facies architecture etc.) that are either similar or dissimilar to those observed in the real sedimentary system. If the synthetic and real features are similar, and modelled processes have been represented in a physically realistic way, this indicates that the conceptual model is a physically reasonable explanation (one of possibly several) for what is observed in the real sedimentary system. In this case, the *conceptual model is supported by the quantitative investigation.* If the numerical model however does not recreate the features seen in the real system, this suggests that the conceptual model may not be physically plausible. In this case, the *conceptual model is not supported by the quantitative investigation*. Such a result would indicate that the original conceptual model should be revised.

Non-uniqueness analysis (*green boxes in flow chart*)

A non-unique model (*sensu* Burgess & Prince, 2015) is one which develops indistinguishable results that occur as a result of different processes or parameter values in a conceptual or numerical. Non-unique stratal geometries are not demonstrably different from one another, and can occur as a consequence of different parameter values for controlling processes, or from entirely different controlling processes (Burgess & Prince, 2015).

If the numerical model only assesses a single set of processes and parameter rates, the user will not be able to determine if the conceptual model is a unique representation of platform evolution. To investigate issues of non-uniqueness, the user must assesses whether the parameters selected from the conceptual model are uniquely responsible for the features observed in the real sedimentary system or whether the simulation of other parameters and parameter rates can also develop features that are similar to those seen in the real system. Results from sensitivity analysis can develop numerical models that either display features that are distinct or similar to those developed in other numerical models that aim to replicate real sedimentary systems.

Each numerical model realisation, produced as part of a sensitivity analysis, is screened against real strata to determine if it is realistic to a defined degree. If the sensitivity analysis demonstrates that only one numerical model can reconstruct the features observed in the real system, then the realisation produced by the numerical model derived from a conceptual model is unique (unique model realisation). If, however, the sensitivity analysis develops other numerical models that demonstrate features similar to those observed in the real sedimentary system, the numerical models are added to a library of valid results, these are theoretically plausible non-unique scenarios. These are then compared against each other to determine whether they are all unique, or if there is non-uniqueness. If non-uniqueness is present, it can then be mapped, visualised and understood.

This exercise is theoretical in nature and is similar to previous investigations of non-uniqueness (e.g. Burgess & Prince, 2015). However, since the investigations carried out here relate to particular outcrop examples and real sedimentary systems, the theoretically plausible non-unique scenarios can be compared to the real carbonate platform/data. This will determine whether the theoretically non-unique scenario is or is not a good fit to the observed strata. Either outcome helps the user gain insight into platform evolution that would not have been possible without the application of this quantitative method. If the non-unique scenario is a good fit to the observed strata, the user may conclude that several model outputs are equally plausible as explanations for the features observed in the real sedimentary system. Such a result can help focus/direct further research/investigation on the particular sedimentary system and improve our understanding on controls on more or less likely controls platform evolution.

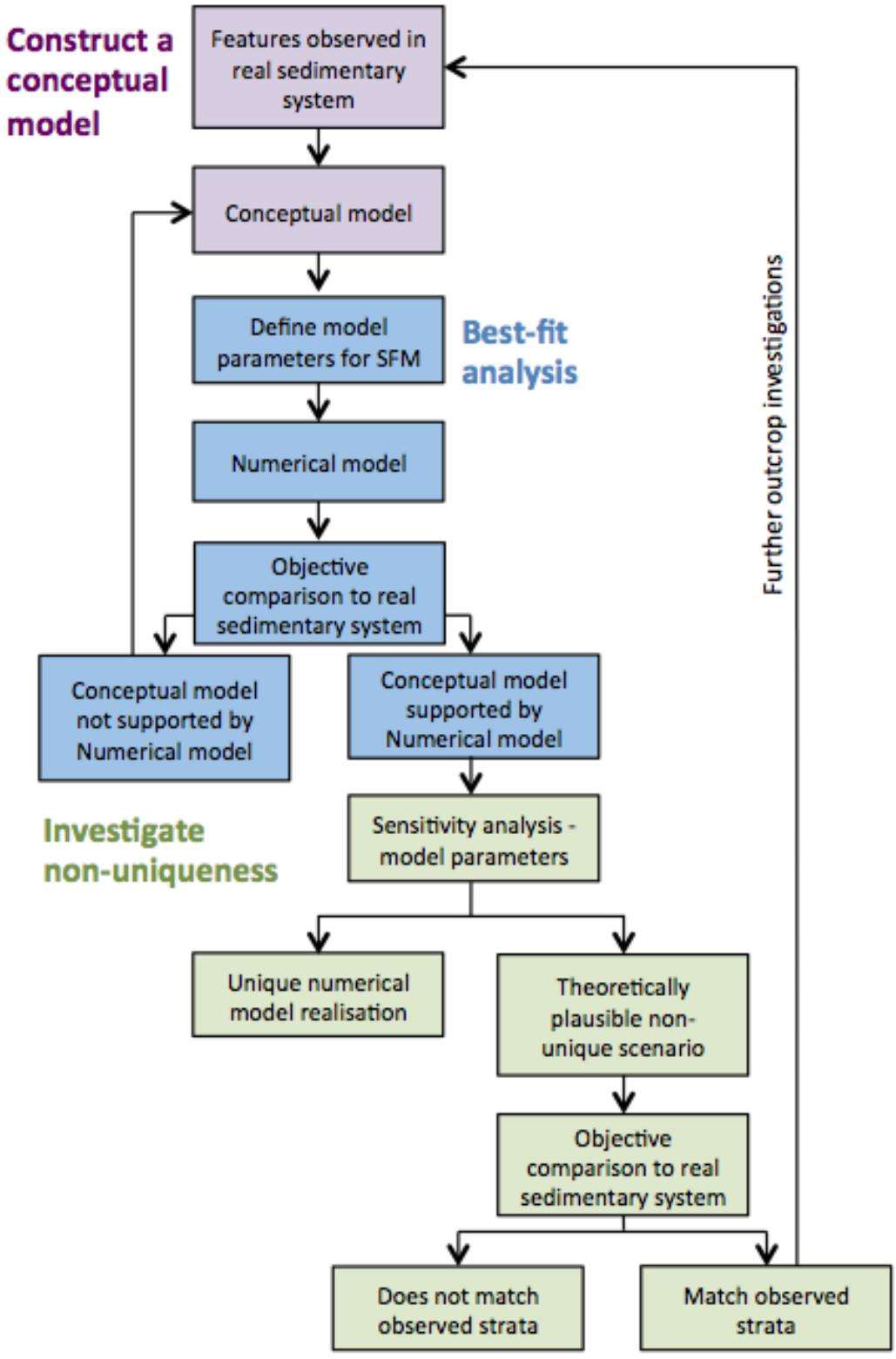

Figure 7.1: Flow chart that summarises the key steps of the method used in this chapter. The method integrates forward modelling with real observations and enables the strengthening or rejecting of conceptual models (best-fit analysis), the investigating of alternative hypothesis and issues of non-uniqueness (non-uniqueness analysis). The method may help sedimentologists strengthen or reject interpretations on controls on platform evolution and help focus/direct further research/investigation on understanding platform evolution.

7.1.2. Chapter aims

During the Late Miocene, the Maltese area formed a shallow marine carbonate platform that deposited the Upper Coralline Limestone (UCL) Formation (e.g. Pedley, 1974, 1976; Bosence & Pedley, 1982; Dart, 1991). A limited data set is available for the UCL Formation and interpretations on platform evolution are based on outcrop observations and shallow subsurface water borehole logs (chapter 5 and 6). In this study the quantitative method (figure 7.1) is applied to evaluate whether it can help assess the validity of the outcrop-based conceptual models of controls on platform evolution *(*best-fit analysis*)* and assess whether other plausible interpretations of controls on platform evolution are possible (non-uniqueness) *(*non-uniqueness analysis*)*.

Best-Fit Analysis

The section applies SFM and investigates whether the concept model and hypothesis are supported by the quantitative investigations. The degree of match between the numerical model and real sedimentary system features is quantitatively assessed on the basis of three factors (stacking patterns, platform margin slope gradients and facies recorded at particular locations) that represent some aspect of the real strata observed in the UCL Formation (table 7.2).

Conceptual model: The UCL Formation is subdivided into three depositional sequences (DS1, 2 and 3) (section 6.3). A distinct carbonate factory dominates each depositional sequence. The first-deposited depositional sequence (DS1) consists of the Coralline Algal Biostrome Facies Association (FA) and Sheltered Shelf Facies Association (FA). These form a distally steepened ramp (DSR) platform. Sediment production within DS1 is predominantly from the coralline red algal factory (heterozoan factory). The upper surface of DS1 is bounded by an erosional surface (sequence boundary 2) that is then overlain by depositional sequence 2. The latter depositional sequence consists of Reef-Core FA and the Fore-Reef Slope and Shelf FA. These form a flat top steep margin (FTSM) platform. Sediment production within DS2 is predominantly from the scleractinian coral factory (photozoan factory). The upper surface of DS2 demonstrates a sharp erosive contact (sequence boundary 3) that separates the underlying Reef-Core FA from the overlying Sand Shoal FA and Fore-Reef Slope and Shelf FA of depositional sequence 3 (DS3).

Interpretation/hypothesis: There is a marked change in platform geometry from DSR platform in DS1 to FTSM platform in DS2. Across the sequence boundary, there is a marked change in lithology and carbonate factories. DS1 is dominated by the heterozoan factory (produces deposits that are not bound together during deposition) while DS2 is dominated by the photozoan factory (produces deposits that are bound together during deposition).

The hypothesis is that the change in platform geometry is the result of a change from heterozoan to photozoan factories. The distinct platform geometries are interpreted to be the result of a

change of sediment production and transport ratios (chapter 3 and 4) brought about by the change in carbonate factories across the depositional sequences. This hypothesis is based on an understanding of how the heterozoan and photozoan factories are distinct from each other in terms of sediment production profiles, sediment production rates, and production of different grain-size proportions (chapter 3). Quantitative SFM-based investigations (chapter 3) indicate that the different platform geometries, ramp to FTSM platforms, are the result of distinct sediment production rates relative to sediment transport rates. The photozoan factory has a greater sediment production rate and produces grain-sizes that are less easily transported than the heterozoan factory. Consequently, the heterozoan factory has a high transport rate relative to production rate (low PR/TR ratio) and forms a ramp to DSR while the photozoan factory has a high sediment production rate relative to transport rate (high PR/TR ratio) and develops FTSM platforms (chapter 3 and 4).

Non-uniqueness analysis

Model sets (MS) 1, 2 and 3 investigate whether there are several sets of controlling factors that can plausibly explain the change in platform geometry observed from DS1 (DSR) to DS2 (FTSM). The section investigates the following possible alternative controlling factors: (MS1) changes in the rate of accommodation generation (icehouse *versus* greenhouse eustasy), (MS2) time and carbonate factory variable sediment production rates, and (MS3) time and carbonate factory variable sediment transport rates. Model set 4 (MS4) investigates whether a relative sea level curve that is distinct from that developed in the conceptual model, in both temporal and amplitude content (section 6.4 figure 6.6), can produce similar stacking patterns, platform margin slope gradients and facies (recorded at particular locations) to those observed in outcrop.

7.2. Methods

7.2.1. Choice of Stratigraphic Forward Model

Dionisos SFM is used in this study. Refer to chapter 2 (section 2.3.3.2) for a detailed description of the stratigraphic forward model.

A summary table (table 7.1) is presented below that indicates what model parameters were applied in this chapter. The parameter rates are described in more detail in the following sections within the chapter.

SFM parameters applied in section	7.4.2.1	7.4.2.2	7.4.2.3	7.4.2.4
DIONISOS	✓	✓	✓	✓
Model iterations	4	3	3	1
Duration (My)	2.1	2.1	2.1	2.1
Time step (My)	0.05	0.05	0.05	0.05
Cell size (km)	0.5	0.5	0.5	0.5
Initial bathymetry (figure)	4.1	4.1	4.1	4.1
Sea level history (figure)	7.8	7.11	7.11	7.11
Sediment production equalised production profile	✓	✓	✓	✗
Sediment production natural production profile	✗	✗	✗	✓
Single grain size	✓	✓	✓	✗
Multiple grain size	✗	✗	✗	✓
Sediment transport by diffusion ($km^2\ ky^{-1}$)	0 to 1	0 to 1	0 to 1	0 to 1
Wave and current modelling.	✗	✗	✗	✗
Sediment transport by slope failure	✓	✓	✓	✓
Sub-aerial erosion	✓	✓	✓	✓

Table 7.1: Summary of initial model conditions and input parameters.

7.2.2. Choice of 2D over 3D SFM

A comparison of dip transects in the Malta Horst and North Malta Graben shows that dip sections do not significantly vary along strike (figure 7.2, compare OCS 3, 4, 5 and 6). The dip line transects (W to E) are similar in terms of facies architectures, stacking patterns and platform geometry, but thicknesses varies. Since the sections are similar, it is unlikely that strike oriented sedimentary processes exerted significant control on platform evolution. In view of this, SFM in 2.5D or 3D are unnecessary and 2D simulations are sufficient. The simulation of platform evolution in 2D does not prevent the investigation of non-uniqueness.

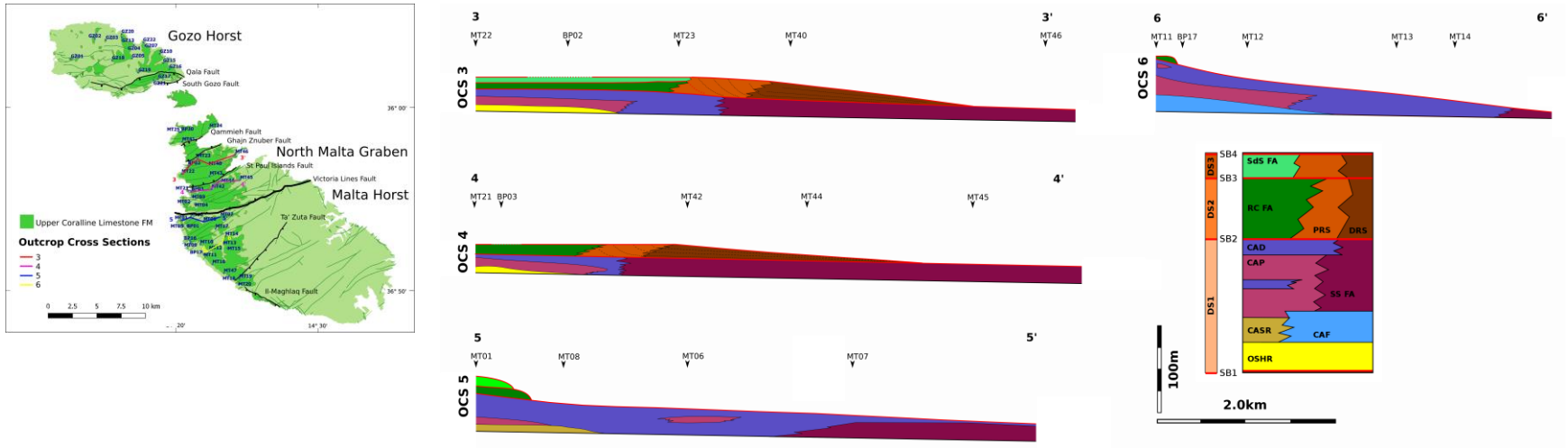

Figure 7.2: (A) Map showing the distribution of outcrop cross sections (OCS) 3, 4, 5 and 6, (B) Outcrop cross section across the North Malta Graben, and (B) outcrop cross sections across the Malta horst. Base of OCS logs corresponds to top of Blue Clay Formation.

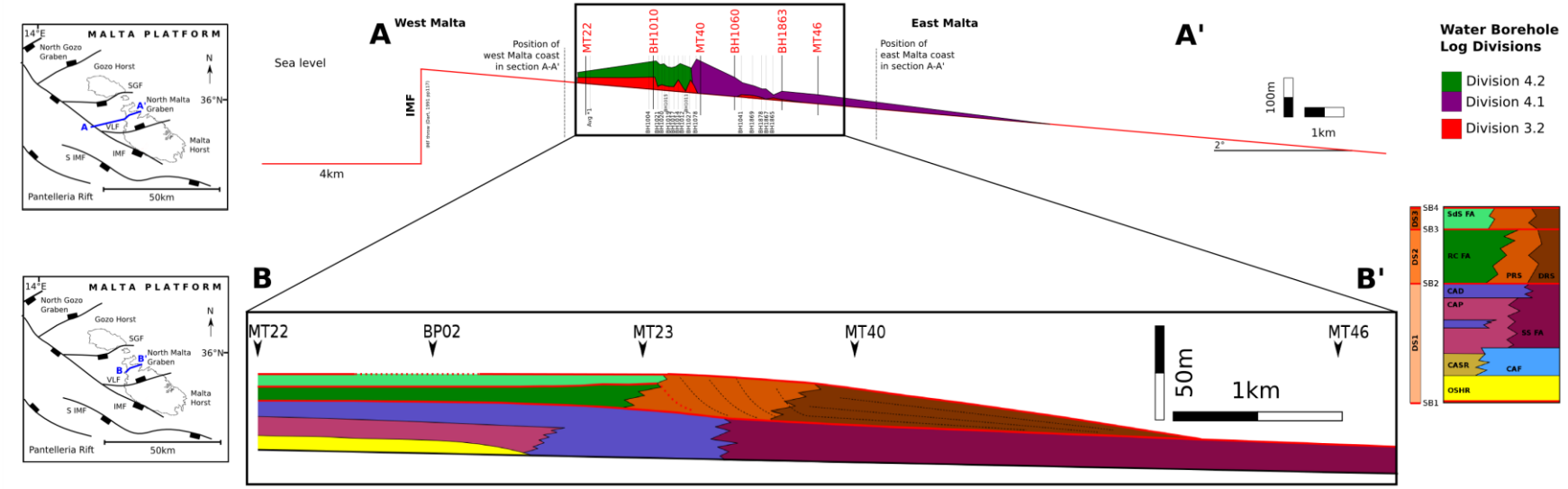

Figure 7.3: Section A-A' shows a transect across the IMF and shows thicknesses of divisions 3.2, 4.1 and 4.2 as identified from water bore hole logs (BH) and outcrop logs (MT). The red line shows the initial surface applied in numerical model. Section B-B' is of OCS3 transect.

7.2.3. Choice of dip transect for modelling

The North Malta Graben contains a thicker accumulation of the three depositional sequences (DS1, 2, and 3) than the Malta Horst. The North Malta Graben transect OCS3 (figure 7.2 and 7.3) is therefore preferred for the numerical simulations in this chapter. The facies observed in OCS3 and the interpreted depositional history is briefly described in section 7.3.1.2.

7.2.4. Functions to describe model match to real sedimentary system

The degree of match between the numerical model and real sedimentary system features is quantitatively assessed on the basis of three factors (table 7.3) that represent some aspect of the real strata observed in the UCL Formation (table 7.2).

The first factor (F_1) compares stacking patterns (aggradation, aggradation, retrogradation) [equation 1]. The second factor (F_2) compares maximum platform margin slope gradients [equation 2]. A quantitative metric was developed so as to compare the resulting simulated stratal architecture in terms of maximum topographic gradient (MaxS) along the depositional profile (measured in degrees). The third factor (F_3) compares the facies recorded at particular locations in real sedimentary system to the simulated facies at the same locations (table 7.2) [equation 3]. The facies recoded at the outcrop (MT22, MT40, MT46) and water boreholes (BH) (BH1010, BH1014, BH1027, BH1078, BH1041, BH1863) were compared to those simulated at the same positions (figure 7.3 for position of outcrop and borehole logs). The more matches expressed along the vertical section, the greater the factor match. A 100% match (1.00 F_3) requires each facies to be exactly the same thickness and exactly the same position within the three vertical sections. Such a match however does not imply a perfect match across the entire simulated 2D section. The top of the UCL Formation is in most cases the top of the studied outcrops. However, sub-aerial Quaternary deposits can locally cap the formation. Consequently, the true thickness of DS3 is not known.

Equation 4 quantifies the model match for entire simulation (MMS) relative to the real strata and depends on the results of the three individual factors (F_1, F_2 and F_3 in table 7.3).

Factor 1 (F_1) Stacking patterns	**Factor 2 (F_2)** Maximum platform margin slope gradients	**Factor 3 (F_3)** Approximate facies thickness. Outcrop logs (MT) and water bore hole logs (BH)
Photozoan Reef-Core FA: progradation Heterozoan CAP facies: aggradation - progradation	Photozoan Reef-Core FA and PRS facies: 10 to 30° Heterozoan CAP facies: up to 5°	MT22/BH1010 (figure 7.3) MT40/BH1060 (figure 7.3) MT46/BH1863 (figure 7.3)

Table 7.2: The match between model run and UCL Formation outcrop is based on outcrop data and depends on three quantitative functions: stacking patterns, maximum platform margin slope gradient and approximate facies architecture.

The degree of model match in F_1, F_2, F_3 and MMS [equations 1 to 4] is quantitatively expressed as a fraction where a score of 1 is a perfect match between the simulated and real factor. The three factors (F_1, F_2 and F_3) are given equal importance in equation 4. Consequently, models that have different factor values (F_1, F_2, F_3) may develop similar values of model match for simulation (MMS) [equation 4]. However, a high model match for simulation (MMS) is required for and reflects a good match in all three factors (F_1, F_2 and F_3).

[Equation 1] F_1: Stacking patterns (aggradation, progradation, retrogradation)
Score of 1 if sequence of stacking patterns in real sedimentary system matches SFM
Score of 0 if sequence of stacking patterns in real sedimentary system does not match SFM

[Equation 2] F_2: Maximum platform margin slope gradients
$F_2 = (SF_1/OF_1)$ *(use this equation when simulated MaxS ≤ UCL Formation MaxS)*
$F_2 = (OF_1/SF_1)$ *(use this equation when simulated MaxS ≥ UCL Formation MaxS)*
F_2 = Model Match Factor 1 (maximum platform gradient)
SF_2 = Simulated Factor 2 (simulated maximum platform margin slope gradient)
OF_2 = Real sedimentary system Factor 2 (observed maximum platform margin slope gradient)

[Equation 3] F_3: Facies at borehole logs BH1010, BH1060 and BH1863 (figure 7.3 for location and vertical facies)
$F_3 = (TM / TOL)$
F_3 = Model Match Factor 3 (facies comparison)
TM = Thickness of Match between the simulated facies and outcropping facies
TOL = Total Outcrop Log height (m) that compared against simulated facies

[Equation 4]
$MMS = F_1 * F_2 * F_3$
MMS = Model Match for Simulation (MMS units)

Table 7.3: Mathematical equations/functions that quantitatively assess which combination of sediment production and diffusional transport develop stacking patterns (F_1), maximum platform margin slope gradients (F_2), and facies architectures (F_3) similar to those observed in outcrops of the UCL Formation. Equation 4 quantifies the model match for simulation (MMS) based on the results of the three individual factors (F_1 to F_3).

7.2.5. Selection of grid size and time step

Sensitivity tests assessing a variable of gird sizes (1 km, 0.5 km and 0.25 km applying same 0.1 My time step) were carried out in chapter 3. Within the grid size range tested, a grid size of 0.25 km was select as suitable for this study. This grid size is sufficient to accurately simulate facies architecture at a scale similar to that assessed in outcrop. Sensitivity tests assessing variable SFM time steps (0.5 My, 0.05 My and 0.005 My) were also carried out in chapter 3. A time step of 0.03 My was applied in this study. This time step produces consistent and accurate maximum platform gradient (MaxS) results.

7.3. Best-fit analysis

7.3.1. Constraining model parameters from the conceptual model

The parameters and processes that are thought to influence the evolution of the Malta UCL carbonate platform include: initial surface, relative sea level curve, time of formation, sediment production, sediment transport, and sub-aerial erosion (chapters 5 and 6).

Model parameter	**Explanation**	**Certainty (decreasing order):** (i) Direct observation, (ii) Robust interpretation, (iii) Speculative interpretatoin
Initial surface	Based on the distribution of CAP, MCAD and PCAD Facies and their interpreted depth of deposition (chapter 6).	Robust interpretation
Sea level curve	Based on (i) facies and their interpreted palaeobathymetries, (ii) relative elevations of successive facies, (iii) thickness of platform facies, and (iv) stratal geometries (chapter 5 and 6).	Speculative interpretation
Time of formation	Based on Cornee *et al.* (2004) who identify and correlate three lithological units across the Late Tortonian–Messinian carbonate complexes of western and central Mediterranean (including the Maltese UCL Formation) (chapter 6).	Speculative interpretation
Sediment production	Based on the carbonate factories interpreted from outcrop. Factory sediment production rates, depth distribution of sediment production, and grain-sizes produced from Holocene carbonate platforms (Chapter 3).	Direct observation
Slope failure	Based on literature data on outcropping Mediterranean Miocene carbonate platforms were reviewed in terms of the slope angle, overall sediment texture and other details that may influence these two parameters (Chapter 4).	Direct observation
Diffusional transport	Based on inverse modelling in Chapter 4.	Speculative interpretatoin

Table 7.4: Evidence used to define/constrain model parameters. The table indicates the basis on which the modelling is being done – which model parameters are more robust and which are more speculative interpretation. This is in order to avoid issues of circular reasoning (section 4.2.2.1). Model parameters that are defined from direct outcrop observations are essential (e.g. sediment production rates). These model parameters are independent of the interpreted platform evolution and ground the model in observational truths. However, various model parmaters (e.g. relative sea level curve) are invariably interpreted from features observed in outcrop. These model parameters when input into SFM, may be subject to an element of circular reasoning.

7.3.1.1. Initial surface

Accumulations of the *in situ* CAF and CAP Facies in western Malta thin eastwards (figure 7.2) suggesting either eastward flowing currents that upwell on the westerly facing margins of the Il-Maghlaq Fault (IMF) footwall or an increase in depositional water depth to the east (section 6.2.2). During deposition of the Coralline Algal Biostrome FA and Sheltered Shelf FA, the Malta Platform (Malta Horst and Graben) is interpreted to have a <2° dip to the east (figure 7.3A). The interpretation is based on the distribution of CAP, MCAD and PCAD Facies and their interpreted depth of deposition (section 6.2.2).

Dart (1991 pp.114-117) and Dart *et al*. (1993) indicate that depth converted seismic sections of the Pantelleria Rift IMF show thickness increases (up to 250 m) down hanging-wall dip slopes. Depth conversion was using the Dix equation and internal velocity analyses were used to derive specific depths for specific locations on the seismic section (Dart, 1991 p.114). The deposits that accumulated within the hanging-wall during the early syn-rift include the Middle and Upper Globigerina Limestone Members, the Blue Clay Formation, OSGR Facies, and depositional sequences 1 and 2 of the UCL Formation (Dart *et al*., 1993; section 2.2.1.3). This suggests that the IMF developed fault related bathymetric relief during the Late Miocene. In view of this, the IMF is used to define the westernmost border of the Malta Horst and Graben in the numerical model (figure 7.3A red line).

7.3.1.2. Depositional model

A detailed description of the depositional model generated in this thesis for the Maltese UCL Formation is available in chapter 6 (section 6.2). On the basis of this both a sequence stratigraphic scheme (section 6.3) and a chronostratigraphic scheme (section 6.4) were developed. This information was used to develop a relative sea level curve (section 6.5). The parameters interpreted in chapter 6 are applied in this chapter (table 7.5).

Parameter	Description	Reference to chapter and section for detail
Stratigraphic relations (3D facies relations & correlations) and depositional history	Six facies associations (FA) and fifteen facies were identified in the study area within the Greensand and Upper Coralline Limestone formations.	Chapter 5 and section 6.2
Sequence stratigraphic scheme	Three depositional sequences identified (DS1, DS2 and DS3) and four sequence boundaries (SB1, SB2, SB3 and SB4). A distinct carbonate factory dominates each depositional sequence.	Chapter 6 section 6.3
Chronostratigraphic scheme and time of formation	SFM modelled to run from 7.0 to 5.5 Ma (a total run time of 1.5 My). Sediment production during DS1 is simulated from 7 to 6.7 Ma (EMT 0.3 My), sediment production during DS2 is from 6.7 to 5.9 Ma (EMT 0.8 My), and sedient production during DS3 is simulated from 5.9 to 5.6 Ma (EMT 0.3 My).	Chapter 6 section 6.4
Relative sea level	Interpreted relative sea level (RSL) curve defined from palaeobathymetric and stratal geometry data, dating and correlation of depositional sequences from central Mediterranean area.	Chapter 6 section 6.5

Table 7.5: Summary of SFM parameters applied in chapter 7 and interpreted from chapter 5 and 6.

7.3.1.4. Sediment production and synthetic facies

The simulated sediment production rates for each depositional sequence is based on the carbonate factories observed in outcrop. Sediment production in DS1 (figure 7.4A) is the sum of sediment produced by the rhodalgal (coralline red algae) factory (figure 3.1C) and the foramol/bryomol factory (figure 3.1D) - corresponding to the heterozoan factory. Sediment production in DS2 (figure 7.4B) is the sum of chlorozoan (scleractinian coral) factory (figure 3.1A), chloralgal (calcearous green algae) factory (figure 3.1B) and the foramol/bryomol (mollusc and bryozoan) factory (figure 3.1C). The chlorozoan and chloralgal factories correspond to the photozoan factory. Sediment production in DS3 (figure 7.4C) consists of non-skeletal grains (peloids and oods) and skeletal grains (calcareous green algea).

Sediment production by carbonate factories falls within a range (section 3.2.2). In view of this, seven distinct sediment production rates were tested for each of the four carbonate factories (figure 7.4); PR 100, PR 500, PR 1000, PR 1500, PR 2000, PR 2500, and PR 3000. PR 1000 represents the average sediment production by the carbonate factories (figure 7.4), PR 100 represents one tenth of sediment produced in PR 1000, and PR 3000 represents three times the average sediment production of PR 1000. All seven tested sediment production rates fall within the natural range of sediment production of the carbonate factory (section 3.2.2).

7.3.1.5. Sub-aerial erosion

In view of modern day analogues for rates of sub-aerial karst dissolution (section 4.2.2.1.7), an average sub-aerial dissolution rate of 0.03 m ky^{-1} was calculated from warm/tropical climates that may have existed in the Late Miocene (e.g. DS2 and 3) in the Malta Platform. This sub-aerial dissolution rate is simulated in the numerical model. Since the platform top is very infrequently and briefly sub-aerially exposed, and rates of sub-aerial erosion are relatively low, sub-aerial dissolution does not significantly impact platform evolution.

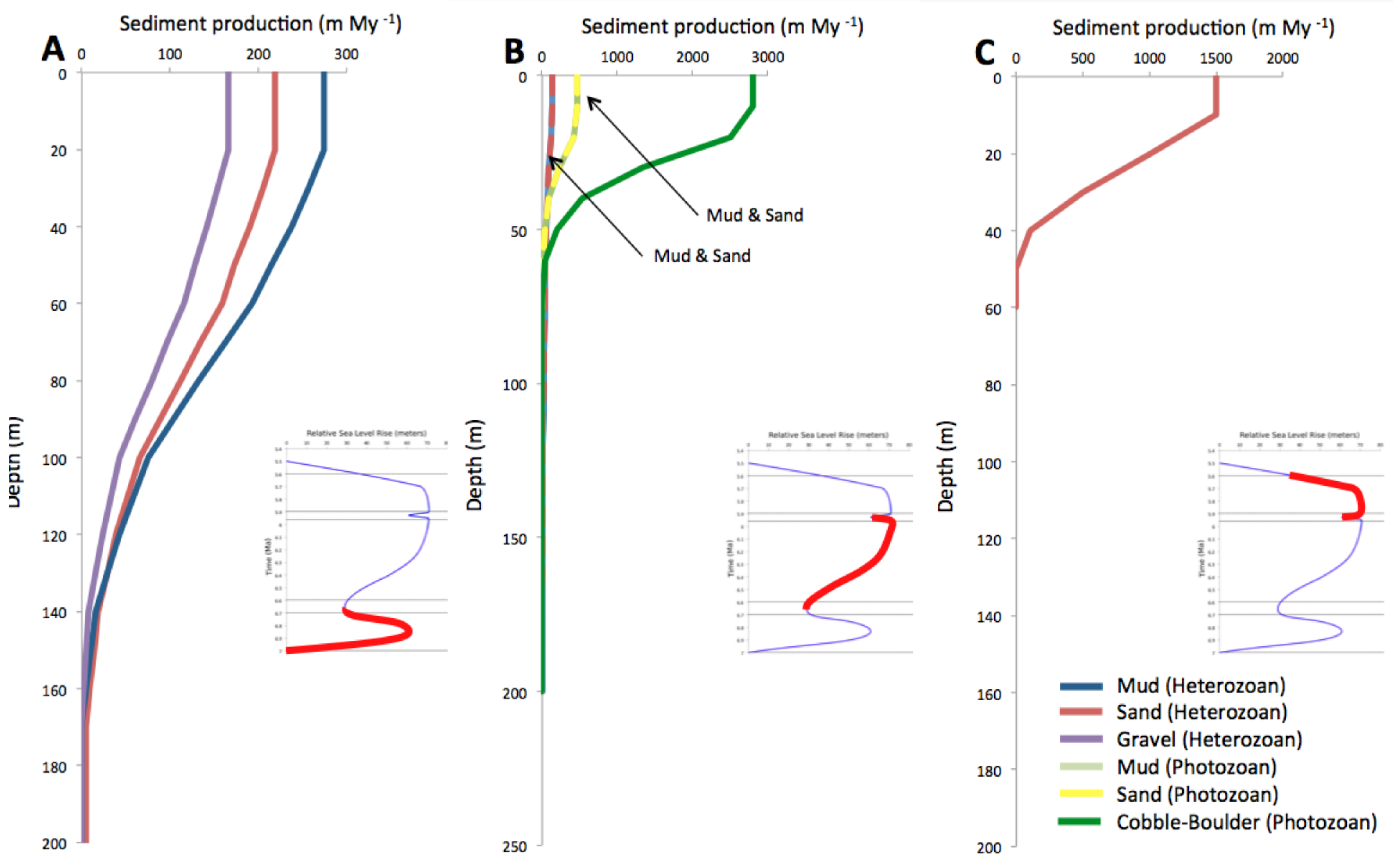

Figure 7.4: Grain size productoin profiles for (A) PR 1000 DS1, (B) PR 1000 DS2, and (C) PR 1000 DS3. Photozoan grain association includes sediment production from the scleractinian coral factory and the calcearous green algae factory (figure 3.1). Heterozoan grain association includes sediment production from the the coralline red algae factory and the foramol/bryomol factory (figure 3.1).

7.3.1.6. Sediment transport (slope failure and diffusional transport)

Slope failure

In circumstances where sediment accumulation rates exceed transport rates, slope gradients steepen. A threshold may eventually be reached where gravitational sheer stress exceeds the shear strength of the constituent materials. Beyond this critical slope threshold, sediment becomes unstable and is transported down-slope to gradients below the critical threshold (Schlager and Camber, 1986). Chapter 4 (section 4.2.2.1.6) investigates slope angle and sediment texture and develops slope failure angles for different textures. These are applied in this chapter.

Diffusion coefficeint

Calcareous grains produced by carbonate factories may be transported at different rates depending on grain-size and bulk density. In this study, the relation between grain-size and transport rate has been expressed by attributing a sediment transport by diffusion coefficient that is inversely proportional to grain-size. In this context, coarser material is expressed as sediment with a low diffusion coefficient and hence a lower diffusional transport rate than finer-grade material.

Chapter 4 (section 4.3.1) investigated which combination of sediment production and diffusional transport develops distinct platform types (e.g. flat top steep margin and ramp). Results indicated that stratal geometry observed in outcrops of the reef-rimmed Llucmajor FTSM platform form with a high PR/TR ratio (sediment production rate of PR 2000 and grain-size diffusion coefficients mud 0.1 km^2 ky^{-1}, sand 0.033 km^2 ky^{-1}, gravel 0.0083 km^2 ky^{-1} and cobble 0.0021 km^2 ky^{-1}). Since both the Llucmajor and Maltese carbonate systems have similar platform geometries, similar PT/TR ratios were applied. Sediment transprt rates may vary across carbonate systems with similar platform geometries. To take this factor into account, this chapter tests a range of diffusion coefficients one order of magnitude greater and lower than those identified in chapter 4 (from 0.01 km^2 ky^{-1}, sand 0.0033 km^2 ky^{-1}, gravel 0.00083 km^2 ky^{-1} and cobble 0.00021 km^2 ky^{-1} to 1.0 km^2 ky^{-1}, sand 0.33 km^2 ky^{-1}, gravel 0.083 km^2 ky^{-1} and cobble 0.021 km^2 ky^{-1}).

7.3.1.7. Relative sea level curve

The relative sea level curve applied in this chapter (figure 7.11 red line) is based on on the chronostratigraphic scheme (section 6.4) and the interpreted depositional environments (chapter 5 and section 6.2) for the observed facies in the UCL Formation.

7.3.2. Best-fit analysis conceptual model – SFM

7.3.2.1. Describe model parameters (PR and DC) that produce best match

Across the tested range of sediment production rates (section 7.3.1.4) and diffusional transport rates (section 7.3.1.6), the highest model match achieved between the numerical model and outcrop features is 0.80 MMS [equation 4] (figure 7.6). The match was achieved simulating a sediment production rate displaed in figure 7.5. These sediment production rates fall within the natural range of sediment production of Holocene carbonate factories (Chapter 3). The same grain size diffusion coefficients were applied across the three depositional sequences: mud 0.0165 km^2 ky^{-1}, sand 0.0042 km^2 ky^{-1}, gravel 0.002 km^2 ky^{-1} and cobble 0.001 km^2 ky^{-1}. These diffusion coefficient rates are of the same order of magnitude as those developed in chapter 4 (section 4.3.1.1) (table 7.6).

Diffusional transport rate (km^2 ky^{-1})	Mud (mudstone)	Sand (grainstone)	Gravel (rudstone)	Cobble (framestone)
Llucmajor	0.1	0.033	0.0083	0.0021
Malta	0.0165	0.0042	0.002	0.001

Table 7.6: Comparison of diffusion coefficients applied to develop highest model match achieved between the numerical model and outcrop features.

Despite the inverse and iterative method, a perfect match between SFM and UCL Formation conceptual model was not achieved. Two issues are thought to contribute towards this non-zero mismatch. Firstly, SFM simulations of sediment transport do not perfectly represent the natural processes that actively contribute different volumes of sediment towards total sediment transport. Sediment transport processes active in natural systems may not be accurately represented by the simplified diffusion formulation and therefore a perfect match may not be possible. Secondly, a more precise model match might be achieved with a more extensive exploration of the sediment production and diffusional transport parameter space tested in the simulations.

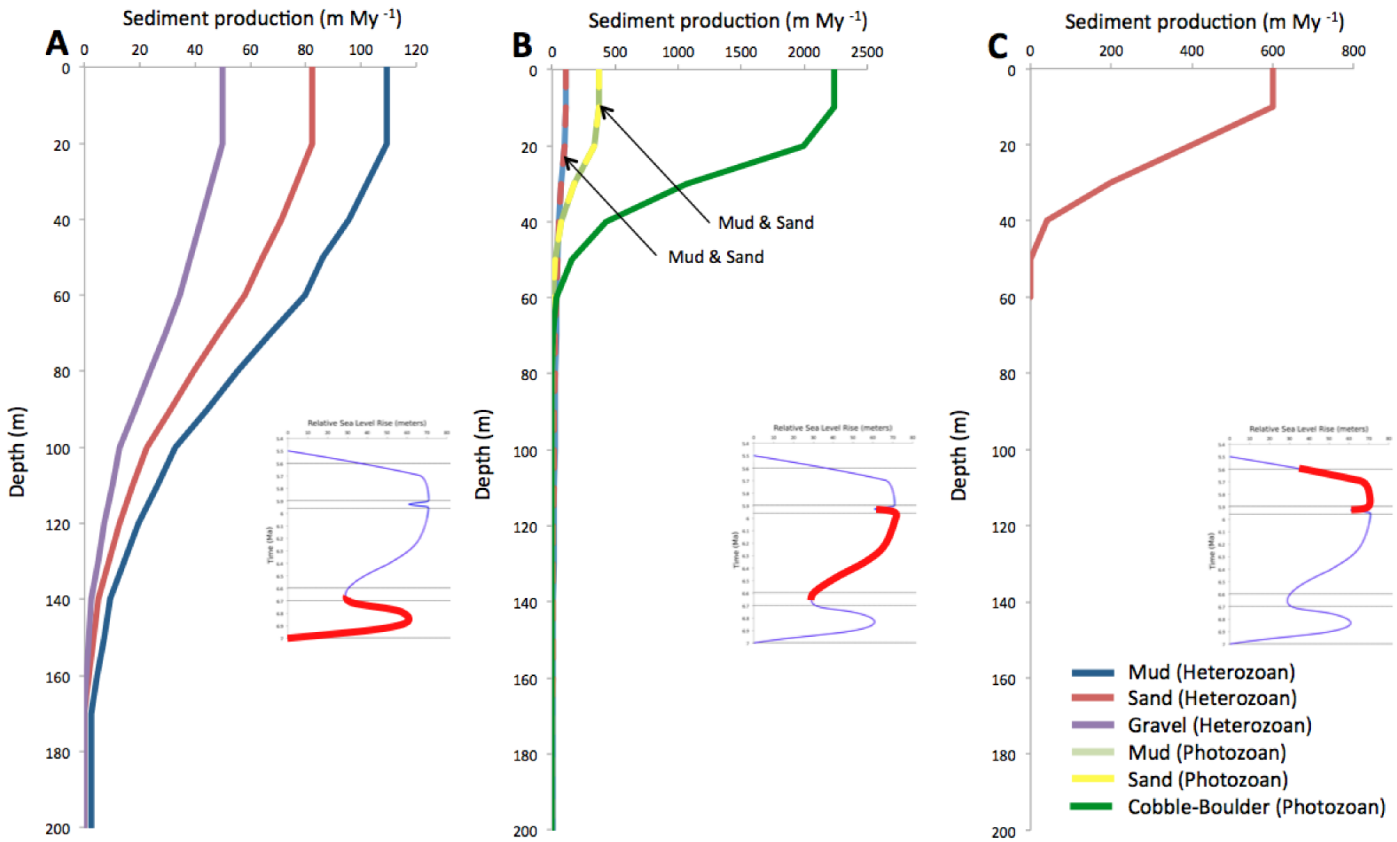

Figure 7.5: Grain size productoin profiles that develop the highest match between numerical model and outcrop features: (A) PR during DS1 corresponding to the heterozoan factory, (B) PR during DS2 corresponding to the photozoan factory, and (C) PR during DS3. Photozoan grain associaiotn includes sedimet production from the scleractinian coral factory and the calcearous green algae factory (figure 3.1). Heterozoan grain association includes sediment production from the the coralline red algae factory and the foramol/bryomol factory (figure 3.1).

7.3.2.2. Comparison between numerical model displaying highest MMS and outcrop features

The following section compares the best matching numerical model (figure 7.6) to the outcrop features observed in the UCL Formation (figure 7.3). The comparison is in terms of stacking patterns (F_1), maximum platform margin slope gradients (F_2) and facies (F_3) (table 7.3).

Stacking patterns (F_1)

The interpreted relative sea level curve for DS1 consists of an initial rapid relative sea level rise that peaks at 6.83 Ma and subsequently rapidly declines to a minimum at 6.65 Ma to form the sequence boundary 2 (SB2) (figure 7.6). Outcrop observations indicate that the Coralline Algal Pavement (CAP) Facies, within the Coralline Algal Biostrome FA (DS1), develops aggradational and progradation bedforms (section 5.2.3). The numerical model displays initially aggradational and then progradational stacking patterns composed of rudstones in DS1 (figure 7.6). The simulated rudstone textures correspond to the observed CAP facies that consists of rhodolith rich rudstone beds. The simulated aggradational to progradational bedforms indicate that sedimentation rates gradually outpace the rates of base-level rise and progressively reduced marine water depths via normal regression. The conceptual model interprets the CAP Facies as late transgressive and highstand deposits. The numerical model indicates this interpretation is physically possible within the sediment production and diffusional transport rates simulated. The numerical model is therefore consistent with the conceptual model of DS1 for the UCL Formation.

DS2 overlies the SB2. The interpreted relative sea level curve for DS2 consists of a more gradual relative sea level rise that plateaus at 6.2 Ma, remains level until 5.95 Ma and subsequently rapidly declines to a minimum at 5.92 Ma forming sequence boundary 3 (SB3) (figure 7.6). Outcrop observations indicate that the Reef-Core FA and Fore-Reef Slope and Shelf FA (DS2) develop progradation bedforms (section 5.3.5 figure 5.63). The numerical model displays progradational stacking patterns composed of framestone and rudstone-packstone textures (figure 7.6) corresponding to the Reef-Core FA and the Fore-Reef Slope and Shelf FA respectively. The high chlorozoan sediment production rates clearly outpaced the rates of base-level rise leading to normal regression and relative sea level shallowing that further accelerated progradation. The conceptual model interprets the Reef-Core FA as late transgressive and highstand deposits. The numerical model indicates this interpretation is physically possible within the sediment production and diffusional transport rates simulated. The numerical model is therefore consistent with the conceptual model of DS2 for the UCL Formation.

DS3 overlies SB3 and consists of the Sand Shoal FA. The numerical model simulates

grainstone textures, corresponding to the Sand Shoal FA. In the SFM, these packstone/grainstones overlie and sharply contrast with the framestone texture representing the Reef-Core FA. Above this contact, reef growth is abruptly terminated and the facies are dominated by grainstones of the Sand Shoal FA. This relationship is observed in northwest and west areas of Malta where a sharp contact separates the Sand Shoal FA from the underlying Reef-Core FA (section 5.3.6). In the numerical model, the packstone deposits of the Sand Shoal FA (DS3) are also observed eastwards of the Reef-Core FA framestones within the grainstones of the Fore-Reef Slope and Shelf FA (figure 7.9). In the numerical model, these grainstones occur in depths greater than that in which they are simulated to form (>40 m). This indicates that the grainstones originated from shallow marine western areas and were subsequently transported eastwards. In outcrop, oolitic sediments were also observed eastward of the Sand Shoal FA in Fore-Reef Slope and Shelf FA (PRS Facies section 5.3.5.1). These were interpreted as contemporaneous with and sourced from the Sand Shoal FA. This interpretation is therefore consistent with the conceptual model of DS3 for the UCL Formation.

In view of the high match between the stacking patterns and textures of the synthetic and real sedimentary system, the factor was set at $1.00F_1$ [Equation 1] (figure 7.6).

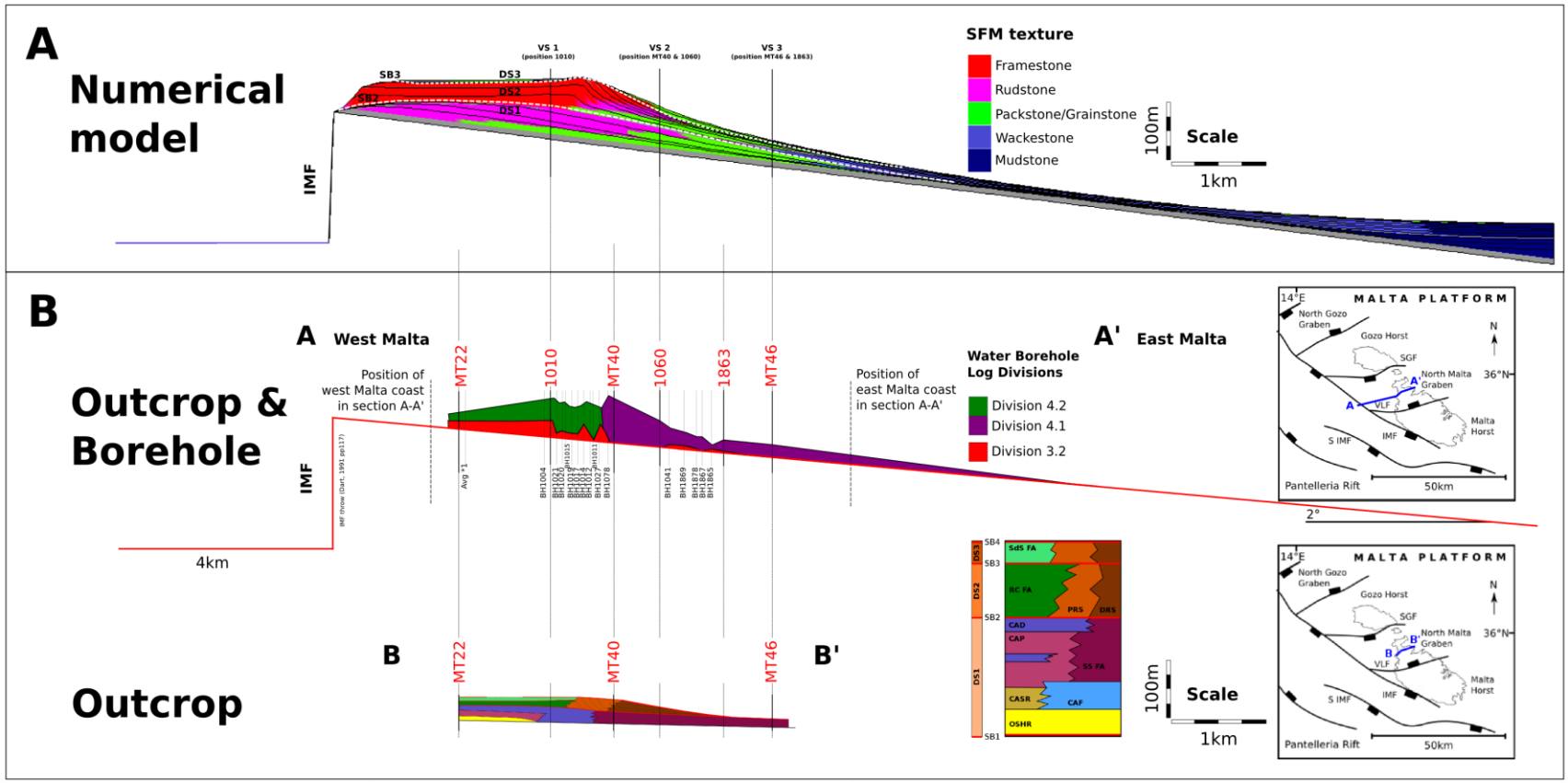

Figure 7.6: (A) 2D SFM simulation of section A-A' and B-B' (figure 7.3 and 7.6B) that develops best match to the UCL Formation in terms of stacking patterns (F_1), platform margin slope gradients (F_2) and facies recorded at particular locations (VS1, VS2 and VS3) (F_3). The figure presents 2D simulation of stacking patterns (F_1), platform margin slope gradients (F_2) that can be compared to section A-A' and B-B' (figure 0.0) from real platform. A comparison of simulated and real facies recorded at particular locations is available in figure 7.7. One time step (black line in 2D SFM) of 0.12 My EMT. (B) Transect across the IMF and shows thicknesses of divisions 3.2, 4.1 and 4.2 and facies architecture as identified from water bore hole logs (BH) and outcrop logs (MT).

Maximum platform margin slope gradients (F_2)

In terms of the platform maximum gradient factor (F_2), the best model match develops maximum gradients of 5.1° for DS1 and 10.7° for DS2. The simulated gradients correspond to those measures in outcrops up to 8° for the CAP Facies (DS1) and 10 to 30° for the Proximal Reef Slope (PRS) Facies deposited in proximal reef slope settings (Chapter 4). In view of this, the factor was calculated as $1.00F_2$ [Equation 2].

Facies at borehole logs BH1010, BH1060 and BH1863 (F_3)

The depositional textures in outcrop logs (MT22, MT40 and MT46) and in boreholes (BH1010, BH1060 and BH1863) (figure 7.7) are compared against the facies simulated at the same positions (vertical sections - VS) in the best-fit model. The quantitative comparison is through factor (F_3). Results demonstrate an overall (VS1, VS2 and VS3) depositional texture and facies match of 90% and an overall thickness match of 80% (0.80 F_3 [Equation 3]) to boreholes (BH1010, BH1060 and BH1863).

The facies observed in outcrop log MT22 consist of a succession of CAP Facies (rudstone) and CAD Facies (rudstone to packstone) of DS1. An unconformity (SB2) caps DS1, over which the CPR Facies (framestone) of DS2 occurs. DS2 is terminated by an unconformity (SB3) that is in turn overlain by Sand Shoal FA of DS3. Borehole log BH1010 reflects this sequence and consists of Division 3.2 that corresponds to the Coralline Algal Biostrome FA, and Division 4.2 that corresponds to the Reef-Core FA and Sand Shoal FA (table 5.2 and appendix C 1.2). The facies recoded at the outcrop MT22 and BH1010 are compared to those simulated at the same positions VS1 (figures 7.6 and 7.7). VS1 demonstrates a 91% depositional texture and facies match and an 88% thickness match to borehole BH1010 (figures 7.6 and 7.7). VS1 develops a succession of packstone to rudstone textures, corresponding to the Coralline Algal Pavement Facies and Coralline Algal Debris Facies (DS1). This is then overlain by framestone textures, corresponding to the Reef-Core FA (DS2) that is subsequently overlain by grainstone textures that correspond to the Sand Shoal FA (DS3).

Outcrop log MT40 consists of Sheltered Shelf FA (packstone to wackestone) of DS1 and is overlain by PRS-DRS Facies (packstone) of DS2 and DS3. Borehole log BH1060 reflects this sequence and consists of Division 4.1 that corresponds to both Sheltered Shelf FA (PCAD Facies) and Fore-Reef Slope and Shelf FA (table 5.2 and appendix C 1.2). VS2 demonstrates an 84% depositional texture and facies match and a 71% thickness match to BH1060 (figures 7.6 and 7.7). The facies recoded at the outcrop MT40 and BH1060 are compared to those simulated at the same positions VS2 (figure 7.6 and 7.7). VS2 develops a vertical succession of packstone to rudstone that corresponds to the Sheltered Shelf FA and CAP Facies (DS1). The facies mismatch is from the simulated rudstone textures in DS1. The simulated rudstone textures

(DS1) are from the CAP Facies, however, outcrop and borehole logs indicate wackestone-packstone textures of the Sheltered Shelf FA should be present. In terms of progradation distance the modelled rudstone strata in DS1 have a greater progradation distance than that occurring in the Malta platform.

Outcrop log MT46 consists of Sheltered Shelf FA (packstone to wackestone) of DS1. Borehole log BH1863 reflects this sequence and consists of Division 4.1 that corresponds to the PCAD Facies of the Sheltered Shelf FA. The facies recoded at the outcrop MT46 and BH1863 are compared to those simulated at the same positions VS3 (figure 7.6 and 7.7). VS3 demonstrates a 100% depositional texture and facies match and a 72% thickness mismatch to borehole BH1863 (figure 7.6 and 7.7). VS3 develops a vertical succession of packstone, corresponding to PCAD Facies.

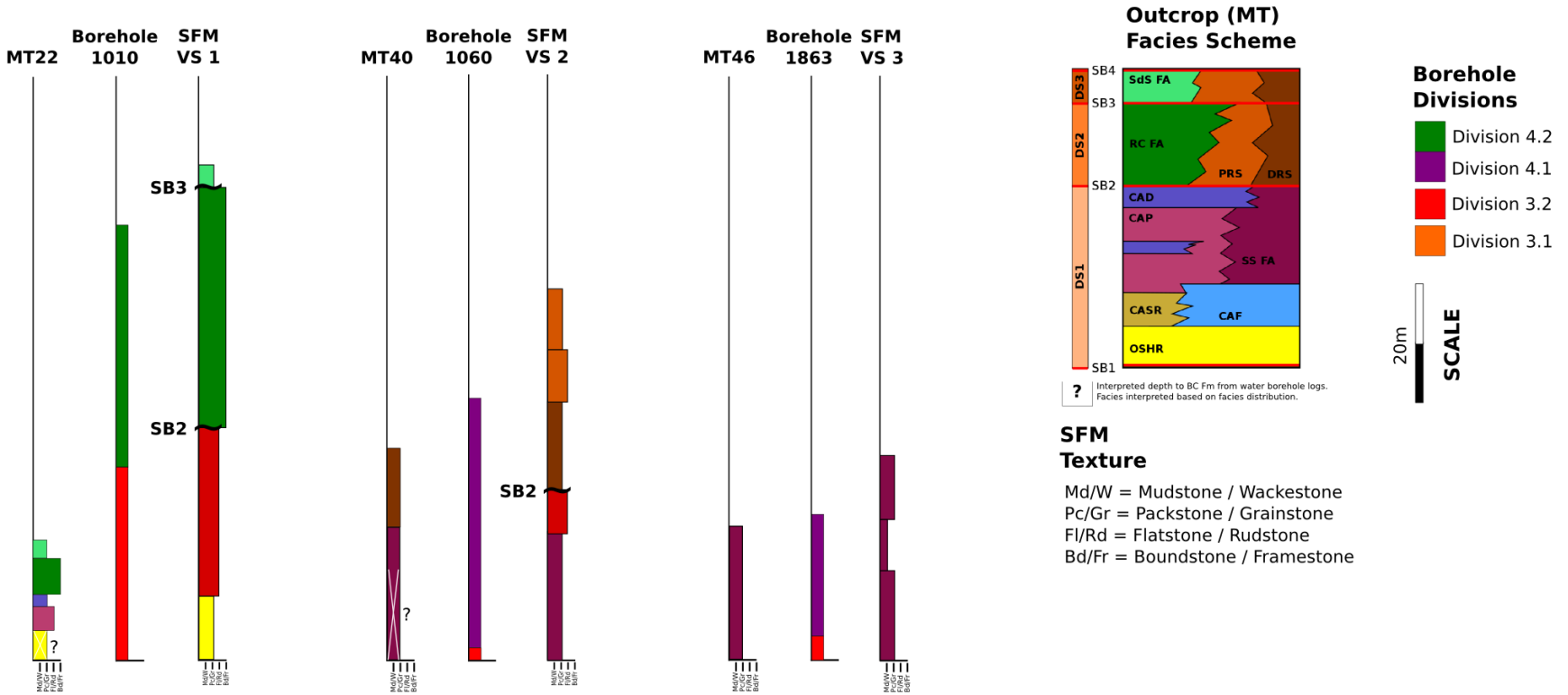

Figure 7.7: 2D model outputs showing (F_3) stratal thickness match between real facies (outcrop and borehole) and simulated facies (SFM VS1, 2 and 3). A systematic comparison of borehole to nearby outcrops (<50 m) was carried out in Chapter 5. This allowed the development of a scheme that indicates which descriptive terms used in the borehole logs relate to stratigraphic divisions (Appendix C5.2). See table 5.2 for description on which borehole log divisions relate to which stratigraphic divisions (facies associations & facies).

7.3.2.3. Does the numerical model support the conceptual model and the hypothesis?

The numerical model replicates key stacking patterns, platform margin slope gradients, facies architecture and facies belts observed in Maltese UCL Formation strata (compare figure 7.3 and 7.9). For DS1, the numerical model demonstrates a basinward transition from rudstone, packstone, wackestone-mudstone textures (figure 7.9). This corresponds to the CAP and CAD Facies, that transition basinward to Sheltered Shelf FA (MCAD and PCAD Facies) (figure 7.3). For DS2, the numerical model demonstrates a basinward transition from framestone, rudstone, packstone, and wackestone-mudstone textures (figure 7.9). This corresponds to the Reef-Core FA (CFR and CPR Facies) that transition basinward to the Fore-Reef Slope and Shelf FA (PRS and DRS Facies) (figure 7.3). For DS3, the numerical model develops grainstone textures that overlie the framestone textures (figure 7.9). This corresponds to the Sand Shoal FA that overlie the Reef-Core FA (figure 7.3).

In the numerical model there is a marked change in platform geometry from DSR platform in DS1 to FTSM platform in DS2. In the numerical model, the distinct platform geometries are the result of distinct sediment production and transport ratios brought about by the change in carbonate factories across depositional sequences – DS1 heterozoan and DS2 photozoan. This hypothesis is further investigated in MS2 (section 7.4.2.2). The photozoan factory, relative to the heterozoan factory, has a greater sediment production rate and produces grain-sizes that are less easily transported. Consequently, the heterozoan factory has a high transport rate relative to production rate (low PR/TR ratio) and forms a ramp while the photozoan factory has a high sediment production rate relative to transport rate (high PR/TR ratio) and develops FTSM platforms.

The close match between outcrop and numerical model indicates that the conceptual model – expressed as model parameters (e.g. relative sea level curve, timing of deposition etc.) and processes (sediment production and transport) in the numerical model - are physically reasonable explanation for the features observed in outcrop. The numerical model also indicates that a change in platform geometry is a result of a shift in carbonate factories is a physically reasonable hypothesis.

The match does not prove the conceptual model and the interpretation/hypothesis are correct. One should also be aware of an important caveat. The SFM parameters selected from the conceptual model might not be uniquely responsible for the features observed in outcrop. One should further investigate whether the simulation of other parameters and process rates can also develop similar features to those seen in outcrop (section 7.4).

7.4. Non-uniqueness analysis

The following section assesses whether numerical models that simulate parameters and process rates that are distinct from those applied in the previous section (best-fit analysis) can also develop synthetic features that are similar to those seen in the Maltese UCL Formation. These tests also assess wheter seemingly non-realistic rates can produce a good match to observed strata. This additional examination eliminates elements of circular reasoning - our understanding and assumption on how sedimentary processes operate influence the conceptual model. Additionally, this investigation helps rule out or confirm other plausible conceptual models on platform evolution that helps focus future research on platform evolution.

Section 7.4.1 describes the model sets (MS) and the model parameter/process that are focused upon in the sensitivity analysis. Section 7.4.2 quantitatively investigates the degree of match between the MS and real strata. If any models also produce a good match, this would indicate non-uniqueness.

7.4.1. Model parameters

Four model sets (MS) are investigated in this section. Each MS performs a sensitivity analysis on a single process while keeping all other parameters constant, allowing assessment of the degree of control this single process may have on the model fit, and on the observed strata. *MS1* - changes in the rate of accommodation generation due to icehouse *versus* greenhouse eustasy; *MS2* - time and carbonate factory variable sediment production rates; *MS3* - time and carbonate factory variable sediment transport rates; and *MS4* - variable total SFM run time (table 7.7).

Model Set (MS)	**Relative sea level (RSL)**	**Sediment production** Heterozoan (H) (7 to 6.6 Ma) and Photozoan (P) (6.6 to 5.5 Ma)	**Diffusional sediment transport** Heterozoan (H) (km^2 ky^{-1}) and Photozoan (P) (km^2 ky^{-1})
MS 1.1	**Greenhouse** 100 ky period 2 m amplitude, 40 ky period 2 m amplitude (figure 7.8)	Equalised single grain size type H = P (figure 7.8B)	H 0.0001 = P 0.0001
MS 1.2	**Icehouse** 400 ky period 70 m amplitude, 100 ky period 20 m amplitude (figure 7.8)	Equalised single grain size type H = P (figure 7.8B)	H 0.0001 = P 0.0001
MS 1.3	**Icehouse to Greenhouse** Icehouse (from 7 to 6.6 Ma), Greenhouse (from 6.6 to 5.5 Ma) (figure 7.8)	Equalised single grain size type H = P (figure 7.8B)	H 0.0001 = P 0.0001
MS 1.4	**Greenhouse to Icehouse** Greenhouse (from 7 to 6.6 Ma), Icehouse (from 6.6 to 5.5 Ma) (figure 7.8)	Equalised single grain size type H = P (figure 7.8B)	H 0.0001 = P 0.0001
MS 2.1	Original RSL (figure 7.11 red line)	Equalised single grain size type **H = P (figure 7.9A)**	H 0.002 = P 0.002
MS 2.2	Original RSL (figure 7.11 red line)	Equalised single grain size type **H > P (figure 7.9B)**	H 0.002 = P 0.002
MS 2.3 Similar PR to best-fit analysis (section 7.3.2.1)	Original RSL (figure 7.11 red line)	Equalised single grain size type **H < P (figure 7.9C)**	H 0.002 = P 0.002
MS 3.1	Original RSL (figure 7.11 red line)	Equalised single grain size type H = P (figure 7.10)	**H 0.0165 = P 0.0165**

MS 3.2	Original RSL (figure 7.11 red line)	Equalised single grain size type H = P (figure 7.10)	**H 0.001 < P 0.0165**
MS 3.3 Similar DC to best-fit analysis (section 7.3.2.1)	Original RSL (figure 7.11 red line)	Equalised single grain size type H = P (figure 7.10)	**H 0.0165 > P 0.001**
MS 4	Different **RSL and SFM run time** within uncertainty range (figure 7.11 black line) RSL is common to late Miocene central and western Mediterranean carbonate platforms	Multiple grain size type H < P (figure 7.15) PR rate applied in MS4 is 37% less for the P factory and 88% less for the H factory than that applied in the best-fit analysis (section 7.3.2.1)	Md 0.0165, Sd 0.042, Grv 0.002, Cbl-Bld 0.001 DC rate same as that applied in the best-fit analysis (section 7.3.2.1)

Table 7.7: Non-uniqueness analysis. Text in green indicates the model parameter subject to the sensitivity analysis. Sediment production for the heterozoan and photozoan factories was equalised (photozoan factory made to match heterozoan factory production rates) following the method described in section 3.2.3.

7.4.1.1. MS1: Accommodation (sea level cycles)

MS1 investigates four different relative sea level curves (table 7.7 and figure 7.8). The sea level curves are distinct from one another in their frequency and amplitude content, but are the same in terms of total duration (1.5 My). MS1.1 simulates a greenhouse system and MS1.2 simulates an icehouse system through the entire model run. MS1.3 simulates a system that is initially subject to icehouse (from 7 to 6.6 Ma) and then to greenhouse (from 6.6 to 5.5 Ma) conditions. MS1.4 simulates a system that is initially subject to greenhouse (from 7 to 6.6 Ma) and then icehouse (from 6.6 to 5.5 Ma) conditions. Greenhouse eustasy is modelled with two components: 100 ky period with 2 m amplitude and a 40 ky period with 2 m amplitude. The icehouse eustasy is modelled with two components: a 400 ky period with 70 m amplitude and 100 ky period with 20 m amplitude.

Total sediment production and diffusional transport for the heterozoan and photozoan factories were made equal in MS1 simulations. This is to ensure that the differences in the platform evolution are known to be the consequence of differences in relative sea-level history (and to a lesser extent the production profile see Chapter 3), and not due to variations in sediment production or diffusional transport between the two factories. To that end, all MS1 models only simulate one grain size type with the same diffusion coefficient (0.0001 km^2 ky^{-1}) and total sediment production was equalised between the heterozoan and photozoan factories (figure 7.8B for equalised production profile).

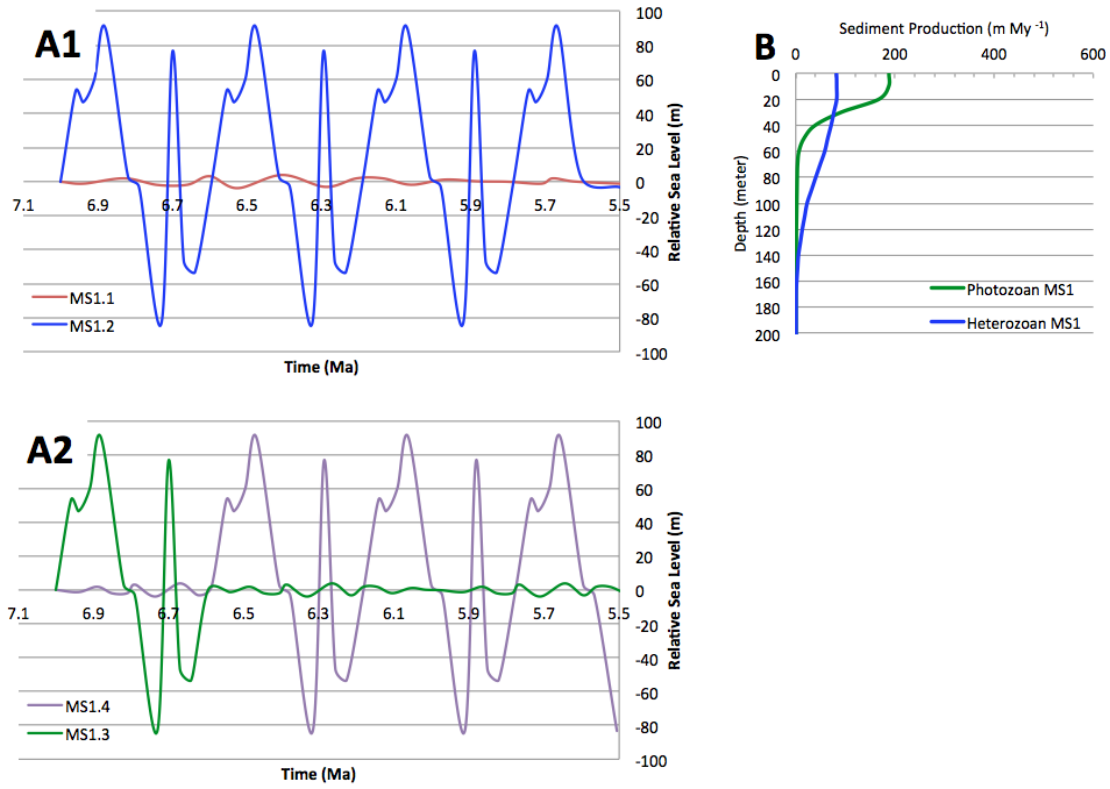

Figure 7.8: (A1 and A2) Relative sea level curves for MS1.1 greenhouse, MS1.2 icehouse, MS1.3 icehouse to greenhouse and MS1.4 greenhouse to icehouse. (B) MS1 equalised photozoan and heterozoan production profiles.

7.4.1.2. MS2 Time and carbonate factory variable sediment production

MS2 investigates different production rates for different factories and variable production rate through (table 7.7). MS2.1 assesses a baseline scenario where the total sediment production from the heterozoan factory production is equal to that of the photozoan factory (figure 7.9A). MS2.2 simulates a scenario where sediment production by the heterozoan factory is greater than that of the photozoan factory (figure 7.9B). MS2.3 simulates a scenario where sediment production by the heterozoan factory production is less than that of the photozoan factory (figure 7.9C). The latter scenario is similar to that in numerical model from the best-fit analysis (section 7.3.2), to the extent that sediment production by the photozoan factory is greater than

the heterozoan factor. All models only simulate one grain size type with the same diffusion coefficient (0.0001 km^2 ky^{-1}). This represents depositional systems where both factories produce the same grain size types that can be transported down slope at the same rate. All models also apply the same relative sea level curve (figure 7.11 red line).

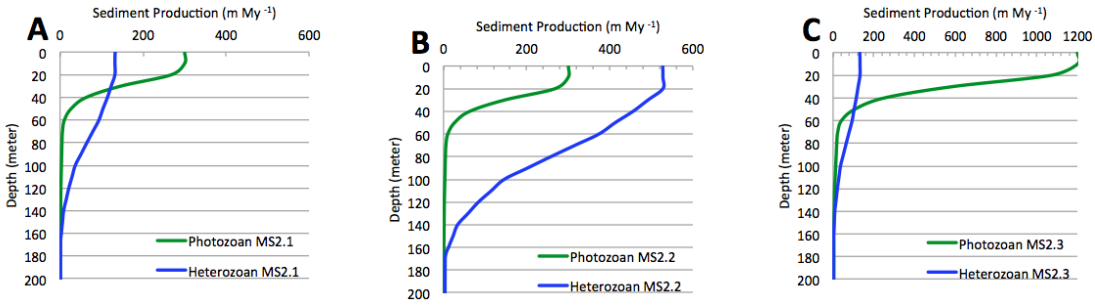

Figure 7.9: MS2 production profiles (A) equalised photozoan and heterozoan production profiles, (B) sediment production by the heterozoan factory is greater than that of the photozoan factory and (C) sediment production by the heterozoan factory production is less than that of the photozoan factory.

7.4.1.3. MS3 Time and carbonate factory variable sediment transport

MS3 investigates time and carbonate factory variable sediment transport rates (table 7.7). MS3.1 assesses a baseline scenario where sediment diffusional transport rates for the heterozoan and photozoan factories are equal. This represents a depositional system where both factories produce sediment that is transported down slope at the same rate (e.g. both factories produce the same grain size types). MS3.2 simulates a scenario where sediment diffusional transport rates of the heterozoan factory transport rates (0.001 km^2 ky^{-1}) are less than those of the photozoan factory (0.0165 km^2 ky^{-1}) (table 7.7). This represents a depositional system where sediment produced by the heterozoan factory is less easily transported than the photozoan factory (e.g. heterozoan grain size coarser than chlorozoan). MS3.3 simulates a scenario where sediment diffusional transport rates of the heterozoan factory (0.0165 km^2 ky^{-1}) are higher than those of the photozoan factory (0.001 km^2 ky^{-1}). This represents a depositional system where sediment produced by the heterozoan factory is more easily transported than the photozoan factory (e.g. photozoan grain size coarser than heterozoan). All models simulate the same total sediment production rate (figure 7.10) and apply the same relative sea level curve (figure 7.11 red line).

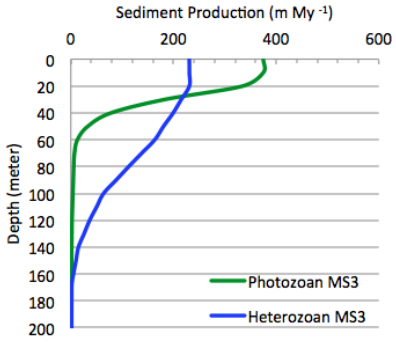

Figure 7.10: MS3 equalised photozoan and heterozoan production profiles.

7.4.1.4. MS4: Uncertainty in relative sea level periodicity

A relative sea level curve was constructed for the Maltese Late Miocene UCL Formation (section 6.5, figure 7.11) and applied in section 7.3.2 of this chapter (figure 7.11 red line). This relative sea level curve is based on the chronostratigraphic scheme (chapter 6 section 0.0) and the interpreted depositional environments (chapter 5) for the observed facies in the UCL Formation. However, both the chronostratigraphic scheme and the depositional environments are somewhat uncertain (section 6.6). By varying the RSL temporal and amplitude component across the uncertainty range (e.g. figure 7.11 black line applied in MS4), one can assess if other RSL curves can produce an equally good match with outcrop interpretations. This helps us better understand the impact of the uncertainty on our interpretation of depositional sequence geometries.

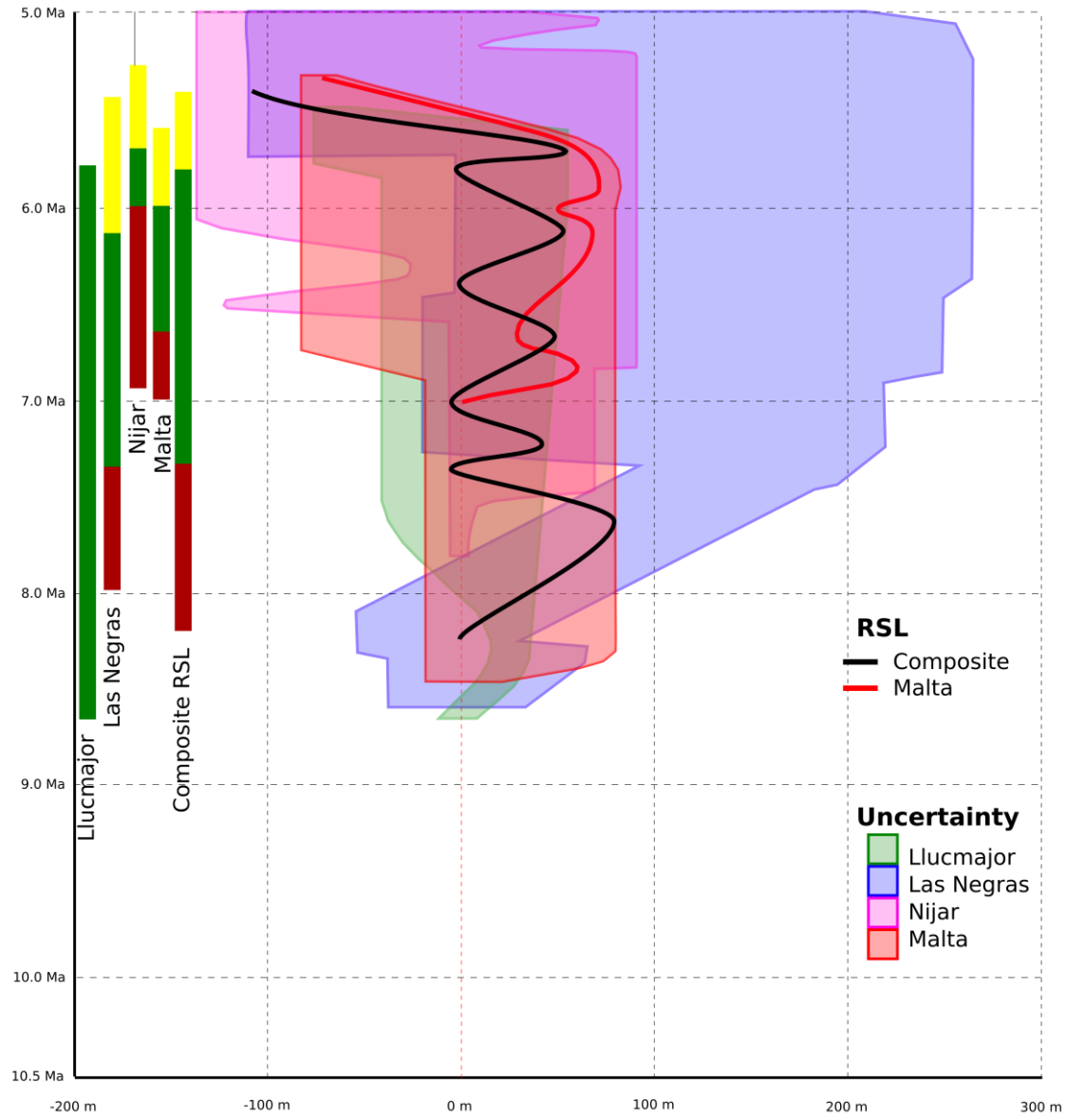

Figure 7.11: Relative sea level curve for each platform and associated uncertainty due to a combination of uncertainty in ages of strata, and uncertainty in the water-depth interpretations. Shaded zones, colour coded for each platform, indicate the range of possible oscillation amplitude and frequency. Red line represents the RSL applied in section 7.3.2, and black line represents the RSL applied in MS4 (see section 6.6.2 for details on how composite curve was constructed).

7.4.2. Non-uniqueness analysis

The degree of match between the MS and UCL strata is quantitatively assessed on the basis of three factors that compare (F_1) stacking patterns, (F_2) platform margin evolution and maximum platform margin slope gradients for the heterozoan and photozoan factories and (F_3) stratal thickness match [table 7.3].

7.4.2.1. MS1: Accommodation (sea level cycles)

MS1.1 simulates a greenhouse relative sea-level curve. While the heterozoan factory is active, the platform initially forms a distally steepened ramp with a maximum platform margin slope gradient of 3.63°. The platform margin then rapidly steepens to form a FTSM platform (maximum platform margin slope gradient of 9.90°) when the photozoan factory is active (table 7.8 and figure 7.12). MS1.2 simulates an icehouse relative sea-level curve. This produces a distally steepened ramp (maximum platform margin slope gradient of 4.87°) while the heterozoan factory is active. The platform geometry and platform margin slope gradient is maintained (4.93°) when the photozoan factory is active (table 7.8 and figure 7.12). MS1.3 initially produces a distally steepened ramp (maximum platform margin slope gradient of 6.17°) during the icehouse relative sea level that rapidly steepens to form a FTSM platform (maximum platform margin slope gradient of 9.07°) during the greenhouse relative sea level curve (table 7.8 and figure 7.12). MS1.4 produces a distally steepened ramp (maximum platform margin slope gradient of 3.63°) during the greenhouse relative sea level that is largely maintained during the icehouse relative sea level curve (maximum platform margin slope gradient of 6.55°) (table 7.8 and figure 7.12). MS1.1 and MS1.3 develop progradational stacking patterns while MS1.2 and MS1.4 develop progradational and retrogradational stacking patterns. The match between the simulated stratal thickness and borehole thickness across the three vertical sections assessed (VS1, 2 and 3) is 44% for MS1.1, 42% for MS1.2, 52% for MS1.3 and 62% for MS1.4 (table 7.8 and figure 7.12). The large-scale platform geometries and platform margin positions for the heterozoan and photozoan factories in MS1.1 and MS1.3 correspond to the conceptual model developed from outcrop observations. This is not the case for MS1.2 and MS1.4.

MS	Stacking patterns (F_1) and platform margin position	Maximum platform margin slope gradients (F_2) for Heterozoan (H) and Photozoan (P) factory	Stratal thickness match (F_3)	MMS [Equation 4]
MS1.1	Progradational, correct platform margin position	(H) 3.63° to (P) 9.90°	44%	0.44MMS
MS1.2	Progradational and retrogradational, incorrect platform margin position	(H) 4.87° to (P) 4.93°	42%	0.00MMS
MS1.3	Progradational, correct platform margin position	(H) 6.17° to (P) 9.07°	52%	0.42MMS
MS1.4	Progradational and retrogradational, incorrect platform margin position	(H) 3.63° to (P) 6.55°	62%	0.00MMS

Table 7.8: Degree of match between MS1 and real strata quantitatively assessed in terms of (F_1) stacking patterns, (F_2) platform margin evolution and maximum platform margin slope gradients for the heterozoan and photozoan factories and (F_3) stratal thickness match (table 7.3). MMS is colour coded to show poor (red) and better (green) match.

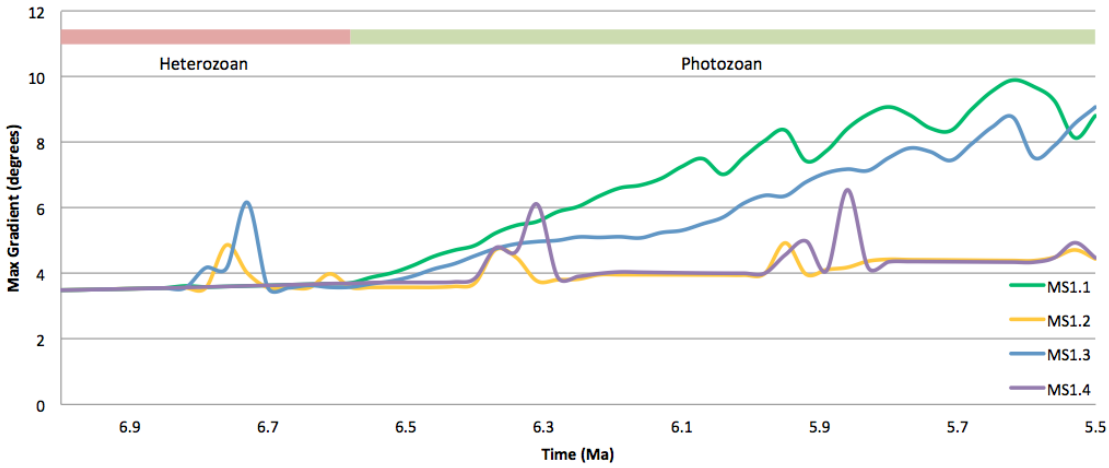
Heterozoan
Photozoan
Max Gradient (degrees)
Time (Ma)
MS1.1
MS1.2
MS1.3
MS1.4

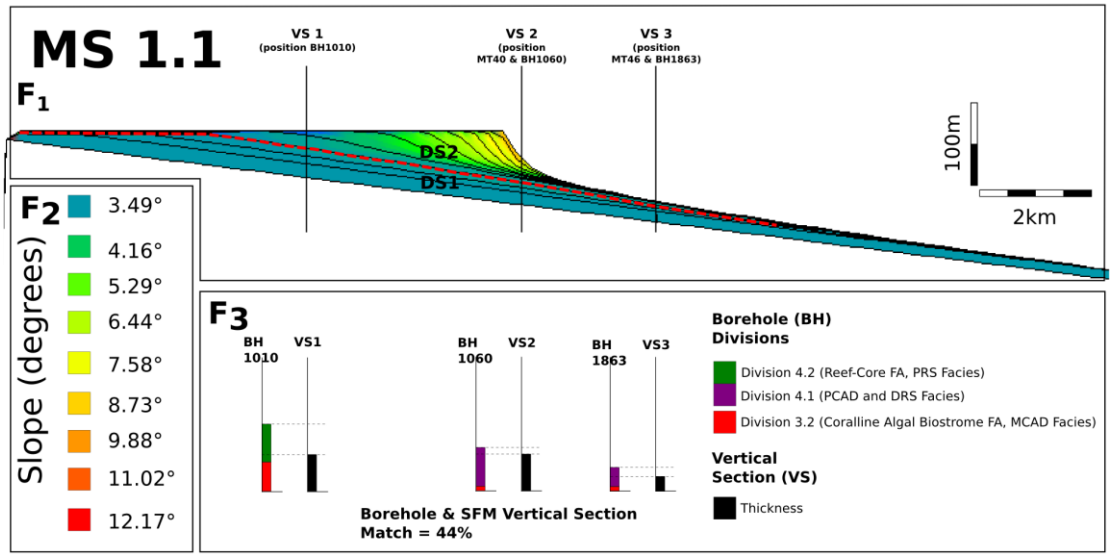
MS 1.1
VS 1 (position BH1010)
VS 2 (position MT40 & BH1060)
VS 3 (position MT46 & BH1863)
F1
DS2
DS1
100m
2km
F2
Slope (degrees)
3.49°
4.16°
5.29°
6.44°
7.58°
8.73°
9.88°
11.02°
12.17°
F3
BH 1010
VS1
BH 1060
VS2
BH 1863
VS3
Borehole & SFM Vertical Section Match = 44%
Borehole (BH) Divisions
Division 4.2 (Reef-Core FA, PRS Facies)
Division 4.1 (PCAD and DRS Facies)
Division 3.2 (Coralline Algal Biostrome FA, MCAD Facies)
Vertical Section (VS)
Thickness

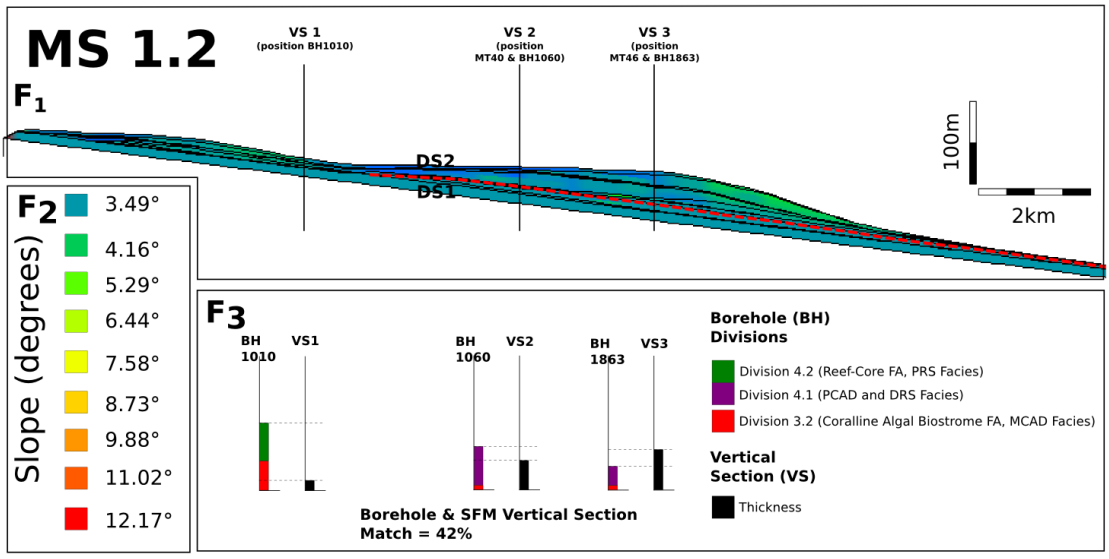
MS 1.2
VS 1 (position BH1010)
VS 2 (position MT40 & BH1060)
VS 3 (position MT46 & BH1863)
F1
DS2
DS1
100m
2km
F2
Slope (degrees)
3.49°
4.16°
5.29°
6.44°
7.58°
8.73°
9.88°
11.02°
12.17°
F3
BH 1010
VS1
BH 1060
VS2
BH 1863
VS3
Borehole & SFM Vertical Section Match = 42%
Borehole (BH) Divisions
Division 4.2 (Reef-Core FA, PRS Facies)
Division 4.1 (PCAD and DRS Facies)
Division 3.2 (Coralline Algal Biostrome FA, MCAD Facies)
Vertical Section (VS)
Thickness

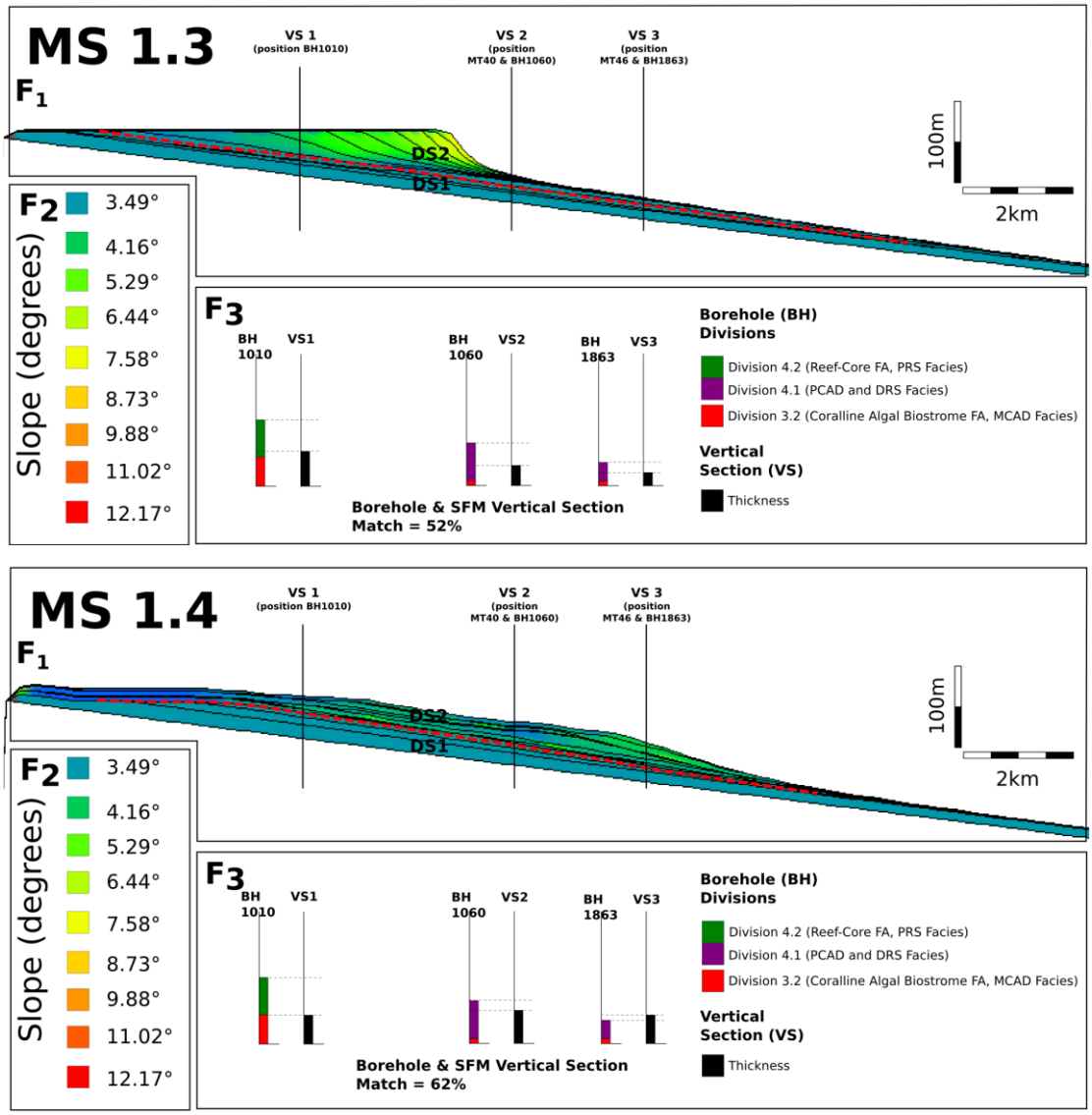

Figure 7.12: Graph depicting MS1 maximum platform margin slope gradient (MaxS) over model run time. 2D model outputs for MS1 showing stacking patterns (F_1), platform margin evolution and maximum platform margin slope gradients for the heterozoan and photozoan factories (F_2) and stratal thickness match (F_3). Red dashed line demarcates the heterozoan (underlying) and photozoan (overlying) factories. One time step (black line in 2D SFM) of 0.12My EMT.

The rates of sediment accumulation relative to the amplitude and frequency of oscillations in sea level influence platform geometry. The extent of relative sea-level oscillations spread out carbonate production either allowing or preventing focused accumulation and steepening. Ramps will be favoured when the rate at which the horizontal shifts in the position of maximum sediment production across the platform outweighs the rate of sediment accumulation at the position of maximum sediment production (e.g. MS1.1) (Wright, 1992; Read, 1995, 1998; Williams *et al*., 2011). Conversely, FTSM will be developed when the rate of sediment accumulation at the position of maximum sediment production outweighs the rate at which the horizontal shifts in the position of maximum sediment production across the platform (e.g. MS1.2).

MS1 model behaviour and results (figure 7.12) show that changes in sediment production and/or transport rates are not required to develop the change in platform geometry. The shift in platform geometry from ramp (DS1) to FTSM (DS2) may be the product of particular sea level oscillations. Two theoretically plausible non-unique scenarios can be envisioned that may control this platform evolution.

The first scenario (MS1.1) suggests that both depositional sequences (DS1 and 2) were subject to low-amplitude sea level oscillations (greenhouse conditions). The short duration (0.4 My) of sediment production (relative to transport rates) by the heterozoan factory (DS1) would have prevented significant aggradation, progradation and platform margin steepening resulting in ramp geometries. As the photozoan factory was established, sediment production in shallow waters accumulated leading to rapid progradation and platform margin steepening to form a FTSM platform. The second scenario (MS1.3) suggests that DS1 was affected by high-amplitude sea level oscillations (icehouse conditions) and the DS2 was affected by low-amplitude sea level oscillations (greenhouse conditions).

The Cenozoic climate is characterized by marked climatic fluctuations. During the Cenozoic, a world without significant polar ice sheets (Greenhouse World) was transformed into one with large ice sheets at both poles (Icehouse World) (Miller *et al*., 1991). Deep-sea isotope records document stepwise combined cooling and glaciation (Miller *et al*., 2001). The Paleocene-Eocene Thermal Maxima (*circa* 55 Ma) and Early Eocene Climatic Optimum are extremely warm periods. This is followed with a gradual prolonged cooling that is occasionally punctuated by warm periods such as the Late Oligocene warming and Mid Miocene Climatic Optima (MMCO) (Mudelsee *et al*., 2014; Zachos *et al*., 2001). The MMCO (from ~17 to ~14.5 Ma) represents the last warm time interval during the Miocene in Earth history. The establishment of the Antarctic cryosphere (*circa* 15 Ma) (Wright & Faulkner, 1990; Shevenell *et al*., 2004; Mudelsee *et al*., 2014) led to the Mid-Miocene Climatic Transition (MMCT) between ~ 14.2 and ~ 13.8 Ma (Flower and Kennett, 1994; Shevenell *et al*., 2008). The MMCT marks the end

of the MMCO and the onset of a long-term global cooling (Flower and Kennett, 1994; Zachos *et al*., 2001).

In view of the Late Miocene climate evolution described above, the low-amplitude sea level oscillations (greenhouse conditions) of MS1.1 are unlikely. The general interpretation of long-term global cooling of the Late Miocene also suggests that the switch from high-amplitude sea level oscillations (icehouse conditions) to low-amplitude sea level oscillations (greenhouse conditions) of MS1.3 is unlikely. The interpretation developed from MS1.3 therefore does not agree with the prevailing model of long-term cooling.

It is useful to review how the quality of the information about a gradual increase in icehouse eustatic oscillations amplitude compares to the quality of information from matching the SFM with outcrop to the degree that one can, and given non-uniqueness. When and where cooling occurred, when the ice sheets started to form on each hemisphere, whether they persisted once formed, and the cause(s) of the cooling have long been debated (e.g., Thomas *et al*., 2006). MS1.3 could thus support notions that the sea-level history and hence ice sheet growth history may have been more complicated than the prevailing model of long-term cooling suggests. MS1.3 may suggest an increase ice sheet size earlier in the Miocene (DS1) that is followed by a decrease ice sheet size (DS2) that interrupted this longer-term trend. In theory, the platform could show an early change to high-amplitude eustasy (DS1) and back to low-amplitude eustasy (DS2), which may represent a small perturbation in the overall cooling trend. This outcome helps the user question/gain insight into platform evolution that would not have been possible without the application of this quantitative method.

7.4.2.2. MS2 Time and carbonate factory variable sediment production

MS2.1 initially develops a distally steepened ramp geometry (maximum platform margin slope gradient 3.71°) that then gradually steepens to form a FTSM platform (maximum platform margin slope gradient 6.99°) (table 7.9 and figure 7.13). In MS2.2, the high sediment production rate within the heterozoan factory develops a FTSM platform (maximum platform margin slope gradient 4.92°). The low sediment production rate for the photozoan factory prevents substantial platform margin steepening (maximum platform margin slope gradient 7.39°) (table 7.9 and figure 7.13). In MS2.3, low heterozoan sediment production leads to development of a distally steepened ramp (maximum platform margin slope gradient 3.71°). The platform margin slope gradients rapidly steepen with the onset of high photozoan sediment production that in turn forms a FTSM platform (maximum platform margin slope gradient 10.80°) (table 7.9 and figure 7.13). All MS2 develop progradational stacking patterns (figure 7.13). The match between the simulated stratal thickness and borehole thickness across the three vertical sections assessed (VS1, 2 and 3) is 60% for MS2.1, 47% for MS2.2, 74% for MS2.3 (table 7.9 and figure 7.13). Relative to the conceptual model, the FTSM platform margin in MS2.1 has insufficient

progradation and the platform margin in MS2.2 has excessive progradation. The large-scale platform geometries and platform margin positions for the heterozoan and photozoan factories in MS2.3 correspond to the conceptual model developed from outcrop observations.

MS	Stacking patterns (F_1) and platform margin position	Maximum platform margin slope gradients (F_2) for Heterozoan (H) and Photozoan (P) factory	Stratal thickness match (F_3)	MMS [Equation 4]
MS2.1	Progradational, incorrect platform margin position	(H) 3.71° to (P) 6.99°	60%	0.42MMS
MS2.2	Progradational, incorrect platform margin position	(H) 4.92° to (P) 7.39°	47%	0.35MMS
MS2.3	Progradational, correct platform margin position	(H) 3.71° to (P) 10.80°	74%	0.74MMS

Table 7.9: The degree of match between the MS2 and real strata is quantitatively assessed on the basis of three factors that represent some aspect of the strata observed in the UCL Formation. The quantitative comparison is in terms of (F_1) stacking patterns, (F_2) platform margin evolution and maximum platform margin slope gradients for the heterozoan and photozoan factories and (F_3) stratal thickness match (table 7.3). MMS is colour coded to show poor (red) and better (green) match.

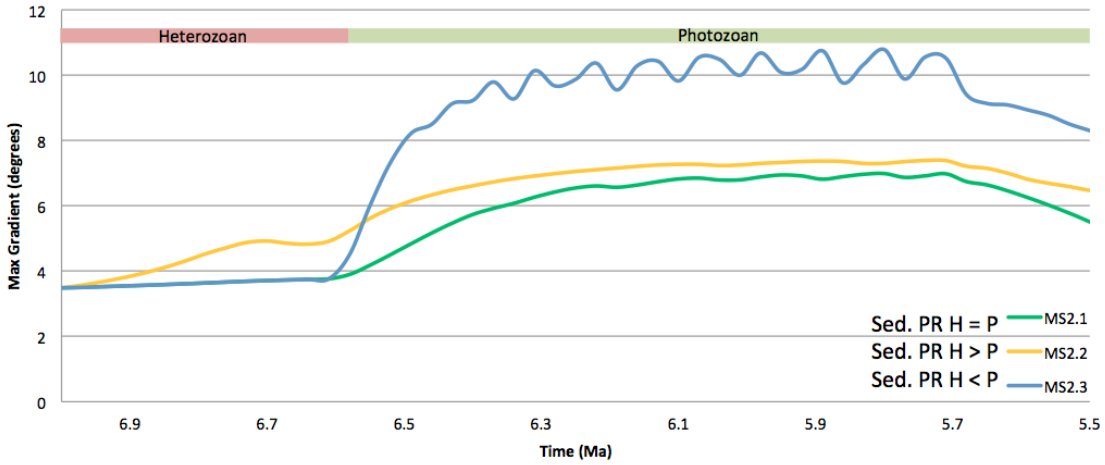
Heterozoan
Photozoan
Max Gradient (degrees)
Time (Ma)
Sed. PR H = P
Sed. PR H > P
Sed. PR H < P
MS2.1
MS2.2
MS2.3

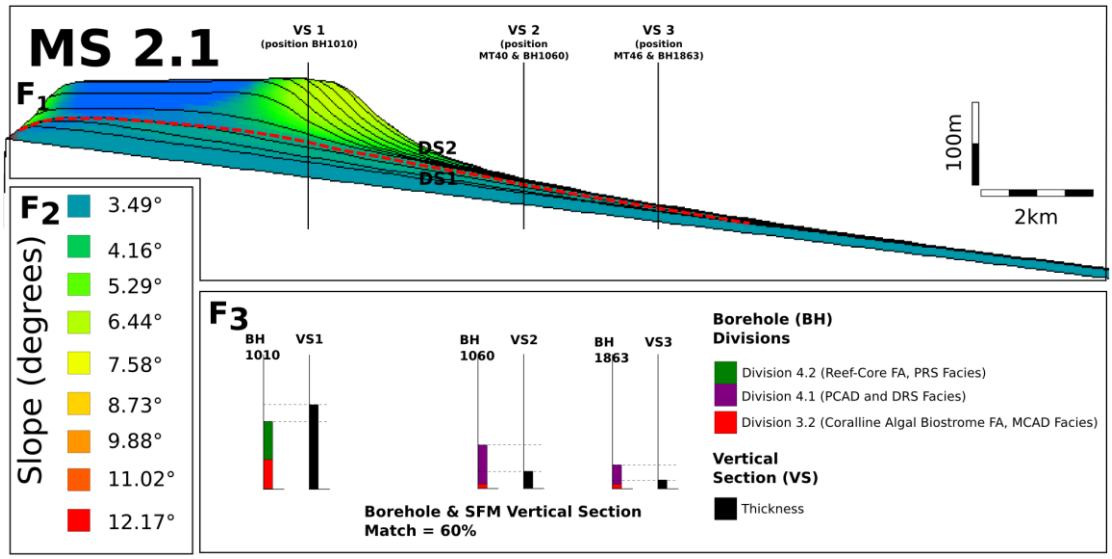
MS 2.1
VS 1 (position BH1010)
VS 2 (position MT40 & BH1060)
VS 3 (position MT46 & BH1863)
F1
DS2
DS1
100m
2km
F2
Slope (degrees)
3.49°
4.16°
5.29°
6.44°
7.58°
8.73°
9.88°
11.02°
12.17°
F3
BH 1010
VS1
BH 1060
VS2
BH 1863
VS3
Borehole & SFM Vertical Section
Match = 60%
Borehole (BH) Divisions
Division 4.2 (Reef-Core FA, PRS Facies)
Division 4.1 (PCAD and DRS Facies)
Division 3.2 (Coralline Algal Biostrome FA, MCAD Facies)
Vertical Section (VS)
Thickness

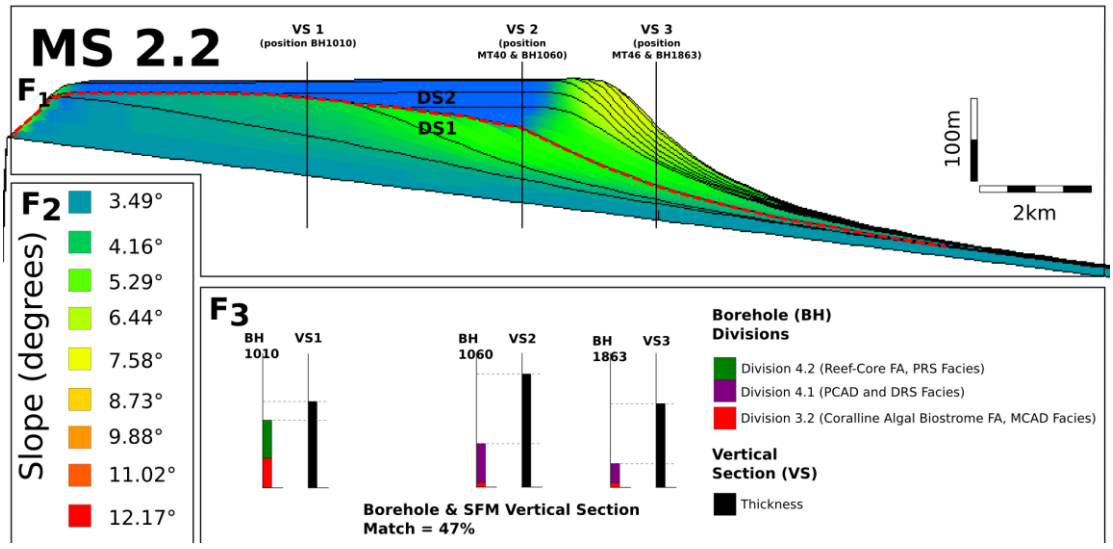
MS 2.2
VS 1 (position BH1010)
VS 2 (position MT40 & BH1060)
VS 3 (position MT46 & BH1863)
F1
DS2
DS1
100m
2km
F2
Slope (degrees)
3.49°
4.16°
5.29°
6.44°
7.58°
8.73°
9.88°
11.02°
12.17°
F3
BH 1010
VS1
BH 1060
VS2
BH 1863
VS3
Borehole & SFM Vertical Section
Match = 47%
Borehole (BH) Divisions
Division 4.2 (Reef-Core FA, PRS Facies)
Division 4.1 (PCAD and DRS Facies)
Division 3.2 (Coralline Algal Biostrome FA, MCAD Facies)
Vertical Section (VS)
Thickness

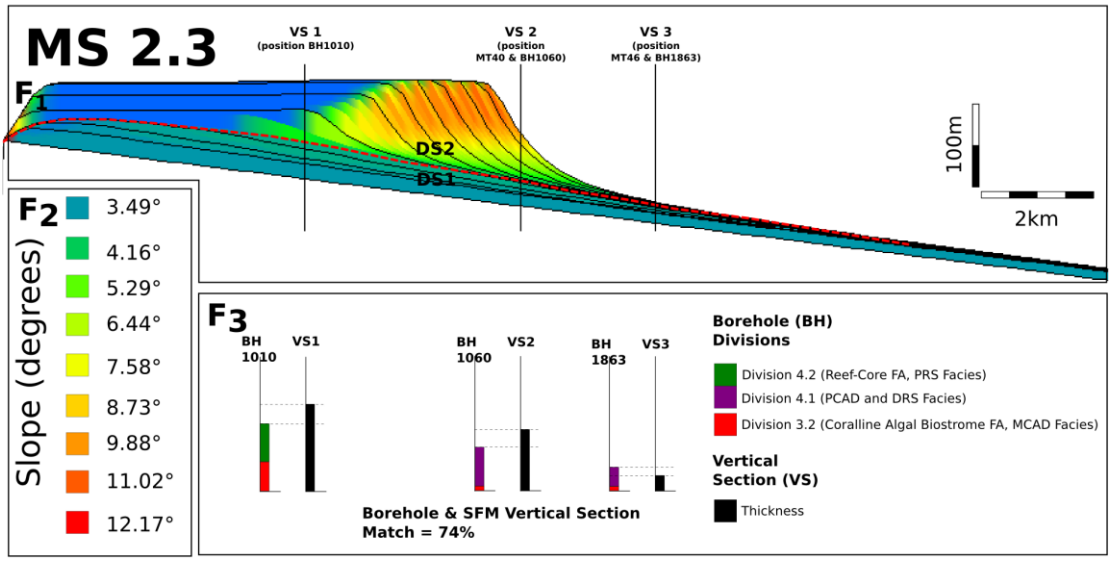

Figure 7.13: Graph depicting MS2 maximum platform margin slope gradient (MaxS) over model run time. 2D model outputs for MS2 showing stacking patterns (F_1), platform margin evolution and maximum platform margin slope gradients for the heterozoan and photozoan factories (F_2) and stratal thickness match (F_3). Red dashed line demarcates the heterozoan (underlying) and photozoan (overlying) factories. One time step (black line in 2D SFM) of 0.12 My EMT.

Model behaviour suggests that MS simulating higher sediment production rates, relative to sediment transport rates, tend to develop steeper platform margin slope gradients. These models accumulate sediment and aggrade at a faster rate than models simulating lower sediment production rates. Aggradation in turn reduces the marine depth which consequently enhances sediment production in both heterozoan and photozoan factories. This then drives progradation and enables the development of rapidly steepening platform margins. The duration over which sediment is produced is also an important control; the greater the time during which sediment is produced the steeper the resulting platform margin. The type of production profile (euphotic *versus* oligophotic), in conjunction with the time component, is also an important parameter. The euphotic production profile concentrates sediment production in the shallow-water depths. This focuses sediment production in a narrow area in the platform. This leads to rapid shallow-water accumulation, progradation and platform margin steepening. Conversely, sediment production by the oligophotic production profile is spread over a wider area of the platform. This slows accumulation in a single area and suppresses progradation rates. However, the oligophotic production profile enables steeper platform margins to be developed later on in the model time (chapter 3).

Previous authors suggested that euphotic production-depth curves form FTSM platforms while oligophotic production-depth curves construct ramp systems (e.g., Wright and Faulkner, 1990; Bosscher and Schlager, 1992; Bowman and Vail, 1999; Pomar, 2001). More recent numerical

SFM based research (Williams *et al*., 2011 and chapter 3) however clearly indicate that equalised oligophotic production profiles develop steeper platform margins than equalised euphotic profiles. The distinct platform geometries developed by the rhodalgal and coralgal factories are unlikely therefore to result from distinct production-depth profiles.

MS2 model behaviour and results (figure 7.13) suggest that the ramp (DS1) to FTSM (DS2) shift in platform geometry in the Maltese UCL Formation may be the product of distinct heterozoan and photozoan factories sediment production rates. Changes in sediment transport rates across the two carbonate factories are not required to develop the change in platform geometry. The theoretically plausible non-unique scenario that emerges from MS2 is a heterozoan factory that produces less sediment than photozoan factory (MS2.3). Assuming ideal marine conditions, the coralgal factory produces significantly larger quantities of sediment than the rhodalgal factory (section 3.2.2). Sediment production rates of the scleractinian coral factory ranges from 0.35 to 23.00 m ky^{-1} across the depth range producing sediment and sediment production for the coralline red algal factory ranges from 0.10 and 8.30 m ky^{-1}. The cycle of rhodalgal-dominated ramps to coralgal-dominated FTSM platforms is well recorded in various Upper Miocene Mediterranean platforms, namely the Llucmajor area, Balearic Islands (e.g. Pomar, 1991, 1993; Pomar & Ward, 1994, 1995; Pomar *et al*., 1996), the Las Negras platform, Southern Spain (e.g. Franseen, 1989; Goldstein *et al*., 1990; Franseen & Mankiewicz, 1991), the Nijar Basin, South Eastern Spain (e.g. Mankiewicz, 1987, 1996; Warrlich, 2000) and the Malta platform (e.g. Pedley, 1974, 1976; Bosence & Pedley, 1982; Dart, 1991). The theoretically plausible non-unique scenario MS2.3 is plausible in terms of real world rates and is a valid explanation for the switch (ramp to FTSM) in platform geometry observed in various Late Miocene carbonate platforms.

7.4.2.3. MS3 Time and carbonate factory variable sediment transport

MS3.1 and 3.2 both develop and maintain distally steepened ramp geometries during heterozoan and photozoan factory sediment production (maximum platform margin slope gradients 5.09° and 5.10° respectively) (table 7.10 and figure 7.14). MS3.2, however, produces moderately steeper platform margin slope gradients (4.01°) than MS3.1 (3.83°), particularly during heterozoan sediment production. MS3.3 initially simulates a distally steepened ramp during heterozoan production that rapidly steepens to form a FTSM platform during photozoan production (3.83° to 10.33°) (table 7.10 and figure 7.14). All MS3 develop progradational stacking patterns. The match between the simulated stratal thickness and borehole thickness across the three vertical sections assessed (VS1, 2 and 3) is 55% for MS3.1, 58% for MS3.2, 80% for MS3.3 (table 7.10 and figure 7.14). MS3.1 and MS3.2 develop distally steepened platform geometries for both the photozoan and heterozoan factories. This is distinct from the conceptual model. Conversely, the large-scale platform geometries and platform margin

positions for the heterozoan and photozoan factories in MS2.3 correspond to the conceptual model developed from outcrop observations.

MS	Stacking patterns (F_1) and platform margin position	Maximum platform margin slope gradients (F_2) for Heterozoan (H) and Photozoan (P) factory	Stratal thickness match (F_3)	MMS [Equation 4]
MS3.1	Progradational, incorrect platform margin position	(H) 3.83° to (P) 5.09°	55%	0.28MMS
MS3.2	Progradational, incorrect platform margin position	(H) 4.01° to (P) 5.10°	58%	0.30MMS
MS3.3	Progradational, correct platform margin position	(H) 3.83° to (P) 10.33°	80%	0.80MMS

Table 7.10: The degree of match between the MS3 and real strata is quantitatively assessed on the basis of three factors that represent some aspect of the strata observed in the UCL Formation. The quantitative comparison is in terms of (F_1) stacking patterns, (F_2) platform margin evolution and maximum platform margin slope gradients for the heterozoan and photozoan factories and (F_3) stratal thickness match (table 7.3). MMS is colour coded to show poor (red) and better (green) match.

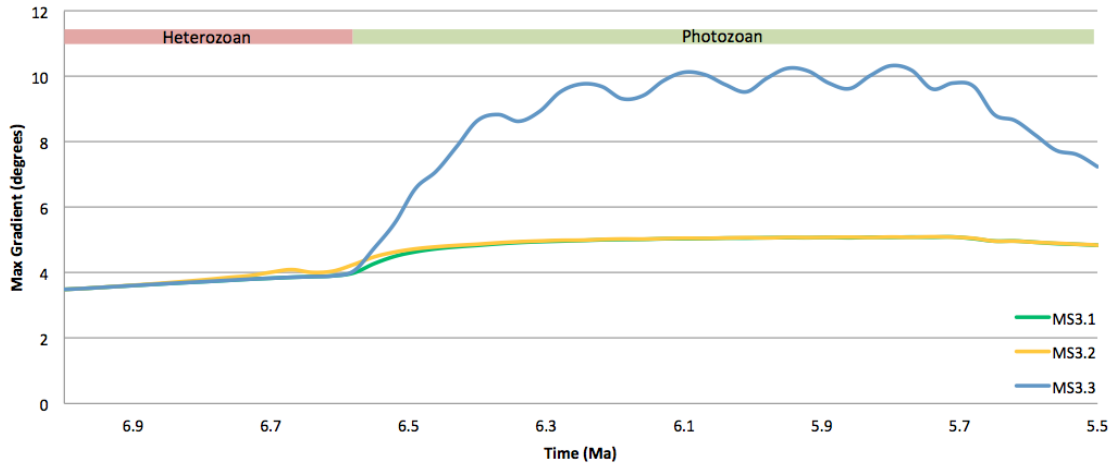
Heterozoan
Photozoan
Max Gradient (degrees)
Time (Ma)
MS3.1
MS3.2
MS3.3

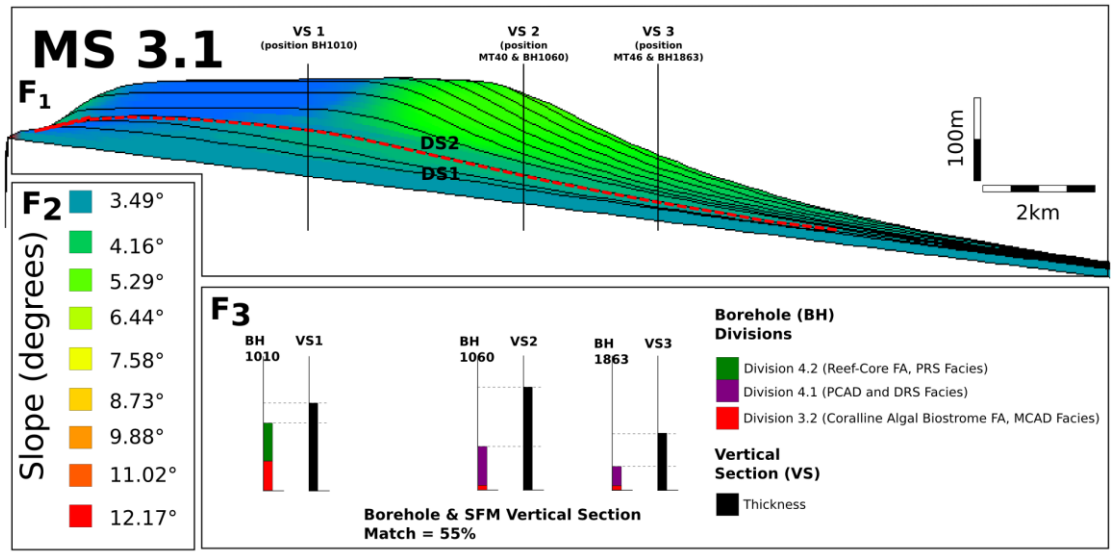
MS 3.1
VS 1 (position BH1010)
VS 2 (position MT40 & BH1060)
VS 3 (position MT46 & BH1863)
F1
DS2
DS1
100m
2km
F2
Slope (degrees)
3.49°
4.16°
5.29°
6.44°
7.58°
8.73°
9.88°
11.02°
12.17°
F3
BH 1010
VS1
BH 1060
VS2
BH 1863
VS3
Borehole & SFM Vertical Section
Match = 55%
Borehole (BH) Divisions
Division 4.2 (Reef-Core FA, PRS Facies)
Division 4.1 (PCAD and DRS Facies)
Division 3.2 (Coralline Algal Biostrome FA, MCAD Facies)
Vertical Section (VS)
Thickness

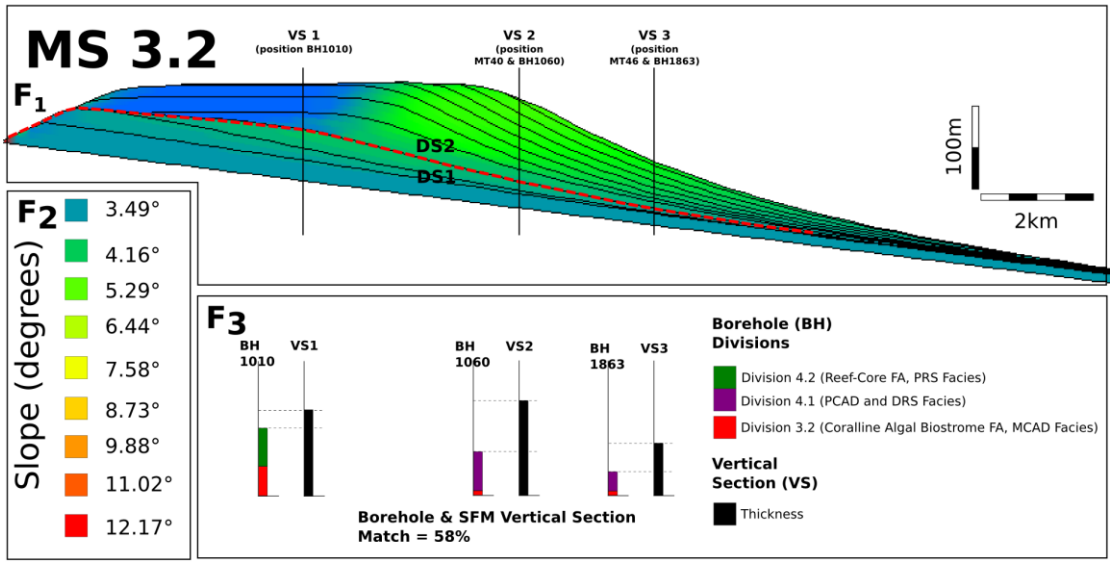
MS 3.2
VS 1 (position BH1010)
VS 2 (position MT40 & BH1060)
VS 3 (position MT46 & BH1863)
F1
DS2
DS1
100m
2km
F2
Slope (degrees)
3.49°
4.16°
5.29°
6.44°
7.58°
8.73°
9.88°
11.02°
12.17°
F3
BH 1010
VS1
BH 1060
VS2
BH 1863
VS3
Borehole & SFM Vertical Section
Match = 58%
Borehole (BH) Divisions
Division 4.2 (Reef-Core FA, PRS Facies)
Division 4.1 (PCAD and DRS Facies)
Division 3.2 (Coralline Algal Biostrome FA, MCAD Facies)
Vertical Section (VS)
Thickness

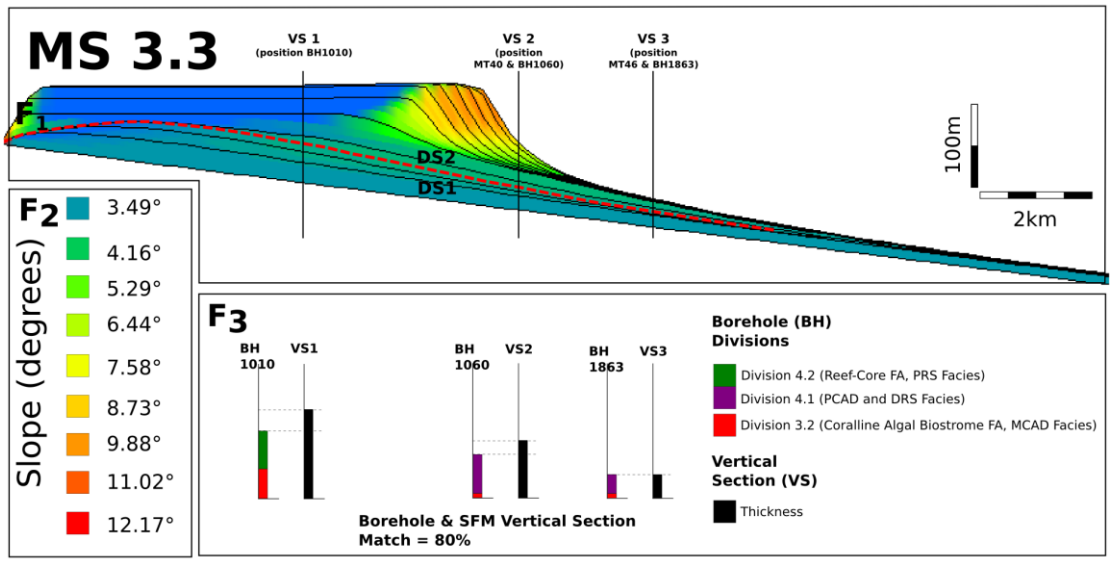

Figure 7.14: Graph depicting MS3 maximum platform margin slope gradient (MaxS) over model run time. 2D model outputs for MS3 showing stacking patterns (F_1), platform margin evolution and maximum platform margin slope gradients for the heterozoan and photozoan factories (F_2) and stratal thickness match (F_3). Red dashed line demarcates the heterozoan (underlying) and photozoan (overlying) factories. One time step (black line in 2D SFM) of 0.12My EMT.

Model behaviour suggests that MS simulating lower diffusional transport rates tend to develop steeper platform margin slope gradients. These models accumulate sediment, aggrade and develop steeped platform margins than models simulating higher sediment diffusional transport rates. MS3 model behaviour and results (figure 7.14) suggest that MS simulating lower diffusional transport rates tend to develop steeper platform margin slope gradients (chapter 3 for discussion on effects sediment transport rate has on sediment accumulation, aggradation and platform margins). The theoretically plausible scenario that emerges from MS3 is a heterozoan factory that is characterised by higher transport rates than the photozoan factory (MS3.3).

The shift in platform geometry (ramp to FTSM) is recorded on Upper Miocene Mediterranean platforms, for example the Llucmajor area, Balearic Islands (e.g. Pomar, 1991, 1993; Pomar and Ward, 1994, 1995; Pomar *et al*., 1996), the Las Negras platform, Southern Spain (e.g. Franseen, 1989; Goldstein *et al*., 1990; Franseen & Mankiewicz, 1991), the Nijar Basin, South Eastern Spain (e.g. Mankiewicz, 1987, 1996; Warrlich, 2000) and the Malta platform (e.g. Pedley, 1974, 1976; Bosence & Pedley, 1982; Dart, 1991). The rhodalgal factory produce fine-to-coarse bioclastic grains that form wackestone/packstone/rudstone textures while the coralgal factory build rigid organic buildups/frameworks and produce framework/rudstone textures (chapter 3). These distinct textures are resistant to gravity and current-driven sediment transport and as a result the sediments produced by the rhodalgal and coralgal factories are subject to different sediment transport regimes. Assuming equal sediment production rates between the two

factories, the sediment produced by the rhodalgal factory is subject to greater transport rates than sediments produced by the coralgal factory. Numerical SFM-based research (e.g. Bosence & Waltham, 1990; Williams *et al*., 2011; chapter 3) has demonstrated that carbonate platforms that are dominated by fine-grained sediment production form transport-dominated systems and develop ramp geometries. Conversely, carbonate platform that are dominated by framework and coarse-grained sediment production are deposition-dominated systems and develop FTSM platforms.

Within the UCL Formation, DS1 contains rhodalgal lithofacies that are characterised by fine-to-coarse bioclastic grains that form wackestone/packstone/rudstone textures. The coralgal lithofacies of DS2 build rigid organic buildups/frameworks and produce framework/rudstone textures (Chapter 5). These distinct textures are more or less resistant to gravity and current-driven sediment transport and as a result the sediments produced by the rhodalgal and coralgal factories are subject to different sediment transport regimes. In view of the above, the theoretically plausible non-unique scenario MS3.3 is plausible in terms of real world rates and is a valid explanation for the switch (ramp to FTSM) in platform geometry observed in various Late Miocene carbonate platforms.

Pomar & Kendall (2008) argue that the interplay between different sediment production and redistribution processes form the various depositional profiles and facies belt distributions. Their conceptual model however does not quantitatively assess how individual or multiple parameters influence platform geometry. Quantitative SFM-based results MS and MS3 show that the sediment production rate (MS2) and diffusional transport rate (MS3) significantly influence platform evolution and geometry.

7.4.2.4. MS4: Uncertainty in relative sea level periodicity

Across the tested range of sediment production rates and diffusional transport rates, the highest model match achieved between the numerical model and the outcrop features is 0.80MMS [equation 4] (figures 7.16 and 7.17). This is the same MMS achieved in the best-fit analysis (section 7.3.2).

The match in MS4 was achieved when simulating a sediment production rate of PR300 during DS1 (corresponding to the heterozoan factory), PR100 during DS2 (corresponding to the photozoan factory) and PR200 during DS3 (figure 7.15). These sediment productoin rates are distinct from those applied in the best-fit analysis (section 7.3.2, figure 7.5) and also fall within the natural range of sediment production of Holocene carbonate factories (see Chapter 3). Relative to the sediment production rate applied in the best-fit analysis (figure 7.5) the production rate applied in MS4 is 37% less for the heterozoan factory (DS1) and 88% less for the photozoan factory (DS2). The diffusion coefficient rates applied in MS4 are of the same as those applied in the best-fit analysis (section 7.3.2) and are of the same order of magnitude as

those developed in Chapter 4 (section 4.3.1). Across the three depositional sequences: mud 0.0165 km^2 ky^{-1}, sand 0.0042 km^2 ky^{-1}, gravel 0.002 km^2 ky^{-1} and cobble 0.001 km^2 ky^{-1}.

Stacking patterns (F_1)

Within DS1, the numerical model displays initially aggradational and then progradational rudstone textures in DS1 (figure 7.16). The simulated rudstone textures correspond to the observed CAP facies that consists of rhodolith-rich rudstone beds. The model simulates aggradational to progradational bedforms. For DS2, the numerical model displays rapidly prograding framestone and rudstone textures (figure 7.16) corresponding to the Reef-Core FA and the Fore-Reef Slope and Shelf FA respectively. In DS3, grainstones overlie and sharply contrast with the framestone texture representing the Reef-Core FA. Above this contact, reef growth is abruptly terminated and the facies are dominated by grainstones of the Sand Shoal FA. These grainstones are also observed eastwards of the Reef-Core FA framestones and correspond to the Fore-Reef Slope and Shelf FA.

The stacking patterns developed by the numerical model are therefore consistent with the conceptual model of DS1, DS2 and DS3 for the UCL Formation. The numerical model indicates the new RSL (figure 7.11 black line) assessed in MS4 is physically possible within the sediment production and diffusional transport rates simulated. In view of the above, the factor was set at $1.00F_1$ [Equation 1]. Factor (F_1) compares stacking patterns (aggradation, aggradation, retrogradation) [equation 1] and a score of 1 is a perfect match between the simulated and real factor.

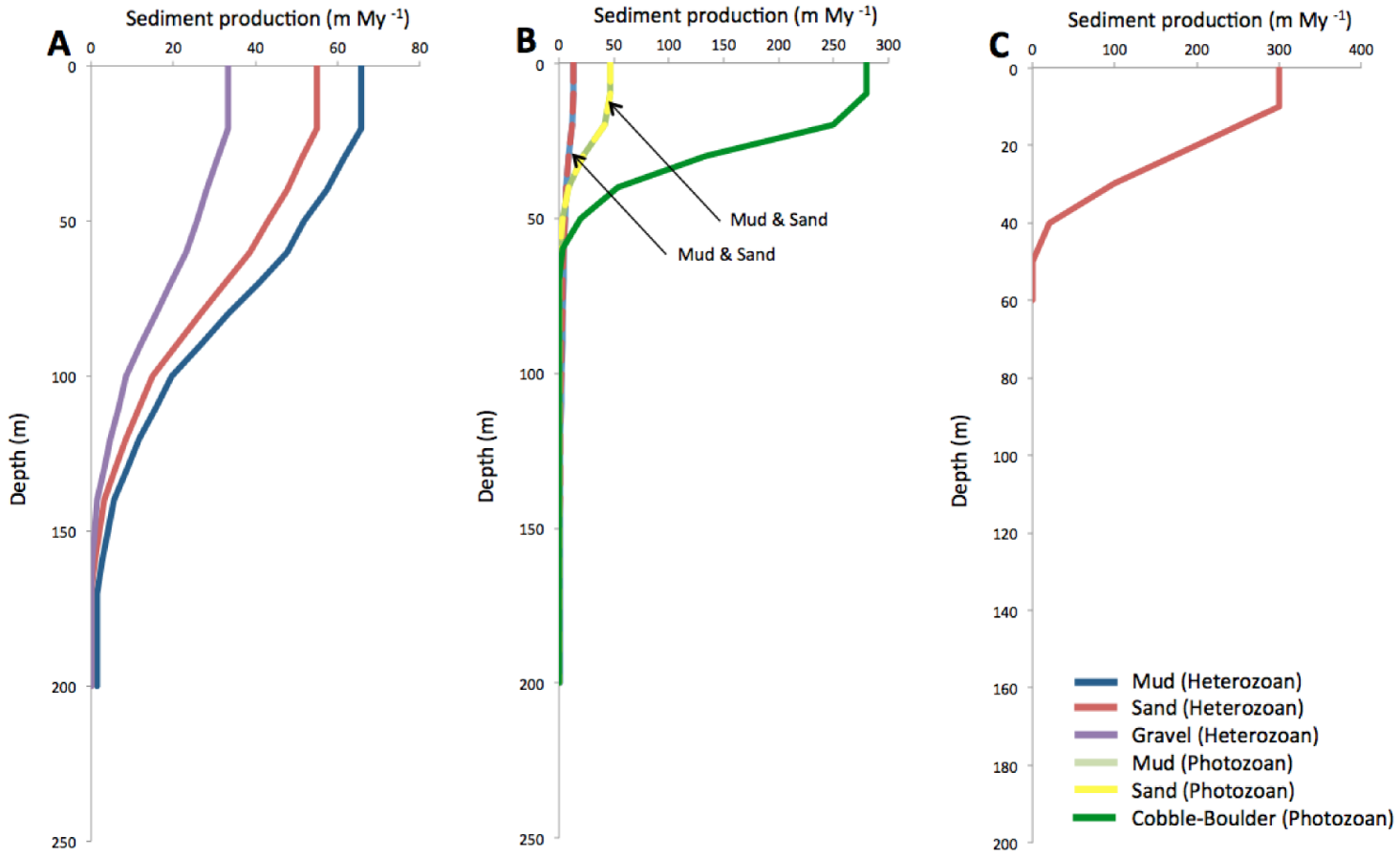

Figure 7.15: Grain size productoin profiles for (A) depositional sequence 1, (B) depositional sequence 2, and (C) depositnal sequence 3. Relative to the PR applied in the best-fit analysis (figure 7.5), PR applies in MS4 is 88% less for DS1 (the heterozoan factory) and 37% less for DS2 (the photozoan factory). Photozoan grain associaiotn includes sedimet production from the scleractinian coral factory and the calcearous green algae factory (figure 3.1). Heterozoan grain association includes sediment production from the the coralline red algae factory and the foramol/bryomol factory (figure 3.1).

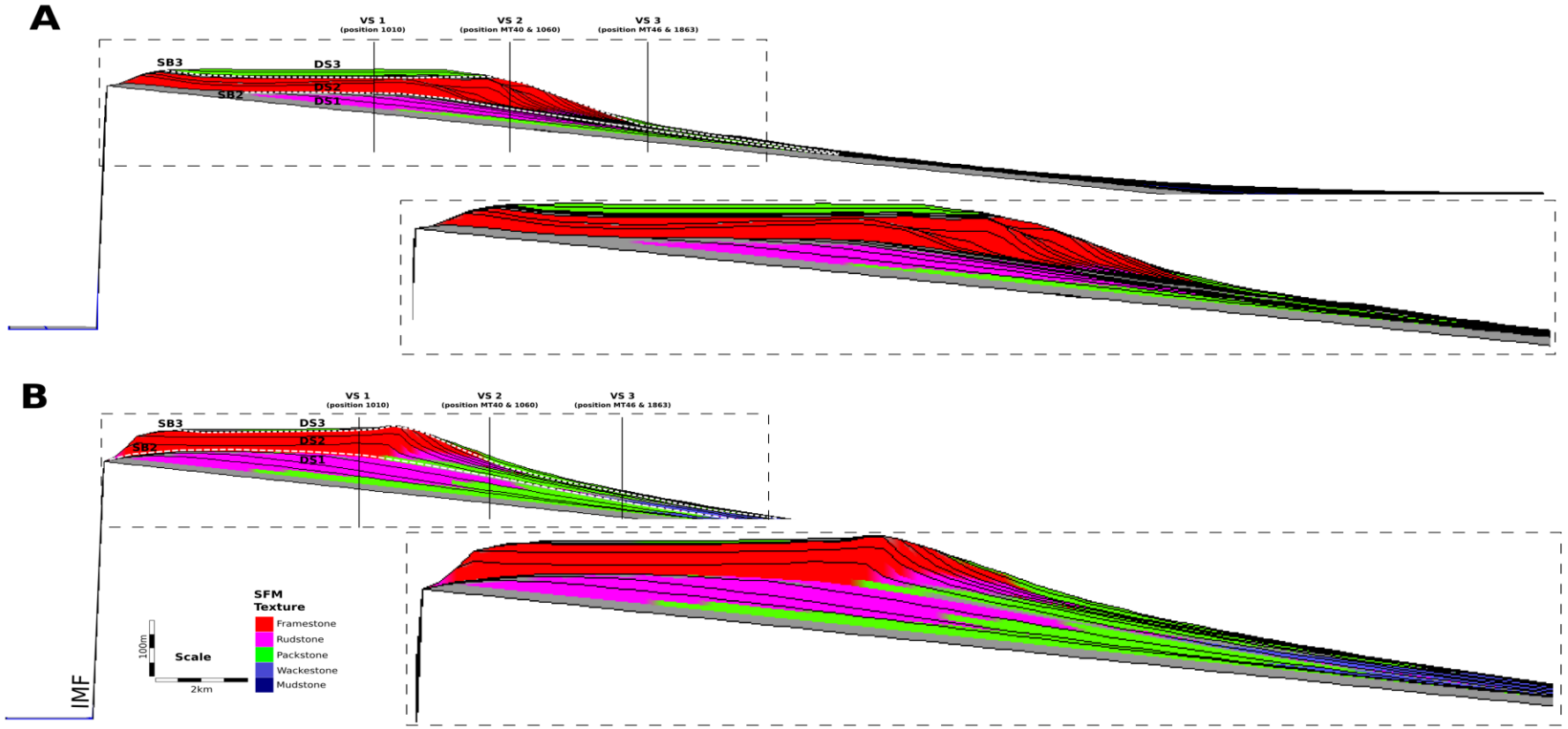

Figure 7.16: (A) 2D section of MS4 that applies a different set of model parameters relative to the simulation that best-fits the conceptual model (section 7.3.2 figure 7.16B). MS4 demonstrates issues of non-uniqueness within the investigated parameter range. White dashed line (SB2) demarcates the heterozoan (underlying) and photozoan (overlying) deposits. White dashed line (SB3) demarcates the photozoan (underlying) and oolitic (overlying) deposits. One time step (black line in 2D SFM) of 0.12 My EMT. Compare (A) non-unique simulatin with (B) simulation that best-fits the conceptual model (section 7.3.2) in terms of stacking patterns (F1), platform margin slope gradients (F2) and facies recorded at particular locations (VS1, VS2 and VS3) (F3).

Maximum platform margin slope gradients (F_2)

In terms of the platform maximum gradient factor (F_2), the best model match develops maximum gradients of 4° for DS1 and 10° for DS2. The simulated gradients correspond to those measures in outcrops up to 8° for the CAP Facies (DS1) and 10-30° for the Proximal Reef Slope (PRS) Facies deposited in proximal reef slope settings (Chapter 4). In view of this, the factor was calculated as $1.00F_2$ [Equation 2].

Facies at borehole logs BH1010, BH1060 and BH1863 (F_3)

The depositional textures in outcrop logs (MT22, MT40 and MT46) and in boreholes (BH1010, BH1060 and BH1863) are compared against the facies simulated at the same positions (vertical sections - VS) in MS4 (figure 7.17). The quantitative comparison is through factor (F_3). Results demonstrate an overall (VS1, VS2 and VS3) depositional texture and facies match of 82% and an overall thickness mismatch of 80% (0.80 F_3 [Equation 3]) to boreholes (BH1010, BH1060 and BH1863).

VS1 demonstrates a 93% depositional texture and facies match and a 100% thickness match to borehole BH1010. VS1 develops a succession of packstone to rudstone textures, corresponding to the Coralline Algal Pavement Facies and Coralline Algal Debris Facies. This is then overlain by framestone textures, corresponding to the Reef-Core FA. These deposits are subsequently overlain by grainstone textures that correspond to the Sand Shoal FA.

VS2 demonstrates a 54% depositional texture and facies match and a 58% thickness match to borehole BH1060. VS2 develops a vertical succession of packstone to rudstone textures that corresponds to the Sheltered Shelf FA and CAP Facies respectively. The rudstones are overlain by framestone textures corresponding to the Reef-Core FA. The facies mismatch is from the simulated rudstone (DS1) and framestone (DS2) textures. The simulated rudstone textures (DS1) are from the CAP Facies, however, outcrop and borehole logs indicate wackestone-packstone textures of the Sheltered Shelf FA should be present. The simulated rudstone textures in DS1 suggest that MS4 has a greater component of progradation than that occurring in the Malta platform. This facies mismatch is similar to that developed in best-fit analysis (section 7.3.2). The simulated framestone textures (DS2) are from the Reef-Core FA, however, outcrop and borehole logs indicate wackestone-packstone-floatstone-rudstone textures of the Fore-Reef Slope and Shelf FA should be present. This textural mismatch in MS4 is also the result of progradation rates that are possibly greater than in the Malta platform.

VS3 demonstrates a 100% depositional texture and facies match and an 89% thickness match to borehole BH1863. VS3 develops a vertical succession of packstone-rudstone, corresponding to PCAD Facies.

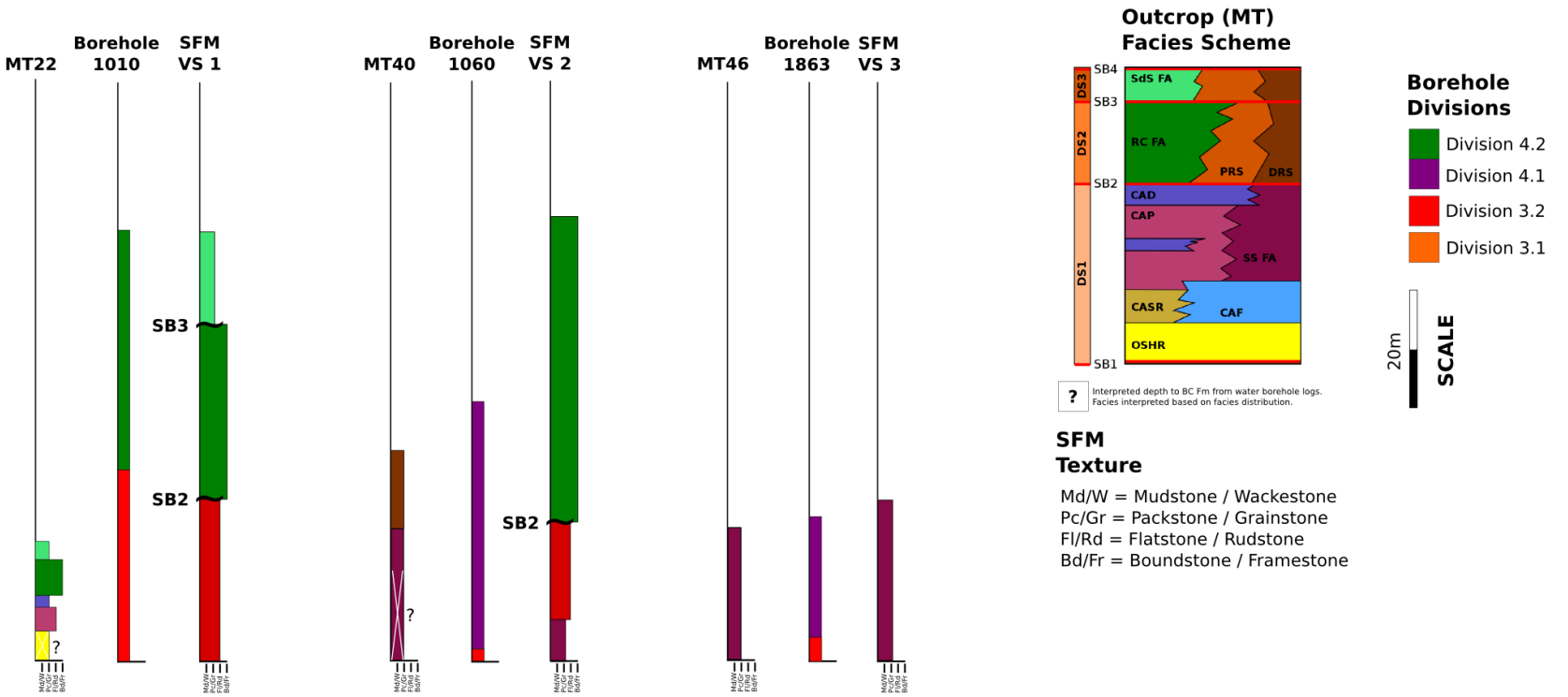

Figure 7.17: 2D model outputs for MS4 showing (F_3) stratal thickness match between real facies (outcrop (MT) and borehole (BH)) and simulated facies (SFM VS1, 2 and 3). See table 5.2 for description on which borehole log divisions relate to which stratigraphic divisions (facies associations & facies).

Does the numerical model support the alternative conceptual model?

The large-scale observations of MS4 are similar to those of the best-fit analysis (section 7.3.2) SFM. At a larger scale, MS4 displays the key facies associations and facies belts (compare figure 7.3 outcrop and borehole cross section with figure 7.16 2D SFM cross section). For DS1, the numerical model demonstrates a basinward transition from rudstone, packstone, wackestone-mudstone textures. This corresponds to the CAP and CAD Facies, that transition basinward to Sheltered Shelf FA (MCAD and PCAD Facies). For DS2, the numerical model demonstrates a basinward transition from framestone, rudstone, packstone, and wackestone-mudstone textures. This corresponds to the Reef-Core FA (CFR and CPR Facies) that transition basinward to the Fore-Reef Slope and Shelf FA (PRS and DRS Facies). For DS3, the numerical model develops grainstone textures that overlie the framestone textures. This corresponds to the Sand Shoal FA that overlie the Reef-Core FA.

The composite sea level curve (figure 7.11 black curve) occupies the temporal and amplitude uncertainty of sea level curves interpreted for the Late Miocene Llucmajor, Las Negras, Nijar and Maltese carbonate platforms (figure 7.11 space between polygons). The composite relative sea level curve is distinct from that applied in the best-fit analysis section (section 7.3.2, figure 7.11 red curve) in both the sea level cycle frequency/amplitude as well as the total duration. Despite the difference in simulated RSLs, a quantitative comparison of the two models that developed the best match to outcrop features from MS4 and best-fit analysis (section 7.4.2.4) reveals that both numerical models have the same MMS (0.80 MMS [equation 4]). This is achieved by lowering sediment production rates in MS4 relative to that simulated in the best-fit analysis. In both cases, the simulated sediment production rates fall within the natural range of sediment production of Holocene carbonate factories. This indicates that in the absence of well-bracketed sea level cycle, in terms of frequency/amplitude and total duration, a variety of relative sea level curves can plausibly explain the features observed in outcrop. In view of the above, the theoretically plausible non-unique scenario MS4 is plausible in terms of real world uncertainties tied to relative sea level.

There exists a large range of naturally plausible sediment production (section 3.2.2) and transport rates (section 2.3.3.1). Results from this section show that different combinations of these rates, over different time spans, can produce the same platform geometries and facies architectures. Thus, similar stacking patterns and stratal geometries can be formed over different simulated model run times that may represent different sea level order cycles. These different (non-unique) solutions indicate that in the absence of direct information (e.g. well-constrained isotope dates) several different time spans may need to be considered in terms of platform evolution. The implication of this observation is that unless there is direct evidence supporting the interpretations of particular sea level cycle orders, the temporal scale of the investigated

Late Miocene relative sea level curves are tentative at best. Additionally, since there are significant uncertainties in the age of these units, this calls in to question the evidence for long distance cyclostratigraphic correlations and interpretations of Mediterranean-wide controls (e.g. Esteban, 1996; Cornée *et al*., 2004) (section 6.6).

Suggestions for future work

There is a scope to further investigate the relative sea level curves that affected Late Miocene Mediterranean carbonate platforms. Research should be directed towards refining relative sea level temporal and amplitude uncertainty and the possible role of autocyclic effects. A better understanding of regional Late Miocene relative sea levels may shed light on the possible control on carbonate platform evolution, cycles in rhodalgal and coralgal facies, and facilitate/support arguments for long distance cyclostratigraphic correlations (e.g. Esteban, 1997; Cornée *et al*., 2004).

7.5. Conclusions

7.5.1. Discussion best-fit analysis (section 7.3.2)

Quantitative comparison between numerical model and outcrop features is 0.80 MMS [equation 4]. The numerical model displays the key stacking patterns, platform margin slope gradients, facies architecture and facies belts observed for the Maltese UCL Formation (compare figure 7.3 and 7.6). The close match between outcrop and numerical model does not *prove* the conceptual model and the interpretation/hypothesis are correct. Rather, it indicates that the conceptual model expressed in the numerical model (section 7.3.2) is physically reasonable. The numerical model also indicates that the interpretation/hypothesis - that a change in platform geometry is a result of a shift in carbonate factories - is physically reasonable. The SFM parameters selected from the conceptual model might however not be uniquely responsible for the features observed in outcrop (investigations of non-uniqueness section 7.4.2).

7.5.2. Discussion non-uniqueness analysis (section 7.4.2)

The investigation of non-uniqueness assesses whether numerical models that simulate process rates that are distinct from those applied in best fit analysis (section 7.3.2) can also develop synthetic features that are similar to those seen in the Maltese UCL Formation.

MS1 - changes in the rate of accommodation generation (icehouse *versus* greenhouse eustasy); *MS2* - time and carbonate factory variable sediment production rates; *MS3* - time and carbonate factory variable sediment transport rates; and *MS4* - variable total SFM run time.

Two theoretically plausible non-unique scenarios emerge from MS1. MS1.1 suggests that both depositional sequences (DS1 and 2) were subject to low-amplitude sea level oscillations (greenhouse conditions) and MS1.3 suggests that DS1 was affected by icehouse conditions and DS2 was affected by greenhouse conditions. However, given the Late Miocene climate evolution, both theoretically plausible non-unique scenarios are unlikely given the general interpretation of long-term global cooling of the Late Miocene. When and where cooling occurred, when the ice sheets started to form on each hemisphere, whether they persisted once formed, and the cause(s) of the cooling have however long been debated (e.g., Thomas *et al*., 2006). MS1.3 could thus support notions that the sea-level history and hence ice sheet growth history may have been more complicated than the prevailing model of long-term cooling suggests..

The theoretically plausible non-unique scenario that emerges from MS2 is a heterozoan factory that produces less sediment than photozoan factory (MS2.3). A comparison of theoretically plausible non-unique scenario and platform context indicates that the non-unique scenario is plausible in terms of the real carbonate system. A switch in carbonate factory (heterozoan to photozoan) does occur and may influence/control the shift in platform geometry within the context of the Late Miocene carbonate platforms. This outcome helps the user gain insight into platform evolution that would not have been possible without the application of this quantitative method. The theoretically plausible scenario that emerges from MS3 is a heterozoan factory that is characterised by higher diffusional transport rates than the photozoan factory (MS3.3). Within the UCL Formation, DS1 contains rhodalgal lithofacies that are characterised by fine-to-coarse bioclastic grains. The coralgal lithofacies, tied to DS2, build rigid organic buildups/frameworks. Sediments produced by the rhodalgal are more easily transported relative to those provide by the coralgal factories. In view of the above, the theoretically plausible non-unique scenario MS3.3 is plausible in terms of real world rates and is a valid explanation for the observed switch (ramp to FTSM) platform geometry.

Quantitative SFM-based results MS and MS3 show that the sediment production rate (MS2) and diffusional transport rate (MS3) significantly influence platform evolution and geometry. These results support Pomar and Kendall (2008) who argue that the interplay between different sediment production and redistribution processes form the various depositional profiles and facies belt distributions. Thus, this aspect of the modelling supports what previous authors have been suspecting in terms of the impact of carbonate producing biota on platform architecture and can explain the transition from ramp to FTSM platforms (e.g. Pomar & Kendall, 2008; Pomar *et al.,* 2012).

Despite simulation of distinct RSLs (figure 7.11 red and black lines), two models are developed that have similar stacking patterns, maximum platform gradients and facies (MS4 and best-fit

analysis). This indicates that in the absence of well-bracketed sea level cycle, in terms of frequency/amplitude and total duration, a variety of relative sea level curves can plausibly explain the features observed in outcrop. Similar stacking patterns and stratal geometries were also formed for models that simulate different model run times that may represent different sea level order cycles. These different (non-unique) solutions to the depositional geometries, which are also observed in the Mediterranean platforms, indicate that the geometries/platforms may be could be produced by one of several different sea-level curves, each with a different order of cyclicity.

CHAPTER 8: KEY RESULTS, DISCUSSIONS AND CONCLUSIONS

8.1. Introduction

This chapter summarises the key results of this study, discusses these in a broader context and describes how the study has advanced knowledge in the field. The main results are addressed through discussion based on a number of commonly asked questions concerning the evolution of carbonate platforms and the applicability of quantitative methods to further our understanding of platform evolution. Final conclusions are drawn at the end.

8.2. Controls on platform evolution

Various authors have discussed the influence carbonate associations may have on stratal architecture and platform geometry (section 2.1.3). They propose qualitative conceptual models on the influence that carbonate factories may have on platform evolution. Issues of scale and internal consistency however limit conceptual models (section 2.3.2). In view of these limitations, conceptual models are often insufficient to quantitatively assess how individual or multiple parameters influence platform geometry. Numerical stratigraphic forward modelling (SFM) is a quantitative approach that relies on equations and algorithms that ensure internal consistency (section 2.3.3). In view of this, this thesis incorporates quantitative methodologies (Dionisos SFM).

8.2.1. How do carbonate factories influence carbonate platform development in natural systems?

Previous SFM based investigations on how carbonate factories influence carbonate platform development in natural systems do not fully consider realistic values for the various carbonate factory parameters (e.g. Bosence & Waltham, 1990; Bosence *et al*., 1994; Warrlich *et al*., 2008; Williams *et al*., 2011) such as sediment production profiles, sediment production rates, sediment grain-size, sediment transport rates or a combination of these. As a result, our understanding of how these different aspects of carbonate factories influence carbonate platform development in natural systems remains incomplete.

This study involved an extensive literature search to gather data to bracket average sediment production rates, depth distribution of sediment production, and proportions of grain-sizes produced for five carbonate factories from Holocene systems (section 3.2.2 and Appendix A). As a result, *grain-size production profiles* developed in this study better represent the key aspects of particular natural carbonate factories than has been achieved before.

The grain-size production profiles were applied using SFM to simulate sediment production of particular natural carbonate platforms from the literature (e.g. Llucmajor reef-rimmed platform

of Mallorca) and an outcropping example (Upper Coralline Limestone (UCL) Formation of Malta). This approach more accurately simulates sediment production of particular natural carbonate platforms than realised in previous SFM-based attempts. This work contributes to the building of more realistic forward models, in terms of their parameter rates, that enables the testing of sequence stratigraphic interpretations (section 7.3.2), the reconstruction of partially exposed or imaged carbonate stratigraphies, the locating and quantifying of likely reservoir facies, the illustration of the development and likely interconnections of reservoir facies, analysing the primary depositional controls on reservoir heterogeneities, and the prediction of stratigraphies around a basin margin.

The grain-size production profiles were also used in SFM-based investigations to assess the influence various carbonate factories have on platform evolution. The carbonate factory dependent parameters and processes investigated in chapters 3 and 4 are sediment production profiles, sediment production rates and sediment grain-sizes and how these influence sediment transport rates.

8.2.1.1. Production-Depth profiles

Williams *et al.* (2011) use SFM to quantitatively investigate the influence that euphotic and oligophotic production-depth profiles have on platform geometry. The authors conclude that oligophotic profiles produce FTSM platforms, not ramps as previously assumed. The result is however misleading since Williams *et al*. (2011) simulate significantly distinct sediment production rates, applying higher production rates for the oligophotic production profiles. Thus, the oligophotic profiles may have developed steeper platform margins as a result of higher overall production rates rather than a result of the shape of the tested production-depth profiles. Given the limitations of the forward modelling methods applied, their conclusions have been investigated further in this thesis.

Two distinct carbonate production profiles are tested in this study. To better assess the influence distinct production-depth profiles have on platform geometry, the tested euphotic and oligophotic production profiles were made equal in terms of total sediment that could be produced within a defined time interval across the depth-range of sediment production. This method ensures that the only difference being compared between production profiles is the depth distribution of sediment production. These production profiles are termed - *equalised production profiles* (section 3.2.3).

In all the tested sediment production and diffusion transport rates, equalised single grain-size oligophotic production profiles develop steeper platform margins at the end of the model run time than equalised single grain-size euphotic profiles. Thus, the result is consistent with Williams' *et al.* (2011) conclusions. This is despite using a different approach on the production

profiles where the maximum production rates are the same even if the volume of sediment produced on an evolving bathymetry is still different.
Sediment production and accumulation by the oligophotic production profile is less limited by the available accommodation space, which in these tests uses a published late Miocene sea level curve. Additionally, as sediment accumulates at depth, the deeper bathymetries are brought within the oligophotic and euphotic sediment production zone. Consequently, in these equalised production profile runs, the oligophotic profile has a greater sediment production rate over the entire platform slope (per unit time) that leads to greater rates of sediment accumulation, progradation and platform margin steepening.

These results do not support previous ideas that euphotic production-depth curves form FTSM platforms while oligophotic production-depth curves construct ramp systems (e.g., Wright & Faulkner, 1990; Bosscher & Schlager, 1992; Bowman & Vail, 1999; Pomar, 2001).

8.2.1.2. Sediment production and transport rate

When applying a common diffusion coefficient rate, both equalised euphotic and oligophotic single grain-size production profiles develop maximum platform margin gradients (MaxS) that are lowest with low production rates and highest for high production rates (section 3.3.2). When applying a common sediment production rate, MaxS is lowest for high diffusion coefficient rates and highest for the lowest diffusion coefficient rates (section 3.3.2). These results indicate that independently of the production profile tested, ramps form when diffusion coefficients are high relative to production rates and FTSM platforms form when diffusion coefficients are low relative to production rates. These results suggest that hypotheses emphasising sediment production rates or transport rates, as separate, more-or-less dominant, controls are misleading. Rather, hypotheses suggesting the dual control of sediment production and sediment transport, relative to each other, are supported in this research (see section 8.2.2). This is consistent with ideas developed by Williams *et al*. (2011).

8.2.1.3. Grain size type & diffusional transport rate

Results from the modelling also clearly indicate that the relative proportions of grain-size produced, and their attributed diffusion coefficients, significantly influence platform evolution and geometry (section 3.3.3). Tests confirm a strong positive correlation between the maximum platform margin gradient and the proportions of grain-sizes simulated. Platform margin gradients increase as the proportion of coarse, low transport rate grains increases. Maximum platform margin gradients increase linearly with an increase in the contribution of low diffusion coefficient grain-sizes.

These results may be a consequence of the Dionisos diffusional transport computation and is consequently only a hypothesis for how natural systems might work. This result thus requires further testing.

8.2.2. Influence of carbonate factories on platform geometry

Quantitative SFM-based results from this thesis show that the sediment production rate and diffusional transport rate, relative to each other, significantly influence platform evolution and geometry. Over the naturally plausible range of sediment production and diffusion coefficient rates tested, a spectrum of platform geometries (MaxS of 0.2 up to 20.8°) are developed (section 3.3). This work thus demonstrates that platform evolution and geometry is controlled by a combination of sediment production (PR) and sediment transport (TR) rates. Carbonate factories determine sediment production rates (PR) and the quantity and the grain-sizes produced (section 3.2.2) that in turn influence sediment transport rates (TR). The photozoan factory has a greater total sediment production rate than the heterozoan factory. The photozoan factory also produces coarser grain-sizes that are less easily transported than those produced by the heterozoan factory. SFM-based investigations in this thesis show that the simulations of photozoan factories, characterised by a high PR relative to TR, produce FTSM platforms while the simulation of heterozoan factory, characterised by a high TR relative to PR, forms ramps (section 3.3.1).

The quantitative analysis carried out in this thesis thus shows that carbonate factories, through their influence on sediment production and types of sediment being produced (grain size, effective density, etc.), can produce the critical differences between carbonate platform geometries. The quantitative results obtained in this thesis therefore support Pomar & Kendall's (2008) suggestion that "*the interplay between different sediment production and redistribution processes form the various depositional profiles and facies belt distributions*".

8.2.2.1. Can the variable character of carbonate platforms be explained in terms of a PR/TR ratio?

Previous research (e.g. Williams *et al*., 2011) introduces the notion that relative rates of sediment production and transport are key controls on platform geometry. However, it does not provide a quantitative means of comparing the two rates and assessing their influence on platform geometry. In this thesis, the control has been expressed as a production-transport ratio (PR/TR) (section 3.3.2, 3.3.3 and 4.3.2). SFM-based results show that models that simulate high PR relative to TR (high PR/TR ratio) develop steep platform margin gradients and FTSM platforms. Thus, FSTM form when PR/TR > 1 and form quickly when PR/TR >> 1. In these scenarios, sediments rapidly accumulate to sea level and prograde, forming steep platform

margins. Conversely, models that simulate low PR relative to TR (low PR/TR ratio) develop low platform margin gradients and form ramps. In such scenarios, high sediment transport rates redistribute sediment across the underlying topography, preventing the steepening of platform margins. The PR/TR ratio is a key control on the evolution and geometry of carbonate platform. This is the case in both euphotic and oligophotic production profiles and in mixed-grain-size and mixed transport rate systems (section 3.3.3). It is the PR/TR ratio, not the absolute values of each parameter, that influences platform geometry. Carbonate factories strongly influence the PR/TR ratio and platform geometry through their control on sediment production rate (PR) and the quantity and type of grain-sizes produced. The PR/TR ratio is a simple, but new and useful way of considering the spectrum of carbonate platform geometries.

To replicate flat-top steep margin (FTSM) platform geometries, similar to those observed in the Llucmajor platform in Mallorca, a relatively high sediment production rate and relatively low diffusional transport are required (section 4.4.1). These rates are relative to the ranges of these parameters recorded in natural systems (section 3.2.2). The sediment production and diffusional transport (diffusion coefficient) parameter values (section 4.3.1) that replicate the Llucmajor platform stratal geometries may be used in other SFM studies that seek to simulated similar FTSM platform geometries such as those used in chapter 7 in the simulation of the Malta UCL Formation.

8.2.2.2. Accommodation in carbonate platforms

Accommodation has been a fundamental concept in interpreting the controls on large-scale stratal patterns and platform geometry. Jervey (1988) defines accommodation as "*the space available for potential accumulation*" and suggests relative sea level as a major control on accommodation. Later authors (e.g. Posamentier & Allen, 1999; Coe *et al.,* 2002; Catuneanu, 2002) emphasise sedimentation rates as at least a co-equal control of accommodation. Helland-Hansen & Martinsen (1996) suggest that hydrodynamic regimes influence sedimentation rates (sediment flux) through sediment transport and redistribution processes. SFM-based tests carried out in this thesis support notions that large-scale stratal patterns and platform geometry are affected by relative sea level (7.4), sediment production and transport rates (sections 3.3, 4.3, 7.4). Pomar (2001) and Pomar & Kendall (2008, 2009) further qualitatively investigate sediment production and transport dynamics and subdivide Jervey's (1988) accommodation into physical (siliciclastic systems) and ecological (carbonate systems). They argue that siliciclastic sediments accumulate (physical accommodation) until a base level, at which point hydrodynamic conditions (waves and currents) move sediments down-shelf to flatten the depositional profile and establish the "*shelf equilibrium profile*" (*sensu* Swift & Thorne, 1991). For carbonate systems, the base level for sediment accumulation is controlled by local hydrodynamic conditions (physical accommodation) and the capacity of organisms to

accumulate sediments above (ecological accommodation) the hydrodynamic thresholds associated with siliciclastic systems.

Muto & Steel (2000) argue that accommodation, in terms of its original definition (Jervey, 1988), is conceptually flawed since it is inherently unspecifiable and un-measurable in so far as it is linked with potential sedimentation. Using arguments of unspecifiability of lateral extent of accommodation and the dimensional confusion in the creation of accommodation (A) (m yr^{-1}) / rate of sediment input (S) (m^3 y^{-1}) ratio, Muto & Steel (2000) demonstrate that the current definition of accommodation limits its practical use in quantitative sequence stratigraphic analysis. Muto & Steel (2000) suggest a possible redefinition of (realised) accommodation as "*the thickness, measured at a specified site and time, of a space which becomes filled with sediments during a specified time interval*".

There is a scope to further quantitatively investigate qualitative concepts on accommodation, particularly Pomar (2001) and Pomar & Kendall's (2008) distinction between physical and ecological accommodation. SFM-based investigations can aim to assess similarities and differences between accumulation in carbonate and siliciclastic systems and the consequent effects on large-scale stratal patterns and platform geometry. The analysis can be in terms of (i) sediment input (siliciclastic sediment discharge *versus in situ* carbonate production), (ii) grain size distributions across the depositional profile, (iii) sediment redistribution processes across the depositional profile, and (iii) sediment accumulation across the depositional profile. The TR/PR ratio developed in this study (section 3.3.2, 3.3.3 and 4.3.2) could be a unifying way to think about how siliciclastic and carbonate platforms evolve. Further quantitative research on accommodation may thus be in terms of TR/PR ratio and the revised Muto & Steel (2000) concept of accommodation.

8.2.2.3. Do similar sediment production and diffusional transport ratios produce similar platform geometries?

Bosence *et al.* (1994) applied SFM to investigate whether computer models can simulate sedimentary processes of carbonate platforms. Their results indicate that the simulation contains the major elements of the Llucmajor platform of Mallorca including amount of progradation and aggradation. They however emphasize that results are not unique and similar stratigraphies may be generated with different combinations of the controlling parameters (Bosence *et al*., 1994). Burgess & Prince (2015) further investigate issues of non-uniqueness and demonstrate, with SFM, that multiple different controls and process rates may generate similar geometries.

Investigations thus far are however limited in that the parameter values assessed might not be sufficiently realistic or representative of natural systems (Burgess & Prince, 2015).

Investigations carried out in this thesis attempt to assess whether distinct parameter rates for controlling parameters and processes that are representative of natural carbonate systems may also present issues of non-uniqueness.

Across the range of distinct sediment production and diffusional transport rates tested, each simulating a unique combination sediment production and diffusional transport, 19 of the 1085 simulated models develop practically indistinguishable platform geometries (section 4.3.2). The distribution of non-unique results within the tested sediment production and diffusional transport parameter space (section 4.3.1.1) indicates that models simulating a lower sediment production rate and a higher diffusional transport rate can develop similar platform geometries to models that simulate a higher sediment production rate and a lower diffusional transport rate. Results thus indicate that models simulating distinct sediment production and transport rates, but that have similar PR/TR ratios, develop similar platform features. Conversely, models that have a different PR/TR can develop distinct platform features.
These results demonstrate that the simulation of distinct rates for key processes (sediment production and diffusional transport) can develop similar non-unique platform features. This shows that similar (non-unique) stratal geometries and facies architectures can occur across a range of parameter values for particular processes. Thus, non-uniqueness of stratal geometries challenges the assumed ability to identify a single explanation or history for a given stratal geometry, for example, when attempting to interpret sediment bypass and RSL histories (Burgess & Prince, 2015). This provides support for a need to shift towards sequence stratigraphic methods based on constructing and evaluating multiple hypotheses and scenarios (e.g. Burgess and Prince, 2015). Further SFM-based research can investigate whether the PR/TR ratio has predictive power over the stratal and platform evolution and geometry.

Bosence *et al*. (1994) and Burgess & Prince (2015) and this study use different SFM that simulate platform dynamics with distinct algorithms. Despite the different numerical modeling programs, the three studies demonstrate issues of non-uniqueness. This supports the notion that non-uniqueness is not the product of particular functions of specific modeling programs. However, an important limitation to the study of non-uniqueness, within the framework of SFM, is that the simulations used might not be sufficiently realistic or representative of natural systems (Burgess & Prince, 2015). For instance, the applied parameter rates might not realistic, and/or the mathematical functions that aim to simulate particular natural processes are inadequate. Evidence of non-uniqueness in numerical simulations might therefore not necessarily imply issues of non-uniqueness in natural systems.

A good way to assess whether the simulations are sufficiently realistic or representative of natural systems is to reproduce a well-understood real stratigraphy with input parameters that

are characteristic of that particular depositional system. Since the simulations of the Llucmajor and Malta platforms are based on realistic parameter values, and the SFM does simulate the real stratigraphy with these bracketed parameters (sections 4.3.1. and 7.3.2), it can be assumed that the processes are simulated adequately and '*the program weighs parameters much as nature does*' (Eberli *et al*., 1994). If the model simulations in this work are sufficiently realistic, the modelled stratal geometries are important examples of non-uniqueness that may also occur in natural carbonate systems. This would suggest that issues of non-uniqueness in SFM might also occur in natural systems and emphasises the need for a shift towards constructing and quantitatively evaluating multiple rather than single hypotheses and scenarios when investigating the controls on platform evolution.

To further investigate whether non-unique stratal geometries occur natural systems one would have to (i) utilise more advanced numerical models that more accurately simulate natural processes, and (ii) investigate natural systems where the controls on facies architecture and platform evolution are better understood and constrained. These aspects may be better constrained in Holocene systems rather than ancient examples because sedimentary processes are actively underway in modern systems and can thus be more directly observed, measured and quantified.

8.3. Late Miocene Upper Coralline Limestone Formation, Malta (chapters 5 and 6)

8.3.1. Facies model and sequence stratigraphy of Upper Coralline Limestone Formation

Six facies associations (FA) and fifteen facies (section 5.3) were identified in the study area (figure 8.1). These are typical for those also reported for other parts of the Upper Miocene of the central Mediterranean region (e.g. Esteban, 1996; Pedley, 1996; Pedley, 1998; Pomar *et al.,* 1996; Franseen and Goldstein, 1996). Pedley (1974; 1975; 1978; 1979) assessed the UCL Formation across the Maltese Islands and developed a lithostratigraphic scheme and palaeoenvironmental interpretations. Pedley, however, does not develop chronostratigraphic or sequence stratigraphic schemes for the Maltese UCL Formation. Dart (1991) develops the first sequence stratigraphic scheme for the Maltese UCL Formation based on two study areas representing 23% of the outcropping UCL Formation across the Maltese Islands. The investigation carried out in this thesis is a broader study throughout Malta and Gozo that adds more observations and new data on sequence boundary identification. A chronostratigraphic scheme, based on local and regional correlations, and a sequence stratigraphic scheme for the UCL across the islands were also developed (chapter 6).

The following section compares the depositional model and sequence stratigraphic scheme developed for the Maltese UCL Formation in this study with that proposed by previous authors.

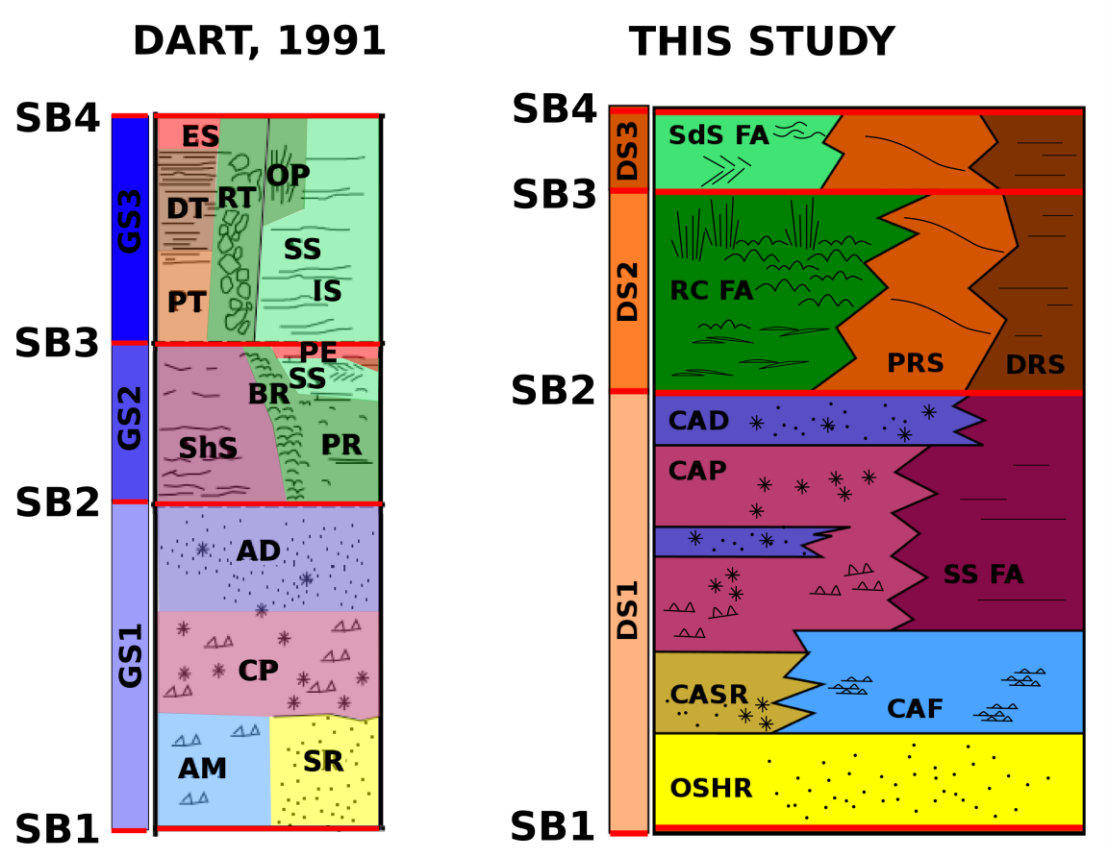

Figure 8.1: Stratigraphic chart comparing the sequence stratigraphic scheme developed by Dart (1991) to this thesis. See table 5.4 for facies abbreviations.

Key similarities/differences Facies & Depositional models

A relative sea level fall ended the deposition of the pelagic Blue Clay sediments and started the deposition of shallow marine Open Shelf Glauconite-rich Packstone (OSGR) Facies. Relative sea level continued to fall across the Maltese Islands and extensively eroded into the OSGR Facies to form the "*basal Upper Coralline Limestone erosion surface"* (Pedley, 1978) identified as sequence boundary 1 (SB1) in this study (section 6.2.1). This is different from previous interpretations by Dart (1991 p.272) who argued that the basal sequence boundary (his SB1) is marked by a hiatus and a condensed sequence of Greensand Formation glauconite sands.

Relative sea level subsequently rose and wave ravinement in nearshore environments in western areas - within the Il-Maghlaq Fault (IMF) footwall high - eroded into seabed deposits that consisted of OSGR deposits. These sediments, interpreted as a transgressive lag, were subsequently transported eastwards (basinwards) forming the OSHR Facies (section 6.2.1). As relative sea level continued to rise, less material was eroded and re-deposited within the Maltese Islands thus ending deposition of the OSHR facies.

Pedley (1978) subdivides the Ghajn Melel Member into the Zebbug Beds in the west of Gozo and the Ghajn Znuber Beds in the east of Gozo and west of Malta. While certain of Pedley's

(1978) criteria to distinguish between the two beds are observed in petrographic/microfacies analysis of this thesis, both beds are rich in *Heterostegina* and share many common features at outcrop scale. Research from this thesis suggests that the beds in Gozo and Malta are similar and contemporaneous (*cf.* Pedley, 1978). In view of this, the two beds of the Ghajn Melel Member have been treated as one facies (section 5.3.1).

The Coralline Algal Biostrome FA conformably overlies the OSHR facies. The biostrome consists of a mosaic of sedimentary facies that are arranged in a NNW-SSE oriented facies belt that trends obliquely across the IMF footwall high in Malta (section 5.3.2). Accumulations of the *in situ* Coralline Algal Floatstone (CAF) and Coralline Algal Pavement Rudstone to Framestone (CAP) Facies are limited to the western areas of Malta and gradually diminish eastwards. This suggests eastern Maltese areas may have been deeper than the maximum depth at which coralline algal development occurs, that is > *circa* 100 m. These observations suggest that the bathymetric relief of the IMF footwall high produced gently easterly tilted fault blocks for both the North Malta Graben and Malta Horst (section 6.2.2).

Previous studies have identified a facies that outcrops in the Fomm ir-Rih area and along the Victoria Lines Fault (VLF) footwall as the Ghajn Znuber Beds (Pedley, 1974, 1978; Bosence & Pedley, 1982; Dart, 1991). In this study, these outcrops have been interpreted as a new distinct facies, the Coralline Algal Sand Ridge Packstone (CASR) Facies (section 5.3.2.1 and figure 8.2). The better-illuminated VLF footwall areas accumulated CASR Facies while deeper and more sheltered areas accumulated the CAF Facies (MT16 to BP1). The CASR Facies demonstrates a fining upward sequence that suggests that the VLF footwall area was subject to increasingly deep and low energy marine environments. Relative sea level rise outpaced CASR Facies sedimentation rates and the deposition of this facies diminished while deposition of the lower energy CAF Facies may have continued. Both CASR and CAF Facies are thus interpreted as transgressive deposits (section 6.2.2). As the rate of sea level rise diminished and stabilised, sedimentation rates of the CAP Facies outpaced the rates of base-level rise to form aggradational and progradational geometries. The stacking patterns suggest the CAP represent late transgressive and highstand deposits (section 6.2.2). Relative sea level then gradually fell, exposing the Coralline Algal Debris Packstone Facies (CAD) Facies to increasingly turbulent and higher energy environments possibly within or close to the storm/fair weather wave base that brought to an end the shallowing-upward trend of the Coralline Algal Biostrome (section 6.2.2). The CAP is interpreted as late highstand and falling stage deposits (section 6.3.2). This corresponds to Dart's (1991) interpretation.

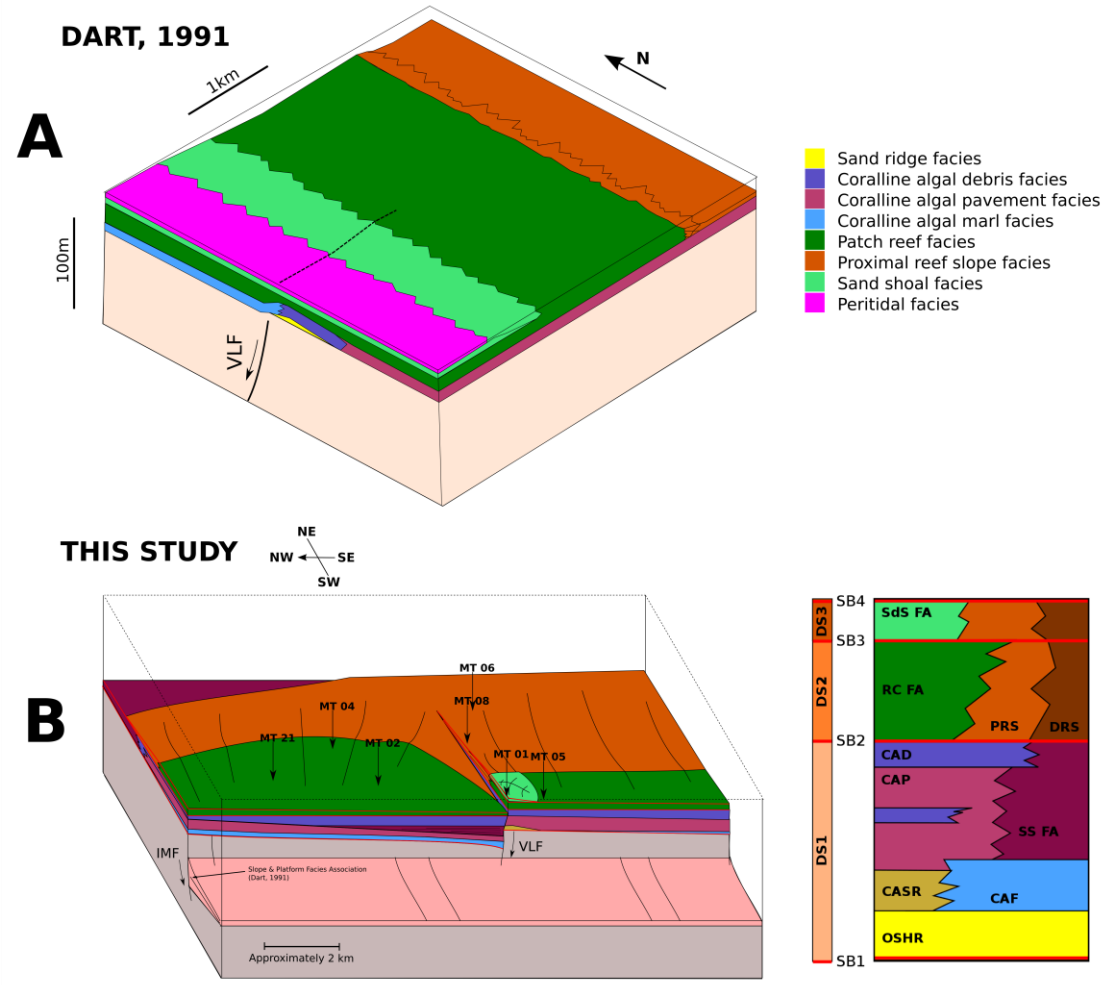

Figure 8.2: Comparison of 3D conceptual depositional models of Dart (1991) and this thesis at a small scale across the VLF and IMF. See table 5.4 for facies abbreviations. Key differences between the conceptual models are described in detail throughout chapters 5 and 7 and summarised in section 8.3.1. Detailed 3D conceptual models developed in this thesis are available in chapter 6 section 6.3.4. These show depositional sequence (DS1, DS2 and DS3), facies distribution within the depositional sequence and key sedimentary geometries.

The CASR, CAP and CAD Facies are the first to record thickening along the VLF footwall high and along the Saint Paul Islands Fault (SPIF) footwall (chapter 6 section 6.2.2). This corresponds to interpretations by Dart (1991 pp.269, 373). These observations suggest that VLF and SPIF developed bathymetric footwall relief during deposition of the Coralline Algal Biostrome FA. A more detailed interpretation of the depositional history across the VLF is provided in this thesis than previous studies of the area (figure 8.2 compare section across VLF by Dart and this study). During early stages of Coralline Algal Biostrome FA deposition, the VLF produced sufficient bathymetric relief to develop the CASR Facies on the VLF footwall and not within the hanging-wall. Following the deposition of CASR, the CAP Facies was deposited in both the VLF footwall and hanging-wall. The uplifted footwall highs of the IMF, VLF and SPIF faults may have been shallower, better-illuminated areas than the hanging-wall

lows allowing for enhanced coralline algal production and accumulation (chapter 6 section 6.2.2). As throw on the VLF increased, the deposition of CAP Facies within the VLF footwall declined and gave way to Plane Bedded Coralline Algal Debris (PCAD) Facies. Thus, within the VLF footwall, high-energy, shallow marine environments predominated and deposition of the CAP Facies continued (MT01) while in the VLF hanging wall depressions, sheltered deeper-marine environments were formed leading to the deposition of PCAD Facies (figures 6.9 and 8.2).

The Sheltered Shelf FA consists of the Massive Coralline Algal Debris Wackestone (MCAD) and PCAD Facies. The facies association lies immediately to the east of the Coralline Algal Biostrome FA and forms a broad N-S oriented facies belt across the eastern areas of Malta. The MCAD is equivalent to Pedley's (1974) Gebel Mtarfa Beds and the PCAD is equivalent to Pedley's (1974) Rdum il-Hmar Beds (figure 8.3). On the basis of facies relationships, the Sheltered Shelf FA is interpreted in interpreted as the eastern seaward lateral equivalent of, and contemporaneous with, the Coralline Algal Biostrome FA (section 5.3.3). New evidence from this study thus supports the interpretations of Pedley (1974; 1978), but not those of Dart (1991 p.222) who suggests his Sheltered Shelf Facies are contemporaneous with the Fore-Reef Slope and Shelf FA and Reef-core FA that overlie the Coralline Algal Biostrome (section 5.3.3 and figure 8.1).

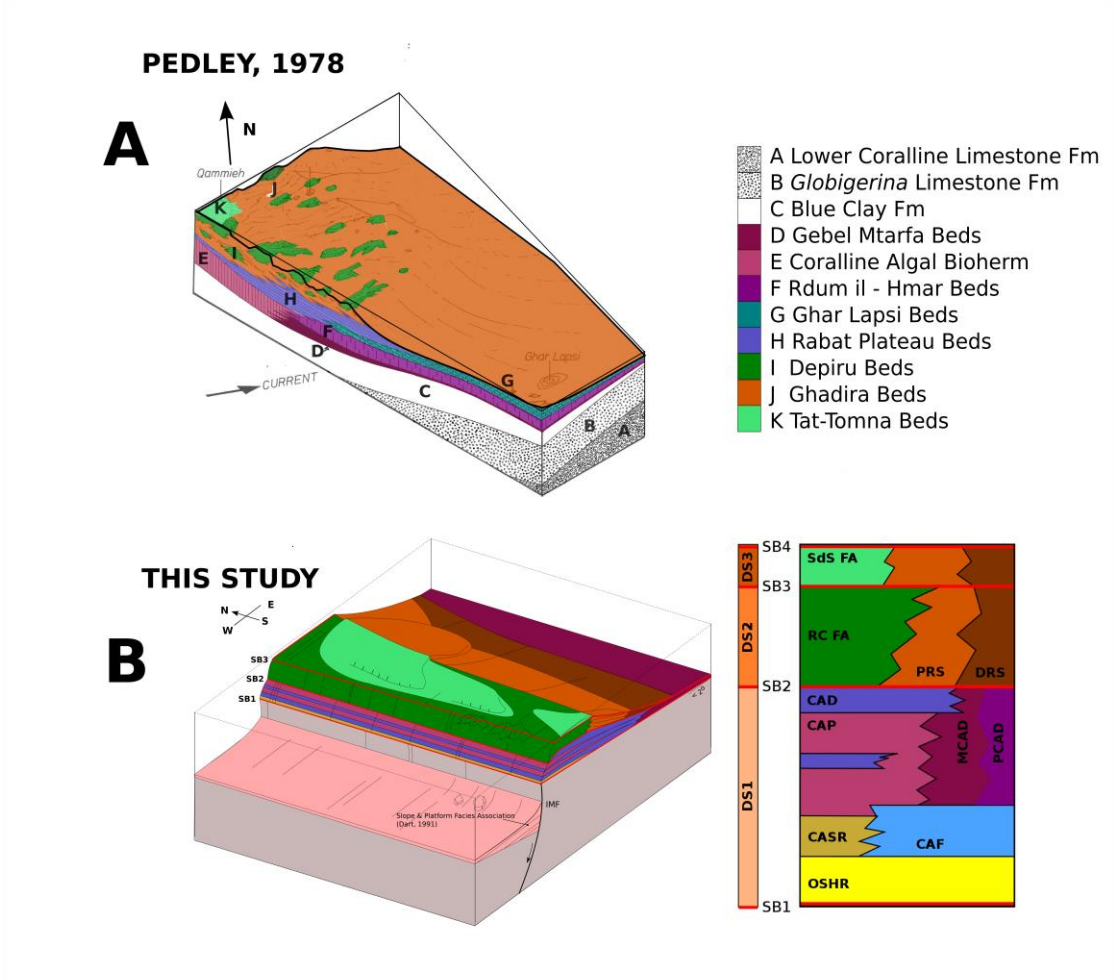

Figure 8.3: Large-scale comparison of 3D conceptual depositional models of Pedley (1978) and this thesis. See table 5.4 for facies abbreviations. Key differences between the conceptual models are described in detail throughout chapters 5 and 7 and summarised in section 8.3.1. Detailed 3D conceptual models developed in this thesis are available in chapter 6 section 6.3.4. These show depositional sequence (DS1, DS2 and DS3), facies distribution within the depositional sequence and key sedimentary geometries.

Widespread shallowing in the Maltese Islands reworked the rhodalgal sediments of the Coralline Algae Biostrome FA and generated the CAD Facies that cap the Coralline Algal Biostrome FA in the west of the Maltese Islands. This study identifies an extensive sharp erosive sequence boundary (SB2) across the westernmost outcrops of the Maltese Islands between the Reef-Core FA and the underlying CAD Facies (figures 8.1, 8.2 and 8.3). Outcrop and carbon and oxygen stable isotope-based evidence gathered in this study indicates that the erosive surface was the result of a substantial relative sea level fall that exposed the upper levels of the Coralline Algal Biostrome FA to sub-aerial conditions in the west of Malta (section 6.3.2.1). The surface is interpreted as a sequence boundary (SB2) and is a key horizon that marks the shift from a rhodalgal (heterozoan) factory (dominant in DS1) to a coralgal (photozoan) factory (dominant in DS2). Dart (1991 p.275) also interprets a sequence boundary

between the rhodalgal dominated and coralgal dominated deposits (his GS1 and GS2). He however suggests that his SB2 (figure 8.1) is not marked by a sharp erosive surface, but by a regional up sequence increase in the degree of colonisation by coral knobs, patches and barriers.

Following the sequence boundary, relative sea level subsequently rose and western areas of the Maltese Islands (along the IMF footwall) formed shallow marine environments within which a chlorozoan factory became established to produce the Reef-Core FA (section 5.3.4 and figures 8.2 and 8.3). This FA records an upward-shallowing marine succession and represents transgressive to highstand deposits (section 6.3.3). The FA is observed in western areas of the Maltese Islands in a NNW-SSE oriented facies belt across the Maltese Islands and trends obliquely across the IMF footwall high (Pedley, 1979; Dart, 1991).

The shallow marine Reef-Core FA is replaced eastwards (basinwards) by the deeper marine Fore-reef slope and Shelf FA that consists of the Proximal Reef Slope Packstone (PRS) and Distal Reef Slope Wackestone (DRS) Facies (figures 8.2 and 8.3). The Fore-Reef Slope and Shelf FA occurs immediately eastward of the Reef-Core FA and Sand Shoal FA and forms a NNW-SSE oriented facies belt across the Maltese Islands (section 5.3.5). Pedley (1978) and Dart (1991) suggest that the sediment supply of the PRS, that contains coarse bioclastic and oolitic material, was the Reef-Core FA. Observations made in this thesis suggest that the stratigraphically lower PRS bioclastic sediments may be contemporaneous with and sourced from the Reef-Core FA while the stratigraphically higher PRS oolitic sediments may be contemporaneous with and sourced from the Sand Shoal FA (section 5.3.5 and figure 8.1).

The Sand Shoal FA caps the Reef-Core FA in western areas of both the Malta Horst (MT01, MT16) and Graben (MT22, MT23). This suggests that western areas of Malta were of similar paleodepth and the ENE-WSW VLF and SPIF did not express bathymetric relief significant enough to cause facies partitioning/distribution (section 6.2.6, figure 8.2). This interpretation is consistent with that made by Dart (1991 p.269).

Following the deposition of the Reef-Core FA, marine shallowing continued in western areas and a sharp erosive contact (SB3) was developed that separates the underlying Reef-Core FA from the overlying Sand Shoal FA (section 5.3.6 and figure 8.1). Depositional sequence 2, which consists of the Reef-Core FA and the Fore-Reef Slope and Shelf FA, is thus terminated at SB3. Above SB3, reef growth is abruptly ended and the facies are dominated by cross-bedded packstones and grainstones of the Sand Shoal FA of depositional sequence 3 (section 6.3.4). This interpretation is different from Dart (1991 p.276) who interprets his Coralgal Patch Reef Facies, Sand Shoal Facies and Peritidal Facies as highstand deposits of the same genetic sequence (GS2) (figure 8.1).

Dart (1991) interprets deposits observed in the Ghar Lapsi area (hanging wall sub-basin of the IMF) as constituting a distinct genetic sequence (his GS3) that only is developed in the area. Dart (1991) interprets deposits observed in the Ghar Lapsi area as constituting a distinct genetic sequence (his GS3) that is only developed in the Ghar Lapsi area. Dart (1991 p.276) suggests that in the Il-Maghlaq area the boundary between his GS2 and 3 is a sequence boundary (his SB3). Dart (1991 pp.235-245) proposes that the deposits observed in Ghar Lapsi consist of Platform Facies Association and Slope Facies Association. Dart's (1991) Platform FA consists of Sand Shoal Facies, Inter Sand Shoal Facies and Organ Pipe Porites Reef Facies. In this thesis, the original source material of these facies is observed in western areas of the Maltese Islands and corresponds to the CR Facies (GS2) and Sand Shoal FA (GS3). In view of this, Dart's distinct GS3 for the Ghar Lapsi deposits is questioned. Rather, research from this thesis suggests the deposits observed in Ghar Lapsi are part of DS2 and DS3 and do not constitute a distinct genetic sequence (figure 8.1).

Following the deposition of the Sand Shoal FA, the central Mediterranean region is subject to the Messinian evaporitic drawdown (Hsü, 1973). The Maltese region may have been subaerialy exposed and formed an upland karst plateau for much of its subsequent history (Dart *et al*., 1993). This marks the sequence boundary 4 (SB4) and terminates depositional sequence 3 and the UCL Formation.

8.3.2. Regional or local controls on Late Miocene Mediterranean carbonate platform evolution?

The Mediterranean Miocene carbonates are remarkably similar in terms of their sedimentary units dominated by rhodalgal, coralgal and stromatolitic/oolitic deposits (e.g. Esteban, 1996; Cornée *et al*., 2004). The following section investigates what controls may have caused the occurrence and timing of these grain associations and whether the interpreted cycles of deposition are contemporaneous or not.

8.3.2.A. Contemporaneous

Regional chronostratigraphic correlation is in a state of flux and further chronostratigraphic research is necessary to reduce the temporal uncertainty of the distinct rhodalgal, coralgal and stromatolitic/oolitic deposits (section 6.6). Esteban (1996), Pedley (1996) and Cornée *et al*. (2004) however argue that the sedimentary cycles of rhodalgal, coralgal and stromatolitic/oolitic units across the Mediterranean are contemporaneous. In this thesis it is suggested that the cyclical development of these units is largely contemporaneous (figures 6.6 and 8.4). The notion is supported in view of (i) cycles of greater or lesser reefal diversity across the Mediterranean

during the Miocene (e.g. Pomar, 1996), (ii) monogeneric *Porites* reefs that display aberrant reef growth (BB features) during the Late Miocene (e.g. Esteban, 1996), and (iii) surface A (maximum flooding surface) and B (regional marine planation surface) (Cornée et al., 2004) being the same age in Sorbas and Melilla-Nador and correlatable across various Mediterranean platforms (section 6.4.3 and figure 6.10).

8.3.2.A.1. Regional sea-level change as control

The Esteban (1996), Pedley (1996) and Cornée *et al*. (2004) models propose regional sea-level changes as a key controlling factor to the widespread occurrence of the sedimentary cycles.

Esteban (1996) suggests that Miocene carbonates in the Mediterranean have a marked cyclicity at different orders of magnitude (figure 8.5). On the basis of data available on Miocene platforms, Esteban (1996) presents a hypothesis for the occurrence of cycles in different frequencies of rhodalgal, coralgal and stromatolitic/oolitic units that correspond to a semi-isolated Mediterranean-type seaway scenario that he considers to be valid for 2nd, 3rd and 4th order cycles. The rhodalgal carbonates are interpreted as a transgressive systems tract (TST) of 3rd order depositional sequences (Esteban, 1996). Coral reefs are characteristic of the 3rd order highstand systems tract (HST) and the early lowstand during the 2nd order highstands (Esteban, 1996). Coral reef development was extensive during the climatic optimum of the Chattian-Aquitanian, Langhian and Late Tortonian-Messinian times, which correspond to global 2nd-order highstands or supercycles of relative sea level. The largest stromatolitic mounds and oolitic shoals appear to occur in the late TST and early HST (Esteban, 1996).

Cornée *et al*. (2004) later proposed distance correlations of Late Tortonian–Messinian littoral carbonate complexes from eight platforms in the western and central Mediterranean. Correlations are based on the identification of two major biological sedimentary cycles (C1 a 3rd order cycle and C2 a 4th order cycle), consisting of three main lithological units (T1 + T2 = C1, TC = C2) and of two index surfaces (A and B) (figures 6.10 and 8.5). The lithological units of Cornée *et al*. (2004) corresponds to Esteban's (1996) in the following way; T1 to the rhodalgal unit, T2 to the coralgal units, T3 to the stromatolitic/oolitic unit. Cornée *et al*. (2004, figure 3) also suggest that these deposits are characterised by similar sequential-biological trends through time and interpret T1 retrograding deposits to a TST, T2 prograding units as HST and T3, while difficult to interpret, is attributed to TST/HST. Cornée *et al*. (2004) interpret surface A as a condensation surface and a maximum flooding surface and surface B as a marine planation surface with little erosion. Both the Esteban (1996) and Cornée *et al*. (2004) models thus show some important similarities, particularly with respect to the organisation of sedimentary cycles (rhodalgal, coralgal, TC) and the systems tracts they are interpreted to correspond to (figure 8.5 compare Esteban (1996) and Cornée *et al*., (2004)).

Pedley (1996) also suggests that Late Tortonian-Early Messinian central Mediterranean reef episodes are cyclic and that sequence stratigraphic events represent 3rd – 4th order basinwide

eustatic cycles. Pedley (1996) suggests that continued global regression from late Burdigalian until Tortonian brought drowned platforms back within reach of reefal communities. During Tortonian times, the deeper water coralline algal communities first regained a foothold in these shallowing depths and coral subsequently colonised the later Tortonian times. Pedley (1996) refers to the Maltese carbonate platform where, through the aforementioned regression, the Tortonian deeper water coralline algal communities regained a foothold in the shallowing water depths of *circa* 65 m (Pedley, 1976).

Studies of the Maltese Platform carried out in this thesis and a literature review of other Late Miocene Mediterranean carbonate platforms however show a number of significant departures from the Esteban (1996) and Cornée *et al*. (2004) models. Esteban (1996) and Cornée *et al*. (2004) suggest that the rhodalgal (TST), coralgal (HST) occur in the first 3rd order sea level cycle and the stromatolitic/oolitic (TST/HST) units occur in subsequent 3rd – 4th order relative sea level cycles. This is not the case for the Llucmajor, Nijar, Malta and Las Negras platforms. In the Llucmajor the coralgal unit forms across three 3rd order cycles and in the Nijar platform the coralgal unit forms across one 3rd order cycle (figure 8.5). In the Malta and Las Negras platforms, each unit forms during a distinct 3rd – 4th order cycle (figure 8.5). Consequently, rhodalgal units are not restricted to TST, the coralgal units not restricted to HST and the stromatolite/oolite units not restricted to TST/HST. In the Malta and Las Negras platforms, different grain types form with each successive 3rd – 4th order sea level cycle to form distinct depositional sequences dominated by distinct carbonate factories (figure 8.4).

Esteban (1996) and Cornée *et al*. (2004) also suggest that the surface between the rhodalgal and coralgal units is a maximum flooding surface. In the Maltese succession, the rhodalgal and coralgal units are separated by a sequence boundary (SB2) (figure 8.4). If the lithological units are contemporaneous and correlatable across the Mediterranean, differences between the Malta model and that of Esteban (1996) and in relative sea level curves across the Late Miocene Mediterranean platforms (section 6.6.2), may be the result of local Maltese conditions superposed (imprint of local events) onto broader Mediterranean-wide conditions. Since Malta is stratigraphically isolated and still inadequately dated, it is difficult to tie the SB to other Mediterranean platforms to determine if local (tectonic driven) or regional (eustatic) processes produced the SB (section 6.2 and 6.3). If the SB is local, this implies a local RSL fall of *circa* 30 m. If the SB can be correlated to a wider extent, this would confirm a key departure from the Esteban (1996) and Cornée *et al*. (2004) models. Further research is needed to investigate whether SB2 observed in Malta also occurs between two rhodalgal and coralgal units in other contemporaneous Mediterranean platforms.

Esteban (1996), Pomar (1996) and Cornée *et al*. (2004) propose 3rd and 4th order basinwide

eustatic sea level cycles as key controls to the sedimentary cycles. The same units observed in different Mediterranean carbonate platforms are however affected by distinct RSL curves both in frequency and in amplitude (section 6.6 and figure 8.4). This suggests that processes in addition to/other than RSL cycles may have controlled the cycle of rhodalgal to coralgal to stromatolite/oolite development during the Late Miocene (see section 8.3.2.A.2).

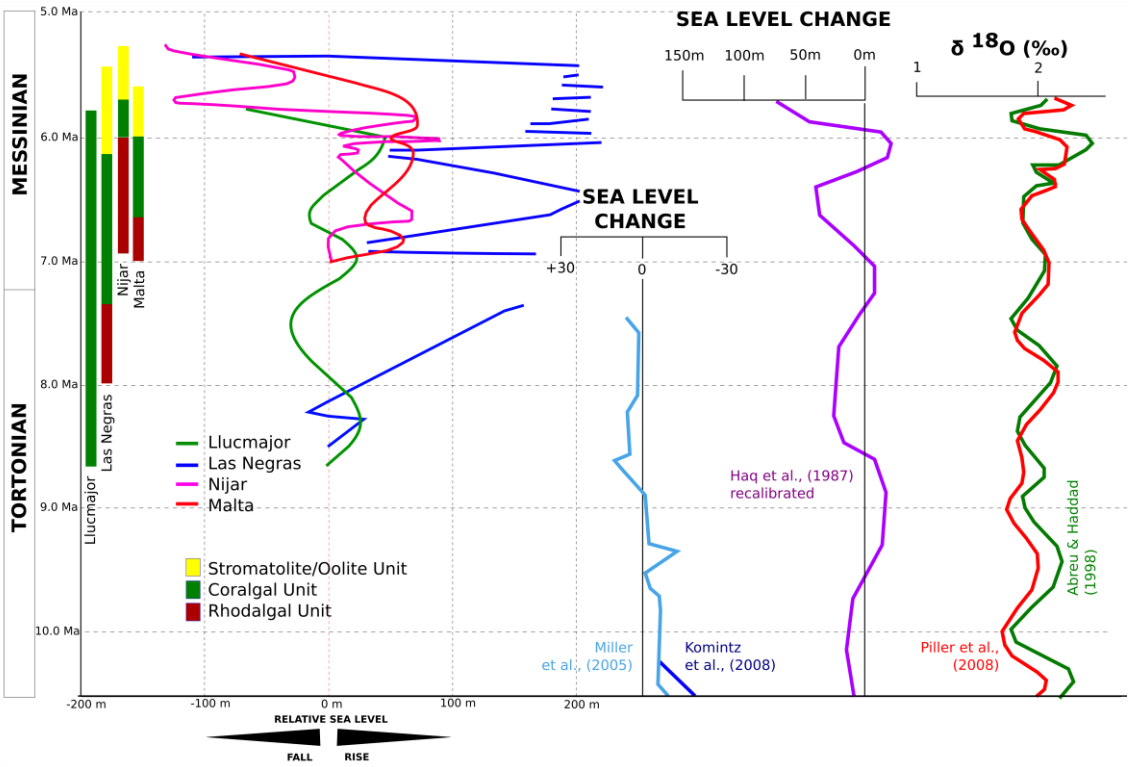

Figure 8.4: Relative sea level curve for the Mediterranean Late Miocene platforms (Llucmajor, Las Negras, Nijar and Malta), temporal occurrence of rhodalgal, coralgal and stromatolite/oolite deposits (section 6.5 and 6.6) and associated eustatic sea level curves. Tzanova *et al.,* (2015) Mediterranean SST Sea Surface Temperature. 3rd order sea level cycle duration range 5 to 0.5 My, 4th order sea level cycle duration range 0.5 to 0.1 My.

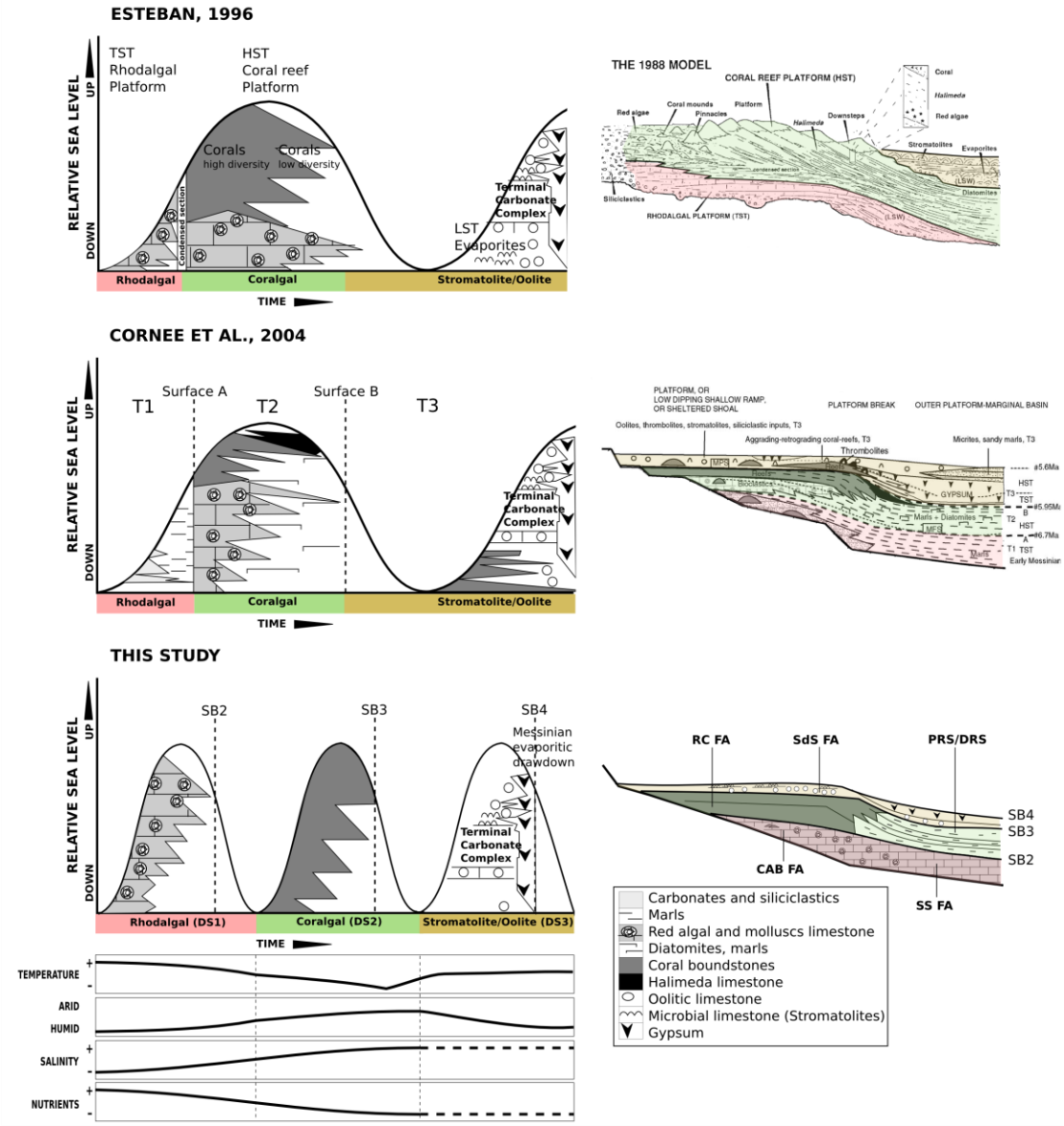

Figure 8.5: Comparison of depositional sequence of Esteban (1996), Cornée *et al*., (2004), and this study with interpretation of controls on rhodalgal, coralgal and oolitic units proposed in this study. 2nd order sea level cycle 50 to 5 My, 3rd order sea level cycle duration range 5 to 0.5 My, 4th order sea level cycle duration range 0.5 to 0.1 My.

8.3.2.A.2. Paleoenvironmental conditions (excluding RSL) as control

While Esteban (1996), Pedley (1996) and Cornée *et al*., (2004) emphasise regional sea level as a key control on the Miocene biological sedimentary cycles, they also acknowledge the influence of region-wide paleoenvironmental changes of seawater. In this thesis it is proposed that changes in climate, water circulation and water chemistry affected the region and gradually altered the local-scale marine conditions (figure 8.5). This in turn controlled the biological-sedimentary organisation (the shift from rhodalgal to coralgal to stromatolite/oolite) of Late Miocene deposits across the Mediterranean such that these are *broadly* contemporaneous.

During the Tortonian, sediment production in the euphotic zone from several Mediterranean carbonate platforms changed from rhodalgal to coralgal (figure 8.4 for platforms, time and carbonate units) (Pomar *et al*., 2012). Esteban (1996) suggests that rhodalgal units correspond to the transition from climatic minimums (glacial periods) towards climatic optimums (de-glaciation) that correspond to pluvial periods in the Mediterranean. This setting would be characterised by decreased salinity and increased nutrient concentration and can be considered as estuarine-type circulation (outflow of surface Mediterranean waters and entry of deep nutrient-rich Atlantic waters). Coral reefs would have developed during interglacial (climatic optimum) periods that tend to evolve into semi-arid or arid climates in the Mediterranean-type settings that would have increased evaporation and salinity and decreases nutrients in the upper water layer.

The suggested shift from glacial periods to later interglacial climatic optima as a control on the shift from rhodalgal to coralgal associations is questioned here in view of the more recent attempts to measure the Late Miocene Mediterranean regional temperatures through A $U^{K'}_{37}$ – derived sea surface temperature (SST), hydrology, floral and faunal studies. These suggest the Mediterranean was subject to long-term global cooling during the Late Miocene (e.g. Zachos *et al.,* 2001; Shevenell *et al.,* 2004; Ivanov *et al.,* 2002; Mudelsee *et al.,* 2014; Jimenez-Moreno *et al.,* 2010; Pound *et al.,* 2011, 2012; Tzanova *et al.,* 2015).

Tzanova *et al.* (2015) propose that the Monte dei Corvi section (Northern Italy) shows extraordinarily warm tropical-like A $U^{K'}_{37}$ – derived sea surface temperature (SST) of ~ 28 °C from 13 to ~ 8 Ma. Mediterranean SST then rapidly cooled beginning at ~ 8 Ma, with an episode of intense cooling to ~ 19 °C between 7.2 and 6.6 Ma. This they argue was followed by a rebound to ~ 25 °C preceding the Messinian Salinity Crisis at 5.9 Ma. SST minima decline in limestone layers which suggests colder and more arid excursions. The pronounced cooling spanning the Tortonian/Messinian boundary coincides with the lowest clay influx to the basin and the absence of sapropels.

Records of SST during the Late Miocene from the Pacific Ocean and the Arabian Sea (Huang *et al.,* 2007; La Riviere *et al.,* 2012) are similar to those observed in the Mediterranean by Tzanova *et al.* (2015). This suggests that the Mediterranean cooling and drying was concurrent to that in the Arabian Sea and Pacific Ocean and points to a large-scale mid-latitude shift in temperatures and aridity. Tzanova *et al.* (2015) suggest that the long-term increase in aridity was likely linked to cooling and a retraction in the latitudinal extent of the Hadley cell. This mechanism links the ocean cooling that Tzanova *et al.* (2015) and others have begun to document with previous evidence for aridification on land (Griffin, 2002; Steinke *et al.,* 2010; Tipple and Pagani, 2010). Thus, the interpreted Late Miocene cooling of the Mediterranean

correlates to the major shift in the European and North African landscape to cooler and dryer, with an increasingly open landscape inhabited by fauna and flora adapted to such conditions (Ivanov *et al*., 2002; Jimenez-Moreno *et al*., 2010; Pound *et al*., 2011, 2012). These floral and faunal changes are interpreted as both a response to cooling and drying during the Tortonian. Additionally, the long-term cooling and increase in aridity of the Tortonian/Messinian boundary is also linked to the appearance of the Sahara desert at ~7 Ma (Schuster *et al*., 2006; Zhang *et al*., 2014).

Under warm tropical-like humid/high rainfall conditions (at least 13 to ~ 8 Ma) (Tzanova *et al.*, 2015), the Mediterranean would have received greater freshwater input, increased terrigenous input, dilution of marine $CaCO_3$, a diminishment in vertical circulation and increased productivity (Schenau *et al*., 1999). This is supported by research by Kohler *et al*. (2008) who investigate the sedimentary archive of Monte Gibliscemi (Sicily). The section provides a Late Miocene record of North African palaeoenvironmental conditions (~9.7 to 7.0 Ma) and disruptions in the Mediterranean–Atlantic connection. Their research shows that North Africa was humid with rivers draining into the central Mediterranean, and fluvial input dominating over aeolian contributions from 9.5 Ma throughout the section (~7.0 Ma). Conversely, a cool arid (~ 8 to 6.6 Ma) Mediterranean region would receive less freshwater input and the dryer conditions would lead to a decrease in terrigenous input and the concentration of marine $CaCO_3$.

In view of the above, it is proposed that the rhodalgal association (DS1) occurred under warm tropical-like humid/high rainfall conditions where large quantities of terrigenous material were delivered in the Mediterranean and nutrient levels increased. The coralgal association (DS2) formed during as climates cooled, conditions became more arid and subsequently nutrient delivery declined. This interpretation is supported by previous research by Halfar & Mutti (2005) who suggest that enhanced tropic resources associated with a global increase in productivity may have triggered the dominance of red algae over coral reefs during Burdigalian-early Tortonian. Wilson & Vecsei (2005) also demonstrate that nutrient-rich marine environments, in humid low-latitude areas subject to high terrestrial runoff and nutrient upwelling, promote oligophotic production (rhodalgal). Brandano & Corda (2002) argue that elevated nutrient levels enhanced oligophotic red algae production in the Middle Miocene Latium-Abruzzi platform. Conversely, a decrease in nutrients may have controlled the shift from the mesotrophic, foramol-rhodalgal deposits into the oligotrophic, chloralgal units during the Tortonian in the Balearic Islands (Pomar *et al*., 2012).

Marine gateways play a critical role in the exchange of water, heat, salt and nutrients between oceans and seas. Consequently, changes in gateway geometry can significantly alter both the pattern of global ocean circulation and associated heat transport and climate, as well as having a

profound impact on local environmental conditions (Flecker *et al*., 2015). During the Messinian, plate tectonic convergence between Africa and Iberia progressively closed these connections (e.g. Duggen *et al*., 2003; Gutscher *et al*., 2002). This tectonic forcing combined with eustatic (e.g. Manzi *et al*., 2013) and climatic (Hilgen *et al*., 2007) factors resulted in a complex history of varied Mediterranean–Atlantic exchange and high amplitude environmental fluctuations in the Mediterranean. The Mediterranean's near-landlocked configuration makes it sensitive to subtle changes in climate (e.g. Thunell *et al*., 1988). Consequently, the first environmental responses to gradual restriction of exchange with the Atlantic recorded in the Mediterranean (e.g. faunal and isotopic changes) predate any evaporite precipitation there by a million years or more. The age of the base of the stromatolitic/oolitic units is similar in age to the SST rebound to ~ 25 °C preceding the Messinian Salinity Crisis at 5.9 Ma (Tzanova *et al.,* 2015) and the onset of the Messinian evaporite deposition inferred from basinal areas of the Mediterranean (Gautier *et al.,* 1994; Krijgsman *et al*., 1999, 2001). The change from chloralgal to stromatolitic/oolitic units, corresponding to the sand shoal FA (TC), may thus be in part the result of surface waters subject to an increase in salinity and temperature.

8.3.2.B. Not contemporaneous

The successive cycles of the three units (Esteban, 1996) and lithological units, sedimentary cycles and index surfaces (Cornée *et al*., 2004) observed in Miocene Mediterranean platforms are interpreted as contemporaneous and correlatable across the Mediterranean (e.g. Esteban, 1996; Cornée *et al*., 2004; this study). Cyclostratigraphic arguments are however flawed with issues of circular reasoning. Additionally, there is limited direct evidence that these units are in fact contemporaneous and there are more scenarios where they are not correlative (section 6.6.2). Differences between the UCL Formation conceptual model, and various other Late Miocene Mediterranean platforms (section 6.6), and that of Esteban (1996) and Cornée *et al*. (2004) may therefore reflect uncertainties in the temporal component. The timing and frequencies (2^{nd}, 3^{rd} and 4^{th} order cycles) of alternating cycles of rhodalgal, coralgal and stromatolitic units are imprecisely determined. The consequence is that similar alternating cycles may be incorrectly correlated to different order cycles (2^{nd}, 3^{rd} and 4^{th}) across the Miocene carbonate platforms in the Mediterranean. This would then incorrectly reinforce the notion that a set of common regional controls act and influence the successive cycles of units observed in Miocene across the Mediterranean. This uncertainty calls into question the evidence for long distance/regional cyclostratigraphic correlations and interpretations of regional or local controls (section 6.6).

In view of these issues and limitation, there still is a need for detailed stratigraphy and chronostratigraphy. This will in turn enable analysis on whether Miocene reef events in the

Mediterranean are contemporaneous or non-contemporaneous and shed light on the possible nature of the controls on the cycle of units.

8.3.3. What may have caused the change in platform geometry from ramp to FTSM in Mediterranean?

Various Upper Miocene platforms record a change in platform geometry from ramp/distally steepened ramp (DRS) to flat top steep margin (FTSM), namely the Llucmajor area, Balearic Islands (e.g. Pomar, 1991, 1993; Pomar & Ward, 1994, 1995; Pomar *et al*., 1996), the Las Negras platform, Southern Spain (e.g. Franseen, 1989; Goldstein *et al*., 1990; Franseen & Mankiewicz, 1991), the Nijar Basin, South Eastern Spain (e.g. Mankiewicz, 1987, 1996; Warrlich, 2000) and the Malta platform (e.g. Pedley, 1974, 1976; Bosence & Pedley, 1982; Dart, 1991; this thesis).

The Late Miocene carbonate platforms occur in a variety of tectonic settings, relative sea level cycles (Appendix D) and substrates (Esteban, 1996). The following section provides a detailed review of these Upper Miocene carbonate complexes in terms of platform types, facies architecture, carbonate factories and external controls on platform evolution (e.g. sea-level fluctuations) (table 8.1). The aim is to assess which of these features may have contributed towards the development of the distinct ramp and FTSM platforms.

Platform	Platform geometry	Age	Carbonate factory	Carbonate depositional texture	Relative sea level curve (see figure 8.4)
Llucmajor	FTSM (Reef Complex Unit) Ramp (*Heterostegina* Calcisiltites Unit)	~8.4 to 6.3Ma ~10.2 to 8.4Ma	Coralgal Rhodalgal	Framestone Packstone to Grainstone	Reef complex relative sea level *megasets of sigmoids* Pomar *et al*., 2012 figure 6
Las Negras	FTSM (DS2 and DS3) Ramp (DS1A and DS1B)	~7.3 to 6.2Ma ~8.5 to 7.3Ma	Coralgal Rhodalgal	Framestone Packstone to Rudstone	Franseen and Goldstein, 1996 figure10
Nijar	FTSM (DS G) Ramp (DS E and DS F)	~6 to 5.7Ma ~6.2 to 6Ma	Coralgal Rhodalgal	Framestone Packstone to Rudstone	Warrlich, 2000 pp.154, 172, 180
Malta	FTSM Ramp	~6.7 to 5.95 Ma ~6.9 to 6.7Ma	Coralgal Rhodalgal	Framestone/ Rudstone Packstone to Rudstone	Chapter 5

Table 8.1: Summary of Late Miocene carbonate platform features. A detailed description and review of the information used to construct the table is available in Appendix D. Information for the age and relative sea level from Llucmajor (Pomar *et al*., 1996; Pomar, 2001; Pomar *et al*., 2012), Las Negras (Franseen & Goldstein, 1996), Nijar (Warrlich, 2000), Malta see chapters 5 and 6.

Carbonate factories

The feature that corresponds to the change in platform geometry (ramp to FTSM), and that is common to Late Miocene platforms assessed, is a change in carbonate factory. The rhodalgal factory and ensuing lithofacies tend to develop ramp and distally steepened ramp platform geometries while the coralgal factory and ensuing lithofacies tend to develop FTSM platforms with reefs and fore-reef slopes with gradients that are up to 45°. A key difference between the ramp and FTSM platforms is therefore the carbonate factory (rhodalgal *versus* coralgal) that dominates sediment production within the carbonate systems.

The rhodalgal and coralgal factories are distinct from one another in three ways: production-depth profiles, sediment production rates, and production of different grain-size types and proportions (with distinct transport rates) (section 3.2.2). The following section draws on research, carried out in this study and in literature, to assess whether these features may contribute to the development of different platform geometries.

The coralgal factory is typified by a euphotic sediment production profile while the rhodalgal factory by an oligophotic production profile. SFM based research (section 3.3.2) however indicates that the distinct platform geometries developed by the rhodalgal and coralgal factories cannot be the result of distinct production-depth profiles. Assuming ideal marine conditions, sediment production by the coralgal factory produces is significantly greater than that of the rhodalgal factory. Sediment production rates of the scleractinian coral factory ranges from 0.35 to 23.00 m ky^{-1} across the depth range producing sediment and sediment production for the coralline red algal factory ranges from 0.10 and 8.30 m ky^{-1} (section 3.2.2). Numerical SFM-based research has demonstrated that the platform margins of carbonate platforms subject to higher sediment production rates steepen faster than those subject to lower sediment production rates (e.g. Williams *et al*., 2011; chapter 3 and 6-MS2). This assumes sediment transport rates are equal between carbonate systems. The rhodalgal factory produces fine-to-coarse bioclastic grains while the coralgal factory build rigid organic buildups/frameworks (section 3.2.2). Numerical SFM-based research (e.g. Williams *et al*., 2011; chapter 3 and 6-MS3) has demonstrated that carbonate platforms that are dominated by fine-grained sediment production form transport-dominated systems and develop ramp geometries. Conversely, carbonate platform that are dominated by framework and coarse-grained sediment production are deposition-dominated systems and develop FTSM platforms.

The coralgal factory therefore has a significantly higher sediment production rate, in a shallower depth range and produces a larger proportion of coarse grains (characterised by a lower-transport rate) than the rhodalgal factory. SFM-based investigations have shown that the combination of high sediment production rates and low transport rates (higher PR to TR ratio) for the coralgal factory tends to favour the development of FTSM platforms (section 3.3.1).

Conversely, the relatively low sediment production rates over a greater depth range and high transport rates (higher TR to PR ratio) of the rhodalgal factory favours the formation of ramp and distally steepened ramp (section 3.3.1). In view of this, the shift from ramp/DSM to FTSM platform observed in the Late Miocene carbonate platforms is attributed to a change (from rhodalgal to coralgal) in carbonate factories.

Other ways same stratal patterns could occur

There may be other possible controls on the shift in carbonate factories. Model behaviour show that changes in sediment production and/or transport rates are not required to develop the change in platform geometry (section 7.4.2.1). The rates of sediment accumulation relative to the amplitude and frequency of oscillations in sea level also influence platform geometry (e.g. Williams *et al*., 2011; section 7.4.2.1). The amplitude of RSL oscillations determines whether carbonate production is focused in a limited area thereby allowing accumulation and steepening or spread over a large area thereby prevent accumulation and steepening. The shift in platform geometry from ramp (DS1) to FTSM (DS2) may also be the product of particular sea level oscillations (section 7.4.2 MS1.1 and 1.3). Field data suggest that RSL curves are broadly the similar in amplitude and frequency for DS1 (rhodalgal dominated) and DS2 (coralgal dominated). Additionally no evidence of high amplitude RSL was observed from field data for DS1 and DS2, for example though several well-developed subaerial exposure surfaces. This suggests that RSL did not influence the platform geometry. The uncertainty in RSL curve across the Late Miocene (sections 6.6 and 7.4.2.1) does however open arguments that RSL may also have influenced the evolution of Late Miocene platform geometry. Further investigation is necessary to that end.

8.4. Quantitative methods

8.4.1. Can SFM accurately simulate the facies architecture of naturel carbonate systems?

Carbonate facies architectures have characteristically been poorly represented in SFM studies that seek to simulate real platforms. This is since facies architectures are either not considered (e.g. Bosence & Waltham, 1990), or are inferred on the basis of depth, hydraulic energy, the *in situ* or transported nature of grains (e.g. Bosence *et al*., 1994; Warrlich *et al*., 2008; Borgomano *et al*., 2014). Boylan *et al*. (2002) later introduces a new scheme that enables forward models to output simulated facies defined by a range of values for each of the controlling processes and thereby predicts rock texture within simulated stratigraphies. The types of grain texture and compositions simulated are the result of the sedimentary processes that the SedTec 2000 SFM program simulates (Boylan *et al*. 2002).

In all the above cases, synthetic facies are not defined by the nature of the grains accumulated in a unit area in the numerical model. While these approaches can simulate large-scale platform

architecture (e.g. stacking patterns), these shortcomings have limited the use of SFM simulation of real facies architecture and in adequately answering questions that conventional sedimentological analyses have difficulty answering.

Williams *et al.* (2011) simulate a simplified representation of various carbonate factory aspects different proportions. Consequently, the simulated facies architectures and stratal geometries might not be characteristic of the more complex/real carbonate factories and depositional systems that the SFM initially sought to represent. A method was developed and applied in this study (sections 4.2.2 and 7.3.1) that better adjusts the simulated sediment production to that produced in natural carbonate system. Through the method, a high match between simulated and real facies was achieved for the Llucmajor (section 4.3.1) and Malta (section 7.3.2) conceptual models. The study thus shows that SFMs can accurately simulate facies architecture of natural carbonate systems.

8.4.2. Can the application of quantitative techniques improve our understanding of platform evolution?

Paola (2000) notes that when quantitative techniques '*allow us to ask sharper questions, make our hypotheses less ambiguous and hence easier to test, rules out some apparently plausible explanations and suggests new ones that would never have occurred to our unaided intuition*'. Several authors have applied certain aims of these quantitative techniques in their investigations of platform dynamics (e.g. Bosence & Waltham, 1990; Warrlich, 2000; Burgess and Prince, 2015). This study presents and applies a step-by-step quantitative method that builds on Paola's (2000) described potential application of quantitative techniques (section 7.1.1).

The application of the method developed various similar features between outcrop observations of the Maltese UCL Formation and SFM simulations (section 7.3.2). While this result does not *prove* the conceptual model and the interpretation/hypothesis are correct, it does indicate that the conceptual model and associated interpretation/hypothesis are physically reasonable.

The study also investigates whether the simulation of other scenarios, with distinct process rates, can develop similar features to those seen in outcrop (section 7.4.2). The scenarios investigated include variable rate of accommodation space generation, variable sediment production and transport rates, and reduced model run time. A comparison of these scenarios to the outcropping platform indicates which non-unique scenarios are not possible or plausible in terms of the real carbonate system (section 7.4.2). Simulations of distinct relative sea level curves indicates that in the absence of a well-defined sea level cycle (frequency/amplitude and total duration), a variety of relative sea level curves can plausibly explain the features observed in outcrop. These results show that various non-unique scenarios are plausible in terms of the real carbonate system. The results help direct further research on platform evolution and

substantiate a need for quantitative methods based on constructing and evaluating multiple hypotheses and scenarios.

8.5. Fundamental contributions

The following briefly highlights the key contributions the thesis has made towards the fields of numerical SFM and carbonate geology (particlarly Late Miocene carbonates in the Mediterranean).

Quantitative SFM-based results show that it is the sediment production and transport (PR/TR) ratio, not the absolute values of each parameter, that influence platform geometry. Carbonate factories strongly influence the PR/TR ratio through their control on (i) sediment production rate (PR) and (ii) the quantity and type of grain-sizes produced which in turn influences transport rate (TR). The PR/TR ratio is a new, simple and useful way of considering the spectrum of carbonate platform geometries.

Models simulating distinct sediment production and transport rates, but that have similar PR/TR ratios, develop similar platform features. These results demonstrate that the simulation of distinct rates for key processes (sediment production and diffusional transport) can develop similar non-unique platform features. Issues of non-uniqueness in SFM might also occur in natural systems. This emphasises the need for a shift towards constructing and quantitatively evaluating multiple, rather than single, hypotheses and scenarios when investigating the controls on platform evolution.

Conceptual models developed by Esteban (1996), Pedley (1996) and Cornée et al. (2004) suggest regional sea-level changes are the key controlling factor to the widespread occurrence of Late Miocene Mediterranean sedimentary cycles. In this study, it is proposed that changes in climate, water circulation and water chemistry affected the region and gradually altered the local-scale marine conditions. This in turn controlled the biological-sedimentary organisation (the shift from rhodalgal to coralgal to stromatolite/oolite) of Late Miocene deposits across the Mediterranean such that these are broadly contemporaneous.

Lastly, this study presents and applies a novel step-by-step quantitative method that integrates forward modelling with outcrop observations and enables the strengthening or rejecting of conceptual models, the investigating of alternative hypothesis and issues of non-uniqueness. The quantitaive method may replace qualitative conceptual methods and models. Such a shift would improve our understanding of platform evolution, facies distribtions and may help direct and refine further research on platform evolution.

APPENDIX A

	Depth (m)		*In situ* sediment production						
			g $CaCO_3$ m^2 y^{-1}			m ky^{-1}			
	Range		Avg.	Range		Avg.	Range		Location, Time	Depositional environment	*Species*
SCLERACTINIAN CORAL FACTORY											
Bosscher & Schlager, 1992	0	0				9.87	6.81	13.06	Carribean, Present		*Montastrea annularis*
Bosscher & Schlager, 1992	5	5				9.31	5.82	12.37	Carribean, Present		*Montastrea annularis*
Bosscher & Schlager, 1992	10	10				8.48	5.84	11.12	Carribean, Present		*Montastrea annularis*
Bosscher & Schlager, 1992	15	15				6.39	3.48	8.62	Carribean, Present		*Montastrea annularis*
Bosscher & Schlager, 1992	20	20				1.95	1.07	2.60	Carribean, Present		*Montastrea annularis*
Bosscher &	2	25				1.90	1.67	2.55	Carribean, Present		*Montastrea*

Schlager, 1992	5								*annularis*
Bosscher & Schlager, 1992	30	30		1.60	1.11	2.09	Carribean, Present		*Montastrea annularis*
Bosscher & Schlager, 1992	35	35		1.11	1.11	1.11	Carribean, Present		*Montastrea annularis*
Bosscher & Schlager, 1992	49	40		1.11	1.11	1.11	Carribean, Present		*Montastrea annularis*
Bosscher & Schlager, 1992	45	45		0.80	0.80	0.80	Carribean, Present		*Montastrea annularis*
Shinn *et al.,* 1989		6				8.20	Florida, Present	Inshore	*Montastrea annularis*
Shinn *et al.,* 1989		6				6.30	Florida, Present	Offshore	*Montastrea annularis*
Shinn *et al.,* 1989		3				11.20	Florida Present	Platform margin	*Montastrea annularis*
Weber & White, 1977	0	20				5.80	Key West, Florida, Present		*Montastrea annularis*
Hutson, 1985	0	5				6.00	Florida, Present		*Montastrea annularis*
Baker & Wever, 1975		9				10.40	Virgin Islands, Present		*Montastrea annularis*
Baker and Wever,		14				9.60	Virgin Islands, Present		*Montastrea*

1975						*annularis*
Gladfelter *et al.,* 1978		10		7.60	Virgin Islands, Present	Forereef	*Montastrea annularis*
Huston, 1985		5		7.40	Jamaica, Present		*Montastrea annularis*
Dustan, 1979		45		1.60	Jamaica, Present		*Montastrea annularis*
Huston, 1985	6	15		7.80	Curacao, Present		*Montastrea annularis*
Weber & White, 1977	0	20		12.00	Belize, Present		*Montastrea annularis*
Shinn *et al.,* 1989	0	20		5.00	Pleistocene, Florida, Present Pleistocene, Florida, Present		*Montastrea annularis*
Huston, 1985		10		3.60	Jamaica, Present		*Montastrea cavernosa*
Huston, 1985		20		6.80	Jamaica, Present		*Montastrea cavernosa*
Huston, 1985		30		4.10	Jamaica, Present		*Montastrea cavernosa*
Weber & White, 1977	0	20		4.10	Key West, Florida, Present		*Montastrea cavernosa*

Ghiold & Enos, 1982	0	20	1180 0	2.20	6.60	5.70	Florida, Present	*Diploria labyrinthiformis*
Landon, 1975	0	20				17.00	Florida, Present	*Porites porites*
Landon, 1975	0	20				10.50	Pleistocene, Florida, Present	*Porites porites*
Ghiold & Enos, 1982	0	20				23.00	Florida & Bahamas, Present	*Porites furcata*
Huston, 1985		0				5.00	Jamaica, Present	*Porites asteroides*
Huston, 1985		5				5.00	Jamaica, Present	*Porites asteroides*
Huston, 1985		10				3.30	Jamaica, Present	*Porites asteroides*
Huston, 1985		30				2.30	Jamaica, Present	*Porites asteroides*
Gladfelter *et al.,* 1978		5				3.40	Virgin Islands, Present	*Porites asteroides*
Gladfelter *et al.,* 1978		10				3.00	Virgin Islands, Present	*Porites asteroides*
Ghiold & Enos, 1982	0	20				4.30	Florida, Present	*Porites asteroides*
Ghiold & Enos, 1982	0	20				13.00	Florida, Bahamas, Present	*Porites asteroides*
Huston, 1985	0	5				13.50	Enewetak, Present	*Porites lutea*
Huston, 1985	6	15				11.00	Enewetak, Present	*Porites lutea*
Huston, 1985	1	25				9.50	Enewetak, Present	*Porites lutea*

Huston, 1985	6	25				6.00	Enewetak, Present		*Porites lutea*
Huston, 1985	6	15				11.50	Enewetak, Present		*Porites lobata*
Huston, 1985	16	25				6.00	Enewetak, Present		*Porites lobata*
Kinsey, 1978	0	5		4600	3.39		One Tree Island, Present	Reef-flat coral zone	
Kinsey, 1978	0	5		2700	1.99		Lizard Island, Present	Seaward pinnacle	
Kinsey, 1978	0	5		2400	1.77		Lizard Island, Present	Seaward reef flat - algal pavement	
Kinsey, 1978	0	5		4600	3.39		Lizard Island, Present	Seaward reef flat	
Kinsey, 1978	0	5		3100	2.29		Lizard Island, Present	Lagoon reef flat	
Kinsey, 1978	0	5		3100	2.29		Lizard Island, Present	Lagoonal reef-flat	
Kinsey, 1978	0	5		1700	1.25		Lizard Island, Present	Lagoonal reef-flat - small heads	
Kinsey, 1978	0	5		8800	6.49		Kaneohe Bay, Present	Coral	
Kinsey, 1978	0	5		4400	3.25		Johnston Island, Present	Pavement coral / algal	
Kinsey, 1978	0	5		9600	7.08		Johnston Island, Present	Back-reef	
Kinsey, 1978	0	5		6400	4.72		Johnston Island, Present	Lagoon	
Kinsey, 1978	0	5		1400	1.03		Johnston Island, Present	Lagoon, reticulated reefs	
Stearn *et al.,* 1977	0	20	9000		6.64		Carribean, Belize Reef,	Reef	

									Present	
Smith & Kinsey, 1978	20	50				1.70			Carribean, Holocene	Reef
Smith, 1981	0	20	12000			8.86			Houtman Abrolhos Islands, W. Australia, Present	Abrolhos reefs
Hart & Kench, 2007	0	4	1660			1.23			Warraber Island, Torrest Strait, Present	0-4m deep intertidal reef flat
Hart & Kench, 2007	5	15				2.25		6.34	Warraber Island, Torrest Strait, Present	Outer reef flat
Hart & Kench, 2007	0	10				0.35		0.56	Warraber Island, Torrest Strait, Present	Reef rim
Hart & Kench, 2007	0	20	1394	767	2021	1.03	0.57	1.49	Warraber reef flat, Torrest Strait, Present	
Hart & Kench, 2007	0	20	19242	10818	27666	14.20	7.98	20.42	Warraber reef flat, Torrest Strait, Present	*Acropora*
Hart & Kench, 2007	0	20	16160	7680	24640	11.93	5.67	18.18	Warraber reef flat, Torrest Strait, Present	
Hart & Kench, 2007	0	20	17000	3000	31000	12.55	2.21	22.88	Warraber reef flat, Torrest Strait,h Present	
Yamano *et al.,* 2000	5	30	1600			1.18			Green Island, Great Barrier Reef, Present	Reef flat and slope
Smith & Kinsey,	1	3	4000			2.95			Mode of Several, Pacific	1-3m deep, seaward

1978						reefs, Present	reef flat	
Odum & Odum, 1955	0	5	3050		22.50	Japan Inter-Island Reef, Eniwetok, Present	Inter-Island reef flat	
Harney, 2000	0	3	3180		2.35	Kailua Bay, Hawaii, Present	Fringing reef with large sand bodies and diverse benthic community	
Kinsey, 1981	0	3	4700		3.47	Kaneohe Bay, Hawaii, Present	Shallow (<3m) reef flat	
Kinsey, 1981	0	3	4400	8000	3.25	5.90	Discovery bay, Jamaica, Present	Shallow (<3m) reef flat	*Acropora palmata reef*
Stearn *et al.,* 1977	0	5	1500		11.00	Bellaris Reef, Barbados, Present	5m deep fringing reef	
Sadd, 1984	2	60	1900		1.40	Cane Bay, St. Croix, Virgin Islands, Present	Fringing reef, including hard ground, reef flat and shelf	
Hubbard *et al.,* 1990	0	40	1210		0.61	Cane Bay, St. Croix, Virgin Islands, Present	Fringing reef, including hard ground, reef flat and shelf	
Hughes, 1987	0	20	1616		10.1	Present	Massive coral	

			0			0				
Hughes, 1987	0	20	17000			8.50		Present	Foliaceous, mushroom and encrusting ramose	*Acropora*
Scoffin *et al.,* 1980	0	10	9000			6.64		Barbados, present	Reef	
Kinsey, 1985	0	10	10000			7.38		Present	Very shallow, submerged fore-reefs and reef patches	
Vecsei, 2001	0	10		10000	17300		7.38	12.77	Caribbean, Present	Framework reefs dominated by ramose corals
Vecsei, 2001	10	20		4500	8100		3.32	5.98	Caribbean, Present	
Vecsei, 2001	20	30	3000			2.21			Caribbean, Present	
Vecsei, 2001	30	40		800	3000		0.59	2.21	Caribbean, Present	
Vecsei, 2001	0	10		5000	6700		3.69	4.94	Indian Ocean islands and GBR, Present	Fore-reefs
Vecsei, 2001	0	10		8600	9800		6.35	7.23	Indian Ocean islands and GBR, Present	Fore-reefs

Vecsei, 2001	0	10		9200	16400		6.79	12.10	Pacific Ocen islands, Present	Fore-reef	
Smith, 1981	0	10	11700			8.63			Houtman Abrolhs Islands, Present	Reef	*Acroporan* dominated reef
Grigg, 1982	0	10	15000			11.07			Southern Hawaii Chain, Pacific, Present	Shallow reef	
Glynn & Macintyre, 1977; Glynn *et al.,* 1979	0	10	5000			3.69			Panama and Galapagos Islands, Present	Shallow fore-reef	
Gischler & Hudson, 2004	0	20				3.25	0.87	6.59	Belize Barrier Reef, Carribean, Pleistocene	Shallow water, Reef margin	*Montastraea annularis*
Macintyre et al. 1977	0	10				12.00			Alcaran, Mexico, Holocene (8.9-7ky)	Shallow-water coral reefs	Zooxanthellate scleractinian corals
Macintyre et al. 1977	0	10				6.00			Alcaran, Mexico (Holoence 6.0-5ky)	Shallow-water coral reefs	Zooxanthellate scleractinian corals
Macintyre & Glynn, 1976	0	10				3.90			Galeta Point, Panama, Present	Shallow-water coral reefs	Zooxanthellate scleractinian corals
Shinn *et al.,* 1982	0	10				6.00			Belize, Caribbean, Present	Shallow-water coral reefs	Zooxanthellate scleractinian corals
Macintyre & Glynn, 1976	0	10				5.00			Panama, Caribbean, Present	Shallow-water coral reefs	Zooxanthellate scleractinian corals
Fairbanks, 1989	0	10				13.0			Barbados, Holocene (8.8-	Shallow-water	Zooxanthellate

Adey *et al.,* 1977	0	10	0 15.2 0	7ky) St. Croix, Holocene (9.4-5ky)	coral reefs Shallow-water coral reefs	scleractinian corals Zooxanthellate scleractinian corals
Adey *et al.,* 1977	0	10	6.00	St. Croix, Holocene (9.4-5ky)	Shallow-water coral reefs	Zooxanthellate scleractinian corals
Adey, 1978	0	10	10.0 0	St. Croix, Holocene (9.4-6ky)	Shallow-water coral reefs	Zooxanthellate scleractinian corals
Shinn *et al.,* 1981	0	10	4.85	Florida, Present	Shallow-water coral reefs	Zooxanthellate scleractinian corals
Shinn *et al.,* 1981	0	10	1.30	Florida, lagoon, Present	Shallow-water coral reefs	Zooxanthellate scleractinian corals
Lighty *et al.,* 1978	0	10	6.50	Florida Bay, Present	Shallow-water coral reefs	Zooxanthellate scleractinian corals
Davies *et al.,* 1985	0	10	8.00	Central GBR, Holocene (7-5ky)	Shallow-water coral reefs	Zooxanthellate scleractinian corals
Gray *et al.,* 1992	0	10	2.20	Cook Islands, Holocene (9-1ky)	Shallow-water coral reefs	Zooxanthellate scleractinian corals
Eisenhauer *et al.,* 1993	0	10	7.57	Houtman Abrolhos Aqaba, Holocene (9.8-6.5ky)	Shallow-water coral reefs	Zooxanthellate scleractinian corals
Dullo, 2005	0	10	1.69	Aqaba, Holcene (2.8-2.0ky)	Shallow-water coral reefs	Zooxanthellate scleractinian corals
Dullo, 2005	0	10	1.60	Sanganeb, Holocene (9.6-	Shallow-water	Zooxanthellate

Dullo, 2005	0	10		6.00	0ky)	coral reefs	scleractinian corals
Dullo, 2005	0	10		2.82	Sanganeb, Holocene (9.6-5.5ky)	Shallow-water coral reefs	Zooxanthellate scleractinian corals
Dullo, 2005	0	10		8.57	Mayotte, Holocene (9.8-2ky)	Shallow-water coral reefs	Zooxanthellate scleractinian corals
Dullo, 2005	0	10		1.70	Mayotte, Holocene (9.6-7.2ky)	Shallow-water coral reefs	Zooxanthellate scleractinian corals
Camoin *et al.,* 1977	0	10		4.44	Reunion, Holocene (8-1ky)	Shallow-water coral reefs	Zooxanthellate scleractinian corals
Camoin *et al.,* 1977	0	10		4.41	Reunion, Holocene (7.4-6.9ky)	Shallow-water coral reefs	Zooxanthellate scleractinian corals
Collins *et al.,* 1983	0	20		3.30	Indo-Pacific average, Present	Shallow-water coral reefs	Zooxanthellate scleractinian corals
Collins *et al.,* 1983	0	20		10.20	Houtman Abrolhos reef, W. Australia, Holocene		
Collins *et al.,* 1983	0	20		6.00	Houtman Abrolhos reef, W. Australia, Holocene		
Adey, 1978	0	20		10.00	Houtman Abrolhos reef, W. Australia, Holocene		
Smith, 1983	5	25		3.00	Carribean, Holocene	Reefs	
					Holocene	Reef margin	

BIODETRITAL CORAL FACTORY										
Vecsei, 2001	0	20	1500			1.11			Caribbean, Present	Biodetrital reefs (BR)
Vecsei, 2001	20	40	100			0.07			Caribbean, Present	Biodetrital reefs (BR)
Sadd, 1984	0	10		1200	3200		0.89	2.36	St. Croix, Cane Bay, Present	Biodetrital reefs
Hubbard *et al.,* 1990	0	10	5800			4.28			St. Croix, Cane Bay, Present	Biodetrital reefs
Hubbard *et al.,* 1990	20	40	100			0.07			St. Croix, Cane Bay, Present	Biodetrital reefs
CALCAREOUS GREEN ALGEA										
Hart & Kench, 2007	0	10		400	1667		0.30	1.23	Warraber, Australia, Present	Reef flat, green algae	*Halimeda* (Green alga)
Wefer, 1980	0	5	50			0.04			Bermuda, Present	Shallow lagoon	*Halimeda incrassata*
Multer, 1988	0	10		114	760		0.08	0.56	Antigua, Present	Barrier reef	*Halimeda incrassata*

Multer, 1988	0	10		62	413		0.05	0.30	Antigua, Present	Fringing lagoon	*and Halimeda monile Halimeda incrassata*
Multer, 1988	0	10		61	406		0.05	0.30	Antigua, Present	Open lagoon	*and Halimeda monile Halimeda incrassata*
Hudson, 1985	0	5	108			0.08			Florida, Present	Lagoon	*and Halimeda monile Halimeda opuntia*
Chave *et al.,* 1972; Bosence *et al.,* 1985	0	30	400			0.30				Shallow-waver	
Hart & Kench, 2007	0	10	1066	400	1667	0.79	0.30	1.23	Warraber reef flat, Torrest Strait, Present		
MOLLUSC, BRYOZOAN & FORAMINIFERAL FACTORY											
Langer *et al.,* 1997	0	5	70.33			0.05			Asiatic, Present	Reef	Reef Foraminifera, various
Langer *et al.,* 1997	0	5	70.34			0.05			Indian, Present	Reef	Reef Foraminifera, various
Langer *et al.,* 1997	0	5	70.26			0.05			South Pacific, Present	Reef	Reef Foraminifera, various

Langer *et al.,* 1997	0	5	70.26			0.05			North Pacific, Present	Reef	Reef Foraminifera, various
Langer *et al.,* 1997	0	5	70.35			0.05			Caribbean, Present	Reef	Reef Foraminifera, various
Langer *et al.,* 1997	0	5	70.31			0.05			North Atlantic, Present	Reef	Reef Foraminifera, various
Langer *et al.,* 1997	0	5	70.37			0.05			Red Sea, Present	Reef	Reef Foraminifera, various
Langer *et al.,* 1997	0	5	70.00			0.05			Persian Gulf, Present	Reef	Reef Foraminifera, various
Langer *et al.,* 1997	0	5	56.25			0.04			South Atlantic, Present	Reef	Reef Foraminifera, various
Yamano *et al.,* 2000	0	10		210.0	480.0		0.15	0.35	Green Island, Great Barrier reef, Present	Reef flat	*Amphistegina* dominated
Tudhope & Scoffin, 1988	0	50	40.0			0.03			North GBR, Holocene	Continental shelf	*Amphistegina* dominated
Hallock, 1981	0	10		187.0	2762.0		0.14	2.04	Caroline Islands, Present	Reef flat	*Amphistegina* dominated
Hallock, 1981	10	30		57.0	568.0		0.04	0.42	Caroline Islands, Present	Reef slope	*Amphistegina* dominated
Hallock, 1981	5	30		38.0	145.0		0.03	0.11	Hawaii, Present	Reef flat and slope	*Amphistegina* dominated

Muller, 1974	0			305.0	512.0		0.23	0.38	Hawaii, Present	Rock pool	*Amphistegina* dominated
Muller, 1976	5	15	263.0			0.19			Hawaii, Present	Nearshore	*Amphistegina* dominated
Sakai & Nishihira, 1981	0	5		500.0	700.0		0.37	0.52	Japan, Present	Shallow tidal pool	*Baculogypsina shpaerulata*
Hallock *et al.,* 1986	0	5		60.0	100.0		0.04	0.07	Florida, Present	Shallow lagoon	*Archaias angulatus*
Richard, 1981	0	10	4.8			0.00			French Polynesia, Present	Reef	Molluscs
Richard, 1981	0	10	0.2			0.00			French Polynesia, Present	Reef	Molluscs
Hart & Kench, 2007	0	10	100.0	10.0	200.0	0.07	0.00	0.15	Warraber Island, Torrest Strait, Present		Molluscs
Bosence, 1989	0	40		0.3	1.8		0.00	0.00	Upper Cross Bank & Buchanan Keys, Florida Bay, Present	Shallow water, bank and lake environment	
Smith & Nelson, 1994	0	10		90.0	400.0	0.22	0.04	0.40	New Zealand, Present		
Masse & Masse, 2006	0	10		19.0	200.0	0.10	0.03	0.40	Marseille, France, Present		
Richard, 1982; 1985	0	30	20.0			0.01			French Polynesia, Present	Atoll lagoons	*Tridacna maxima*
Richard, 1982;	0	30	30.0			0.02			French Polynesia, Present	Atoll lagoons	*Chama iostoma*

1985										
Richard, 1982; 1985	0	30	200.0			0.15			French Polynesia, Present	Atoll lagoons
Moore, 1972	0	30	8.0			0.01			Florida Bay, Present	Shallow water - Intertidal
Moore, 1972	0	40	309.0			0.23				Shallow water – Sub-tidal
Hart & Kench, 2007	0	10	120.0	30.0	230.0	0.09	0.02	0.17	Warraber, Torrest Strait, Present	Reef flat
Hart & Kench, 2007	0	10	100.0	10.0	200.0	0.07	0.01	0.15	Warraber, Torrest Strait, Present	Reef flat
LAGOON ENVIRONMENT (sediment production from mollusk & bryozoan and calcareous green algal factories)										
Bosence, 1989	0	20				0.40	0.30	0.50	Florida Keys, Present	Back Reef
Bosence, 1989	0	30				0.20	0.01	0.40	Florida Keys, Present	Lagoonal

Smith & Kinsey, 1976	0	20				0.60				Lagoonal	
Hubbard *et al.,* 1990	0	10				0.73			St. Croix, Holcene (6-3ky)	Lagoon or shallow-water coral reefs	Zooxanthellate scleractinian corals
Kinsey, 1978	0	5			1500.0			1.11	One Tree Island, Present	Lagoon: reticulum	
Kinsey, 1978	0	5			500.0			0.37	One Tree Island, Present	Lagoon: open	
Kinsey, 1978	0	5			300.0			0.22	Lizard Island, Present	Lagoonal reef-flat - sand alagl flat	
Kinsey, 1978	0	5			120.0			0.09	Kaneohe Bay, Present	Sand-flat	
Smith & Kinsey, 1976	5	6	800.0			0.59			Mode of Several, Pacific reefs, Present	Protected 5-6m deep lagoon/bank	
SEAGRASSES (corallines; benthic foraminifer; bryozoans; spirorbids; bivalves factories)											
James *et al.,* 2009	0	10	210.0	49.0	661.0	0.07	0.02	0.24	Southern continental margin of Australia,	Seagrass epiphytes *	

									Present	
									Southern continental	
			254.		402.	0.19	0.07	0.30	margin of Australia,	Seagrass epiphytes
James *et al.,* 2009	0	5	0	99.0	0				Present	*
									Southern continental	
			187.		295.	0.14	0.07	0.22	margin of Australia,	Seagrass epiphytes
James *et al.,* 2009	5	10	0	98.0	0				Present	*
										Shallow water
										bank, epiphyte
						0.09	0.02	0.62		
Nelsen & Ginsburg,			118.		846.				Tavernier Key, Florida	production on
1986	0	5	0	30.0	0				Reef tract, Preset	seagrass
Frankovitch &			119.		282.					
Zeiman, 1994	0	10	0	1.9	0	0.09	0.00	0.21	Florida Bay	Seagrass epiphytes
									Florida Bay, Upper Cross	
			281.		1042	0.21	0.04	0.77	Bank + Buchanan Keys,	Epiphytes on
Bosence, 1989	0	10	0	55.0	.0				Present	*Thalassia*
			180.							Inshore, Seagrass
Land, 1970	0	10	0			0.13			Jamaica, Present	epiphytes
Gostin *et al.,* 1984;										
Burne & Colwell,										
1982	0	10					0.20	2.70	Quaternary	Seagrass epiphytes
James, 1997	0	20					0.10	1.00		Seagrass epiphytes

Perry & Beavington-Penney, 2005	0	5		33.4	43.9		0.02	0.03	Inhaca Island, Mozambique, Present	Seagrass epiphytes	*Hydrolithon farinosum, Thalassodendron ciliatum, Thalassia hemprichii*
Gacia *et al.,* 2003	0	10	133.7	91.5	735.6	0.10	0.07	0.54	SE Asia, Present	Seagrass epiphytes	
Frankovitch & Zieman, 1994	0	10	119.0	1.9	282.0	0.09	0.00	0.21	Florida Bay, Present	Seagrass epiphytes	
CORALLINE RED ALGAE											
Kinsey, 1978	0	5			4000.0			2.95	One Tree Island, Present	Algal pavement	
Kinsey, 1978	0	5			300.0			0.22	Kaneohe Bay, Present	Algal-flat	
Hart & Kench, 2007	0	10	1872.0	1500.0	2500.0	1.38	1.11	1.85	Warraber, Torrest Strait	Reef flat	
Bosence & Wilson, 2003	0	30					0.10	1.00	NW Spain, Present	Maerl, ocean facing coastal waters	
Bosence & Wilson, 2003	0	30		30.0	250.0		0.10	1.00	W Ireland, Present	Maerl, ocean facing coastal waters	

Bosence & Wilson, 2003	0	30		895.0	1423.0		0.80	1.00	Norway, Present	Maerl, ocean facing coastal waters	
Bosence & Wilson, 2003	0	30	876.0			0.65			NW France, Present	Maerl, ocean facing coastal waters	
Bosence & Wilson, 2003	0	30				0.08			Orkney, NE Scotland, Present	Maerl, ocean facing coastal waters	
Bosence & Wilson, 2003	0	30				0.50			Cornwall, SW England, Present	Maerl, ocean facing coastal waters	
Bosence & Wilson, 2003	0	30				1.40			Norway, Present	Maerl, ocean facing coastal waters	
Adey & McKibbin, 1970	5	6				0.11			Ria de Vigo, NW Spain, Present		*Lithothamnion corallioides*
Adey & McKibbin, 1970	5	6				0.49			Ria de Vigo, NW Spain, Present		*Phymatolithon calcareum*
Bosence, 1976; 1980	0	10		29.0	164.0		0.02	0.12	Mannin Bay, Ireland, Present	Open marine, shallow waters < 10m	*Lithothamnion corallioides*
Bosence, 1976; 1980	0	10		79.0	249.0		0.06	0.18	Mannin Bay, Ireland, Present	Open marine, shallow waters < 10m	*Phymatolithon calcareum*
Bosence, 1976		3				0.50			St Mawes Bank, Falmouth, Present		

Fazakerley & Guiry, 1998	0	30		895.0	1432.0		0.66	1.06	Norway, Present	*L. glaciale*
Fazakerley & Guiry, 1998	0	5				1.00			Connemara, western Ireland, Present	Very shallow, well lit water
Potin *et al.,* 1990	0	30	879.0			0.65			France, Present	*L. corallioidies*
Bosence *et al.,* 1985	0	30		100.0	900.0	0.58	0.50	0.66	Florida, Present	*S. Strictum*
Payri, 1997	0	30		20.0	50.0		0.01	0.04	Tahiti, Present	*H. reinboldii*
Payri, 1997	0	30		120.0	175.0		0.09	0.13	Tahiti, Present	*H. oncoides*
Bosence, 1976; 1980	0	30				0.58	0.50	0.65	Falmouth, Present	
Farrow *et al.,* 1984	0	30				0.20	0.08		Orkney, Present	Maerl
Freiwald & Henrich, 1994	7	18		895.0	1423.0	1.15	0.80	1.50	Norway, Present	Maerl *Lithothamnium cf.glaciale*
Bosence, 1985	0	30				0.65			Forida, Travernier Key, Present	Maerl
Harlfar *et al.,* 2001	0	30					0.25	0.45	Newfoundland, Canada, Present	*Lithothamnium glaciale*
Freiwald, 1998	0	30						1.40	Raised beach Kvalo, Islands off Norway, Present	

Freiwald, 1998	0	30					0.80	1.00	Tromso, Islands off Norway, Present	
Ballesteros, 1994	0	30		123.0	181.0		0.09	0.13	W Mediterranean , Present	*Peyssonnelia rosamarina*
Chisholm, 2000	0	30		1500.0	1030 0.0		1.11	7.60	Lizard Island, Australia, Present	Windward reef	*Hyrolithon spp. and Neogoniolithon spp.*
Benzoni *et al.,* 2011	0	30				8.30			NW cost Gulf of Aden, Yemen, Present		*Hydrolithon rupestre and H. murakoshii*
Pichon, 1985; Payri, 2000	0	30	7400 .0			5.46			Rangiroa, Polynesia, Present	CCA - dominated reef flat	*Porolithon onkodes*
El Haikali *et al.,* 2004	0	1	5037 .0			3.72			Marseille, NW Mediterranean, Present		*Corallina elongata*
Kinsey, 1985	0	1	4000 .0			2.95			One Tree Island, Australia, Present	Surf zone	*Coralline pavement*
Martin *et al.,* 2006	0	10		145.0	3100 .0		0.11	2.29	Bay of Brest, France, Present		*Lithothamnion corallioides*
Stearn *et al.,* 1977	0	30	2378 .0			1.75			Barbados, Present	Fringing reef	*Porolithon*
Stearn *et al.,* 1977	0	30	1225 .0			0.90			Barbados, Present		*Neogoniolithon*
Stearn *et al.,* 1977	0	30	1355 .0			1.00			Barbados, Present		*Lithophyllum*

Stearn *et al.,* 1977	0	30	167.0			0.12			Barbados, Present		*Mesophyllum*
Agegian *et al.,* 1988	4 0	100	2100.0			1.55			Penguin Bank, Hawaii, Present		*Porolithon onkodes*
Matsuda, 1989	0	10	2044.0			1.51			Ishigaki Is, Ryukyu Island, Present	Upper fore reef	*Hydrolithon onkodes*
Freiwald & Henrich, 1994		7		895.0	1432.0		0.66	1.06	Troms, Norway, Present		*Lithothamnion cf. glaciale*
Freiwald & Henrich, 1994		18		420.0	630.0		0.31	0.46	Troms, Norway, Present		*Lithothamnion cf. glaciale*
Potin *et al.,* 1990	0	10	876.0			0.65			Bay of Brest, Brittany, France, Present	Maerl occurring at LWST	*Lithothamnion corallioides*
Walker & Woelkerling, 1988	0	30	500.0			0.37			Shark Bay, W Australia, Present		*Epiphyte corallines on seagrass*
Bosence, 1980	0	30		88.0	165.0		0.06	0.12	Galway, Ireland, Present	Maerl	*Lithothamnion corallioides*
Bosence, 1980	0	30		79.0	422.0		0.06	0.31	Galway, Ireland, Present		*Phymatolithon calcareum*
Edyvean & Ford, 1987	0	30	379.0			0.28			SW Wales, UK, Present	Intertidal pools	*Lithophyllum incrustans*
Hart & Kench, 2007	0	10	299.0			0.22			Warraber Island, Australia, Present	Reef flat	*Crustose coralline algae*

Martin & Gattuso, 2009		25	292.0			0.22			NW Mediterranean, Present	25m aquarium simulation	*Lithophyllum cabiochae*
Canals & Ballesteros, 1997	0	10	289.0			0.21			Mallorca-Menorca shelf, NW Mediterranean, Present		*Neogoniolithon brassicaflorida (as Spongites notarisii) and geniculate*
Bosence, 1980; Bosence & Wilson, 2003	0	10		29.0	164.0	0.14	0.02	0.12	Mannin Bay, NE Atlantic, Present	Maerl from the Bank and Muddy Algal Gravel facies	*Lithothamnion corallioides*
Bosence, 1980; Bosence & Wilson, 2003	0	10		79.0	249.0	0.25	0.06	0.18	Mannin Bay, NE Atlantic, Present	Maerl from the Bank and Muddy Algal Gravel facies	*Phymatolithon calcareum*
Canals & Ballesteros, 1997	0	85	210.0			0.15			Mallorca-Menorca shelf, NW Mediterranean, Present	Maerl	*Several coralline species*
Eakin, 1996	0	10	190.0			0.14			Uva Island, Panama, Present	Reef flat	*Crustose coralline algae*
James *et al.,* 2009	0	10		79.0	164.0		0.06	0.12	Southern Australia, Present		*Epiphyte corallines on seagrass*
Canals & Ballesteros, 1997	0	90	170.0			0.13			Mallorca-Menorca shelf, NW Mediterranean, Present	Coralligenous build-ups	*Several coralline species*
Savini *et al.,* 2012		47	91.0			0.07			Cilento shelf, W Mediterranean, Present	Maerl	*Lithothamnion corallioides*

Canals & Ballesteros, 1997	0	35	68.0			0.05			Mallorca-Menorca shelf, NW Mediterranean, Present	*Epiphyte corallines on seagrass*
Bracchi & Basso, 2012	40	70	32.0			0.02			Pontian Islands shelf, W Mediterranean, Present	*Lithothamnion spp. and lithophylloids*
Bracchi & Basso, 2012	70	100	8.0			0.01			Pontian Islands shelf, W Mediterranean, Present	*Lithothamnion spp. and lithophylloids*
Matsuda & Iryu, 2011	50	130				0.10			Okinawa-jima, Ryukyu Islands, Japan, Present	Deep fore-reef to shelf
Tsuji, 1993	0	30					0.01	0.03	Miyako-jima, Present (?)	
Reid & Macintyre, 1988	0	30					0.01	0.09	Caribbean, Present (?)	
Martin *et al.,* 2006	0	10		150.0	3000.0		0.11	2.21	Bay of Brest, W Brittany, France, Present	*Lithothamnion corallioides*
Bosence, 1980	0	30		30.0	160.0		0.02	0.12	Mannin bay, Ireland, Present	*Lithothamnion corallioides*
Edyvean & Ford, 1987	0	30	380.0			0.28				*Lithophyllum incrustans*
Potin *et al.,* 1990	0	30	880.0			0.65				*Lithothamnion corallioides*
Bosence & Wilson, 2003	0	30		200.0	1200.0		0.15	0.89		*Lithothamnion corallioides*
Chisholm, 2000;	0	30		100.0	1000		0.07	7.38		

Payri, 2000				0.0						
Adey & Vassar, 1975	0	10		1560.0	8112.0		1.00	5.20	Virgin Islands, Present	Algal ridge and reef
Matsuda, 1989	0	10		1560.0	1872.0		1.00	1.20	Japan, Present	Upper fore-reef and reef crest
Stearn *et al.,* 1977	0	10		167.0	2378.0		0.10	1.50	Barbados, Present	Fore reef
Eakin, 1992	0	10	1872.0			1.90			Panama, Present	Reef flat
PLANKTONIC FORAMINIFERA										
Scholle *et al.,* 1983	6 0	200				0.10	0.01	0.20		
Ku & Broecker, 1965		>200					0.00 1	0.002	Arctic, past 150,000 years	Deep sea *Foraminifera*
Cita *et al.,* 1978		>200					0.03	0.09	Mediterranean, onset of the Messinian salinity crisis	Deep sea
Cita *et al.,* 1978		>200				0.06	0.00 1	0.30	Mediterranean, Pliocene/Pleistocene	Deep sea

Figure A.1: Sediment production rates for scleractinian and biodetrital coral, calcareous green algae, coralline red algae and mollusc & bryozoan carbonate factories from various literature sources. Where production rates (g $CaCO_3$ m^2 yr^{-1}) are provided and production rates (m yr^{-1}) are not, the latter have been calculated following the method applied by Bosence and Waltham (1990) (assuming 100% cover). The calculated sediment production (m yr^{-1}) values are distinguished by being underlined. Underlined values in the depth zone columns indicate approximate depth zone dependent on literature descriptions. Accumulation rates (m yr^{-1}) are provided for ancient carbonate factories. Both accumulation rates (m yr^{-1}) and sediment production rates (g $CaCO^3$ m^2 yr^{-1}) are provided for modern carbonate factories.

APPENDIX B

Platform name & Type, Location, Time of formation, Literature	**- Cementation** **- *In situ versus* Transported**	**Depositional environment, Depth, Light conditions, Nutrient environment**	**Calcareous associations (*sensu* Lees & Buller, 1972)**	**Sediment textural classes** (Dunham, 1964 and Embry ad Klovan, 1971) M mudstone; W wackestone; P packstone; G grainstone; R rudstone; Fl floatstone; Fr framestone	**Slope (in degrees)**
Kenter, 1990			Grainy mud-free cohesionless fabrics Grain supported sediment fabric with mud matrix Mud supported fabric Pure mud	G & R P & G W M	30 – 40 (maximum slope angles) 12 – 20 <15 <5 (under 5)
Brione Mountain, Trento Region, S	Difference between facies 1 and 2. Differences in texture	Platform (horizontally bedded platform)	Shell fragments, echinoid spines, Small	P (fine sand Facies 3)	0 – 5

Alps - Platform to slope - Oligocene - Bosellini, 1989	cannot explain the differences in inclination. The significant difference is in bedding pattern_ alternating grainy and muddy layers. The angle of repose of the muddy layers between the packstone and grainstone layers could have been the controlling factor (Eberli, 1988). This cannot be confirmed due to pressure solution.	Slope deposits Slope deposits	& Large Benthic Forams (S&LBF) Oyster fragments, coralline algae, echinoid spines, LBF Shell fragments, coralline algae, echinoid spines, S&LBF	 Skeletal P & G (coarse and Facies 1) P (fine-medium sand Facies 2)	 15 – 17 12 – 17 (20 - 25)
Saraceno Mountain, Apulia platform, Gargano Promontory - Toe of slope to basin - Eocene - Bosellini & Neri, 1999	No mention of early cementation	Reef Slope deposits Slope deposits Toe of slope & Basin deposits	Corals, coral fragments, coralline algae, echinoid spines, S&LBF Shell fragments, echinoid spines, S&LBF Shell fragments, echinoid spines, S&LBF Shell fragments, echinoid spines, S&LBF	*In situ* corals, coral P - Fr Skeletal P & G Skeletal P & R Foraminifer P	 10-15 10-15 0 – 10

Gorbea Platform - Gorbea platform succession accumulated in the Basque–Cantabrian Basin, eastern Pyrenees, during the Late Aptian to Early Albian - Evolved consecutively from a mixed carbonate-siliciclastic ramp into a carbonate ramp and finally into a rimmed platform - Gómez-Pérez *et al.,*., 1999	These bioherms were created by automicrite precipitation, a certain degree of frame binding, and early cementation on the slope.	Upper slope Mid slope Downslope Downslope Note: Depositional depth has been estimated to be in the range of 20 m down to 120m (Gómez-Pérez *et al.,*., 1999).	Rudists, algae, and Chondrodonta skeletal boundstone and floatstone Massively bedded coral boundstone, with lenses of skeletal grainstone and packstone Massive slope clinobeds change into calcareous sponge (chaetetid) wackestone and boundstone, locally with meter- to decameter-scale coral–rudist bioherms Marl and marly limestone at the toe of slope. Thin-bedded, fine-grained bioclastic marl and marly	B & Fr M & W	< 35 (depositional dips) 12 – 1 (depositional dip decreases from)

			limestone interbedded with locally graded skeletal floatstone, and packstone		
Sella Mountain, Dolomites, Italy - Middle Triassic - Kenter, 1990	Consist of non-cohesive rudstones and grainstones alternating with in-situ precipitated micritic carbonate layers. The slope inclination there is about 35'. Keim & Schlager (1999) proposed that the angle of repose of these alternations is determined by the non-cohesive layers and that the stiff in-situ precipitation of micritic layers of automicrite break up and slide before they can significantly change the slope gradient.	*Slope (upper two-thirds)*		G & R	*35*
Djebel Bou Dahar, High Atlas,	Non-cohesive rudstones and grainstones	Upper slope		G & R	26 – 29

Morocco - Lower Jurassic - Kenter & Campbell, 1991					
Belize - Quaternary - James & Ginsburg, 1979	???	Reef talus		G & R	35 – 45
Tongue of the Ocean, Bahamas - Quaternary - Grammer *et al.,*., 1993	Cementation of the talus slope in the Tongue of the Ocean (Grammer *et al.,*., 1993), and steep carbonate slopes elsewhere have been interpreted to be established by early cementation. Re cementation (Gischler & Hudson, 2003) The degree of reef consolidation is negatively correlated with Holocene thicknesses, indicating that	Reef talus		G & R	35 – 46

	slowly growing reefs are better cemented than fast growing ones.				
Migjorn Ramp, Mallorca, Spain - DSR - Lower Tortonian - Pomar, 2001	No mention of early cementation DSR represents accumulation of loose grains of foramol-rhodalgal associations produced in the euphotic and oligophotic zone.	Inner ramp Basinwards of Middle ramp (break of slope) Ramp slope (toe of slope)	Echinoid fragments, bivalves, gastropods Red algal fragments, echinoids, bryozoan, molluscs & rhodoliths Echinoid spines, plankton, SBF	P Fl & R (P & G matrix) W & P	5 (to 10) (individual units 10-20cm thick) 15-20 (large scale clinoforms) <5 (basinwards dipping beds)
Llucmajor Platform, Mallorca, Spain - RRP - Upper Tortonian-Lower Messinian - Pomar *et al.,*., 1996; Pomar *et al.,*., 2012	No mention of early cementation Un-cemented, fine-grained sediments shed off the reef and lagoon accumulated to form a fore-reef depositional slope. The scarcity of talus deposits at the toe of the slope indicates low rates of	Reef wall Proximal reef slope Distal reef slope	Massive corals, coral fragments, red algae, forams, bryozoans, molluscs Mollusc, rhodolites, red algal biostromes, *Halimeda*	Fr P – R W & P	>45 10 – 30 (dipping clinobeds) 5 – 10 (dipping clinobeds)

	sediment export from the platform top. Abundance of submarine cement is another common feature on many of these platform margins, and its origin is still poorly understood.				
Ermenek Platform, S Turkey - LAR (late Burdigalian) - DSR (lower Langhian) - RRP (middle Langhian) - Pomar *et al.,*., 2012	No mention of early cementation	LAR- no additional data RRP- Reef wall	Echinoderm fragments, bivalves & oysters Coral, red algae, coral debris, foraminifers & bivalves	No data R, B & Fr	5 – 10 >45
Ragusa Ramp, SE Sicily - DSR	Massive, well-cemented, coral-bearing mudstones and wackestones compose the	DSR- Ramp slope (toe of slope) FTP- Ramp slope (toe	Small foraminifer Small foraminifer	W & P W & P	3 5

(Serravallian) - FTP (Tortonian) - Pomar *et al.,*., 2012	innermost part of the lower Tortonian ramp, overlying an erosion surface on the rhodalgal lithofacies of the Serravallian ramp	of slope)			
Nijar Basin, SE Spain - Miocene - Warrlich *et al.,*., 2005; Warrlich *et al.,*., 2008	No mention of early cementation	Reef core Proximal slope Distal slope Proximal facies Low energy, sub-wavebase	*Porites* Reef core Fossiliferous Packstone Fine Wackestone & Packstone Packstone Wackestone	Fr & R P W & P P W	<40 (*) 10-30 (*) 8 – 10 (*) <16 (*) <14 (*) * *Interpreted as depositional slope*
Melilla Basin, NE Morocco - Upper Miocene - Cunningham & Collins, 2002	Lithofacies that comprises the ramp is a widespread, poorly cemented, bryozoan-red algal packstone and grainstone	- Platform margin	Bryozoans, red algae, bivalves & foraminifers Bivalve grainstone	P & G (minor W), medium sand - pebble G, medium sand – pebble	>16 (large scale accretion slopes with basinward dips up to 16°) <25 (very large-scale, prograding oblique-tangential clinoforms)
Nijar Basin, SE Spain - Miocene	Syndepositional alteration (micro- and macro-boring) and cementation, fabric-	Low energy marine environment	Planktonic foraminifers	W & P, Md (fine sand)	<10 (bedding that consistently dips 10° or less to SE)

- DSR - RRP - Mankiewicz, 1996	selective dissolution of predominantly aragonitic components, dolomitization, and calcite cementation modified original mineralogy, fabric and porosity. The coral *Porites* and associated micritic coatings constructed the reef framework. Most of the rigidity of the framework may have resulted from the	- - - - - -	Mollusks, serpulids, benthic foraminifers, bryozoans, echinoids (all transported) Mollusks, serpulids, benthic foraminifers, echinoids (all transported) Planktonic & SBF *(isopachous calcite cement)* Rhodoliths, molluscs, *Porites*, bryozoan (all transported) *(isopachous calcite cement)* *Porites* reef *in situ (dolomite cement)*	P P & G (medium – coarse sand) P P & G Fr	10 – 20 <10 (beds dip 10° or less to SE) <12 10 – 25 (within each wedge, dips of beds decrease basinwards from 25° to 12° forming clinoforms) 20 – 30

	thick micritic crusts that coat *Porites* sticks. Volumetrically, the micritic crusts can be more important that the *Porites* (Mankiewicz, 1996 pp147-149). Entire section shows evidence of dolomitization, but most prevalent in the reef facies. [Note Dan S.: good detail about how such cementing form in "*health"* conditions in modern reefs. Might lead to saying that cementation is predominant in reefal systems and therefore slope angle is also commonly influenced by similar type cementation].				
Las Negras, SE Spain - Miocene		Shallow-water ramp		W & P P & G	<10 (primary dips less than 10°)

- DSR - RRP - Franseen & Goldstein, 1996	Early encrusters such as red algae, serpulid worms, foraminifera and bryozoans enhanced framework rigidity of *Porites*. Fibrous marine cements and micritic coatings.	*In situ* Reef core and reef talus	Red algae (abundant) Porites	P & G, coarse sand Fr	<10 – >35 (primary dips range from less than 10° to more than 35°) <12 (primary dips less than 12°) 35
Livornesi Mountains, Tuscany, Central Italy - Messinian - RRP - Bossio *et al.,*., 1996	No mention of early cementation	Off-reef talus-slope	*Halimeda*, mollusc, red algae, bryozoans, with rare planktonic forams and *Porites*	P & G	<25 (dips up to 25°)
Ofaqim, Pattish Fort, Israel - Middle to Upper Miocene - RRP	Dolomitized rhodoliths	Shelf-edge -	Calcareous claystone with occasional beds of skeletal debris Dolomitized rhodolith grainstone and	M & claystone P & G & Claystone	<10 (gentle dips up to 10° to the N) 20 (steeply dipping 20° clinoforms)

- Buchbinder, 1996		-	packstone alternating with calcareous claystoanes Echinoderm grainstones	G	10 – 15 (steeply inclined clinoforms)
Wadi Sharm el Bahari, Red Sea - Miocene - FTP - Purser & Plaziat, 1998	No mention of early cementation	Off-reef	Bioclastic packstone with scattered coral detritus interbedded in terrigenous marine slope deposits	P	<25 (reefs dip progressively up to 25° towards SE)
Sharm el Luli, NW Red Sea - Miocene - RRP - Purser & Plaziat, 1998	No mention of early cementation	Reef core Pre-reef	R1_ Massive coral colonies forming coral wackestone to floatstone deposit. Mixed siliciclastic-carbonate sands and conglomerates	W – Fl Sand	10 (top of reef is inclined at about 10°) 20 (reef front is an inclined surface 20°) 10 (dips are inclined at about 10° to the NE)
Abu Shaar Complex, Gulf of Suez, Egypt - Miocene	No mention of early cementation? Carbonates are entirely dolomite. Calcite and other	Reef	2 to 4m thick “reef veneer” that extends from the basal for reef to the reef crest at the top	Fr	35 – 40 (unit dips 35-40° from the platform margin)

- RRP - Coniglio *et al.,*., 1990	cements are ubiquitous although are of minor importance, all postdate dolomitization. Timing of dolomitization; recrystallisation hypothesis, first stage of dolomitization could have reslted from gradual restriction of the platform, possibly during Mid to Late Miocene.	Reef and fore-reef	of the wedge and then as intermittent biostromes and patch reefs Prograding reef and fore-reef complex. The upper, more massive par is mostly a Framestone composed of *Porites*	G & Fr	25 – 30 (bedding is obvious and dips S at 25-30°)
Middle Triassic carbonate platforms in the Western Dolomites (Southern Alps, Italy) - Maurer and Rettori, 2002	Cementation: most limestone fragments occurring on the flanks of the Duerrnstein carbonate platform were lithified by marine cementation and organic framebuilding However, the abundance of breccias in the slope deposits suggests that these sediments	Middle slope (G) Lower slope (M&W)			30 5

	were rich in coarse-grained material. This assumption could also explain the high angle of repose, which is typical for grainy, non-cohesive, virtually mud-free sediments (Kenter, 1990).				

Figure B.1: Gradients and sediment textural class (Dunham, 1964; Embry Klovan, 1971) in outcropping carbonate slopes.

Note: Literature descriptions of the Miocene Zug al Bohar, Pre-reef facies and late Miocene Mellila, NE Rif, Morocco carbonate systems suggest that the platforms may have been influenced by tectonic movements. Recorded slope gradients for these platforms may not be representative of their original slope inclinations and may therefore be imprecise. These values have been marked with a distinguishing [*] symbol in the appendix. Literature descriptions for other reviewed platforms do not indicate that tectonic processes influenced the recorded slope inclinations. Differential compaction may also alter initial slope gradient. The assessed literature however does no mention compaction processes. The assessed outcrops are also fairly homogeneous in texture. Adams et al. (2012) suggest that when this is the case, the effect of differential compaction is probably negligible. However, the homogeneity necessary for the effects of differential compaction to be negligible is not known.

APPENDIX C

Appendix C1: outcrop logs and water borehole logs

C1.1. Outcrop logs

In the course of the study 48 sedimentary logs were measured at outcrop and recorded in a standard format. These represent the better-developed and thicker depositional sequences within the study area. The studied outcrops were also selected to ensure, as far as possible, an even high-density distribution of outcrop data (figure 5.1). All logs are referenced to 0 m at the top of the Blue Clay Formation that is the most widely distributed and recognisable horizon (figure 5.3). The Greensand Formation is only locally present and was not studied in detail in outcrop.

Textures

M Mudstone
W Wackestone
F Floatstone
P Packstone
G Grainstone
R Rudstone
Fr Framestone

Facies

Peloids
Ooids
Halimeda
Domal corals
Head like corals
Wavy and platey corals
Corals
Bioturbation
Foraminifers
Gastropods (Mollusc)
Serpulids
Echinoderm
Bivalves (Mollusc)
Brachiopods
Bryozoans
Lithophaga
Terebratula
Heterostegina
Rhodoliths
Crustose pavemet
Millimeter coralline algal crust
Coralline algal debris

Sedimentary structures

Normal bedding
Planar lamination
Wavy lamination
Cross-Stratification
Cross-Bedding
Erosional channels and scours
Large-scale clinoform
Sharp bed contact
Gradual bed contact
Sharp erosional bed contact
Limestone

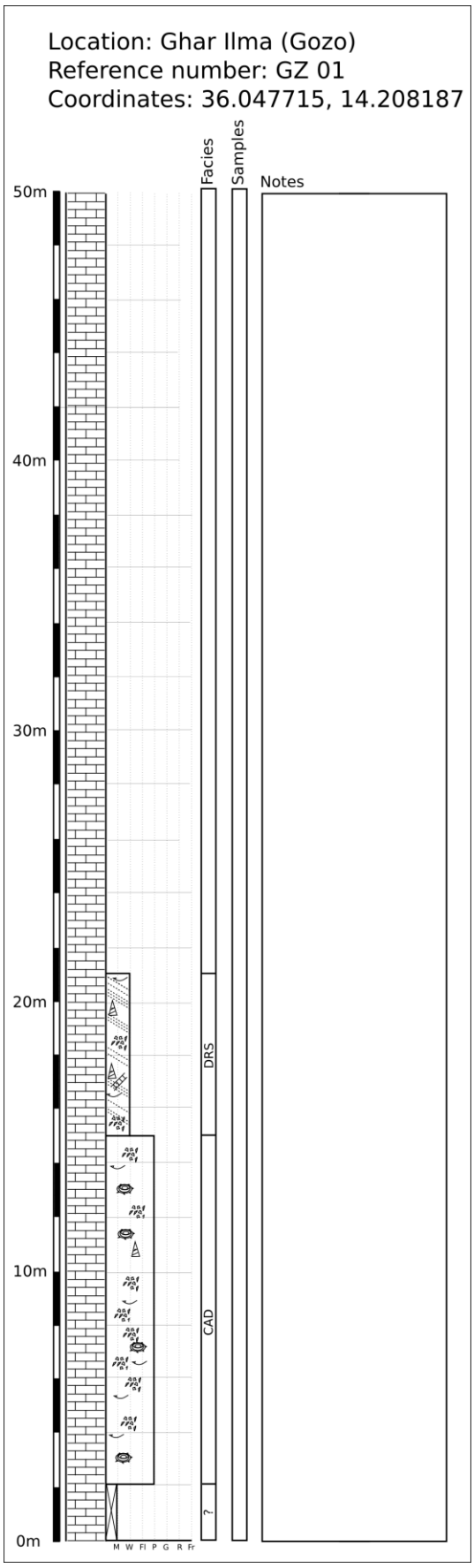
Location: Ghar Ilma (Gozo)
Reference number: GZ 01
Coordinates: 36.047715, 14.208187
Facies
Samples
Notes
50m
40m
30m
20m
10m
0m
DRS
CAD
?
M W Fl P G R Fr

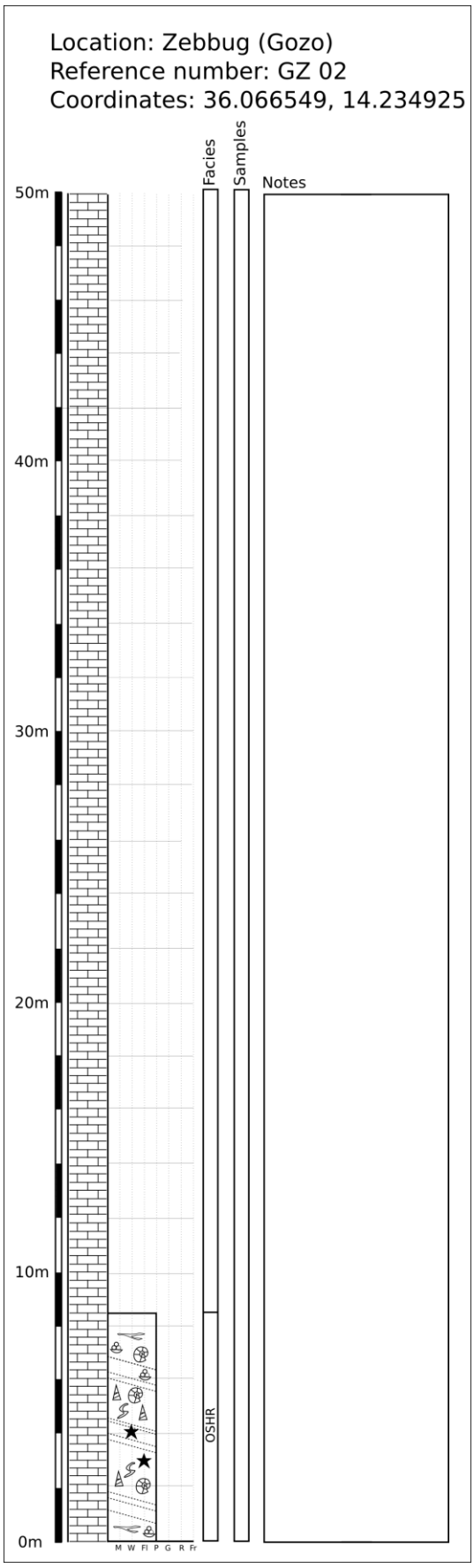
Location: Zebbug (Gozo)
Reference number: GZ 02
Coordinates: 36.066549, 14.234925
Facies
Samples
Notes
50m
40m
30m
20m
10m
0m
OSHR
M W Fl P G R Fr

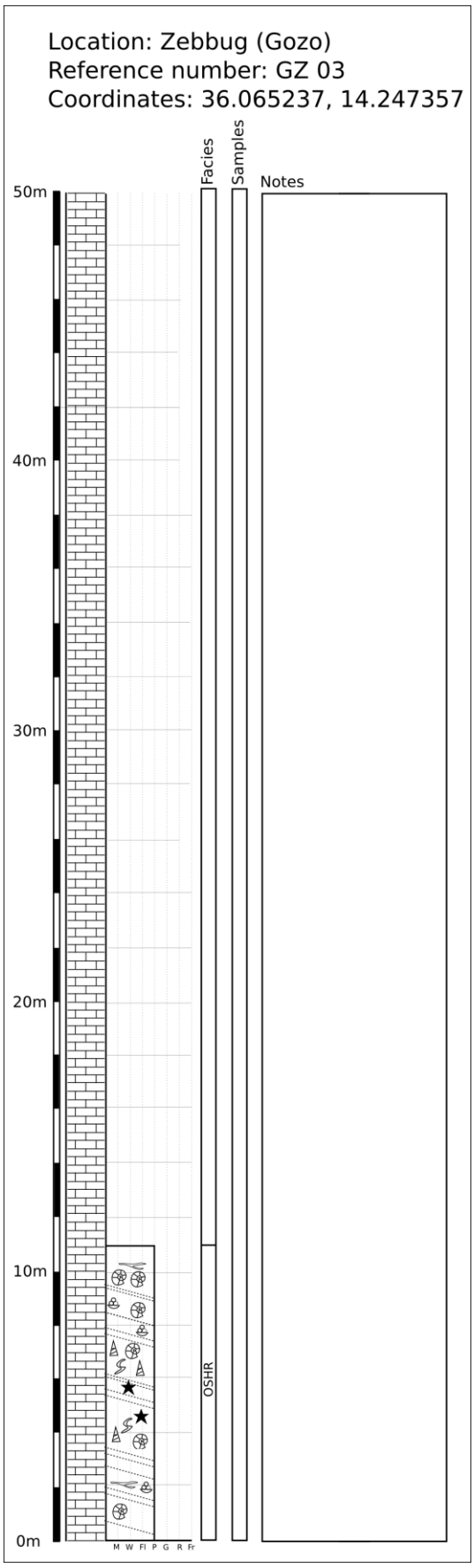
Location: Zebbug (Gozo)
Reference number: GZ 03
Coordinates: 36.065237, 14.247357
Facies
Samples
Notes
50m
40m
30m
20m
10m
0m
OSHR
M W Fl P G R Fr

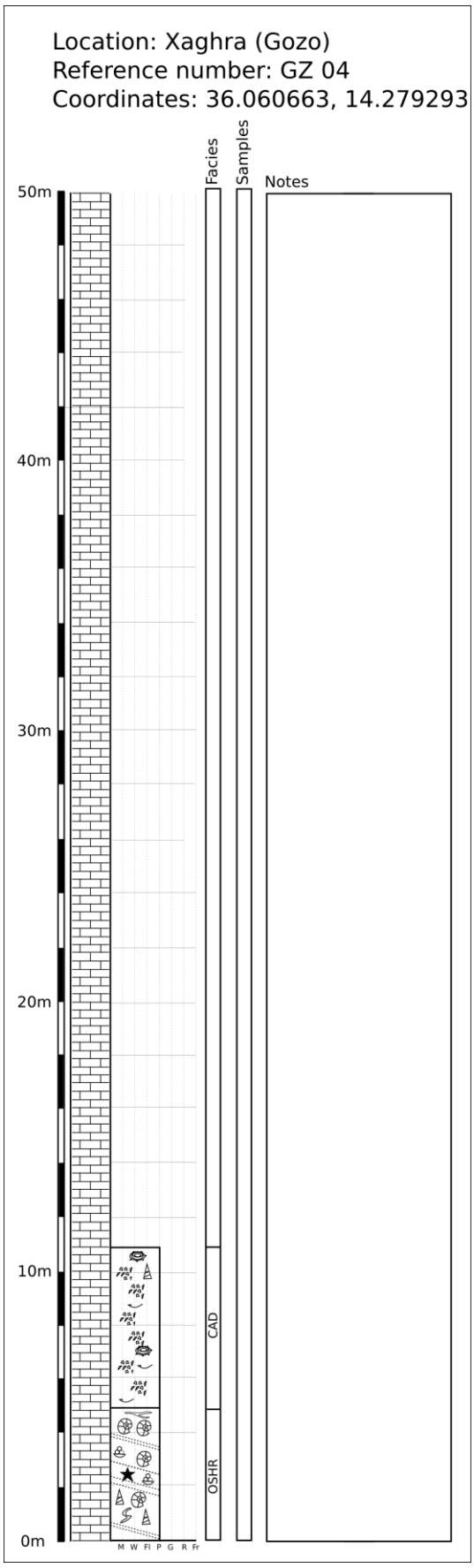
Location: Xaghra (Gozo)
Reference number: GZ 04
Coordinates: 36.060663, 14.279293
Facies
Samples
Notes
50m
40m
30m
20m
10m
0m
CAD
OSHR
M W Fl P G R Fr

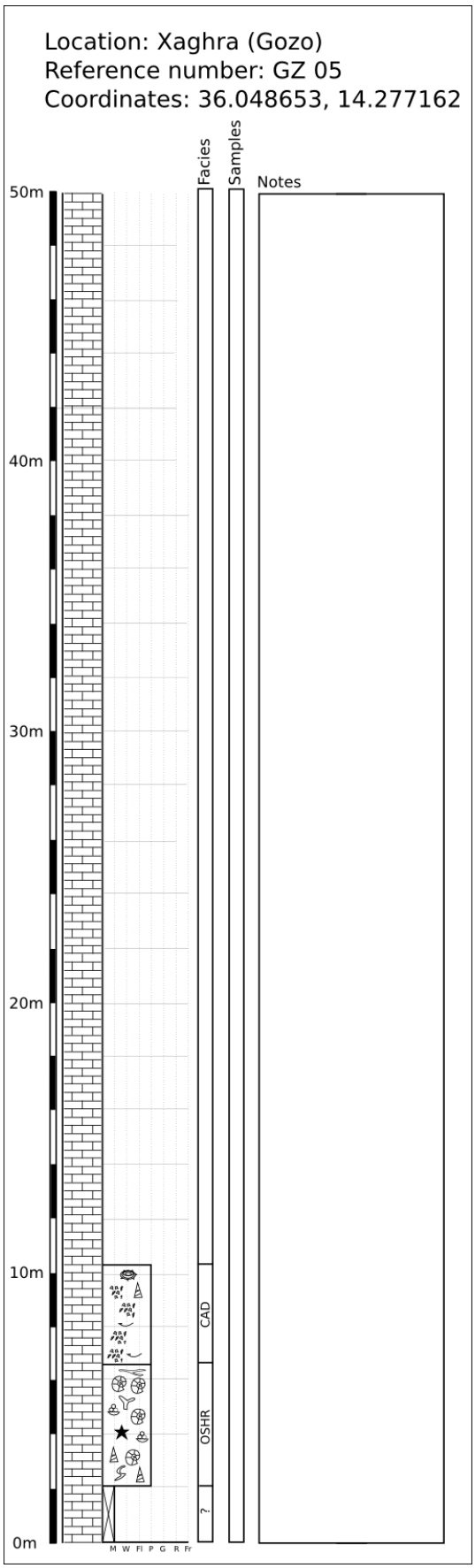
Location: Xaghra (Gozo)
Reference number: GZ 05
Coordinates: 36.048653, 14.277162
Facies
Samples
Notes
50m
40m
30m
20m
10m
0m
CAD
OSHR
?
M W Fl P G R Fr

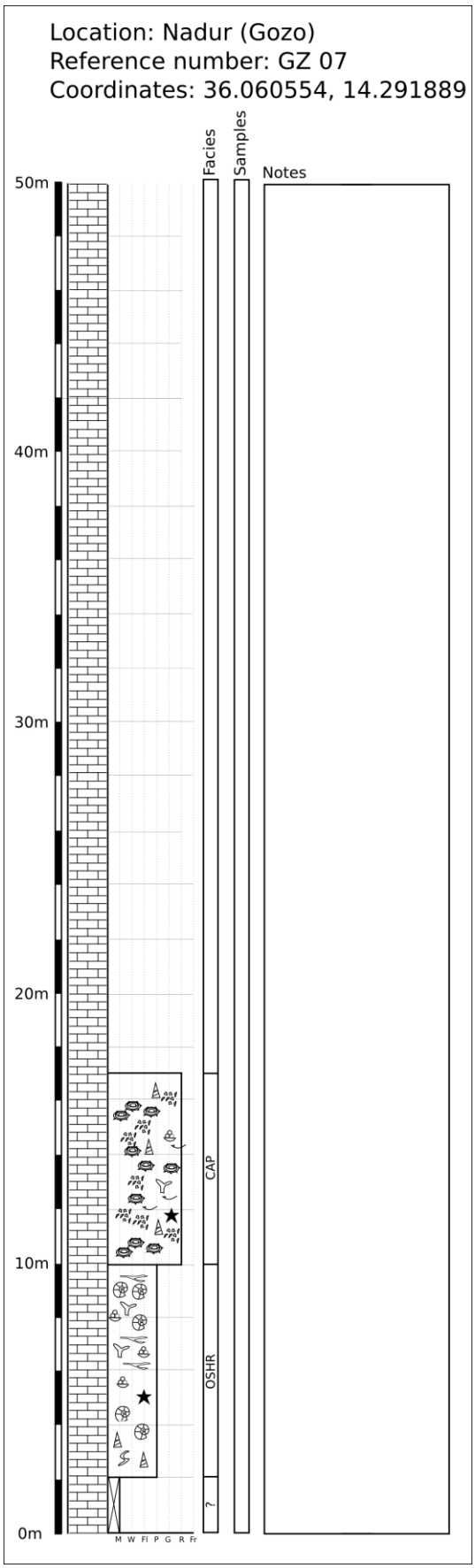
Location: Nadur (Gozo)
Reference number: GZ 07
Coordinates: 36.060554, 14.291889
Facies
Samples
Notes
50m
40m
30m
20m
10m
0m
CAP
OSHR
?
M W Fl P G R Fr

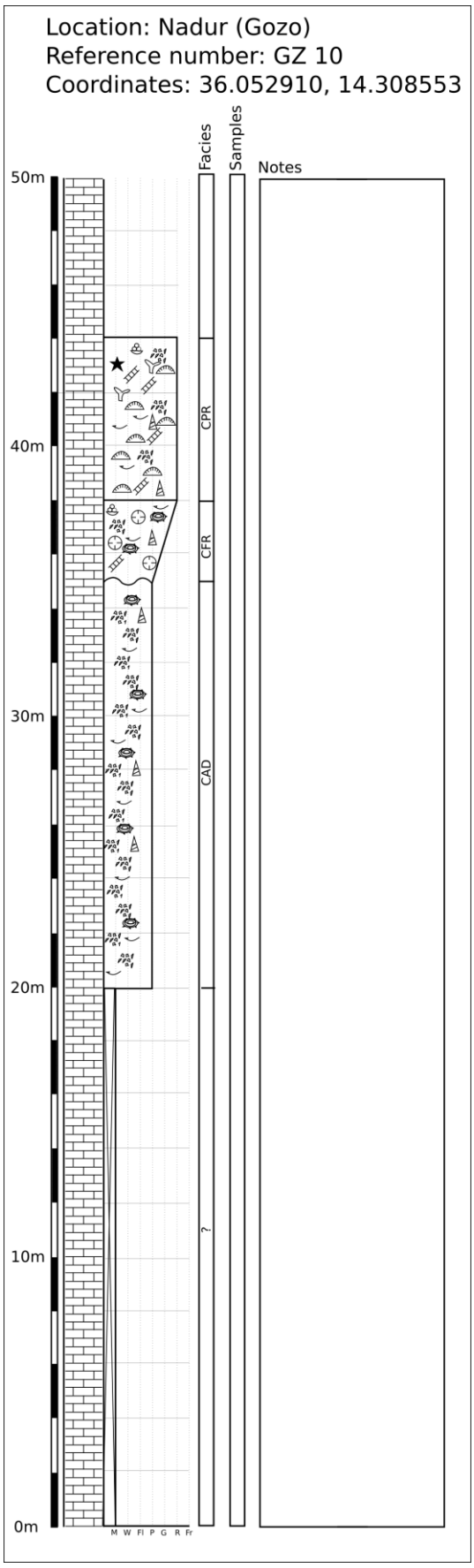
Location: Nadur (Gozo)
Reference number: GZ 10
Coordinates: 36.052910, 14.308553
Facies
Samples
Notes
50m
40m
30m
20m
10m
0m
CPR
CFR
CAD
?
M W Fl P G R Fr

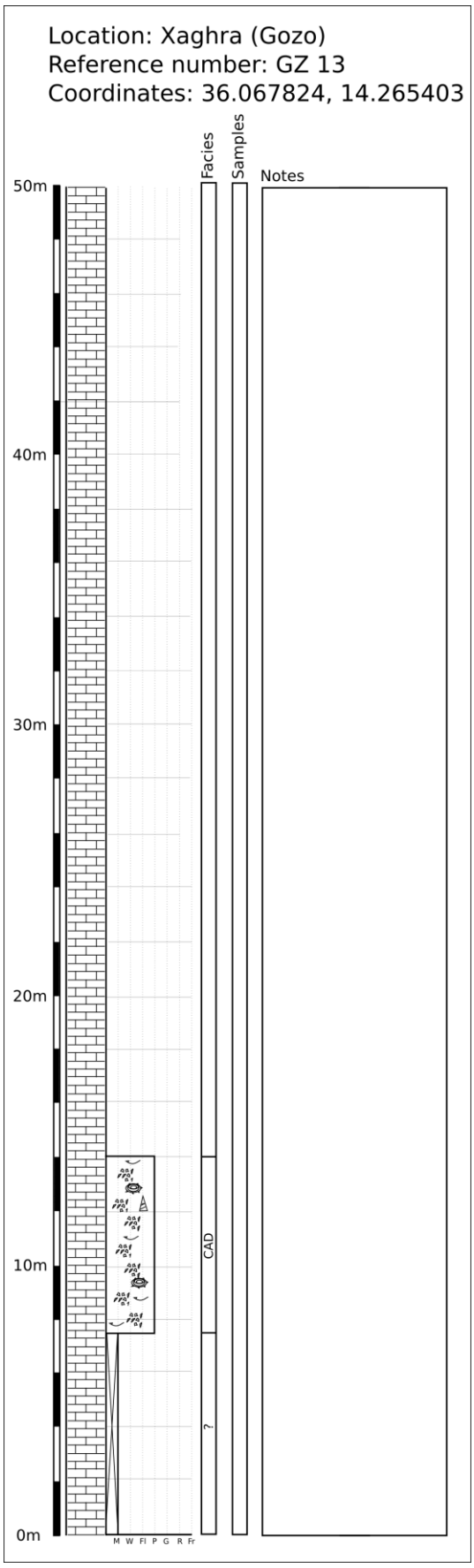
Location: Xaghra (Gozo)
Reference number: GZ 13
Coordinates: 36.067824, 14.265403
Facies
Samples
Notes
50m
40m
30m
20m
10m
0m
CAD
?
M W Fl P G R Fr

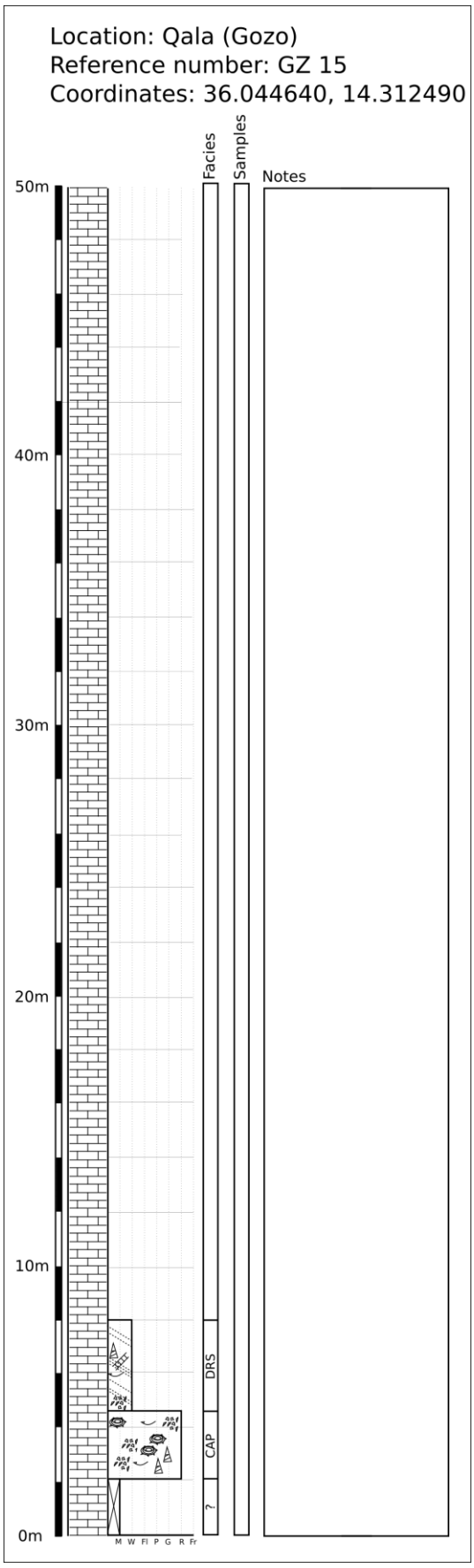
Location: Qala (Gozo)
Reference number: GZ 15
Coordinates: 36.044640, 14.312490
Facies
Samples
Notes
50m
40m
30m
20m
10m
0m
DRS
CAP
?
M W Fl P G R Fr

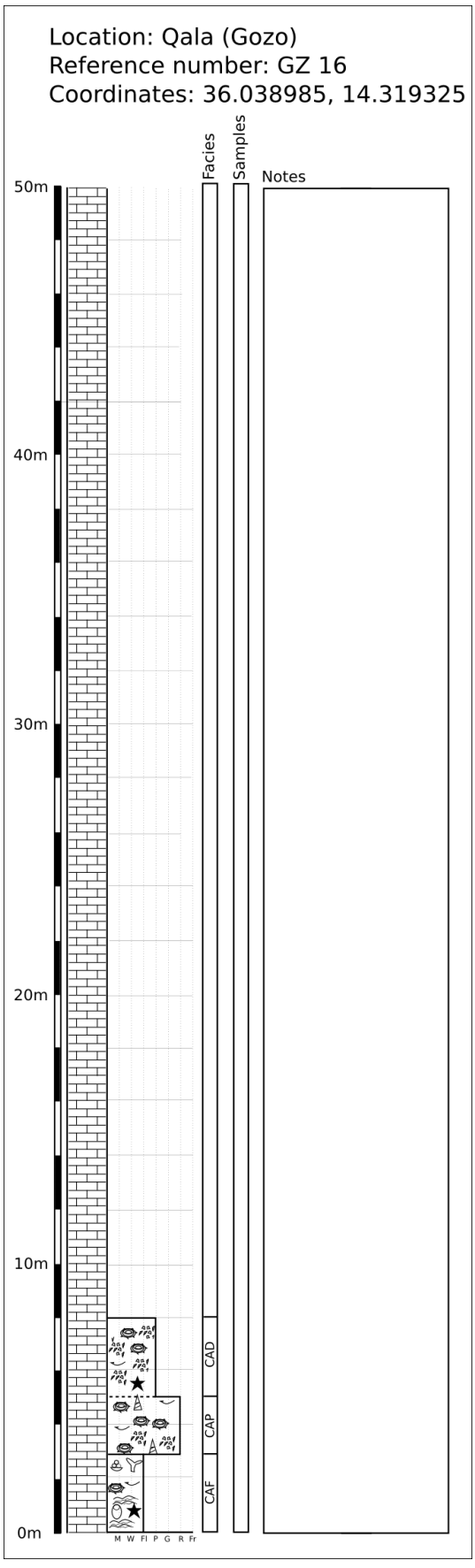
Location: Qala (Gozo)
Reference number: GZ 16
Coordinates: 36.038985, 14.319325
Facies
Samples
Notes
50m
40m
30m
20m
10m
0m
CAD
CAP
CAF
M W Fl P G R Fr

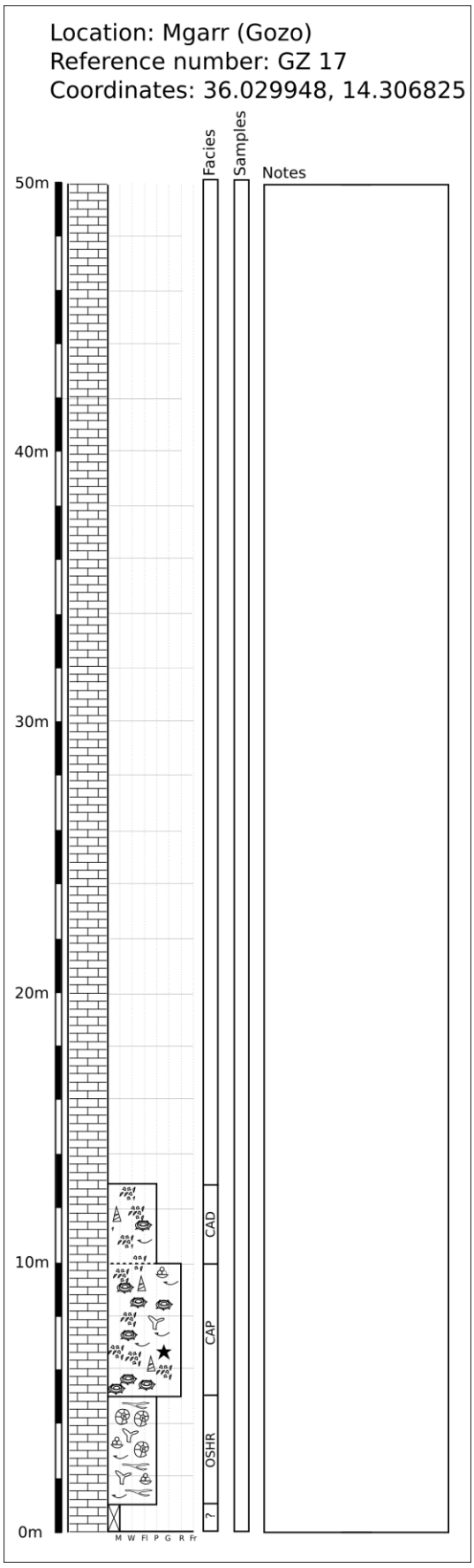
Location: Mgarr (Gozo)
Reference number: GZ 17
Coordinates: 36.029948, 14.306825
Facies
Samples
Notes
50m
40m
30m
20m
10m
0m
CAD
CAP
OSHR
?
M W Fl P G R Fr

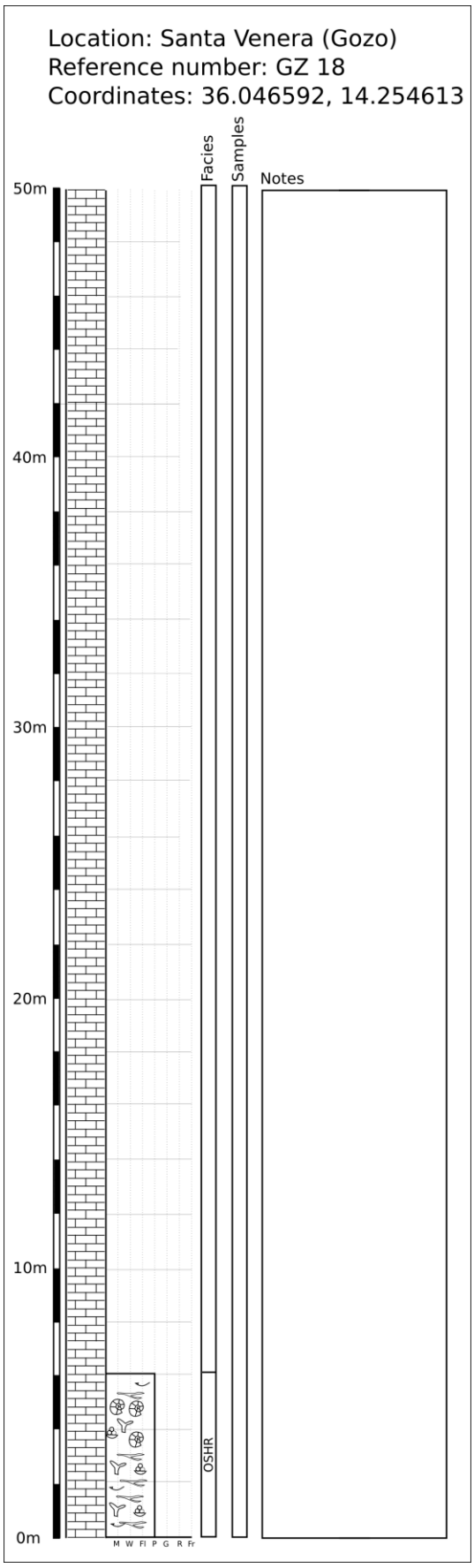
Location: Santa Venera (Gozo)
Reference number: GZ 18
Coordinates: 36.046592, 14.254613
Facies
Samples
Notes
50m
40m
30m
20m
10m
0m
OSHR
M W Fl P G R Fr

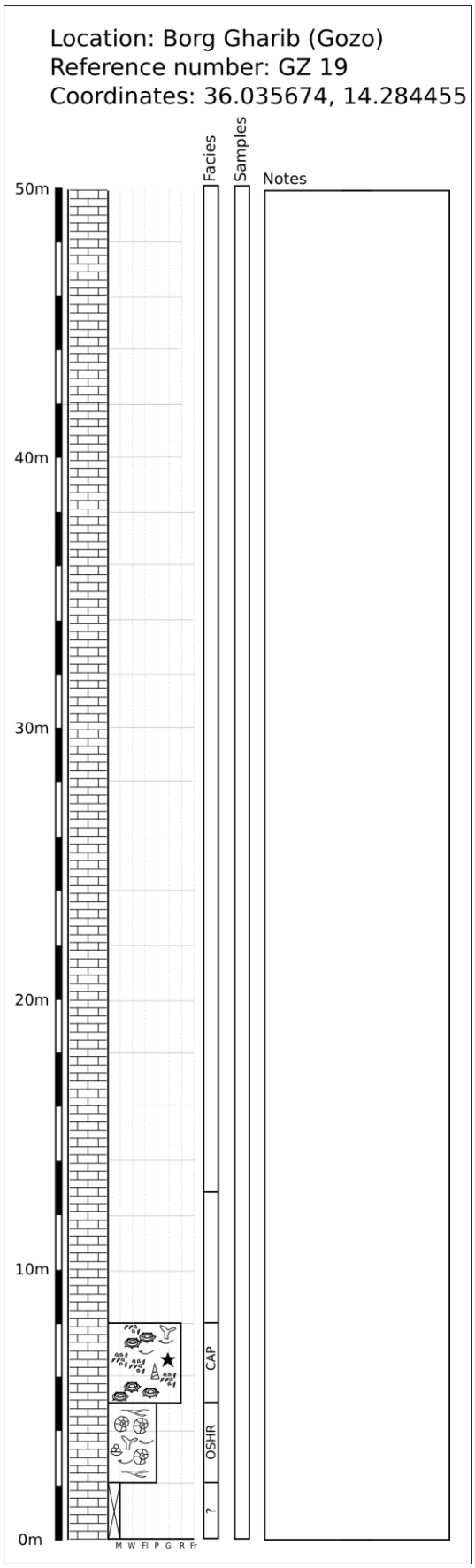
Location: Borg Gharib (Gozo)
Reference number: GZ 19
Coordinates: 36.035674, 14.284455
Facies
Samples
Notes
50m
40m
30m
20m
10m
0m
CAP
OSHR
?
M W Fl P G R Fr

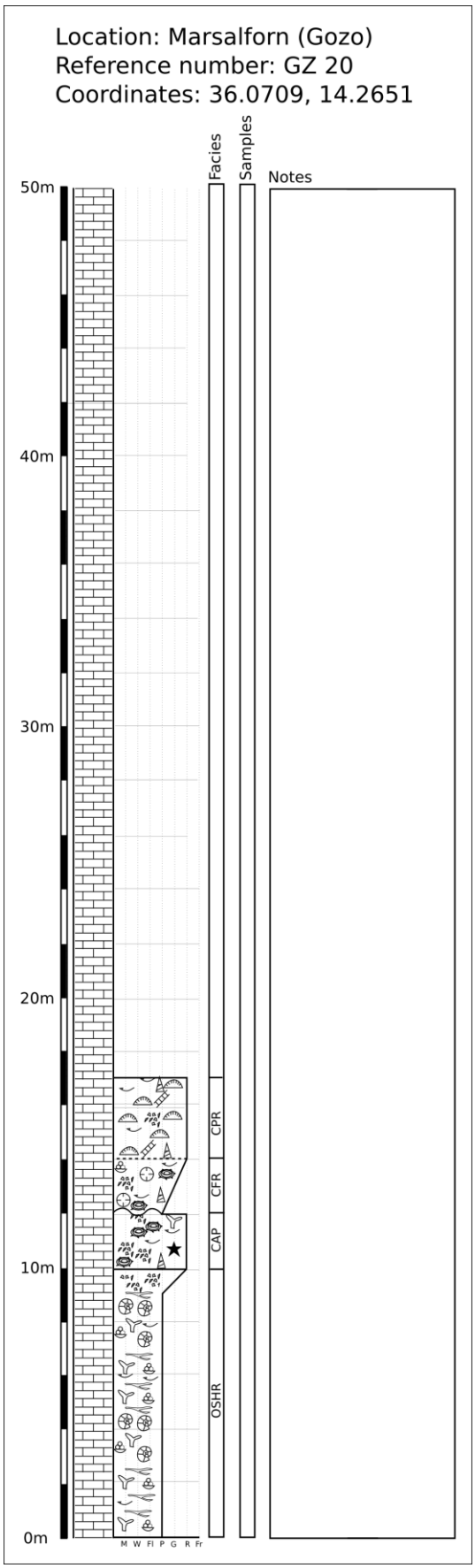
Location: Marsalforn (Gozo)
Reference number: GZ 20
Coordinates: 36.0709, 14.2651
Facies
Samples
Notes
50m
40m
30m
20m
10m
0m
CPR
CFR
CAP
OSHR
M W Fl P G R Fr

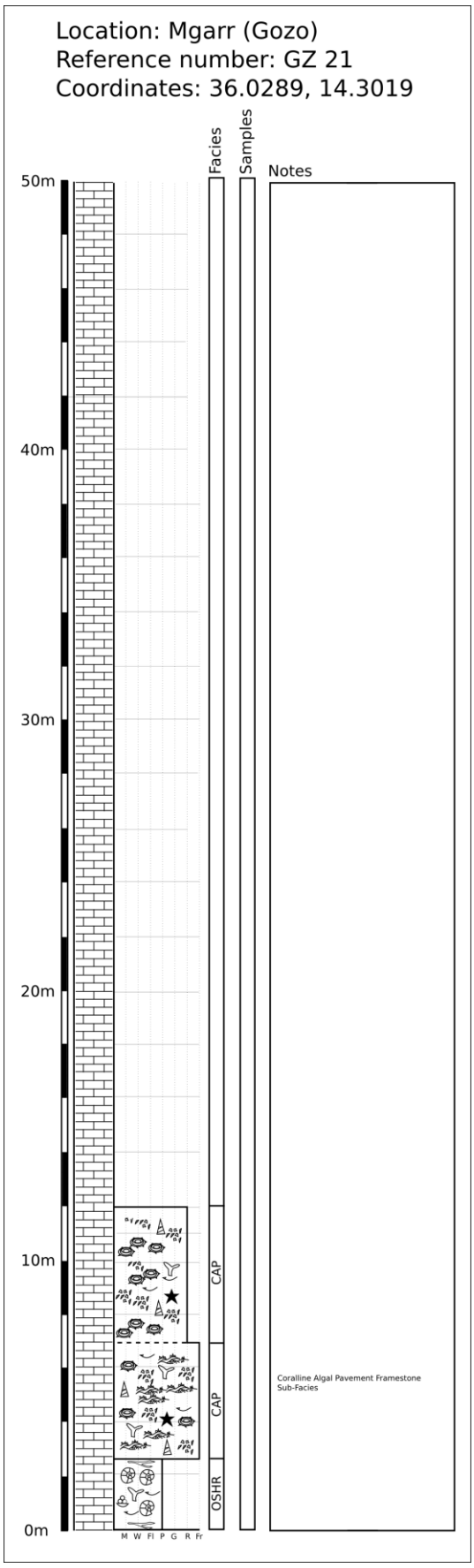
Location: Mgarr (Gozo)
Reference number: GZ 21
Coordinates: 36.0289, 14.3019
Facies
Samples
Notes
50m
40m
30m
20m
10m
0m
CAP
CAP
OSHR
Coralline Algal Pavement Framestone Sub-Facies
M W Fl P G R Fr

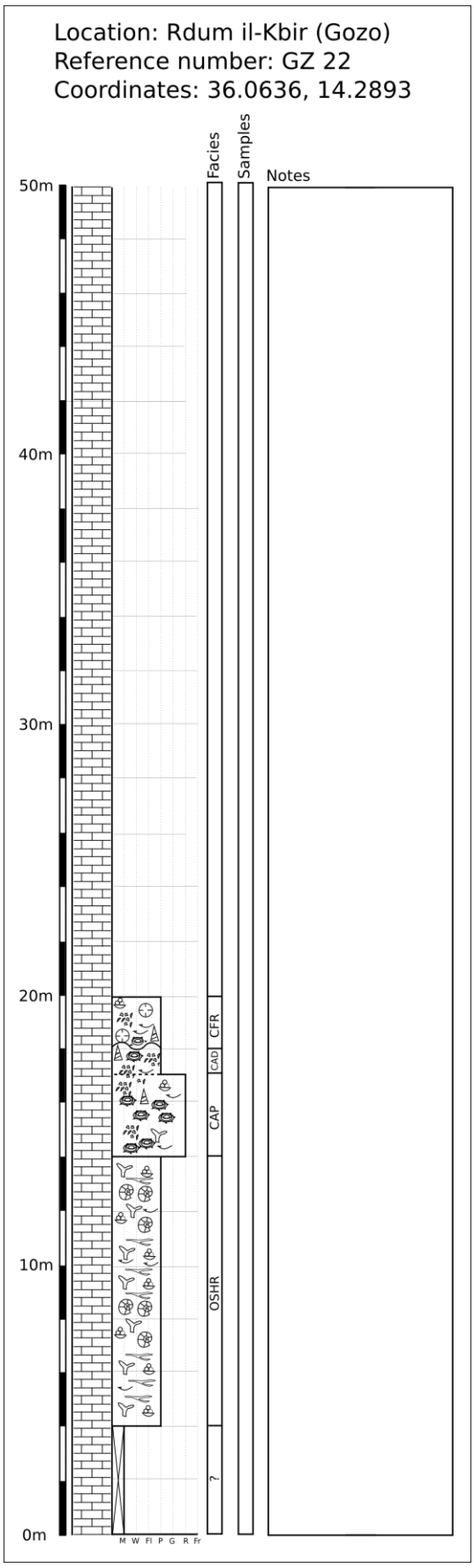
Location: Rdum il-Kbir (Gozo)
Reference number: GZ 22
Coordinates: 36.0636, 14.2893
Facies
Samples
Notes
50m
40m
30m
20m
10m
0m
CFR
CAD
CAP
OSHR
?
M W Fl P G R Fr

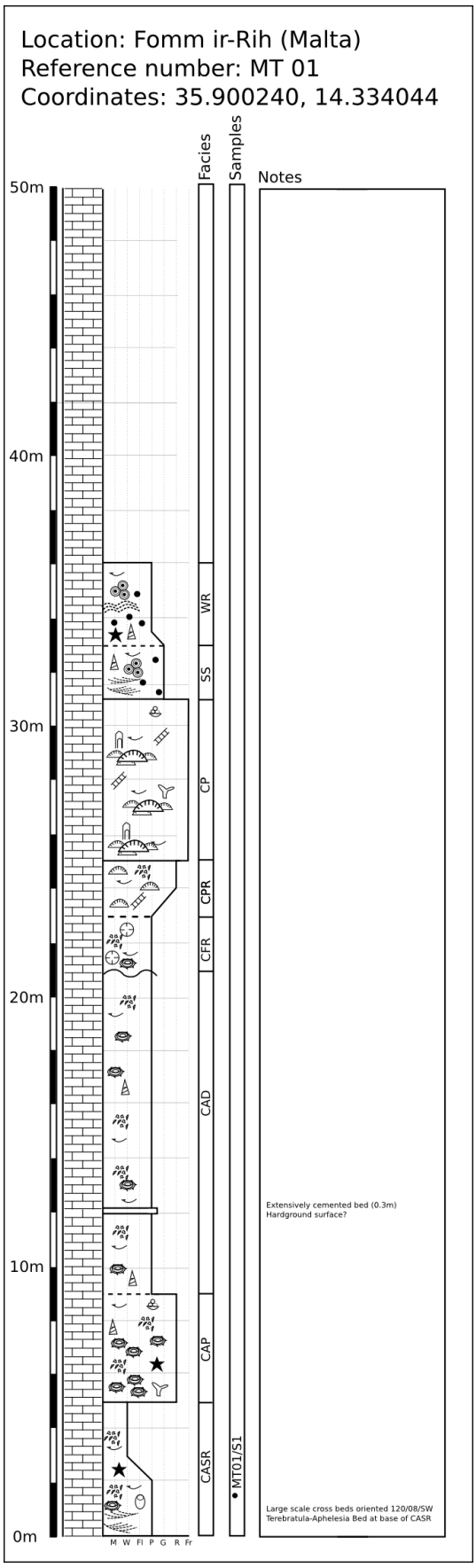
Location: Fomm ir-Rih (Malta)
Reference number: MT 01
Coordinates: 35.900240, 14.334044
Facies
Samples
Notes
50m
40m
30m
20m
10m
0m
WR
SS
CP
CPR
CFR
CAD
CAP
CASR
MT01/S1
M W Fl P G R Fr
Extensively cemented bed (0.3m)
Hardground surface?
Large scale cross beds oriented 120/08/SW
Terebratula-Aphelesia Bed at base of CASR

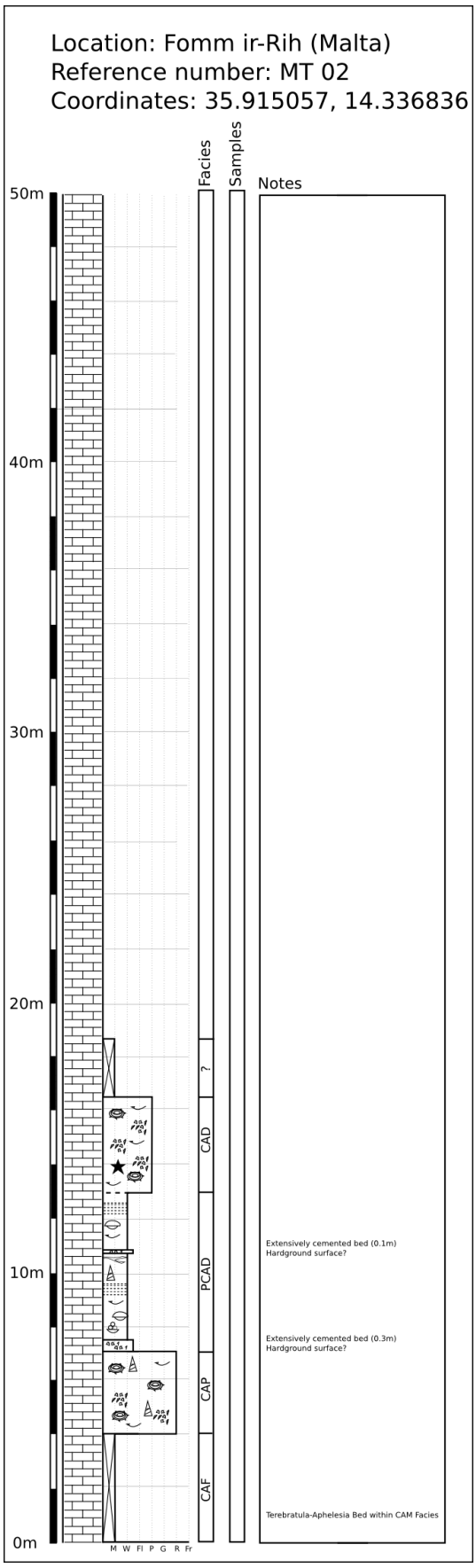
Location: Fomm ir-Rih (Malta)
Reference number: MT 02
Coordinates: 35.915057, 14.336836
Facies
Samples
Notes
50m
40m
30m
20m
10m
0m
?
CAD
PCAD
CAP
CAF
M W Fl P G R Fr
Extensively cemented bed (0.1m)
Hardground surface?
Extensively cemented bed (0.3m)
Hardground surface?
Terebratula-Aphelesia Bed within CAM Facies

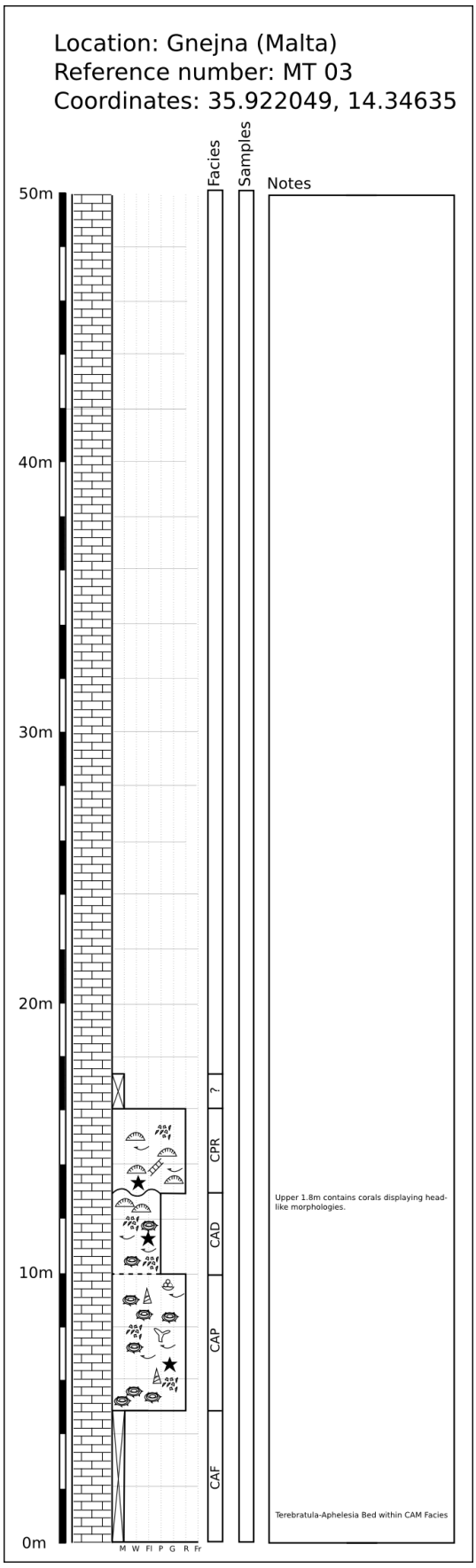
Location: Gnejna (Malta)
Reference number: MT 03
Coordinates: 35.922049, 14.34635
Facies
Samples
Notes
50m
40m
30m
20m
10m
0m
?
CPR
CAD
CAP
CAF
Upper 1.8m contains corals displaying head-like morphologies.
Terebratula-Aphelesia Bed within CAM Facies
M W Fl P G R Fr

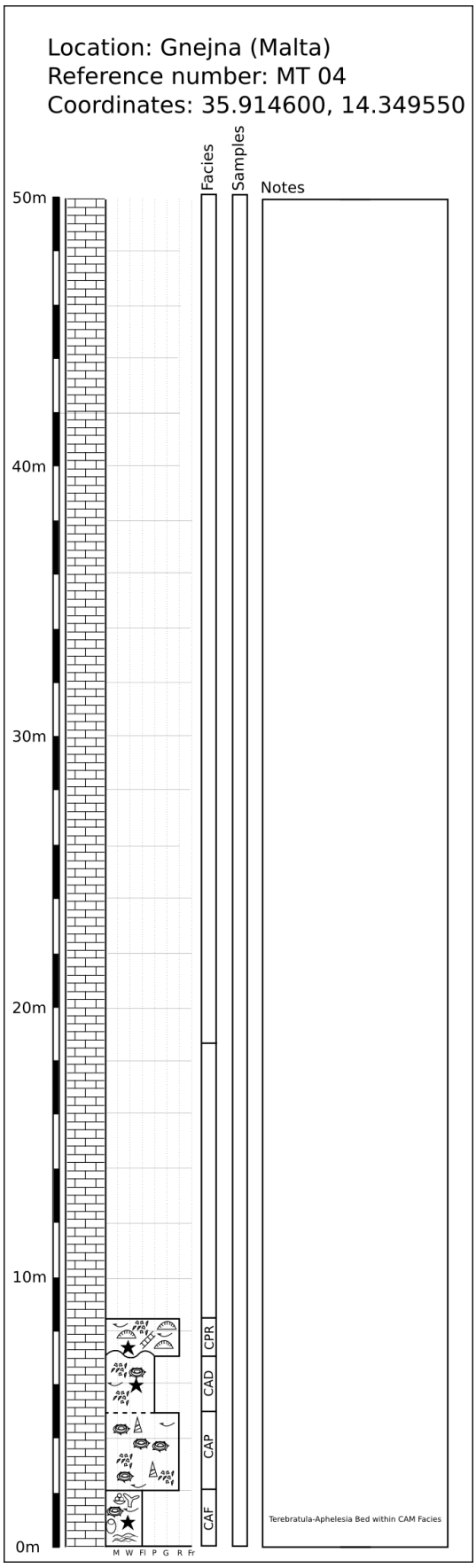
Location: Gnejna (Malta)
Reference number: MT 04
Coordinates: 35.914600, 14.349550
Facies
Samples
Notes
50m
40m
30m
20m
10m
0m
CPR
CAD
CAP
CAF
Terebratula-Aphelesia Bed within CAM Facies
M W Fl P G R Fr

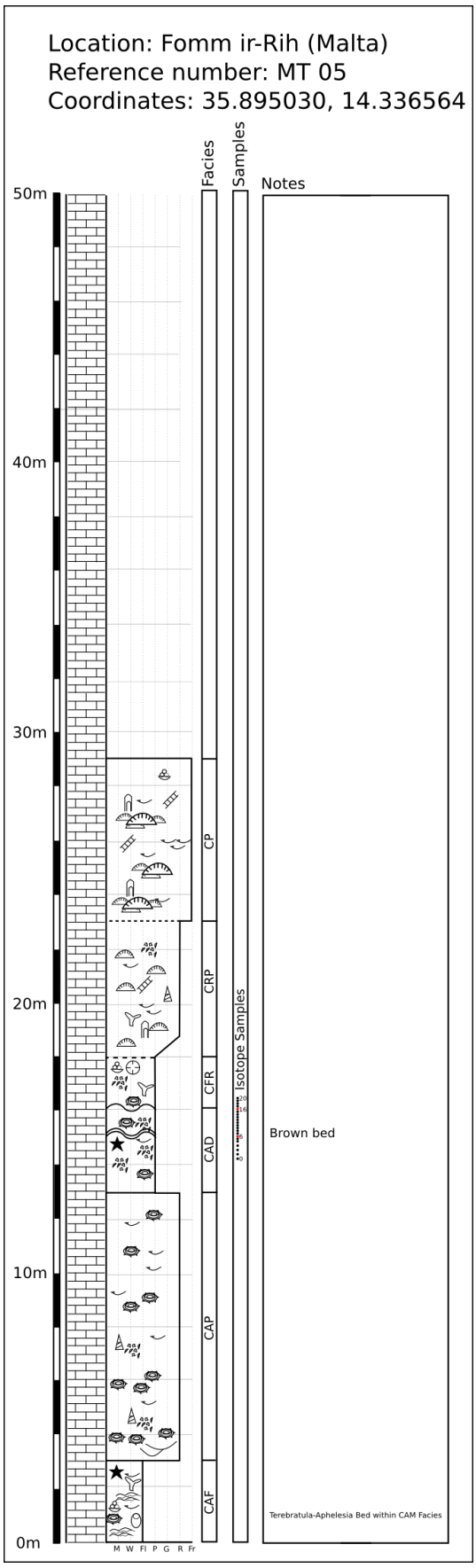
Location: Fomm ir-Rih (Malta)
Reference number: MT 05
Coordinates: 35.895030, 14.336564
Facies
Samples
Notes
50m
40m
30m
20m
10m
0m
CP
CRP
CFR
CAD
CAP
CAF
Isotope Samples
Brown bed
Terebratula-Aphelesia Bed within CAM Facies
M W Fl P G R Fr

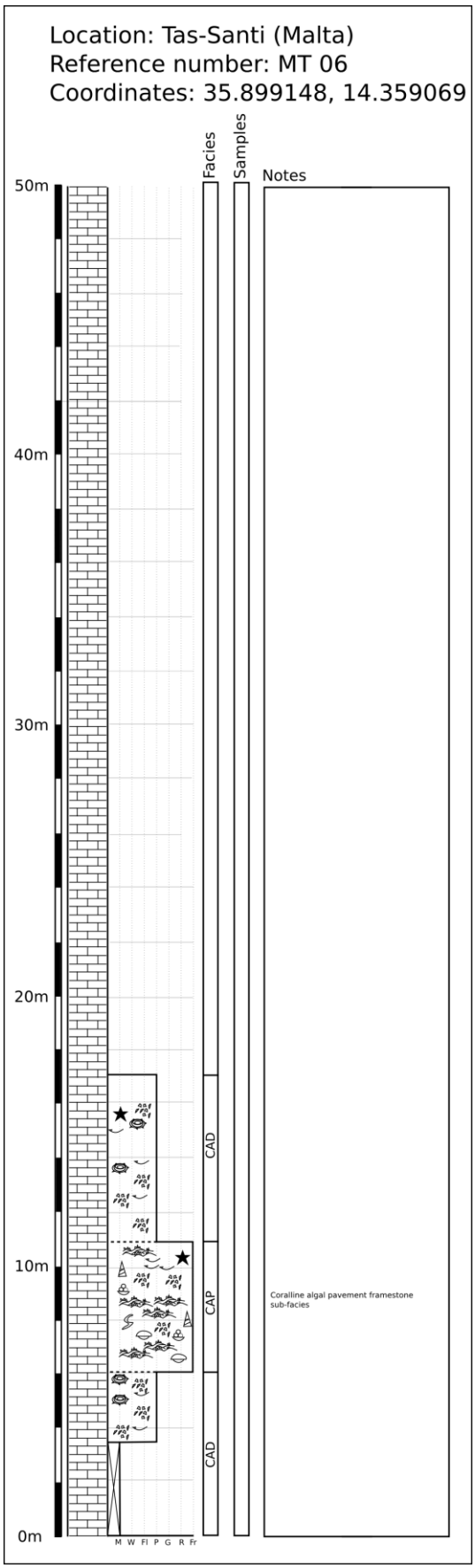
Location: Tas-Santi (Malta)
Reference number: MT 06
Coordinates: 35.899148, 14.359069
Facies
Samples
Notes
50m
40m
30m
20m
10m
0m
CAD
CAP
CAD
Coralline algal pavement framestone sub-facies
M W Fl P G R Fr

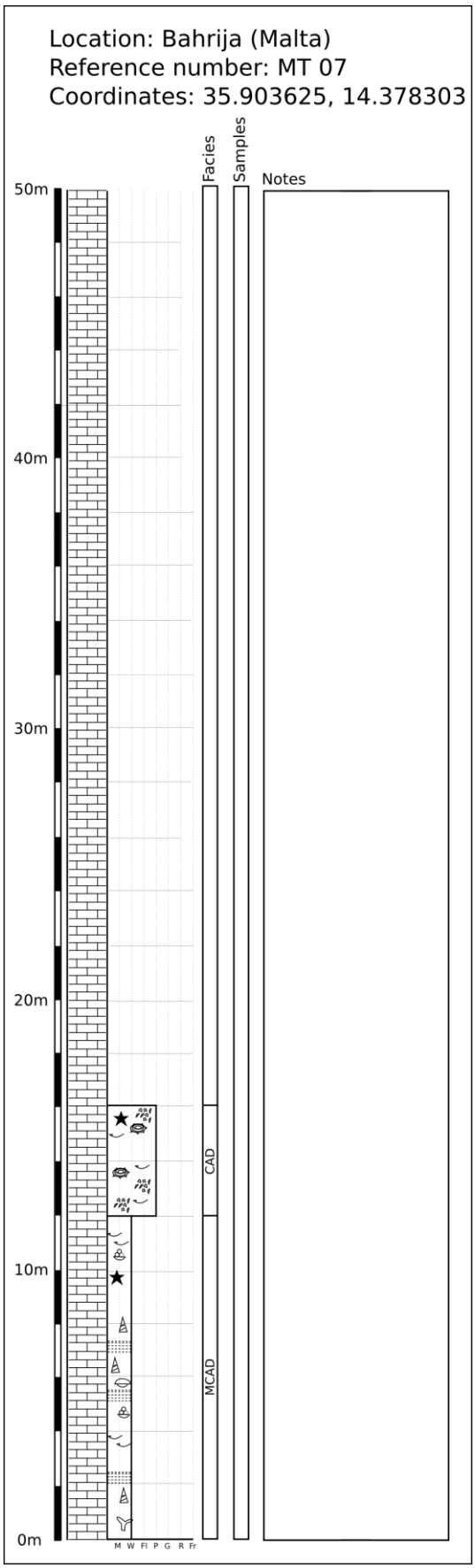
Location: Bahrija (Malta)
Reference number: MT 07
Coordinates: 35.903625, 14.378303
Facies
Samples
Notes
50m
40m
30m
20m
10m
0m
CAD
MCAD
M W Fl P G R Fr

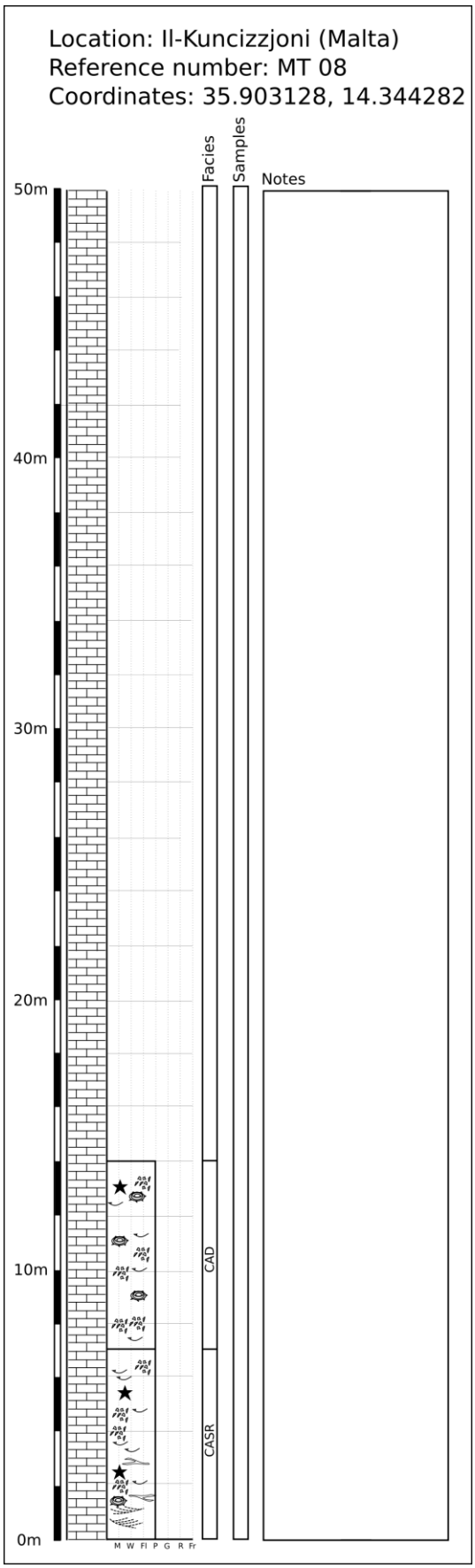
Location: Il-Kuncizzjoni (Malta)
Reference number: MT 08
Coordinates: 35.903128, 14.344282
Facies
Samples
Notes
50m
40m
30m
20m
10m
0m
CAD
CASR
M W Fl P G R Fr

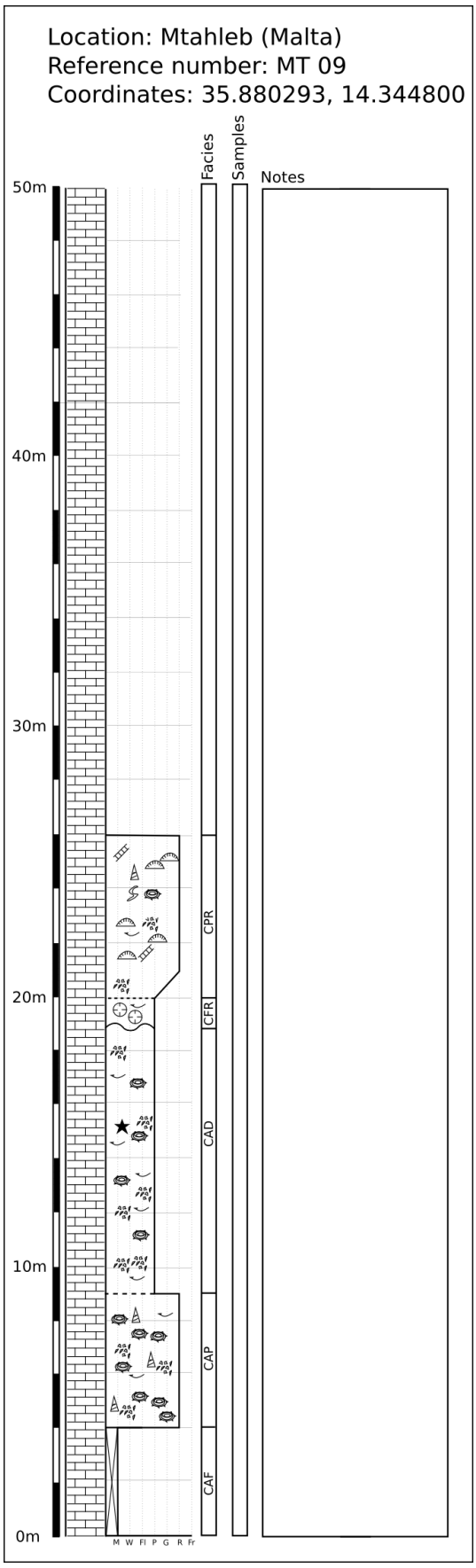
Location: Mtahleb (Malta)
Reference number: MT 09
Coordinates: 35.880293, 14.344800
Facies
Samples
Notes
50m
40m
30m
20m
10m
0m
CPR
CFR
CAD
CAP
CAF
M W Fl P G R Fr

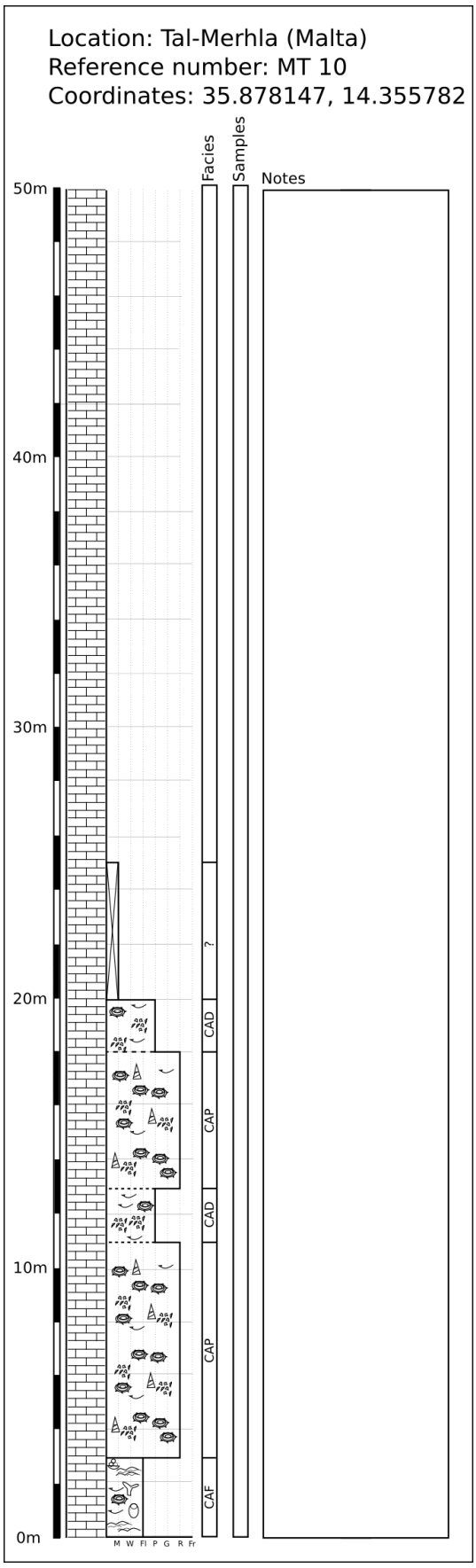
Location: Tal-Merhla (Malta)
Reference number: MT 10
Coordinates: 35.878147, 14.355782
Facies
Samples
Notes
50m
40m
30m
20m
10m
0m
?
CAD
CAP
CAD
CAP
CAF
M W Fl P G R Fr

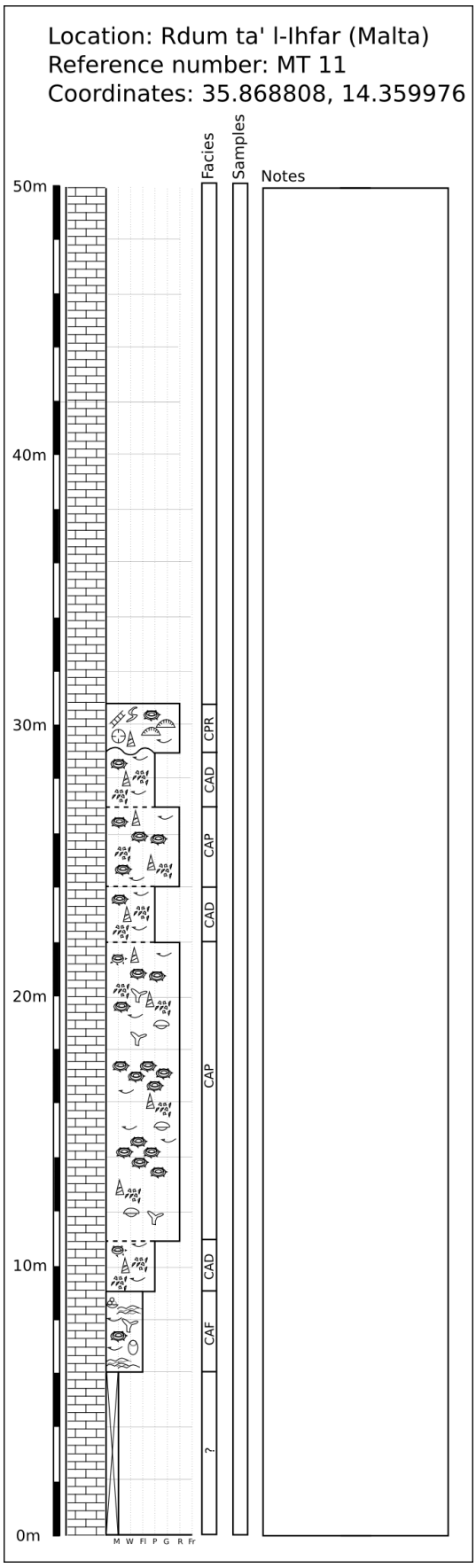
Location: Rdum ta' l-Ihfar (Malta)
Reference number: MT 11
Coordinates: 35.868808, 14.359976
Facies
Samples
Notes
50m
40m
30m
20m
10m
0m
CPR
CAD
CAP
CAD
CAP
CAD
CAF
?
M W Fl P G R Fr

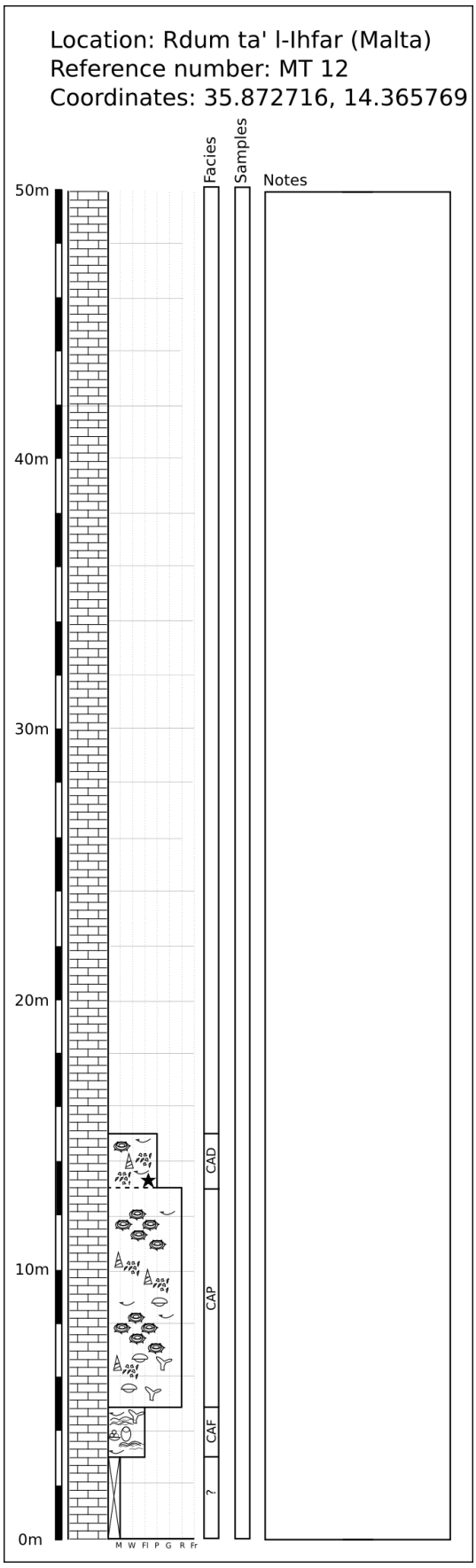
Location: Rdum ta' l-Ihfar (Malta)
Reference number: MT 12
Coordinates: 35.872716, 14.365769
Facies
Samples
Notes
50m
40m
30m
20m
10m
0m
CAD
CAP
CAF
?
M W Fl P G R Fr

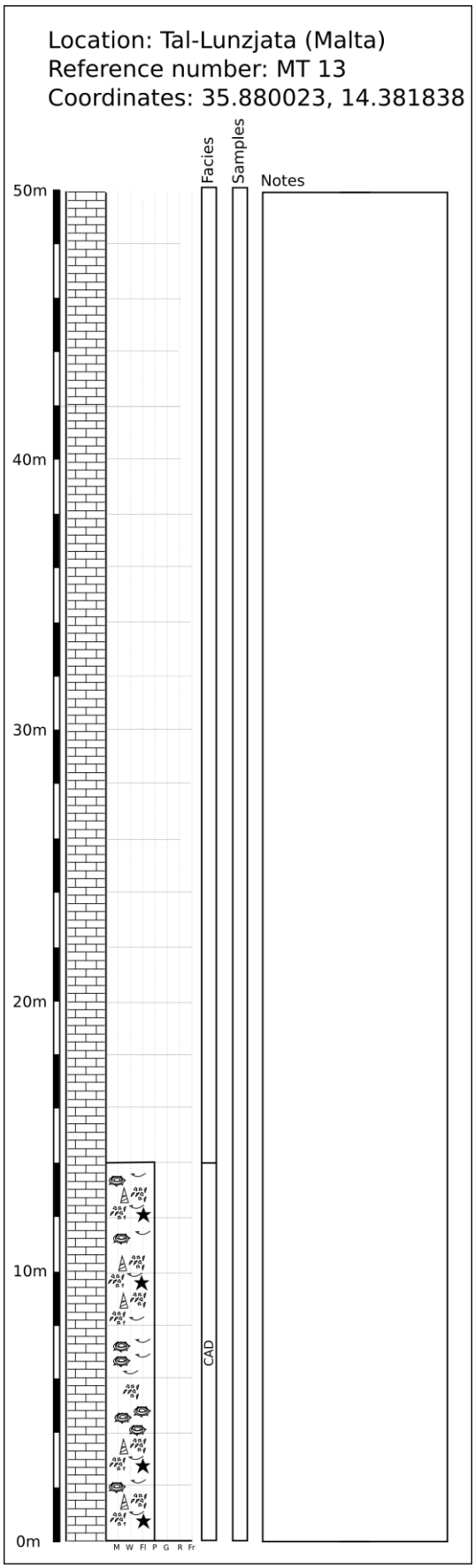
Location: Tal-Lunzjata (Malta)
Reference number: MT 13
Coordinates: 35.880023, 14.381838
Facies
Samples
Notes
50m
40m
30m
20m
10m
0m
CAD
M W Fl P G R Fr

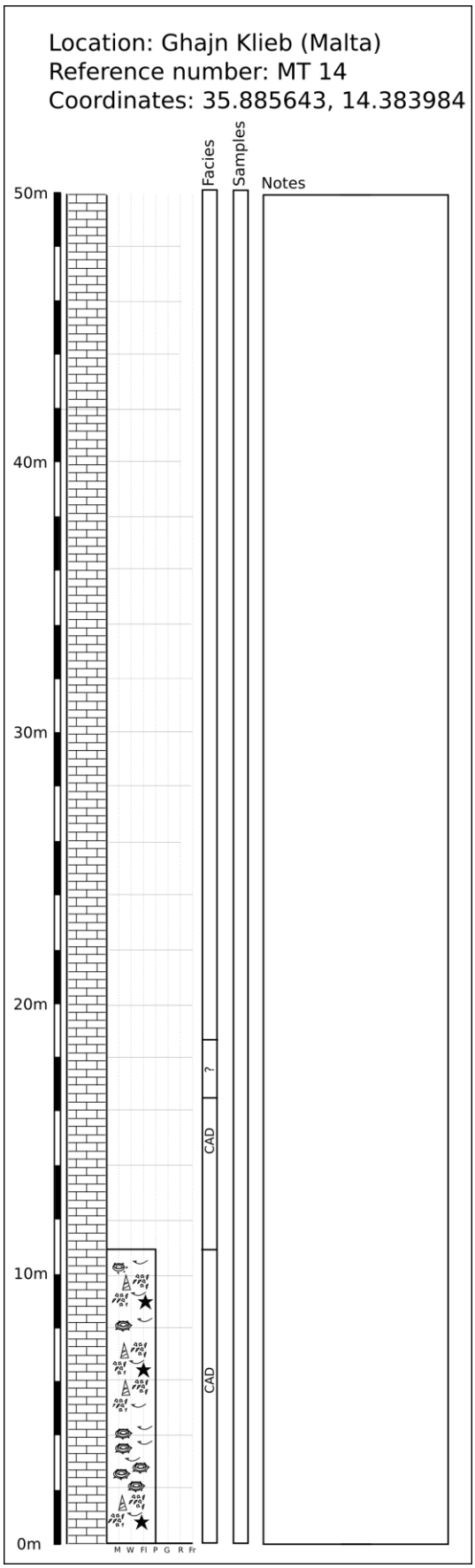
Location: Ghajn Klieb (Malta)
Reference number: MT 14
Coordinates: 35.885643, 14.383984
Facies
Samples
Notes
50m
40m
30m
20m
10m
0m
?
CAD
CAD
M W Fl P G R Fr

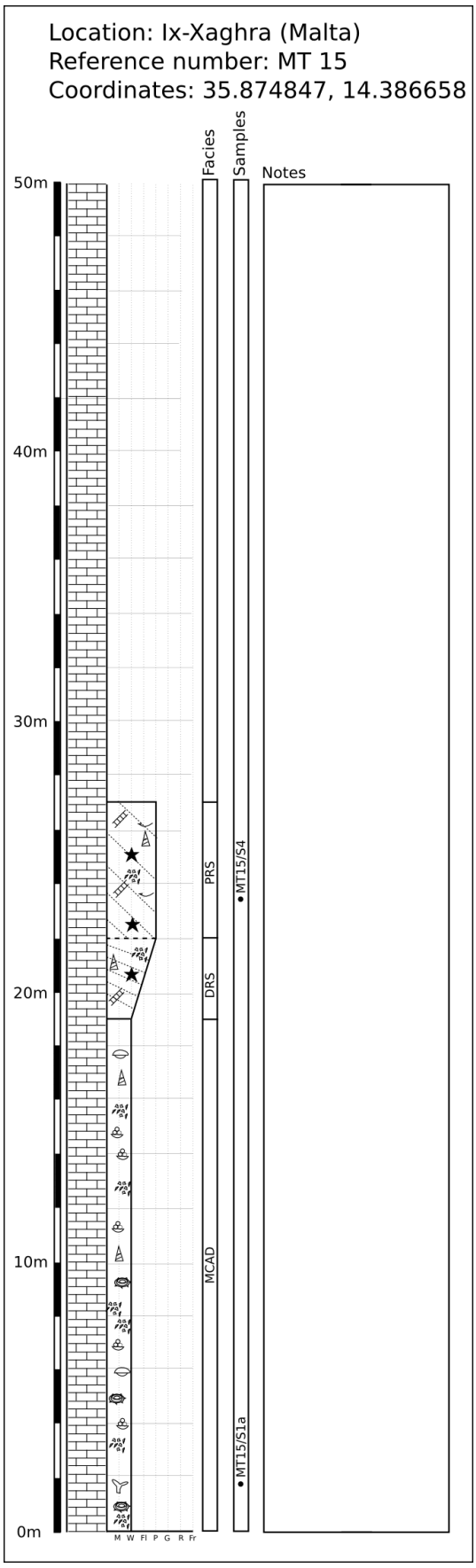
Location: Ix-Xaghra (Malta)
Reference number: MT 15
Coordinates: 35.874847, 14.386658
Facies
Samples
Notes
50m
40m
30m
20m
10m
0m
PRS
DRS
MCAD
MT15/S4
MT15/S1a
M W Fl P G R Fr

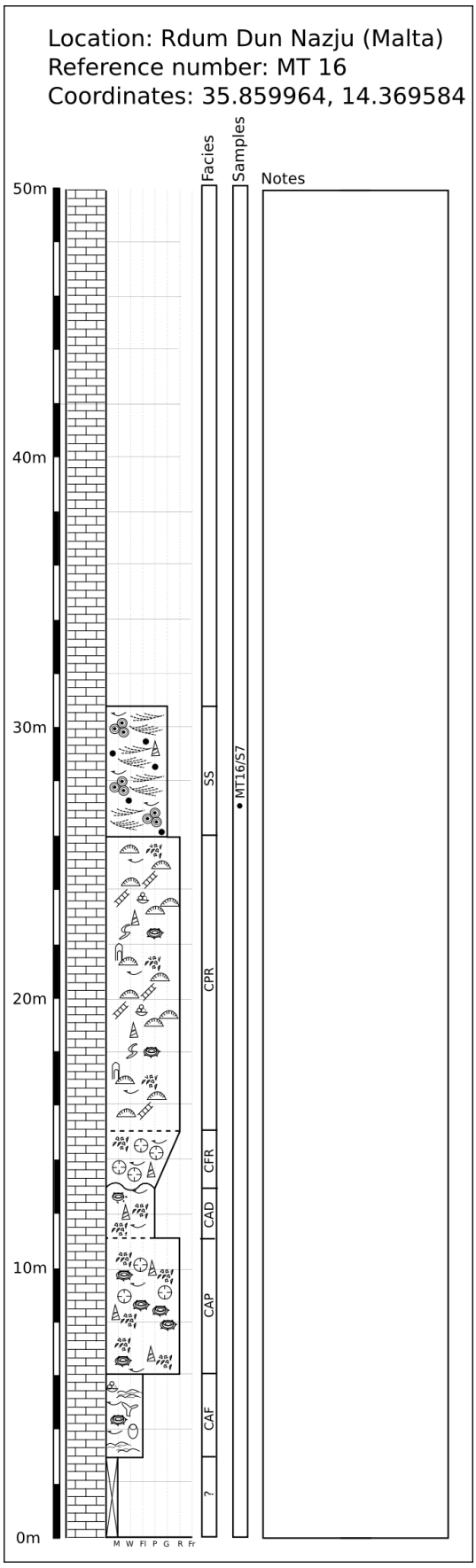
Location: Rdum Dun Nazju (Malta)
Reference number: MT 16
Coordinates: 35.859964, 14.369584
Facies
Samples
Notes
50m
40m
30m
20m
10m
0m
SS
CPR
CFR
CAD
CAP
CAF
?
MT16/S7
M W Fl P G R Fr

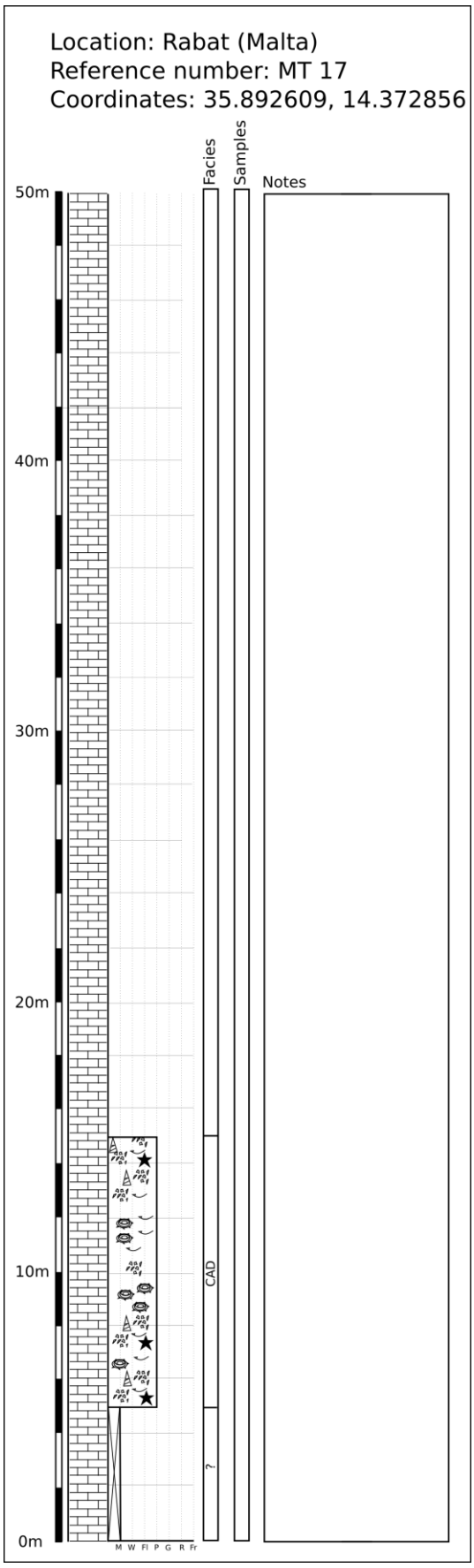
Location: Rabat (Malta)
Reference number: MT 17
Coordinates: 35.892609, 14.372856
Facies
Samples
Notes
50m
40m
30m
20m
10m
0m
CAD
?
M W Fl P G R Fr

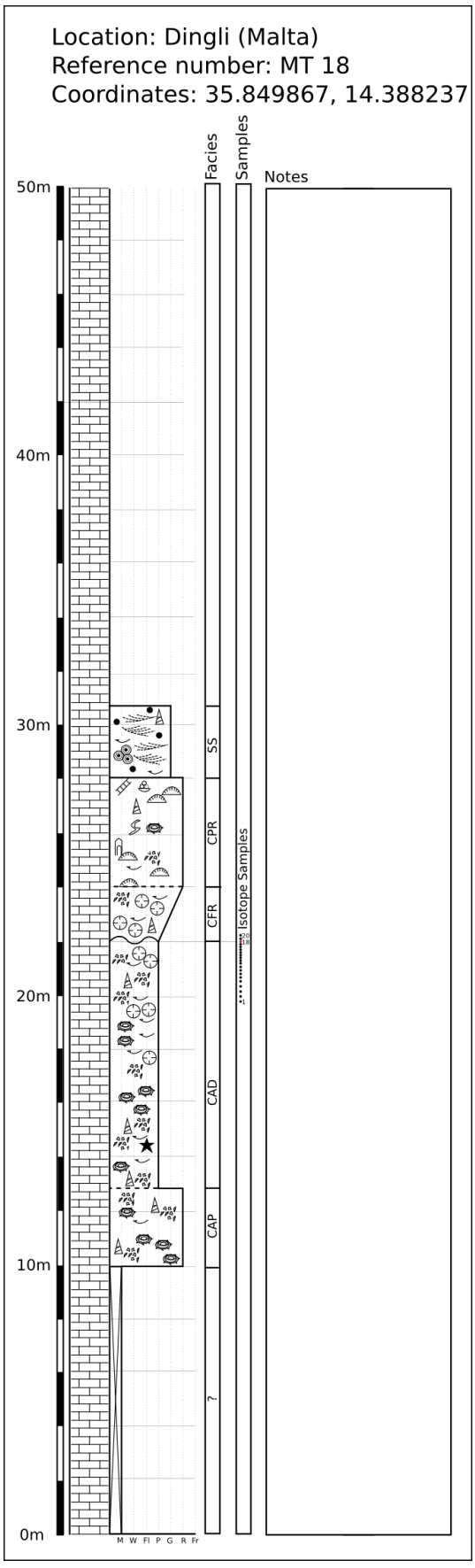
Location: Dingli (Malta)
Reference number: MT 18
Coordinates: 35.849867, 14.388237
Facies
Samples
Notes
50m
40m
30m
20m
10m
0m
SS
CPR
CFR
CAD
CAP
?
Isotope Samples
M W Fl P G R Fr

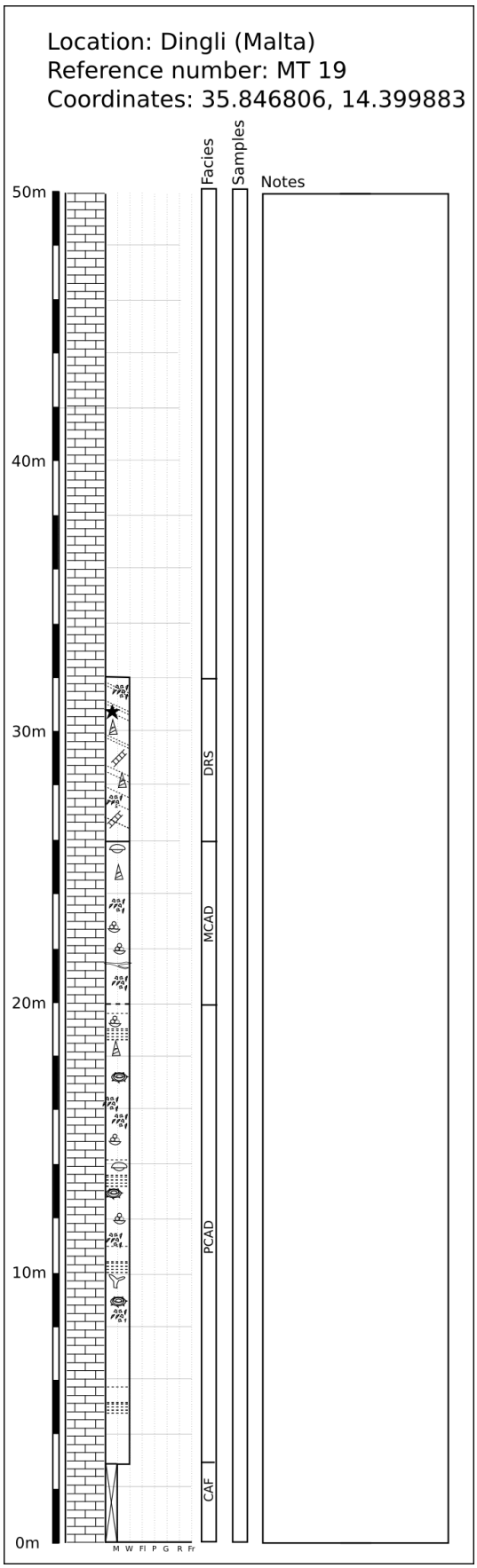
Location: Dingli (Malta)
Reference number: MT 19
Coordinates: 35.846806, 14.399883
Facies
Samples
Notes
50m
40m
30m
20m
10m
0m
DRS
MCAD
PCAD
CAF
M W Fl P G R Fr

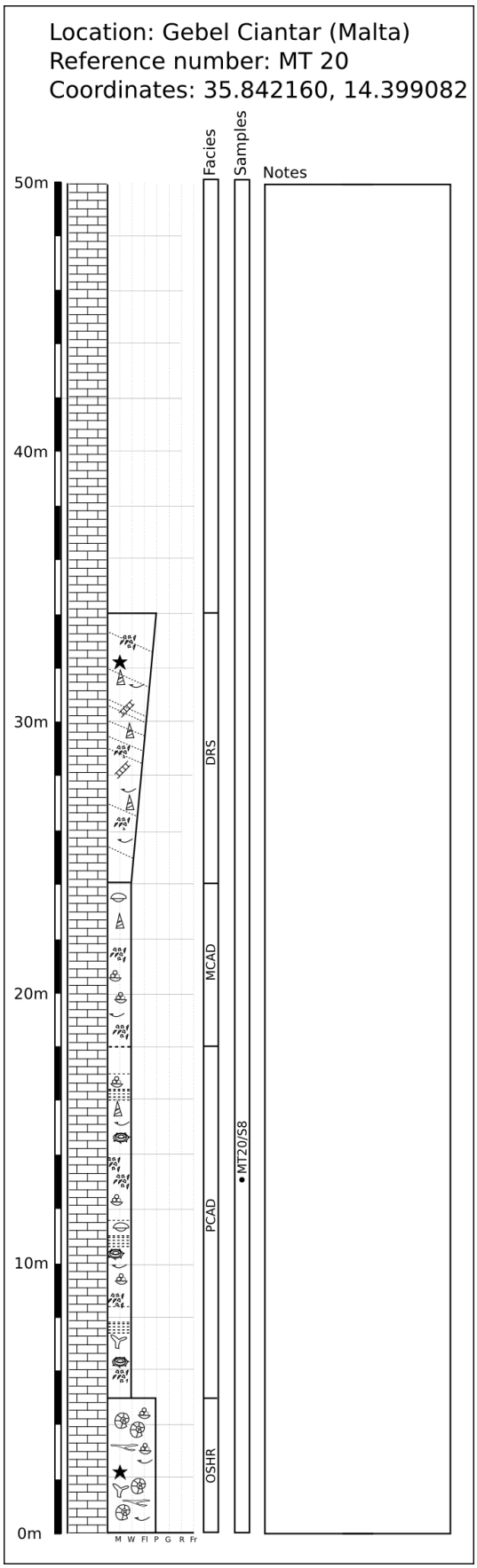
Location: Gebel Ciantar (Malta)
Reference number: MT 20
Coordinates: 35.842160, 14.399082
Facies
Samples
Notes
50m
40m
30m
20m
10m
0m
DRS
MCAD
PCAD
OSHR
MT20/S8
M W Fl P G R Fr

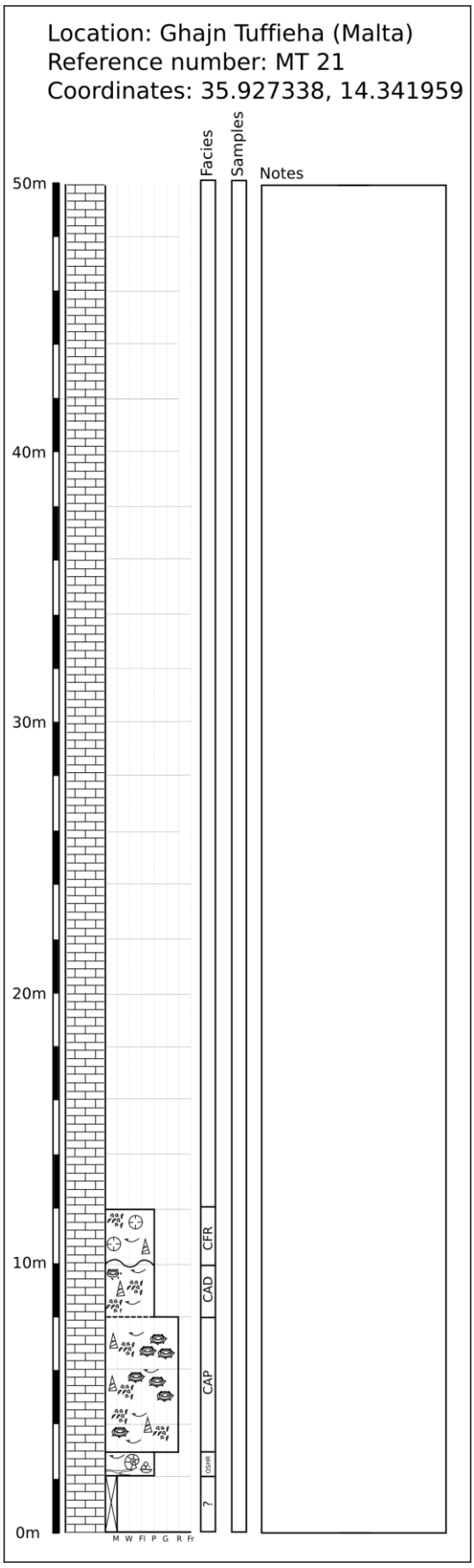
Location: Ghajn Tuffieha (Malta)
Reference number: MT 21
Coordinates: 35.927338, 14.341959
Facies
Samples
Notes
50m
40m
30m
20m
10m
0m
CFR
CAD
CAP
?
M W Fl P G R Fr

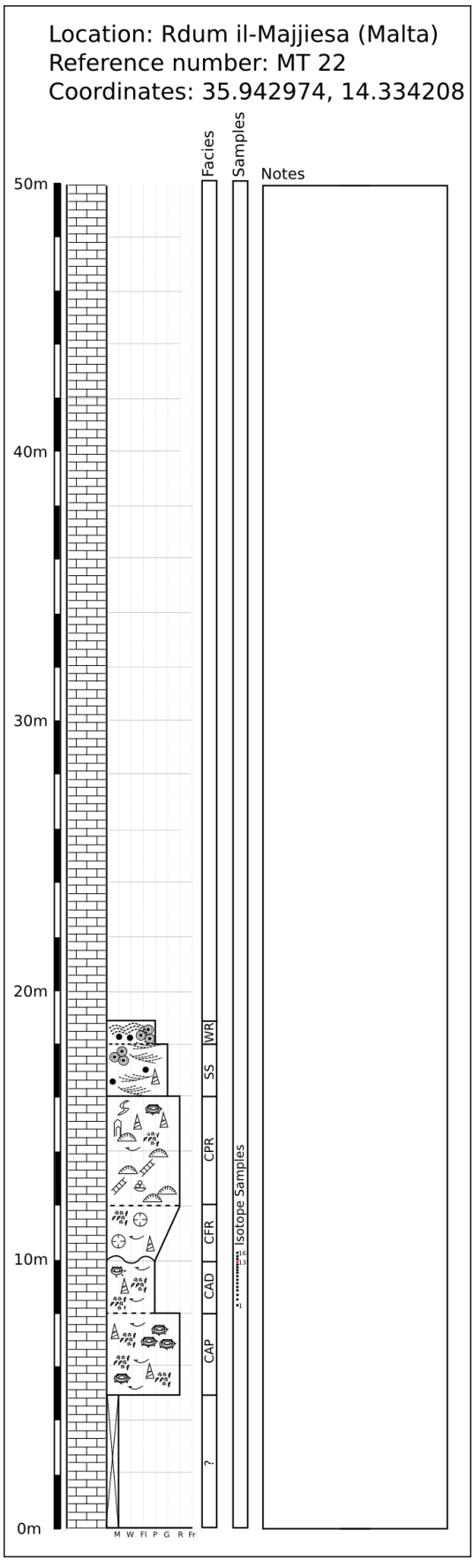
Location: Rdum il-Majjiesa (Malta)
Reference number: MT 22
Coordinates: 35.942974, 14.334208
Facies
Samples
Notes
50m
40m
30m
20m
10m
0m
WR
SS
CPR
CFR
CAD
CAP
?
Isotope Samples
M W Fl P G R Fr

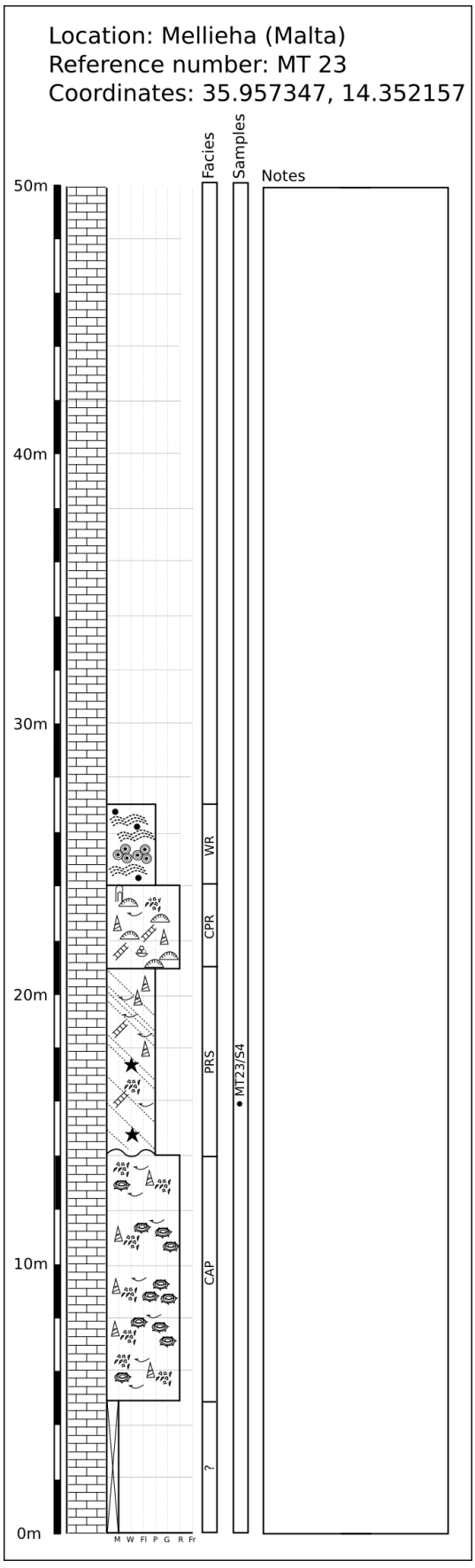
Location: Mellieha (Malta)
Reference number: MT 23
Coordinates: 35.957347, 14.352157
Facies
Samples
Notes
50m
40m
30m
20m
10m
0m
WR
CPR
PRS
CAP
?
MT23/S4
M W Fl P G R Fr

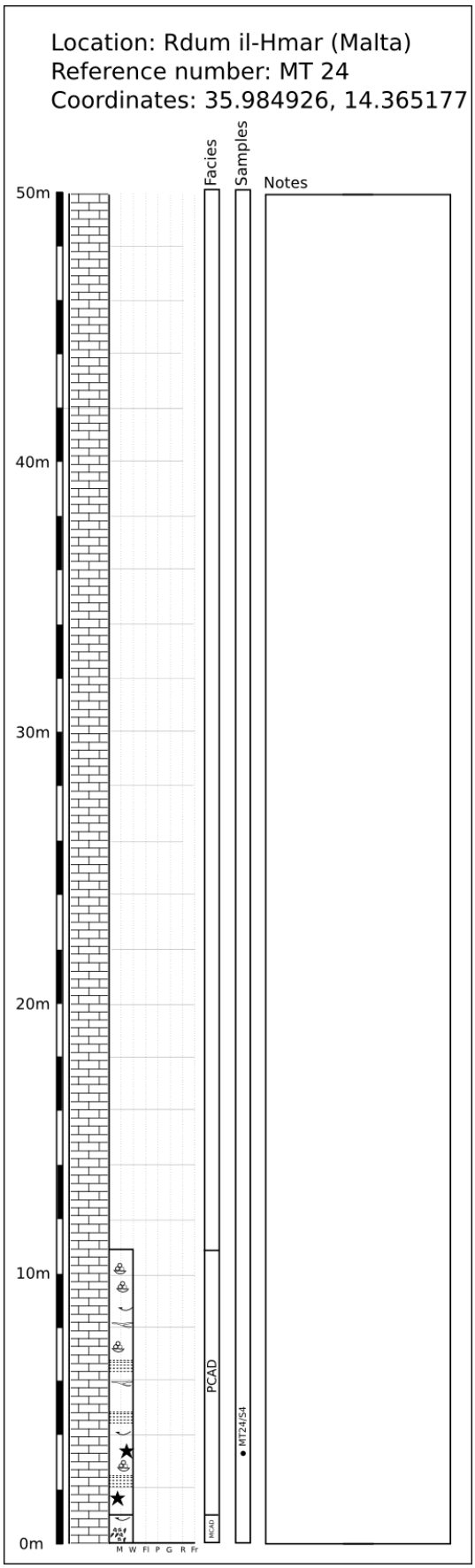
Location: Rdum il-Hmar (Malta)
Reference number: MT 24
Coordinates: 35.984926, 14.365177
Facies
Samples
Notes
50m
40m
30m
20m
10m
0m
PCAD
MT24/S4
M W Fl P G R Fr

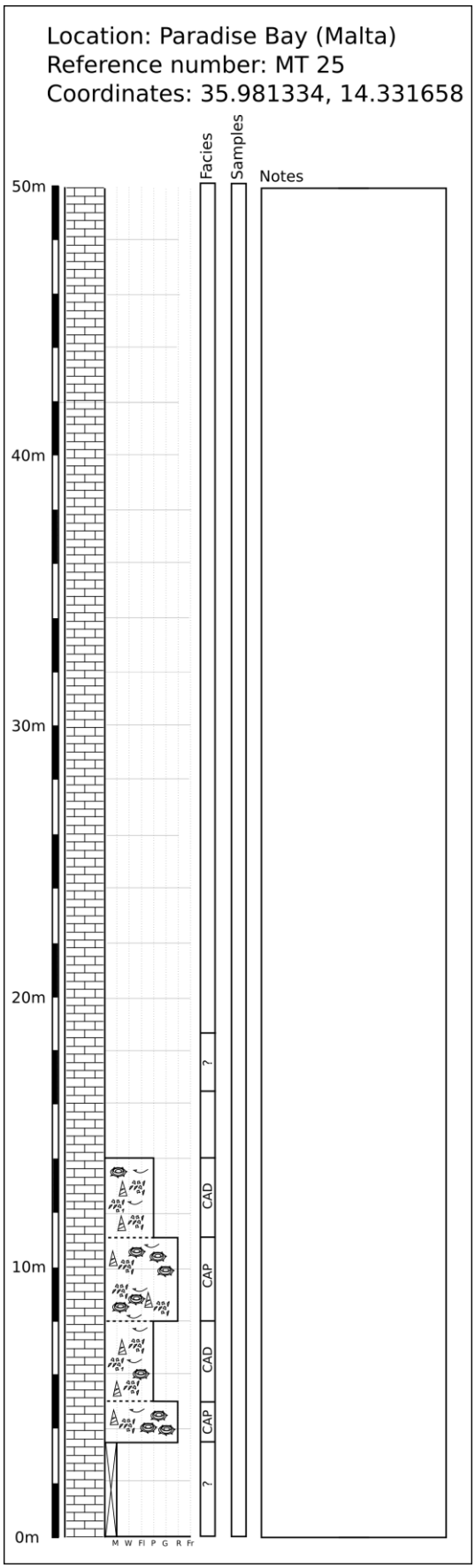
Location: Paradise Bay (Malta)
Reference number: MT 25
Coordinates: 35.981334, 14.331658
Facies
Samples
Notes
50m
40m
30m
20m
10m
0m
?
CAD
CAP
CAD
CAP
?
M W Fl P G R Fr

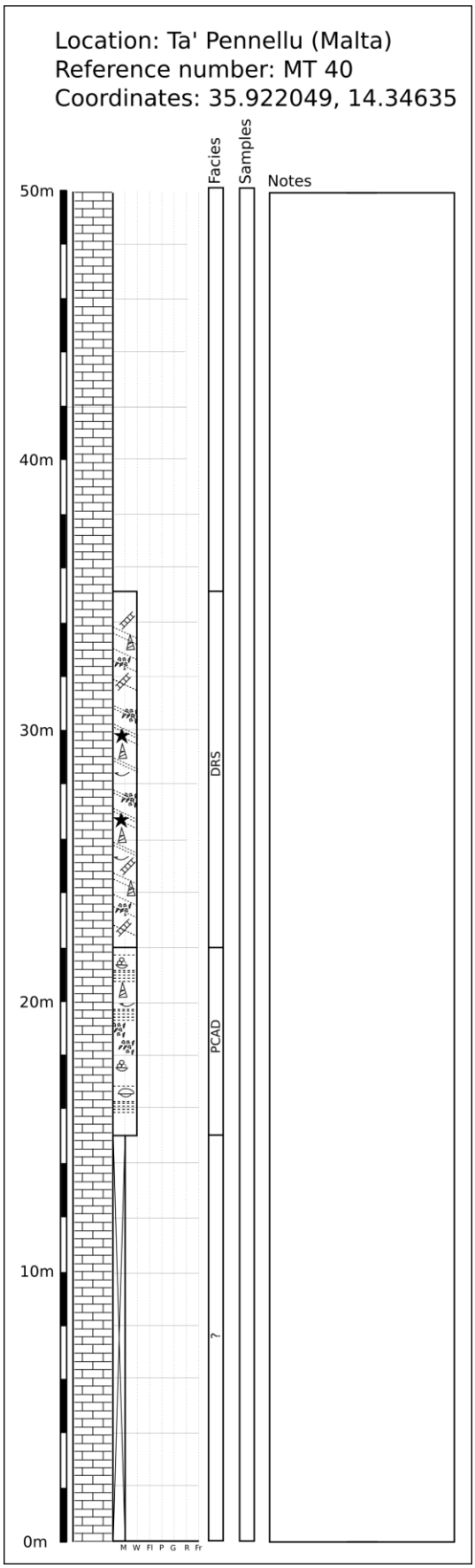
Location: Ta' Pennellu (Malta)
Reference number: MT 40
Coordinates: 35.922049, 14.34635
Facies
Samples
Notes
50m
40m
30m
20m
10m
0m
DRS
PCAD
?
M W Fl P G R Fr

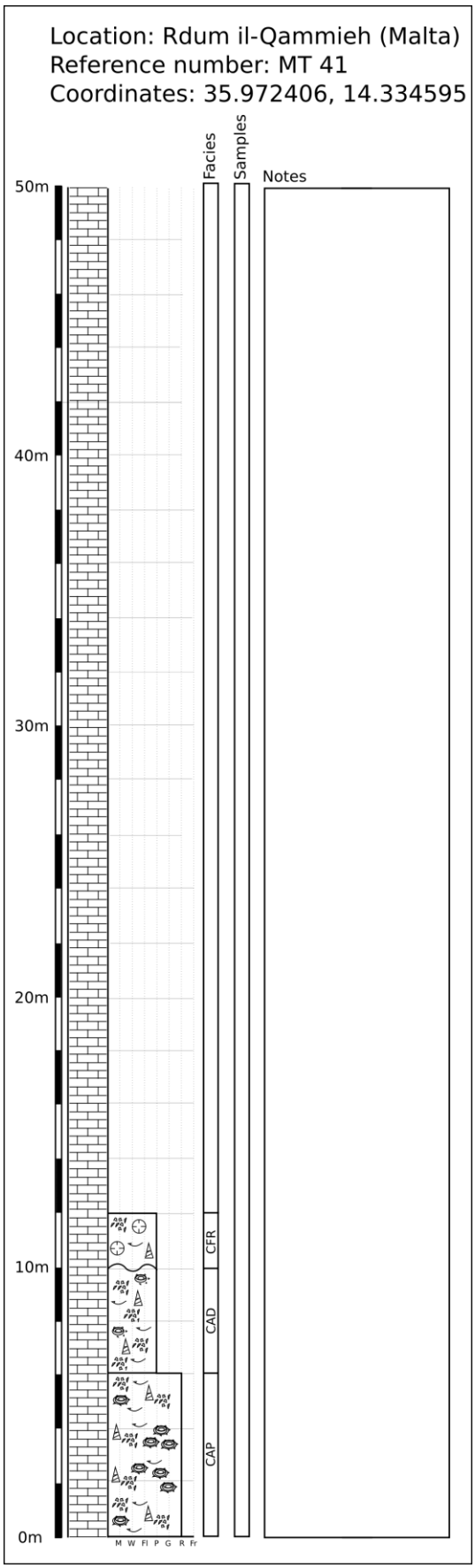
Location: Rdum il-Qammieh (Malta)
Reference number: MT 41
Coordinates: 35.972406, 14.334595
Facies
Samples
Notes
50m
40m
30m
20m
10m
0m
CFR
CAD
CAP
M W Fl P G R Fr

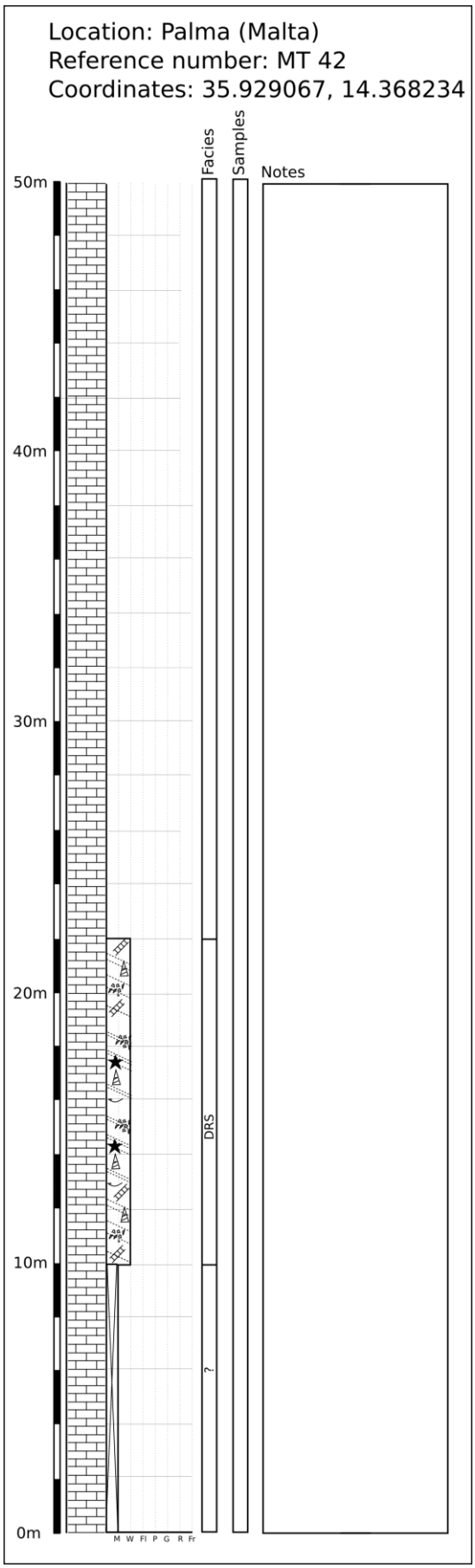
Location: Palma (Malta)
Reference number: MT 42
Coordinates: 35.929067, 14.368234
Facies
Samples
Notes
50m
40m
30m
20m
10m
0m
DRS
?
M W Fl P G R Fr

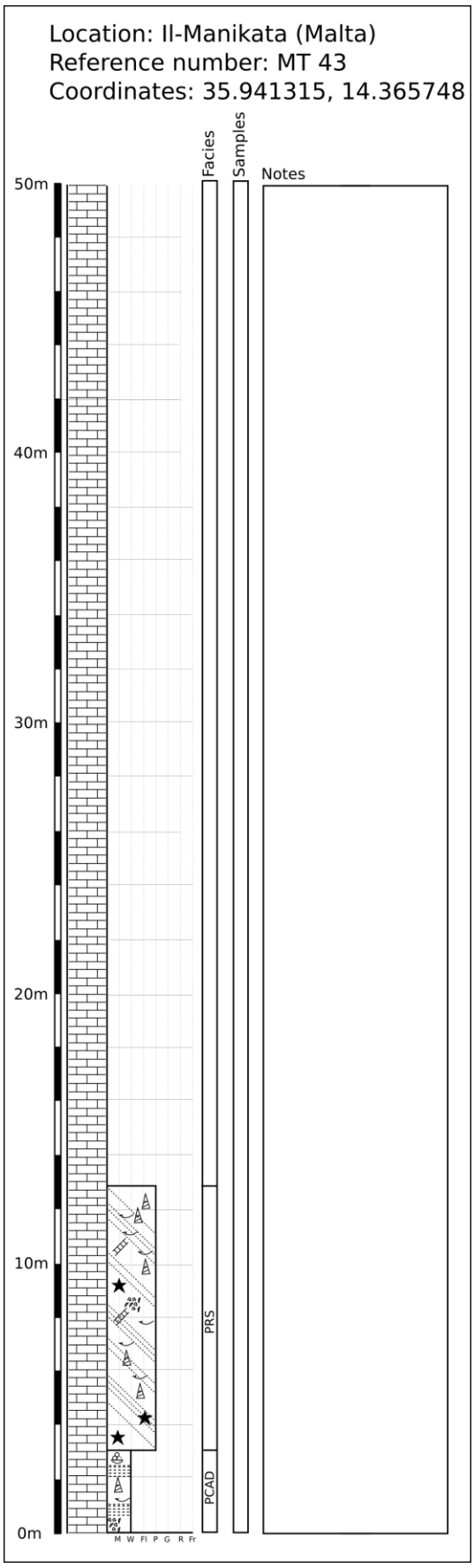
Location: Il-Manikata (Malta)
Reference number: MT 43
Coordinates: 35.941315, 14.365748
Facies
Samples
Notes
50m
40m
30m
20m
10m
0m
PRS
PCAD
M W Fl P G R Fr

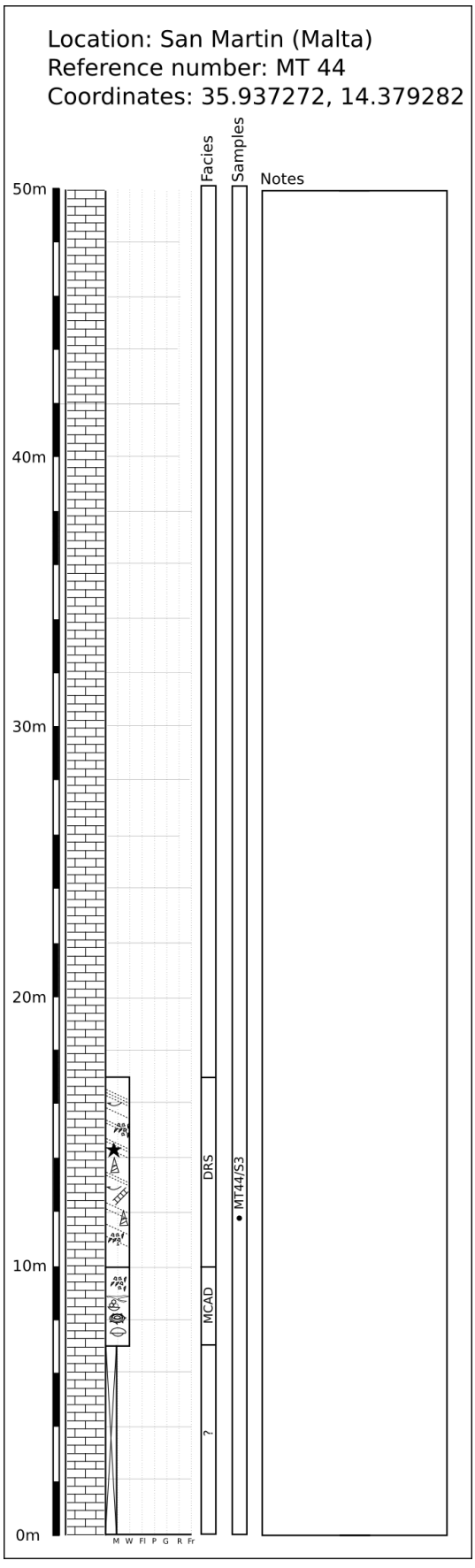
Location: San Martin (Malta)
Reference number: MT 44
Coordinates: 35.937272, 14.379282
Facies
Samples
Notes
50m
40m
30m
20m
10m
0m
DRS
MCAD
?
MT44/S3
M W Fl P G R Fr

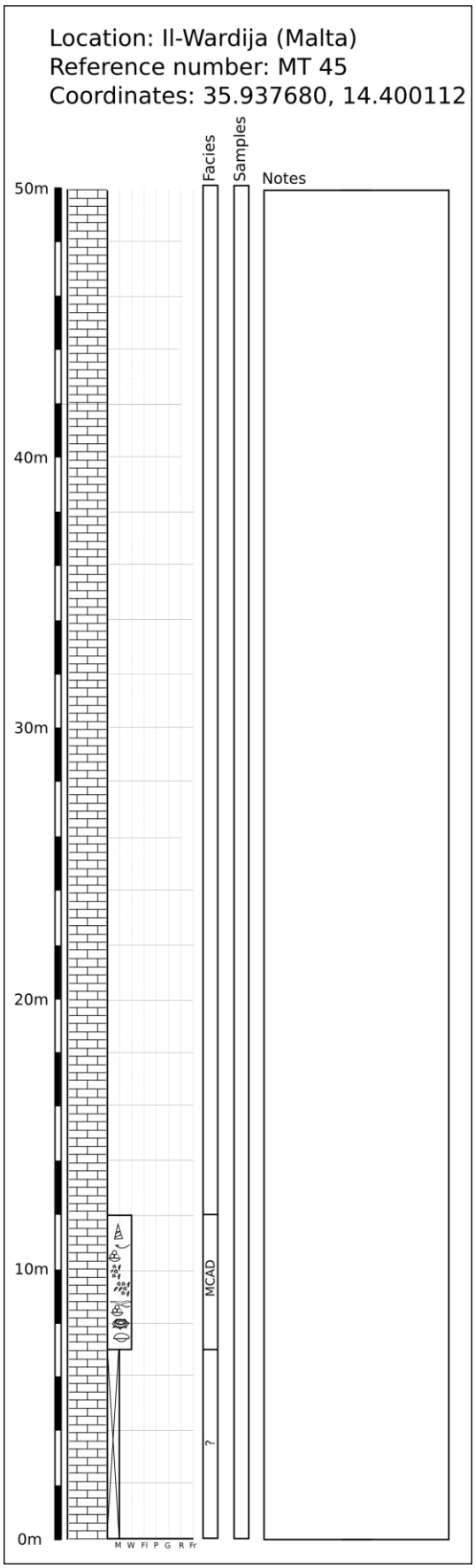
Location: Il-Wardija (Malta)
Reference number: MT 45
Coordinates: 35.937680, 14.400112
Facies
Samples
Notes
50m
40m
30m
20m
10m
0m
MCAD
?
M W Fl P G R Fr

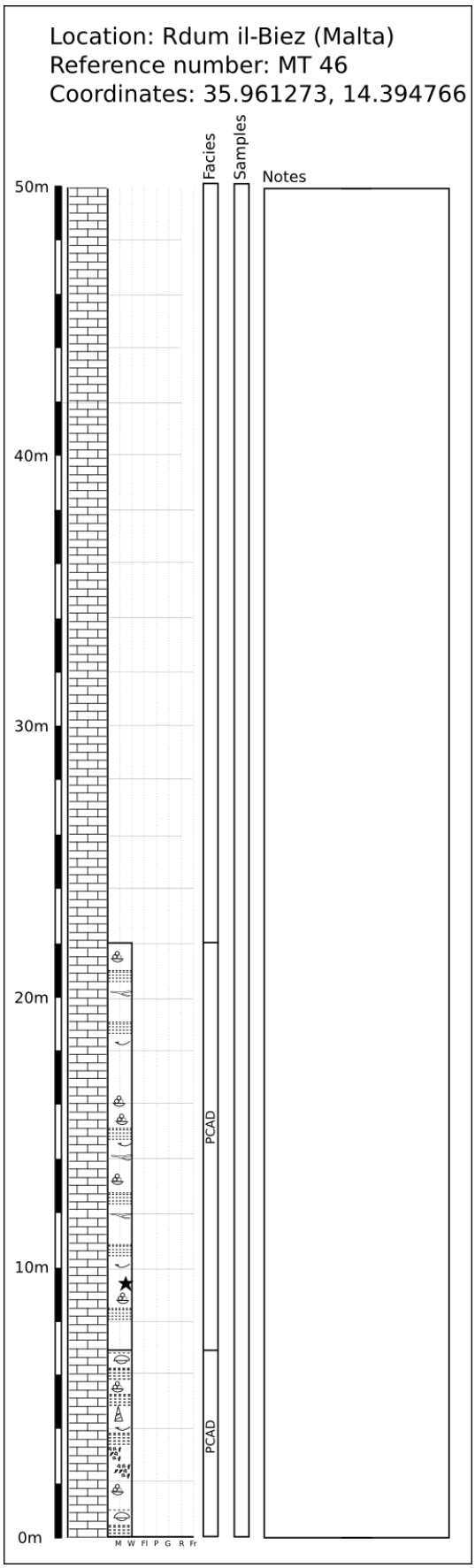
Location: Rdum il-Biez (Malta)
Reference number: MT 46
Coordinates: 35.961273, 14.394766
Facies
Samples
Notes
50m
40m
30m
20m
10m
0m
PCAD
PCAD
M W Fl P G R Fr

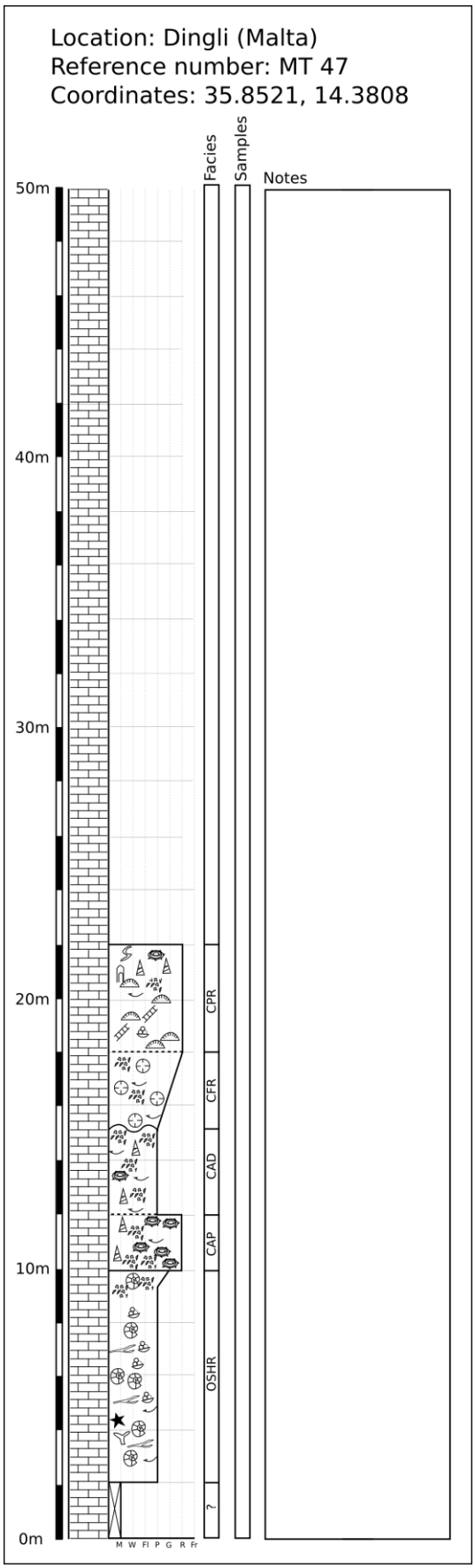
Location: Dingli (Malta)
Reference number: MT 47
Coordinates: 35.8521, 14.3808
Facies
Samples
Notes
50m
40m
30m
20m
10m
0m
CPR
CFR
CAD
CAP
OSHR
?
M W Fl P G R Fr

C1.2. Borehole logs

A systematic comparison of borehole to nearby outcrops (<50 m) carried out in the course of this study has allowed a scheme to be developed that indicates which descriptive terms used in the borehole logs relate to stratigraphic divisions (table 5.2 and table C1.1). This exercise was carried out by comparing 36 outcrop logs to 54 nearby water borehole logs.

Division	Descriptive term in borehole report	Stratigraphic / sedimentological units
Division 0	"Blue plastic clay", "yellow plastic clay"	Blue Clay Formation
Division 1	"Orange glauconite", "green glauconite",	Greensand Formation
Division 2	"Blue marl limestone"	Coralline Algal Matrix Rich Wackestone Facies (CAM)
Division 3.1	"Orange marl", "brown marl"	Open Shelf Heterostegina Rich Packstone Facies (OSHR)
Division 3.2	"Yellow marl", "yellow algal marl"	Coralline algal biostrome Facies Association (except for Coralline Algal Matrix Rich Wackestone Facies), and Massive Coralline Algal Debris Wackestone Facies (MCAD)
Division 4.1	"White chalky limestone", "pink chalky limestone", "cream chalky limestone", "creamy fine grained limestone", "interbedded white limestone and marl bands"	Planar Bedded Coralline Algal Debris Wackestone Facies (PCAD), Off-Reef Shelf Wackestone Facies (ORS) and Distal Reef Slope Mudstone Facies (DRS)
Division 4.2	"Hard white crystalline limestone", "hard pink crystalline limestone",	- Reef-Core FA and Proximal Reef Slope Packstone Facies (PRS)

Table C1.1: Scheme indicating which borehole log descriptive terms relate to which stratigraphic divisions.

Appendix C2: Outcrop-based cross-sections (OCS)

The top of the Blue Clay and Greensand Formation is used as a datum in the cross-sections of the Upper Coralline Limestone Formation. The major faults are shown but their fault throw has been removed so there is no displacement to the top Blue Clay surface.

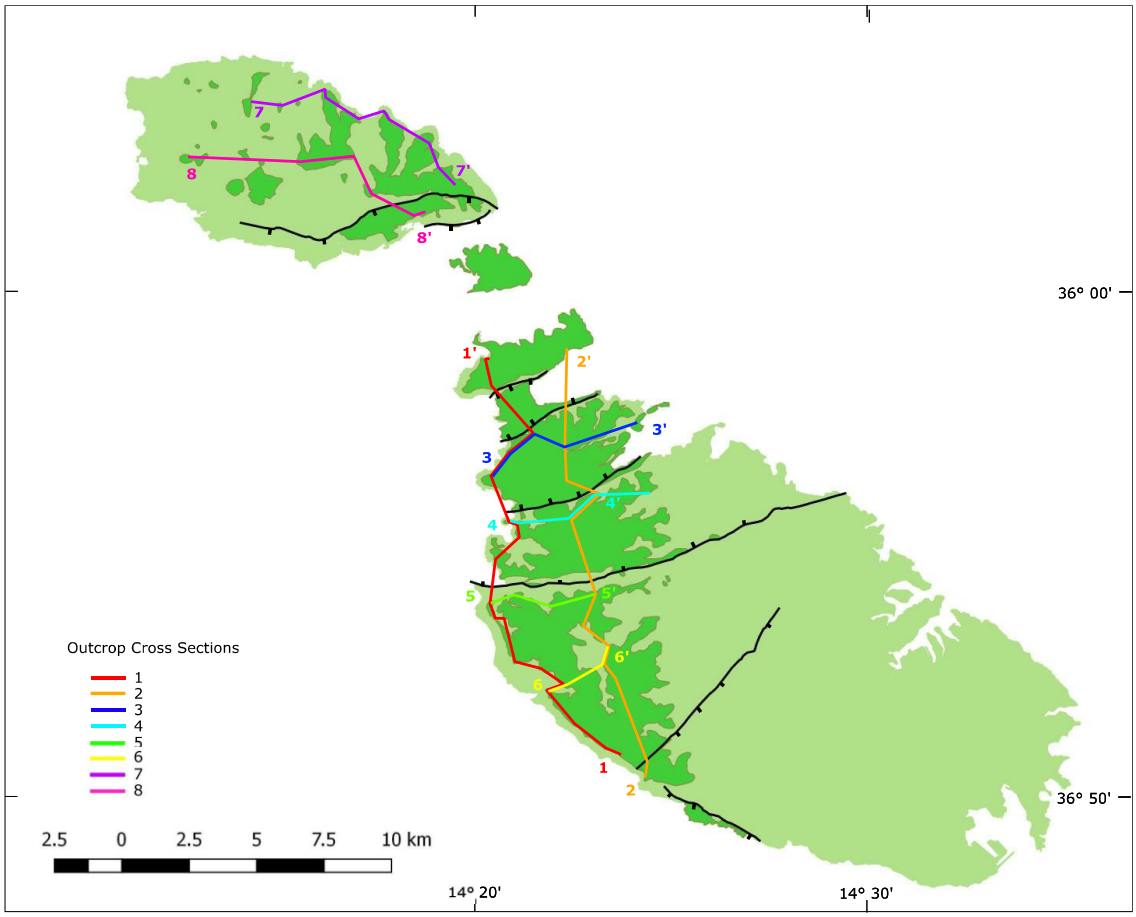

Figure C2.1: Outcrop-based cross-sections (OCS) reference map. Reference numbers (1 to 8) close to sections in map make reference to Outcrop Cross-Section numbers (OCS1 to 8). Base of OCS logs corresponds to top of Blue Clay Formation.

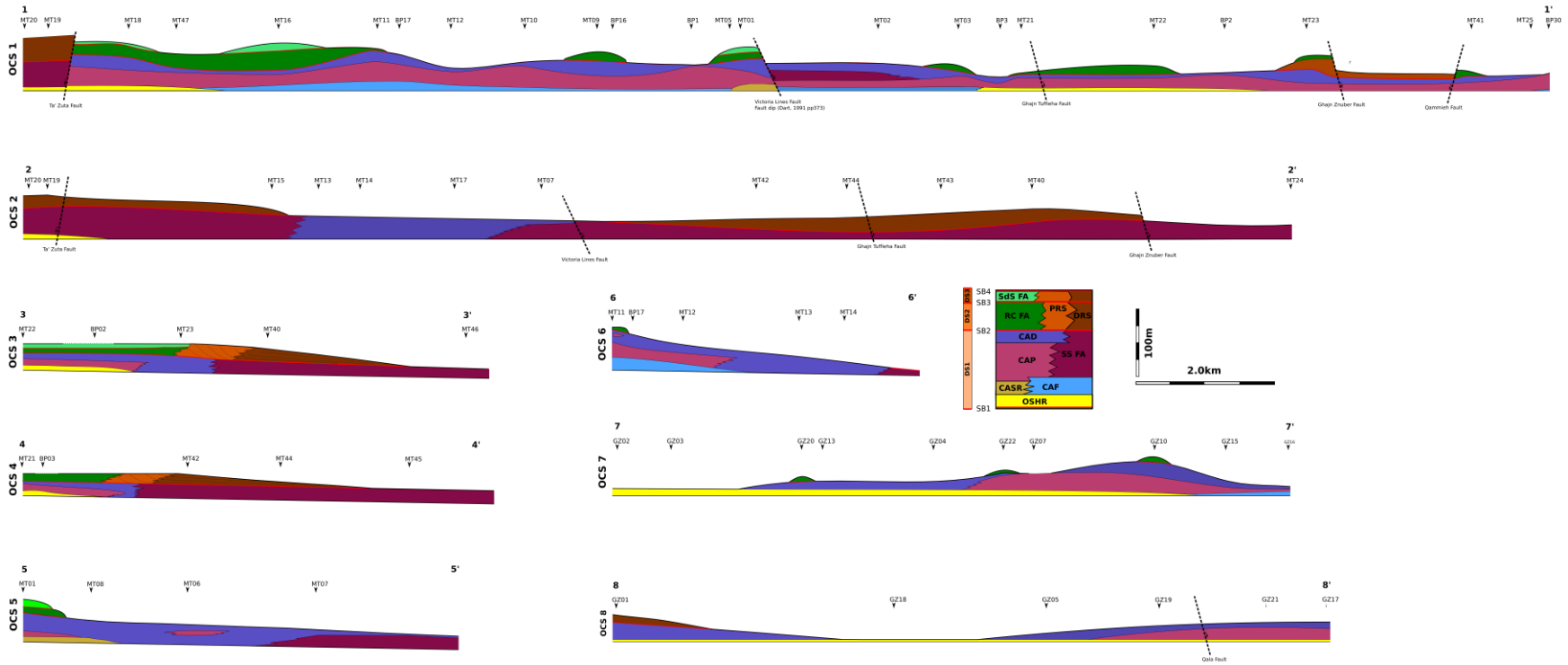

Figure C2.2: Outcrop-based cross-sections (OCS). Base of OCS logs correspond to top of Blue Clay Formation. Fault dips are from Dart, 1991 (pp. 370, 373 and 374). Note: bold black line represents modern day surface, bold red line represents Miocene sequence boundaries.

Appendix C3: Fossil fauna and flora

Fossils identified from literature (Pedley, 1974; Bosence & Pedley, 1982; Dart, 1991; Gatt, 2006) and from investigations carried out in this the course of this study are listed hereunder.

		OSGR Facies (Greensand Fm)	OSHR Facies (Ghajn Melel Member)	Coralline Algal Biostrome FA	MCAD Facies (Gebel Mtarfa Beds)	PCAD Facies (Rdum il-Hmar Beds)	CFR and CPR Facies (Tal-Pictal Beds)	RC Facies (Depiru Beds)
Annelida	*Serpula sp.*			X				
	Rotularia Rotularia			X				
Arthropoda, Crustacea	*Scylla sp.*			X				
	Creusia Costata							X
	Creusia Creusia Rangii							X
	Necronectes				X			
	Necronectes schaferi.	X						
	Callianassa sp.				X			
	Callianassa Pagurus			X				
	Petrochius Priscus			X				X
	Calappa Heberti			X				
	Maja Maja			X				
	Necronectes Schafferi							
Arthropoda, Ostracoda	*Aurila sp.*	X						
	Bairdia sp.	X						
Brachiopoda	*Aphelesia Bipartita*			X	X			
	Terebratula terebratula	X	X	X	X			X
	Terebratulina caputserpentis			X				
	Terebratula Sinuosa			X				
	Terebratula Caput-Serpentis			X				

	Megathiris sp.			X				
	Megathiris Decollata			X	X			X
	Megerlia Truncata				X			
	Maltaia Maltensis			X	X			
	Argyrotheca sp.			X				
	Argyrotheca Cordata			X		X		X
	Mererlia sp.			X				
Bryozoa	*Cellepora sp.*	X		X				
	Cellepora cf. polythele	X						
	Cellaria sp.	X						
	Canda sp.	X						
	Crisia sp.	X						
	Scrupocellaria sp.	X						
	Cellepora mammalata		X					
	Membraniporiform types.	X		X				
	Vinculariform bryozoans		X					
	Calpensia impressa			X				
Chlorophyta, Bryopsidophyceae	*Halimeda sp.*						X	
Chordata	*Carcharias Carcharias*			X	X			
	Syngnathus sp.				X			
	Hemipristis Serra	X						
Chordata, Mammalia	*Phocidae Phoca sp.*	X						
	Cetacea	X	X					
Chordata, Reptilia	*Gaudensis*	X						
Chordata, Vertebrata	*Cretoxyrhina Oxyrhina sp.*	X						
	Odontaspis Odontaspis sp.	X	X					
	Isurus sp.					X		
	Isurus Hastalis	X		X				
	Isurus Desori	X						

	Isurus Retroflexus	X						
	Carcharocles Megalodon	X	X	X				
	Carcharhinues Egertoni	X						
	Negaprion							
	Eurybathrodon	X						
	Myliobatis Stokeri	X						
	Myliobatis Micropleurus	X						
	Myliobatis Myliobatis	X						
	Bregmaceros Albyi	X			X			
	Sparus Cinctus	X						
	Sparus aurata	X						
	Sparus	X						
	Xiphiorhynchus							
	Xiphiorhynchus	X						
	Stereodus Melitensis	X						
	Diodon Scillae	X						
	Stephanophyllia							
Cnidaria, Anthozoa	*Imperialis*							X
	Coenocyathus Adamsi	X						
	Acanthocyathus							
	Hastingsae	X						
	Flabellum Extensum	X						
	Tarbellastraea					X	X	
	Diploastrea ravlini						X	
	Favites sp.						X	
	Acropora sp.						X	
Echinodermata	*Clypeaster altus*	X	X	X	X		X	X
	Clypeaster marginatus	X	X	X				X
	Arbacina Piae			X				
	Echinolampas pignatari	X	X					
	Echinolampas Lucae							X
	Echinolampas wrighti	X			X			X
	Echinolampas							
	Hemisphaerica			X				X
	Echinocyamus Stellatus			X				X
	Echinoneus Echinoneus			X				

	Psammechinus							
	Tortonicus			X				
	Cidaris melitensis			X				
	Echinus duciei			X	X	X		
	Spatangus Delphinus				X			X
	Stylocidaris Melitensis			X	X			X
	Prenaster Excentricus			X	X			X
	Plagiobrissus Imbricatus			X				
	Schizaster eurynotus	X		X	X	X		X
	Schizaster Scillae			X		X		X
	Schizechinus Duciei					X		
	Spatangus sp	X						
	Echinolampas Manzoni	X						
	Brissus Cordieri	X		X				
	Brissus oblongus			X	X	X		
	Eupatagus De Koninckii	X						
	Meoma Latus	X		X				
	Trachypatagus							
	Tuberculatus	X		X				
	Spatangus Pustulosus	X			X			
Foraminifera	*Globigerina sp.*	X						
	Orbulina sp.	X						
	Elphidium sp.	X						
	Heterostegina depressa	X	X					
	Textularia sp.	X						
	Eponides sp.	X						
	Nodosaria sp.	X						
Mollusca, Bivalvia	*Pecten tournali.*	X						
	Pecten cristatum	X						
	Pecten substriatus.	X						
	Pecten senensis		X					
	Pecten Vigolenensis			X	X	X	X	
	Pecten Dunkeri			X	X	X		
	Pecten Revolutus							X
	Pecten Larteti							X
	Pecten Fraterculus							X

	Pecten Haueri							X
	Anadara Turonica				X	X		
	Pleurotoma sp.						X	
	Tapes sp.						X	
	Tapes sallomocensis				X			
	Tapes vetusta	X						
	Glycymeris sp.,		X			X		X
	Ostma digitalia	X					X	
	Spondylus crassicosta	X	X	X				
	Area fichtelii	X						
	Isocardia sp.	X						
	Thracia Thracia					X		
	Thracia (Thracia)							
	pubescens	X		X	X	X		
	Cytherea pedomontana	X						
	Venus sp.						X	
	Venus umbonara	X						
	Venus (Ventricoloidea)							
	multilamella	X						
	Chama pseudounicornis						X	
	Tellina sp.						X	
	Tellina plantata	X				X		
	Carclium hians	X		X		X		
	Loripes incrassata	X			X		X	
	Lucina sp.		X					
	Lucina haidingeri.	X						
	Lucina columbella					X		
	Glycimeris deshayesi	X	X			X	X	
	Pleuromya sp.	X			X			
	Arca sp.,		X		X	X		X
	Arca turonica				X		X	
	Lima sp.						X	
	Lima Squamosa			X				X
	Cardita Calyculata							X
	Glossus Glossus							X
	Dosinia Umbonaria							X
	Pholadomya Pholadomya							X
	Amusium Cristatum var.							X

	Badense							
	Chlamys burdigalensis	X						
	Chlamys multistriatus	X	X		X			
	Chlamys scrabella	X	X	X	X			X
	Chlamys solarium	X	X					X
	Chlamys (Macrochlamis)							
	latissima		X	X	X			X
	Chlamys Squamulosus							X
	Chlamys Pusio			X		X		X
	Chlamys Fasciculata			X				X
	Hinnites Hinnites			X				
	Ostrea virleti	X	X	X				
	Ostrea lamellosa	X						
	Ostren frondosa	X						
	Ostrea edulis var.							
	boblayei	X						
	Ostrea Serrodentata			X				
	Ostrea Boblayei			X				
	Anadara Fichtelii							X
	Lithophaga Lithophaga							X
	Lithophaga Lithodomus							X
	Ostrea Navicularis	X						
	Pinna sp.					X		
	Cardium sp.		X			X	X	
	Cardium Hians	X			X	X		
	Cardium Multicostatum	X				X		
	Lutraria lutraria				X			
	Lutraria Oblonga	X				X		
Mollusca,								
Cephalopoda	*Aturia Aturi*							X
	Sepia Sepulta							X
Mollusca, Gastropoda	*Xenophoria sp.*	X						
	Xenophora Incertissima							X
	Epitonium melitensis	X						
	Conus sp.	X	X				X	
	Conus Betulinoides	X						

	Conus Mercati var Melitensis							X
	Conus Melitosiculus							X
	Cassis Gulia							X
	Galeodea Echinophora							X
	Natica sp.	X						
	Dentalium sp.	X						
	Strombus sp.	X		X			X	
	Aporrhais pespelecani			X				
	Trochus Patulus				X			
	Genota sp.				X			
	Oliva Oliva							X
	Fusinus Iongirostris							X
	Cypraea Fabagina							X
	Turritella sp.		X		X		X	
	Turritella Catherdralis	X						
	Turritella Turris			X				
	Fissurella Fissurella							X
	Haliotis sp.						X	
	Haliotis Tuberculata			X				X
	Cirsotrema Ducei	X						
	Schilderia sp.						X	
	Gibbula sp.						X	
Porifera	*Entobia sp.*			X		X	X	
Rhodophyta	*Lithophyllum rhodolites*			X		X	X	
	Lithoporella sp.						X	
	Dermatolithon cf. nitida						X	
	Mesophyllum sp			X			X	
	Archaeolithothamnion sp.			X			X	
	Lithothamnion sp.						X	
	Corallina sp.						X	

Appendix C4: Oxygen and carbon isotope analysis

Mineralogical stabilization and geochemical changes

The stable isotopic compositions of unstable grains change from a marine to a meteoric signature during mineralogical changes and cementation (Tucker & Wright, 1990). These changes have been observed and documented in numerous studies of Quaternary limestones (e.g. Gross et al., 1969; Allan & Matthews, 1977, 1982; Beier, 1987). The key characteristics are an addition of light carbon (^{12}C) from the soil causes a more negative $\delta^{l3}C$ and the addition of lighter, meteroric-derived ^{16}O develops a more negative $\delta^{18}O$ (Tucker & Wright, 1990). Additional features include the notion that the upper part of the profile - where more organic 'soil' carbon (enriched in ^{12}C) is available - should develop the lightest $\delta^{l3}C$ values. It has been suggested that as a result of a loss of ^{16}O by evaporation, $\delta^{18}0$ values become heavier in the vadose zone (James & Choquette, 1984). Various authors have used these isotope trends to detect palaeoexposure surfaces (Videtich & Matthews, 1980; Allan & Matthews, 1982; Wagner & Matthews, 1982; Beeunas & Knauth, 1985).

Stable Isotope Sampling

Across the sampled interval sample spacing diminishes towards the surface of interest (the suspected palaeoexposure surface/sequence boundary); from 40cm spacing at the base, 20 to 10cm spacing at the middle and 5cm spacing 30 cm below and 20cm above the surface of interest. A drill was used to collect the powdered rock. The rock was drilled approximately 8-10cm into the rock after which the hole, surrounding rock face and drill bit were cleared of powdered rock with compressed air. Drilling was then resumed and 5 grams of powdered rock were collected in silicon containers. The drill bit was cleaned between each sampling. Samples were collected across the available width of the bed, from base to top. In all locations the isotope samples were collected along a continuous vertical line.

Location	Facies	Thickness sampled (m)	No. of Samples	Sample ID
Mellieha MT22	Coralgal fore-reef Facies	0.15	4	MLH 013-016
	Coralline Algal Debris packstone Facies	1.45	12	MLH 001-012
Dingli MT18	Coralgal fore-reef Facies	0.55	6	DNG 015-020
	Coralline Algal Debris packstone Facies	1.90	14	DNG 001-014
Bahrija MT05	Coralgal fore-reef Facies	0.25	5	BHR 016-020
	Coralline Algal Debris packstone Facies	2.25	15	BHR 001-015

Table C4.1: Number and naming of isotope samples collected, which facies they were sampled from and the thicknesses of facies sampled. Sample spacing and sample distribution across the investigated facies is available in stratigraphic logs (Appendix C1).

Methodology: Stable Isotope Analysis: $\delta^{13}C$ and $\delta^{18}O$ Analysis using a Mass Spectrometer

Sample preparation and analysis were performed at Royal Holloway. Carbonates were analysed using the GV Instruments Multiflow prep system on line to an IsoPrime mass spectrometer. Dr. Dave Lowry from Royal Holloway University of London provided details regarding preparation, reaction, analysis and data correction (email on the 23/09/2016).

Preparation

Standards used are NBS-19 and LSVEC international standards and RHBNC internal calcite. Carbonate samples are analysed in batches of 18, plus 6 standards. Between 300 and 400 microgrammes of each pure carbonate is weighed and placed at the bottom of a 7ml Labco Exetainer. Sample weight increases as carbonate content of the analysed material decreases, up to a maximum weight of 4 mg.

Reaction

The hot block is set at 90°C. The auto-run programme of the Gilson auto-sampler flushes each vial in the hot block with helium for 210 seconds at a flow of 90 ml / min to ensure that all air is removed from the vial. Then approximately 0.25ml (5 drops) of orthophosphoric acid is dispensed manually to the first 12 vials. After 90 minutes acid is added to the second 12 vials.

The vials are allowed to equilibrate for an additional 90 minutes, so that all samples have a minimum of 3 hours to fully react and equilibrate.

Analysis

The liberated CO_2 is extracted sequentially from each vial in a flow of helium. The CO_2 peak is then focussed using a GC column and admitted to the Isoprime mass spectrometer. Each analysis takes 4.5 minutes and each sample is analysed twice. A reference gas pulse of known isotopic ratio is injected after each sample peak, which allows the isotopic ratio of the sample relative to the reference gas to be calculated.

Data Correction

Analysed samples give peak heights of between 6 and 8 nano Amps (nA), The reference gas peak height is 5 nA. The peak height of the second sample injection is between 70 and 75% of the size of the first injection. Data are corrected using a calibration based on the known and raw values of the 3 standards used. External precision (1sd) on multiple analyses of the carbonate standards during the sample analysis period is better than ±0.05‰ for $\delta^{13}C$ and ±0.10‰ for $\delta^{18}O$ after scale stretching correction.

Results

Mellieha

Results indicate that $\delta^{13}C$ values become more negative from the base of the sampled interval (MLH1) to the surface of interest (MLH13): from -6.21 $\delta^{13}C$ PDB ‰ to -9.61 $\delta^{13}C$ PDB ‰. The $\delta^{13}C$ values rapidly become more positive from the surface of interest (MLH13) to the top of the sampled interval (MLH16): from -9.61 $\delta^{13}C$ PDB ‰ to -4.92 $\delta^{13}C$ PDB ‰. The most negative $\delta^{13}C$ PDB ‰ value occurs at the surface of interest. These results suggest the addition of light carbon (^{12}C) from soil, which in turn indicates a palaeoexposure surfaces.

Compared to $\delta^{13}C$ results, $\delta^{18}O$ results do not demonstrate as significant shift in values across the studied interval and at the surface of interest. General trends can however be discussed. The basal to middle (MLH1 to 7) portion of the studied interval demonstrates a linear trend of increasingly positive $\delta^{18}O$ values. The three samples immediately below and at the surface of interest (MLH 10 to 13) demonstrate a trend of increasingly negative $\delta^{18}O$ values; $\delta^{18}O$ values at the surface of interest being the most negative (-4.27 $\delta^{18}O$ PDB ‰). $\delta^{18}O$ values become more positive immediately above the surface of interest (-4.09 $\delta^{18}O$ PDB ‰). Isotope trends of $\delta^{18}O$ broadly match those of $\delta^{13}C$ and support the idea that the surface of interest may have been sub-aerially exposed.

Bahrija

Note: a laterally extensive "*brown bed*", interpreted as a palaeosol preserved in karstic features, is observed 20 to 50cm below the surface of interest that is interpreted as an sub-aerial exposure surface.

Results indicate that there are two cycles of $\delta^{13}C$ values; values more negative up-section, peak and subsequently values become more positive. The most negative $\delta^{13}C$ value (BHR4, -6.80 $\delta^{13}C$ PDB ‰) in the first cycle occurs 20cm beneath the "brown bed" (BHR6), then $\delta^{13}C$ values become more positive up to a maximum in BHR8 (-5.64 $\delta^{13}C$ PDB ‰) 20cm above the "brown bed". Following this peak, $\delta^{13}C$ values again become more negative up-section towards the surface of interest (BHR16). The most negative $\delta^{13}C$ values (BHR14, -7.03 $\delta^{13}C$ PDB ‰) occur 10cm below the surface of interest (BHR16). The $\delta^{13}C$ values then become more positive, peaking at -5.55 $\delta^{13}C$ PDB ‰ 5cm above the surface of interest (BHR17).

$\delta^{18}O$ follow the same trends developed by $\delta^{13}C$ values. $\delta^{18}O$ values are at their most negative in BHR4 (-4.37 $\delta^{18}O$ PDB ‰), 20cm below the "brown bed" (BHR6). $\delta^{18}O$ values then become more positive to a maximum in BHR8 (-2.21 $\delta^{18}O$ PDB ‰) 20cm above the "brown bed". $\delta^{18}O$ values then progressively become more negative and are at their lowest at the surface of interest BHR16 (-4.26 $\delta^{18}O$ PDB ‰). $\delta^{18}O$ values become more positive immediately above the surface of interest.

Dingli

Both $\delta^{13}C$ and $\delta^{18}O$ isotopic trends closely match one another. Both $\delta^{13}C$ and $\delta^{18}O$ isotopic trends develop more positive values from the base of the sampled interval (-9.23 $\delta^{13}C$ PDB ‰ and -4.24 $\delta^{18}O$ PDB ‰) and peak at DNG10 (-2.62 $\delta^{13}C$ PDB ‰ and +3.75 $\delta^{18}O$ PDB ‰) 45cm below the surface of interest (DNG18). Following the peak in positive values, both $\delta^{13}C$ and $\delta^{18}O$ isotopic trends become more negative and are at their lowest (-9.22 $\delta^{13}C$ PDB ‰ and -3.99 $\delta^{18}O$ PDB ‰) at the surface of interest (DNG15). The isotopic trends of both $\delta^{13}C$ and $\delta^{18}O$ become more positive up-section of the surface of interest. These results suggest that the isotopic trends developed at the surface of interest may be the result of sub-aerial exposure.

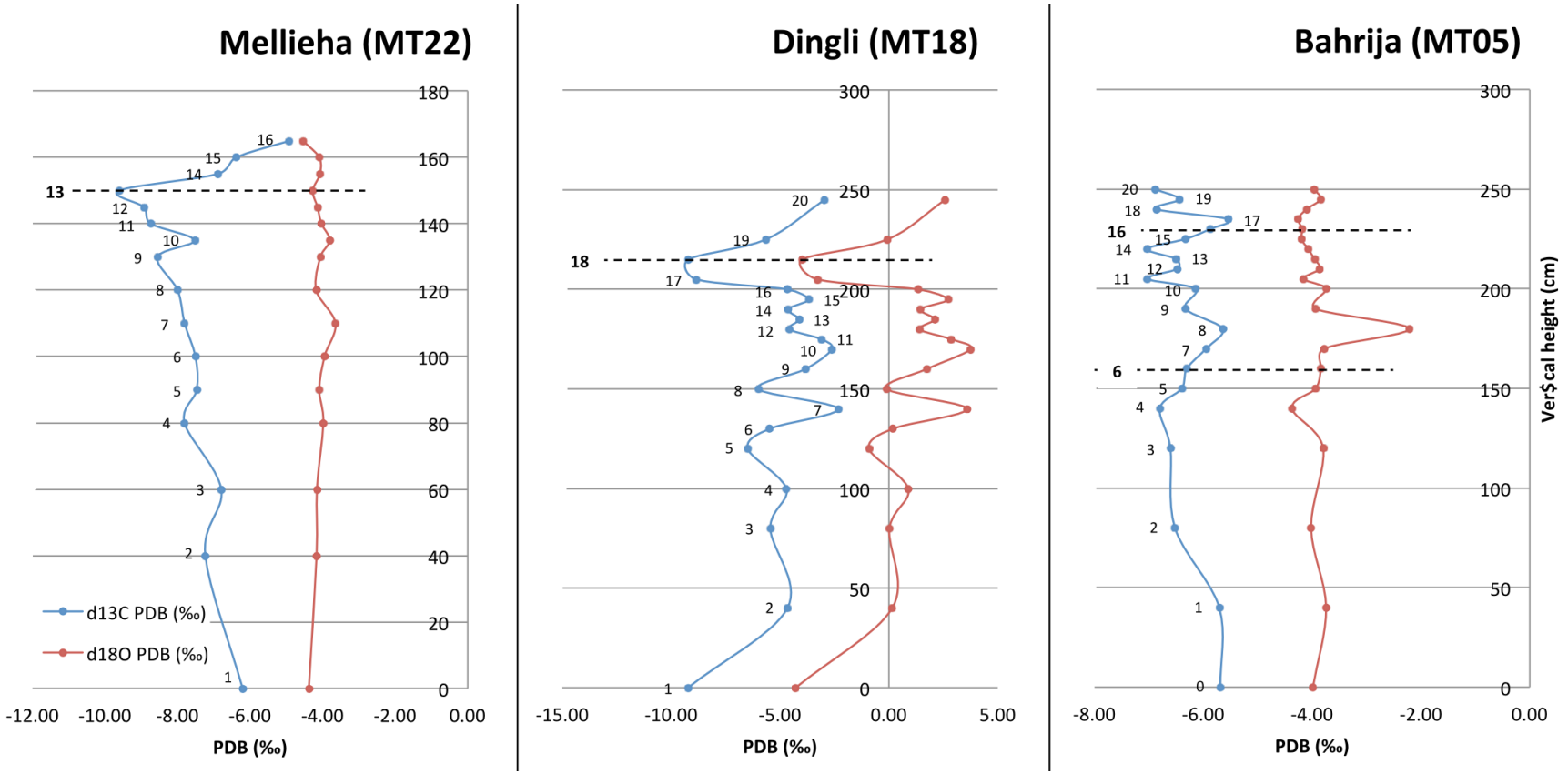

Figure C4.1: Isotope graphs. Note: "Surface" denotes surface of interest – possible subaerial exposure. Mellieha (locality MT22), Bahrija (locality MT05), Dingli (locality MT18). Black dashed lines represent surfaces of interest in the assessed sections. Numbers at the side of blue dots are isotope sample reference numbers – refer to outcrop logs for their positions.

Discussion

The Mellieha section in particular demonstrates $d^{13}C$ and $d^{18}O$ isotopic trends that suggest the surface of interest may have been sub-aerially exposed. The Bahrija section develops two cycles of $d^{13}C$ and $d^{18}O$. Both $d^{13}C$ and $d^{18}O$ isotopic trends closely match one another and develop isotopic signatures that are indicative of palaeoexposure surfaces were developed in both the surface of interest and the associated "brown bed". The isotopic signature supports the interpretation of a "brown bed" palaeosol preserved in karstic features developed during sub-aerial exposure that formed the surface of interest. This isotopic investigation supports field-based evidence (refer to chapter 5 section 5.3.4) that indicate the surface of interest may have been sub-aerially exposed during the late Miocene and may be a regionally extensive sequence boundary.

REFERENCES

Abreu, V.S. & Haddad, G.A. 1998. Glacioeustatic fluctuations: the mechanism linking stable isotope events and sequence stratigraphy from the Early Oligocene to Middle Miocene. In: de Graciansky, P.C., Hardenbol, J., Jacquin, T., Vail, P.R. (Eds.), Mesozoic and Cenozoic Sequence Stratigraphy of European Basins: SEPM Special Publication, 60, 245–259.

Adey, W.H. 1987. Coral reef morphogenesis- a multidimensional model. Science 202, 831-837.

Adey, W.H. & McKibbin, D.L. 1970. Studies on the maerl species *Phymatolithon calcareum* (Pallas) nov. comb. and *Lithothamnium corallioides* Crouan in the Ria de Vigo. Botanica Marina 13: 100–106.

Adey, W. H. & MacIntyre, I. G. 1973. Crustose coralline algae: a reevaluation in the geological sciences. Geol. Soc. Am. Bull. 84:883–904.

Adey, W.H. & Vassar, J.M. 1975. Succession and accretion rates in Caribbean crustose corallines. Phycologia 14, 55–70.

Adey, W.H., Macintyre, I.G. & Stuckenrath, R. 1977. Relict barrier reef system off St. Croix: its implications with respect to Late Cenozoic coral reef development in the western Atlantic. Proc. 3rd Int. Coral Reef Symp. Miami, 2, 15– 21.

Adey, W.H., Townsend, R.A. & Boykins, W.T. 1982. The crustose coralline algae (Rhodophyta: Corallinaceae) of the Hawaiian Islands. Smithson. Contrib. Mar. Sci. 15, 1–74.

Agegian, C.R., Mackenzie, F.T., Tribble, J.S. & Sabine, C. 1988. Carbonate production and flux from a mid-depth bank ecosystem. Penguin Bank, Hawaii, in AGEGIAN C. R. (ed.), Biogeochemical cycling and fluxes between the deep euphotic zone and other oceanic realms. National Undersea Research Program, 88(1), 5-32.

Ahr, W.M. 1973. Carbonate Ramp–Alternative to Shelf Model. American Association of Petroleum Geologists, Bulletin, 57, 1826–1826.

Allan, J.R. & Matthews, R.K. 1977. Carbon and oxygen isotopes as diagenetic and stratigraphic tools: data from surface and subsurface of Barbados, West Indies. Geology 5, 16-20.

Allan, J. & Matthews, R.K. 1982. Isotope signatures associated with early meteoric diagenesis. Sedimentology, 29, 797-817.

Alvaro, M., Barnolas, A., Del Olmo, P., Ramirez del Pozo, J. & Simo, A. 1984. El Neogeno de Mallorca: caracterizacion sedimentologica y bioestratigrafica. Bol. Geol. Min., 95, 3–25.

Argnani, A. 1990. The Strait of Sicily rift zone: Foreland deformation related to the evolution of a back-arc basin. Journal of Geodynamics, 12, 311-331.

Aurell, M., Badenas, B., Bosence, D.W.J. & Waltham, D.A. 1998. Carbonate production and offshore transport on a Late Jurassic carbonate ramp (Kimmeridgian, Iberian basin, NE Spain): evidence from outcrops and computer modeling, in Wright, V.P., and Burchette, T.P., eds., Carbonate Ramps: The Geological Society of London, Special Publication 149,

137-161.

Baker, P.A. & Weber, J.N. 1975. Coral growth rate – variation with depth. Earth Planet Sci Lett, 27, 57–61.

Ballesteros, E. 1994. The deep-water *Peyssonnelia* beds from the Balearic Islands (western Mediterranean). Marine Ecology, 15, 233-253.

Basso, D. 1998. Deep rhodolith distribution in the Pontian Islands, Italy: a model for the paleoecology of a temperate sea. Palaeogeogr, Palaeoclimatol, Palaeoecol, 137, 173-187.

Beavington-Penney, S. J. 2004. Analysis of the effects of abrasion on the test of *Palaeonummulites venosus*: implications for the origin of nummulithoclastic sediments. Palaios, 19, 143-155.

Beeunas, M.A. & Knauth, L.P. 1985. Preserved stable isotopic signature of subaerial diagenesis in the 1.2-b.y. Mescal Limestone, central Arizona. Implications for the timing and development of a terrestrial plant cover. Bull. geo. Soc. Am, 96, 737-745.

Begin, A.B., Ehrlich, A. & Natilan, Y. 1974. Lake Lisan, the Pleistocene precursor of the Dead Sea. Bull. geo!. Surv. Israel 63, 30.

Beier, J.A. 1987. Petrographic and geochemical analysis of caliche profiles in a Bahamian Pleistocene dune. Sedimentology 34, 991-998.

Bennett, R.H., Bryant, W.R. & Keller, G.H. 1979. Clay fabric and related pore geometry of selected submarine sediment: Mississippi Delta. In: 0. Johars (Editor), Scanning Electron Microscopy, I. O'Hare, Ill., 519-524.

Benzoni, F., Basso, D., Caragnano, A. & Rodondi, G. 2011. Hydrolithon spp. (Rhodophyta, Corallinales) overgrow live corals (Cnidaria, Scleractinia) in Yemen. Mar. Biol, 158, 2419– 2428.

Bice, D. 1988. Synthetic stratigraphy of carbonate platform and basin systems: Geology, 16, 703–706.

Bitzer, K. & Salar, R. 2002. SIMSAFADIM: Three dimensional simulation of stratigraphic architecture and facies distribution modelling of carbonate sediments. Computers & Geoscience, 28, 1177-1192.

Bizon, G., Bizon, J.J., Bourrouilh, R. & Massa, D. 1973. Presence aux I lles Baleares (Mediterranee Occidentale) de sediments ‘messiniens’ deposses dans une mer ouverte a salinite normale. CR Acad. Sci. Paris, 277, 985–988.

Blanc, J.J. 1968. Sedimentary geology of the Mediterranean Sea. Oceanogr. Mar. Biol. Annu. Rev, 6, 377-454.

Bonham-Carter, G.F. & Sutherland, A.J. 1968. Mathematical model and FORTRAN IV program for computer simulation of deltaic sedimentation. Computer Contribution, Kansas Geological Survey, 24:56.

Borgomano, J., Lanteaume, C., Ridet, O., Rousseau, M. & Vilasi-Marmier, N. 2014. 3D Stratigraphic Forward Modelling for the Prediction of Carbonate Platform Architectures: Evaluation o Stratigraphic Trap Potential in Middle Eastern Mesozoic Carbonate Sequences. Search and Discover Article 41328(2014).

Bosellini, F.R., 2006. Biotic changes and their control on Oligocene-Miocene reefs: a case study from the Apulia Platform margin (southern Italy). Palaeogeography, Palaeoclimatology, Palaeoecology, 241, 393-409.

Bosellini, F.R. 1989. Dynamics of Tethyan carbonate platforms. In: Crevello, P.D.,Wilson, J.L., Sarg, J.F., Read, F.R. (Eds.), Controls on Carbonate Platform and Basin Development: SEPM Special Publication, 44, 3–13.

Bosence, D.W.J. 1976. Ecological and sedimentological studies on some carbonate sediment-producing organisms, CoGalway, Eire. Unpublished PhD thesis: University of Reading.

Bosence, D.W.J. 1980. Sedimentary facies, production rates and facies models for Recent coralline algal gravels. Geological Journal, 15, 91–111.

Bosence, D.W.J. 1983. The occurrence and ecology of recent rhodoliths. In: Peryt,T.M. (Ed.), Coated grains. Springer-Verlag, Berlin, 225–242.

Bosence, D.W.J. 1985. The morphology and ecology of a mound-building coralline alga *Neogoniolithon strictum* from the Florida Keys. Palaeontology, 28, 189-206.

Bosence, D.W.J. 1989. Biogenic carbonate production in Florida Bay. Bulletin of Marine Sciences, 44, 419-433.

Bosence, D.W.J. 2005. A genetic classification of carbonate platforms based on their basinal and tectonic settings in the Cenozoic. Sedimentary Geology, 175, 49–87.

Bosence, D.W.J. & Pedley, H. M. 1982. Sedimentology and Palaeoecology of a Miocene coralline algal bioherm from the Maltese islands. Palaeogeography, Palaeoclimatology & Palaeoecology, 38, 9-43.

Bosence, D.W.J. & Waltham, D. 1990. Computer modelling the internal architecture of carbonate platforms: Geology, 18, 26–30.

Bosence, D.W.J. & Wilson, J. 2003. Mearl growth, carbonate production rates and accumulation rates in the NE Atlantic. Aquatic conservation, marine and freshwater ecosystems, 13, 23-27.

Bosence, D.W.J., Rowlands, R.J. & Quine, M.L. 1985. Sedimentology and budget of a Recent carbonate mound, Florida Keys. Sedimentology, 32, 317-343.

Bosence, D.W.J., Pomar, L., Waltham, D.A. & Lankester, T.H.G. 1994. Computer modelling a Miocene carbonate platform, Mallorca, Spain. AAPG Bulletin, 78, 247–266.

Bosscher, H. & Schlager, W. 1992. Computer simulations of reef growth: Sedimentology, 39, 503-512.

Bossio, A., Esteban, M., Mazzanti, R., Mazzei, R. & Salvatorini, G. 1996. Rosignano reef

complex (Messinian), Livornesi Mountains, Tuscany, central Italy. In: Franseen, E.K., Esteban, M., Ward, W.C., Rouchy, J.-M. (Eds.), Models for Carbonate Stratigraphy from Miocene Reef Complexes of Mediterranean Regions: SEPM Concepts in Sedimentology and Paleontology, 5, 277–294.

Bowman, S.A. & Vail, P.R. 1999. Interpreting the stratigraphy of the Baltimore Canyon section, offshore New Jersey with Phil a straigraphic simulator. In: Harbaugh, J, W., Watney, W. L., Rankey, E.C., Slingerland, R., Goldstein, R. H., Franseen, E.K. (Eds.), Numerical experiments in stratigraphy: Recent advances in stratigraphic and sedimentologic computer simulations. SEPM Spec. Publ. 62, 117-138.

Boylan, A., Waltham, D.A., Bosence, D.W.J., Badenas, B. & Aurell, M. 2002. Digital rocks: linking forward modelling to carbonate facies. Basin Research, 14, 401–415.

Bracchi, V.A. & Basso, D. 2012. The contribution of calcareous algae to the biogenic carbonates of the continental shelf: Pontian Islands, Tyrrhenian Sea, Italy, in Basso D. and Granier B. (eds), Calcareous algae and global change: from identification to quantification. Geodiversitas, 34, 61-76.

Braga, J.C. & Martin, J.M. 1996. Geometries of reef advance in response to relative sea-level changes in a Messinian (uppermost Miocene) fringing reef (Cariatiz reef, Sorbas Basin, SE Spain). Sed. Geol., 107, 61–81.

Brandano, M. & Corda, L. 2002. Nutrients, sea level and tectonics: constrains for the facies architecture of a Miocene carbonate ramp in central Italy. Terra Nova 14(4), 257-262.

Brownell, W.N. 1977. Reproduction, laboratory culture, and growth of *Strombus gigas*, *S . gostatus* and *S . pugilis* in Los Roques, Venezuela . Bull. Mar. Sci., 27, 668-680.

Buchbinder, B., 1996. Middle and upper Miocene reefs and carbonate platforms in Israel. In: Franseen, E.K., Esteban, M., Ward, W.C., Rouchy, J.-M. (Eds.), Models for Carbonate Stratigraphy from Miocene Reef Complexes of Mediterranean Regions: SEPM Concepts in Sedimentology and Paleontology, Tulsa, 5, 227–237

Burchette, T.P. & Wright, V.P. 1992. Carbonate ramp depositional systems. Sedimentary Geology, 79, 3-57.

Burgess, P.M. 2012. A brief review of developments in stratigraphic forward modelling 2000-2009. In: Roberts, D.G., Bally, A.W., 2012. Regional geology and tectonics: principles of geologic analysis.

Burgess, P.M. & Emery, D.J. 2004. Sensitive dependence, divergence and unpredictable behaviour in a stratigraphic forward model of a carbonate system. In: Curtis, A., Wood, R. (Eds.), Geological Prior Information: Special Publication, 239. Geological Society of London, London, 240.

Burgess, P.M. & Steel, R. 2008. Stratigraphic forward modeling of basin-margin clinoform systems: implications for controls on topset and shelf width and timing of formation of

shelf-edge deltas. In: Recent Advances in Models of Siliciclastic Shallow-Marine Stratigraphy (Ed. by Hampson G.J., Steel R.J., Burgess P.M. & Dalrymple R.W.) SEPM Special Publication, 90, 35–45.

Burgess, P.M. & Prince, G.D. 2015. Non-unique stratal geometries: implications for sequence stratigraphic interpretations. Basin Research, 27, 351-365.

Burgess, P.M., Lammers, H., van Oosterhout, C. & Granjeon, D. 2006. Multivariate sequence stratigraphy: tackling complexity and uncertainty with stratigraphic forward modelling, multiple scenarios and conditional frequency maps. AAPG Bulletin, 90, 1883–1901.

Burne, R.V. & Colwell, I.B. 1982. Temperate carbonate sediments of northern Spencer Gulf, South Australia; a high-salinity 'foramol' province. Sedimentology, 29, 223-238.

Burton, R., Kendall, C.G.St.C. & Lerche, I. 1987. Out of our depth: On the impossibility of fathoming eustasy from the stratigraphic record: Earth-Science Reviews, 24, 237-277.

Buxton, M. & Pedley, H.M. 1989. A standardized model for Tethyan Tertiary carbonate ramps. Journal of the Geological Society of London, 46, 746-748.

Calvo, J.P., Daams, R., Morales, J., Lopez-Martinez, N., Agusti, J., Anadon, P., Armenteros, I., Cabrera, L., Civis, J., Corrochano, A., Diaz-Molina, M., Eliaga, E., Hoyos, M., Martin-Suarez, E., Martinez, J., Moissenet, E., Muñoz, A., Perez-Garcia, A., Perez-Gonzalez, A., Portero, J.M., Robles, F., Santisteban, C., Torres, T., Van der Muelen, A.J., Vera, A. & Mein, P. 1993. Up-to-date Spanish continental Neogene synthesis of the paleoclimatic interpretation. Revista de la Sociedad Geologica España, 6, 29–40.

Camoin, G.F., Colonna, M., Montaggioni, L.F., Casanova, J., Faure, G. & Thomassin, B.A. 1997. Holocene sea level changes and reef development in the southwestern Indian Ocean. Coral Reefs, 16, 247–259.

Canals, M. & Ballesteros, E. 1997. Production of carbonates particles by phytobenthic communities on the Mallorca-Menorca shelf, northwestern Mediterranean Sea. Deep-Sea Research, Part 2, Topical studies in Oceanography, 44(3-4), 611-629.

Carannante, G., Esteban, M., Milliman, J.D. & Simone, L. 1988. Carbonate lithofacies as paleolatitude indicators: problems and limitations. Sedimentary Geology, 60, 333–346.

Carminati, E., Corda, L., Mariotti, G. & Brandano, M. 2007. Tectonic control on the architecture of a Miocene carbonate ramp in the Central Apennines (Italy): Insights from facies and backstripping analyses. Sedimentary Geology, 198, 233–253.

Carvajal, C., Steel, R. & Petter, A. 2009. Sediment supply: the main driver of shelf-margin growth. Earth Science Reviews, 96, 221–248.

Cedric, M.J. & Mutti, M. 2005. Relative control of paleoceanography, climate, and eustasy over heterozoan carbonates: a perspective from slope sediments of the Marion Plateau (ODP LEF 194). Journal of Sedimentary Research, 75(2), 216–230.

Challis, G.R., 1980. Palaeoecology and Taxonomy of Mid-Tertiary Maltese Echinoids. Ph.D. Thesis (unpublished). Department of Geology, Bedford College, University of London, London, 401 pp.

Charvin, K., Gallagher, K., Hampson, G.L. & Labourdette, R. 2009. A Bayesian approach to inverse modelling of stratigraphy, part 1: method. Basin Res. 21, 5–25. Charvin, K., Hampson, G.L., Gallagher, K., Labourdette, R., 2009. A Bayesian approach to inverse modelling of stratigraphy, part 2: Validation tests. Basin Research, 21, 27–45.

Chave, K.E., Smith, S.V. & Roy, K.J. 1972. Carbonate production by coral reefs. Mar Geology, 12, 123- 140.

Chayes, F. 1956. Petrographic modal analysis. New York (Wiley), 113.

Chennouf, R., Ben Moussa, A., El Hajjaji, K., Andr, J.P., Boukli-Hacene, S., Corne, J.J., Mnch, P., Muller, J. & Saint Martin, J.P. 1996. La plateforme messinienne de la bordure NE des Kebdana (Maroc nord-oriental): organisation, dynamique. Geol Mediterranean, 13, 227–234

Chisholm, J.R.M. 2000. Calcification by crustose coralline algae on the northern Great Barrier Reef, Australia. Limnology and Oceanography, 45, 1476-1484.

Chukwu, J.N., Okosun, E.A. & Alkali, Y.B. 2012. Foraminiferal Biostratigraphy and Depositional Environment of Oloibiri-1 Well, Eastern Niger Delta, Nigeria. Journal of Geography and Geology, 4(4), 114-122.

Cita, M.B., Ryan, W.B.F. & Kidd, R.B. 1978. Sedimentation rates in Neogene deep-sea sediments from the Mediterranean and geodynamic implications of their changes. Initial Reports – Deep Sea Drilling Project, 42(A), 991-1002.

Colantoni, P., Cremona, G., Ligi, M., Borsetti , A.M. & Cate, F. 1985. The Adventure Bank (off Southwestern Sicily): a present day example of carbonate shelf sedimentation. Giornali Geologico Serie, 3(47), 165-180.

Collins, M.D., Jones, D., Keddie, R.M., Kroppenstedt, R.M. & Schleifer, K.H. 1983. Classification of some coryneform bacteria in a new genus Aureobacterium. Systematic and Applied Microbiology, 4, 236-252.

Conesa, G. & Babinot, J.F. 1999. Le Messinien inferieur des marges carbonatedddes du bassin de Sorbas (Sud-Est Espagne): organization sedimentaire, microfaunes et paleoenvironnements. Rev Micropaleontol Paris, 42, 255–267.

Conesa. G., Saint Martin, J.P., Cornee, J.J. & Muller, J. 1999. Nouvelles contraintes sur la crise de salinite messinienne par l'etude d'une plate-forme carbonatee marginale (bassin de Sorbas, Espagne). Comptes Rendus 'Acad Sci Paris, 328, 81–87.

Cornée, J.J., Saint Martin, J.P., Conesa, G. & Muller, J. 1994. Geometry, palaeoenvironments, and relative sea-level (accommodation space) changes in the Messinian Murdjadjo carbonate platform (Oran, Western Algeria). Consequences. Sedimentary Geology, 89, 143–158.

Cornée, J.J., Saint-Martin, J., Conesa, G., Andre, J.P., Muller, J. & Benmoussa, A. 1996. Anatomie de quelques plates-formes carbonatees progradantes messiniennes de Mediterranee. Bulletin de la Societe Geologique France, 167, 495–507

Cornée, J.J., Roger, S., Mench, P., Saint Martin, J.P., Feraud, G., Conesa, G. & Pestrea, S. 2002. Messinian events: new constraints from sedimentological investigations and new $^{40}Ar/^{39}Ar$ ages in the Melilla–Nador basin (Morocco). Sedimentary Geology, 151, 127–147.

Cornée, J.J., Saint Martin, J.P., Conesa, G., Mench, P., Andree, J.P., Saint Martin, S. & Roger, R. 2004. Correlations and sequence stratigraphic model for Messinian carbonate platforms of the western and central Mediterranean. International Journal of Earth Sciences (Geologische Rundschau, 93, 621–633.

Costain, L.T.D. 1957-1958. Reports on geological investigations. Government of Malta Water Supply, Malta.

Cross, T.A. 1999. Quantitative dynamic stratigraphy. Prentice Hall, New Jersey, 622

Cross, T.A. & Lessenger, M.A. 1999. Construction and application of stratigraphic inverse model. In: Harbaugh, J.W., Watney, W.L., Rankey, E.C., Slingerland, R., Goldstein, R.H. & Franseen, E.K. (eds.) Numerical Experiments in Stratigraphy: Recent Advances in Stratigraphic and Sedimentologic Computer Simulations, SEPM Special Publication, 62, 69-83.

Cunningham, K.J. & Collins, L.S. 2002. Controls on facies and sequence stratigraphy of an upper Miocene carbonate ramp and platform, Melilla basin, NE Morocco. Sedimentary Geology, 146, 285– 304.

Cunningham, K.J., Farr, M.R. & Rakic-El Bied, K. 1994. Magnetostratigraphic dating of an Upper Miocene shallow marine and continental succession in northeastern Morocco and correlation to regional events. Earth and Planet Science Letters, 127, 77–93.

Cunningham, K.J., Benson, R.H., Rakic-El Bied, K. & McKenna, L.W., 1996. Eustatic implications of late Miocene depositional sequences in the Melilla Basin, northeastern Morocco. Sedimentary Geology, 107, 1–19.

Dart, C.J. 1991. Carbonate sedimentation and extensional tectonics in the Maltese graben system. PhD thesis, University of London.

Dart, C.J., Bosence, D.W.J. & McClay, K.R. 1993. Stratigraphy and structure of the Maltese graben system. Journal of the Geological Society, London, 150, 1153–1166.

Davies, P.J., Marshall, J.F., Hopley, D., 1985. Relationships between reef growth and sea level in the Great Barrier Reef. Proc. Fifth Int. Coral Reef Congress, Tahiti, pp. 95 – 103.

Dinesen, Z.D. 1983. Patterns in the distribution of soft corals across the central Great Barrier Reef. Coral Reefs 1, 229–236.

Done, T.J. 1982. Patterns in the distribution of coral communities across the Great Barrier Reef.

Coral Reefs 1, 95–107.

Duggen, S., Hoernle, K., Wan den Bogaard, P., Rupke, L. & Phipps Morgan, J. 2003. Deep roots of the Messinian salinity crisis. Nature, 422, 602– 606.

Dullo, W.C. 2005. Coral growth and reef growth: a brief review. Facies, 51, 33-48.

Dunham, R.J. 1962. Classification of carbonate rocks according to depositional texture. In Ham, W.E. Classification of carbonate rocks. American Association of Petroleum Geologists Memoire, 1, 108–121.

Dustan, P. 1979. Distribution of zooxanthellae and photosynthetic chloroplast pigments of the reef-building coral Montastrea annularis Ellis and Solander in relation to depth on the West Indian coral reef. Bulletin of Marine Science, 29, 79–95.

Eakin, C.M. 1992. Post-El Niño Panamanian reefs: less accretion, more erosion and damselfish protection. Proceedings 7th International. Coral Reef Symposium, 1, 387–396.

Eakin, C.M. 1996. Where have all the carbonates gone? A model comparison of calcium carbonate budgets before and after the 1982-1983 El Nino at Uva Island in the eastern Pacific. Coral Reefs, 15, 109-119.

Eberli, G.P. & Ginsburg, R.N. 1989, Cenozoic progradation of northwestern Great Bahama Bank, a record of lateral platform growth and sea-level fluctuations, in Crevello, P.D., Wilson, J.L., Sarg, J.F., and Read, J.F., eds., Controls on Carbonate Platform and Basin Development, SEPM, Special Publication, 44, 339–351.

Eberli, G.P., Kendall, C.G.St.C., Moore, P., Whittle, G.L. & Cannon, R. 1994. Testing a seismic interpretation of Great Bahama Bank with a computer model. American Association of Petroleum Geologists, Bulletin, 78, 981–1004.

Eder, W., Briguglio, A. & Hohenegger, J. 2016. Growth of Heterostegina depressa under natural and laboratory conditions. Marine Micropaleontology, 122, 27–43.

Edyvean, R.G.J. & Ford, H. 1987. Growth rates of *Lithophyllum incrustans* (Phil) from S.W.Wales. British Phycological Journal, 22, 139-146.

Eisenhauer, A., Wasserburg, G.J., Chen, J.H., Bonani, G., Collins, L.B., Zhu, Z.R. & Wyrwoll, B.G. 1993. Holocene sea-level determinations relative to the Australian continent: U/Th (TIMS) and14C (AMS) dating of coral cores from the Abrolhos Islands. Earth and Planetary Science Letters, 114, 529–547.

El Haikali, B., Bensoussan, N., Romano, J.C. & Bousquet, V. 2004. Estimación de tasas de fotosíntesis y de calcificación en *Corallina elongata* Ellis y Solander, 1786, a través de medidas de oxígeno disuelto, pH y alcalinidad total. Scientia Marina, 68.

El-Sorogy, A.B.S., Abdelwahab, M., Ziko, A.M., El-Dera, N., Saber, N. & Abu Elkair, N. 2004. Recent bryozoans from southern Safaga Bay, Red Sea Coast. Egyptian Journal of Paleontology, 4, 199-230

Embry, A.F. & Klovan, J.E. 1971. A Late Devonian reef tract on Northeastern Banks Island, NWT: Canadian Petroleum Geology Bulletin, 19, 730-781.

Emmerich, A., Zuehlke, R. & Bechstaedt, T. 2003. Carbonate slope clinoforms from outcrop to numerical model: the growth of the Rosengarten Platform (Middle Triassic, Dolomites, Italy) (abs.). Geological Society of America, Annual Meeting.

Esteban, M. 1996. An overview of the Miocene reefs from the Mediterranean areas: general trends and facies models. In: Models for Carbonate Stratigraphy from Miocene Reef Complexes of Mediterranean Regions (Eds E.K. Franseen, M. Esteban, W.C. Ward and J.M. Rouchy), SEPM Concepts Sedimentology and Paleontology, 5, 3–47.

Fairbanks, R.G. 1989. A 17000-year glacio-eustatic sea-level record: Influence of glacial melting rates on the Younger Dryas event and deep-ocean circulation. Nature, 342, 637–642.

Farrow, G.E., Allen, N.H. & Ekpan, E.B. 1984. Bioclastic carbonate sedimentation on a high-latitude, tide-dominated shelf: northeast Orkney Islands, Scotland. Journal of Sedimentary Petrology, 54, 373–393.

Fazakerley H. & Guiry, M.D. 1998. The distribution of maerl beds around Ireland and their potential for sustainable extraction: phycological section. Report to the Marine Institute, Dublin. National University of Ireland, Galway.

Feldmann, M. & Mckenzie, J.A. 1993, Neogene Stromatolites from Santa Pola, SE-Spain: Strasburg, EUG VII, Abstract supplement n° 1 Terra Nova, 5, 278.

Felix, R. 1973. Oligo-Miocene Stratigraphy of Malta and G020. H. Veenman and Zonen, B.V., Wageningen.

Finetti, I. 1982. Structure, stratigraphy and evolution of the Central Mediterranean Boll. Geofisica Teorica e Applicata, 24(96), 247-312.

Finetti, I. 1984. Geophysical study of the Sicily Channel Zone. Boll. Geofisica Teorica e Applicata, 26(101-102), 3-28.

Flake, G.W. 2000. The Computational Beauty of Nature: Computer Explorations of Fractals. Chaos, Complex Systems, and Adaptation, The MIT Press 514.

Flecker, R., Krijgsman, W., Capella, W., de Castro Martíns, C., Dmitrieva, E., Mayser, J.P., Marzocchi, A., Modestu, S., Ochoa, D., Simon, D., Tulbure, M., van den Berg, B., van der Schee, M., de Lange, G., Ellam, R., Govers, R., Gutjahr, M., Hilgen, F., Kouwenhoven, T., Lofi, J., Meijer, P., Sierro, F.J., Bachiri, N., Barhoun, N., Alami, A.C., Chacon, B., Flores, J.A., Gregory, J., Howard, J., Lunt, D., Ochoa, M., Pancost, R., Vincent, S. & Yousfi, M.Z. 2015. Evolution of the Late Miocene Mediterranean-Atlantic gateways and their impact on regional and global environmental change' Earth-Science Reviews, 150(2154), 365-392. DOI: 10.1016/j.earscirev.2015.08.007.

Flemings, P. & Grotzinger, J. 1996. STRATA: freeware for analyzing classic stratigraphic problems. Geological Society of America, 6(12), 1–7.

Flower, B.P. & Kennett, J.P. 1993. Relations between Monterey Formation deposition and middle Miocene global cooling: Naples Beach section, California: Geology, 21, 877–880.

Flugel, F. 2010. Microfacies of carbonate rocks—analysis, interpretation and application. Springer, Berlin Heidelberg New York.

Follmi, K.B., Weissert, H., Bisping, M. & Funk, H. 1994. Phosphogenesis, carbon-isotope stratigraphy, and carbonate-platform evolution along the Lower Cretaceous northern Tethyan margin. Bulletin of the Geological Society of America, 106, 729-746.

Follows, M.J., Williams, R.G. & Marshall, J.C. 1996. Subduction of carbon in the North Atlantic subtropical gyre. Journal of Marine Research, 54, 605–630.

Frankovich, T.A. & Zieman, J.C. 1994. Total epiphyte and epiphytic carbonate production on *Thalassia testudinum* across Florida Bay. Bulletin of Marine Science, 54, 679–95.

Franseen, E.K. & Mankiewicz, C. 1991. Depositional sequences and correlation of middle (?) to late Miocene carbonate complexes, Las Negras and Nijar areas, southeastern Spain. Sedimentology, 38, 871–898.

Franseen, E.K. & Goldstein, R.H. 1996. Paleoslope, sea-level and climate controls on upper Miocene platform evolution, Las Negras Area, Southeastern Spain. In: Franseen, E.K., Esteban, M., Ward, W.C., Rouchy, J.-M. (Eds.), Models for Carbonate Stratigraphy from Miocene Reef Complexes of Mediterranean Regions: SEPM Concepts in Sedimentology and Paleontology, 5, 159–177.

Franseen, E.K., Goldstein, R.H. & Farr, M.R. 1998. Quantitative controls on location and architecture of carbonate depositional sequences: Upper Miocene, Cabo de Gata region, SE Spain. Journal of Sedimentary Research, 68, 283–298.

Freiwald, A. 1998. Geobiology of *Lophelia pertusa* (Scleractinia) reefs in the North Atlantic. Unpublished Thesis, University of Bremen, Bremen.

Freiwald A. & Henrich, R. 1994. Reefal coralline algal build-ups within the Arctic Circle: morphology and sedimentary dynamics under extreme environmental seasonality. Sedimentology, 41, 963-984.

Freneix, S., Saint Martin, J.P. & Moissette, P. 1988. Huîtres du Messinien d'Oranie (Algérie occidentale) et paléobiologie de l'ensemble de la faune de bivalves. Bulletin du Muséum National d'Histoire Naturelle, 10(4), 1–21.

Froese, R. and D. Pauly (2015). Sparus aurata. Linnaeus, 1758. Gilthead sea bream. World Wide Web electronic publication.

Gacia, E., Duarte, C.M., Marba, N., Terrados, J., Kennedy, H. & Fortes, M.D. 2003. Sediment deposition and production in SE-Asia seagrass meadows. Estuarine, Coastal and Shelf Science, 56, 909– 19.

Gatt, M. 2006. Il-Geologija u l-Paleontologija tal-Gzejjer Maltin (The geology and palaeontology of the Maltese Islands). Pubblikazzjonijiet Indipendenza, Pieta', Malta, 1(1-10), 1–264.

Gatt, P.A. 2012. Carbonate facies, depositional sequences and tectonostratigraphy of the Palaeogene Malta Platform. University of Durham theses, Durham.

Gatt, P.A. & Gluyas, J.G. 2012. Climate controls on facies in Palaeogene Mediterranean subtropical carbonate platforms. EAGE/Geological Society of London, 3(18), 355-367.

Gautier, F., Clauzon, G., Suc, J.P., Cravatte, J. & Violanti, D. 1994. Age et duree de la crise de salinite messinienne. Comptes Rendus Academy of Science Paris, 318, 1103–1109.

Ghiold, J. & Enos, P. 1982. Carbonate production of the coral Diploria labyrinthiformis in south Florida patch reefs. Marine Geology, 45, 281-296.

Gianelli, L. & Salvatorini, G. 1975. I formaminiferi planctonici dei sedimentari terziari del l'Archipelago Maltese 11 Biostratgrafia di (Blue Clay), (Greensand) and (Upper Coralline Limestone). Atti della Societa Toscana di Scienze Naturali, Pisa, Memorie Serie A, 82, 1-24.

Gischler, E. & Hudson, J.H. 2004. Holocene development of the Belize Barrier Reef: Sedimentary Geology, 164, 233-236.

Gladfelter, E.H., Monahan, R.K. & Gladfelter, W.B. 1978. Growth rates of five reef-building corals in the northeastern Caribbean. Bulletin of Marine Science, 28, 728–734.

Glynn, P.W. & Macintyre, I.G. 1977. Growth rate and age of coral reefs on the Pacific coast of Panama. Third International Coral Reef Symposium, Proceedings, Miami, Florida, 2, 252-259.

Glynn, P.W., Wellington, G,M. & Birkeland, C. 1979. Coral reef growth in the Galapagos: limitation by sea urchins. Science, 203, 47-49.

Goldstein, R. H., Franseen, E. K. & Mills, M.S., 1990. Diagenesis associated with subaerial exposure of Miocene strata, southeastern Spain: implications for sea-level change and preservation of low temperature fluid inclusions in calcite cement: Geochimica et Cosmochimica Acta, 54, 699-704.

Gomez-Perez, I., Fernandez-Mendiola, P.A. & Garcia-Mondejar, J. 1999. Depositional architecture of a rimmed carbonate platform (Albian, Gorbea, western Pyrenees): Sedimentology, 46, 337– 356.

Gostin, V.A., Hails, J.R. & Belperio, A.P. 1984. The sedimentary framework of northern Spencer Gulf, Southern Australia. Marine Geology, 61, 111-138.

Gradstein, F.M., Ogg, J.G., Smith, A.G., Bleeker, W. & Lourens, L.J. 2004. A new geologic time scale, with special reference to Precambrian and Neogene. Episodes, 2, 83–100.

Grammer, G. M., Ginsburg, R.N. & Harris, P.M. 1993. Timing of deposition, diagenesis, and failure of steep carbonate slopes in response to a high-amplitude/high-frequency fluctuation in sea level, tongue of the ocean, Bahama's, in R. G. Loucks, and J. F. Sarg, eds., Carbonate sequence stratigraphy: American Association of Petroleum Geologists Memoir, 107-132.

Granjeon, D. & Joseph, P. 1999. Concepts and applications of a 3-D multiple lithology, diffusive model in stratigraphic modeling, in Harbaugh, J.W., Watney, W.L., Rankey, E., Slingerland, R., Goldstein, R., and Franseen, E., eds., Numerical Experiments in Stratigraphy: Recent Advances in Stratigraphic and Sedimentologic Computer Simulations, SEPM, Special Publication, 62, 197-210.

Granjeon, D., Casa, M.C., Eschard, R. & Joseph, P. 2002. Stratigraphic modeling: A new tool to construct 3-D geological models for basin modeling purposes: (abstract). American Association of Petroleum Geologists, Annual Meeting Program, 11, 66.

Grasso, M. & Reuther, C. 1988. The western margin of the Hyblean Plateau (SE Sicily). Dynamics of collisional processes within a neotectonic strike-slip regime. Anna. Tecton. 2(2), 107-120.

Gray, S.C., Hein, J.R., Haumann, R. & Radtke, U. 1992. Geochronology and subsurface stratigraphy of Pukaputa and Rakahanga atolls, Cook Islands; Late Quaternary reef growth and sea level history. Palaeogeography, Palaeoclimatology and Palaeoecology, 91, 377–394.

Griffin, D.L. 2002. Aridity and humidity: two aspects of the late Miocene climate of North Africa and the Mediterranean. Palaeogeography Palaeoclimatology Palaeoecology, 182, 65–91.

Grigg, R.W. 1982. Darwin point: a threshold for atoll formation? Coral Reefs 1, 29-34.

Gross, M.G., Milliman, J.D., Tracey, J.I. & Ladd, H.S. 1969. Marine geology of Kure and Midway Atolls, Hawaii: A preliminary report. Pacific Science, 33, 17-25.

Gutscher, M.A., Malod, J.,Rehault, J.P., Contrucci, I., Klingelhoefer, F., Mendes-Victor, L. & Spakman, W. 2002. Evidence for active subduction beneath Gibraltar. Geology, 30(12), 1071–1074.

Halfar, J. 1999. Warm-temperate to subtropical shallow water carbonates of the southern Gulf of California and geochemistry of rhodoliths. Ph.D. Thesis, Stanford University, USA.

Halfar, J. & Mutti, M. 2005. Global dominance of coralline red-algal facies: A response to Miocene oceanographic events. Geology, 33, 481–484.

Halfar, J., Godinez-Orta, L., Goodfriend, G.A., Mucciarone, D.A., Ingle, J.C. & Holden, J. 2001. Holocene–late Pleistocene non-tropical carbonate sediments and tectonic history of the western rift basin margin of the southern Gulf of California. Sedimentary Geology, 144(1–2), 149–157, 161–178.

Hallock, P. 1981. Production of carbonate sediments by selected large benthic foraminifera on two Pacific coral reefs. Journal of Sedimentary Petrology, 51, 467-474.

Hallock, P. & Schlager, W. 1986. Nutrient excess and the demise of coral reefs and carbonate platforms. Palaios, 1, 389-398.

Hallock, P., Cottey, T.L., Forward, L.B. & Halas, J. 1986. Population biology and sediment production of *Archaias angulatus* (Foraminiferida) in Largo Sound, Florida. Journal of Foraminifer Research, 16, 1-8.

Haq, B.U., Hardenbol, J. & Vail, P.R. 1987. Chronology of fluctuating sea level since the Triassic. Science, 235, 1156–1167.

Haq, B.U., Hardenbol, J. & Vail, P.R. 1988. Mesozoic and Cenozoic chronostratigraphy and cycles of sea-level change, in SeaLevel Changes - An Integrated Approach, eds. C.K. Wilgus, B.S. Hastings, C.A. Ross, H. Posamentier, J. Van Wagoner and C.G.S.C. Kendall: SEPM Special Publication, 42, 71-108.

Hara, U., 2015. Bryozoan internal moulds from the La Meseta Formation (Eocene) of Seymour Island, Antarctic Peninsula. Polish polar research. 36(1), 25–49.

Harbaugh, J.W. & Bonham-Carter, G. 1970. Computer Simulation in Geology. Wiley Interscience, New York, 575.

Harney, J.N. & Fletcher, C.H. 2003. A budget of carbonate framework and sediment production, Kailua Bay, Oahu, Hawaii. Journal of Sedimentary Research, 73, 856-868.

Hart, D.E. & Kench, P.S. 2007. Carbonate production of an emergent reef platform, Warraber Island, Torres Strait, Australia. Coral Reefs, 26(1), 53-68.

Hayton, S., Nelson, C.S. & Hood, S.D. 1995. A skeletal assemblage classification system for non-tropical deposits based on New Zealand Cenozoic limestones. Sedimentary Geology, 100, 123-141.

Hayward, A.B., Robertson, A.H.F., Scoffin, T.P., 1996. Miocene patch reefs from a Mediterranean marginal terrigenous setting in southwest Turkey. In: Franseen, E.K., Esteban, M., Ward, W.C., Rouchy, J.-M. (Eds.), Models for Carbonate Stratigraphy from Miocene Reef Complexes of Mediterranean Regions: SEPM Concepts in Sedimentology and Paleontology, Tulsa, 5, 317–332.

Helland-Hansen, W. & Gjelberg, J.G. 1994. Conceptual basis and variability in sequence stratigraphy: a different perspective. Sedimentary Geology, 92, 31–52.

Helland-Hansen, W. & Martinsen, O.J. 1996. Shoreline trajectories and sequences: description of variable depositional-dip scenarios. Journal of Sedimentary Research, 66, 671.

Henrich, R., Freiwald, A., Betzler, C., Bader, B., Schafer, P., Samtleben, C., Brachert, T.T.C., Wehrmann, A., Zankl, H. & Kuhlmann, D.H.H. 1995. Controls on modern carbonate sedimentation on warm-temperate to Arctic coasts, shelves and seamounts in the Northern Hemisphere: Implications for fossil counterparts. Facies, 32, 71–108.

Hilgen, F., Kuiper, K., Krijgsman, W., Snel, E. & van der Laan, E. 2007. Astronomical tuning as the basis for high resolution chronostratigraphy: the intricate history of the Messinian Salinity Crisis. Stratigraphy, 4(2-3), 231-238.

Hine, A.C., Hallock, P., Harris, M.W., Mullins, H.T., Belknap, D.F. & Jaap, W.C., 1988. *Halimeda* bioherms along an open seaway: Miskito Channel, Nicaraguan Rise, SW Caribbean Sea. Coral Reefs, 6, 173– 178.

Hodell, D.A., Benson, R.H., Kennett, J.P. & Rakic-El Bied, K. 1989. Stable Isotope Stratigraphy of Late Miocene-Early Pliocene Sequences in Northwest Morocco: The Bou Regreg Section. Paleoceanography, 4, 467-482.

Holcová, K. & Zágoršek, K. 2008. Bryozoa, foraminifera and calcareous nannoplankton as environmental proxies of the ‘‘bryozoan event’’ in the Middle Miocene of the Central Paratethys (Czech Republic). Palaeogeography, Palaeoclimatology, Palaeoecology, 267, 216–234.

Hottinger, L. 2006. Illustrated glossary of terms used in foraminiferal research. Notebooks on Geology, Brest, Memoir 2, 83.

House, M.R., Dunham, K.C. & Wigglesworth. J.C. 1961. Geology of the Maltese Islands. In Malta: Background for Development. Bowen-Jones, H., Dewdney J.C. & Fisher, W.B. (Eds.), 24-33. Univ. Durham.

Hsü, K.J., Ryan, W.B.F. & Cita, M.B. 1973. Late Miocene desiccation of the Mediterranean. Nature, 242, 240–244.

Hubbard, J.A.E.B. & Pocock, Y.P. 1972. Sediment rejection by recent scleractinian corals: a key to palaeoenvironmental reconstruction: Geologische Rundschau, v. 161, 598-626.

Hubbard, D.K., Miller, A.I. & Scaturo, D. 1990. Production and cycling of calcium carbonate in shelf-edge reef systems (St Croix, U.S. Virgin Islands): Applications to the nature of reef systems in the fossil record. Journal of Sediment Petrology, 60, 335-360.

Hudson, J.H. 1985. Growth rate and carbonate production in *Halimeda opuntia*: Marquesas Keys, Florida. In: Toomey DF, Nitecki MH (eds) Paleoalgology: contemporary research and applications. Springer-Verlag, Berlin, 257-263.

Huessner, H., Roessler, J., Betzler, C., Petschick, R. & Peinl, M. 2001. Testing 3D computer simulation of carbonate platform growth with REPRO: the Miocene Llucmajor carbonate platform (Mallorca). Palaeogeography, Palaeoclimatology, Palaeoecology, 175, 239–247.

Hughes, O.L. 1987. Quaternary Geology. In: Guidebook to Quaternary Research in Yukon, Morison, S.R. and Smith, C.A.S. (eds.) XII INQUA Congress, Ottawa, Canada. National Research Council of Canada, Ottawa, 12-16.

Husing, S.K., Hilgen, F.J., Aziz, H.A. & Krijgsman, W., 2007. Completing the Neogene geological time scale between 8.5 and 12.5 Ma. Earth Planetary Science Letters, 253, 340–358.

Huston, M. 1985. Variation in coral growth rates with depth at Discovery Bay, Jamaica. Coral Reefs, 4,19-25.

Illes, J. H. 1980. Form and function of graben structures: The Maltese Islands, in Cloos, H., Von Gehlen, K., Illies, J. H., Kuntz, E., Neumann, J., and Seibold, E., eds., Mobile Earth: Berlin, Harald Boldt Verlag Boppard, 161-184.

Iryu, Y., Nakamori, T. Matsuda, S. & Abe, O. 1995. Distribution of marine organisms in the modern reef complex of the Ryukyu Islands and its geological significance. -Sedimentary Geology, 99, 243-258.

Ivanov, D., Ashraf, A.R., Mosbrugger, V. & Palamarev, E. 2002. Palynological evidence for Miocene climate change in the Forecarpathian Basin (Central Paratethys, NW Bulgaria). Palaeogeography Palaeoclimatology Palaeoecology, 178, 19–37.

Jacobs, E., Weissert, H., Shields, G. & Stille, P. 1996. The Monterey event in the Mediterranean: A record from shelf sediments of Malta. Paleoceanography, 11, 717–728.

James, N.P. 1979. Facies models 11. Reefs, in R.G. Walker et., Facies models: Geoscience Canada Reprint Series, 1, 121-132.

James, N.P. 1997. The cool-water carbonate depositional realm. In: James, N.P., Clarke, J. (Eds.), Cool-water Carbonates. SEPM Special Publication, 56, 1-20.

James, N.P. & Ginsburg, R.N. 1979. The seaward margin of Belize barrier and atoll reefs. Spec. Publ. into Assoc. Sedimentology, 3, 191

James, N.P. & Choquette, P.W. 1984. Diagenesis 9. Limestones- the meteoric diagenetic environment. Geoscience Canada, 11,161-194.

James, N.P. & Bone, Y. 1991. Origin of a cool water Oligo-Miocene deep shelf limestone, Eucla -Platform, southern Australia: Sedimentology, 38, 323-341

James, N.P., Collins, L.B. & Bone, Y. 1999. Subtropical carbonates in a temperate realm: Modern sediments on the southwest Australian Shelf. Journal of Sedimentary Research, 69, 1297-1321.

James, N.P., Bone, Y., Brown, K.M. & Cheshire, A. 2009. Calcareous Epiphyte Production in Cool-Water Carbonate Seagrass Depositional Environments — Southern Australia, in Perspectives in Carbonate Geology: A Tribute to the Career of Robert Nathan Ginsburg (eds Swart, P.K., Eberli, G.P., McKenzie, J.A., Jarvis, I. & Stevens, T.), John Wiley & Sons, Ltd, Chichester, West Sussex, UK.

Jervey, M.T. 1988. Quantitative geological modeling of siliciclastic rock sequences and their seismic expression. In: Sea-level changes: an integrated approach (Eds C.K. Wilgus et al.), SEPM Special Publication, 42, 47-69.

Jimenez-Moreno, G., Fauquette, S. & Suc, J.P. 2010. Miocene to Pliocene vegetation reconstruction and climate estimates in the Iberian Peninsula from pollen data. Review of Palaeobotany and Palynology, 162, 403–415.

Johansen, H. W. 1981. Coralline Algae, A First Synthesis. CRC Press, Boca Raton, Florida, 239.

Jongsma, D., Van Hinte, J. E. & Woodside, J. M. 1985. Geologic structure and neotectonics of the north African continental margin south of Sicily. Marine and Petroleum Geology, 2, 156-177.

Jongsma, D., Woodside, J.M., King, G.C.P. & Vanhinte, J.E. 1987. The Medina wrench: A key to the understanding to the kinematics of the central and eastern Mediterranean over the past 5 Ma. Earth and Planetary Science Letters, 82, 87-106.

Kenter, J.A.M. 1990. Carbonate platform flanks, slope angle and sediment fabric. Sedimentology, 37, 777-794.

Kenter, J.A.M. & Compbell, A.E. 1991. Sedimentation on a Lower Jurassic carbonate platform flank, geometry, sediment fabric and related depositional structures (Djebel Bou Dahar, High Atlas, Morocco). Sedimentary Geology, 72, 1-34.

Kenyon, P.M. & Turcotte, D.L. 1985. Morphology of a delta prograding by bulk sediment transport. Geological Society of America, Bulletin, 96, 1457-1465.

Kinsey, D.W. 1978. Productivity and calcification estimates using slack-water periods and field enclosures. In: D.R. Stoddart and R.E. Johannes (Editors), Coral reefs: research methods. UNESCO, 439-468.

Kinsey, D.W. 1981. The Pacific/Atlantic reef growth controversy. Proc. 4th International Symposium Coral Reefs, Manila, 1, 493-498.

Kinsey, D.W. 1985. Metabolism, calcification and carbon production. I. System level studies. Proceedings of the 5th International Coral Reef Symposium, 4, 505-526.

Koerschner, W.F. & Read, J.F. 1989. Field and modelling studies of Cambrian carbonate cycles, Virginia Appalachians: Journal of Sedimentary Petrology, 59, 654-687.

Köhler, C.M., Heslop, D., Dekkers, M.J., Krijgsman, W., van Hinsbergen, D.J.J. & von Dobeneck, T., 2008. Tracking provenance changes during the late Miocene in the Eastern Mediterranean Metochia section using geochemical and environmental magnetic proxies. Geochemistry, Geophysics, Geosystems, 9.

Kominz, M. A., Browning, J.V., Miller, K.G., Sugarman, P.J., Mizintseva, S. & Scotese, C.R. 2008. Late Cretaceous to Miocene sea-level estimates from the New Jersey and Delaware coastal plain coreholes: An error analysis, Basin Research, 20, 211 –226, doi:10.1111/j.1365-2117.2008.00354.x.

Krijgsman, W., Hilgen, F.J., Raffi, I., Sierro, F.J. & Wilson, D.S. 1999. Chronology, causes and progression of the Mediterranean salinity crisis. Nature, 400, 652-655.

Krijgsman, W., Fortuin, A.R., Hilgen, F.J. & Sierro, F.J. 2001. Astrochronology for the Messinian Sorbas basin (South East Spain) and orbital (precessional) forcing for evaporite cyclicity. Sedimentary Geology, 140, 43–60.

Ku, T.L. & Broecker, W.S. 1965. Rates of sedimentation in the Arctic ocean. Progress in Oceanography, 4, 95-104.

Ku Shafie, K.R. & Madon, M. 2008. A review of stratigraphic simulation techniques and their applications in sequence stratigraphy and basin analysis. Bulletin of the Geological Society of Malaysia, 54, 81-89.

Laborel, J. 1961. La constru ctionnment algal 'coralligene' et son importance geomorphologique en Mediterrante. Rec. Trav. Stn. mar. Endoume, 37, 37-60.

Lacour, D., Nraudeau, D., Saint Martin, J.P., Lauriat-Rage, A. & Goubert, E. 2000. Paleoecologie des associations de bivalves du Messinien du bassin de Sorbas (SE Espagne). Geodiversitas, 23, 641–657.

Land, L.S. 1970. Carbonate mud: production by epibiont growth on Thalassia testudinum. Journal of Sedimentary Petrology, 40, 1361-1363.

Land, L.S. 1979. The fate of reef-derived sediment on the north Jamaican island slope. Marine Geology, 29, 55– 71.

Landon, S.M. 1975. Environmental controls on growth rates in hermatypic corals from the lower Florida Keys. MS thesis. State Univ New York, Binghamton.

Langer, M.R., Silk, M.T. & Lipps, J.H. 1997. Global ocean carbonate and carbon dioxide production: The role of reef foraminifera. Journal of Foraminifer Research, 27, 271-277.

LaRiviere, J., Ravelo, A.C., Crimmins, A., Dekens, P.S., Ford, H.L., Lyle, M. & Wara, M.W. 2012. Late Miocene decoupling of oceanic warmth and atmospheric carbon dioxide forcing. Nature, 486, 97–100.

Lawrence, D.T., Doyle, M. & Aigner, T. 1990. Stratigraphic simulation of sedimentary basins: Concepts and calibration. American Association of Petroleum Geologists, 74, 273–295.

Lees, A. 1975. Possible influence of salinity and temperature on modern shelf carbonate sedimentation. Marine Geology, 19, 159-198.

Lees, A. & Buller, A.T. 1972. Modern temperate-water and warm-water self carbonate sediments contrasted. Marine Geology, 13, 67-73.

Lehr, J.H. 1990. The scientific process-part 1: do we understand it? Groundwater, 28(5), 658-663.

Lesser, M.P. & Farrell, J.H. 2004. Exposure to solar radiation increases damage to both host tissues and algal symbionts of corals during thermal stress. Coral Reefs, 23, 367–377.

Liddell, W.D., Ohlhorst, S.L. & Boss, S.K. 1988. The significance of Halimeda as a space-occupier and sediment-producer, 1-750m, North Jamaica. Proceedings of the Sixth International Coral Reef Symposium, Townsville, Australia, 3, 127-132.

Lighty, R.G., Macintyre, I.G. & Stukenrath, R. 1978. Submerged early Holocene barrier reef, southeast Florida shelf. Nature, 175, 59–60.

Litter, M.M. & Doty, M. 1975. Ecological components structuring the seaward edges of tropical Pacific reefs: the distribution, communities and productivity-ecology of Porolithon. Journal of Ecology, 63, 117-29.

Longman, M. 1981. Carbonate Diagenesis as a Control on Stratigraphic Traps, Presented at AAPG Fall Education Conference, Calgary, Canada.

Lourens, L.J., Sluijs, A., Kroon, D., Zachos, J.C., Thomas, E., Rohl, U., Bowles, J. & Raffi, I. 2005. Astronomical pacing of late Palaeocene to early Eocene global warming events. Nature, 435, 1083–1087.

Macintyre, I.G. & Glynn, P.W. 1976. Evolution of modern Caribbean fringing reef, Galeta Point, Panama. American Association of Petroleum Geologists, 60, 1054–1072.

Macintyre, I.G., Burke, R.B. & Stuckenrath, R. 1977. Thickest recorded Holocene reef section, Isla Perez core, Alacran Reef, Mexico. Geology, 5, 749–754.

Maldonado, A. & Stanley, D.J. 1976. Late Quaternary sedimentation and stratigraphy in the Strait of Sicily. Smithsonian Contributions to the Earth Sciences, 16.

Mankiewicz, C. 1987. Sedimentology and calcareous algal palaeoecology of middle to upper Miocene reef complexes near Fortuna (Murcia Province) and Nı´jar (Almerı´a Province) south-eastern Spain. PhD thesis, Univ. of Wisconsin, Madison, 341.

Mankiewicz, C. 1996. The Middle to Upper Miocene Carbonate Complex of Nıjar, Almerı´a province, Southeastern Spain. In: Models for Carbonate Stratigraphy from Miocene Reef Complexes of Mediterranean Regions (Eds E.K. Franseen, M. Esteban, W.C. Ward and J. M. Rouchy), SEPM Concepts Sedimentology and Paleontology, 5, 141–157.

Manzi, V., Gennari, R., Hilgen, F., Krijgsman, W., Lugli, S., Roveri, M. & Sierro, F.J. 2013. Age refinement of the Messinian salinity crisis onset in the Mediterranean. Terra Nova 25(4), 315–322.

Martin, J.M. & Braga, J.C. 1993. Discussion (of Franseen E. K., Mankiewicz C., (1991) Depositional sequences and correlation of Middle (?) to Late Miocene carbonate complexes, Las Negras and Níjar areas, southeastern Spain). Sedimentology,

Martin, S. & Gattuso, J.P. 2009. Response of Mediterranean coralline algae to ocean acidification and elevated temperature. Global Change Biology, 15, 2089-2100.

Martin, S., Castets, M.D. and Clavier, J. 2006. Primary production, respiration and calcification of the temperate free-living coralline alga Lithothamnion corallioides. Aquatic Botany, 85, 121-128.

Martin, S., Clavier, J., Chauvaud, L. & Thouzeau, G. 2007. Community metabolism in temperate maërl beds. I Carbon and carbonate fluxes. Marine Ecology Progress Series 335, 31-41.

Masse, J.P. & Masse, M.F. 2006. Carbonate production by rudist bivalves. The record of Late Barremian requieniid communities from Provence (SE France). Palaeogeography, Palaeoclimatology, Palaeoecology 234, 239-257.

Matsuda, S. 1989. Succession and growth rates of encrusting crustose coralline algae (Rhodophyta, Cyptonemiales) in the upper fore-reef environment off Ishigaki Island, Ryukyu Islands. Coral Reefs, 7, 185-195.

Matsuda, S. & Iryu, Y. 2011. Rhodoliths from deep fore-reef to shelf areas around Okinawa-jima, Ryukyu Islands, Japan. Marine Geology, 282, 215-230.

Maurer, F. & Rettori, R. 2002. Middle Triassic Foraminifera for the Seceda core (Dolomites, northern Italy). Rivista Italiana di Paleontologia e Stratigrafia, 108(3), 391-8.

McConnaughey, T.A. & Whelan, J.F. 1997. Calcification generates protons for nutrient and bicarbonate uptake. Earth-Science Reviews, 42, 95–117.

Meijer, P.Th., Slingerland, R. & Wortel, M.J.R. 2004. Tectonic control on past circulation of the Mediterranean Sea: A model study of the Late Miocene. Paleoceanography, 19, 10-26.

Meijer, X.D. 2002. Modelling the drainage evolution of a river-shelf system forced by Quaternary glacio-eustasy. Basin Research, 14, 361–377.

Miall, A. 1992. Exxon global cycle chart: an event for every occasion? Geology, 20, 787-790.

Miall, A.D. 1997. The geology of stratigraphic sequences. Springer, 421.

Miller, K.G., Kominz, M.A., Browning, J.V., Wright, J.D., Mountain, G.S., Katz, M.E., Sugarman, P.J., Cramer, B.S., Christie-Blick, N. & Pekar, S.F. 2005. The Phanerozoic record of global sea-level change. Science, 310, 1293–1298.

Mitchell, S.F., Paul, C.R.C. & Gale, A.S. 1996. Carbon isotopes and sequence stratigraphy. In: Howell, J.A. & Aitken J.F. (eds.): High Resolution Sequence Stratigraphy: Innovation and Application. Geological Society Special Publication, 104, 11-24.

Montgomery, P., Farr, M.R., Franseen, E.K. & Goldstein, R.H. 2001. Constraining controls on carbonate sequences with high resolution chronostratigraphy: Upper Miocene, Cabo de Gata region, SE Spain. Palaeogeography, Palaeoclimatology, Palaeoecology, 176, 11–45.

Moore, H.B. 1972. Carbonate production on seaquarium flats. Marine Biology, 17, 120–132.

Mudelsee, M. & Raymo, M.E. 2005. Slow dynamics of the Northern Hemisphere glaciation. Paleoceanography, 20.

Mudelsee, M., Bickert, T., Lear, C.H. & Lohmann G. 2014. Cenozoic climate changes: A review based on time series analysis of marine benthic δ18O records, Reviews of Geophysics, 52, 333–374.

Muller, P.H. 1974. Sediment production and population biology of the benthic foraminifer Amphistegina madagascariensis. Limnology and Oceanography, 19, 802-809.

Muller, P.H. 1976. Sediment production by shallow-water, benthic foraminifera at selected sites on Oahu, Hawaii. Maritime Sediments Special Publication, 1, 263-265.

Multer, H.G. 1988. Growth rate, ultrastructure, and sediment contribution of *Halimeda incrassata* and *Halimeda monile*, Nonsuch and Flatmouth Bays, Antigua, W.I. Coral Reefs, 45, 763-786.

Münch, P., Roger, S., Martín, J.J., Saint Martin, J.P., Feraud, G. & BenMoussa, A. 2001. Restriction of the sea water exchanges between the Atlantic and the Mediterranean during the Messinian: contribution of the tephrochronology of the Melilla–Nadorarea (northe astern Rif, Morocco). Comptes Rendus de l'Academie des Sciences. Fasciculea-Sci. Terre Planetes, 332(9), 569–576.

Münch, P., Furaud, G., Cornee, J.J., Saint Martin, J.P., Saint Martin, S., Conesa, G., Garcia, F. & Roger, S. 2003. High precision 40Ar/39Ar dating of paleontologic, sedimentologic and paleoceanographic key events within a Messinian carbonate complex (Melilla, Morocco). Edinburgh Geological Society Congress, abstract.

Muto, T., Steel, R. & Swenson, J. 2007. Autostratigraphy: a framework norm for genetic stratigraphy. Journal of Sedimentary Research, 77, 2–12.

Mutti, M. & Hallock, P. 2003. Carbonate systems along nutrient and temperature gradients: some sedimentological and geochemical constraints. International Journal of Earth Sciences, 92(4), 465–475.

Mutti, E., Tinterri, R., Benevelli, G., Di Biase, D. & Cavanna, G. 2003. Delatic, mixed and turbidite sedimentation of ancient foreland basins: Marine and Petroleum Geology, 20, 733-755.

Nelson, D.M. 1988. Biogenic silica and carbon accumulation in the Bransfield Strati, Antarctica, Unpublished MSc thesis, Norther Carolina State University, USA.

Nelsen, J.E. & Ginsburg, R.N. 1986. Calcium carbonate production by epibionts on *Thalassia* in Florida Bay. Journal of Sedimentary Petrology, 56, 622-628.

Neumann, A.C. & Land, L.S. 1975. Lime mud deposition and calcareous algae in the Bight of Abaco, Bahamas. Journal of Sedimentary Petrology, 45, 763-786.

Nobes, K., Uthicke, S. & Henderson, R. 2008. Is light limiting factor for the distribution of benthic symbiont bearing foraminfera on the Great Barrier Reef? Journal of Experimental Marine Biology and Ecology, 363, 48–57.

Noble, R.S., Curran, A.H. & Wilson, M.A. 1995. Paleoenvironmental and paleoecological analyses of a Pleistocene mollusc-rich lagoon facies, San Salvador Island, Bahamas, in Curan, H. A., and White, B., Terrestrial and Shallow Marine Geology of the Bahamas and Bermuda: Boulder, Colorado, Geological Society of America Special Paper, 300.

Odum, H.T. & Odum, E.P. 1955. Trophic structure and productivity of windward coral reef community on Eniwetok Atoll. Ecological Monographs, 25, 291-320.

Osleger, D. & Read, J.F. 1991. Relation of eustasy to stacking patterns of meter-scale carbonate cycles, Late Cambrian, U.S.A. J. Sediment. Petroleum, 61, 1225-1252.

Pajaud, D. 1974. Ecologie des Thdciddes????. Lethaia, 7, 203-218.

Paola, C. 2000. Quantitative models of sedimentary basin filling. Sedimentology 47, 121–178.

Paterson, R.J., Whitaker, F.F., Jones, G.D., Smart, P.L., Waltham, D. & Felce, G. 2006. Accommodation and sedimentary architecture of isolated icehouse carbonate platforms: Insights from forward modelling with CARB3D+. Journal of Sedimentary Research, 76, 1162–1182.

Payri, C.E. 1997. *Hydrolithon reinboldii* rhodolith distribution, growth and carbon production of a French Polynesian reef. Proceedings 8th International Coral Reef Symposium, Panama, 1, 755–760.

Payri, C.E. 2000. Production primaire et calcification des algues benthiques en milieu corallien. Océanis, 26, 427-463.

Pedley, H.M. 1974. Miocene sea floor subsidence and later sub aerial solution subsidence structures in the Maltese islands. Proceedings of the Geologists' Association, 11(5), 533-547.

Pedley, H.M. 1975. The Oligo-Miocene sediments of the Maltese Islands. PhD thesis, University of Hull.

Pedley, H.M. 1976. A palaeoecological study of the Upper Coral line Limestone Terebratula-Aphelesia Bed (Miocene, Malta) based on bryozoan growth forms and brachiopod distributions: Palaeogeography, Palaeoclimatology, Palaeoecology, 20, 209- 234.

Pedley, H. M. 1978. A new lithostratigraphical and palaeoenvironmental interpretation for the coralline limestone formations (Miocene) of the Maltese Islands: Institute of Geological Sciences, Overseas Geology and Mineral Resources, 54, 17.

Pedley, H.M., 1979. Miocene bioherms and associated structures in the Upper Coralline Limestone of the Maltese Islands; their lithification and palaeoenvironment: Sedimentology, 26, 577-591.

Pedley, H.M., 1987. Controls on Cenozoic carbonate deposition in the Maltese Islands: review and reinterpretation: Memofie della Societa Geologica Italiana, 38, 81-94.

Pedley, H.M. 1996. Miocene reef distributions and their associations in the central Mediterranean region: an overview. In: Models for Carbonate Stratigraphy from Miocene Reef Complexes of Mediterranean Regions (Eds Franseen, E.K., Esteban, M., Ward, W.C. & Rouchy, J.M.), SEPM Concepts Sedimentology Paleontology, 5, 3–47.

Pedley, H.M. 1998. A review of sediment distributions and processes in Oligo-Miocene ramps of southern Italy and Malta (Mediterranean divide), in Wright, V.P. & Burchette, T.P., eds., Carbonate Ramps: The Geological Society of London, Special Publication, 149, 163–179.

Pedley, H. M. & Bennett, S. M. 1985. Phosphorites, hardgrounds and syndepositional solution subsidence structures: a palaeoenvironmental model from the Miocene of the Maltese Islands Sediment. Geology, 45, 1-34.

Pedley, M.H., House, M.R., Wilson, A.A., Debono, G. & Xerri, S. 1993. Geological maps of the Maltese Islands: Valetta, Malta, Oil Exploration Directorate, Office of the Prime Minister, scale 1:25,000, 1 sheet.

Pedley, M.H., & Grasso, M. 1992. Miocene syntectonic sedimentation along the western margins of the Hyblean-Malta Platform: a guide to plate margin processes in the Central Mediterranean. Journal of geodynamics, 15, 19-37.

Peres, J.M. 1967. The Mediterranean benthos. In: BARNES, H. (ed.). Oceanography and marine biology; Annual review, 5, 449-533.

Peres, J.M. & Picard, J. 1964. Nouveau manuel de bionomie benthique de la Mer Méditerranée. Rec. Trav. Stn. Mar. Endoume, Marseille. Fascicule Hors Série Supplément 31(47), 5–138.

Perrin, C. 2002. Tertiary: the emergence of modern reef ecosystems, SEPM. Special Publication, 72, 587–624.

Perry, C.T. & Beavington-Penney, S.J. 2005. Epiphytic calcium carbonate production and facies development within sub-tropical seagrass beds, Inhaca Island, Mozambique. Sedimentary Geology, 174, 161-176.

Pestrea-Saint Martin, S., Conesa, G. & Saint Martin, J.P. 2003. Signification paleoecologique des assemblages de diatomees du Messinien de Melilla–Nador (Maroc). Rev Micropalontol, 46, 161–190.

Pestrea, S. & Saint Martin, J.P. 2002. La microflore de diatomees du Messinien de Gibellina (Sicile occidentale, Italie). Geodiversitas, 23, 585–610.

Pestrea, S., Mansour, B. & Saint Martin, J.P. 1999. Les diatomites du Messinien d'Afrique du Nord (Maroc, Algerie): principaux enseignements. Cryptogamie-Algologie, 20, 109–110.

Philippe, M. & Lary, C. 1990. Premières découvertes du genre *Trachypatagus Pomel* (*Echinoidea, Spatangoida*) dans les terrains miocènes du Bassin du Rhône, in: De Ridder, C. et al. (Ed.) Echinoderm Research. Proceedings of the Second European Conference on Echinoderms, Brussels, Belgium, 18-2, 33-40.

Pichon, M. 1985. Organic production and calcification in some coral reefs of Polynesia. Proceedings of the 5th International Coral Reef Symposium, 6, 173-177.

Playton, T.E., Janson, X. & Kerans, C. 2012. Carbonate slopes. In: Facies Model, Response to Sea Level Change, Walker, RG and James, N. (Eds.), Geological Association of Canada Press, 447-474.

Pomar, L. 1991. Reef geometries, erosion surfaces and high-frequency sea-level changes, upper Miocene Reef Complex, Mallorca, Spain. Sedimentology, 38, 243–269.

Pomar, L. 1993. High-resolution sequence stratigraphy in prograding carbonates: Application to Seismic Interpretation. In: Louks, B., Sarg, R.J. (Eds.), Carbonate Sequence Stratigraphy: Recent Advances and Applications: AAPG Memoir, 57, 389–407.

Pomar, L., 2001. Ecological control of sedimentary accommodation: evolution from a carbonate ramp to rimmed shelf, Upper Miocene, Balearic Islands: Palaeogeography, Palaeoclimatology, Palaeoecology 175, 249–272.

Pomar, L. & Ward, W.C. 1994. Response of a Miocene carbonate platform to high-frequency eustasy. Geology 22, 131–134.

Pomar, L. & Ward, W.C. 1995. Sea level change, carbonate production and platform architecture. In: Haq, B. (Ed.), Sequence stratigraphy and depositional response to eustatic, tectonic and climatic forcing. Kluwer Academic Press, 87–112.

Pomar, L. & Hallock, P. 2007. Changes in coral-reef structure through the Miocene in the Mediterranean: adaptative vs. environmental influence. Geology, 35, 899–902.

Pomar, L. & Hallock, P. 2008. Carbonate factories: a conundrum in sedimentary geology. Earth-Science Reviews, 87, 134–169.

Pomar, L. & Kendall, C.G.S.C. 2008. Architecture of carbonate platforms: A response to hydrodynamics and evolving ecology. In: Lukasik, J., Simo, A. (Eds.), Controls on Carbonate Platform and Reef Development: SEPM Special Publication, 89, 187–216.

Pomar, L., Ward, W.W. & Green, D.G. 1996. Upper Miocene reef complex of the Llucmajor Area, Mallorca, Spain. In: Franseen, E.K., Esteban, M., Ward, W.C., Rouchy, J.-M. (Eds.), Models for Carbonate Stratigraphy from Miocene Reef Complexes of Mediterranean Regions: SEPM Concepts in Sedimentology and Paleontology, Tulsa, 5, 227–237

Pomar, L., Brandano, M. & Westphal, H. 2004. Environmental factors influencing skeletal grain sediment associations: a critical review of Miocene examples from the western Mediterranean. Sedimentology, 51, 627-651.

Pomar, L., Bassant, P., Brandano, M., Ruchonnet, C. & Janson, X. 2012. Impact of carbonate producing biota on platform architecture: Insights from Miocene examples of the Mediterranean region. Earth-Science Reviews, 113(3–4), 186-211.

Pontin, P., Floch, J.Y., Augris, C. & Cabioch, J. 1990. Annual growth rate of the calcareous red alga Lithothamnion corallioides (Corallinales, Rhodophyta) in the Bay of Brest, France. Hydrobiologia 204, 263-267.

Popp, B.N. & Wilkinson, B.H. 1983. Holocene lacustrine ooids from Pyramid Lake, Nevada. In: Coated Grains (Ed. by T.M. Peryt), 142-153.

Potin, P., Floch, J.Y., Augris, C. & Cabioch, J., 1990. Annual growth rate of the calcareous red algae Lithothamnion corallioides (Corallinales, Rhodophyta) in the Bay of Brest, France. Hydrobiologia, 204, 263–267.

Poulain, P.M., Zambianchi, E. (2007) Surface circulation in the central Mediterranean Sea as deduced from Lagrangian drifters in the 1990s. Continental Shelf Research, 27, 981-1001.

Pound, M.J., Haywood, A.M., Salzmann, U., Riding, J.B., Lunt, D.J. & Hunter, S.J. 2011. A Tortonian (Late Miocene, 11.61–7.25 Ma) global vegetation reconstruction. Palaeogeography Palaeoclimatology Palaeoecology, 300, 29–45.

Pound, M.J., Haywood, A.M., Salzmann, U. & Riding, J.B., 2012. Global vegetation dynamics and latitudinal temperature gradients during the Mid to Late Miocene (15.97–5.33 Ma). Earth-Science Reviews, 112, 1–22.

Pratt, S. K. 1990. Hardground genesis in pelagic carbonates from the Miocene of Malta and Cretaceous of southern England. PhD thesis, University of London.

Prince, G. & Burgess, P. 2013. Numerical modeling of fallingstage topset aggradation: implications for distinguishing between forced and unforced regressions in the geological record. Journal of Sedimentary Research, 83, 767–781.

Purser, B.H. & Plaziat, J.C. 1998. Miocene periplatform slope sedimentation in the northwestern Red Sea rift, Egypt. In: Purser BH, Bosence DWJ, editors. Sedimentation and tectonics of rift basins: Red Sea–Gulf of Aden. London (UK)7 Chapman Hall-Kluwers, 320– 46.

Purser, B.H., Barrier, P., Montenat, C., Orszag-Sperber, F., Ott d'Estevou, J.C., Plaziat, J.C., et al. 1998. Carbonate and siliciclastic sedimentation in an active tectonic setting: Miocene of the Northwest Red Sea rift Egypt. In: Purser, B.H., Bosence, D.W.J., editors. Sedimentation and tectonics of rift basins: Red Sea–Gulf of Aden. London (UK)7 Chapman Hall-Kluwers, 239–270.

Raffi, I., Backman, J., Fornaciari, E., Palike, H., Rio, D., Lourens, L. & Hilgen, F. 2006. A review of calcareous nannofossil astrobiochronology encompassing the past 25 million years. Quaternary Science Reviews 25, 3113–3137.

Read, J.F. 1982. Carbonate platforms of passive (extensional) continental margins types, characteristics and evolution: Tectonophysics, 81, 195–212.

Read, J.F. 1985. Carbonate platform facies models: American Association of Petroleum Geologists, Bulletin, 69, 1-21.

Read, J.F. 1998, Phanerozoic carbonate ramps from greenhouse, transitional and icehouse worlds: clues from field and modelling studies, in Wright, V.P., and Burchette, T.P., eds., Carbonate Ramps: The Geological Society of London, Special Publication 149, 107–135.

Reid, R.P. & MacIntyre, I.G. 1988. Foraminiferal–algal nodules from the eastern Caribbean: growth history and implications on the value of nodules as paleoenvironmental indicators. Palaios, 3, 424–435.

Reiss, Z. & Hottinger, L. 1984. The Gulf of Aqaba In: Ecological Micropaleontology, Ecological Studies, Analysis and Synthesis, 50 (Eds O.L.L.W.D. Billings and H.

Remmert), Springer, Berlin, 354.

Reuther, C.D. & Eisbacher, G.H. 1985. Pantelleria rift; crustal extension in a convergent intraplate setting: Geologische Rundschau, 74, 585–597.

Richard, G. 1981. A first evaluation of the findings on the growth and production of lagoon and reef molluscs in French Polynesia. Proc 4th International Coral Reef Symposium 2, 637-641.

Richard, G. 1982. Mollusques lagunaires et recifaux de Polynesie francaise. Inventaire faunistique, bionomie, bilan quantitatif, croissance, production. These, Universite Pierre et Marie Curie, Paris VI. 312.

Richard, G. 1985. Richness of the great sessile bivalves in Takapoto lagoon. In: Salvat, B., Richard, G. (Eds.), Atoll de Takapoto, Archipel des Tuamotu. Field Trip, 5eme Congres Int. Recifs coralliens, Tahiti, Polynesie Francaise, 1, 368–371.

Ries, J.B. 2010. Review: geological and experimental evidence for secular variation in seawater Mg/Ca (calcite-aragonite seas) and its effects on marine biological calcification. Biogeosciences, 7, 2795–2849.

Roman, F. & Roger, J. 1939. Observations sur la faune de pectinides de Malte. [Observations on the pectinid fauna of Malta.] *Bulletin de la Societe Geologique, France,* 5' Serie, 9, 59-79.

Russell, N.A.C. 1955. Report on the Geological Survey of the Maltese islands. D'Arcy Exploration Co. Ltd. 36p. plus Appendices. (Unpublished).

Sadd, J.L. 1984. Sediment transport and CaCO3 budget on a fringing reef, Cane Bay, St Croix, U.S. Virgin Islands. Bulletin of Marine Science, 35, 221-238.

Saint-Martin, J.P. 1990. Les formations récifales coralliennes du Miocène supérieur d'Algérie et du Maroc. Paris, Mémoires du Muséum National d'Histoire Naturelle, C, Sciences de la Terre, 56, 366.

Saint-Martin, J. P. 2001. Implications de la présence de mud-mounds microbiens au Messinien (Sicile, Italie). Comptes Rendus de l'Académie des Sciences de Paris, Série, 332, 527–534.

Saint Martin, J.P. & Rouchy, J.M. 1990. Les plateformes carbonatées messiniènnes de la Méditerranée occidentale: leur importance pour la reconstitution des variations de niveau marin au Miocène terminal. Bulletin de la Societe Géologique, France, 8(6), 83–94.

Saint Martin, J.P. & André, J.P. 1992. Les constructions coralliennes de la plateforme messinienne de Malte (Méditerranée centrale). Géologie Méditerranéenne 19(3), 145–163.

Saint-Martin, J.P. & Cornée, J. J. 1996. The Messinian reef complex of Melilla, northeastern Rif, Morocco. In: Franseen, E.K., Esteban, M., Ward, W.C., Rouchy, J.-M. (Eds.), Models for Carbonate Stratigraphy from Miocene Reef Complexes of Mediterranean Regions: SEPM Concepts in Sedimentology and Paleontology, Tulsa, 5, 227–237.

Saint-Martin, J.P., Cornée, J.J. & Muller, J. 1995. Nouvelles données sur le système de plate-forme carbonatée du Messinien des environs d'Oran (Algérie). Conséquences. Comptes Rendus de l'Académie des Sciences de Paris, Série IIA, 320, 837–843.

Saint-Martin, J.P., Néraudeau, D., Lauriat-Rage, A., Secrétan, S., Goubert, E., Babinot, J.F., Boukli-Hacene, S., Pouyet, S., Lacour, D., Pestrea, S. & Conesa, G. 2000. La faune interstratifiée dans les gypses messiniens de Los Yesos (Bassin de Sorbas, SE Espagne): Implications paléoenvironnementales, Géobios, 33, 637–649.

Sakai, K. & Nishihira, M. 1981. Population study of the benthic foraminifer *Baculogypsina sphaerulata* on the Okinawan Reef flat and preliminary estimation of its annual production. Proc 4th International Coral Reef Symp 2, 763-766.

Sandberg, P. A.: New interpretations of Great Salt Lake ooids and of ancient nonskeletal carbonate mineralogy, Sedimentology, 22, 497–538, 1975.

Savini, A., Basso, D., Bracchi, V.A., Corselli, C. & Pennetta, M. 2012. Maerl-bed mapping and carbonate quantification on submerged terraces offshore the Cilento peninsula (Tyrrhenian Sea, Italy), in BASSO D. & GRANIER B. (eds), Calcareous algae and global change: from identification to quantification. Geodiversitas, 34(1), 77-98.

Scaturo, D.M., Strobel, J.S., Kendall, C.G.St.C., Wendte, J.C., Biswas, G., Bezedek, J. & Cannon, R. 1989. Judy Creek. A case study of two dimensional sediment deposition simulation. In: Crevello, P.D., Wilson, J.J., Sarg, J.F., Read, J.F. (Eds.), Controls on Carbonate Platform Development: SEPM Special Publication, 44, 64–76.

Schlager, W. 1981. The paradox of drowned reefs and carbonate platforms: Geological Society of America, Bulletin, 92, 197-211.

Schlager, W. 2005. Carbonate Sedimentology and Sequence Stratigraphy: SEPM, Concepts in Sedimentology and Paleontology, Series, 8, 200.

Scholle, P.A., Arthur, M.A. & Ekdale, A.A. 1983. Pelagic environment, in Scholle, P.A., Bebout, D.G., and Moore, C.H., (eds.), Carbonate Depositional Environments: American Association of Petroleum Geologists Memoir, 33, 620-691.

Schreiber, B.C. & El Tabakh, M. 2000. Deposition and early alteration of evaporites. Sedimentology, 47, 215-238.

Schuster, M., Duringer, P., Ghienne, J.F., Vignaud, P., Mackaye, H.T., Likius, A. & Brunet, M. 2006. The age of the Sahara desert. Science, 311, 821.

Scoffin, T.P., Stearn, C.W., Boucher, D., Frydl, P., Hawkins, C.M., Hunter, I.G. & MacGeachy, J.K. 1980. Calcium carbonate budget of a fringing reef on the west coast of Barbados. Bulletin of Marine Science, 30, 475-508.

Sebe, O.G., Crasquin, S. & Grădinaru, E. 2013. Early and middle Anisian (Triassic) deep-water ostracods (Crustacea) from North Dobrogea (Romania). *Revue de Paléobiologie, Genève,* **32**, 509-529.

Sepkoski, J.J. 2002. A Compendium of Fossil Marine Animal Genera. Paleontology Research Institution, Ithaca, New York, 500.

Shevenell, A.E., Kennett, J.P. & Lea, D. 2004. Middle Miocene southern ocean cooling and Antarctic cryosphere expansion. Science, 305, 1766–1770.

Shevenell, A.E., Kennett, J.P. & Lea, D.W. 2008. Middle Miocene ice sheet dynamics, deep-sea temperatures, and carbon cycling: A Southern Ocean perspective, Geochemistry, Geophysics and Geosystems, 9.

Shinn, E.A., Hudson, J.H., Halley, R.B., Lidz, B., Robbin, D.M. & Macintyre, I.G. 1982. Geology and sediment accumulation rates at Barrie Bow Cay, Belize. In: The Atlantic Barrier Reef Ecosystem at Barrie Bow Cay, Belize, 1 Structure and Communities (Ed. By K. Rutzler and I.G. Macintyre) Smithsonian Contrib. Marine Science, 12, 63-75. Smithsonian Inst. Press, Washington.

Shinn, E.A., Hudson, J.H., Robbin, D.M. & Lidz, B. 1981. Spurs and grooves revisited: Construction versus erosion Looe Key reef, Florida. Proc 4th International Coral Reef Symposium Manila, 1, 475–483.

Shinn, E.A., Lidz, B.H., Kindinger, J.L., Hudson, J.H. & Halley, R.B. 1989. Reefs of Florida and the Dry Tortugas. International Geological Congress, Field Guide T-176, Washington DC, 53.

Simone, L. 1981. Ooids: A review. Earth-Science Reviews, 16, 319-355.

Smith, S.V. 1981. The Houtman Abrolhos Islands: carbon metabolism of coral reefs at high latitudes. Limnology Oceanography, 26, 612-621.

Smith, S.V. 1983. Coral reef calcification. In: Barnes DJ (ed) Perspectives on Coral Reefs. Brian Clouster Publisher, ACT, Australia, 240-247.

Smith, S.V. & Kinsey D. W. 1976. Calcium carbonate production, coral reef growth, and sea level change. Science, 194, 937-939.

Smith, S.V. & Kinsey, D.W. 1978. Calcification and organic carbon metabolism as indicated by carbon dioxide. In: Coral Reefs: Research Methods 469-484, Stoddart, D.R., and Johannes, R.E., (eds.), UNESCO, Paris, 581.

Smith, S.V. & Nelson, C.S. 1994. Calcifcation rates of rapidly colonising bryozoans in Hauraki Gulf, northern New Zealand. N.Z. J. Marine Freshwater Research, 28, 227-234.

Spratt, T.J.U. 1843. On the Geology of the Maltese Islands. Process not correct geology Society London, 4, 225-232.

Stearn, C.W., Scoffin, T.P. & Martindale, W. 1977. Calcium carbonate budget of a fringing reef on the west coast of Barbados. Bulletin of Marine Science, 27, 479-510.

Steinke, S., Groeneveld, J., Johnstone, H., Rendle-Buhring, R., 2010. East Asian summer monsoon weakening after 7.5 Ma: evidence from combined planktonic foraminifera Mg/Ca and $\delta^{18}O$ (ODP Site 1146; northern South China Sea). Palaeogeography

Palaeoclimatology Palaeoecology, 289, 33–43.

Steneck, R.S. 1986. The ecology of coralline algal crusts: convergent patterns and adaptative strategies. Annual Review of Ecological Systems, 17, 273–303.

Stephenson, W.J. & Kirk, R.M. 1996. Measuring erosion rates using the micro-erosion meter – 20 years of data from shore platforms, Kaikoura Peninsula, South Islands, New Zealand. Marine Geology, 130, 209-218.

Steuber, T. & Veizer, J. 2002. Phanerozoic record of plate tectonic control of seawater chemistry and carbonate sedimentation. Geology; 30, 1123–1126.

Stoffers, P. & Kühn, R. 1974. Geochemische und petrographische Untersuchungen an Evaporit-Bohrkernen aus dem Roten Meer. *Kali und Steinsalz, Verlag Glückauf, Essen*, 8, 290-299.

Sweatman, H., Bass, D., Cheal, A., Coleman, G., Miller, I., Ninio, R., Osborne, K., Oxley, W., Ryan, D., Thomson, A. & Tomkins, P. 1998. Long-term monitoring of the Great Barrier Reef. Australian Institute Marine Science, Status Report, 1-303.

Testa, V. & Bosence, D.W.J. 1999. Physical and biological controls on the formation of carbonate and siliciclastic bedforms on the north-east Brazilian shelf. Sedimentology, 46, 279–301.

Tewfik, A. & Guzman, H.M. 2003. Shallow-water distribution and population characteristics of *Strombus gigas* and *S. costatus* (Gastropoda: Strombidae) in Bosca Del Toro, Panama. Jounral of Shellfish Research, 22(3), 7890894.

Thompson, J. 1927. Brachiopod Morphology and Genera Recent and Tertiary. Wellington, New Zealand. 338.

Thunell, R.C., Locke, S.M. & Williams, D.F. 1988. Glacio-eustatic sea-level controlon Red Sea salinity. Nature, 334, 601–604.

Tipple, B.J. & Pagani, M. 2010. A 35 Myr North American leaf-wax compound-specific carbon and hydrogen isotope record: implications for C-4 grasslands and hydrologic cycle dynamics. Earth Planetary Science Letters, 299, 250–262.

Trudgill, S., 1985, Limestone geomorphology: London, Longman, 196.

Tsuji, Y. 1993. Tide influenced high-energy environments and rhodolith-associated carbonate deposition on the outer shelf and slope off Miyako Islands, southern Ryukyu Island Arc, Japan. Marine Geology, 113, 255–271.

Tucker, M.E. & Wright, V.P., 1990. Carbonate Sedimentology. Blackwell Science Public. 462.

Tudhope, A.W. & Scoffin, T.P. 1988. The relative importance of benthic foraminiferas in the production of carbonate sediment on the Central Queensland Shelf. Proc 6th International Coral Reef Symposium, 2, 583-588.

Tzanova, A., Hebert, T.D. & Peterson, L. 2015. Cooling Mediterranean Sea surface temperatures during the Late Miocene provide a climate context for evolutionary transitions in Africa and Eurasia. Earth and Planetary Science Letters, 419, 71–80.

Vail, P.R., Audemard, F., Bowman, S.A., Eisner, P.N. & Perez-Cruz, C. 1991. The stratigraphic signatures of tectonics, eustasy and sedimentology – an overview, in Einsele, G., Ricken, W. & Seilacher, Al., eds., Cycles and Events in Straigraphy: Berlin Springer-Verlag, 617-656.

Vaughan, T.W. & Cole, W.S. 1941. Preliminary report on the Cretaceous and Tertiary larger foraminifera of Trinidad, British West Indies. *Special Paper Geology Society,* 30, 137.

Vecsei, A. 2001. Fore-reef carbonate production: development of a regional census-based method and first estimates. Palaeogeography Palaeoclimatology Palaeoecology, 175, 185-200.

Videtich, P.E. & Matthews, R.K. 1980. Origin of discontinuity surfaces in limestones: isotopic and petrographic data, Pleistocene of Barbados, West Indies. Journal of Sedimentary Petrology, 50, 971-980.

Wagner, P.D. & Matthews, R.K. 1982. Porosity preservation in the Upper Smackover (Jurassic) carbonate grainstone, Walker Creek Field, Arkansas: response of paleophreatic lenses to burial processes. 1. Sedimary Petrology, 52,3-18.

Walker, D.I. & Woelkerling, W.J. 1988. Quantitative study of sediment contribution by epiphytic coralline red algae in seagrass meadows in Shark Bay, western Australia. Marine Ecology Progress Series, 43, 71-77.

Wanless, H.R. & Tedesco, L.P. 1991. A re-evaluation of Mississippian mud mounds based on their internal stratigraphy. Geolgical Society of America Abstracts with Programs, 23(5), 226.

Warrlich, G.M.D. 2001. Computer modeling of carbonate platform evolution. Ph.D. Thesis. University of London, London, 240.

Warrlich, G.M.D., Wood, C., Waltham, D.A. & Bosence, D.W.J. 2002. Quantifying the sequence stratigraphy and drowning mechanisms of atolls using a new forward modeling program (CARBONATE 3-D). Basin Research 14(3), 379–400.

Warrlich, G.M.D., Bosence, D.W.J. & Waltham, D.A. 2005. 3D and 4D controls on carbonate depositional systems: sedimentological and sequence stratigraphic analysis of an attached carbonate platform and atoll (Miocene, Níjar Basin, SE Spain). Sedimentology, 52, 363–389.

Warrlich, G.M.D., Bosence, D., Dave Waltham, D., Charlie Wood, C., Boylan, A. & Badenas, B. 2008. 3D stratigraphic forward modelling for analysis and prediction of carbonate platform stratigraphies in exploration and production. Marine & Petroleum Geology,25, 35–58.

Watney, W.L., Rankey, E.C. & Harbaugh, J. 1999. Perspectives on stratigraphic simulation models: current approaches and future opportunities. In: Harbaugh, J.H., Watney, W.L., Rankey, E.C., Slingerland, R., Goldstein, R.H., Franseen, E.K. (Eds.), Numerical Experiments in Stratigraphy, 3-21, SEPM Special Publication 62.

Weber, J.N. & White, E.W. (1977) Caribbean reef corals *Montastrea annularis* and *Montastrea cavernosa* – long-term growth data as determined by skeletal X-radiography. AAPG Stud Geol, 4, 171–179.

Wefer, G. 1980. Carbonate production by algae *Halimeda, Penicillus* and *Padina*, Nature, 285, 323-324.

Wigglesworth, J.C. 1964. The Tertiary Stratigraphy and Echinoid Palaeontology of Gozo, Malta. Unpublished Ph.D. thesis, University of Durham.

Williams, H.D., Burgess, P.M., Wright, V.P., Della Porta, G. & Granjeon, D. 2011. Investigating carbonate platform types: multiple controls and a continuum of geometries. Journal of Sedimentary Research, 81, 18-37.

Wilson, J.L. 1975. Carbonate Facies in Geologic History: New York, Springer-Verlag, 470.

Wilson, M.E.J. & Vecsei, A. 2005. The apparent paradox of abundant foramol facies in low latitudes: their environmental significance and effect on platform development. Earth-Science Reviews, 69, 133–168.

Winnock, E. 1981. Structure du block pelagien, in: Sedimentary basins of structural margins (Ed. F. C. Wezel) CNR Italian Project of Oceanography, Tecnoprint, Bologna, 445-464

Winnock, E. & Bea, F., 1979. La mer pélagienne. Structure de la mer pélagienne. Géologie Méditerranéenne, 6(1), 35–49.

Wolfram, S., 2001. A New Kind of Science. Wolfram Media, 1197.

Wright, V.P. & Faulkner, T.J. 1990. Sediment dynamics of Early Carboniferous ramps: a proposal: Geological Journal, 25, 139-144.

Wright, V.P. & Burgess, P.M. 2005. The carbonate factory continuum, facies mosaics and microfacies: an appraisal of some of the key concepts underpinning carbonate sedimentology. Facies, 51(1-4), 19-25.

Yamano, H., Miyajima, T., and Koike, I. (2000) Importance of foraminifera for the formation and maintenance of a coral sand cay: Green Island, the Great Barrier Reef, Australia. Coral Reefs, 19, 51-58.

Zachos, J.C., Pagani, M., Sloan, L., Thomas, E. & Billups, K. 2001. Trends, rhythms, and aberrations in global climate change 65 Ma to present: Science, 292, 686–693.

Zammi-Maempel, G. 1977. An outline of Maltese geology. Progress Press.

Zhang, Z.S., Ramstein, G., Schuster, M., Li, C., Contoux, C. & Yan, Q. 2014. Aridification of the Sahara desert caused by Tethys Sea shrinkage during Late Miocene. Nature, 513, 401.